

DEVELOPMENT OF LIGHTWEIGHT MATERIAL COMPOSITES TO INSULATE CRYOGENIC TANKS FOR 30-DAY STORAGE IN OUTER SPACE

Final Report

June 1972

CR-123828



Prepared under Contract No. NAS8-26006
by Advance Propulsion Department
McDonnell Douglas Astronautics Company
Huntington Beach, California

for

NATIONAL AERONAUTICS AND SPACE ADMINISTRATION



(NASA-CR-123797) DEVELOPMENT OF
LIGHTWEIGHT MATERIAL COMPOSITES TO INSULATE
CRYOGENIC TANKS FOR 30-DAY STORAGE IN OUTER
SPACE D. R. Krause (McDonnell-Douglas Co.)
Jun. 1972 515 p

CSCL 11D G3/18
Unclas
15947

N72-30495

PREFACE

This is the final report on a program entitled, "Development of Lightweight Material Composites to Insulate Cryogenic Tanks for 30-Day Storage in Outer Space." This work was performed at McDonnell Douglas Astronautics Company under the direction of the National Aeronautics and Space Administration, George C. Marshall Space Flight Center, Alabama, Contract NAS 8-26006. Dr. J. M. Stuckey served as the principal contracting officer representative. Mr. G. O. Fredrickson served as Program Manager. Significant contributions to this study were made by the following personnel:

M. C. Coes	Material survey, material testing, test sample preparation, specifications
A. J. Dervy	System configuration design
Dr. C. R. Easton	Evacuation and repressurization analyses
J. J. Hutmacher	System configuration design, hardware definition
L. E. Lannon	Heat flux gage calorimeter, system selection
Dr. R. A. Madsen	Thermal analyses
J. M. Salontai	Thermal analyses, heat flux gage calorimeter
S. Saneto	System configuration design, MLI design concepts
G. J. Tiezzi	Structural analyses, material testing, tooling, structural testing
C. S. Wilkinson	Outgassing tests, heat flux gage calorimeter tests
Dr. J. A. Zelik	Inspection techniques

Flat-plate calorimeter and thermal expansion testing was accomplished at MAC, St. Louis, under the direction of V. L. Holmes and L. McCrary. Mr. L. A. Holmes served as a consultant and contributed in the areas of purge analyses, heat flux gage calorimeter test planning, and thermal analyses.

PRECEDING PAGE BLANK NOT FILMED

CONTENTS

Section 1	INTRODUCTION	1
Section 2	SUMMARY	3
	2.1 Material Selection	3
	2.2 System Selection	6
	2.3 Thermal Degradation Testing	8
	2.4 Inspection Technique Evaluation	8
Section 3	COMPOSITE MATERIAL SURVEY AND TESTING—TASK 1	9
	3.1 Material Survey	9
	3.2 Separator Thermal Performance Screening Tests	22
	3.3 Thermal-Cycle Tests	32
	3.4 Effect of Separator Volatiles	58
	3.5 Moisture Degradation Tests	59
	3.6 Outgassing Tests	65
	3.7 Thermal Expansion and Contraction Tests	74
	3.8 Acoustic Environment Tests	84
	3.9 Compression Cycling Effects On Layer Density	92
	3.10 Flat-Plate Calorimeter Tests	114
Section 4	DEFINITION OF ENVIRONMENT, TOOLING, AND DESIGN VERIFICATION TESTS—TASK 2	133
	4.1 Environment	133
	4.2 Tooling and Fixture Requirements	143
	4.3 Composite Survivability Verification Testing	151
Section 5	MLI DESIGN CONCEPTS AND HARDWARE DEFINITION—TASK 3	157
	5.1 Insulation System Concepts	157
	5.2 Tanks and Associated Hardware	162
Section 6	THERMAL ANALYSES—TASK 4	171
	6.1 LH ₂ Tank Thermal Analyses	171
	6.2 LO ₂ Tank Thermal Analyses	201
	6.3 Parametric Study of Effect of MLI Thermal Performance Degradation	222

	6.4	Heat Shorts Due to Tank Penetrations	224
	6.5	Purge, Evacuation, and Repressurization Requirements	230
	6.6	Conclusions and Recommendations	270
Section 7		STRUCTURAL ANALYSES—TASK 5	273
	7.1	MLI Strength Analyses	273
	7.2	Compressive Load on MLI	283
	7.3	Purge-Bag Strength Analyses	284
	7.4	Thermal Contraction Compatibility Analyses	285
Section 8		FASTENER STRUCTURAL TESTS AND THERMAL DEGRADATION TESTS—TASK 6	297
	8.1	Fastener Tests	297
	8.2	Thermal Degradation Test	301
Section 9		SELECTION OF MLI SYSTEM AND MATERIALS—TASK 7	323
	9.1	System Selection	323
	9.2	Reflector Material	324
	9.3	Separator Material	325
	9.4	Face-Sheet System	327
	9.5	Fastener Material	328
	9.6	Purge Bag Material	329
Section 10		INSULATION SYSTEM CONFIGURATION TASK 8	331
	10.1	MLI Composite Assembly Configuration	331
	10.2	Purge Bag	344
	10.3	System Component Weight Summary	346
	10.4	Conclusions and Recommendations	351
Section 11		INSPECTION AND REFURBISHMENT PROCEDURES—TASK 9	353
	11.1	Inspection Technique Evaluation	353
	11.2	Repair of Damaged Areas	381
Section 12		SPECIFICATIONS—TASK 10	383
		Procurement Requirements for Film, Polyimide, Gold Metalized	385
		Procurement Requirements for Net, Polyester, Resinless Finish	391

	Process Requirements for Fabrication of Multilayer Insulation Panels	397
	Application Requirements for Installation of Multilayer Insulation Panels	401
Section 13	REFERENCES	403

PRECEDING PAGE BLANK NOT FILMED

FIGURES

3-1	Separator Fabrics Screening Test	25
3-2	Beta Glass Net Separators Screening Test	27
3-3	Nomex Net Separators Screening Tests	29
3-4	Thermal Cycle—Cyclical Temperature Tests	33
3-5	Thermal Cycling Test Setup	36
3-6	Thermal Cycling Test Apparatus	37
3-7	Double-Aluminized Kapton Reflector— Cyclical Temperature Specimen Cycled to 650°F	37
3-8	Double-Goldized Kapton Reflector—Cyclical Temperature Specimen Cycled to 650°F	38
3-9	Double-Aluminized Mylar Reflector— Cyclical Temperature Specimen Cycled to 650°F	38
3-10	Double-Goldized Mylar Reflector—Cyclical Temperature Specimen Cycled to 650°F	39
3-11	Double-Aluminized Mylar Reflector— Cyclical Temperature Specimen Cycled to 400°F	39
3-12	Double-Goldized Mylar Reflector—Cyclical Temperature Specimen Cycled to 400°F	40
3-13	Nomex HT-287 Separator—Cyclical Temperature Specimens	41
3-14	Nomex HT-96 Separator—Cyclical Temperature Specimens	41
3-15	Beta Glass 1653 Separator—Cyclical Temperature Specimens	42

3-16	Dacron B4A Separator—Cyclical Temperature Specimens	42
3-17	Astrel 360 Fastener Material—Cyclical Temperature Specimens	43
3-18	Silicone/Beta Glass Face Sheet—Cyclical Temperature Specimens	44
3-19	Polyimide/Beta Glass Face Sheet—Cyclical Temperature Specimens	44
3-20	Teflon/Beta Glass Face Sheet—Cyclical Temperature Specimens	45
3-21	Silicone/Nomex Face Sheet—Cyclical Temperature Specimens	45
3-22	Polyimide/Nomex Face Sheet—Cyclical Temperature Specimens	46
3-23	Viton/Beta Glass Face Sheet—Cyclical Temperature Specimens	46
3-24	Viton/Nomex Face Sheet—Cyclical Temperature Specimens	47
3-25	Teflon/Nomex Face Sheet—Cyclical Temperature Specimens	48
3-26	Tensile Test Specimen Dimensions	53
3-27	Test Setup for Ambient Temperature Tensile Tests	54
3-28	Test Setup for -320°F Tensile Tests	55
3-29	Outgassing Test Setup Inside Vacuum Chamber	67
3-30	Outgassing Test Apparatus	67
3-31	Outgassing of Nomex HT-287	69
3-32	Outgassing of Nomex HT-96	70
3-33	Outgassing of Dacron B4A	71
3-34	Outgassing of Double-Goldized Kapton	72
3-35	Sample Area and Flexible Film Holder for Reflector and Separator Specimens	76

3-36	Specimen Holder for Nonflexible Strip Specimens (Face Sheets)	77
3-37	Thermal Expansion Test Apparatus	78
3-38	Thermal Expansion Test Setup	79
3-39	Thermal Expansion and Contraction of Reflector Materials	81
3-40	Thermal Expansion and Contraction of Nomex Face-Sheet Systems, DGK, and Dacron B4A	82
3-41	Thermal Expansion and Contraction of Beta Glass Face-Sheet Systems, DGK, and Dacron B4A	83
3-42	Test Specimens Mounted on Acoustic Test Fixture	85
3-43	Narrow-Band Frequency Spectrum for 140-db Overall Sound Pressure Level Test	87
3-44	Narrow-Band Frequency Spectrum for 150-db Overall Sound Pressure Level Test	88
3-45	Narrow-Band Frequency Spectrum for 160-db Overall Sound Pressure Level Test	89
3-46	Side and Bottom Retaining Frames Removed After 160-db (Overall) Test	90
3-47	Tearing and Separator Unraveling of DGK/Nomex HT-96 After 160-db (Overall) Test	90
3-48	Tearing and Separator Unraveling of DGK/Nomex HT-287 After 160-db (Overall) Test	91
3-49	Compressive Load Test Setup	95
3-50	Test Fixture Used in Compressive Load Tests	95
3-51	Typical Data Trace for One Compressive Load Cycle	97
3-52	Effect of Compressive Load Cycles on Layer Density of DAK/Dacron B4A	98
3-53	Effect of Compressive Load Cycles on Layer Density of DAK/Nomex HT-287	99

3-54	Effect of Compressive Load Cycles on Layer Density of DAK/Nomex HT-96	100
3-55	Effect of Compressive Load Cycles on Layer Density of DGM/Dacron B4A	101
3-56	Effect of Compressive Load Cycles on Layer Density of DGM/Nomex HT-287	102
3-57	Effect of Compressive Load Cycles on Layer Density of DGM/Nomex HT-96	104
3-58	Effect of Number of Compressive Load Cycles on Layer Density of DAK Composites at 1×10^{-4} psi Loading	105
3-59	Effect of Number of Compressive Load Cycles on Layer Density of DGM Composites at 1×10^{-4} psi Loading	106
3-60	Effect of High Compressive Load Cycles on Layer Density of DAK/Dacron B4A	108
3-61	Effect of High Compressive Load Cycles on Layer Density of DAK/Nomex HT-287	109
3-62	Effect of Compressive Loading on Layer Density of 10 and 20 Layer-Pairs of DAK/Dacron B4A—First Loading Cycle	111
3-63	Effect of Compressive Loading on Layer Density of 10 and 20 Layer-Pairs of DAK/Nomex HT-287—First Loading Cycle	112
3-64	Effect of Compressive Loading on Layer Density of 10 and 20 Layer-Pairs of DAK/Nomex HT-96—First Loading Cycle	113
3-65	DAK/Nomex HT-287 Flat-Plate Calorimeter Specimen	115
3-66	Cross-Sectional View of Flat-Plate Calorimeter	117
3-67	Flat-Plate Calorimeter Test Setup	118
3-68	Calorimeter Gas-Pressure Control System	120
3-69	Effective Thermal Conductivity—Flat-Plate Calorimeter Data	124

3-70	k ρ -Flat-Plate Calorimeter Data	129
3-71	Effect of Interstitial Gas Pressure on Effective Thermal Conductivity of DGK/Dacron B4A	132
4-1	Temperature Histories During Reentry- Vicinity of LH ₂ Tank	134
4-2	Temperature Histories During Reentry- Vicinity of LO ₂ Tank	135
4-3	Temperature Histories During Ascent- Vicinity of LH ₂ Tank	136
4-4	Temperature Histories During Ascent- Vicinity of LO ₂ Tank	137
4-5	Pressure Histories During Ascent	140
4-6	Pressure History During Reentry for both LH ₂ and LO ₂ Secondary Tanks	141
4-7	Acceleration Loading History During Ascent	142
4-8	Acceleration Loading History During Reentry	142
4-9	Acoustic Sound Pressure Level-Vicinity of LH ₂ Tank	144
4-10	Acoustic Sound Pressure Level-Vicinity of LO ₂ Tank	145
4-11	Typical Layup Tool for Compound Curvature Panel	148
4-12	Typical Layup Tool for Single Curvature Panel	149
4-13	Assembled Panel on a Layup Tool	149
4-14	Loading of MLI Panel Joint-Test Setup	152
5-1	Shroud Configurations	160
5-2	Single Curvature Shroud Configuration	161
5-3	Secondary LH ₂ Tank and Supports	164
5-4	Tank Equatorial Reinforcing Frames	165
5-5	Manhole Cover Attachment	166

5-6	Typical Tank Support Strut	167
5-7	Secondary LO ₂ Tank and Supports	170
6-1	Thermal Model—Ground Hold	172
6-2	LH ₂ Tank Purge Bag Surface Temperatures— Helium Purge	174
6-3	LH ₂ Tank Purge Bag Surface Temperatures— Nitrogen Purge	174
6-4	LH ₂ Tank Wall Temperatures—Nitrogen Purge	175
6-5	LH ₂ Tank Ground Hold Heat Transfer Rates	176
6-6	LH ₂ Tank Purge Bag Temperature—Ground Hold, No Foam	177
6-7	LH ₂ Tank Ground Hold Heat Transfer—Helium Purge	178
6-8	Effect of Ambient Gas Temperature on LH ₂ Tank Ground Hold Heating Rate	179
6-9	Prelaunch Boiloff (3-Minute Lockup)—Helium, No Foam	180
6-10	Prelaunch Boiloff (3-Minute Lockup)—Helium, Foam	180
6-11	Prelaunch Boiloff (3-Minute Lockup)— Nitrogen, Foam	181
6-12	Typical Ground Hold Temperature Distributions—LH ₂ Tank	182
6-13	Pressure History Assumed During Ascent— LH ₂ Tank	183
6-14	Purge Bag Temperature History During Ascent— LH ₂ Tank	185
6-15	Heat Flux History to LH ₂ —Ascent Phase	186
6-16	Heat Transfer to LH ₂ During Ascent—Helium, Foam	187
6-17	Heat Transfer to LH ₂ During Ascent—Helium, No Foam	187
6-18	Heat Transfer to LH ₂ During Ascent— Nitrogen, Foam	188

6-19	Total Heat Transfer During Evacuated Period-7-Day Mission, LH ₂ Tank	189
6-20	Total Heat Transfer During Evacuated Period-30-Day Mission, LH ₂ Tank	189
6-21	Pressure History During Reentry-LH ₂ and LO ₂ Tanks	192
6-22	Heat Flux History to LH ₂ -Reentry Phase	193
6-23	Purge Bag Temperature History-Reentry Phase	194
6-24	Heat Transfer to LH ₂ During Reentry- Helium, Foam	195
6-25	Heat Transfer to LH ₂ During Reentry- Helium, No Foam	195
6-26	Heat Transfer to LH ₂ During Reentry- Nitrogen Purge, Helium Repressurization, Foam	196
6-27	Effect of System Concept on System Weight- 7-Day Mission, LH ₂ Tank	199
6-28	Effect of System Concept on System Weight- 30-Day Mission, LH ₂ Tank	200
6-29	MLI Composite-7-Day Mission, LH ₂ Tank	202
6-30	MLI Composite-30-Day Mission, LH ₂ Tank	203
6-31	Comparison of DGK and DAM Composites- 7-Day Mission	204
6-32	Comparison of DGK and DAM Composites- 30-Day Mission	204
6-33	Effect of Layer Density on System Weight- 7-Day Mission	205
6-34	Effect of Layer Density on System Weight- 30-Day Mission	205
6-35	LO ₂ Tank Purge Bag Temperature-Ground Hold (Helium Purge)	207
6-36	LO ₂ Tank Purge Bag Temperature-Ground Hold (Nitrogen Purge)	208

6-37	LO ₂ Tank Ground Hold Heat Flux (Helium Purge)	209
6-38	LO ₂ Tank Ground Hold Heat Flux (Nitrogen Purge)	210
6-39	LO ₂ Tank Prelaunch Boiloff (3-Minute Lockup)—Nitrogen	211
6-40	LO ₂ Tank Prelaunch Boiloff (3-Minute Lockup)—Helium	211
6-41	Typical Ground Hold Temperature Distributions—LO ₂ Tank	213
6-42	Heat Transfer to LO ₂ During Ascent—Helium Purge Gas	214
6-43	Heat Transfer to LO ₂ During Ascent—Nitrogen Purge Gas	214
6-44	Heat Flux History to LO ₂ —Ascent Phase	215
6-45	Total Heat Transfer to LO ₂ During Evacuated Period—7-Day Mission	215
6-46	Total Heat Transfer to LO ₂ During Evacuated Period—30-Day Mission	216
6-47	Heat Flux History to LO ₂ —Reentry Phase	217
6-48	Heat Transfer to LO ₂ During Reentry—Nitrogen Repressurization	218
6-49	Heat Transfer to LO ₂ During Reentry—Helium Repressurization	218
6-50	Effect of Purge and Repressurization Gas on System Weight—7-Day Mission	220
6-51	Effect of Purge and Repressurization Gas on System Weight—30-Day Mission	221
6-52	Effect of 1-Percent Thermal Performance Degradation on LH ₂ Tank Boiloff	225
6-53	Effect of 5-Percent Thermal Performance Degradation on LH ₂ Tank Boiloff	226
6-54	Effect of 1-Percent Thermal Performance Degradation on LO ₂ Tank Boiloff	227

6-55	Effect of 5-Percent Thermal Performance Degradation on LO ₂ Tank Boiloff	228
6-56	Schematic of Conceptual Purge, Evacuation, and Repressurization System Design	231
6-57	Effect of Purge Volume and Concentration of Condensibles on Purge Gas Flow Requirements	239
6-58	Friction Loss in Purge Gas Exit Tube	240
6-59	Helium Mass Flow Rates Required During Chiltdown-LH ₂ Tank	242
6-60	Helium Mass Flow Rates Required During Chiltdown-LO ₂ Tank	243
6-61	Ascent Pressure History in MLI Panel-No Outgassing	248
6-62	History of Pressure Drop Across MLI Panel-No Outgassing	250
6-63	Pressure Profiles in MLI During Evacuation-No Outgassing	251
6-64	Distribution of Outgassing Rate Through the MLI	253
6-65	History of Assumed Total Outgassing Rate	254
6-66	Effect of Vents on Purge Bag Pressure History	256
6-67	Effect of Evacuation Valves on Boiloff Weight Penalty	257
6-68	Valve Weights	259
6-69	Total Weight Penalty with Pneumatically Actuated Evacuation Valves	260
6-70	Total Weight Penalty with Torque Motor Actuated Valve	261
6-71	Effect of Purge Bag Pressure History on Reentry Heat Transfer	264
6-72	Pressure History in MLI Panel During Reentry	265
6-73	Pressure Differential Across MLI Panel During Reentry	266

6-74	Pressure Profiles in MLI During Repressurization	268
6-75	Repressurization Gas Flow Rates	269
7-1	Loading Model When Acceleration is Parallel to Tank Axis	276
7-2	Loading Model When Acceleration is Perpendicular to Tank Axis	281
8-1	Specimen Configuration for Loads in Tensile Direction—Fastener Tests	298
8-2	Specimen Configuration for Loads in Shear Direction—Fastener Tests	299
8-3	Heat Flux Gage Calorimeter—Top View	302
8-4	Heat Flux Gage Calorimeter—Bottom View	302
8-5	Heat Flux Gage Calorimeter with MLI End Caps—Top View	304
8-6	Heat Flux Gage Calorimeter with MLI End Caps—Bottom View	304
8-7	Installation of Inner MLI Test Panel	306
8-8	MLI Installed on Heat Flux Gage Calorimeter— Bottom View	306
8-9	MLI Installed on Heat Flux Gage Calorimeter— Top View	307
8-10	Test Setup, Heat Flux Gage Calorimeter	307
8-11	Evacuation and Repressurization System Schematic	308
8-12	MLI Thermocouple Locations	310
8-13	Data Acquisition System, Heat Flux Gage Calorimeter	311
8-14	Calorimeter Fill and Vent System Schematic	312
8-15	Evacuation Pressure History	313
8-16	Repressurization System	314

8-17	Typical Repressurization Pressure Histories	315
8-18	Heat Flux History—Cycles 1 and 50	316
8-19	Heat Flux History—Cycle 101	317
8-20	Heat Flux History During Evacuation	319
8-21	Heat Flux History During Repressurization	320
8-22	Typical Evacuated Steady State Temperature Profile Through MLI	320
8-23	Typical Temperature Profile at a Joint	321
10-1	Conceptual Insulation Installation for Secondary LH ₂ Tank—SK 710511	332
10-2	Panel Attachment to Tank and Manhole Cover—SK 710512	335
10-3	Insulation Design at Aft End of Tank—SK 710513	337
10-4	Insulated Strut Penetration—SK 710514	339
10-5	Typical MLI Gore Panel Assembly—LH ₂ Tank Configuration—SK 710515	341
10-6	Typical Reflector Sheet—SK 710516	343
10-7	Fastener and Lacing Button Detail—SK 710517	345
10-8	Conceptual Purge Bag Design for Secondary LH ₂ Tank—SK 710518	347
11-1	HPI Thickness Gage	356
11-2	Parallel Plate Capacitor Setup	358
11-3	Induction Coil Setup for Corrosion Tests	360
11-4	Induction Coil Setup for Compression Tests	366
11-5	Compression Detection with Induction Core Technique—CP Data	369
11-6	Compression Detection with Induction Coil Technique—RP Data	370
11-7	DAM/2A Elastic Behavior—CP Data	371

11-8	Effect of Test Frequency Induction Coil Technique—CP Data	373
11-9	Effects of Test Frequency Induction Coil Technique—RP Data	374
11-10	Repeatability of CP vs Load—DAM/B2A Without Frequency Reset	376
11-11	Repeatability of Cp vs Load—DAM/B2A With Frequency Reset	377

TABLES

2-1	MLI Materials Selected	4
3-1	Reflector Material Survey	11
3-2	Separator Material Survey—Nets	13
3-3	Separator Material Survey—Fabrics	15
3-4	Face-Sheet Polymers	18
3-5	Fastener Material Survey	20
3-6	Candidate Materials for MLI Composite	21
3-7	Electrical Resistance Test Data—Fabrics	26
3-8	Electrical Resistance Test Data—Beta Glass Nets	28
3-9	Electrical Resistance Test Data—Nomex Nets	30
3-10	Temperature Cycling Test Matrix	34
3-11	Weight Loss Due to Temperature Cycling	49
3-12	Effect of Cyclical Temperatures on Reflector Metal Adhesion	50
3-13	Test Matrix for Tensile Tests	52
3-14	Summary of Tensile Test Results	56
3-15	MLI Material Verified Cyclical Thermal Environments	58
3-16	Effects of Separator Volatiles on Reflector Emissivity	60
3-17	Moisture Degradation Test Data	63
3-18	Weight Loss Due to Outgassing	73
3-19	Thermal Expansion Test Specimens	75

3-20	Test Matrix for Acoustic Test	85
3-21	Compression Load Cycling Effect on Layer Density—Test Matrix	93
3-22	Effect of Number of Layer Pairs on Layer Density—Test Matrix	94
3-23	Effect of 100 Compressive Load Cycles on Layer Density	103
3-24	Layer Density at 1×10^{-4} PSI Compressive Load and in a One-g Field after 100 Compression Cycles to 0.15 PSI	107
3-25	DAK/Nomex HT-287 Flat-Plate Calorimeter Data	125
3-26	DGK/Nomex HT-287 Flat-Plate Calorimeter Data	125
3-27	DGK/Nomex HT-96 Flat-Plate Calorimeter Data	126
3-28	DGK/Dacron B4A Flat-Plate Calorimeter Data	127
3-29	Effect of Interstitial Gas Pressure on Effective Thermal Conductivity of DGK/Dacron B4A	131
5-1	LH ₂ Tank Plumbing	168
5-2	LO ₂ Tank Plumbing	169
6-1	Typical Helium/No-Foam System Weight (lb/ft ²)	197
6-2	Typical Helium/Foam System Weight (lb/ft ²)	198
6-3	Degradation of Effective Thermal Conductivity Using Method A	223
6-4	Degradation of Effective Thermal Conductivity Using Method B	224
6-5	Total Heating Rate Due to Tank Penetrations—LH ₂ Tank	229
6-6	Total Heating Rate Due to Tank Penetrations—LO ₂ Tank	229
6-7	Valve Event Sequence—Purge, Evacuation, and Repressurization System	233

6-8	Summary of Purge System Design Equations (Reference 16)	236
6-9	Ground-Hold Purge Design Parameters	237
6-10	Ground-Hold Purge Helium Usage	244
7-1	Maximum Vehicle g Loads	274
7-2	LH ₂ and LO ₂ Tank Dimensions	275
7-3	Maximum Stresses on MLI Load-Carrying Components	279
7-4	Purge Bag Materials	286
7-5	Operating Temperature Bands—LH ₂ Tank MLI	287
7-6	Physical Properties of Face-Sheet Systems	287
7-7	Operating Temperature Bands—LO ₂ Tank MLI	289
7-8	Face-Sheet Systems Selected for LH ₂ and LO ₂ Tank MLI Panels	289
7-9	LH ₂ and LO ₂ Tank Design Parameters	291
7-10	Changes in Tank Geometry Due to Filling, Pressurization, and Acceleration	294
7-11	Required Oversizing of Inner Face Sheets of Inner Blankets	295
8-1	Tensile Load Limit of Fasteners	299
8-2	Load Limit of Fasteners in Shear Direction	300
8-3	Thermocouples—Thermal Degradation Test	309
9-1	In-Space Boiloff vs Shroud Weight	324
9-2	MLI Composite Materials Selected	327
10-1	MLI System Component Weight Summary— LH ₂ Tank	348
10-2	MLI System Component Weight Summary— LO ₂ Tank	349
10-3	Purge and Repressurization System Hardware Weight Summary	350

11-1	Detection of 10-Percent Corrosion by the Induction Coil Technique	362
11-2	Detection of 2-Percent Corrosion by the Induction Coil Technique	364
11-3	Corrosion Detection by the Induction Coil Technique with Zero Loading of the Test Specimen	365
11-4	Compression Detection with the Induction Coil Technique	368
11-5	Compression Measurements on DAM/B2A MLI at Several Frequencies—Induction Coil Technique	372
11-6	Compression Detection in DGK/Dacron B4A with Induction Coil Techniques	370

Section 1

INTRODUCTION

The storage of cryogenics in space requires the utilization of highly efficient insulation systems to prevent excessive and costly loss of these cryogenics through boiloff. The insulation systems being considered for this application are called high performance multilayer insulation (MLI). These MLI systems consist primarily of numerous layers of reflective material which significantly decrease the heat transfer due to radiation. A separator material is placed between each reflector layer to minimize the heat transfer due to conduction.

Previous MLI studies have principally addressed materials and design concepts applicable to single launch vehicles. Consequently, the additional design constraints associated with a reusable integrated launch and recovery vehicle (ILRV) require further studies. The additional design constraints which must be considered include the reentry environment, the reusability requirement, and the effect of environmental cycling resulting from reuse.

The objective of this program was to define a conceptual design for an MLI system which will meet the design constraints of an ILRV used for 7- to 30-day missions. The program was divided into ten tasks which are briefly described as follows:

- Task 1: Material survey and procurement, material property tests, and selection of composites to be considered.
- Task 2: Definition of environmental parameters and tooling requirements, and thermal and structural design verification test definition.
- Task 3: Definition of tanks and associated hardware to be used, and definition of MLI concepts to be considered.
- Task 4: Thermal analyses, including purge, evacuation, and reentry repressurization analyses.

- Task 5: Structural analyses.
- Task 6: Thermal degradation tests of composite and structural tests of fastener.
- Task 7: Selection of MLI materials and system.
- Task 8: Definition of a conceptual MLI system design.
- Task 9: Evaluation of nondestructive inspection techniques and definition of procedures for repair of damaged areas.
- Task 10: Preparation of preliminary specifications.

Section 2

SUMMARY

Numerous candidate materials and system configurations were considered to accomplish the program objective of defining a conceptual design for an MLI system which will meet the design constraints of an ILRV used for 7- to 30-day missions. The effort to accomplish this program objective included numerous tests and analyses as well as defining conceptual designs. A survey of potential techniques for nondestructive inspection of MLI composites was also included.

2.1 MATERIAL SELECTION

The basic components of an MLI composite are the reflector sheets, the separator material which reduces the thermal conduction between the reflector sheets, the face sheets which provide structural support for the composite, and the fasteners which hold these components together to form an integral composite. The materials selected for each of these components for a maximum use temperature of 350°F are listed in Table 2-1.

A goldized material, Double Goldized Kapton (DGK), was selected as a reflector because of its resistance to moisture degradation. Kapton was chosen over Mylar because Kapton has the capability of withstanding much higher temperatures and the manufacturer experienced fabrication problems with the double goldized Mylar (DGM), particularly at a film thickness of 0.00025 inch or less.

Dacron net, style B4A, was selected as the separator material primarily because of its high thermal insulation performance and light weight. Also, test results indicated that the Dacron B4A net would provide the highest thermal performance, the lowest outgassing, and would meet the current cyclical temperature design criteria (maximum temperature of 350°F). The thermal analyses showed that the DGK/Dacron B4A composite offered the lowest system weight of the candidate composites using the DGK reflectors.

Table 2-1
MLI MATERIALS SELECTED

Component	Material
Reflector	- Double Goldized Kapton (25-30 gage)
Separator	- Dacron Net (Style B4A)
Face Sheets	
Outer surface of MLI composite	- Nomex Fabric (Style HT-287) and Polyimide Resin
Center of MLI composite	- Nomex Fabric (Style HT-287) and Silicone Resin
Inner surface of MLI composite	- Nomex Fabric (Style HT-287) and Silicone Resin
Fastener	- Polysulfone - Astrel 360

The use of Dacron B4A results in relatively higher layer densities but the increase in layer density resulting from 100 compressive load cycles was lowest (approximately 5 percent) for the DGK/Dacron B4A composite.

The face sheets consist of a basic material with reinforced areas fabricated onto this material by impregnating these areas with a resin. Assuming adequate strength properties, the primary criterion for selection of a face sheet is its thermal contraction and expansion characteristics and its weight. Of those systems which could be used on the inner (cold) surface of the MLI and in the center of the MLI composite, the Silicone/Nomex HT-287 system has the lightest weight and the closest match of thermal contraction characteristics to that of the DGK and Dacron B4A. Of those systems which could be used on the outer (warm) surface of the MLI, the Polyimide/Nomex HT-287 system appeared to be the best choice because of its light weight.

The Astrel 360 Polysulfone material was selected as the fastener material because it has both the required temperature capability and fabrication properties.

2.2 SYSTEM SELECTION

Four MLI system configurations and concepts were considered. These included tank-mounted MLI with or without foam on the interior surface of the tank wall and non-tank-mounted MLI with or without foam on the interior surface of the tank wall. Purging of the MLI and the associated purge bag and plumbing hardware was included in each of these systems. A system with the MLI mounted on the tank surface was selected. A light-weight shroud supporting the MLI off of the tank surface was considered and showed an improved performance but the reduction in boiloff did not appear to be adequate to offset the increased weight due to the shroud.

The MLI is prefabricated into panels which are then attached to the tank. Two panels, an inner and outer, are used to obtain the desired MLI thickness. The main panels are gore shaped to conform to the compound curvature of the tank and adjacent panels are butted together to completely cover the surface of the tank. Special panels are placed around the end domes of the tank, tank supports, and plumbing.

The thermal analyses showed that, for the LH₂ tank MLI, a total of approximately 68 layer pairs of DGK/Dacron B4A would be optimum for a 7-day mission and approximately 94 layer pairs would be optimum for a 30-day mission. For the LO₂ tank MLI, a total of approximately 83 layer pairs appears to be optimum for a 7-day mission and approximately 92 layer pairs for a 30-day mission.

Concepts considered for purging and repressurizing the LH₂ tank MLI included: (1) helium purge during ground hold and helium repressurization during reentry, with no foam; (2) helium purge and repressurization as in number 1, but with the minimum practical thickness (0.5 inch) of foam; and (3) nitrogen purge of MLI during ground hold, helium repressurization during reentry, and with sufficient foam to prevent liquefaction of the nitrogen purge gas during ground hold. Helium must be used for repressurization during reentry because the tank temperature during reentry will be well below the liquefaction temperature of nitrogen. The analyses clearly showed

that, for the trajectories considered, the helium-purge and helium-repressurization-with-no-foam system provides the lowest system weight for the LH₂ tank. It should be noted, however, that the use of foam in the system could prove to be desirable if the vehicle trajectories are altered to include a longer reentry period.

Concepts considered for purging and repressurizing the LO₂ tank were: (1) helium purge and repressurization, with no foam; and (2) nitrogen purge and repressurizing with no foam. The thermal analyses showed that the use of nitrogen as the purge and repressurization gas offered the lowest system weight. However, this did not include the potential reduction in weight and system complexity which would result from using common storage and control hardware for the repressurization gas for both the LH₂ and LO₂ tanks. Also, it did not include any cost savings which would result from using common ground support equipment for the purge gas for the two tanks. A final decision as to the optimum choice between using nitrogen or helium for the LO₂ tank MLI will depend on numerous factors beyond the scope of this study. The conceptual design for the repressurization system reported herein was formulated assuming that helium would be used to purge and repressurize the LO₂ tank MLI. A selection of nitrogen in future studies, however, would alter only the repressurization system design.

In the system concept selected, the purge and repressurization gases are introduced under the MLI at three locations near the strut attachment points on the tank equator. The purge gases, after having diffused through the MLI, exit the purge bag at the aft end of the tank. The repressurization gases which are stored on the vehicle are introduced into the MLI through the same inlet flow lines used for the purge gas. An estimated 8.22 and 3.35 pounds of helium will be required to purge the LH₂ and the LO₂ tanks, respectively. The estimated helium gas requirement for repressurization is 2.4 pounds for the LH₂ tank and 0.9 pound for the LO₂ tank. The evacuation of the MLI is facilitated by perforations in the reflector sheets and by four butterfly valves which open during ascent to vent the purge bag. Perforations in the reflector sheets, 0.046 inch in diameter and spaced to provide a 0.85-percent open surface area, were selected.

2.3 THERMAL DEGRADATION TESTING

The effect of numerous evacuation-repressurization cycles on the thermal performance of an MLI composite has been investigated on a MDAC IRAD program. One-hundred-and-one evacuation and repressurization cycles in a vacuum chamber were performed on a MDAC-developed and insulated heat-flux-gage calorimeter. The results showed that an improvement in thermal performance, not a degradation, may be expected with repeated pressure cycling. It is felt that this is primarily due to "fluffing" of the composite resulting from the gas flow through the MLI during evacuation and repressurization.

An evacuated steady-state effective thermal conductivity (k) of approximately 2×10^{-5} Btu/hr ft $^{\circ}$ R was obtained for the 70-layer-pair DAM/Dacron B4A composite. The cold- and hot-side temperatures in the tests were -320 $^{\circ}$ and 70 $^{\circ}$ F, respectively. This (k) value is in good agreement with data obtained in the flat-plate calorimeter tests at similar layer densities.

2.4 INSPECTION TECHNIQUE EVALUATION

Of the several techniques evaluated for nondestructive testing of MLI, an induction coil technique showed greatest promise. Tests indicated that detecting corrosion as low as 2 percent of the surface area is feasible and that accurate measurements of the composite layer density or thickness could be obtained.

PRECEDING PAGE BLANK NOT FILMED

Section 3

COMPOSITE MATERIAL SURVEY AND TESTING—TASK 1

The objective of Task 1 was to obtain data on candidate MLI composite materials to facilitate material selection for an ILRV cryogenic tank application. This objective was accomplished by: (1) conducting a material survey, (2) selecting candidate materials, and (3) performing property and performance tests on these materials. The tests included separator thermal-performance screening, thermal cycling, effects of separator volatiles, moisture degradation, outgassing, thermal expansion, acoustic environment, flat-plate calorimeter, and effects of compression cycling on layer density.

3.1 MATERIAL SURVEY

A survey of materials with potential for compatibility with ILRV environments was conducted, and candidate materials selected. This survey included materials for a purge bag as well as all of the components in an MLI composite (reflectors, separators, face sheets, fasteners, and lacing buttons). The selection of the candidate materials included consideration of material configurations and vendors as well as selection of generic types.

3.1.1 Reflectors

As specified by NASA, the choice of reflectors was limited to metallized Mylar and Kapton films or aluminum foil. Mylar would not be expected to survive the original design temperature of 600°F but was included as a candidate material for the cooler portion of a composite. An aluminum coating was selected for consideration because of its prior usage, relatively low cost, and availability. A gold coating was selected because alternative metallic coatings insensitive to moisture do not appear promising. Nichrome and titanium can be obtained, but only on a laboratory scale in small widths and at high cost. With these metals, coatings having adequate adhesion are

much thinner (40 to 60 Angstroms) than is usual for conventional reflectors. Gold coatings are much less sensitive to moisture than aluminum coatings, an important consideration for an ILRV application.

A double (both sides) coating on smooth films was considered the most attractive metallized configuration. Other types of metallized films—embossed, crinkled, or simply single-coated—were rejected because they have been shown to be unattractive in previous work (Reference 1). Single-coated materials curl under heat, and thin-gage embossed and crinkled materials are more sensitive to compressive loads than are smooth materials.

Aluminum foils are available in a range of thicknesses from 0.17 to 5.0 mils. The very thin gage foil can be obtained only with a matte finish and can be expected to have relatively high emittance. Foils with two polished sides are relatively thick (0.8 mil). Intermediate-thickness foils are polished on one side only. A 0.17-mil (17-gage) foil is the lightest available, but users have indicated severe handling difficulties. A 0.25-mil (25-gage) material was considered the better choice for a foil candidate, but is noncompetitive with Kapton because of its weight.

In view of the above discussion, reflector materials selected (with concurrence of MSFC) as initial candidates were double-goldized Kapton, double-goldized Mylar, and double-aluminized Kapton.

Information pertinent to procurement of double-goldized Kapton, double-goldized Mylar, and double-aluminized Kapton was obtained and is presented in Table 3-1. Items of interest include minimum-buy quantities, unit cost, lead time, available widths, form, and vendor certification. Vendor certification was considered mandatory. Material in roll form was preferred to material in individual sheets. Wider widths were also preferred. Lead time was the same for all suppliers and therefore was not considered in the selection. Norton can supply material in roll form but will not certify emittance properties in small quantities. Schjeldahl will certify but can supply materials only in sheet form and in

Table 3-1
REFLECTOR MATERIAL SURVEY

Material Description						Procurement Data		
Material	Supplier	Width (in.)	Form	Weight (ft ² /lb)	Certification	Minimum Buy	Unit Cost (\$)	Lead Time (wk)
Goldized Kapton 25-30 Gage	National Metallizing	48	Rolls	480-500	Will certify $\epsilon \leq 0.025$	500 ft ² 5,000 ft ²	4.75/ft ² 2.61/ft ²	4
	G. T. Schjeldahl	18	1.5 x 10 ft sheets	480-500	Will certify $\epsilon \leq 0.025$	30 ft ³ 300-600 ft ² 600-12,000 ft ² 4,800-9,600 ft ²	500 ft ² 19.20/ft ² 15.80/ft ² 12.80/ft ²	4
Goldized Mylar 25 Gage	National Metallizing	48	Rolls	550	Will certify $\epsilon \leq 0.025$	500 ft ² 5,000 ft ²	4.44/ft ² 2.06/ft ²	4
	G. T. Schjeldahl	36	3 x 10 ft sheets	550	Will certify $\epsilon \leq 0.025$	30 ft ² 300-600 ft ² 600-12,000 ft ² 4,800-9,600 ft ²	500 ft ² 14.35/ft ² 11.80/ft ² 9.90/ft ²	4
Aluminized Kapton 25-30 Gage	National Metallizing	48	Rolls	480-500	Will certify $\epsilon \leq 0.035$	2 lb 11 lb	1.50/ft ² 1.00/ft ²	4
	G. T. Schjeldahl	18	1.5 x 10 ft sheets	480-500	Will certify $\epsilon \leq 0.035$	30 ft ² 300-600 ft ² 600-1,200 ft ² 4,800-9,600 ft ²	500 ft ² 7.95/ft ² 6.55/ft ² 5.25/ft ²	4
	Norton Co.	48	Rolls	480-500	Best effort only	1 lb	430/lb	4

narrower widths, and at highest cost. National Metallizing (Cranbury, N.J.) was therefore selected as the preferred supplier for these materials.

3.1.2 Separators

Numerous materials were considered for the separators. These included Beta glass, E glass, Nomex, Durette, Tissuglas, Dexiglas, inorganic felts, polyimide foams, polyimide honeycomb, asbestos, Teflon, PBI, Kynol, and nylon. Of these, the Beta Glass, Nomex, and Durette materials were selected. Beta glass and E glass have high strength and relatively high temperature tolerance. Beta glass is preferred over conventional E glass because of the much lower potential for abrasion with the Beta material. Nomex and Durette materials also have relatively high service-temperature stability. Durette is a chemically processed material and could therefore be unacceptable in some environments. Tissuglas (good high-temperature stability) is a potentially useful material, but in the past has been considered less promising than a net. Its fragility makes it particularly undesirable for an ILRV application. Dexiglas is weaker than Tissuglas. Inorganic felts are expected to fail in successive vibration environments. Polyimide foams are still in the development stage, and contaminating chaff can be expected with every foam. High abrasion of adjacent reflectors is one potential disadvantage of a polyimide honeycomb separator. The low strength and high moisture absorption of asbestos materials make them unattractive for an ILRV application. Teflon, polybenzimidazole (PBI), and Kynol appear to have potential as separator materials but their properties are not as well known as those of the Beta glass and Nomex materials. Nylon has a lower temperature capability and has shown relatively high outgassing in previous tests. An additional factor in the selection was the unavailability of lightweight configurations of many of the materials.

A summary of both procurement and material property data for the selected generic types of net materials is presented in Table 3-2. Material property data, weight, thickness, mesh count, elongation, and tensile and tear

Table 3-2
SEPARATOR MATERIAL SURVEY⁽¹⁾ - NETS

Material Description								Mechanical Properties						Procurement Data		
Material	Supplier	Weave	Denier	Mesh Count (meshes/in. ²)	Weight (oz/yd ²)	Thickness (mil)	Width (in.)	Tensile (lb/in. width)		Elongation (%)		Tongue Tear (lb)		Minimum Buy	Unit Cost (\$/lin yd)	Lead Time (wk)
								Warp	Fill	Warp	Fill	Warp	Fill			
Nomex Net HT-96-62	Stern & Stern	Leno	200	120	0.91	12.5	62	38.0	36.7	22.0	20.0	Does not tear threads slip and unravel	None if in stock If not in stock 500 lin yds or \$300 setup + unit cost for 100-500 lin yds	2.30	4-6	
HT-289-42	Stern & Stern	Leno	200	252	1.30	6.8	42	116.0	45.8	25.5	27.0			2.45	1	
HT-62-46	Stern & Stern	Leno	200	451	1.84	9.8	46	109.2	106.4	23.4	35.4			2.80	4-6	
HT-58-43	Stern & Stern	Leno	200	360	2.02	9.9	43	112.0	118.5	32.0	29.7			3.25	1	
HT-65-30	Stern & Stern	Leno	200	750	2.17	9.0	30	145.5	105.0	31.8	27.0			2.55	1	
HT-51-37	Stern & Stern	Mock Leno	200	261	3.31	10.5	37	154.0	150.0	27.0	29.4	21.6	16.9	4.35	1	
HT-140-38	Stern & Stern	Mock Leno	200	222	3.87	13.0	38	182.5	193.3	31.8	30.7	23.3	23.5	4.85	1	
HT-106-45	Stern & Stern	Leno	200	49	4.60	21.4	45	190.0	215.0	25.8	25.0	Does not tear		8.00	4-6	
100 Mesh	Prodesco	Raschel Leno Tricot	200	100	2.0	~18-19 ~10	48							60 lin yds	18.75	2
200 Mesh	Prodesco		200	200	~4.0		48								18.75	2
300 Mesh	Prodesco		200	300	~5.0		48								18.75	2
β Glass Net 1653	J. P. Stevens	Leno	95	64	1.40 See Note 2	5.0 See Note 2	45	55 See Note 2	95 See Note 2					200 lin yds \$500 setup + unit cost	0.17	6-8
1659	J. P. Stevens	Leno	95	100	1.65 See Note 2	4.0 See Note 2	45	70 Note 2	60 Note 2						0.21	6-8
2530	J. P. Stevens	Leno	95	525	2.0 See Note 2	5.5 See Note 2	44	50 See Note 2	75 See Note 2						1.50	6-8
Woven to customer specifications	Prodesco	Any	100	Any 100 200 300	2.3 3.5-5 6-7	Function of weave (6-7 for Leno)	Any width (Additional setup charges)							\$450 setup + unit cost for 36-in. width \$300 setup + unit cost for 12-in. width	36-in. width 14.75 12-in. width 7.38	2
Teflon Coated (2-20%) β Glass woven to customer specifications Typical values are for 2% coating.	Prodesco	Any	100	Any 100 200 300	2.42 3.68-5.25 6.3-7.35	Function of weave (~14 Raschel ~10 Leno ~10 Tricot)									36-in. width 16.75 12-in. width 8.38	4
Teflon Net (FEP)	Prodesco	Any	100	Any 100 200 300	~2 ~4 ~5	Function of weave (~18-19 Raschel ~8-10 Leno ~8-10 Tricot)									36-in. width 8.00 12-in. width 4.00	3-4
PBI Net	Prodesco	Any	200	100 200 300	1.6-1.75 3.2-3.3 4.5	Function of weave (~17 Raschel ~10 Leno ~10 Tricot)									36-in. width 22.00 ⁽³⁾ 12-in. width ⁽³⁾ 11.00 ⁽³⁾	Function of government procurement + 3 wks
Kynol Net	Prodesco	Any	~200	100 200 300	1.92-2.1 3.84-3.96 5.4										36-in. width 12-18 12-in. width 6-9	4

NOTES: (1) All information is vendor data. Price quotes cannot be considered firm commitments by suppliers.
Lead Times are generally dependent upon current stock status.
(2) Values given are for E glass. β glass values should be slightly lower; ~5% for weight and thickness. Strength values should be correct within 10%.
(3) Costs cited for PBI are weaving costs only. Yarn costs are additional.

strengths, where available, are given in addition to type of weave and yarn denier. Procurement data include available widths, minimum-buy quantities, and unit costs.

Preferred configurations incorporate the best combination of low weight and maximum thickness for mesh counts in the range of 50 to 400 meshes per square inch. Strength properties of separator materials are not critical because these components do not carry any load. It was felt that a material which did not exhibit tearing would be preferred to a material that could incur rips.

On the basis of these criteria, three Nomex nets, supplied by Stern and Stern, were selected: styles HT-96, HT-289, and HT-58. Prodesco Nomex nets were unattractive because of potentially higher weights and substantially higher costs. In addition, purchase of initial candidates from a supplier who maintains a current stock of the generic material was preferable to procurement on a weave-to-order basis.

Two configurations of Beta glass nets were selected, again to the same criteria. These are styles 1653 and 1659, supplied by J. P. Stevens. Prodesco nets, although thicker, are also heavier and much more costly and were therefore rejected.

Available configurations of Beta glass, Nomex, and Durette fabrics are presented in Table 3-3. Selection of initial candidates was also based on low weight and maximum thickness with stock-type procurement at reasonable cost. Three fabrics were chosen: Stern and Stern Nomex, style HT-287; Chemstrand Durette, style 6632-27-2; and J. P. Stevens Beta glass, style 81677. The latter material, while slightly heavier than style 8116, is the preferred material. Style 81677 is an updated version of the earlier style 8166 and is slightly thicker and less costly.

Subsequent to the selection, procurement, and initial screening of the separator materials, the design temperature requirement was reduced from 600 to 350° F. This allowed the addition of Dacron as a candidate separator

Table 3-3 (Page 1 of 3)

SEPARATOR MATERIAL SURVEY--FABRICS

Material Description					Mechanical Properties						Procurement Data		
Material	Supplier	Weight (oz/yd ²)	Thickness (mil)	Width (in.)	Tensile (lb/in. width)		Elongation (%)		Tongue Tear (lb)		Minimum Buy	Unit Cost (\$/lin yd)	Lead Time (wk)
					Warp	Fill	Warp	Fill	Warp	Fill			
Nomex Fabric HT-287-45	Stern & Stern	1.11	7.0	45	33.7	32.3	18.5	19.7	Does not tear-- threads slip & unravel		None if in stock. If not in stock, 500 lin yd or \$300 setup + unit cost for 100 to 500 lin yd	2.75	1
HT-286-42	Stern & Stern	2.23	7.3	42	58.5	55.3	21.5	22.5				4.35	3-4
HT-31-36	Stern & Stern	2.23	8.6	36	102.5	95.6	27.8	35.8	27.8	35.8		3.15	1
HT-6-45	Stern & Stern	2.40	6.4	45	109.5	105.5	26.2	26.0	16.8	14.0		3.45	4.5
HT-5-42	Stern & Stern	2.83	6.4	42	126.0	123.5	27.8	29.5	Does not tear			3.95	4.5
HT-92-54	Stern & Stern	3.22	8.5	54	145.0	135.5	35.0	39.3	10.4	8.5		5.65	5-6
HT-26-45	Stern & Stern	3.37	8.4	45	158.0	150.0	25.0	28.0	26.0	24.0		5.15	1
HT-29-41	Stern & Stern	3.38	6.5	41	156.0	158.5	27.0	30.0	Does not tear			4.70	1
HT-18-45	Stern & Stern	3.41	8.0	45	148.5	144.5	27.0	29.0	18.0	17.6		5.15	1
HT-16-45	Stern & Stern	3.43	6.5	45	154.0	149.5	28.0	31.9	15.0	14.6		5.15	1
HT-22-45	Stern & Stern	3.43	8.6	45	146.0	143.5	23.5	28.8	26.0	24.0		5.15	1
HT-23-45	Stern & Stern	3.49	8.2	45	152.3	149.0	22.0	35.0	22.4	22.2		5.15	4-5
HT-3-43	Stern & Stern	3.62	6.9	43	170.5	154.5	31.0	30.1	14.6	15.0		4.95	1
HT-7-55	Stern & Stern	4.29	11.0	55	191.5	124.5	30.0	24.5	12.4	9.8		8.05	1
HT-47-41	Stern & Stern	4.85	10.5	41	223.0	177.0	32.5	33.3	14.2	9.8		6.10	1
HT-1-41	Stern & Stern	5.04	9.3	41	231.0	215.5	29.2	27.5	31.8	30.2		6.65	3-4
HT-48-48	Stern & Stern	5.05	10.4	48	233.5	201.0	33.8	30.8	28.3	21.3		7.35	6-7
HT-152-45	Stern & Stern	5.15	14.7	45	179.5	139.0	40.5	33.0	26.0	21.8		7.10	6
HT-10-41	Stern & Stern	6.17	12.9	41	289.0	222.0	41.1	32.2	18.0	19.0		7.55	1
HT-67-42	Stern & Stern	8.11	14.7	42	580.0	560.0	42.1	39.6	Does not tear			10.60	1
HT-72-54	Stern & Stern	8.56	15.8	54	362.5	345.0	39.6	38.5	Does not tear			12.60	1
HT-80-59	Stern & Stern	11.12	22.2	59	475.0	472.5	33.3	41.6	106.2	90.6		19.75	4-5
HT-122-46	Stern & Stern	12.05	23.5	46	510.2	518.0	33.0	31.2	Does not tear			17.25	1
HT-35-62	Stern & Stern	26.40	55.9	62	1,070.0	1,170.0	48.9	30.2	Does not tear			52.25	1
Woven to customer specifica- tions	Prodesco	2.0	-18-19 for Raschel weave	24 (?)							100ft ²	9.80/100 ft ²	1
		5.7										13.75/100 ft ²	2-3

Table 3-3 (Page 2 of 3)
SEPARATOR MATERIAL SURVEY--FABRICS

Material Description					Mechanical Properties					Procurement Data			
Material	Supplier	Weight ⁽²⁾ (oz/yd ²)	Thickness ⁽²⁾ (mil)	Width (in.)	Tensile ⁽²⁾ (48/in. width)		Elongation (%)		Tongue Tear (lb)		Minimum Buy	Unit Cost (\$/per yd)	Lead Time (wk)
					Warp	Fill	Warp	Fill	Warp	Fill			
βGlass Fabric 8116	J. P. Stevens	3.16	4.0	45	125	120					None if in stock. If not in stock: 200 lin yds + 500 set up charge + unit cost.	1.07	10
81677	J. P. Stevens	3.20	4.8	38	185	125					↓	0.45	6
81528	J. P. Stevens	6.0	7.0	56	250	190					↓	0.85	1
8401	J. P. Stevens	8.5	8.5	38	190	180					↓	1.27	4
84205	J. P. Stevens	8.5	20.0	48	120	100					↓	1.74	1
81564	J. P. Stevens	12.23	15.0	52.5	500	450					↓	0.52	1
81584	J. P. Stevens	25.40	24.6	38 Max	950	800					↓	2.11	10
8120	Prodesco	3.1	7.0	Any width (additional setup charges)							\$450 set up cost + unit cost for 48-in. width. \$300 set up cost + unit cost for 12-in. width.	8.10	2
8578	Prodesco	4.4	7.0	↓	200+	160+					↓	Above	2
881	Prodesco	5.8	7.0	↓							↓	Above	2
7581	Prodesco	8.5	7.0	↓	350	325					↓	Above	2
Durette Fabric 6632-27-2	Chemstrand	2.16	5.0	36			16.7	17.6			1-99 yd ² 100-999 yd ² 1,000-4,999 yd ² 5,000-yd ² & up	\$50/yd ² \$25/yd ² \$15/yd ² Negotiated	1
6632-9-1	Chemstrand	3.34	7.5	43			22.7	27.6	2.56	2.91	↓	↓	1
6632-8-2	Chemstrand	5.05	13.0	58			21.5	22.0	2.77	3.46	↓	↓	5
6632-21-2	Chemstrand	5.3	8.0	54			17.7	19.0			↓	↓	1
6632-17-1	Chemstrand	5.93	11.0	33			24.7	21.8			↓	↓	1

Table 3-3 (Page 3 of 3)
SEPARATOR MATERIAL SURVEY--FABRICS

Material Description					Mechanical Properties				Procurement Data			
Material	Supplier	Weight ⁽²⁾ (oz/yd ²)	Thickness ⁽²⁾ (mil)	Width (in.)	Tensile ⁽²⁾	Elongation (%)		Tongue Tear (lb)		Minimum Buy	Unit Cost (\$/per yd)	Lead Time (wk)
					(48/in. width) Fill	Warp	Fill	Warp	Fill			
PBI Fabric	Prodesco	~5.0	~10 plain or Leno weave	Any width (additional setup charges)						\$450 setup + unit cost for 36-in. width. \$300 set up + unit cost for 12-in. width.	36-in. width 35-40 12-in. width 17.5-20 (See note 4)	Function of Government (Procurement) + 3 weeks
Nylon Fabric	Prodesco	~5.0	~11-12 plain or Leno weave								36-in. width 22-28/lin yd 12-in. width 11-14/lin yd	3
Teflon Fabric	Prodesco	~6	~10-11 plain or Leno weave								36-in. width 15-18 12-in. width 7.5-9	4

- NOTES: (1) All information is vendor data. Price quotes cannot be considered firm commitments by suppliers. Lead times are generally dependent upon current stock status.
- (2) Values given for J. P. Stevens material are for E glass. β glass values should be slightly lower; 5% for weight and thickness. Strength values should be correct within 10%.
- (3) Types of materials are dependent upon current stock status.
- (4) Costs cited for PBI are weaving costs only. Yarn costs are additional.

material. A Dacron net (configuration B4A) manufactured by Apex Mills was shown to give good performance in studies related to contract NAS 8-21400 and was therefore included in this study. Dacron B4A weighs 0.0013 lb/ft² (0.187 oz/yd²) and has a thickness of 6.6 mils.

3.1.3 Face Sheets

A face sheet has two components: basic material and load-carrying strap. The strap is formed by impregnating the basic material with a resin. Nomex and Beta glass fabrics selected as candidate separator materials are also candidate base materials for a face sheet. Nomex fabric, style HT-287, and Beta glass fabric, style 81677, were selected. Low weight was again the major criterion for this selection. Four high-temperature polymeric systems were selected as candidates for impregnating the strap areas. These are Viton (a fluoroelastomer), silicone, polyimide, and Teflon. The manufacturer's designation and the suppliers are shown in Table 3-4.

3.1.4 Fasteners

Three materials were considered for fasteners. These were Teflon, polysulfone (Astrel 360), and polyimide. Three polyimides were included: Vespel, Gemon, and XPI-MC154-60. Pertinent information for selection

Table 3-4
FACE-SHEET POLYMERS

Material	Manufacturer's Designation	Supplier
Viton	CV 328	Connecticut Hard Rubber Co., New Haven, Conn.
Polyimide	Skybond 703	Monsanto Company Plastics Products & Resin Division Los Angeles, Calif.
Silicone	R 7141 resin with Catalyz 15	Ferro Corporation Cordo Division Culver City, Calif.
Teflon S	954-101 Coating	E. I. Du Pont de Nemours Fabrics & Finishes Dept. Los Angeles, Calif.

of candidate fastener materials within the selected generic types is presented in Table 3-5. Available impact and tensile properties are given as well as suggested methods for fabrication and joining. Minimum-buy requirements, unit costs, and comments on each material are also included. The polyimide materials can be expected to be too brittle in the thin sections required by fastener design. A difficult joining problem can be anticipated with Teflon materials. The polysulfone (Astrel 360) was therefore selected for fastener components.

3.1.5 Lacing Buttons

The lacing buttons are exposed to the same environment as the fasteners and can be constructed of the same material. Consequently, the polysulfone (Astrel 360) material was selected for the lacing buttons.

3.1.6 Purge Bag

Teflon-coated Kapton was selected as the most promising purge bag material. Other possible base substrates are Beta glass and Nomex fabrics. A silicone coating on Beta glass or Nomex fabric can be expected to have lower permeability than a Viton or Teflon coating. However, any of these coatings may be adequate. Teflon-coated Kapton and polyimide coatings on E glass are currently available as off-the-shelf items. A similar coating can be applied to alternative base materials. However, these polymers are traditionally brittle.

The critical factor is the method for achieving adequate joints. All the above materials have a high potential for adequate joining. Teflon-coated materials can be heat sealed. Silicone, Viton, and polyimide-coated materials can be bonded with their own respective polymers. Successful sealing should also be achievable with silicone.

3.1.7 Material Survey—Conclusions and Recommendations

As a result of the material survey, candidate materials were selected for each of the components in an MLI system. A summary of the materials selected is given in Table 3-6. The rationale for these selections has been presented in previous sections.

Table 3-5
FASTENER MATERIAL SURVEY

Material Description		Properties		Procurement Data	Fabrication Procedures		Comments
Material	Supplier	IZOD Impact	Tensile Strength (psi)	Unit Cost	Fabrication Method	Joining Method	
Polyimide Vespel	DuPont	0.9	5,000 at 500°F	Sheet - \$0.25/in. ² Rod - \$4.00/in. ²	Machine from bar	Bond	Not recommend for use in thin sections-- brittle
Gemon	General Electric				Transfer or compression mold	Bond	Not recommend for use in thin sections-- brittle
XPI-MC154-60	Cynamid	0.5	10,000 at 392°F	1-20 lb - \$25/lb 20+ lb - \$12.50/lb	Injection mold	Heat seal	Heat distortion Temperature: 450°F
Polysulfone Astrel 360	3M	3.0	4,100 at 500°F	HC-360 pellets 1-4 lb - \$30/lb 5-100 lb - \$25/lb HC-361 powder 1-4 lb - \$29/lb 5-100 lb - \$24/lb	Injection mold	Heat seal or solvent weld	Heat distortion Temperature: 525°F
Teflon	DuPont	3.0	600 at 500°F	Sheet - \$0.82/ft ² Rod - \$3.40/10 ft	Machine or compression mold	?	Difficult joining problem

Table 3-6
CANDIDATE MATERIALS FOR MLI COMPOSITE

Composite Components	Candidate Materials
Reflectors	<ol style="list-style-type: none"> 1. Double-goldized Kapton, 30-gage 2. Double-goldized Mylar, 25-gage 3. Double-aluminized Kapton, 30-gage
Separators	<ol style="list-style-type: none"> 1. Nomex nets <ul style="list-style-type: none"> Styles: HT-96 HT-289 HT-58 2. Beta glass nets <ul style="list-style-type: none"> Styles: 1653 1659 3. Nomex fabric <ul style="list-style-type: none"> Style: HT-287 4. Durette fabric - 6632-27-2 5. Beta glass fabric - 81677 6. Dacron - B4A
Face sheets	<ol style="list-style-type: none"> 1. Nomex fabric - HT-287 2. Beta glass fabric - 81677 <p>(Both with Vitron, silicone, polyimide, and Teflon polymers)</p>
Fasteners and lacing buttons	<ol style="list-style-type: none"> 1. Polysulfone - Astrel 360

Program scope and material availability limitations prevented extensive optimization of the materials and their configuration. Consequently, it is recommended that additional separator materials be evaluated in future work. This identification and evaluation of other configurations could be especially rewarding since significant separator weight reductions appear feasible if lighter-weight nets can be identified.

The Kapton-based reflector materials have a significant advantage over Mylar-based reflectors, because they can withstand much higher temperatures. A disadvantage of the Kapton materials is that they are only available in a thickness of 25 to 30 gage, whereas double-aluminized Mylar is available in a 15-gage thickness. Thus the Kapton reflectors are heavier. Development work to allow fabrication of the Kapton reflectors in a thinner, lighter material is recommended.

The costs of the goldized reflector materials are significantly higher than those of the aluminized materials at the present time. Since the cost of the gold appears to be negligible because it is only a few Angstroms thick, the material cost appears to be primarily due to fabrication costs. Consequently, development work to reduce fabrication costs is recommended. Of particular interest is the goldized Kapton material. Since goldized Kapton appears to offer a greater potential than goldized Mylar, further development work on double-goldized Mylar is not recommended. Although not significant enough to negate the consideration of goldized reflectors as candidate materials, some variations in gold thickness were noted. Consequently, gold-coating development work should include fabrication procedures to obtain a more uniform deposition of gold.

3.2 SEPARATOR THERMAL PERFORMANCE SCREENING TESTS

A low-cost test method for obtaining an indication of the relative thermal performance of separator materials was developed on NAS8-21400 (Reference 2). This test method involves measuring the electrical

resistance between two reflector sheets separated by a candidate separator material. The rationale is that both electrical and thermal resistance are functions of the separator material conductivity and the intimacy of contact between the separator and reflector sheets. Consequently, by assuming that the radiation parameter would be independent of the separator material, a higher thermal insulation performance is anticipated for those separator materials which show a higher electrical resistance.

3.2.1 Test Procedures

The test procedures used in the electrical resistance tests in this study were identical to those used in NAS8-21400 and outlined in Reference 2. The electrical resistance was measured as a function of applied loads with a Mid-Eastern Megatrometer, Model 710. The instrument was located in a shielded room, and an additional small shielded box was used to house the samples during measurements. These precautions were required due to the capacitive nature of the circuit and the sensitivity of the samples to distortion by air currents. Applied loads were generated by posterboard sheets, aluminum sheets, and lead blocks as outlined in Reference 2.

The measurement procedure was identical for all data points. Voltage (25v) was applied and the indicated resistance recorded after 30 sec. Power was then turned off and a shorting bar of 20-gage copper wire was placed across the terminals to bleed off accumulated charges on the reflector sheets. The shorting bar was left in place for 150 sec. During this time the next load element was added to the test stack. At the end of 150 sec, voltage was applied again for the next measurement.

3.2.2 Test Specimen Configuration

The test specimens consisted of two double-goldized Kapton (DGK) reflector sheets, 3 by 3 inches, centered above and below one sheet of the candidate separator material. A single DGK/candidate-separator layer-pair was placed on top to simulate a realistic load distribution. These layers, consisting of the top layer-pair and test specimen layers, were placed on top of 20 layer-pairs of DGK/nylon net. The layers beneath the test specimen provided an elastic base to transmit applied loads and therefore

simulate realistic loading conditions. Only the three sheets of candidate separator material were changed between tests. The candidate separator sheets were larger (5 by 5 inches) than the reflectors to avoid edge shorting.

3.2.3 Fabric Separators - Test Results

Test results for the separator fabric materials are shown in Figure 3-1 and Table 3-7. As shown, the Nomex fabric (HT-287) had a higher electrical resistance and therefore appears to offer a higher thermal insulation performance. The Nomex fabric also is the lightest-weight material; Nomex HT-287 = 0.007 lb/ft^2 ; Durette 6632 = 0.015 lb/ft^2 ; and Beta glass 81677 = 0.0222 lb/ft^2 . Consequently, the Nomex HT-287 fabric was selected as the candidate separator fabric material.

3.2.4 Beta Glass Net Separators - Test Results

Test results for the Beta glass net separator materials are shown in Figure 3-2 and Table 3-8. The 1653 material appears to offer a slightly higher thermal insulation performance than the 1659. The 1653 is also the lightest in weight: 1653 = 0.0097 lb/ft^2 and 1659 = 0.01145 lb/ft^2 . Consequently, of the two materials, the 1653 would be the more optimum.

3.2.5 Nomex Net Separators - Test Results

Test results for the Nomex net separator materials are shown in Figure 3-3 and Table 3-9. The HT-58 material appears to offer the highest thermal resistance. However, the optimum Nomex net separator material of those tested is not obvious since the HT-58 is not the lightest-weight candidate but is the heaviest. The weights of the three materials are: HT-96 = 0.0063 lb/ft^2 , HT-289 = 0.0090 lb/ft^2 , and HT-58 = 0.0140 lb/ft^2 .

Since the HT-58 is not the lightest-weight candidate, a comparison of the composite weights required to provide equivalent thermal performance is needed (kp comparison). It can be shown that if two composites are sized to give equal steady-state thermal performance, the ratio of the kp product for the two composites will be equal to the ratio of their total composite weights;

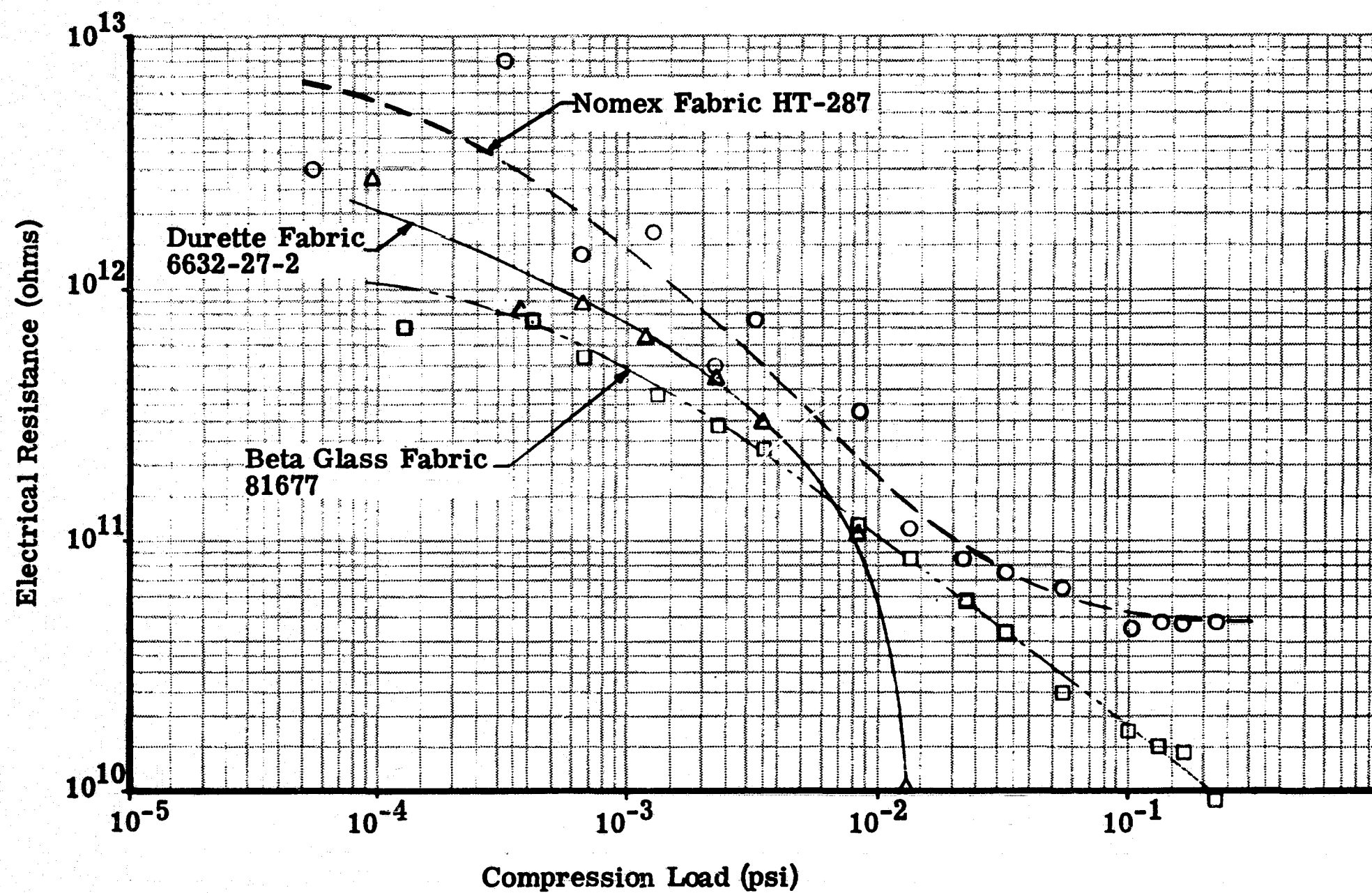


Figure 3-1. Separator Fabrics Screening Test

Table 3-7
ELECTRICAL RESISTANCE TEST DATA - FABRICS

Nomex HT-287		Durette 6632-27		Beta Glass 81677	
Compressive Load (psi)	Resistance (ohms)	Compressive Load (psi)	Resistance (ohms)	Compressive Load (psi)	Resistance (ohms)
5.54×10^{-5}	3×10^{12}	9.34×10^{-5}	2.7×10^{12}	1.31×10^{-4}	7×10^{11}
3.35×10^{-4}	8×10^{12}	3.73×10^{-4}	8.25×10^{11}	4.11×10^{-4}	7.5×10^{11}
6.15×10^{-4}	1.3×10^{12}	6.53×10^{-4}	8.5×10^{11}	6.91×10^{-4}	5.25×10^{11}
1.18×10^{-3}	1.7×10^{12}	1.21×10^{-3}	6.25×10^{11}	1.25×10^{-3}	3.75×10^{11}
2.30×10^{-3}	5×10^{11}	2.33×10^{-3}	4.62×10^{11}	2.37×10^{-3}	2.88×10^{11}
3.42×10^{-3}	7.5×10^{11}	3.45×10^{-3}	2.88×10^{11}	3.49×10^{-3}	2.35×10^{11}
8.28×10^{-3}	3.33×10^{11}	8.31×10^{-3}	1.05×10^{11}	8.35×10^{-3}	1.23×10^{11}
1.31×10^{-2}	11.25×10^{10}	1.32×10^{-2}	Shorted	1.32×10^{-3}	8.88×10^{10}
2.29×10^{-2}	8.25×10^{10}			2.29×10^{-2}	5.75×10^{10}
3.26×10^{-2}	7.38×10^{10}			3.26×10^{-2}	4.25×10^{10}
5.20×10^{-2}	6.75×10^{10}			5.20×10^{-2}	2.5×10^{10}
1.01×10^{-1}	4.5×10^{10}			1.01×10^{-1}	1.75×10^{10}
1.31×10^{-1}	4.75×10^{10}			1.32×10^{-1}	1.53×10^{10}
1.63×10^{-1}	4.75×10^{10}			1.63×10^{-1}	1.38×10^{10}
2.25×10^{-1}	4.75×10^{10}			2.25×10^{-1}	9.5×10^9

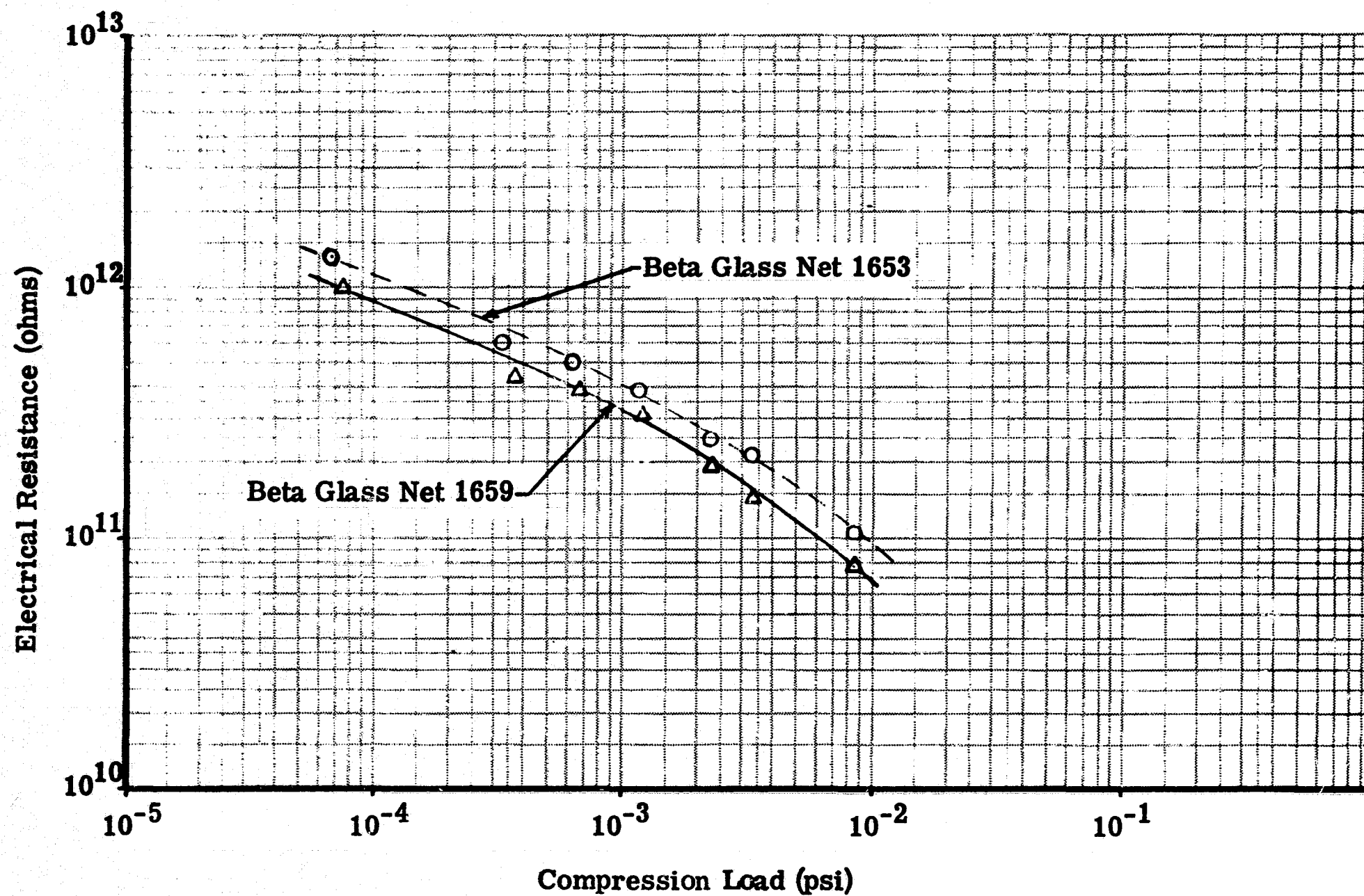


Figure 3-2. Beta Glass Net Separators Screening Test

Table 3-8
ELECTRICAL RESISTANCE TEST DATA - BETA GLASS NETS

Beta Glass Net 1659		Beta Glass Net 1653	
Compressive Load (psi)	Resistance (ohms)	Compressive Load (psi)	Resistance (ohms)
7.64×10^{-5}	1×10^{12}	6.59×10^{-5}	1.3×10^{12}
3.56×10^{-4}	4.25×10^{11}	3.46×10^{-4}	6×10^{11}
6.36×10^{-4}	3.88×10^{11}	6.26×10^{-4}	5×10^{11}
1.20×10^{-3}	3.1×10^{11}	1.19×10^{-3}	3.95×10^{11}
2.32×10^{-3}	1.92×10^{11}	2.31×10^{-3}	2.5×10^{11}
3.44×10^{-3}	1.45×10^{11}	3.43×10^{-3}	2.05×10^{11}
8.30×10^{-3}	7.75×10^{10}	8.29×10^{-3}	1.05×10^{11}

i.e.,

$$\frac{W_A}{W_B} = \frac{(k\rho)_A}{(k\rho)_B}$$

where k is the effective thermal conductivity and ρ is the composite density. This type of comparison is not readily obtained from the electrical resistance tests because the exact relationship between the thermal conductivity, k , and the measured electrical resistance, R , is not known.

However, two cursory relationships were developed and utilized to select one of the Nomex net separators. They are:

$$k\rho \approx D\omega \left(\frac{1}{R}\right)^{0.5} \quad \text{and} \quad k\rho \approx \omega \left(\frac{1}{R}\right)^{0.4}$$

(Relationship 1) (Relationship 2)

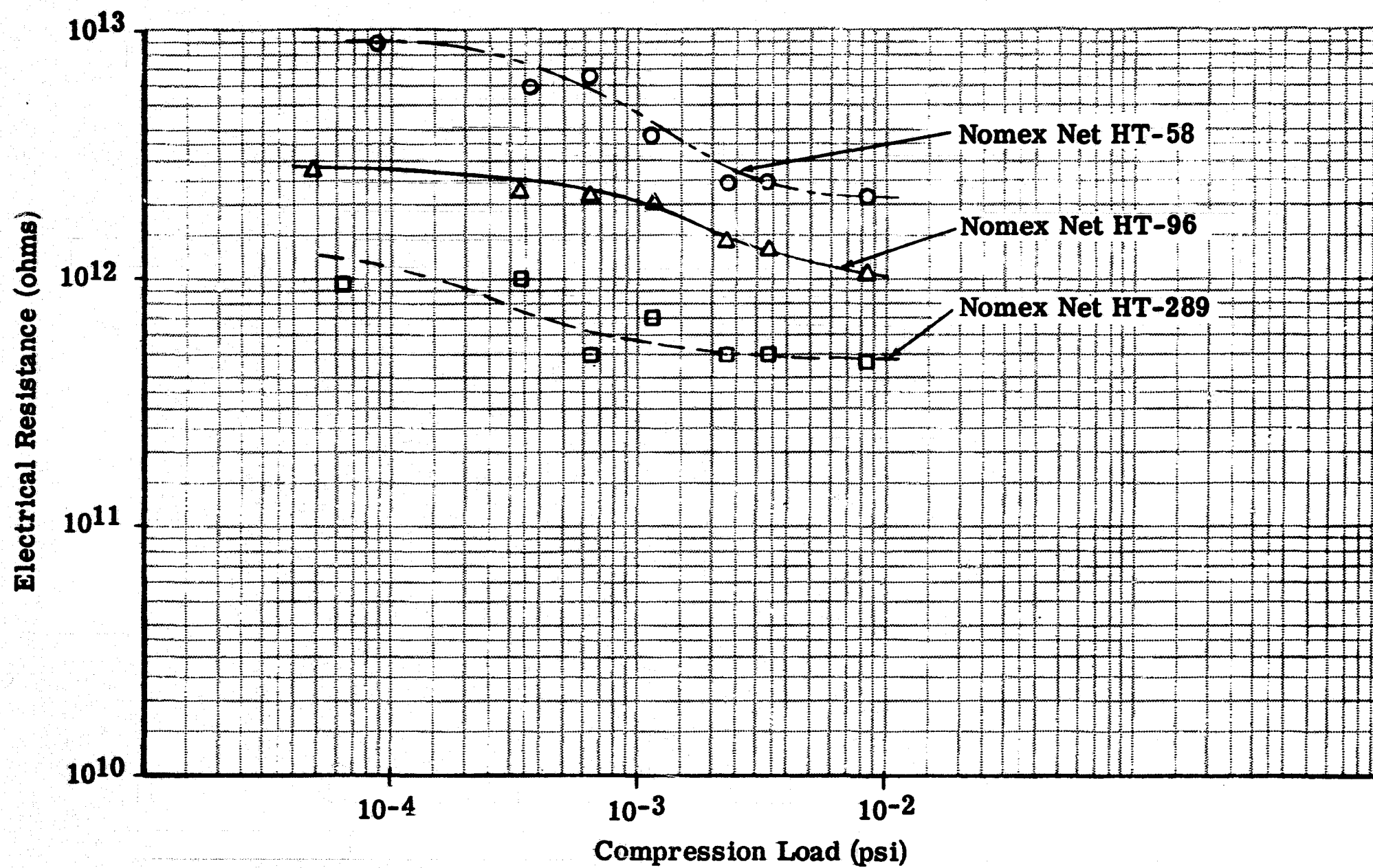


Figure 3-3. Nomex Net Separators Screening Tests

Table 3-9

ELECTRICAL RESISTANCE TEST DATA - NOMEX NETS

Nomex Net HT-289		Nomex Net HT-58		Nomex Net HT-96	
Compressive Load (psi)	Resistance (ohms)	Compressive Load (psi)	Resistance (ohms)	Compressive Load (psi)	Resistance (ohms)
6.23×10^{-5}	9.5×10^{11}	8.83×10^{-5}	9×10^{12}	4.82×10^{-5}	2.75×10^{12}
3.42×10^{-4}	1.0×10^{12}	3.68×10^{-4}	6×10^{12}	3.28×10^{-4}	2.22×10^{12}
6.22×10^{-4}	5.0×10^{11}	6.48×10^{-4}	6.25×10^{12}	6.08×10^{-4}	2.15×10^{12}
1.18×10^{-3}	7.0×10^{11}	1.21×10^{-3}	3.75×10^{11}	1.17×10^{-3}	2.0×10^{12}
2.30×10^{-3}	5.0×10^{11}	2.33×10^{-3}	2.45×10^{11}	2.29×10^{-3}	1.4×10^{12}
3.42×10^{-3}	5.0×10^{11}	3.45×10^{-3}	2.5×10^{11}	3.41×10^{-3}	1.35×10^{12}
8.28×10^{-3}	4.75×10^{11}	8.30×10^{-3}	2.2×10^{11}	8.27×10^{-3}	1.05×10^{12}

where

ω = wt/unit area/layer pair (lb/ft²/layer-pair)

D = layer density (layer-pairs/in.)

R = electrical resistance (ohms)

The development of these relationships is shown in Reference 3. The results which were obtained by using the first relationship and showed approximately equal anticipated composite weights for the HT-96 and HT-58. However, it was felt that the x value of 0.5 is probably high, which penalizes the HT-96. Therefore, the HT-96 would probably be the more efficient material. The results which were obtained by using the second relationship showed that the HT-96 would clearly be the more efficient material. The lower resistance to heat transfer of the HT-96 appears to be more than compensated for by the lower material weight of the HT-96; i.e., if a composite using the HT-96 and a composite using the HT-58 were sized (number of layer-pairs) to give the same thermal performance, the HT-96 composite would have a few more layer-pairs but would still have the lowest total weight.

3.2.6 Selection of Three Separator Candidates

Originally three separators were to be selected for further evaluation: one Nomex net, one Beta glass net, and one fabric. However, at a joint NASA-MSFC and MDAC-W meeting, it was decided to alter this by substituting Dacron B4A net for the Beta glass net. This decision was brought about by: (1) a reduction in the maximum temperature requirement from 600°F to 350°F, which eliminated a potential need for the high-temperature capability of Beta glass; (2) the superior performance of the Nomex materials in the electrical resistance tests as well as the lighter weight of the Nomex materials; and (3) the much lighter weight of the Dacron net. Although it had not been established at that time that the Dacron net could withstand a 400°F cyclical-temperature environment, it was felt that it could be used in the lower (colder) portion of a composite which uses Nomex separators for the outer (hotter) layers. The choice of the B4A over other Dacron nets was based on MSFC calorimeter data.

As discussed in Subsections 3.2.3 and 3.2.5, the Nomex HT-287 fabric and the Nomex HT-96 net appeared to be the optimum fabric and the optimum Nomex net considered. Consequently, the three separator materials selected by joint concurrence of NASA-MSFC and MDAC for further evaluation in the Task 1 material property tests were:

Nomex HT-96 net

Nomex HT-287 fabric

Dacron B4A net

3.3 THERMAL-CYCLE TESTS

Thermal-cycling tests of the candidate reflector, separator, face sheet, and fastener materials were accomplished. These tests were designed to determine the capability of the materials to withstand the thermal cycling anticipated for an ILRV orbiter application. The material degradation resulting from the temperature cycling was determined by visual inspection followed by metal adhesion tests on the reflector materials and strength tests on the separator, fastener, and face-sheet materials.

3.3.1 Thermal-Cycling Test Procedure

Two thermal cycles were used in evaluating the candidate materials. The first cycled the material samples from 650° to -320°F. The second cycled the material samples from 400° to -320°F. Each of these cycles was repeated 100 times. Typical temperature histories of the cycles for both the 650° and 400°F cycles are shown in Figure 3-4. Those materials which did not appear to have the capability to withstand the first (650°F) temperature were rerun in the second series at the lower temperature (400°F). In addition, the DGK reflector and Nomex separator materials and the polyimide/Nomex face-sheet system were rerun in the second series since there was additional room for more samples in the test apparatus. The test matrix is shown in Table 3-10. Four samples of the reflector materials and nine samples of the separator, face sheet, and fastener materials were tested. A separator was placed between the reflector sheets during the 400°F cycles to prevent any adhesion of adjacent reflector layers at the edges.

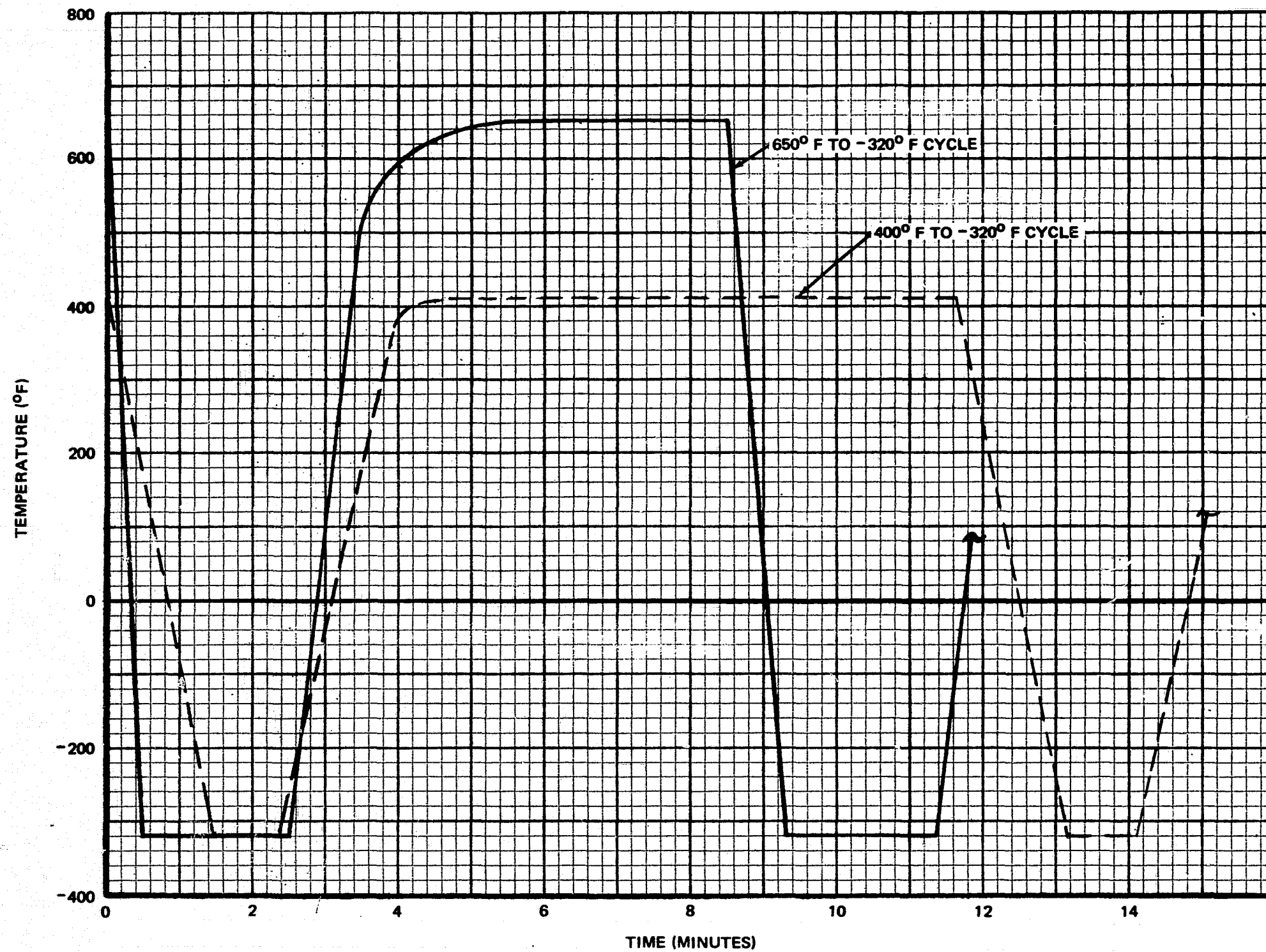


Figure 3-4. Thermal Cycle—Cyclical Temperature Tests

Table 3-10
TEMPERATURE CYCLING TEST MATRIX

Material	Number of Specimens	
	Test Series No. 1 (650 to -320°F)	Test Series No. 2 (400 to -320°F)
Reflectors		
Double-aluminized Kapton	4	
Double-goldized Kapton	4	4
Double-aluminized Mylar	4	4
Double-goldized Mylar	4	4
Separators		
Nomex HT-287	9	9
Nomex HT-96	9	9
Beta glass 1653	9	
Dacron B4A		9
Fastener		
Astrel 360	9	9
Face-Sheet Systems		
Silicone/Beta glass 81677	9	
Polyimide/Beta glass 81677	9	
Teflon/Beta glass 81677	9	
Viton/Beta glass 81677	9	9
Silicone/Nomex 287	9	
Polyimide/Nomex 287	9	9
Teflon/Nomex 287	9	9
Viton/Nomex 287	9	9

The reflector material samples were 6 by 6 in. and the separator and most of the face-sheet samples were approximately 9 by 1 in. Some of the face-sheet samples used in the 400°F cycles were approximately 10 by 1 in. The fastener material samples were of a dog-bone configuration and had a 1/4-in. -wide by 0.025-in. -thick test section.

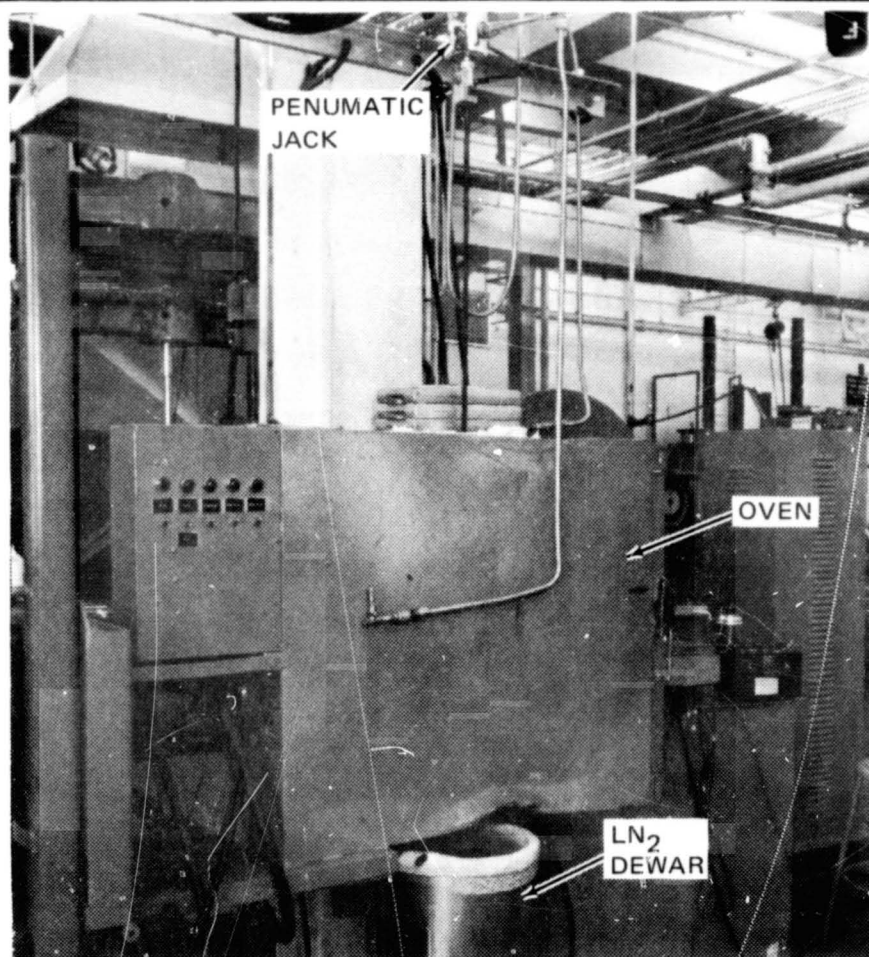
The thermal cycling was accomplished by heating the specimens in an oven to the desired temperature and then lowering the specimen holder through a port in the floor of the oven into a dewar of liquid nitrogen as shown in Figure 3-5. This procedure was controlled by a thermocouple located in the specimen holder which activated a relay switch for a pneumatic jack on which the specimen holder was mounted. The control thermocouple was enclosed in a metal tube to obtain the desired temperature response for the thermocouple. The proper size of the metal tube was determined experimentally prior to testing. The specimen holders (Figure 3-6) consisted of two sheets of stainless steel screen with the specimens lightly sandwiched between them. The specimens were free to expand and contract as they were heated and cooled during the testing.

3.3.2 Visual Test Results

Upon completion of the thermal cycles, the test specimens were visually inspected. The condition of the specimens is discussed and illustrated in the following subsections.

3.3.2.1 Reflectors

The double-aluminized Kapton (DAK) and double-goldized Kapton (DGK) reflector materials both appeared to have survived the 650°F temperature cycles (Figures 3-7 and 3-8). As anticipated, the Mylar reflectors, double-aluminized Mylar (DAM), and double-goldized Mylar (DGM), did not survive the 650°F temperature cycles (Figures 3-9 and 3-10). The DAM reflector material did not survive the second test (400°F) either (Figure 3-11). The material became brittle and easily disintegrated. The DGM



TEST SPECIMENS IN OVEN

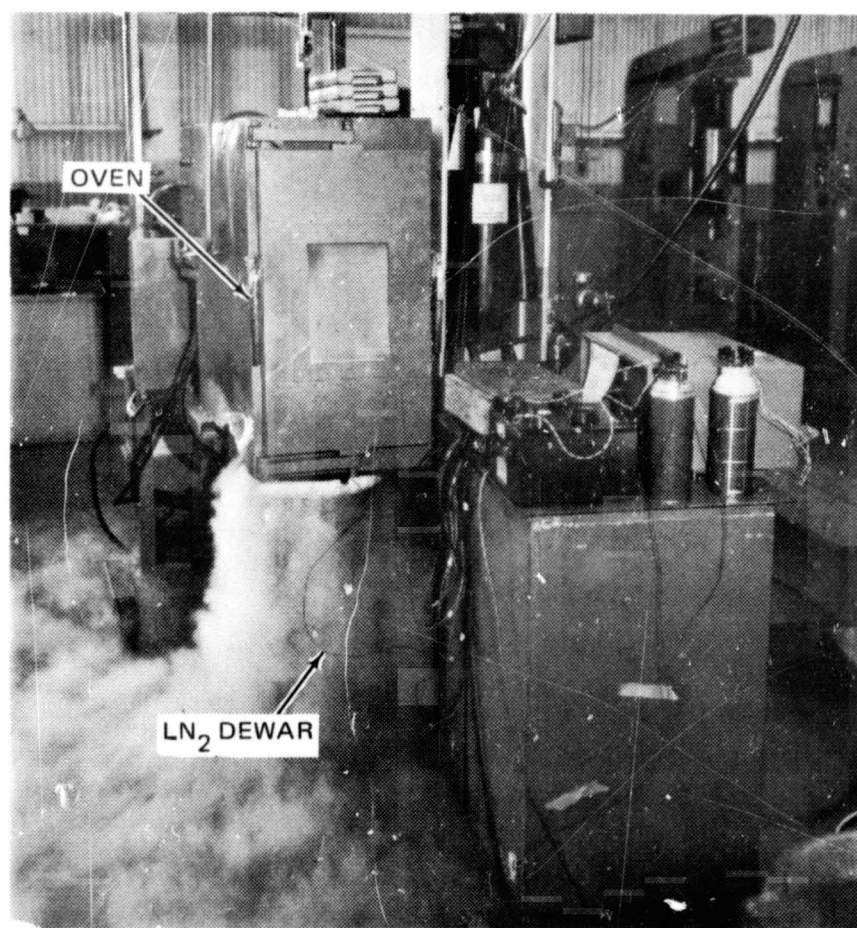
TEST SPECIMENS IN LN₂

Figure 3-5. Thermal Cycling Test Setup

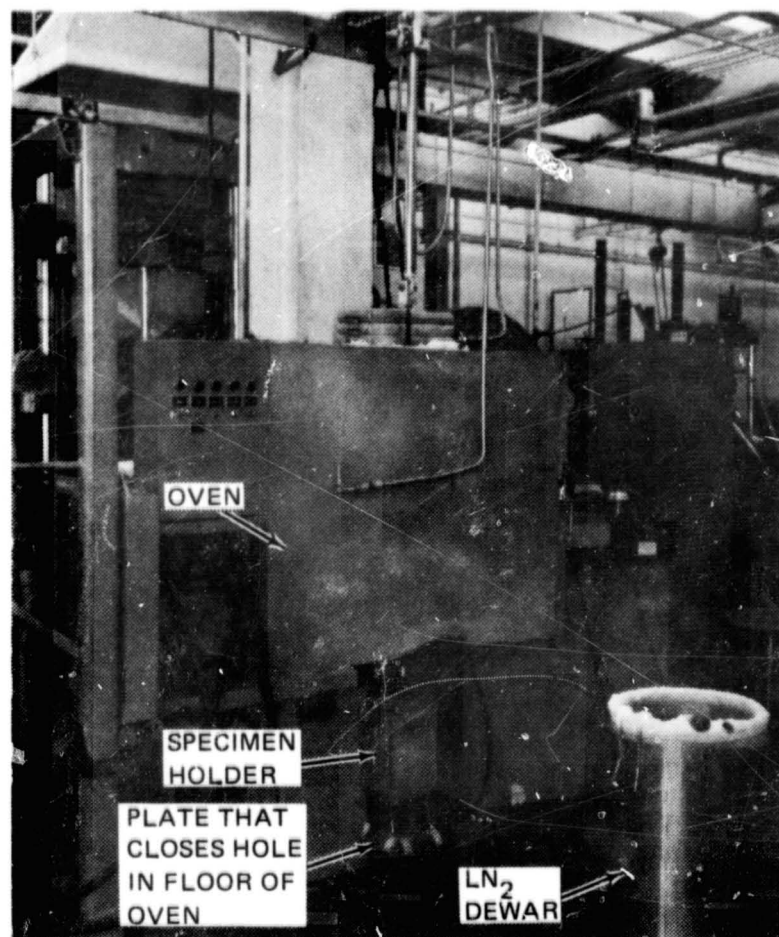


Figure 3-6. Thermal Cycling Test Apparatus



Figure 3-7. Double-Aluminized Kapton Reflector—Cyclical Temperature Specimen Cycled to 650°F

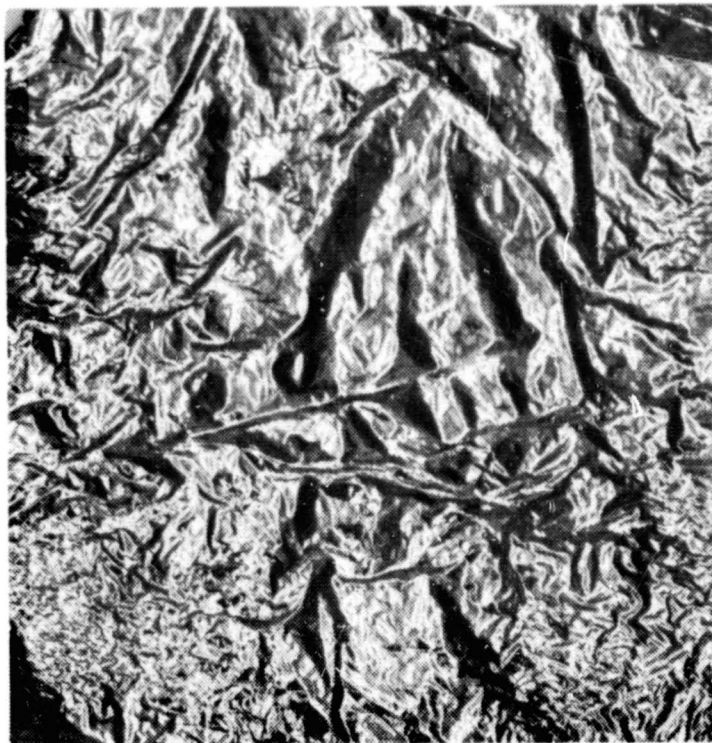


Figure 3-8. Double-Goldized Kapton Reflector – Cyclical Temperature Specimen Cycled to 650° F

CR14

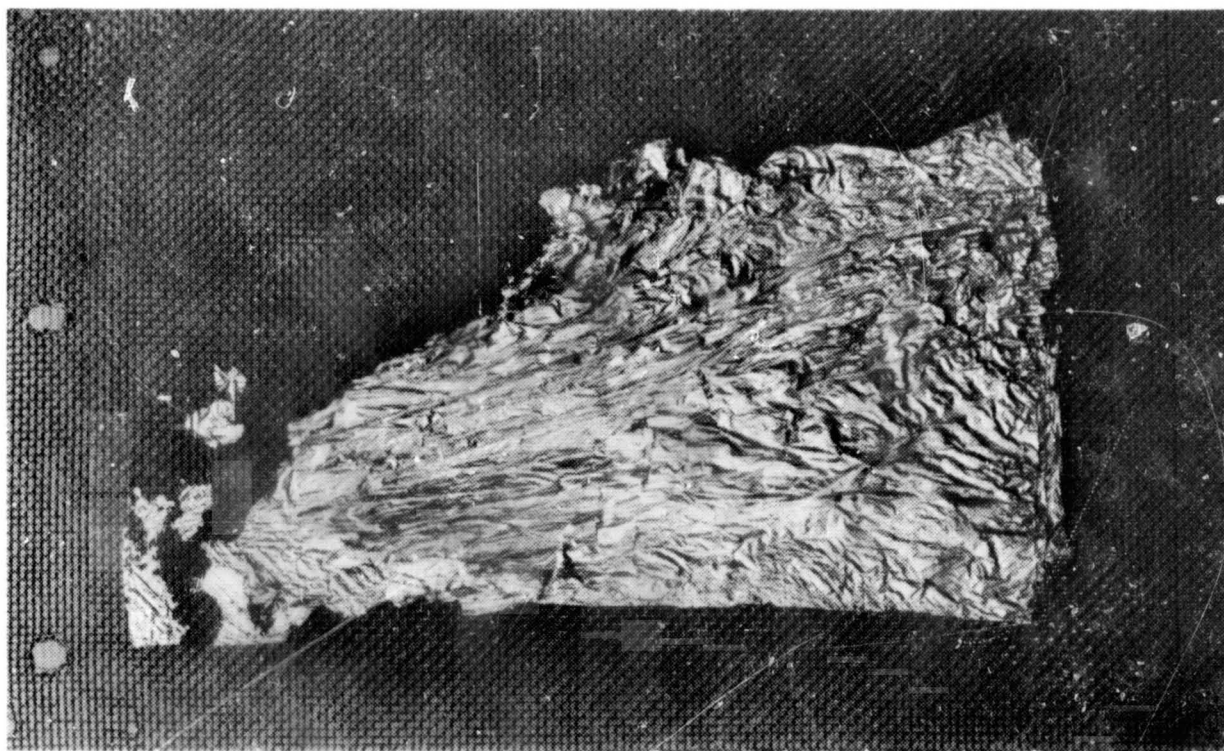


Figure 3-9. Double-Aluminized Mylar Reflector—Cyclical Temperature Specimen Cycled to 650°F

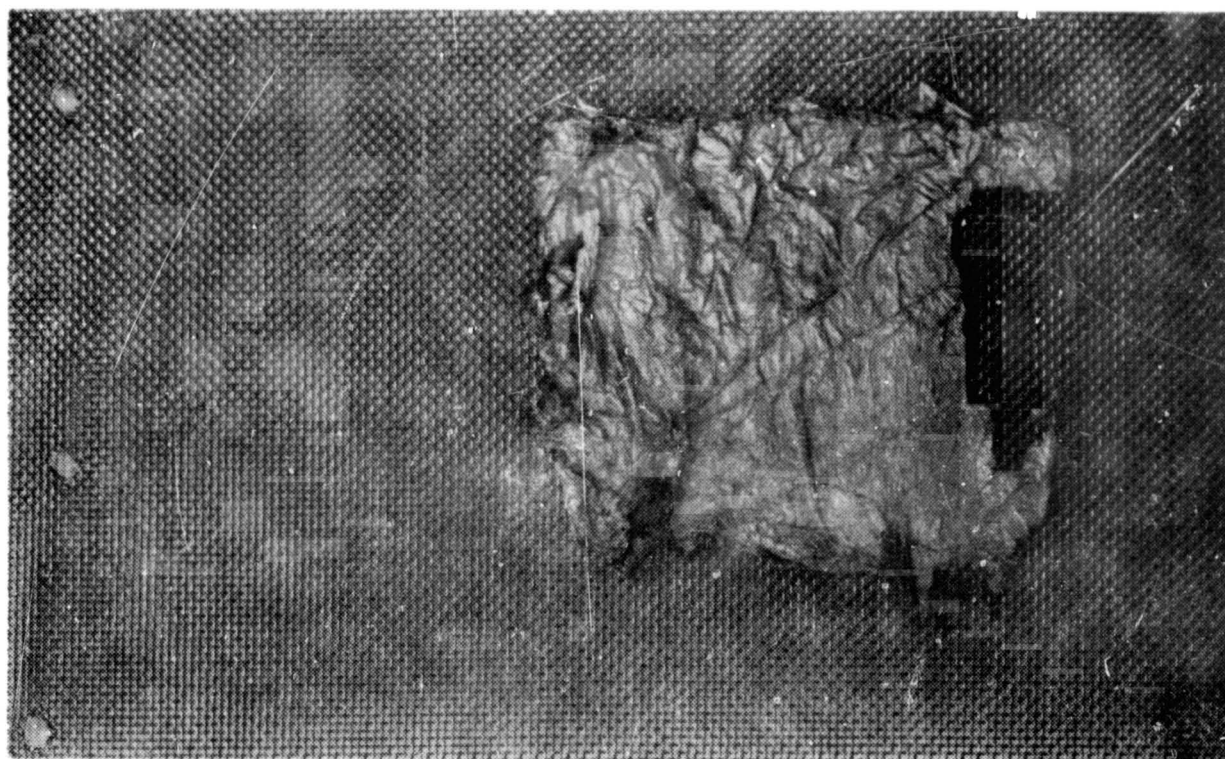


Figure 3-10. Double-Goldized Mylar Reflector—Cyclical Temperature Specimen Cycled to 650°F

CR14



Figure 3-11. Double-Aluminized Mylar Reflector—Cyclical Temperature Specimen Cycled to 400°F

material, however, did not become brittle during the 400°F temperature cycle test and does not appear to have undergone any change (Figure 3-12).

3.3.2.2 Separators

All of the separator materials (Nomex and Beta glass) included in the first test (650°F) appear to have withstood the test environment (Figures 3-13, 3-14, and 3-15). There was no apparent change in the Beta glass material. The Nomex materials changed color from white to light brown, but did not appear to have been structurally degraded. The Nomex materials were also included in the second test (400°F), with results similar to the previous 650°F test except that the color was changed only to a tan color instead of the previous light brown. A Dacron separator material that was included in the 400°F tests was slightly wrinkled by the 400°F cycles (Figure 3-16) but did not appear to have been altered sufficiently to affect its performance.

3.3.2.3 Fastener Material

The Astrel 360 fastener material was badly degraded in the 650°F temperature cycle test. This material, however, showed no degradation due to the 400° to -320°F temperature cycles (Figure 3-17).

CR14



Figure 3-12. Double-Goldized Mylar Reflector—Cyclical Temperature Specimen Cycled to 400°F

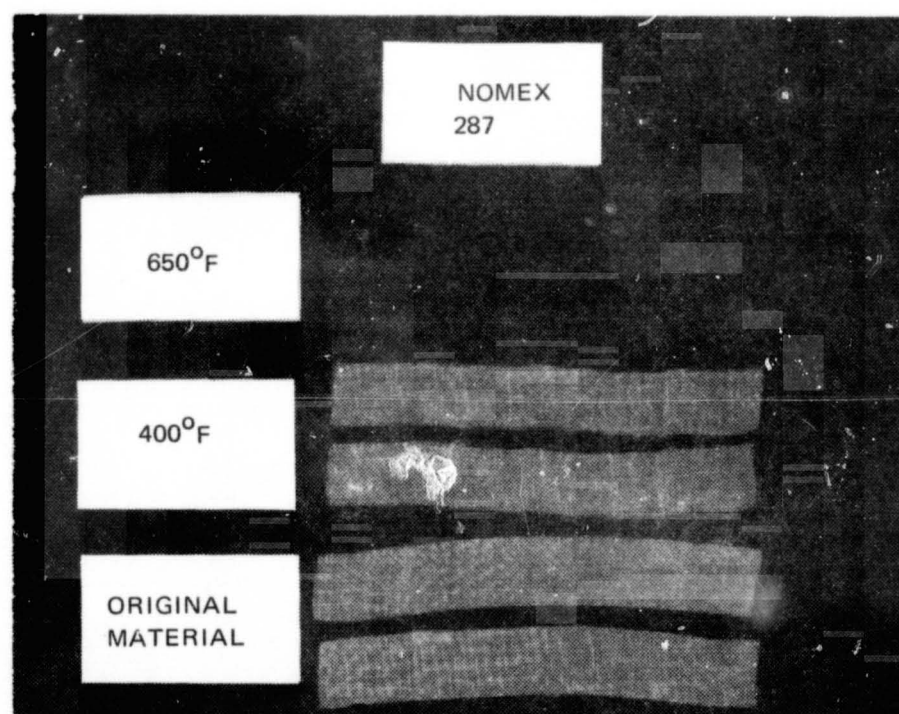


Figure 3-13. Nomex HT-287 Separator – Cyclical Temperature Specimens

CR14

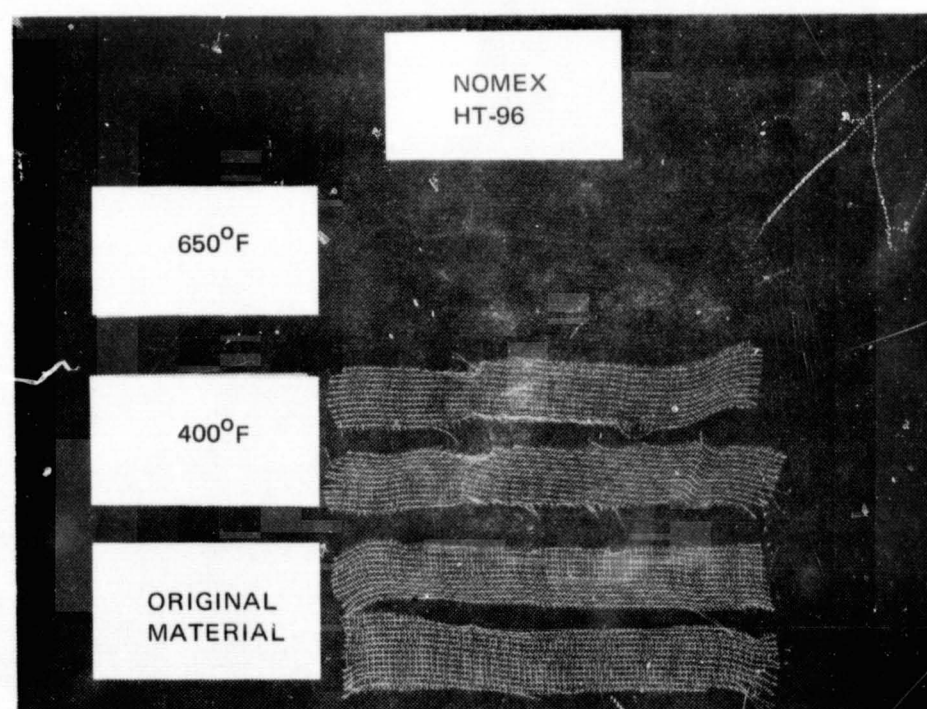


Figure 3-14. Nomex HT-96 Separator – Cyclical Temperature Specimens

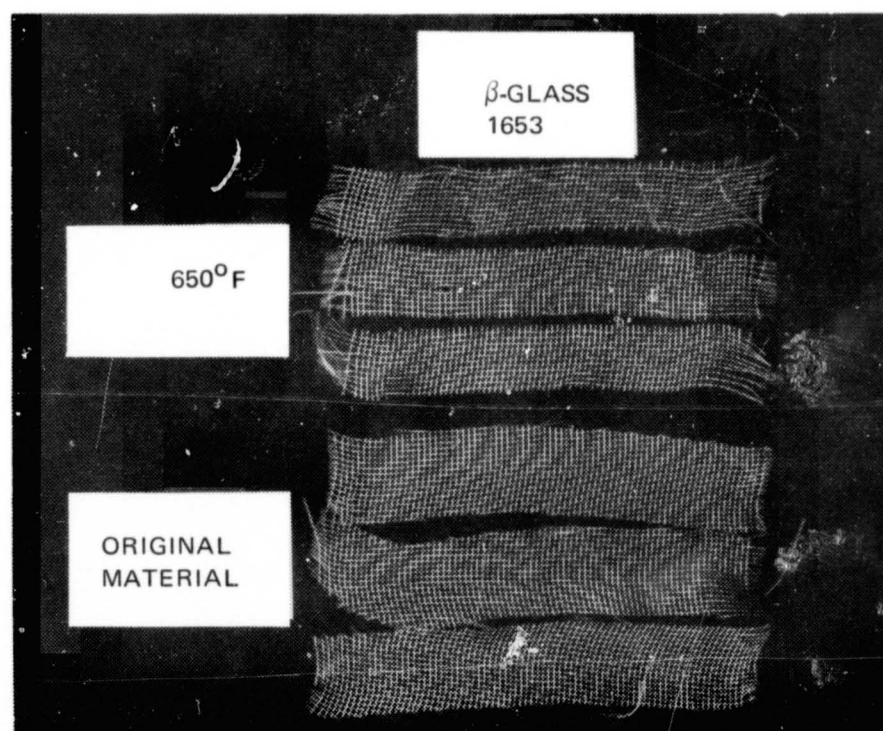


Figure 3-15. Beta Glass 1653 Separator – Cyclical Temperature Specimens

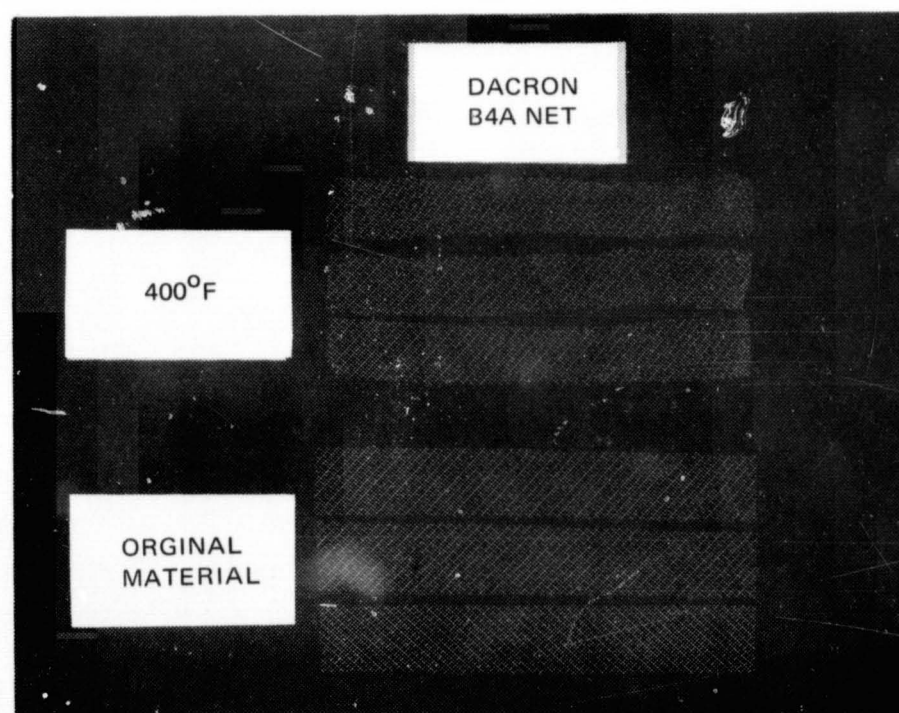


Figure 3-16. Dacron B4A Separator – Cyclical Temperature Specimens

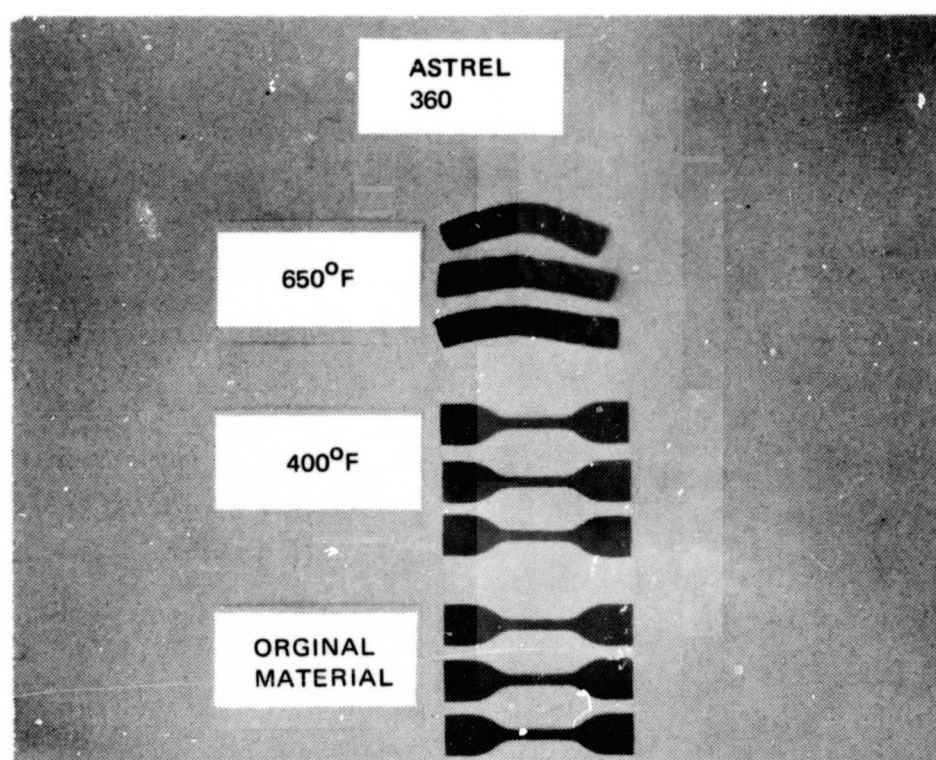


Figure 3-17. Astrel 360 Fastener Material – Cyclical Temperature Specimens

3.3.2.4 Face-Sheet Systems

The silicone/Beta glass, polyimide/Beta glass, Teflon/Beta glass, silicone/Nomex, and polyimide/Nomex face-sheet systems appeared to have survived the 650°F temperature cycle tests (Figures 3-18 through 3-22). The color of the silicone/Beta glass, Teflon/Beta glass, and silicone/Nomex changed from gray yellow to light yellow, green to dark brown, and gray-yellow to medium brown, respectively. There was no change in the polyimide/Beta glass or polyimide/Nomex face-sheet systems.

The Viton was charred and could be rubbed off of the Viton/Beta glass samples included in the 650°F temperature cycle test. The Viton/Beta glass samples, however, showed no degradation from the 400°F temperature cycle tests (Figure 3-23). The Viton/Nomex samples were appreciably distorted, became slightly brittle, and experienced a minor amount of charring in the 640°F temperature cycles. The Viton/Nomex samples, however, appear to have successfully withstood the 400°F temperature cycles (Figure 3-24).

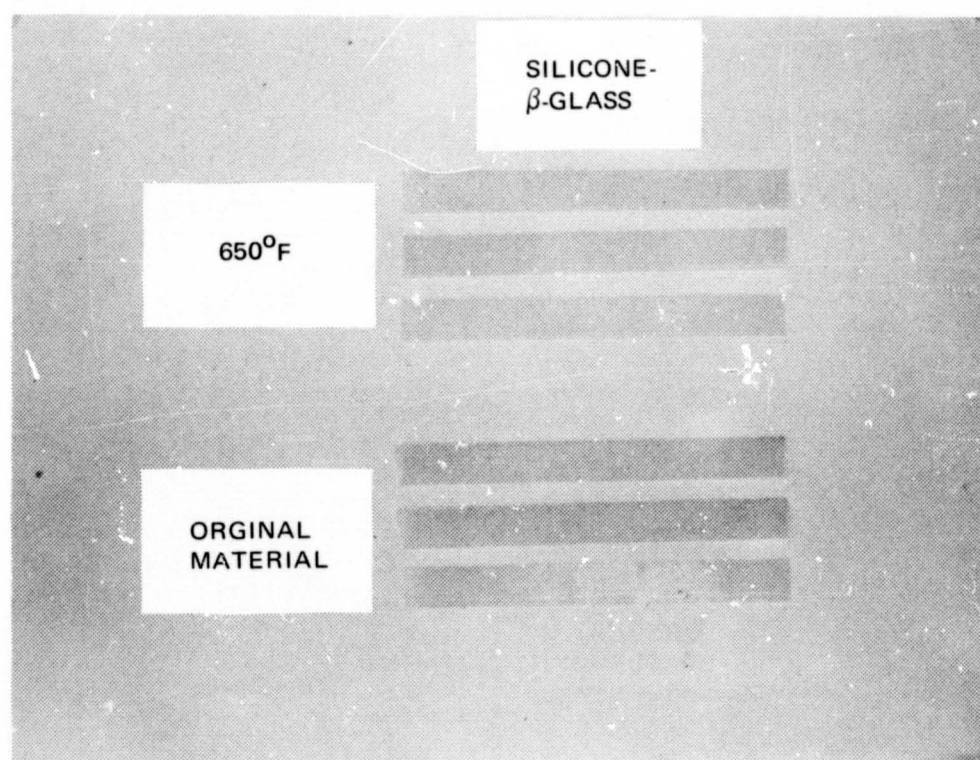


Figure 3-18. Silicone/Beta Glass Face Sheet – Cyclical Temperature Specimens

CR14

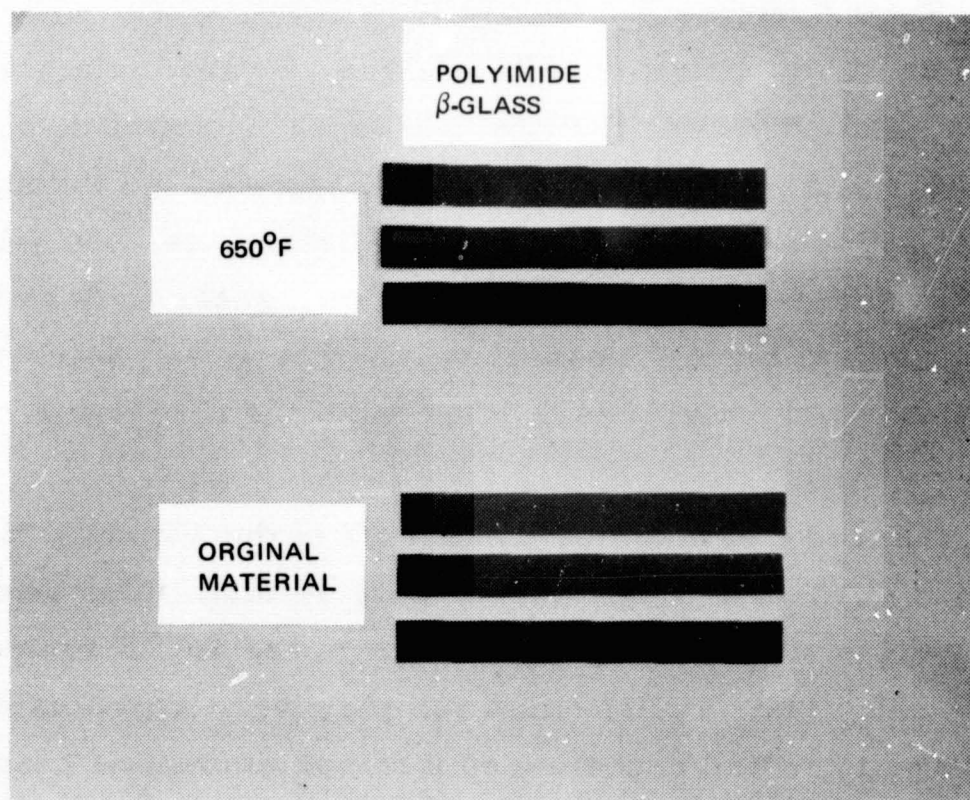


Figure 3-19. Polyimide/Beta Glass Face Sheet – Cyclical Temperature Specimens

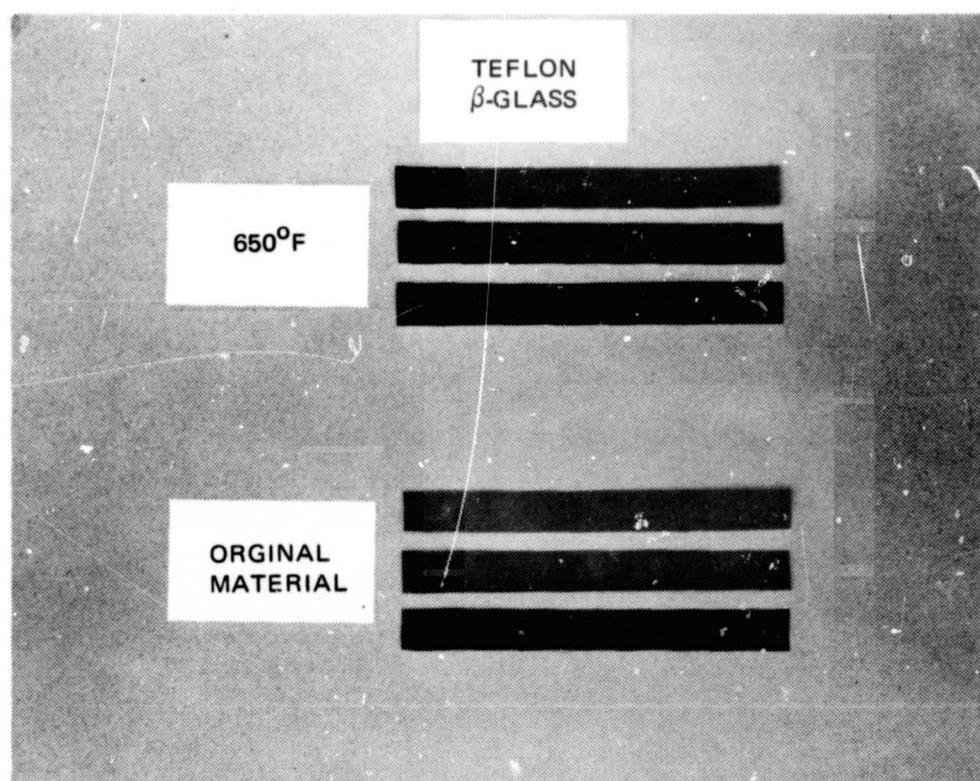


Figure 3-20. Teflon/Beta Glass Face Sheet—Cyclical Temperature Specimens

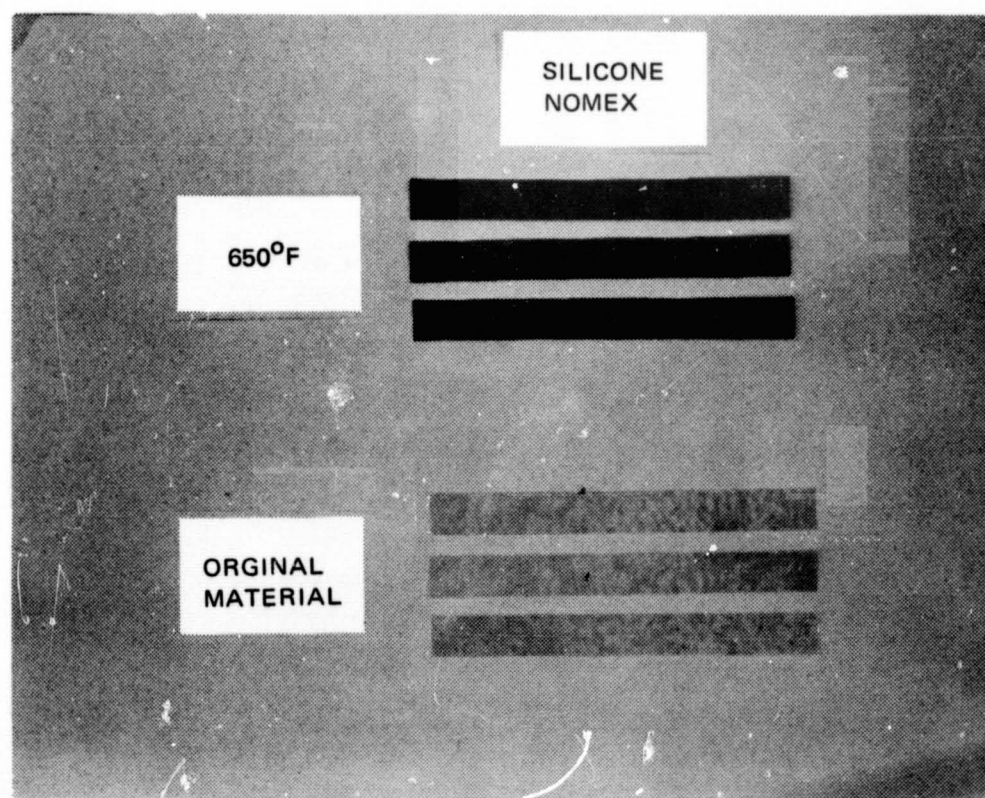


Figure 3-21. Silicone/Nomex Face Sheet—Cyclical Temperature Specimens

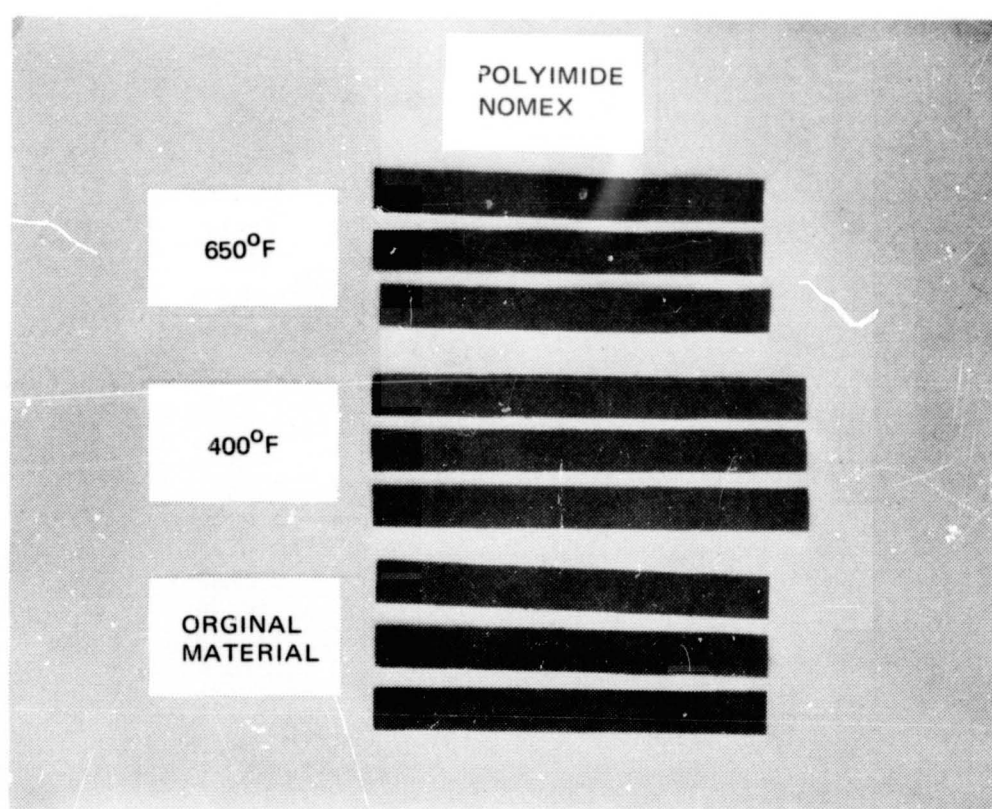


Figure 3-22. Polyimide/Nomex Face Sheet—Cyclical Temperature Specimens

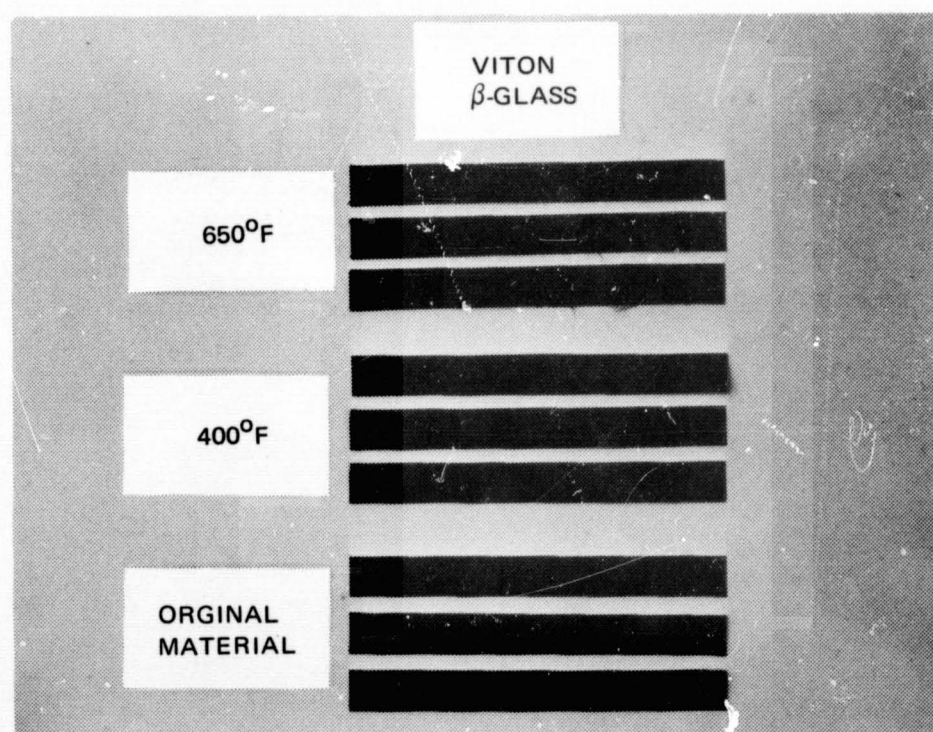


Figure 3-23. Viton/Beta Glass Face Sheet—Cyclical Temperature Specimens

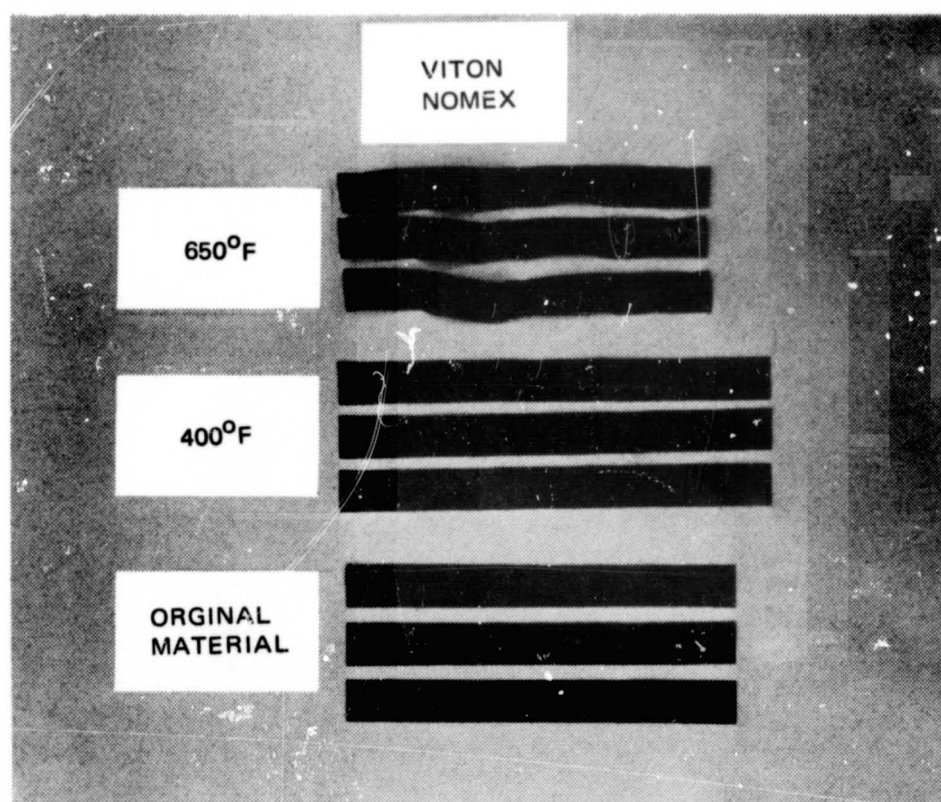


Figure 3-24. Viton/Nomex Face Sheet—Cyclical Temperature Specimens

The Teflon/Nomex samples were badly distorted in the 650° F temperature cycle tests but appear to have survived the 400° F test (Figure 3-25). The color of the specimens was changed to a slightly darker green in the 400° F test, but the samples did not appear to have been degraded.

3. 3. 3 Weight Loss During Thermal Cycling

The material specimens were weighed both before and after the thermal cycling to obtain an indication of material deterioration as evidenced by weight loss. Specimens of a given kind were weighed collectively rather than individually. The results, shown in Table 3-11, reveal that a large amount of material was lost from the Teflon and Viton face-sheet system specimens which were exposed to the 650° F cycles. The percentage weight loss for the face-sheet systems exposed to the 400° F temperature cycle was much less. The polyimide face-sheet systems had the lowest percentage weight loss of the candidate face-sheet systems.

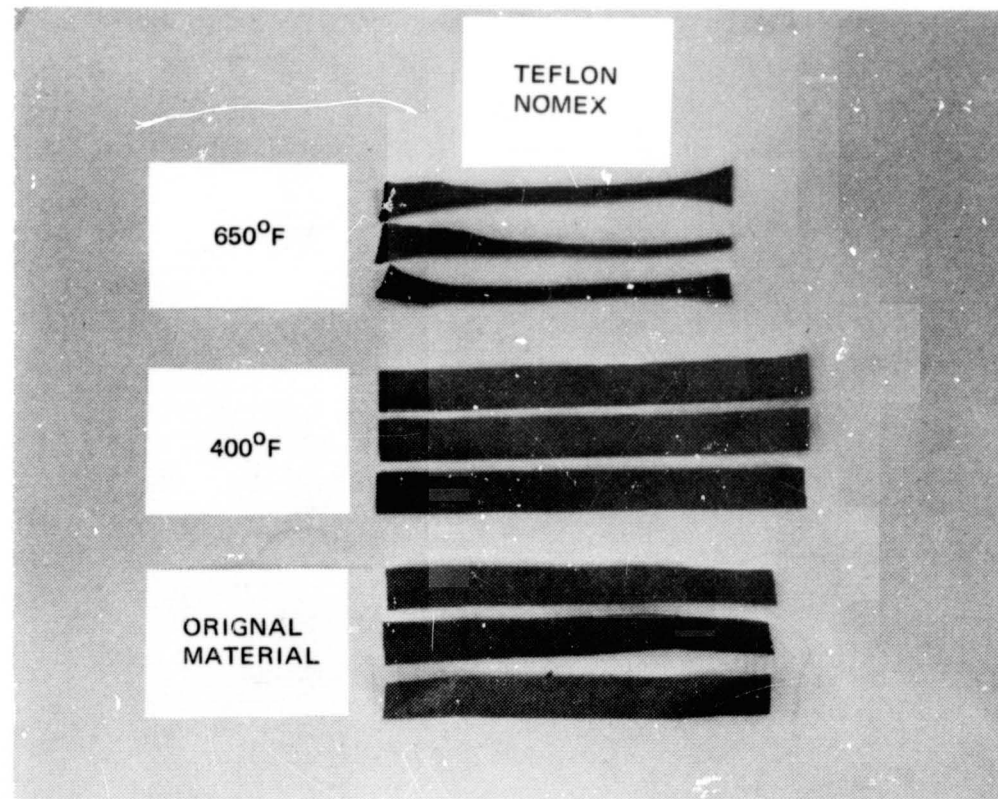


Figure 3-25. Teflon/Nomex Face Sheet—Cyclical Temperature Specimens

The Nomex separators had a weight loss of approximately 4.5 to 4.8 percent when subjected to the 650°F cycles and approximately 1.6 to 1.8 percent when cycled to 400°F. The Dacron B4A net separator had a relatively low weight loss (0.4 percent) when exposed to the 400°F temperature cycles.

3.3.4 Effect of Cyclical Temperatures on Reflector Metal Adhesion

The reflector specimens which visibly survived the thermal cycling were subjected to a tape adhesion test to determine the effect of the cyclical temperatures on the adhesion of the metal to the Kapton or Mylar substrate material. In the tape adhesion test, a piece of Scotch No. 250 tape is applied to the surface of the specimen by rolling it with a 0.9-lb rubber roller. After 5 minutes, the tape is removed by pulling in such a manner that a peeling force is applied to the bond between the tape and the specimen surface. The tape surface and specimen are then examined for evidence of transfer of reflector metal from the specimen to the tape. These tests were performed at 70 ±5°F and 40- to 60-percent relative humidity.

Table 3-11
WEIGHT LOSS DUE TO TEMPERATURE CYCLING

Material	Number of Specimens	Maximum Temperature (°F)	Minimum Temperature (°F)	Weight Before Temperature Cycle (gram)	Weight After Temperature Cycle (gram)	Weight Loss (%)
Beta glass 1653	3	650	-320	1.313	1.293	1.52
Nomex HT-287	9	650	-320	4.616	4.395	4.79
Nomex HT-96	9	650	-320	3.4142	3.257	4.54
Polyimide/Nomex HT-287	9	650	-320	8.111	7.993	1.45
Teflon/Nomex HT-287	9	650	-320	22.405	17.028	23.20
Teflon/Beta glass 81677	9	650	-320	23.438	19.761	15.69
Polyimide/Beta glass 81677	9	650	-320	14.378	14.215	1.13
49 Viton/Nomex HT-287	9	650	-320	33.634	25.472	24.30
Viton/Beta glass 81677	9	650	-320	24.729	14.209	42.54
Silicone/Nomex HT-287	9	650	-320	12.521	11.418	8.81
Silicone/Beta glass 81677	9	650	-320	16.876	16.240	3.77
Astrel 360	3	650	-320	5.567	5.488	1.42
Nomex HT-287	9	400	-320	3.381	3.320	1.80
Dacron B4A	9	400	-320	0.547	0.545	0.37
Nomex HT-96	9	400	-320	2.473	2.433	1.62
Polyimide/Nomex HT-287	9	400	-320	9.087	9.094	(+0.08)
Viton/Nomex HT-287	9	400	-320	35.367	35.273	0.27
Teflon/Nomex HT-287	9	400	-320	26.216	25.880	1.28
Viton/Beta glass 81677	9	400	-320	26.474	26.396	0.29

The test results showed no degradation in the metal adhesion of those reflector materials which appeared to have survived the temperature cycles. As shown in Table 3-12, no metal was removed from any of the faces of the test specimens.

3.3.5 Tensile Strength After Temperature Cycling

The load-carrying ability of the candidate composite structural components (face sheet and fastener) must be known to enable selection and design of these components for an ILRV application. To obtain these data, tensile tests were conducted on material specimens which had undergone temperature cycling. In addition, although they are not structural-load-carrying

Table 3-12
EFFECT OF CYCLICAL TEMPERATURES ON
REFLECTOR METAL ADHESION

Reflector	Separator	Exposure	Specimen		Percent Metal Transfer Using Tape Adhesion
			No.	Side	
Double- goldized Mylar	Nomex 287	400 to -320°F	1	1	0
			1	2	0
			2	1	0
			2	2	0
			3	1	0
			3	2	0
Double- goldized Kapton	Nomex 287	400 to -320°F	1	1	0
			1	2	0
			2	1	0
			2	2	0
			3	1	0
			3	2	0
		650 to -320°F	1	1	0
			1	2	0
			2	1	0
			2	2	0
			3	1	0
			3	2	0
Double- aluminized Kapton	Nomex 287	650 to -320°F	1	1	0
			1	2	0
			2	1	0
			2	2	0
			3	1	0
			3	2	0

members in the composite, the strength of the separators was determined to obtain an indication of any gross degradation of the separator materials.

3.3.5.1 Tensile Test Procedure

The components tested are shown in the test matrix, Table 3-13, and include the separator, face-sheet system, and fastener candidate materials. Three specimens of each material were tested at -320°F , ambient, and an elevated temperature of 400° or 650°F . Tensile strengths of specimens which had not been temperature-cycled were also obtained for comparison purposes.

These tests on the uncycled material were conducted at ambient temperature. The low and high temperatures for the tests on the specimens which had undergone the temperature cycling were selected in an attempt to encompass the temperature range that the materials might be subjected to in an ILRV application, as it was anticipated that the wide variations in temperature would result in significant changes in strength. Although the -320°F temperature is not as low as would be experienced by materials in the lower portion of an MLI composite on an LH_2 tank, the LN_2 temperature of -320°F is the lowest temperature that could be readily obtained within the scope of the program.

The test specimen dimensions are shown in Figure 3-26. The Nomex and Beta glass separator materials were cut with the long axis of the specimen parallel to the warp direction of the material and the edges were raveled for $1/4$ in. on each side. The Dacron B4A separator material is woven so that the yarns are oriented approximately 45° from the usual warp and fill-yarn orientation. Consequently, the yarns in the Dacron B4A specimens were oriented at an angle of approximately 45° to the edges of the specimen. The Nomex and Beta glass material used in the face-sheet systems were all cut so that the long axis of the specimen was parallel to the warp direction. Rectangular face-sheet specimens were used instead of the standard dog-bone configuration tensile test specimen used for the fastener material (Figure 3-26), since previous experience with impregnated net materials has indicated that premature failures can occur at the ends of a reduced section configured specimen.

All of the specimens were grip-loaded and tested to failure in an Instron Universal testing machine. Figure 3-27 shows the test setup for the

Table 3-13

TEST MATRIX FOR TENSILE TESTS

Materials	Uncycled Material Ambient Temp	Temperature Cycled -320 to 650°F			Temperature Cycled -320 to 400°F		
		-320°F	Ambient Temp	+650°F	-320°F	Ambient Temp	+400°F
Separators							
Nomex HT-287	3	3	3	3	3	3	3
Nomex HT-96	3	3	3	3	3	3	3
Beta glass 1653	3	3	3	3			
Dacron B4A	3				3	3	3
Face Sheets							
Silicone/Beta glass 81677	3	3	3	3			
Polyimide/Beta glass 81677	3	3	3	3			
Teflon/Beta glass 81677	3	3	3	3			
Viton/Beta glass 81677	3				3	3	3
Silicone/Nomex HT-287	3	3	3	3			
Polyimide/Nomex HT-287	3	3	3	3	3	3	3
Teflon/Nomex HT-287	3				3	3	3
Viton/Nomex HT-287	3	3	3	3	3	3	3
Fastener Material							
Astrel 360	3				3	3	3

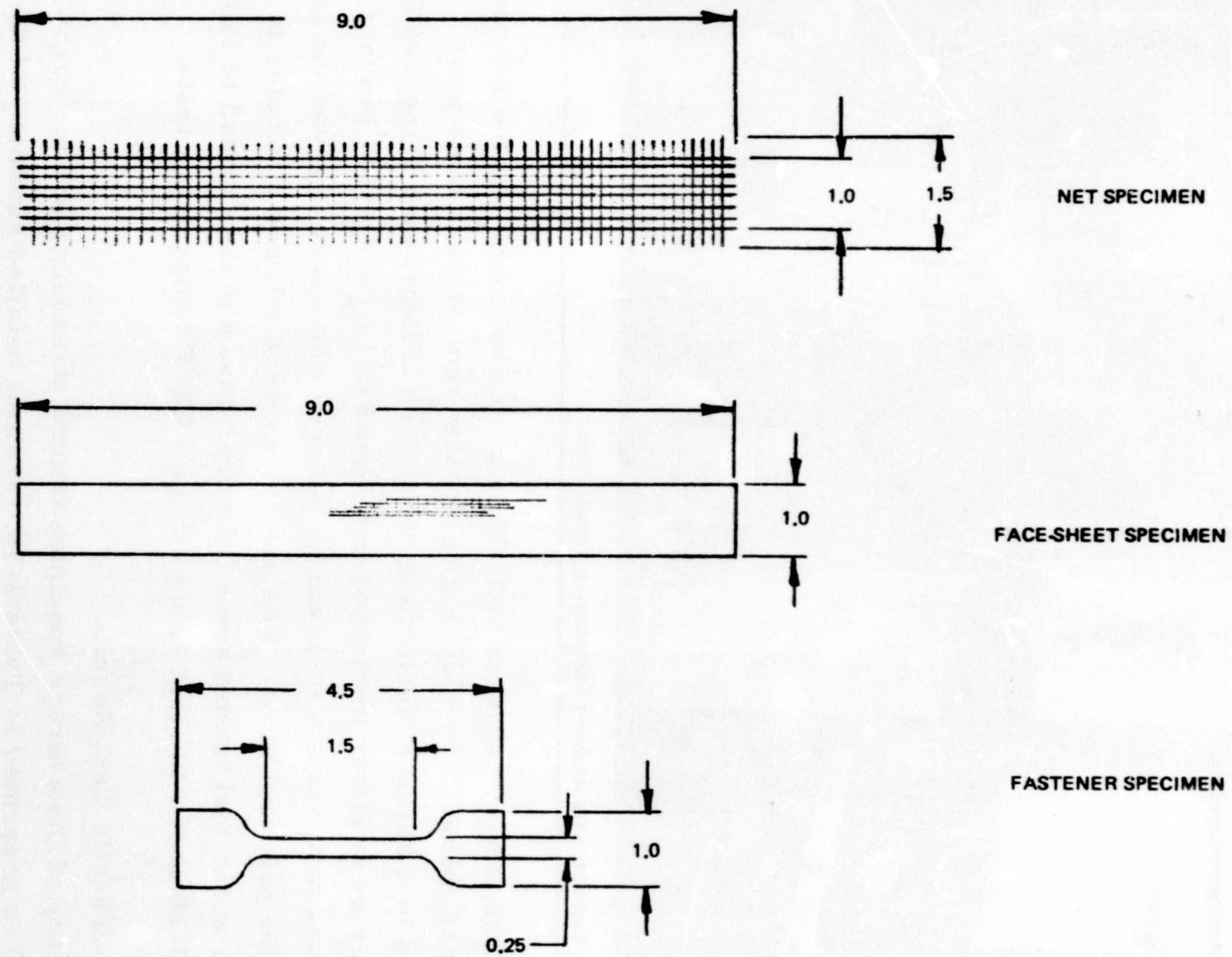


Figure 3-26. Tensile Test Specimen Dimensions

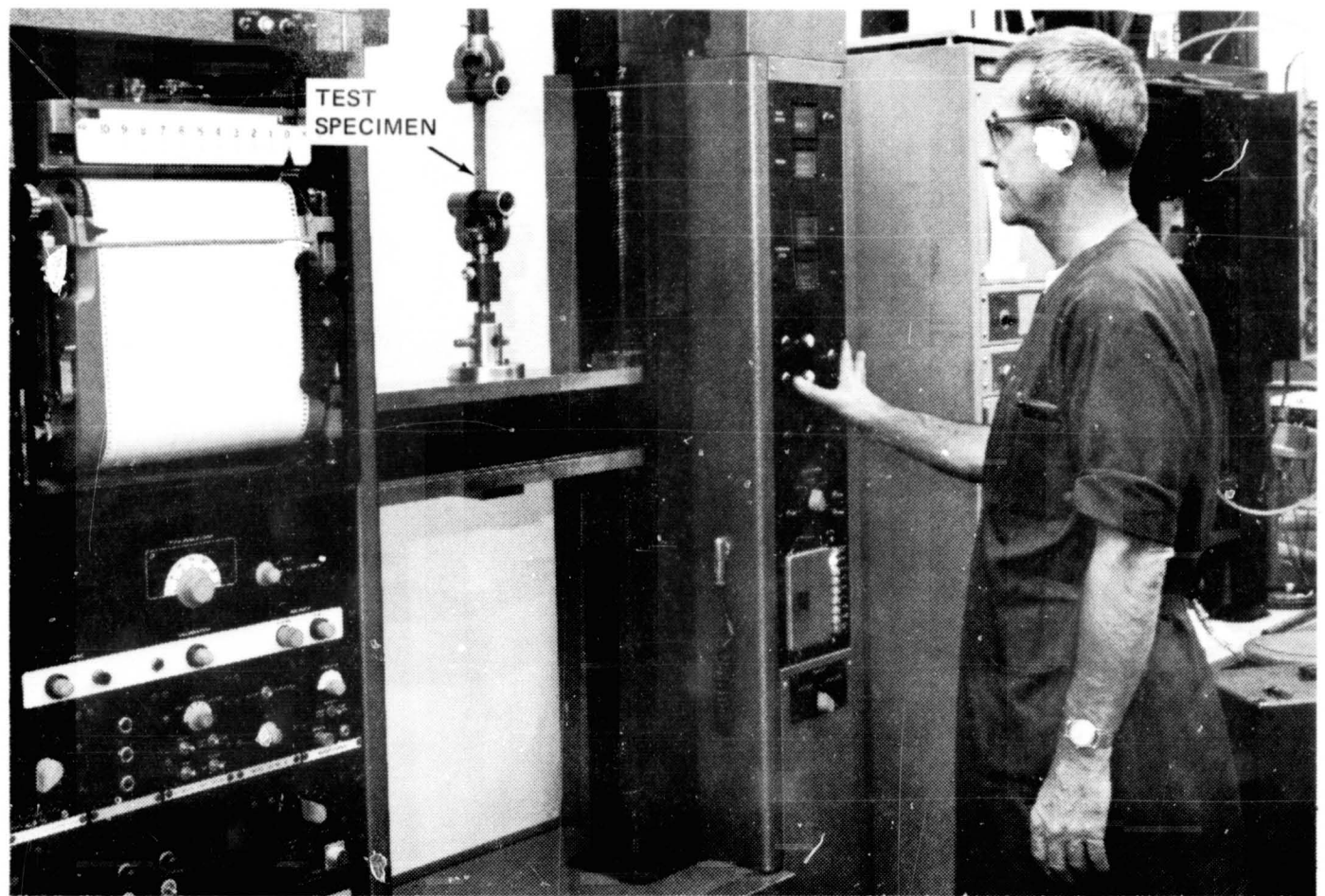


Figure 3-27. Test Setup for Ambient Temperature Tensile Tests

ambient temperature tests of both the control specimens and the thermally cycled specimens. The -320°F and elevated temperature tests were conducted in a similar fashion with the principal difference being that the specimens were either immersed in a dewar of LN_2 until they reached the -320°F test temperature or heated in an oven which fitted around the grip jaws of the test apparatus. The specimens were allowed 5 minutes to stabilize at the test temperature for either case and then loaded to failure. Figure 3-28 shows the test setup for the -320°F temperature tests.

3.3.5.2 Tensile Test Results

A summary of the average specimen failure stress obtained for each material is presented in Table 3-14. A more detailed summary of the test results is presented in References 4 and 5. Of the separator materials tested, the Nomex materials exhibited the highest strength. Of the face-sheet systems tested, the systems containing Beta glass exhibited much higher strength than those containing the Nomex HT-287 fabric. The polyimide/Beta glass 81677 face-sheet system exhibited the highest strength of all the face-sheet systems tested.



Figure 3-28. Test Setup for -320° F Tensile Tests

All of the materials that were thermally cycled between -320° and 650°F appear to have been structurally degraded by the thermal cycling. This degradation varies from approximately 12 percent for the Viton/Nomex HT-287 face-sheet system to approximately 47 percent for the Teflon/Beta glass 81677 face-sheet system. Of the face-sheet systems cycled between -320° and 400°F, the apparent structural degradation varies from essentially none for the polyimide/Nomex HT-287 system to approximately 38 percent for the Viton/Nomex HT-287 systems. In general, all of the systems containing Viton or Teflon appear to have been degraded at least 20 percent. The Nomex separator materials that were thermally cycled between -320° and 400°F do not appear to have been structurally degraded, but the Dacron B4A appears to have been degraded approximately 16 percent. The Astrel 360 fastener material thermally cycled between -320° and 400°F does not appear to have been significantly degraded. All of the materials tested would be acceptable on the basis of strength alone since the HPI system could be designed to function within the strength limits obtained. The separators carry only their own weight between fasteners and consequently have very low strength requirements. The amount of face-sheet area

Table 3-14
SUMMARY OF TENSILE TEST RESULTS
(Average Specimen Failure Stress)

Materials	Uncycled Material (Ambient)	Thermocycled Between 650 and -320°F			Thermocycled Between 400 and -320°F		
		-320°F	Ambient	650°F	-320°F	Ambient	400°F
Separator Materials							
Nomex 287	22.7 lb/in.	25.3 lb/in.	19.5 lb/in.	7.1 lb/in.	32.7 lb/in.	25.6 lb/in.	16.9 lb/in.
Nomex HT-96	35.7 lb/in.	30.7 lb/in.	20.0 lb/in.	10.5 lb/in.	45.6 lb/in.	36.1 lb/in.	24.0 lb/in.
Beta glass 1653	17.5 lb/in.	18.0 lb/in.	13.7 lb/in.	15.4 lb/in.			
Dacron B4A	3.7 lb/in.				1.4 lb/in.	3.1 lb/in.	1.6 lb/in.
Face Sheet Materials							
Silicone/Beta glass 81677	30.1 ksi	32.8 ksi	20.6 ksi	15.8 ksi			
Polyimide/Beta glass 81677	36.0 ksi	42.2 ksi	26.9 ksi	21.2 ksi			
Teflon/Beta glass 81677	23.5 ksi	18.9 ksi	12.4 ksi	5.1 ksi			
Viton/Beta glass 81677	26.9 ksi				55.2 ksi	19.1 ksi	10.2 ksi
Silicone/Nomex HT-287	5.4 ksi	3.0 ksi	3.6 ksi	1.6 ksi			
Polyimide/Nomex HT-287	3.2 ksi	1.46 ksi	2.16 ksi	1.16 ksi	--	3.1 ksi	2.0 ksi
Teflon/Nomex HT-287	4.2 ksi				4.1 ksi	3.4 ksi	2.2 ksi
Viton/Nomex HT-287	3.9 ksi	3.94 ksi	3.45 ksi	1.35 ksi	3.1 ksi	2.4 ksi	1.8 ksi
Fastener Material							
Astrel 360	12.8 ksi				16.6 ksi	12.5 ksi	8.0 ksi

impregnated with the resin could be varied to meet the face-sheet strength requirement.

Two of the Dacron B4A, one of the Astrel 360, and all three of the polyimide/Nomex HT-287 specimens failed during the specimen installation and cool-down period prior to tensile loading. Since the tare weight on the specimen was close to the failure load of the Dacron B4A, it is felt that the premature failure of the Dacron B4A specimens should not cause undue concern. The premature failure of the polyimide/Nomex HT-287 face-sheet system and one of the Astrel 360 specimens are not as readily understood. In a repeat of these tests, reported in Reference 5, none of the Astrel 360 specimens failed prematurely. Consequently, the failure of the one Astrel 360 specimen appears to have been due to improper specimen installation procedures or some other test anomaly. No explanation is apparent for the premature failure of the polyimide/Nomex HT-287 face-sheet system; it may indicate a serious strength reduction or brittleness of the material at -320°F.

3.3.6 Thermal Cycle Test—Conclusions and Recommendations

Reflector, separator, face-sheet, and fastener MLI materials which can withstand 100 temperature cycles from -320° to 400°F and from -320° to 650°F have been identified. A summary list is presented in Table 3-15. As shown, both DGK and DAK reflector materials can be considered for design applications requiring reflectors capable of withstanding temperature cycles with maximum temperatures of 650°F. DGM withstood temperature cycles to 400°F, but the upper temperature limit for thermal cycling of the DAM material is somewhere below 400°F. The Nomex and Beta glass separators can be considered for applications with temperature cycles to 650°F. The Dacron B4A separator material withstood temperature cycles to 400°F. The face-sheet systems utilizing silicone or polyimide for the impregnated strap area successfully withstood temperature cycles to 650°F. However, the polyimide/Nomex HT-287 system may become brittle at cryogenic temperatures and should not be considered for use at cryogenic temperature locations until evaluated further. The Teflon and Viton face-sheet systems should not be considered for applications with thermal cycles which have maximum temperatures greater than 400°F. The Astrel 360 fastener material also should not be considered for applications which include thermal cycles with maximum temperatures greater than 400°F.

TABLE 3-15
MLI MATERIALS VERIFIED FOR CYCLICAL THERMAL ENVIRONMENTS

MATERIAL	SURVIVED CYCLICAL THERMAL ENVIRONMENT	
	-320 TO 400°F	-320 TO 650°F
REFLECTORS		
DOUBLE ALUMINIZED KAPTON (DAK)	YES	YES
DOUBLE GOLDIZED KAPTON (DGK)	YES	YES
DOUBLE ALUMINIZED MYLAR (DAM)	NO	NO
DOUBLE GOLDIZED MYLAR (DGM)	YES	NO
SEPARATORS		
NOMEX HT-287	YES	YES
NOMEX HT-96	YES	YES
BETA GLASS 1653	YES	YES
DACRON B4A	YES	NO
FACE SHEET SYSTEMS		
SILICONE/BETA GLASS 81677	YES	YES
POLYIMIDE/BETA GLASS 81677	YES	YES
TEFLON/BETA GLASS 81677	YES	NO
VITON/BETA GLASS 81677	YES	NO
SILICONE/NOMEX HT-287	YES	YES
POLYIMIDE/NOMEX HT-287	YES	YES
TEFLON/NOMEX HT-287	YES	NO
VITON/NOMEX HT-287	YES	NO
FASTENER		
ASTREL 360	YES	NO

Additional testing in future studies is recommended to determine the upper temperature limit during thermal cycling of the DAM reflector material. An evaluation of the brittleness of the MLI materials at cryogenic temperatures is also recommended for future studies. If feasible, these tests to evaluate brittleness should be conducted at LH₂ temperatures.

3.4 EFFECT OF SEPARATOR VOLATILES

One aspect of the potential effect of any outgassing of separator materials is the possible degradation of optical properties of the reflectors adjacent to outgassing separators. To determine if any such degradation can be expected, tests were designed and conducted. These tests consisted of placing sample composites in an oven at 400°F for 6 hours and then measuring the emissivity of the reflector faces that had been in contact with a separator. To prevent contamination from other samples, composites containing different separator materials were placed in different ovens. The instrument used for the measurements was a Gier-Dunkle DB100 infrared reflectometer.

3.4.1 Test Specimens

The composite test specimens were 6 by 6 inches and contained three reflector and two separator sheets. Three composites of each specimen were tested. The emissivity of both sides of the reflector sheet in the middle and the emissivity of the inner surfaces of the outer reflector sheets in each composite were obtained. The three candidate separators, Nomex HT-96, Nomex HT-287, and Dacron B4A were tested with each of the DGK, DAK, and DGM reflector materials.

3.4.2 Test Results

The test results (Table 3-16) do not indicate any significant effect of separator volatiles on the emissivity of the reflector materials. The range of emissivity values for the DGK control samples encompasses all but one of the emissivity values of the DGK reflector faces exposed to any outgassing. This data point is only slightly higher and is probably due to a material anomaly. Three emissivity values for the DGM material are somewhat higher. These are 0.052 and 0.065 for the DGM/HT-96 and 0.037 for the DGM/HT-287. However, these may also be due to material anomalies as the manufacturer of the DGM material has reported problems in gold deposition on the DGM material. In addition, it should be noted that the gold surfaces apparently were not affected in the DGK reflector material, and the data for the other two DGM composites show no significant increase in emissivity values.

3.4.3 Effect of Separator Volatiles—Conclusions and Recommendations

From the test data results, it was concluded that there was no degradation in reflector emissivity due to any outgassing of the Nomex and Dacron separators considered. Further testing concerned with the effects of separator volatiles on reflector emissivity does not appear warranted for these materials.

3.5 MOISTURE DEGRADATION TESTS

The MLI composite materials used for an ILRV could be exposed to two types of moisture conditions. One would be the humidity and temperature environment expected on the ground between flights. The second would be a high-temperature water vapor environment that could occur during reentry if the MLI is not adequately purged. The composite material of concern is the reflector, as past testing has shown that moisture will readily degrade or remove the aluminum coating from a reflector (Reference 6).

Table 3-16

EFFECTS OF SEPARATOR VOLATILES ON REFLECTOR EMISSIVITY

Reflector	Separator	Exposure	Reflector		Emissivity		
			No.	Side	Composite No. 1	Composite No. 2	Composite No. 3
Double-goldized Kapton	None	None, control	1	1	0.038	0.032	0.029
			1	2	0.023	0.034	0.027
	Nomex HT-96	400°F for 6 hours	1	2	0.034	0.026	0.024
			2	1	0.029	0.024	0.025
			2	2	0.027	0.024	0.028
			3	1	0.028	0.024	0.024
			1	2	0.028	0.031	0.027
	Nomex HT-287		2	1	0.027	0.026	0.028
			2	2	0.031	0.030	0.036
			3	1	0.029	0.026	0.033
			1	2	0.027	0.027	0.031
			2	1	0.028	0.027	0.041
	Dacron B4A		2	2	0.026	0.025	0.031
			3	1	0.030	0.026	0.031
Double-aluminized Kapton	None	None, control	1	1	0.033	0.035	0.035
			1	2	0.033	0.034	0.035
	Nomex HT-96	400°F for 6 hours	1	2	0.034	0.034	0.032
			2	1	0.031	0.034	0.034
			2	2	0.031	0.031	0.034
			3	1	0.031	0.032	0.034
	Nomex HT-287		1	2	0.041	0.033	0.032
			2	1	0.034	0.032	0.034
			2	2	0.034	0.033	0.032
			3	1	0.031	0.033	0.033
	Dacron B4A		1	2	0.033	0.033	0.034
			2	1	0.032	0.033	0.034
			2	2	0.032	0.033	0.033
			3	1	0.034	0.033	0.034
Double-goldized Mylar	None	None, control	1	1	0.029	0.029	0.028
			1	2	0.029	0.029	0.028
	Nomex HT-96	400°F for 6 hours	1	2	0.052	0.027	0.025
			2	1	0.065	0.024	0.025
			2	2	0.032	0.022	0.029
			3	1	0.031	0.026	0.025
	Nomex HT-287		1	2	0.030	0.025	0.024
			2	1	0.027	0.026	0.023
			2	2	0.030	0.026	0.025
			3	1	0.037	0.030	0.031
	Dacron B4A		1	2	0.027	0.028	0.027
			2	1	0.029	0.032	0.028
			2	2	0.026	0.026	0.028
			3	1	0.027	0.030	0.028

3.5.1 Moisture Degradation Test Procedure

Two tests were designed and conducted to determine the effect of moisture on the DGK and DGM reflector candidates being considered for ILRV application. Testing of aluminized reflectors was not necessary because of the availability of previous test data. The first test was designed to simulate a severe between-flights ground environment. The test specimens were placed in a 5 ± 1 percent salt fog atmosphere at 100 percent relative humidity and at $90 \pm 3^\circ\text{F}$ for 96 hours. In the second test, designed to simulate a severe high-temperature water-vapor environment during reentry, the test specimens were subjected to a 300°F steam environment for 6 hours. The test specimens were suspended vertically in the salt-fog atmosphere and were horizontal in the steam test.

Each test specimen consisted of a stack of three reflector sheets with the outer reflector sheets each separated from the inner sheet by a separator, i. e., a total of three reflector sheets and two separator sheets in each composite specimen. The composite specimens were 6 by 6 inches. Each of the three candidate separators, Nomex HT-96, Nomex HT-287, and Dacron B4A, were tested with the DGM and DGK reflectors.

The degradation on each face of the reflector sheets exposed to the test environments was determined by a tape adhesion test in which a piece of Scotch No. 250 tape is applied to the surface of the specimen by rolling it with a 0.9-lb rubber roller. After 5 minutes the tape is removed by pulling in such a manner that a peeling force is applied to the bond between the tape and the specimen surface. The tape surface and specimen face are then examined for evidence of transfer of reflector metal from the specimen to the tape. These tests were performed at $70 \pm 5^\circ\text{F}$ and 40 to 60-percent relative humidity.

The tape test evaluates the effect of any moisture degradation on the adhesion of the metal layer to the substrate material. The metal removal forces exerted by the tape should be much greater than any actual removal forces experienced in an ILRV application. This plus the severe environments chosen for the tests appear to provide for conservative data on the effects of moisture on the metal adhesion.

3.5.2 Moisture Degradation Test Results

The tape adhesion test results are shown in Table 3-17. Also shown are tape adhesion test results for control samples which were not exposed to either of the test environments. No reflector metal was lost on any of the control samples. The tape adhesion test results on the DGK specimens exposed to the salt-fog environment showed no metal loss, except for one reflector face. The 20-percent loss on the No. 3 specimen of DGK/Nomex 287 appears inconsistent with the rest of the data and may have been due to a material anomaly. The DGM reflectors exposed to the salt-fog environment sustained metal loss when used with the Nomex materials. No metal loss was noted on the DGM reflectors used with the B4A separators in the salt fog test.

Gold was removed by the tape adhesion test from most of the reflector surfaces exposed to the 300°F steam. As in the salt-fog tests, the degradation of the DGM appears to be greater than that of the DGK. This may be due to the DGM fabrication problems reported by the manufacturer. The metal loss on the DGM reflectors with B4A separators appears to be much greater than with the Nomex separators. It should be noted that there is no apparent consistent data trend which show that the outer reflector faces of each composite sample were degraded more or less than the inner reflector faces that were in contact with separators. Specimen 1, face 1 and Specimen 3, face 2 were the outer reflector faces of each composite. The reasons for the large differences in amount of metal removed from reflector surfaces within a given composite are not known. One possible reason for the variation in adhesion of the gold to the Kapton is surface contamination of the Kapton prior to deposition of the gold. The variation in adhesion of the gold to the Mylar is probably due to the gold deposition problems noted previously.

3.5.3 Moisture Degradation—Conclusions and Recommendations

The test data indicate that the system design must provide for adequate purging of condensibles from the MLI during reentry if temperatures of 300°F are reached. The data also indicate that control of the condensibles within the MLI while the vehicle is on the ground would be necessary if DGM reflectors were used. It appears, however, that control of the condensibles within the MLI while the vehicle is on the ground may not be required for preventing metal adhesion degradation to DGK reflectors.

Table 3-17
MOISTURE DEGRADATION TEST DATA

Reflector	Separator	Exposure	Specimen		Percent Metal Transfer Using Tape Adhesion
			No.	Side	
Double-goldized Kapton	None	None— control samples	1	1	0
			1	2	0
			2	1	0
			2	2	0
			3	1	0
			3	2	0
Double-goldized Mylar	None	None— control samples	1	1	0
			1	2	0
			2	1	0
			2	2	0
			3	1	0
			3	2	0
Double-goldized Kapton	Nomex HT-96	Salt fog 96 hours	1	1	0
			1	2	0
			2	1	0
			2	2	0
			3	1	0
			3	2	0
	Nomex HT-287		1	1	0
			1	2	0
			2	1	0
			2	2	0
			3	1	0
			3	2	20
	Dacron B4A		1	1	0
			1	2	0
			2	1	0
			2	2	0
			3	1	0
			3	2	0
Double-goldized Mylar	Nomex HT-96		1	1	80
			1	2	55
			2	1	5
			2	2	5
			3	1	1
			3	2	20
	Nomex HT-287		1	1	0
			1	2	2
			2	1	50
			2	2	10

Table 3-17
MOISTURE DEGRADATION TEST DATA (Continued)

Reflector	Separator	Exposure	Specimen		Percent Metal Transfer Using Tape Adhesion	
			No.	Side		
Double-goldized Mylar	Nomex HT-287	Salt fog 96 hours	3	1	0	
			3	2	0	
	Dacron B4A	1	1	0		
		1	2	0		
		2	1	0		
		2	2	0		
		3	1	0		
		3	2	0		
Double-goldized Kapton	Nomex HT-96	Steam at 300 °F for 6 hr	1	1	75	
			1	2	0	
			2	1	0	
			2	2	0	
			3	1	25	
			3	2	0	
	Nomex HT-287	1	1	95		
		1	2	5		
		2	1	80		
		2	2	4		
		3	1	100		
		3	2	5		
	Dacron B4A	1	1	95		
		1	2	0		
		2	1	0		
		2	2	85		
		3	1	0		
		3	2	0		
	Double-goldized Mylar	Nomex HT-96		1	1	98
				1	2	60
			2	1	40	
			2	2	0	
			3	1	98	
			3	2	30	
Nomex HT-287			1	1	60	
			1	2	20	
			2	1	50	
			2	2	50	
			3	1	70	
			3	2	20	

Table 3-17
MOISTURE DEGRADATION TEST DATA (Continued)

Reflector	Separator	Exposure	Specimen		Percent Metal Transfer Using Tape Adhesion
			No.	Side	
Double-goldized Mylar	Dacron B4A	Steam at 300°F for 6 hr	1	1	100
			1	2	70
			2	1	100
			2	2	95
			3	1	100
			3	2	80

The 300°F steam is a severe environment which may not be representative of the ILRV application as well as other future applications of MLI. Consequently, additional moisture degradation tests at temperatures between 100° and 300°F are recommended.

3.6 OUTGASSING TESTS

The outgassing characteristics of the materials are of interest because of the effect outgassing has on the interstitial gas pressure within the MLI, which in turn affects the thermal performance of the MLI. Outgassing measurements were accomplished on the three candidate separator materials (Nomex HT-287, Nomex HT-96, and Dacron B4A) and on the DGK reflector material.

3.6.1 Outgassing Test Procedure

The outgassing measurements were obtained by monitoring a specimen weight history while subjecting it to the test environments. The test procedure included the following steps:

- A. Install specimen in test chamber.
- B. Allow specimen to reach constant weight before purging with dry nitrogen. (This was not done on the first test (Nomex HT-287).)

- C. Purge chamber with dry nitrogen for 1 to 1-1/2 hours.
- D. Allow specimen to reach constant weight before evacuation of chamber.
- E. Evacuate chamber. (A pressure of 10^{-5} torr was reached in approximately 10 minutes; pressure as low as 4×10^{-7} torr was eventually reached.)
- F. Allow specimen to reach constant weight before heating.
- G. Heat specimen to 200 °F at a rate of approximately 8 °F per minute.
- H. Allow specimen to reach constant weight at 200 °F before increasing temperature.
- I. Increase temperature of separator materials to 400 °F at a rate of approximately 8 °F/minute. (The maximum DGK specimen temperature was 350 °F as this was the maximum possible due to the high specimen reflectivity and the small heater used.)
- J. Allow specimen to reach constant weight at the maximum temperature before turning off heater.
- K. Turn off heater.
- L. Allow specimen to reach constant weight before repressurizing chamber.
- M. Repressurize chamber. (Air was used for all tests except the last (DGK), in which dry nitrogen was used.)

One 3- by 3-in. test specimen was used for each of the Nomex HT-287, Nomex HT-96, and DGK materials. Four 3- by 3-in. pieces of the Dacron B4A material were used as the B4A test specimen because of the very light weight of this material.

The weight measurements were obtained with a Cahn RH electrobalance which was mounted inside an Edwards high-vacuum chamber (Figure 3-29). The weight measurements were recorded continuously on a Honeywell chart recorder. The specimen was heated by a resistance heater placed directly below the specimen. A copper constantan thermocouple (2 mil) was attached at the center of the specimen to monitor specimen temperature which was recorded on a Leeds-Northrup potentiometer recorder. The test apparatus and setup are shown in Figure 3-30.

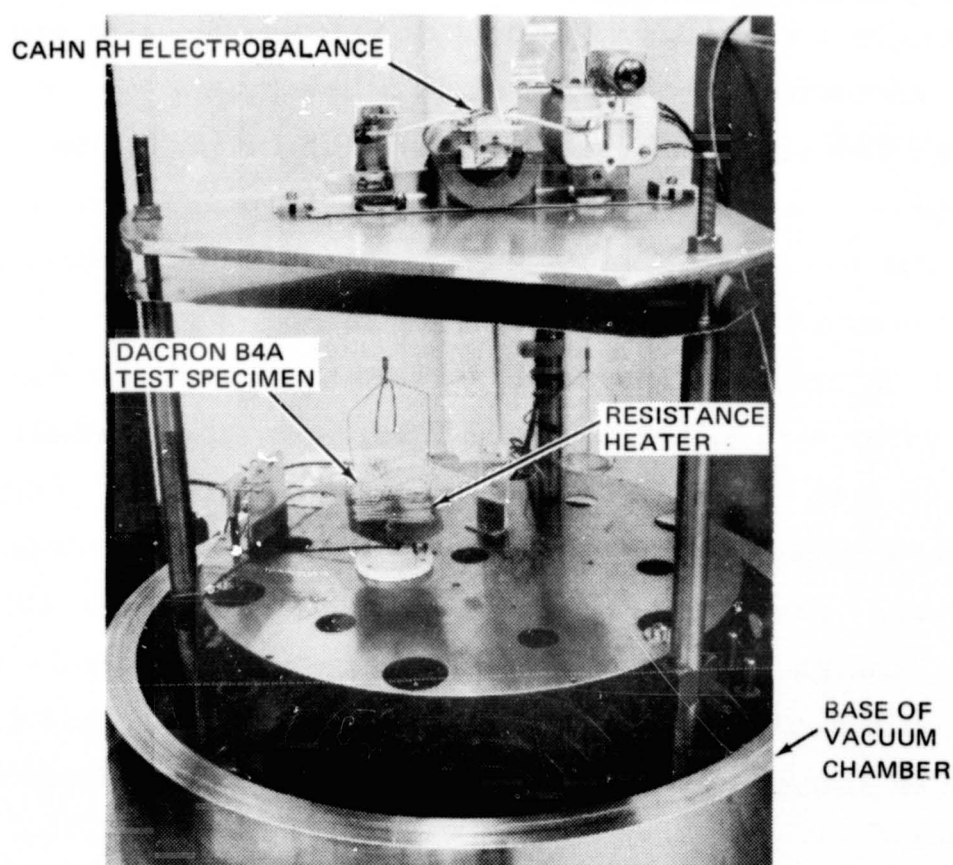


Figure 3-29. Outgassing Test Setup Inside Vacuum Chamber

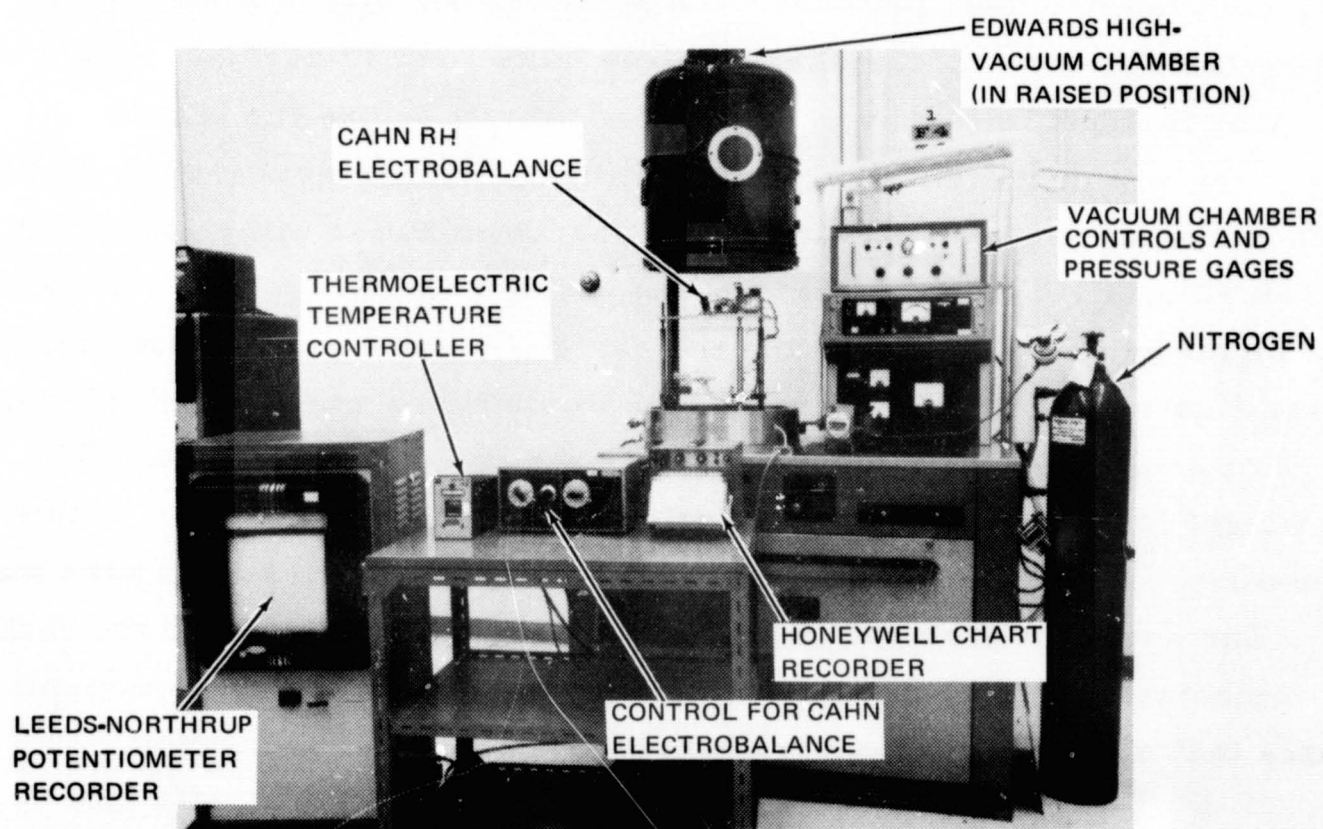


Figure 3-30. Outgassing Test Apparatus

3.6.2 Outgassing Test Results

The outgassing test results are shown in Figures 3-31 through 3-34 and in Table 3-18. As shown, both of the Nomex materials lost weight in both nitrogen purge and vacuum environments. The elevated temperatures, however, appear to have had little effect on the outgassing of the Nomex materials. The results indicate that, for the Nomex materials, approximately 1-1/2 hours are needed in the dry nitrogen gas to remove as much of the outgassing products (probably water) as possible. The results also indicate that after 4 to 4-1/2 hours in a vacuum, there would be no further outgassing. In fact, 86 and 77 percent of the outgassing of the Nomex HT-287 and HT-96 materials, respectively, in a vacuum, was completed in the first hour of vacuum. The slight increase in weight during the 400°F period of testing of the Nomex materials appears to be a test anomaly and was also experienced with heating of the Dacron B4A material. It is felt that this is probably due to some effect of the heat on the very sensitive Cahn electrobalance.

The Dacron B4A specimen lost essentially all of its weight in air prior to purging with the dry nitrogen gas. The relative humidity at the time of installing the specimen in the chamber was quite low (19 percent) and it is evident that the specimen was prepared and stored before the test in a different environment from that in the chamber. There appeared to be no significant outgassing of the Dacron B4A specimen due to either the room temperature or elevated temperature and vacuum environments. The effect of heat on the electrobalance during the 200°F period was apparent, but occurred in a relatively short time, after which there was no gradual weight loss. This indicates that there was no outgassing of the specimen. The small weight loss during the 400°F period may also have been due to this test anomaly. Since the weight loss was in air, it is felt that this loss was water. The apparent ease with which the water was removed and the lack of an immediate increase in weight when the chamber was repressurized indicates that water is not readily absorbed or adsorbed by Dacron.

The outgassing of the DGK specimen appears to have been affected much more by elevated temperatures than were the Nomex and Dacron separator

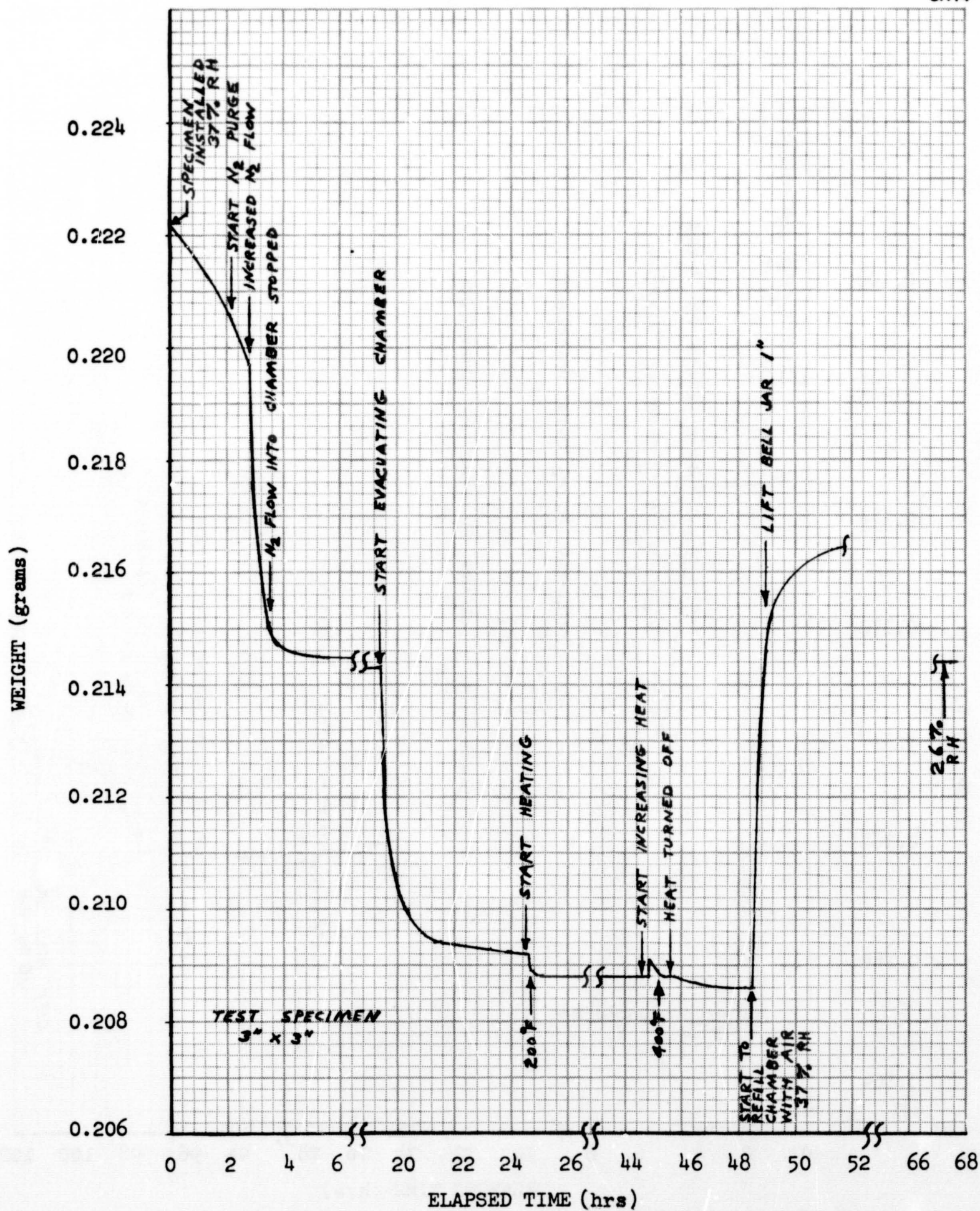


Figure 3-31. Outgassing of Nomex HT-287

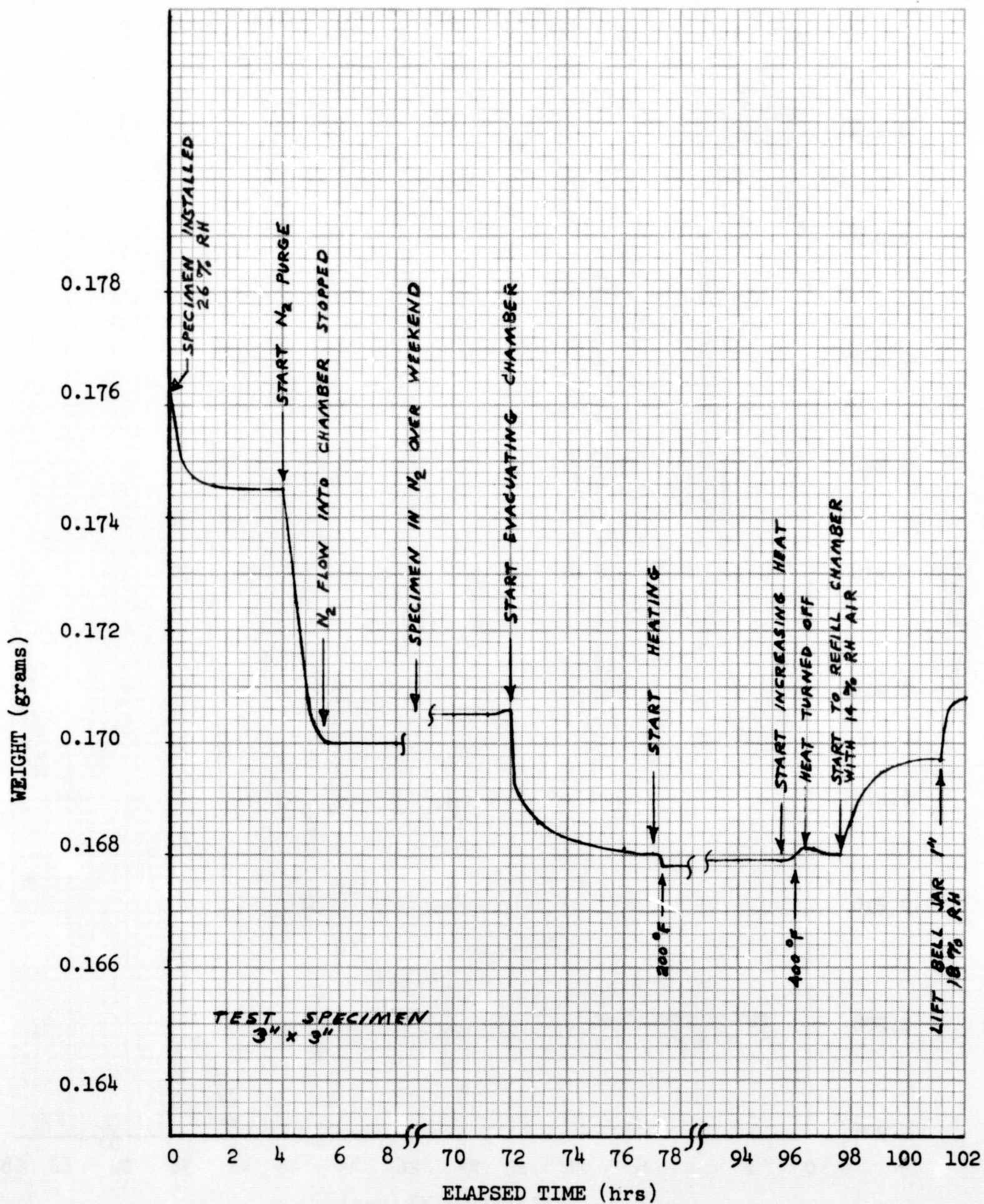


Figure 3-32. Outgassing of Nomex HT-96

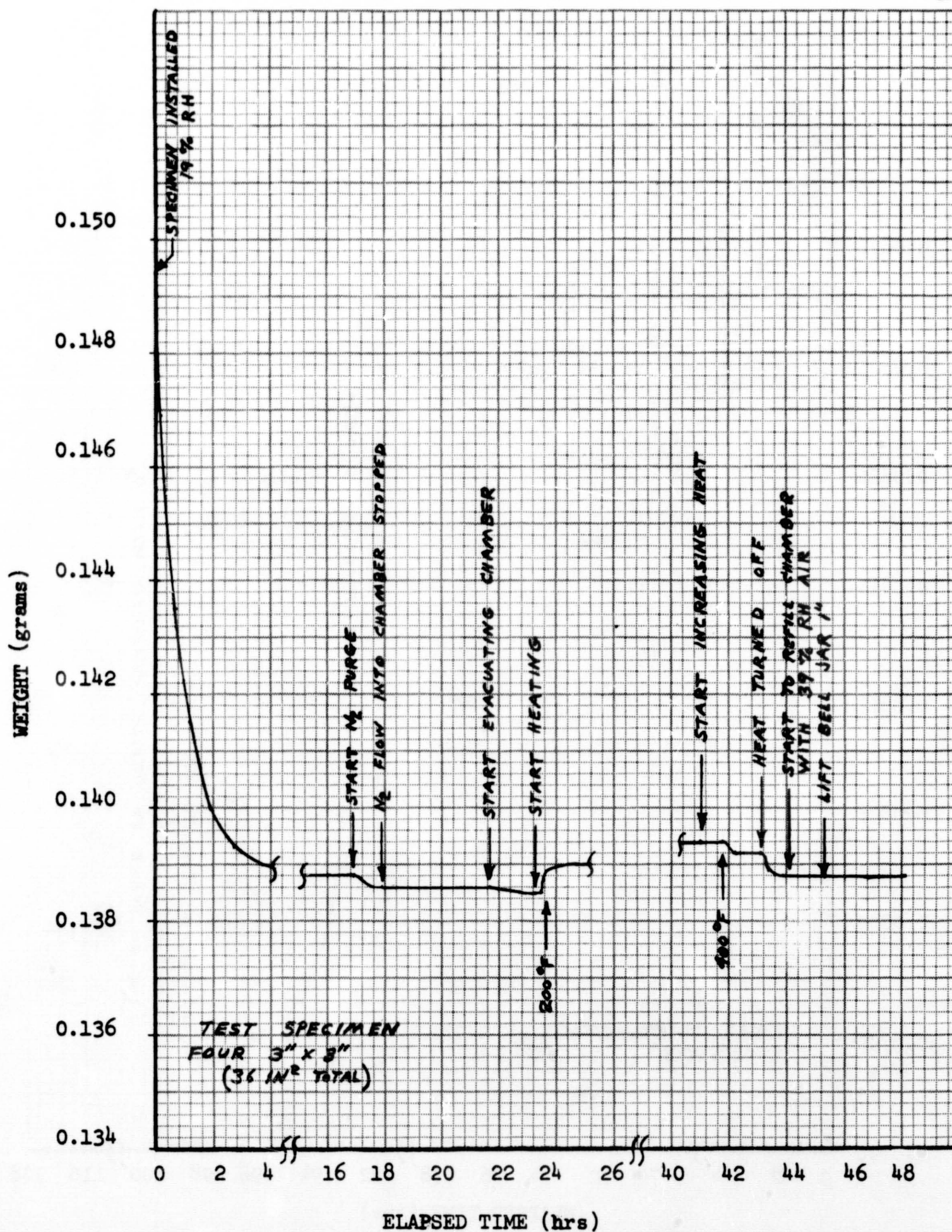


Figure 3-33. Outgassing of Dacron B4A

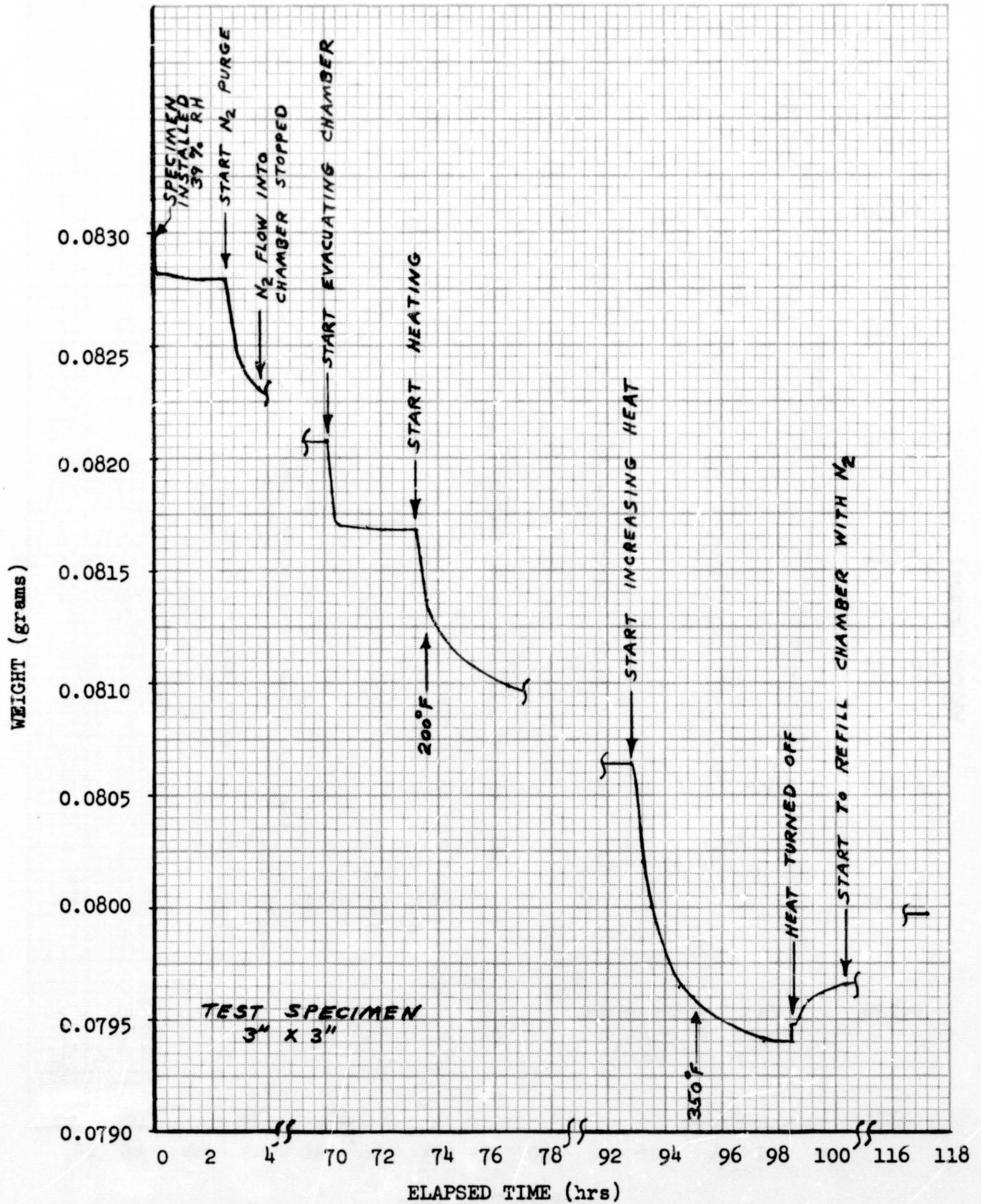


Figure 3-34. Outgassing of Double-Goldized Kapton

Table 3-18
WEIGHT LOSS DUE TO OUTGASSING

Material	Weight Loss Due to Vacuum* (lb/ft ²)	Weight Loss Due to 200°F (lb/ft ²)	Weight Loss Due to 400°F (lb/ft ²)	Total Weight Loss (lb/ft ²)	*⊕Weight Loss After Purging (Percent)
Nomex HT-287	18.0×10^{-5}	1.45×10^{-5}	0.0×10^{-5}	19.45×10^{-5}	2.6
Nomex HT-96	9.17×10^{-5}	0.35×10^{-5}	-	9.52×10^{-5}	1.6
Dacron B4A	0.088×10^{-5}	-	0.176×10^{-5}	0.26×10^{-5}	0.2
DGK	1.48×10^{-5}	3.63×10^{-5}	4.37×10^{-5}	9.49×10^{-5}	3.5

*Constant weight in dry N₂ prior to evacuation.

⊕Weight of thermocouple wire estimated to be 4.5×10^{-3} gram and was subtracted from total measured weight. Percent of total initial weight which was lost due to vacuum and temperature.

materials. In fact, as shown in Figure 3-34 and Table 3-18, most of the weight loss occurred during the elevated temperature test period.

3.6.3 Outgassing Tests—Conclusions and Recommendations

The test results indicate that the Nomex separator materials will outgas more than the Dacron material (Table 3-18). The weight loss after purging for the Nomex materials varied from 1.6 to 2.6 percent, whereas the weight loss for the Dacron B4A was quite low at 0.2 percent. The weight loss after purging (3.5 percent) for the DGK material was higher than anticipated. However, since the weight loss for the DGK material occurred at the elevated temperatures, which were higher and of longer duration than in the baseline ascent trajectory, the total outgassing in the baseline application would be much less. Also, only the outer layers of MLI would be elevated in temperature during a baseline ascent. As a result, it was concluded that the

outgassing characteristics of the materials tested were not severe enough to cause rejection of the materials as candidates.

Three areas are recommended for future study of outgassing characteristics. First, a determination of the products leaving the surface of the material should be made. Vacuum chamber equipment was not available which would allow this within the scope and schedule of this study. Second, a repeat of the tests using elevated-temperature purge gas instead of the room-temperature purge gas would provide valuable data on the advantages of heating the purge gas. Third, tests are recommended on materials which have been cooled to cryogenic temperatures after being purged. These tests would provide data on the effect of cryo-pumping on the outgassing rate.

3.7 THERMAL EXPANSION AND CONTRACTION TESTS

Compatible thermal expansion and contraction between the reflectors, separators, and face-sheet materials in an MLI composite are required to ensure that the support straps in the face sheets will carry the structural load at all times. The face-sheet straps must always have a contraction greater than that of the reflector and separator materials at a temperature lower than ambient and an expansion less than that of the reflector and separator at a temperature higher than ambient. To allow selection of a face-sheet system with the proper thermal expansion and contraction characteristics, testing of the candidate MLI materials was performed.

3.7.1 Test Specimens

Fifteen specimens were tested as shown in Table 3-19. These included all candidate composite materials except the Dacron B4A net separator. Because of the diagonal weave configuration of this net, it could not be readily tested for thermal expansion and contraction characteristics. However, data is available from contract NAS 8-21400 (Reference 1) for a Dacron 15413 net, and the thermal expansion and contraction characteristics

Table 3-19
THERMAL EXPANSION TEST SPECIMENS

Reflectors

Double-goldized Kapton (25 to 30 gage)
Double-aluminized Kapton (25 to 30 gage)
Double-goldized Mylar (25 to 30 gage)

Separators

Nomex HT-287, warp direction
Nomex HT-287, fill direction
Beta glass 1653, warp direction
Beta glass 1653, fill direction

Face-Sheet Systems

Polyimide/Nomex HT-287
Silicone/Nomex HT-287
Viton/Nomex HT-287
Teflon/Nomex HT-287
Polyimide/Beta glass 81677
Silicone/Beta glass 81677
Viton/Beta glass 81677
Teflon/Beta glass 81677

of this net should be similar to those of Dacron B4A. The Nomex HT-96 separator material was not included, as the thermal expansion and contraction characteristics of this material would be expected to be similar to those of the Nomex HT-287 material.

The reflector and separator samples were 0.3 by 10.0-in. strips which formed a loop about the end of the quartz dilatometer rider rod (Figure 3-35). The face-sheet system specimens consisted of two 0.2 by 4.0-in. strips assembled into a modified holder (Figure 3-36) which provided a simulated loop for measurement purposes.

3.7.2 Test Setup

Schematics of the quartz tube dilatometer linear transducer apparatus system used for the measurement of the linear thermal expansion and contraction are shown in Figures 3-35, 3-36, and 3-37. Figure 3-38 is a photograph of the test setup. Electrical heating by means of nichrome wire

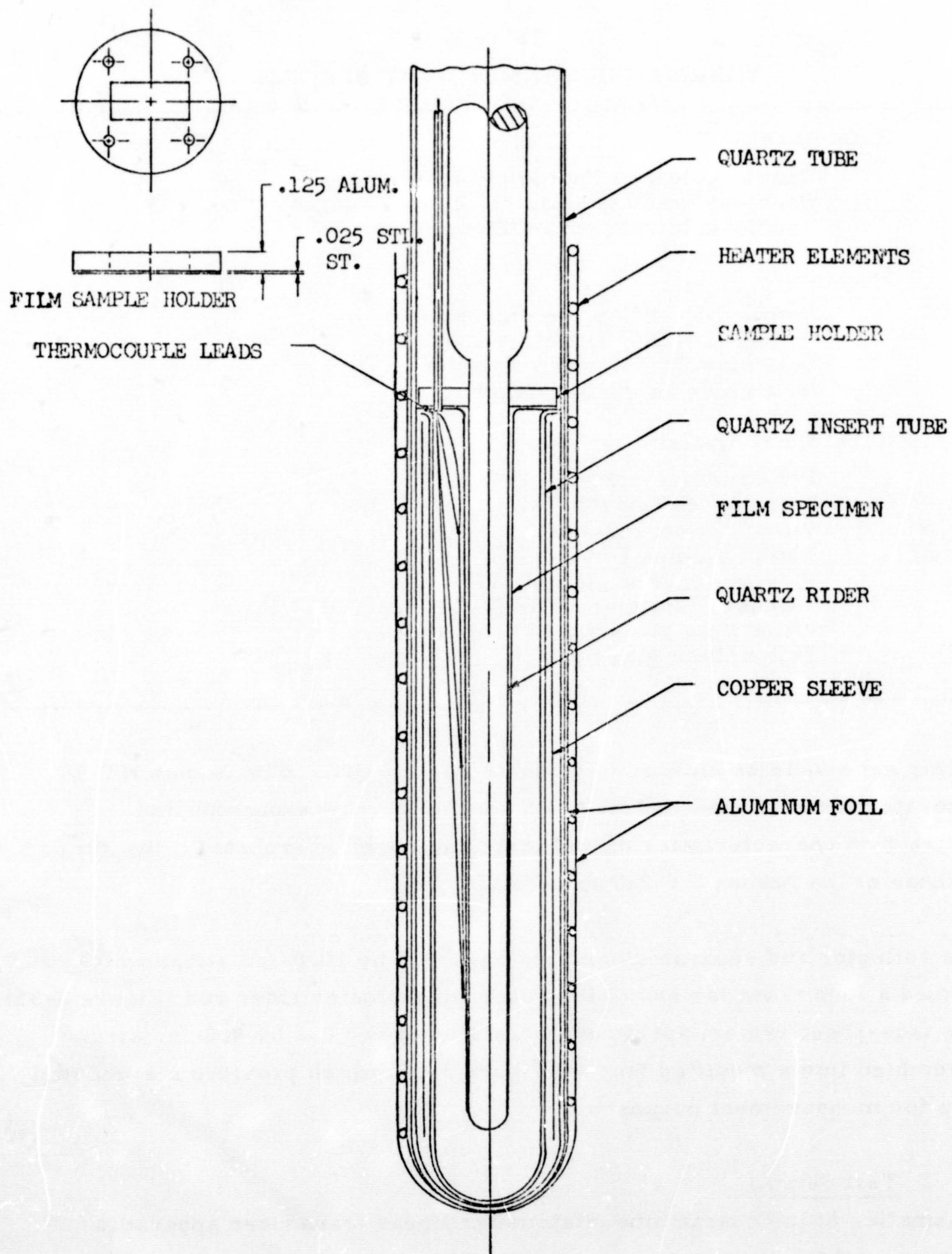


Figure 3-35. Sample Area and Flexible Film Holder for Reflector and Separator Specimens

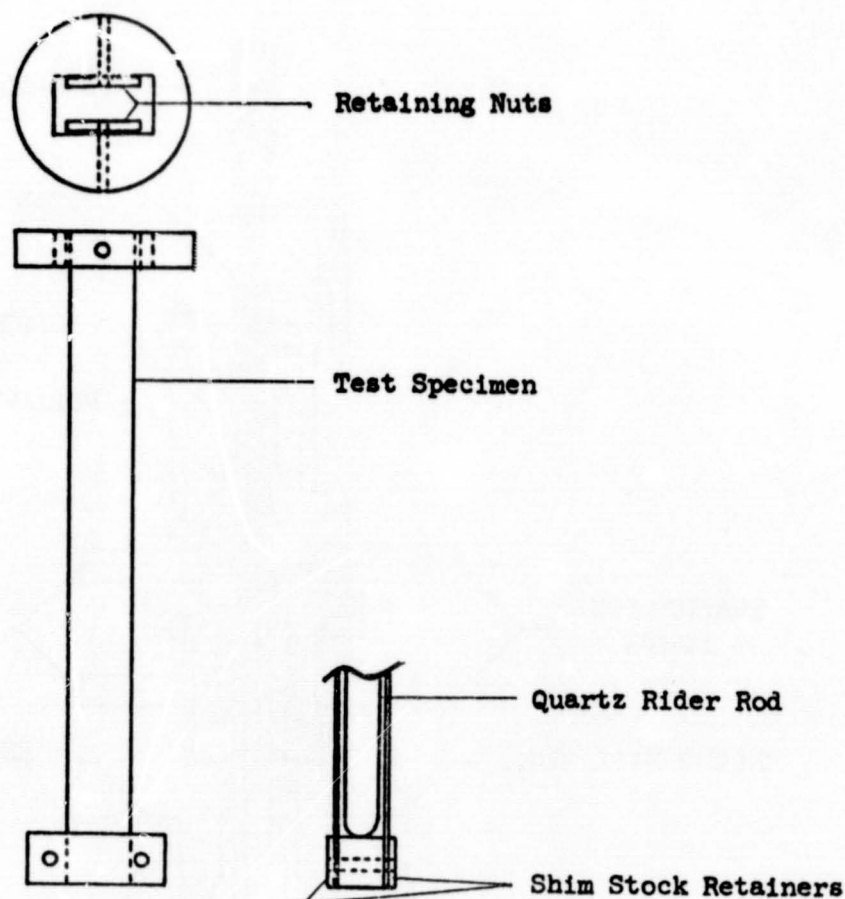


Figure 3-36. Specimen Holder for Nonflexible Strip Specimens (Face Sheets)

wrapped around the quartz tube provided more precise temperature control than possible when an exchange gas is employed as the sole means of energy transfer. Energy exchange by radiation was reduced by a layer of aluminum foil in the annular region between the quartz tube and the cryogen reservoir. A layer of foil was also placed between the heater and the quartz tube to shield the thermocouples from the 60-cycle heater power.

Three iron-constantan thermocouples were positioned along the sample length to monitor its temperature (Figure 3-35). Temperature readout was provided by a stepper switch, a dc preamplifier (Astrodata TDA 875), a Sandborn ac-dc preamplifier 150-1000, and a Sanborn 150 recorder. This system provided 20- μ v resolution, corresponding to a resolution of approximately $\pm 2^{\circ}\text{F}$ below -320°F . In measuring higher temperatures, sensitivity was sacrificed to permit measurement in a wide temperature range without numerous calibrations of equipment during the test. This decrease in sensitivity, coupled with increased output of the thermocouples at the higher temperatures, decreased the resolution of temperature to $\pm 3.5^{\circ}\text{F}$.

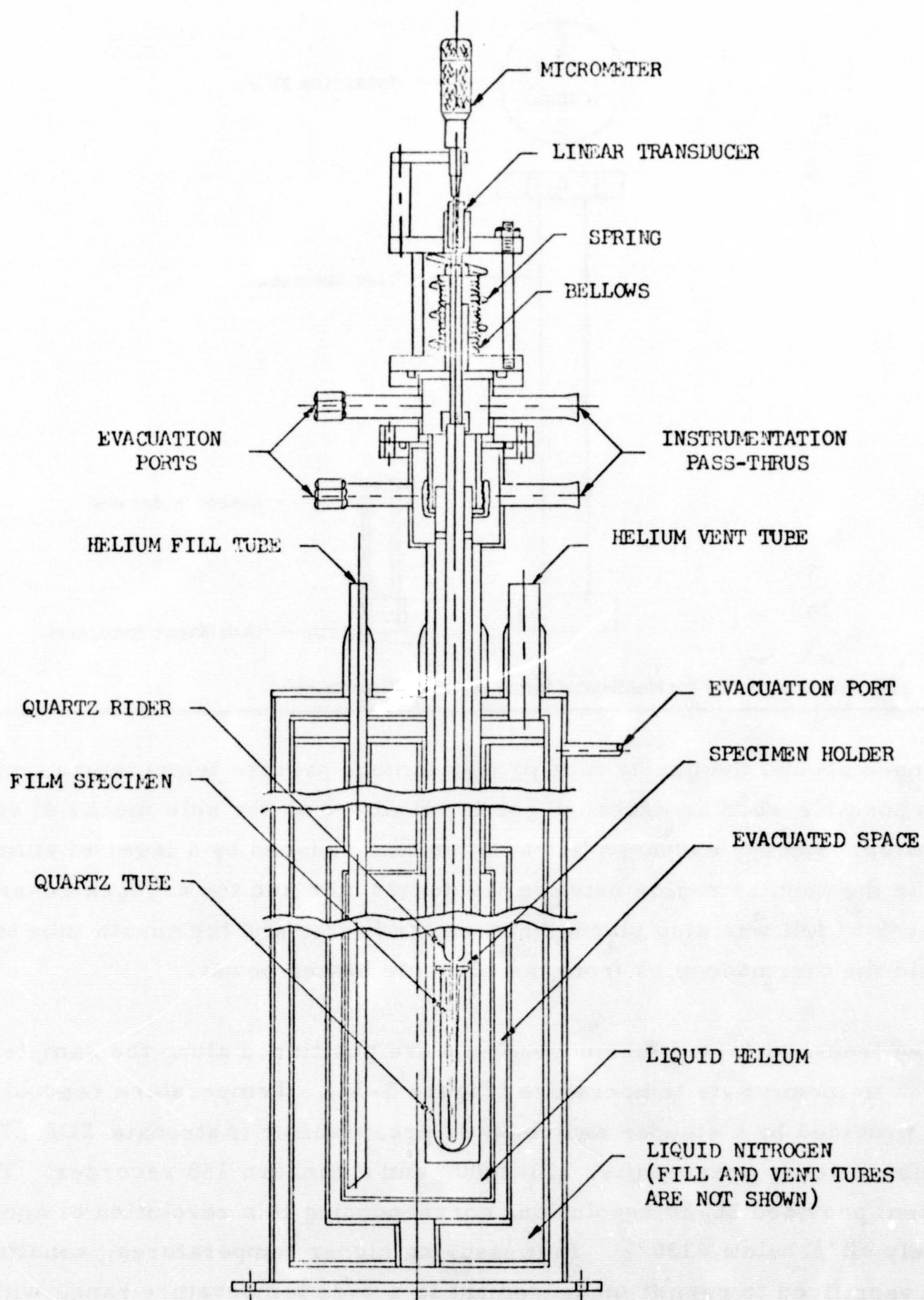


Figure 3-37. Thermal Expansion Test Apparatus

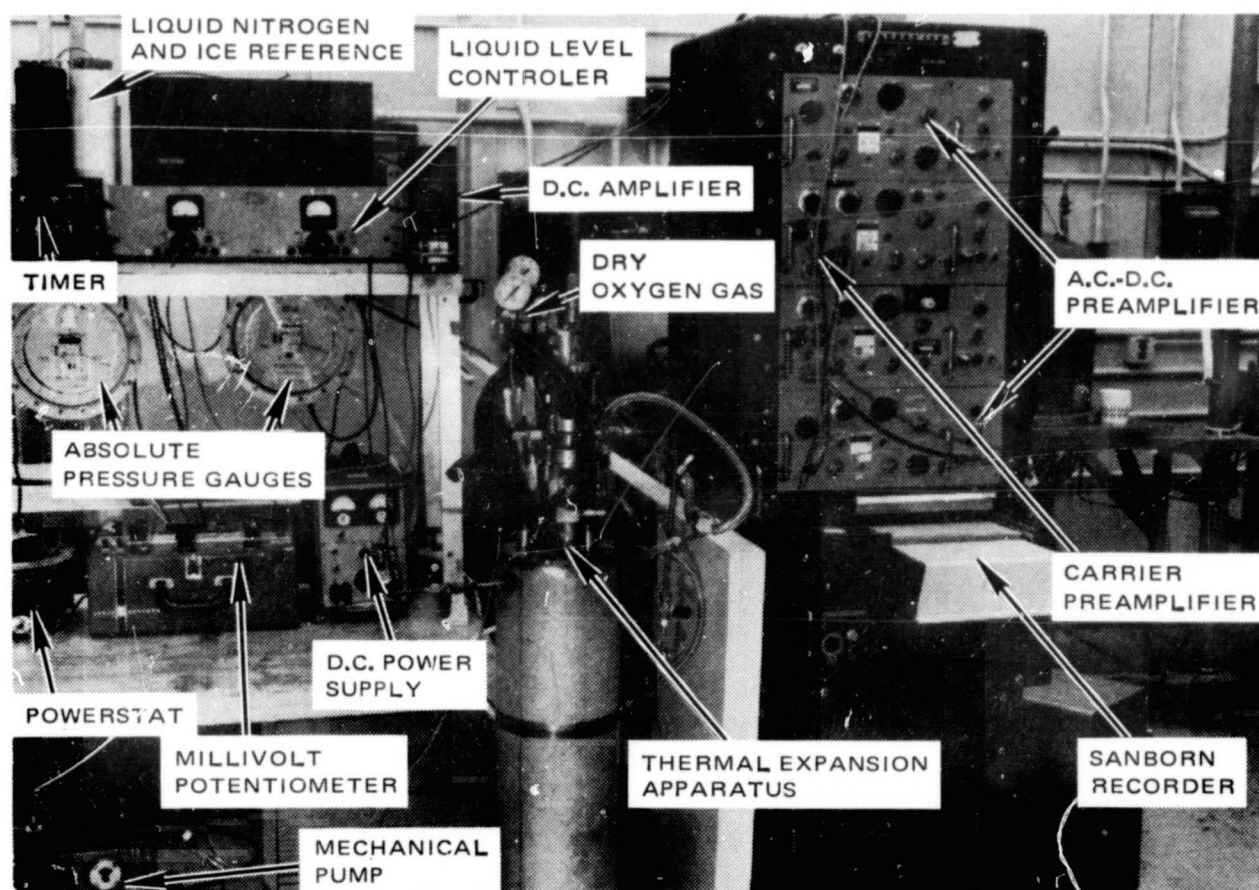


Figure 3-38. Thermal Expansion Test Setup

Dimensional changes in sample length were transmitted to a linear displacement transducer by a quartz rider rod 0.5 in. in diameter (Figures 3-35, 3-36, and 3-37). The linear range of the transducer was 0.025 in.; and by using a Sanborn 150 Carrier preamplifier for readout, the least detectable change in length was 1×10^{-5} in. The range of the transducer was extended past the basic 0.025-in. range by moving the core of the transformer a precisely known distance in the appropriate direction whenever the limit of the linear range of the transducer was approached. Total expansion measurement thus could be extended to 1 in.

3.7.3 Test Procedure

After installation of a sample in the system, the sample area and heat transfer area were evacuated to about 30μ and then were back-filled with dry helium gas to a pressure of approximately 10 mm Hg. Initial specimen length was established at ambient temperature (70°F) and used as the reference length for subsequent measurements of length changes.

After the liquid-nitrogen guard was filled and the liquid-helium reservoir was precooled, liquid helium was transferred to the reservoir and the sample was allowed to cool to a temperature of approximately -430°F . The heat-exchange medium was evacuated to a pressure of approximately 30μ and was held at that pressure throughout the test. Sufficient electrical power was applied to the heater to obtain a sample heating rate of from 2 to 4°F per minute and to maintain sample temperature gradients within 7°F .

The boiloff rate of the liquid helium was such that it was possible to obtain the expansion values from -430°F to -320°F twice for each specimen. After the second set of values was obtained, the specimen was allowed to warm at the same rate to 300°F . Temperature and change in length were recorded continuously.

3.7.4 Test Results

The test results are shown in Figures 3-39, 3-40, and 3-41. Data points shown are taken from a smoothed curve of the original data. In addition, the thermal contraction characteristics of a Dacron separator are shown in Figures 3-40 and 3-41. This data was taken from Reference 1. These data for the DGK reflector material are also included in Figures 3-40 and 3-41 to facilitate a comparison of the expansion and contraction characteristics of the materials. No expansion or contraction was detectable for the Beta glass specimens (Figure 3-41) since the expansion or contraction of the Beta glass specimens and the quartz measuring apparatus are equal. The error introduced into the data for the other samples by the expansion or contraction of the apparatus was negligible and was not included. The data are believed to be accurate to approximately ± 5 percent. No data are shown for the Nomex HT-287 (fill) material below 75°F or for the Viton/Nomex face-sheet system above 140°F (Figure 3-40), as consistent values could not be obtained.

3.7.5 Thermal Expansion and Contraction—Conclusions and Recommendations

Selection of a face-sheet system includes consideration of the system weight, strength, and ability to withstand the anticipated environment as well as the thermal contraction and expansion characteristics. Selection of the face-sheet system is discussed in Section 9.

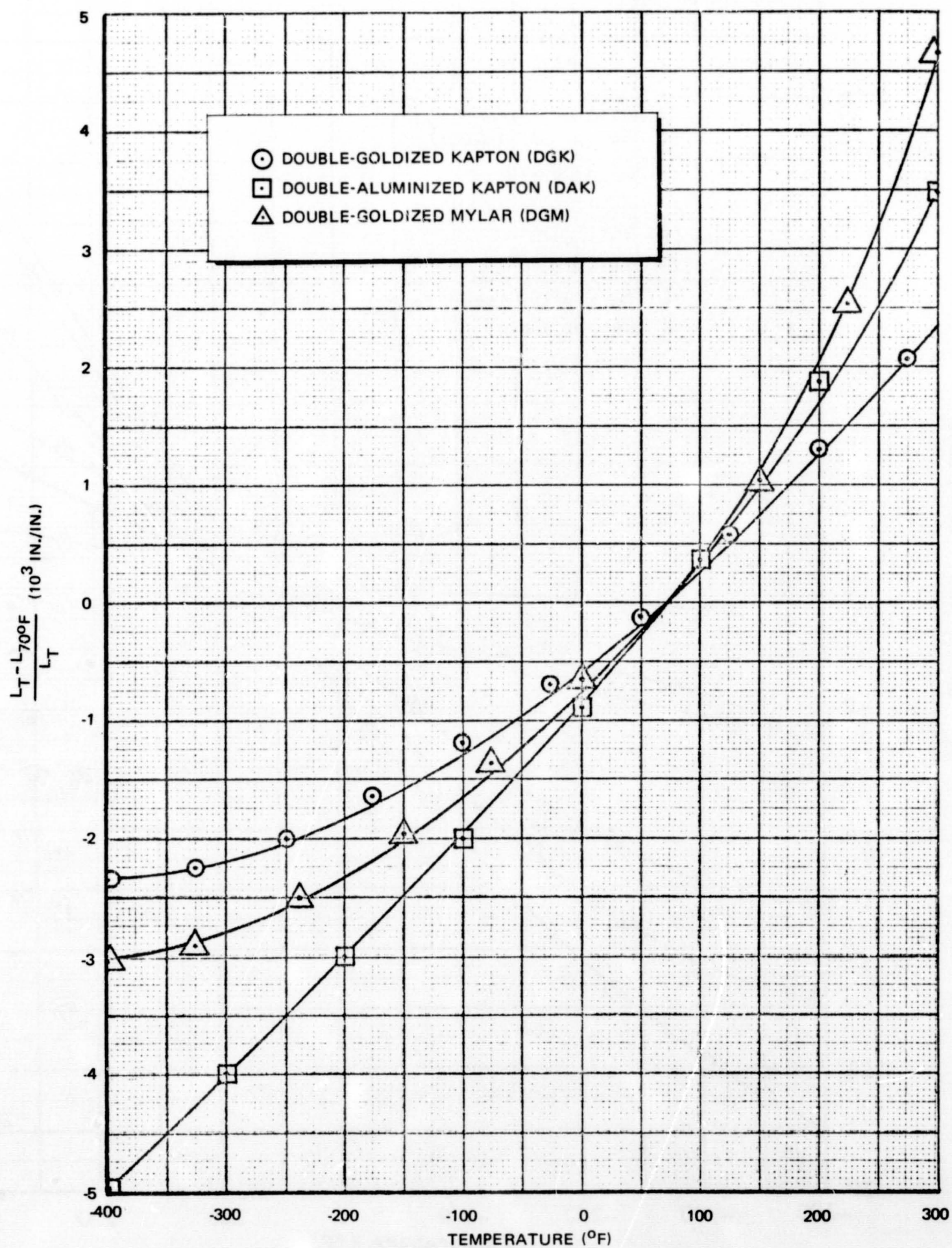


Figure 3-39. Thermal Expansion and Contraction of Reflector Materials

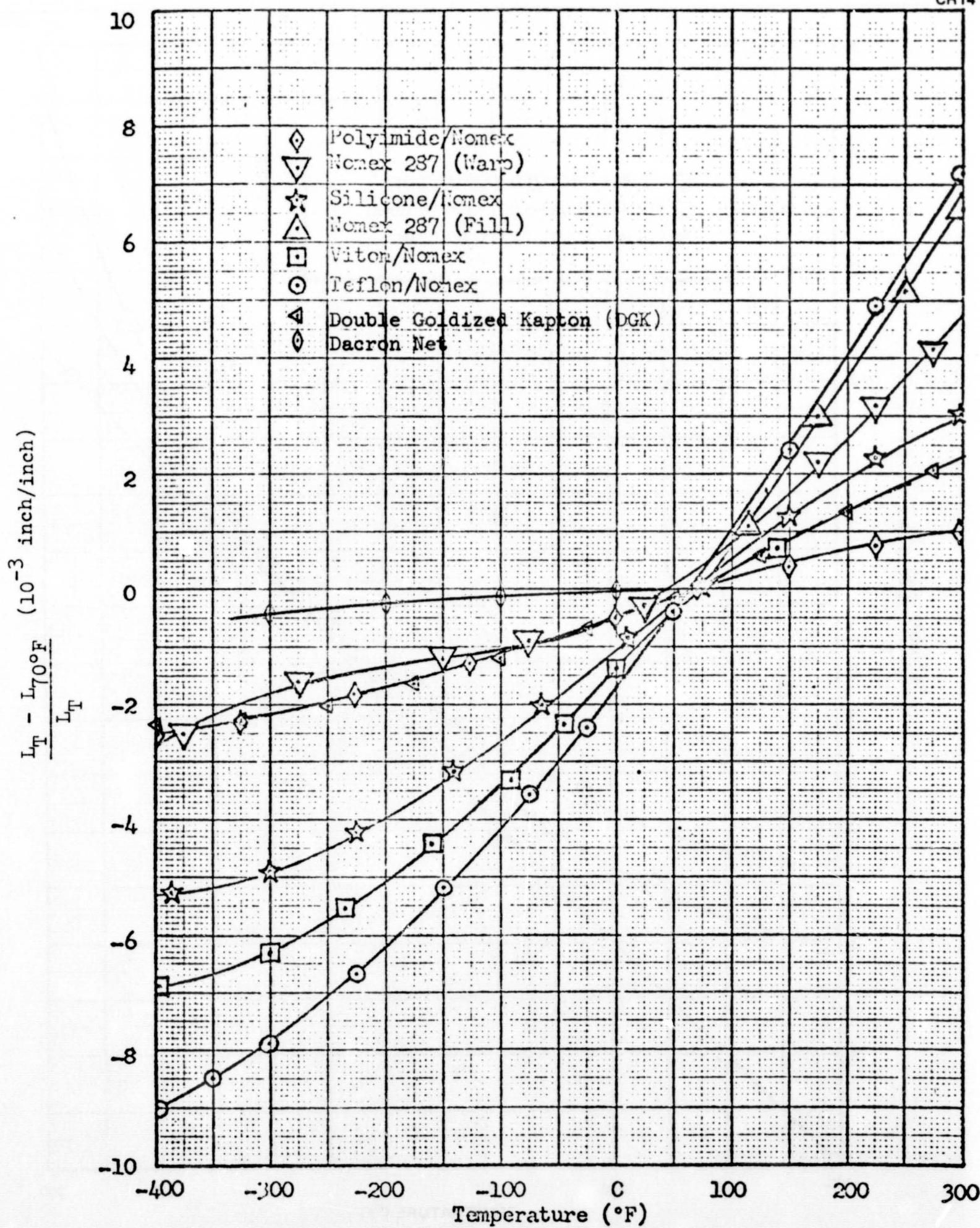


Figure 3-40. Thermal Expansion and Contraction of Nomex Face-Sheet Systems, DGK, and Dacron B4A.

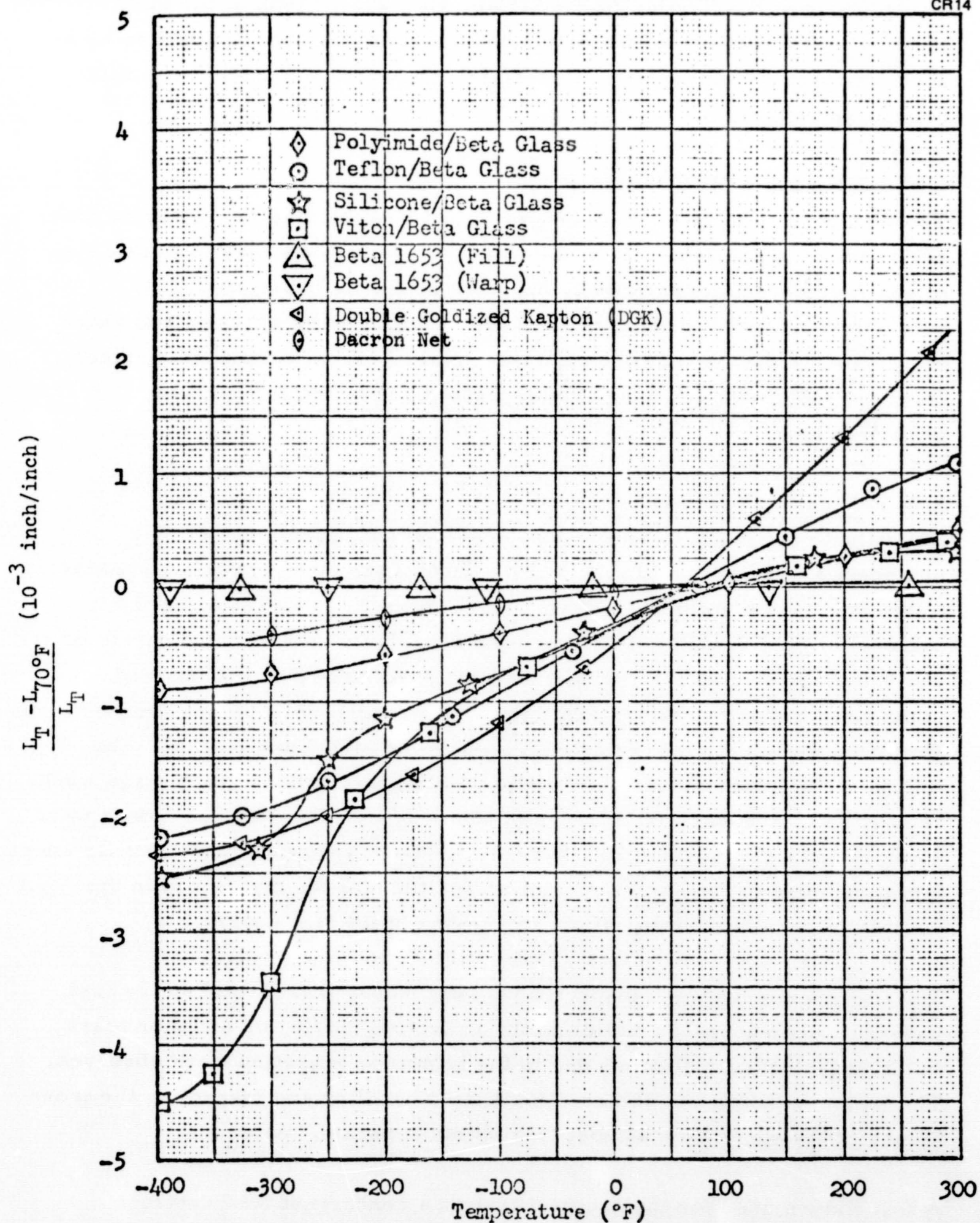


Figure 3-41. Thermal Expansion and Contraction of Beta Glass Face-Sheet Systems, DGK, and Dacron B4A

Using a loop of the flexible materials and a simulated loop of the thin, relatively stiff face-sheet materials as the test specimens appears to be a good approach to testing these materials and is recommended for similar tests in the future.

3.8 ACOUSTIC ENVIRONMENT TESTS

The MLI system to be used on the ILRV will be subjected to a dynamic load environment. Therefore, it is important to evaluate the effects of this type of environment on the various components of the MLI systems. In particular, dynamic loads such as those resulting from acoustic and shock environments may abrade the vapor-deposited gold or aluminum surfaces from the reflectors and seriously degrade the thermal performance of the system.

3.8.1 Acoustic Test Procedure

To evaluate the effect of an acoustic environment, specimens of four composites were tested (Table 3-20). Each of the three candidate separators was tested with a goldized reflector (specimens 2, 3, and 4) since the removal of gold resulting from possible abrasive action of the separators was the primary concern. The remaining specimen (No. 1) contained aluminized Mylar reflectors and therefore provided for a comparison between aluminum and gold surfaces as well as between Mylar and Kapton. The thinner DAM material was tested because 15-gage rather than 25-gage would be used for DAM material in a design application. The test specimens were 14 by 14 in. and contained 20 layer-pairs. Each specimen contained fasteners along one edge to maintain the relative positions of the layers within the composite during mounting of the specimens in the test fixture.

The test specimens were inspected visually before installation on the test fixture. No abnormal variation in the reflective coating or nicks or tears in the edges of the reflectors due to the trimming operation were observed. The fasteners along the one edge facilitated handling and inspecting the inner layers of the specimens without fraying the separator materials.

A test fixture used for the acoustic test on a concurrent MLI contract (Reference 7) was modified and used to hold the test specimens (Figure 3-42).

Table 3-20
TEST MATRIX FOR ACOUSTIC TEST

Specimen	Reflector	Separator
1	15-gage DAM (double-aluminized Mylar)	Dacron B4A
2	25-gage DGK (double-goldized Kapton)	Dacron B4A
3	25-gage DGK (double-goldized Kapton)	Nomex HT-96
4	25-gage DGK (double-goldized Kapton)	Nomex HT-287

Specimens are composed of 20 layer pairs, 14 x 14 in.

The modifications consisted of altering the frame which clamped the test specimens to the fixture. The test fixture was mounted in the MDAC progressive wave tube and was excited from the side opposite that which held

CR14

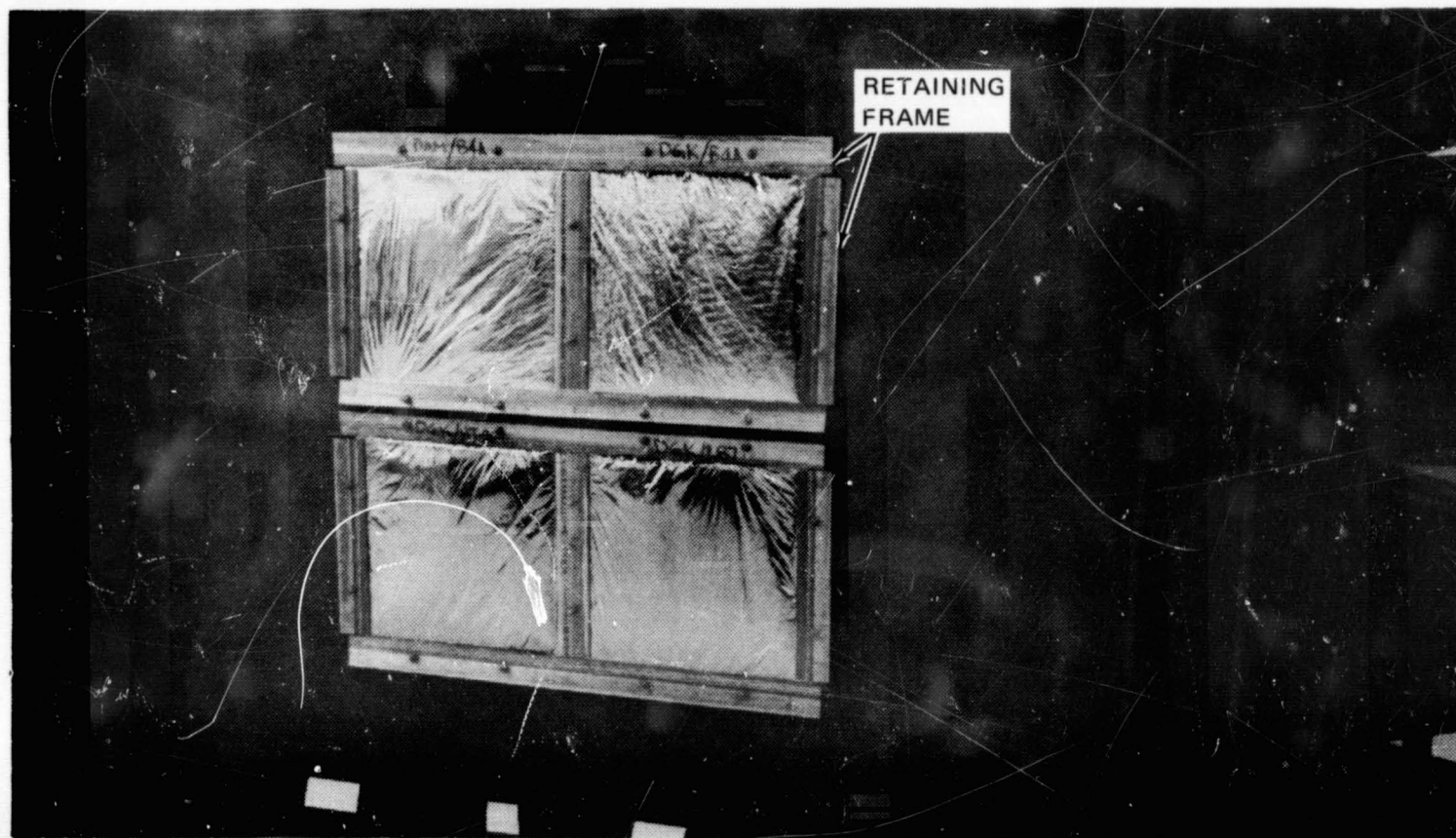


Figure 3-42. Test Specimens Mounted on Acoustic Test Fixture

the MLI samples. The response of the test panel was monitored by three microphones mounted in the progressive wave tube adjacent to the test fixture; one at each end and one at the center of the fixture.

The specimens were tested with an acoustic spectrum shaped like that expected in the vicinity of the ILRV orbiter secondary LH₂ tank (refer to Section 4) at 140-, 150-, and 160-db (overall) sound pressure levels. The narrow band frequency spectrums used in the tests are shown in Figures 3-43, 3-44, and 3-45. The first step in the test sequence consisted of exposing the specimens (simultaneously, as shown in Figure 3-42) to 140 db (overall) for 3 minutes. This was followed by removal of the clamping frame from the bottom and side of each specimen (Figure 3-46) and then by visual inspection of each layer of the composites. The clamping frames were then reattached to the test fixture and the above sequence was repeated for the 150- and 160-db (overall) test levels.

3.8.2 Acoustic Test Results

Inspection of the specimens did not reveal any metal removal or other damage to the surfaces of either the DAM or DGK reflectors from any of the acoustic test environments. The DAM/Dacron B4A and DGK/Dacron B4A specimens showed no tearing of the reflector or unraveling of the separator. However, the acoustic environment did tear the reflector sheets and unravel the separators in the DGK/Nomex HT-96 and DGK/Nomex HT-287 specimens, as shown in Figures 3-47 and 3-48. The separator unraveling of the Nomex HT-96 and Nomex HT-287 can also be seen in Figure 3-46. Tears were noticed in the DGK reflectors of specimens 3 and 4 after the 150-db run and these tears had propagated to lengths of 3 to 4 in. at the conclusion of the 160-db run. In general, the DGK/Nomex HT-287 system had more tearing than the DGK/Nomex HT-96 system. The results show the Nomex HT-96 to be the most susceptible to separator unraveling damage.

3.8.3 Acoustic Test—Conclusions and Recommendations

Since the maximum sound pressure levels expected in the vicinity of the ILRV baseline orbiter secondary LH₂ and LO₂ tanks used in this study are 153.8 and 147.5 db (overall), respectively, as compared to the highest test value of 160 db (overall), it can be concluded that none of the systems tested would sustain any degradation of the reflector surface in the reference ILRV orbiter application. Tearing of the reflectors, however, might be a

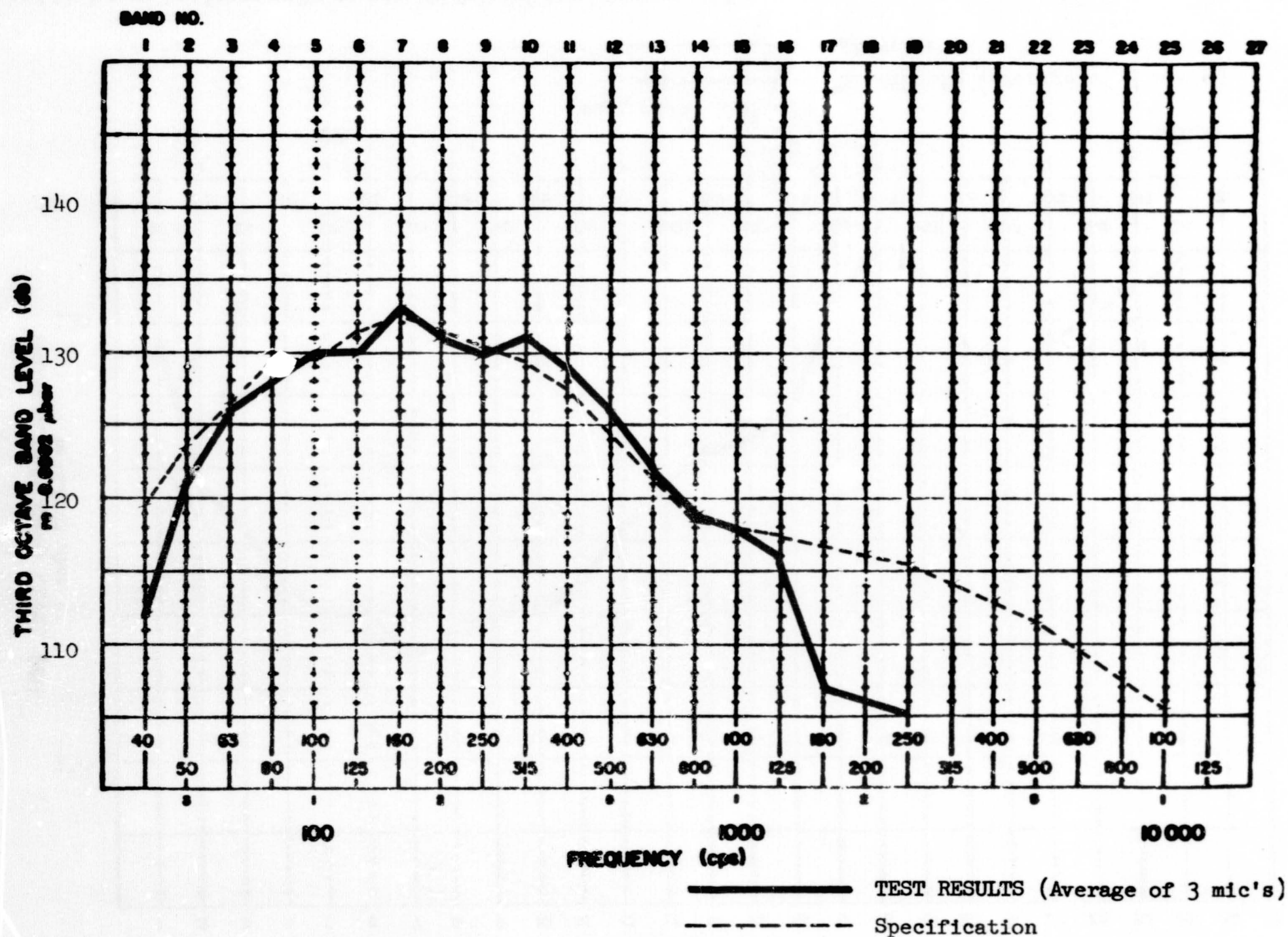


Figure S-43. Narrow-Band Frequency Spectrum for 140-db Overall Sound Pressure Level Test

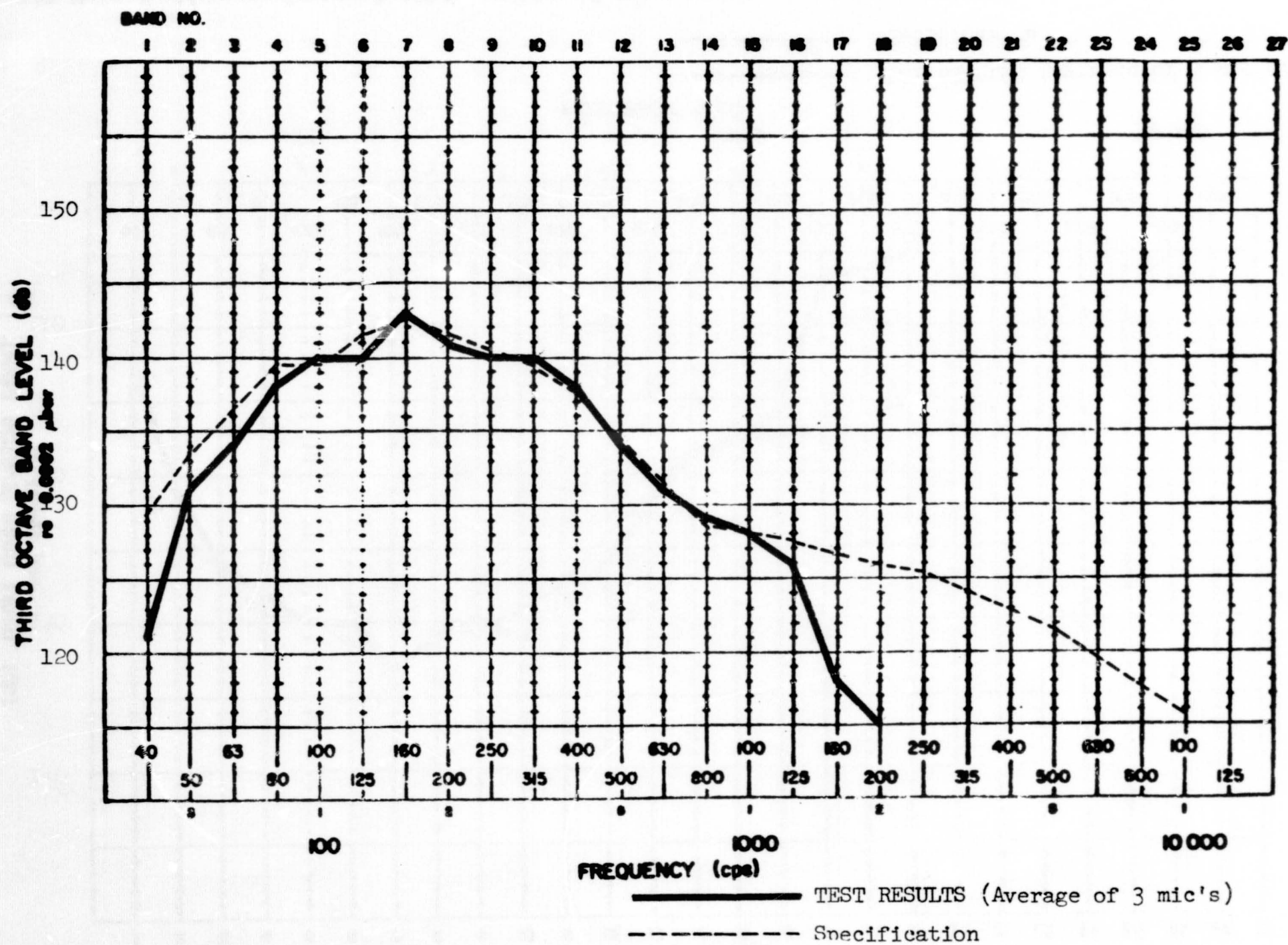


Figure 3-44. Narrow-Band Frequency Spectrum for 150-db Overall Sound Pressure Level Test

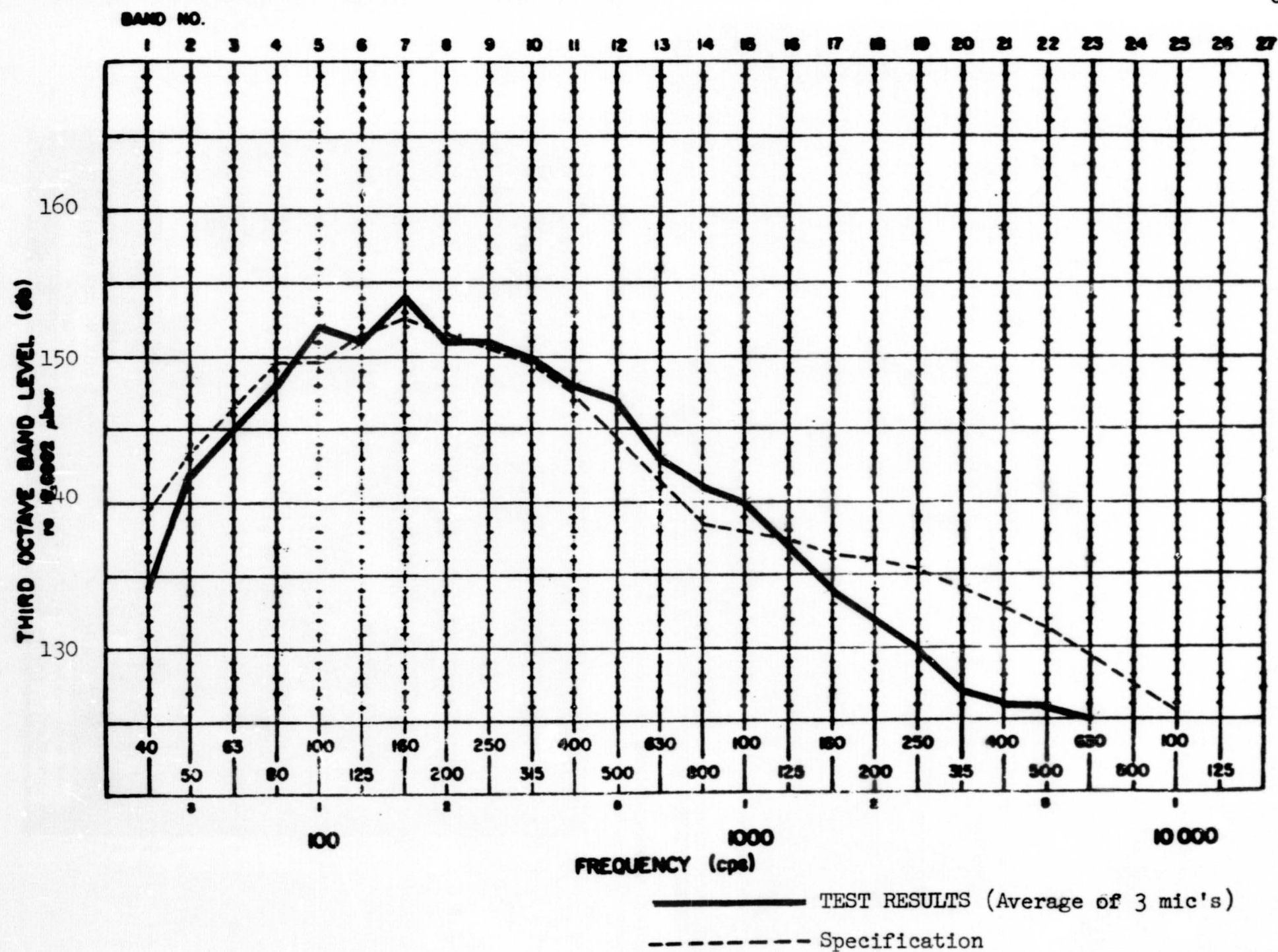


Figure 3-45. Narrow-Band Frequency Spectrum for 160-db Overall Sound Pressure Level Test

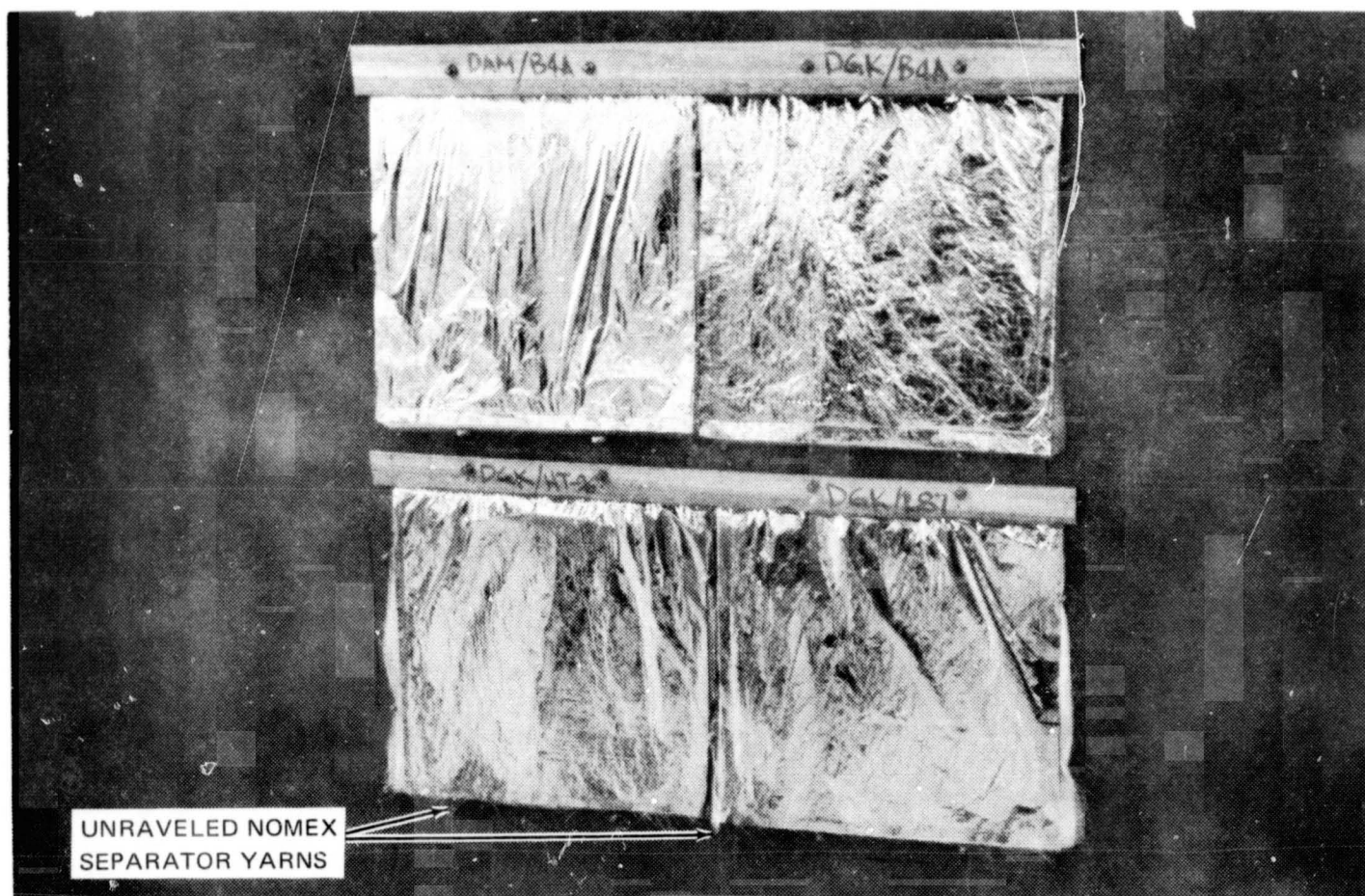


Figure 3-46. Side and Bottom Retaining Frames Removed After 160-db (Overall) Test

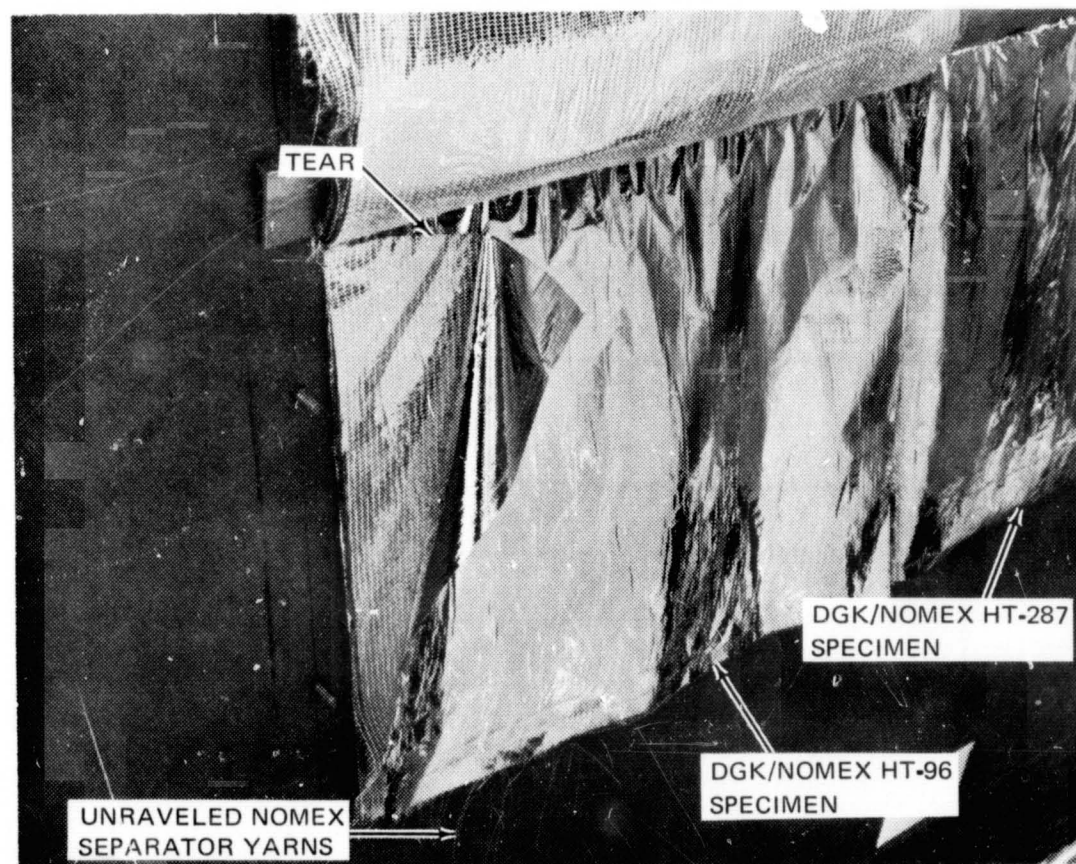


Figure 3-47. Tearing and Separator Unraveling of DGK/Nomex HT-96 After 160-db (Overall) Test

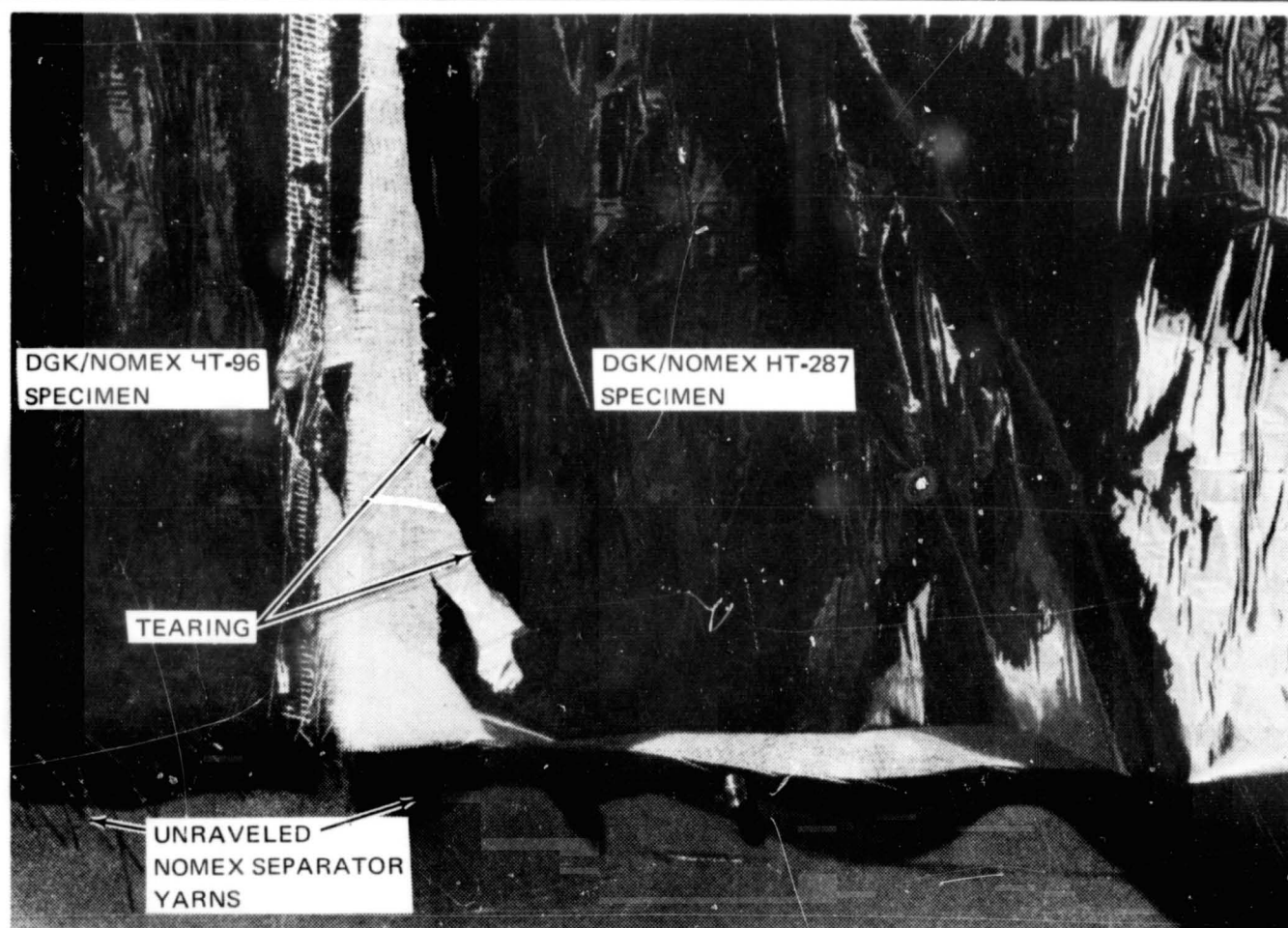


Figure 3-48. Tearing and Separator Unraveling of DGK/Nomex HT-287 After 160-db (Overall) Test

problem in a composite using a heavier separator since the tearing experienced in these tests may have been due to the higher loading resulting from the much heavier Nomex separators. It should be noted that the cause of the tearing is not known and may have resulted from the clamping at the specimen edges rather than the weight of the separator. A fluffing out of the test specimens and an increase in layer density were observed at the end of the tests. This is consistent with the specimen fluffing seen in the acoustic tests conducted on contract NAS 8-21400 (Reference 7). No measurement of the change in layer density was attempted since the specimen size and edge clamping make the interpretation of any such data difficult. However, it appears that this fluffing effect could be significant and could easily eliminate any increase in layer density due to cyclical compressive loads (refer to Section 3.9).

A comparison of the specimens indicates that the Dacron B4A net is the preferred separator for a dynamic environment since it inhibited tearing of the reflectors and was not damaged as were the Nomex separators. Further evaluation of the performance of Nomex materials in a high-level acoustic

environment should be accomplished if these separators are considered in a future application.

3.9 COMPRESSION CYCLING EFFECTS ON LAYER DENSITY

A primary area of interest in designing a multilayer, high-performance insulation system for cryogenic tanks on a reusable vehicle is the effect of the numerous compressive load cycles on the insulation layer density. The magnitude of an increase in layer density is of interest since this will result in a decrease in thermal performance. To evaluate this parameter, the layer density as a function of compressive load and number of compression cycles has been obtained for the six candidate insulation composites.

3.9.1 Compression Cycling Test Procedure

Two test series were conducted. The first series, shown in the test matrix in Table 3-21, was designed to determine the effect of 100 compression cycles on the composite layer density. A 15 by 15 in. square specimen of each of six composites was cycled 100 times from zero to 0.15 psi compressive load. In addition, 8 by 8 in. DAK/Dacron B4A and DAK/Nomex HT-287 specimens were cycled 100 times from zero to 15 psi compressive load. Compressive loadings greater than 0.15 psi are not anticipated for the orbiter ILRV application. However, the tests of the two composites at higher compressive loadings were included to obtain an indication of the ability of this type of composite to spring back to a low layer density should such a loading be encountered. A smaller-size specimen was used for the higher compressive load tests to match the range of the different load cell used in the Instron machine for these tests. All of the composite specimens in the first test series consisted of a stack of 20 layer-pairs. In the lower cyclical compressive load tests, data reduction was not attempted below a load of approximately 1×10^{-4} psi due to the minimal slope of the curve at lower compressive loadings. In the higher cyclical compressive load tests, data reduction was not attempted below 1.5×10^{-2} and 5×10^{-2} psi for the same reason. The uncertainty in reading the data from the curves at the 1×10^{-4} psi and 1.5×10^{-2} or 5×10^{-2} psi loadings was less than 2 percent (less than 1 percent in many tests).

The second test series was designed to determine the effect of the number of layer-pairs (in a 1-g field) on the layer density vs compressive load

Table 3-21
COMPRESSION LOAD CYCLING EFFECT ON
LAYER DENSITY—TEST MATRIX

Composite	Specimen Size (in.)	Number of Layer-Pairs	Compressive Load Range (psi)	Number of Compression Cycles
DAK/Dacron B4A	15 x 15	20	0 to 0.15	100
DAK/Nomex HT-287	15 x 15	20	0. to 0.15	100
DAK/Nomex HT-96	15 x 15	20	0 to 0.15	100
DGM/Dacron B4A	15 x 15	20	0 to 0.15	100
DGM/Nomex HT-287	15 x 15	20	0 to 0.15	100
DGM/Nomex HT-96	15 x 15	20	0 to 0.15	100
DAK/Dacron B4A	8 x 8	20	0 to 15	100
DAK/Nomex HT-287	8 x 8	20	0 to 15	100

DAK: Double Aluminized Kapton, 25 to 30 gage

DGM: Double Goldized Mylar, 25 to 30 gage

relationship and to provide layer density vs compressive load data on 10 layer-pair composites. This data on 10 layer-pair composites was needed to facilitate data reduction of the flat-plate calorimeter tests (Section 3.10) which used 10 layer-pair specimens. The composites tested included DAK/Dacron B4A, DAK/Nomex HT-287, and DAK/Nomex HT-96 as shown in the test matrix in Table 3-22. Only one compression cycle was used in these tests. The compressive load was varied from zero to 0.15 psi. The 15-by-15 in. test specimens used in the previous test series were also used in these tests. The test sequence consisted of testing the 20 layer-pair specimen used in the previous tests, separating this specimen into two 10 layer-pair specimens and testing each, and finally reassembling the material into a 20 layer-pair specimen for the second 20 layer-pair test. Thus, two tests of both 20 and 10 layer-pair specimens were obtained. The handling of the specimens between tests served to restore them to an uncycled layer density condition.

Table 3-22
EFFECT OF NUMBER OF LAYER PAIRS ON
LAYER DENSITY—TEST MATRIX

Composite	Specimen Size (in.)	Number of Layer Pairs	Compressive Load Range (psi)	Number of Compression Cycles
DAK/Dacron B4A	15 x 15	20	0 to 0.15	1
DAK/Dacron B4A	15 x 15	10	0 to 0.15	1
DAK/Dacron B4A	15 x 15	10	0 to 0.15	1
DAK/Dacron B4A	15 x 15	20	0 to 0.15	1
DAK Nomex HT-287	15 x 15	20	0 to 0.15	1
DAK Nomex HT-287	15 x 15	10	0 to 0.15	1
DAK Nomex HT-287	15 x 15	10	0 to 0.15	1
DAK Nomex HT-287	15 x 15	20	0 to 0.15	1
DAK/Nomex HT-96	15 x 15	20	0 to 0.15	1
DAK/Nomex HT-96	15 x 15	10	0 to 0.15	1
DAK/Nomex HT-96	15 x 15	10	0 to 0.15	1
DAK/Nomex HT-96	15 x 15	20	0 to 0.15	1

DAK and DGM reflector materials were used in all of the tests. Since the metal is only approximately 300 to 400 angstroms thick on the surface of the Kapton or Mylar, there should be little if any difference between the layer densities obtained with a DAK and DGK reflector or with a DGM and DAM reflector. Consequently, the DAK data obtained in these tests was also used for composites using DGK since both are the same thickness. Similarly, the DGM data were used for DAM of the same thickness.

All of the tests in both series were conducted in air at room temperature with an Instron Universal testing machine (Figure 3-49). A test fixture consisting of upper and lower platens with flat faces was installed in the Instron machine and the specimen was placed between these platens (Figure 3-50). Before testing, the upper platen was positioned above the lower platen at a distance greater than the free layup thickness of the specimen. This established a no-load reference position for all of the load cycles. The reading on a dial gage that monitored the displacement

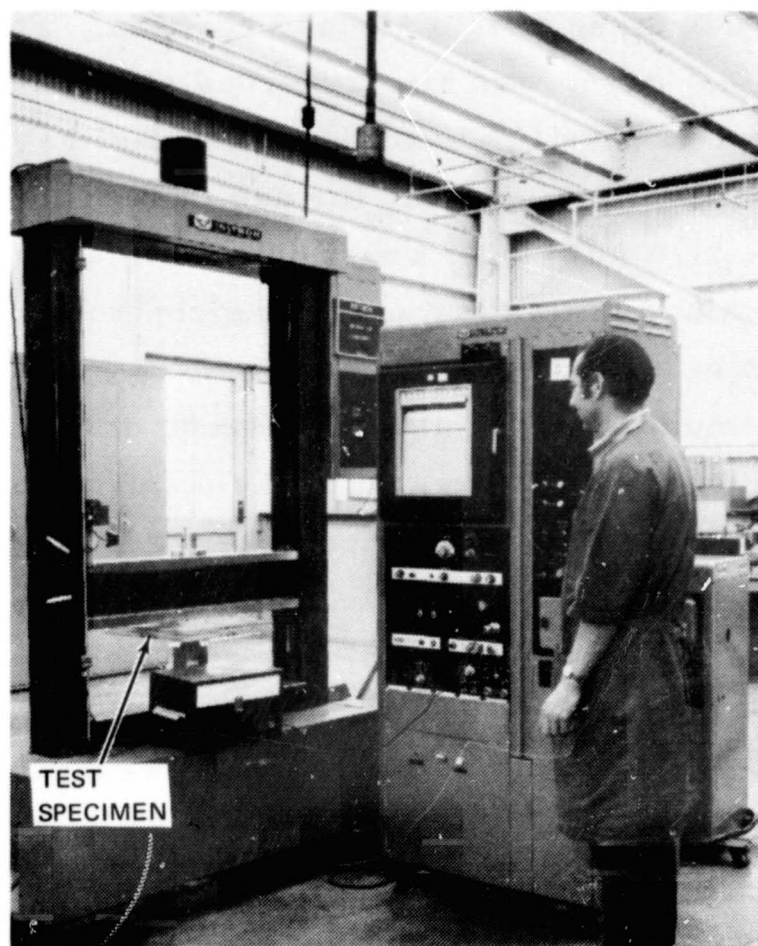


Figure 3-49. Compressive Load Test Setup

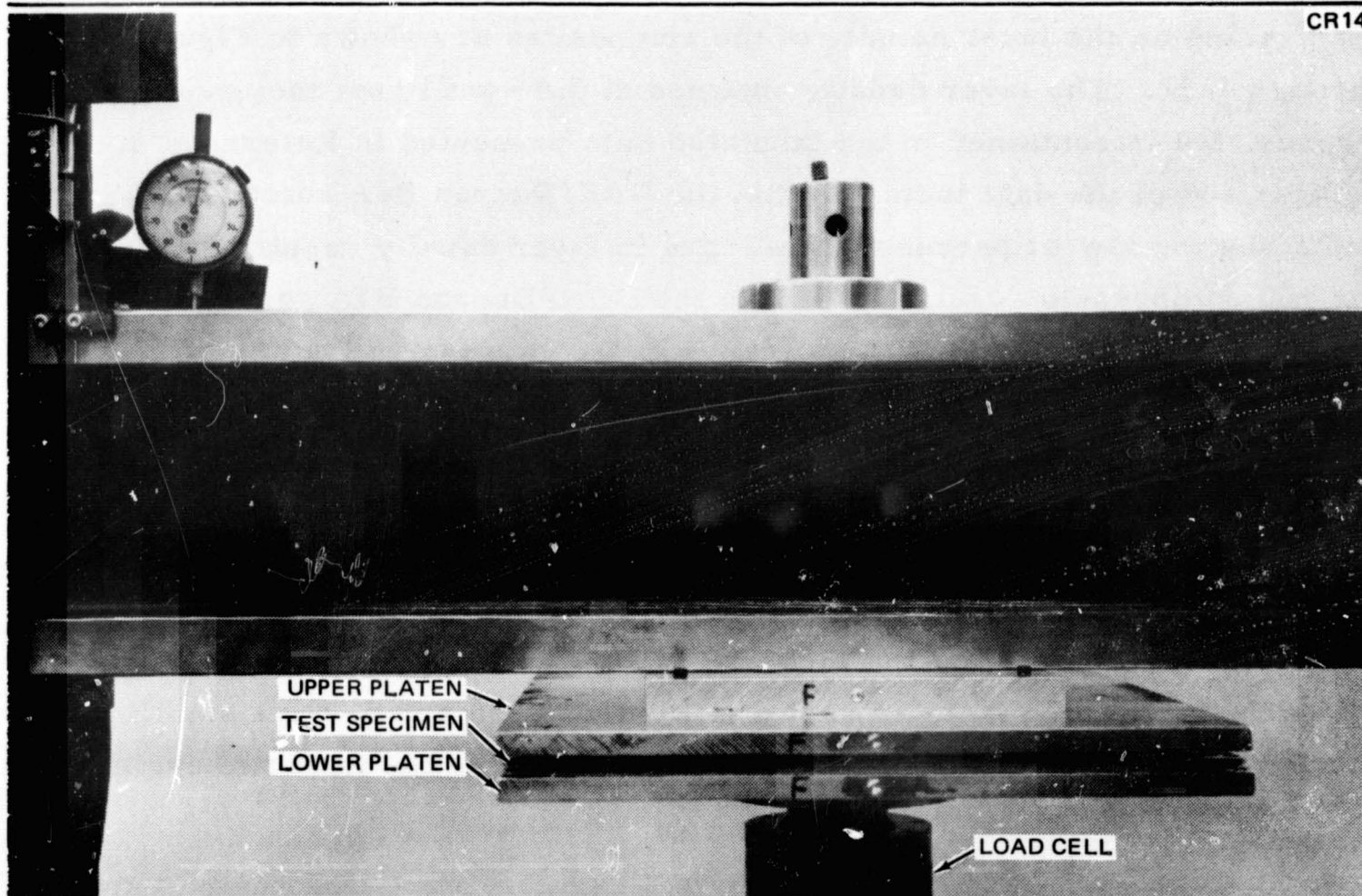


Figure 3-50. Test Fixture Used In Compressive Load Tests

of the upper platen was taken at this no-load position. The platen position, as indicated by the dial gage, was also recorded at the maximum load position of the platen. These two readings of the dial gage were used to determine an accurate deflection scale for use in reading the data trace. For example, the 0.2979 in. = 7.43 chart units deflection scale shown in Figure 3-51 was obtained in this manner. The controls of the Instron were set so that the machine automatically cycled between the no-load machine setting and the maximum test load at a head speed of 0.2 in. per minute. A continuous record of the displacement of the upper platen as a function of the applied load was made on the Instron chart recorder using the most sensitive chart and load ranges available. Figure 3-51 is a typical chart recording of both the loading and unloading of the specimen for one load cycle. The compressive loading in psi and the density in layer-pairs/inch were reduced, at selected points, from the chart recording of the applied load in pounds and the platen displacement in inches.

3.9.2 Compression Cycling Test Results

The test results indicating the effect of 100, zero-to-0.15-psi compressive load cycles on the layer density of the composites are shown in Figures 3-52 through 3-57. The layer density obtained at 0.15 psi is not included in these figures, but is contained in the tabulated data presented in Reference 5. A comparison of the data indicates that the DAK/Dacron B4A composite sustained the lowest percentage increase in layer density resulting from the 100 compression cycles, whereas the DGM/Dacron B4A sustained the highest. These layer density increases at a compressive loading of 10^{-4} psi were approximately 5 and 20 percent for the DAK/Dacron B4A and DGM/Dacron B4A composites, respectively (Table 3-23). The average increase in layer density for all composites at a compressive loading of 10^{-4} psi was 13 percent. The increase in layer density for composites containing the DAK reflectors was consistently less than for those containing the DGM reflectors. Most of the increase in layer density occurred during the early cycles. In fact, as shown in Figures 3-58 and 3-59, a significant portion of the layer density increase occurred during the first two cycles.

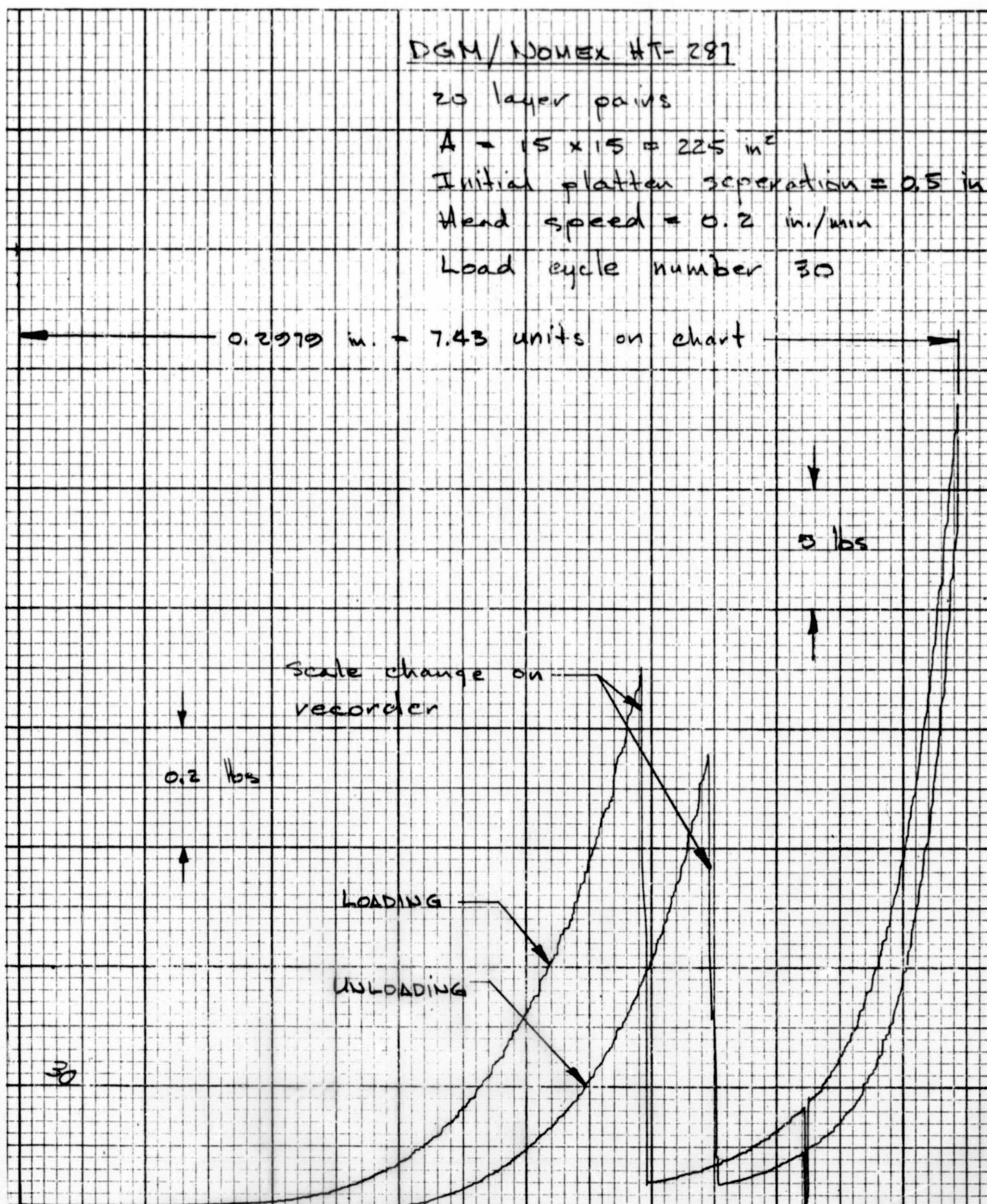


Figure 3-51. Typical Data Trace for One Compressive Load Cycle

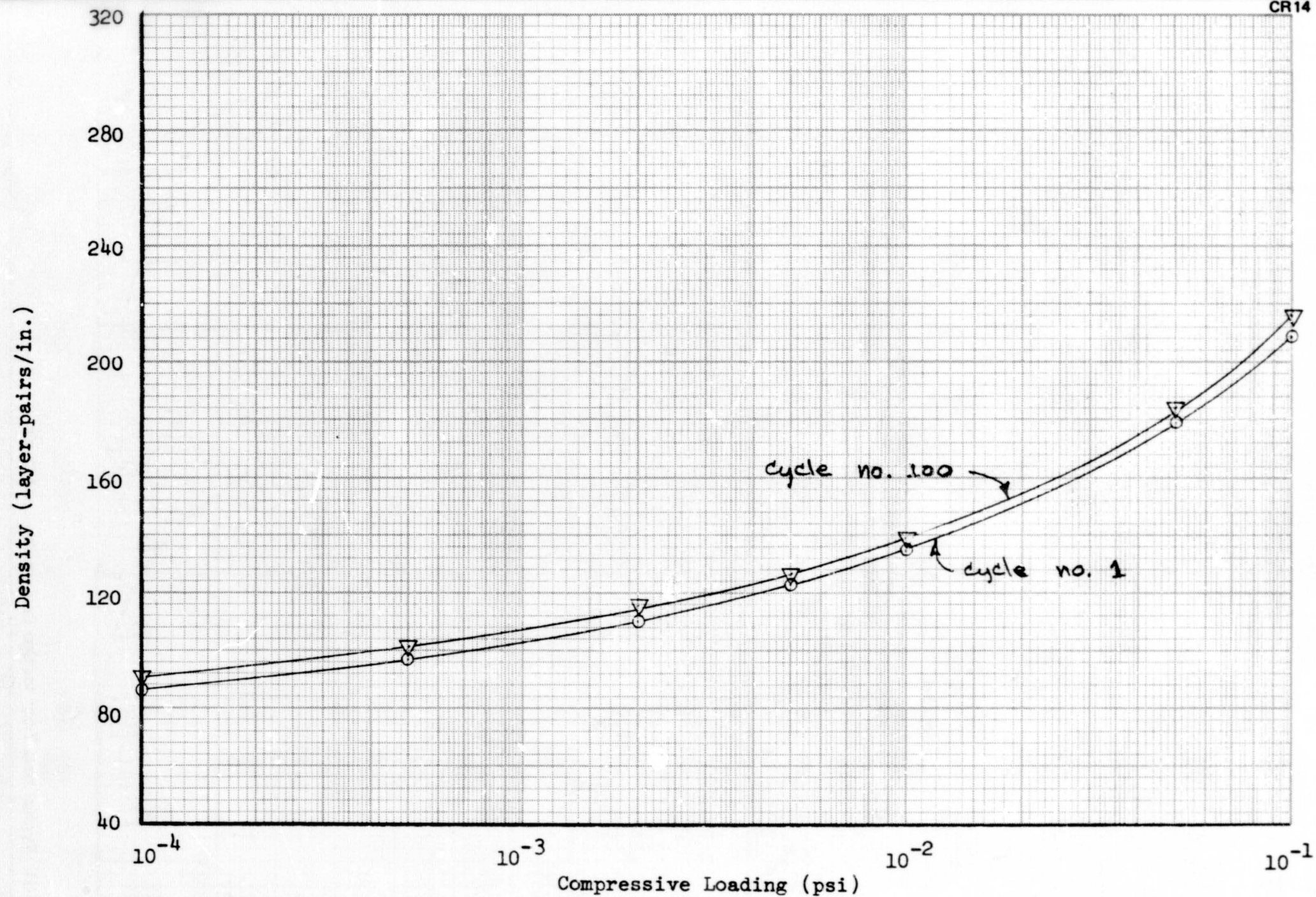


Figure 3-52. Effect of Compressive Load Cycles on Layer Density of DAK/Dacron B4A

56
Density (layer-pairs/in.)

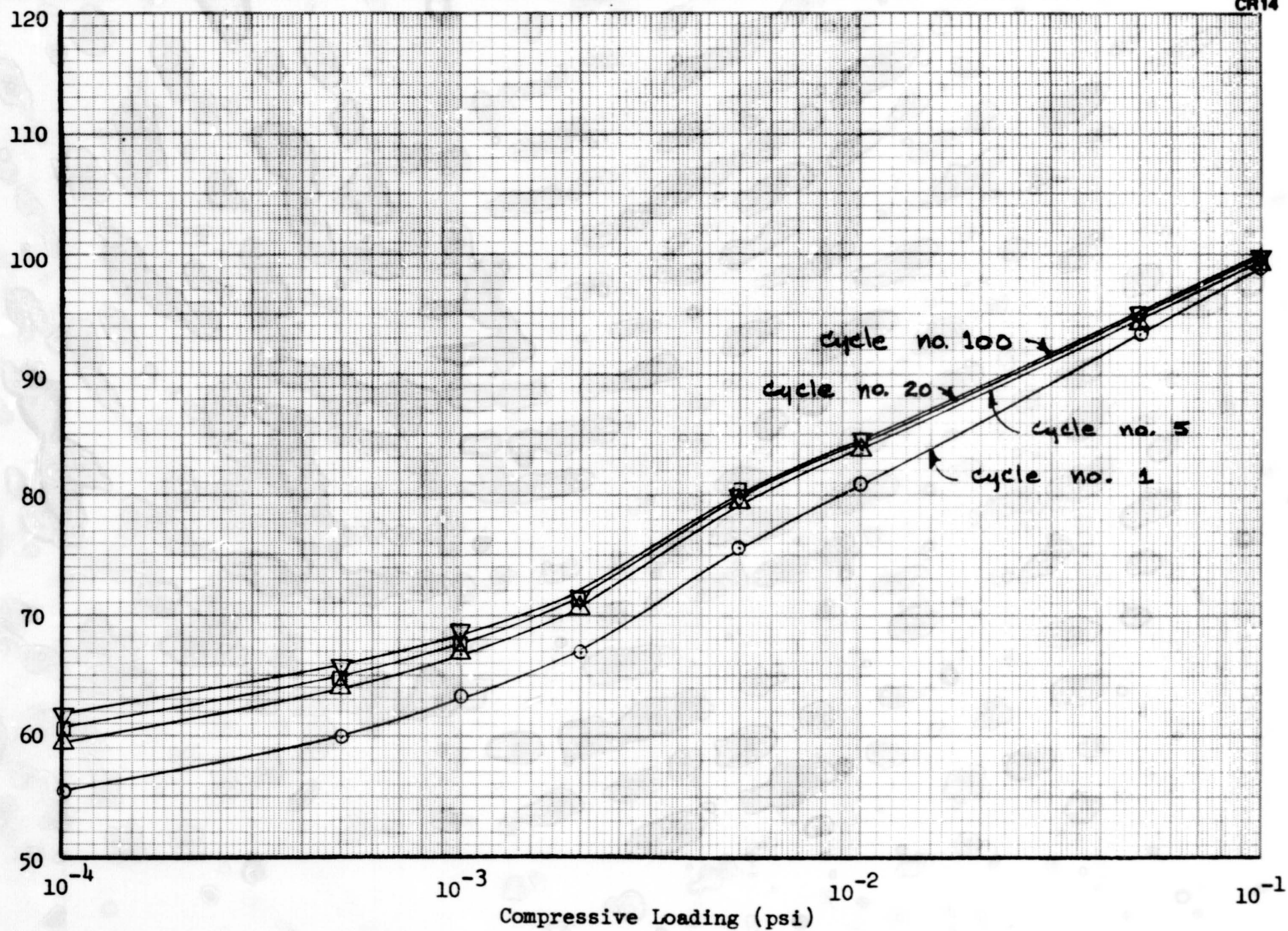


Figure 3-53. Effect of Compressive Load Cycles on Layer Density of DAK/Nomex HT-287

001

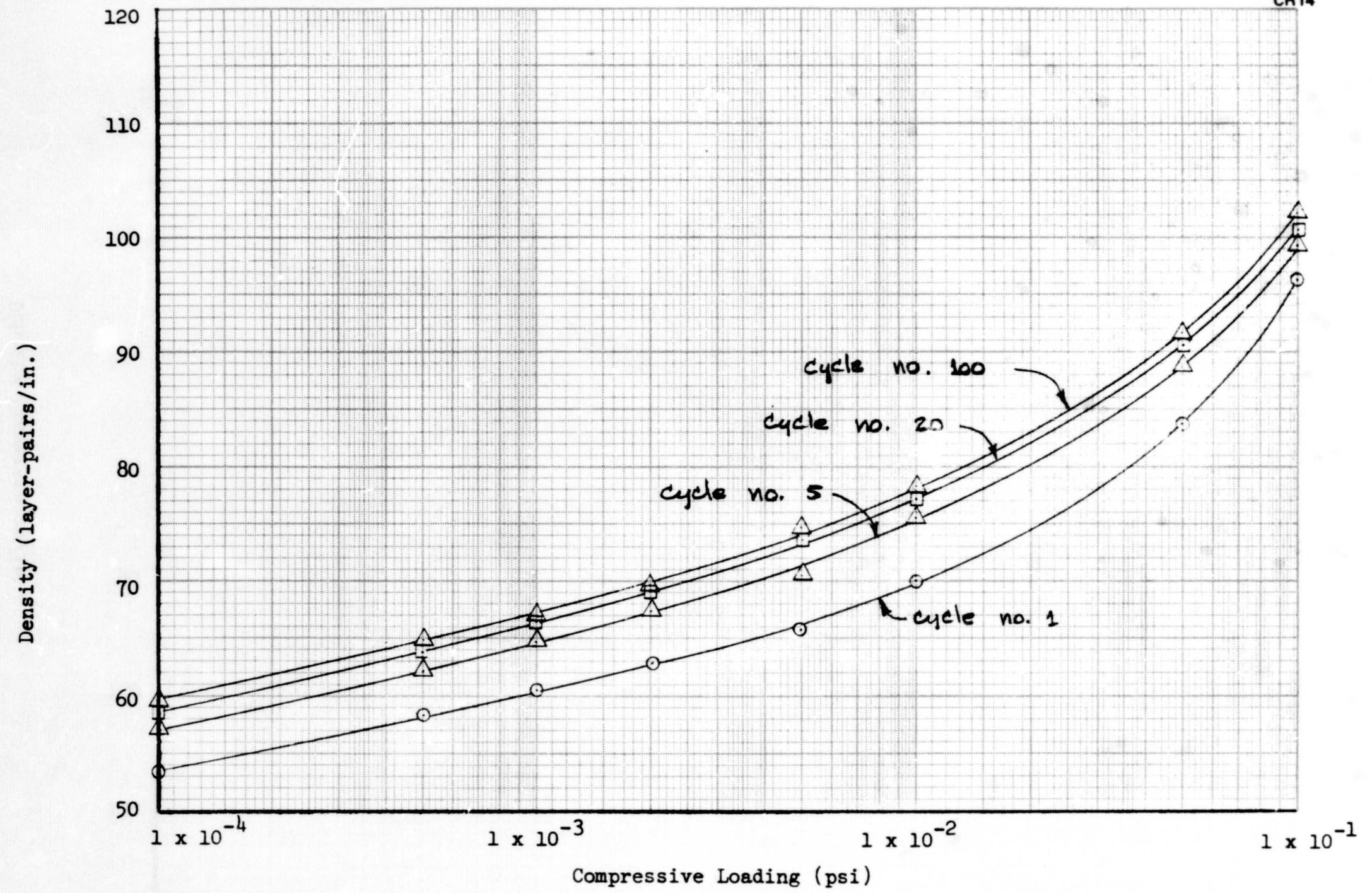


Figure 3-54. Effect of Compressive Load Cycles on Layer Density of DAK/Nomex HT-96

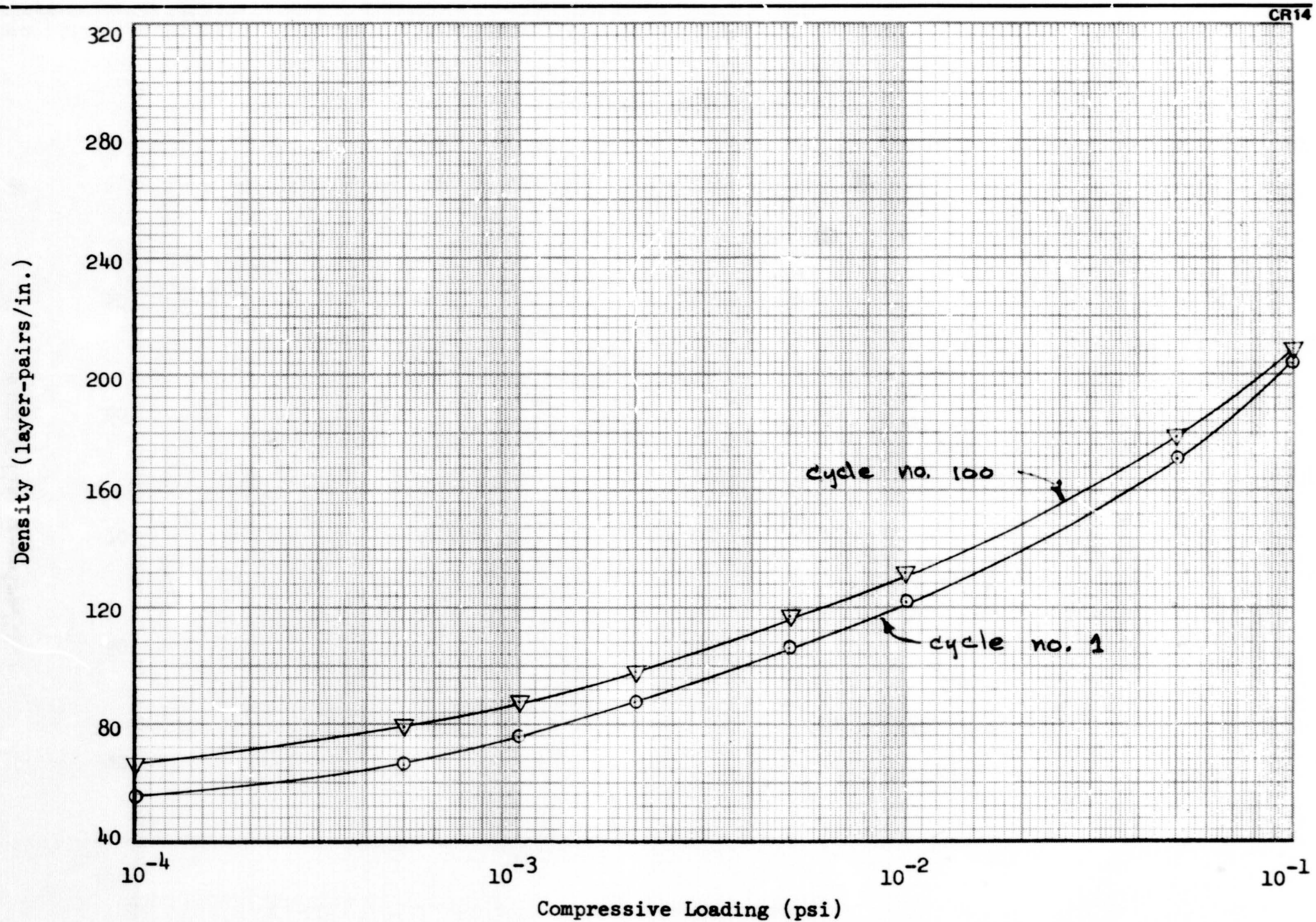


Figure 3-55. Effect of Compressive Load Cycles on Layer Density of DGM/Dacron B4A

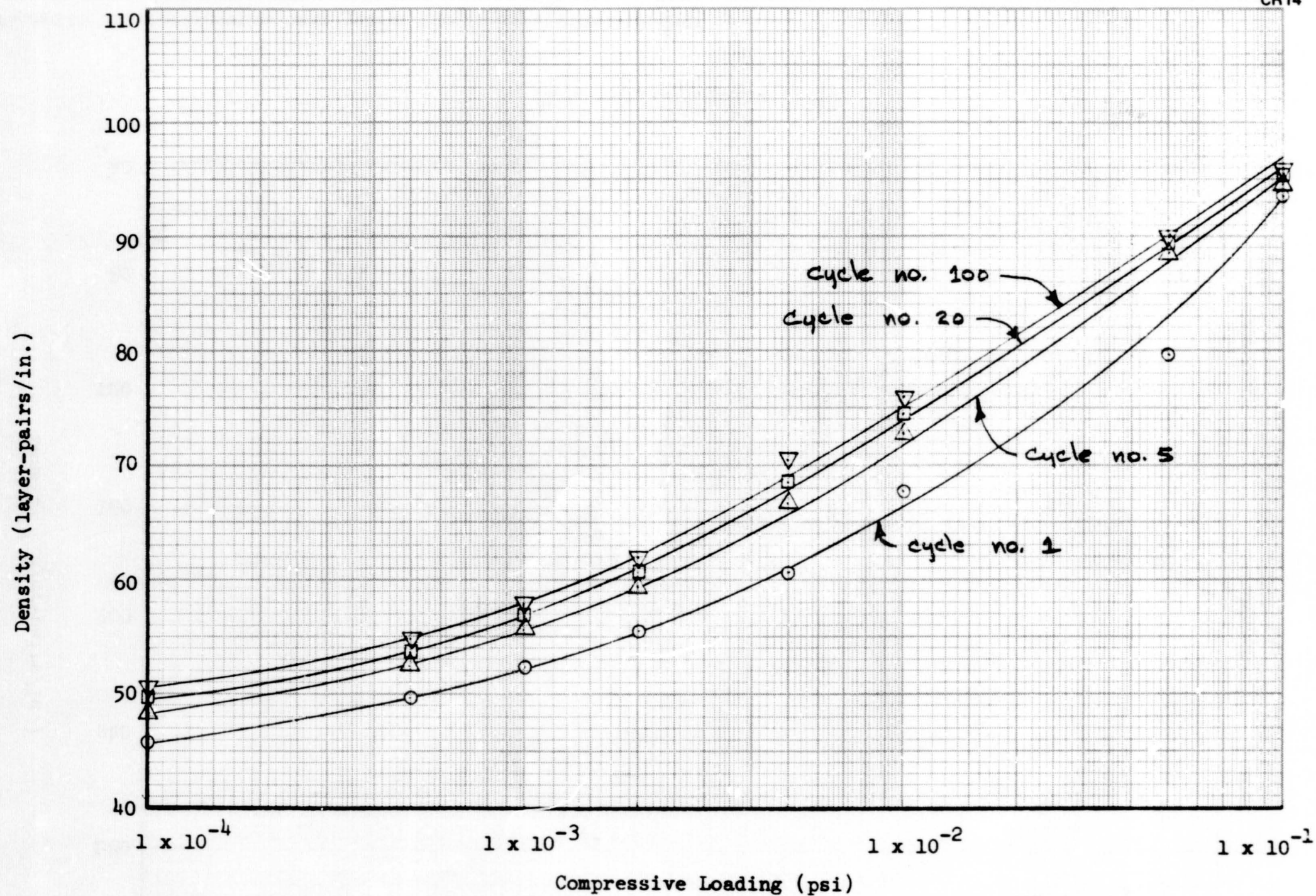


Figure 3-56. Effect of Compressive Load Cycles on Layer Density of DGM/Nomex HT-287

Table 3-23
EFFECT OF 100 COMPRESSIVE LOAD CYCLES
ON LAYER DENSITY

Composite	Layer Density Increase at 10 ⁻⁴ psi Compressive Load (%)
DAK/Dacron B4A	4.75
DAK/Nomex HT-287	11.0
DAK/Nomex HT-96	12.0
DGM/Dacron B4A	20.0
DGM/Nomex HT-287	13.5
DGM/Nomex HT-96	17.5

Figures 3-58 and 3-59 also indicate that there is an exponential relationship between the layer density and the number of load cycles after the second to fifth cycles.

Of the composites tested, the lowest layer density was obtained for the DGM/Nomex HT-96. The layer density obtained for the DGM/Nomex HT-96 composite at 10⁻⁴ psi compressive load was approximately one-half the layer density of the DAK/Dacron B4A at the same compressive load (Table 3-24). The DAK/Dacron B4A has the highest layer density of the composites tested. A comparison of the layer densities for DAK and DGM composites using the same separator shows that, at the very low compressive loads, the use of a DAK reflector consistently resulted in layer densities higher than those obtained with a DGM reflector. However, at the higher compressive loads, the layer densities of the DAK and DGM composites are similar. This is as expected since the thickness of the reflector becomes more significant at higher loads, and the two reflector materials used in these tests are both 25- to 30-gage material. A comparison of the data for the two Nomex separators with the same reflector

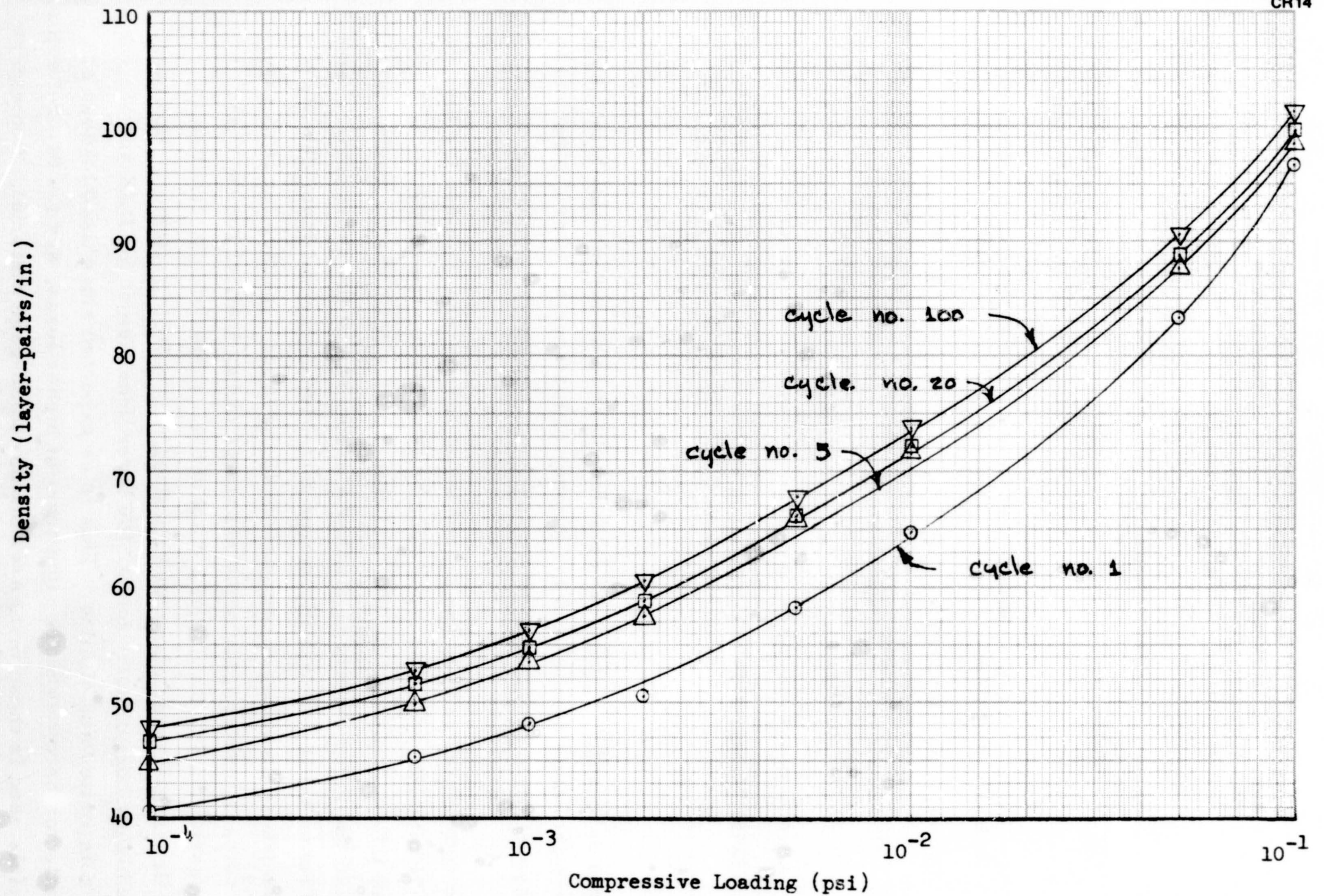


Figure 3-57. Effect of Compressive Load Cycles on Layer Density of DGM/Nomex HT-96

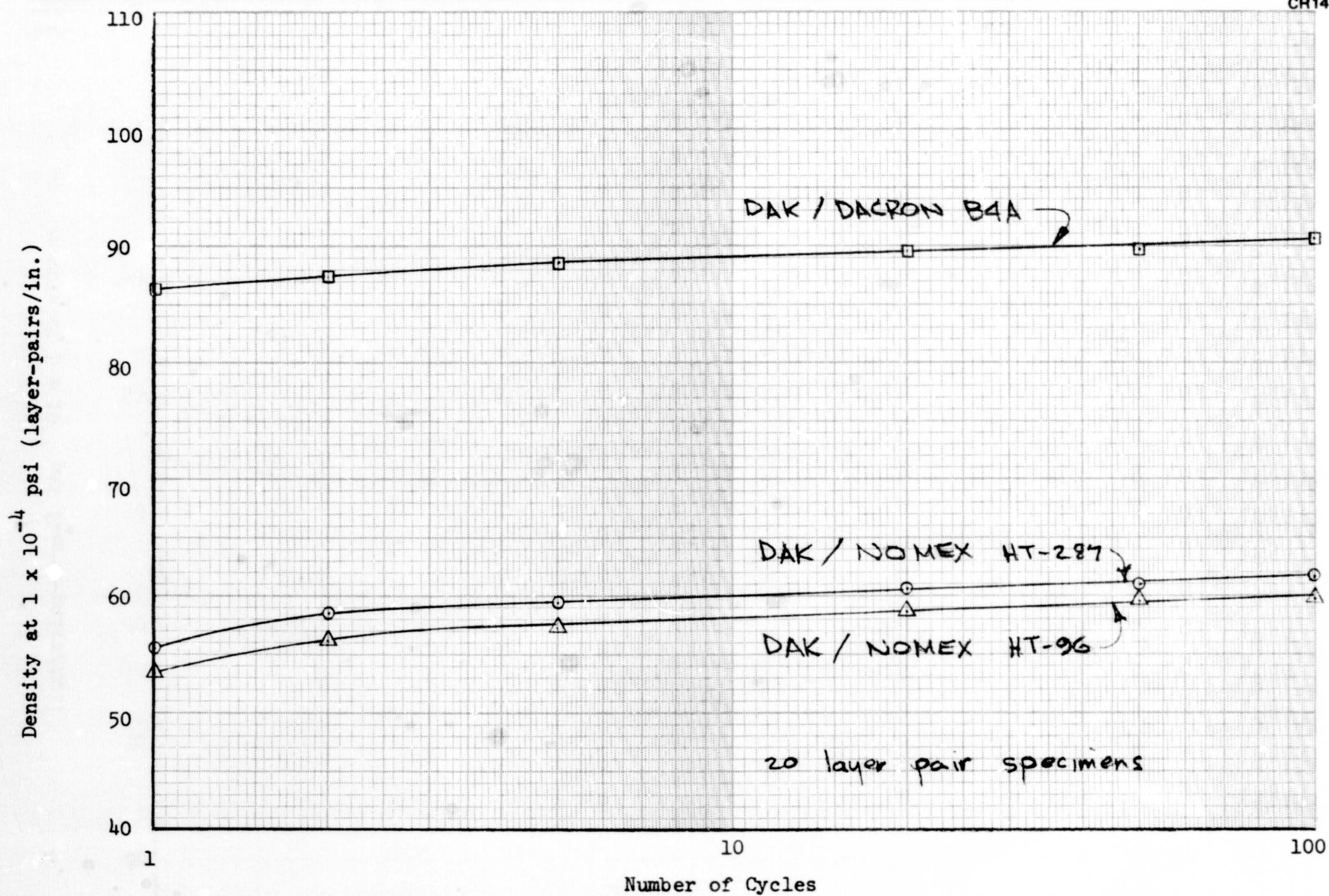


Figure 3-58. Effect of Number of Compressive Load Cycles on Layer Density of DAK Composites at 1×10^{-4} psi Loading

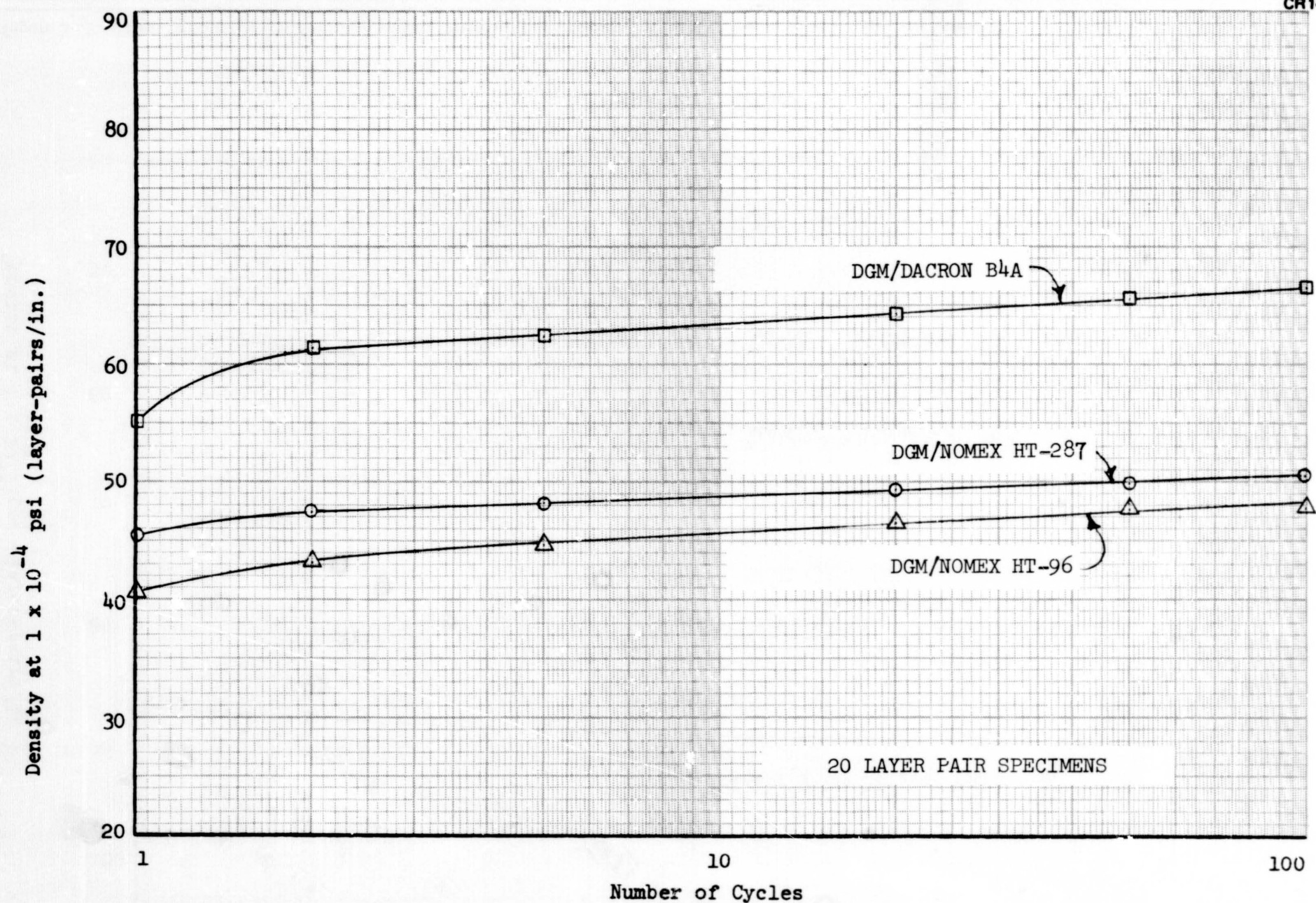


Figure 3-59. Effect of Number of Compressive Load Cycles on Layer Density of DGM Composites at 1×10^{-4} psi Loading

Table 3-24
LAYER DENSITY AT 1×10^{-4} PSI COMPRESSIVE LOAD
AND IN A ONE-G FIELD
AFTER 100 COMPRESSION CYCLES TO 0.15 PSI

Composite	Density (Layer-Pairs/Inch)
DAK/Dacron B4A	90
DAK/Nomex HT-287	61
DAK/Nomex HT-96	60
DGM/Dacron B4A	66
DGM/Nomex HT-287	50
DGM/Nomex HT-96	48

material reveals that the Nomex HT-96 and HT-287 have similar layer densities at a given compressive load.

The DAK/Nomex HT-287 and DAK/Dacron B4A composites which were cycled from zero to 15 psi had sustained, as was expected, much greater increases in layer density at the end of 100 compressive cycles than the same composites cycled only to 0.15 psi (compare Figures 3-60 and 3-61 with Figures 3-52 and 3-53). Because a higher range load cell was used for these tests, the layer density at 10^{-4} psi was not obtained. However, using the layer densities at 0.1 psi after 100 cycles and extrapolating this to 10^{-4} psi, assuming the curve is parallel to the low load curve in Figures 3-52 and 3-53, indicates approximately a 35-percent increase in layer density for the DAK/Nomex HT-287 composite and approximately a 120-percent increase in layer density for the DAK/Dacron B4A composite. Although these layer density increases are significant, it should be noted that the composites showed a good recovery in thickness considering the

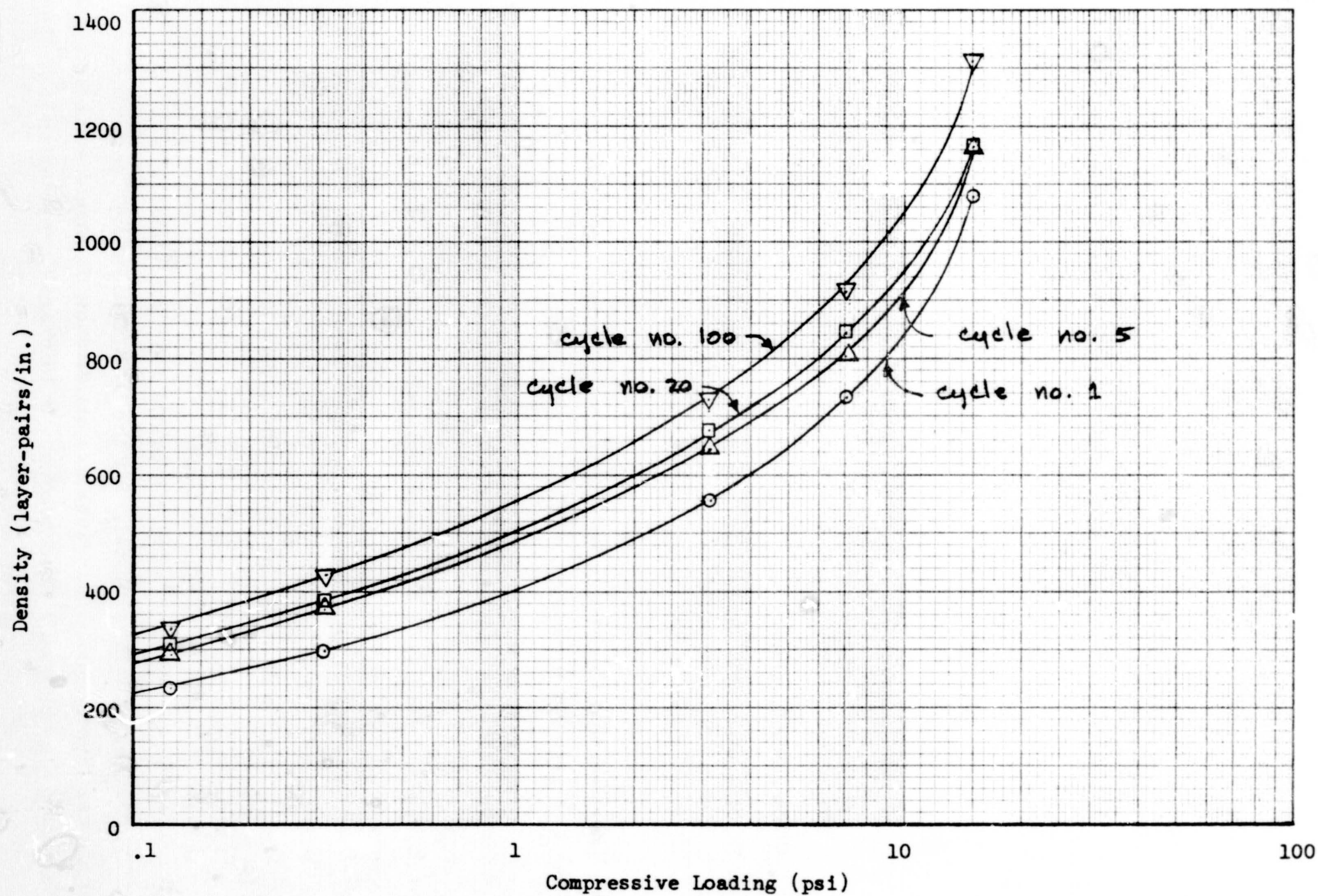


Figure 3-60. Effect of High Compressive Load Cycles on Layer Density of DAK/Dacron B4A

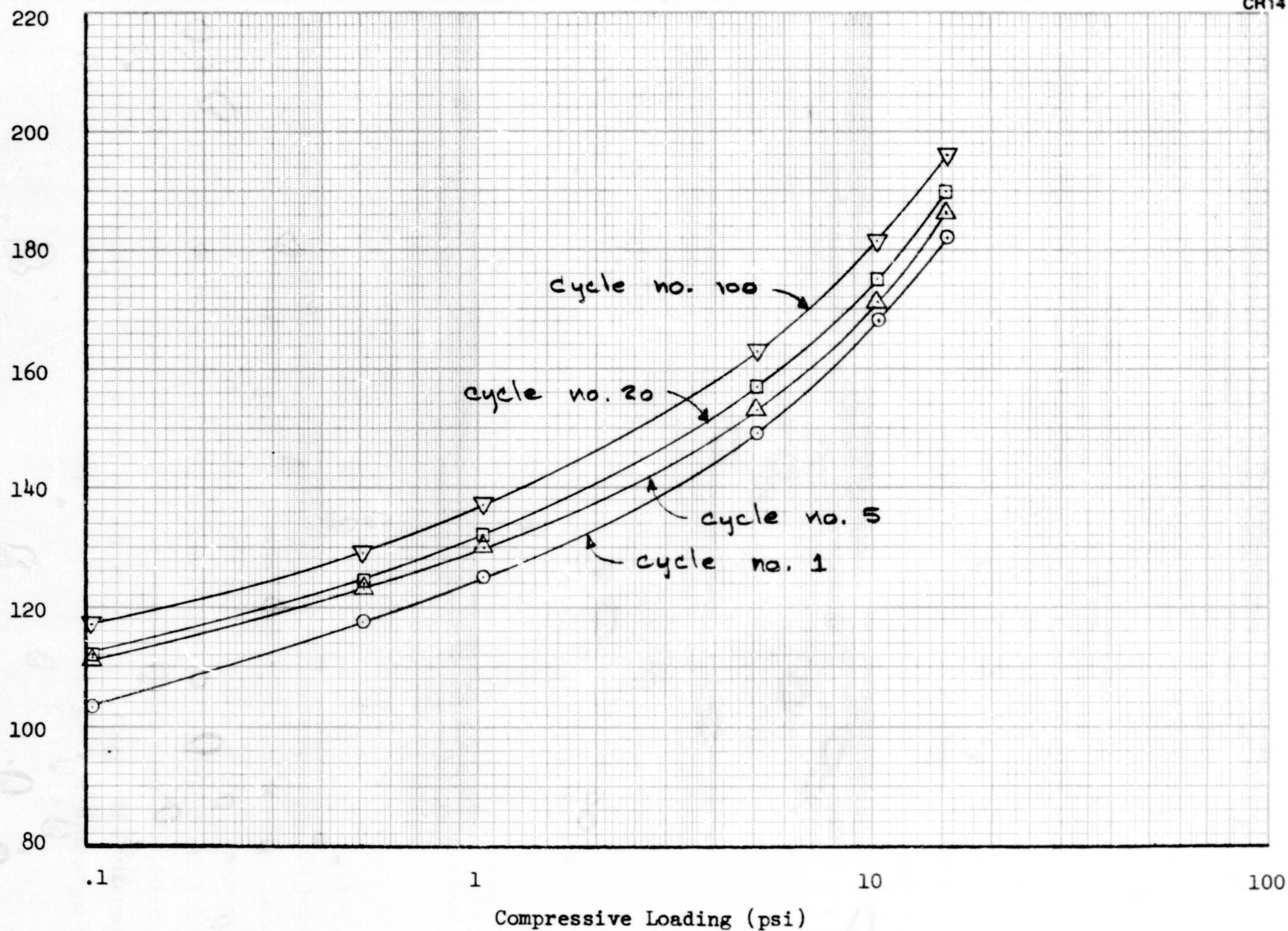
601
Density (layer-pair/in.)

Figure 3-61. Effect of High Compressive Load Cycles on Layer Density of DAK/Nomex HT-287

very heavy load to which they were subjected; fifteen psi is equal to slightly over 1 ton per square foot. Inappropriate emphasis should not be placed on these high load data, since, as stated earlier, compressive loads above 0.15 psi are not anticipated in the orbiter ILRV.

It should be noted that the increase in layer density due to compressive load cycles may be offset in an actual vehicle application by the acoustic vibrations and the evacuation forces. Both of these should tend to fluff out the insulation. It should also be noted that, without exception, the layer density is still decreasing at a compressive load of 10^{-4} psi (Figures 3-52 through 3-57). This reveals that the layer density in the no-load environment of space will be less than that obtained in these tests at 10^{-4} psi. For this reason, and because of the potential fluffing of the insulation, the layer density at 10^{-4} psi after 100 cycles (Table 3-24), should tend to result in a conservative prediction of the in-space layer density.

A comparison of the layer density as a function of compressive loading for 10- and 20-layer-pair specimens is shown in Figures 3-62, 3-63, and 3-64. Tabulated data are given in Reference 5. These data indicate that, in a one-g field, 20 layer-pairs of any of these three composites will have a 15 to 20 percent higher layer density than 10 layer-pairs. It should be noted, however, that these data are applicable only in a one-g field. In a zero-g field (no-load) environment of space, the layer densities should return to a similar low value regardless of the number of layers since the only difference in loading between 10 and 20 layer-pairs in a one-g field is the weight on each layer of the layers above it in the composite. Also, it was shown in the cyclical compression tests that the layer density will return to nearly its previous value after being compressed with a low load. Except for the first 10-layer specimen of DAK/Nomex HT-96, shown in Figure 3-64, the data appear consistent with anticipated results and the two layer-density curves for a given composite and number of layer-pairs are in good agreement.

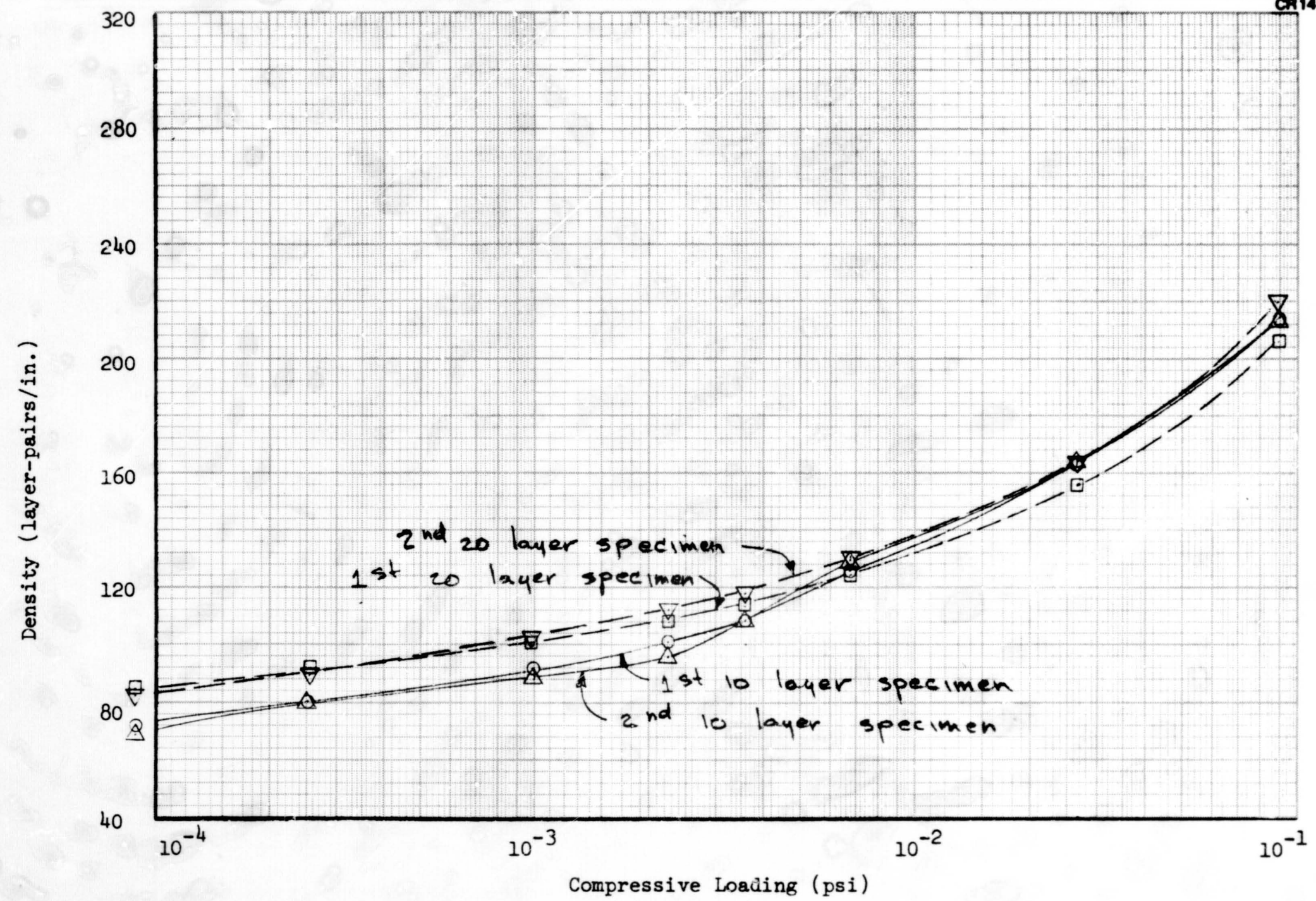


Figure 3-62. Effect of Compressive Loading on Layer Density of 10 and 20 Layer-Pairs of DAK/Dacron B4A—First Loading Cycle

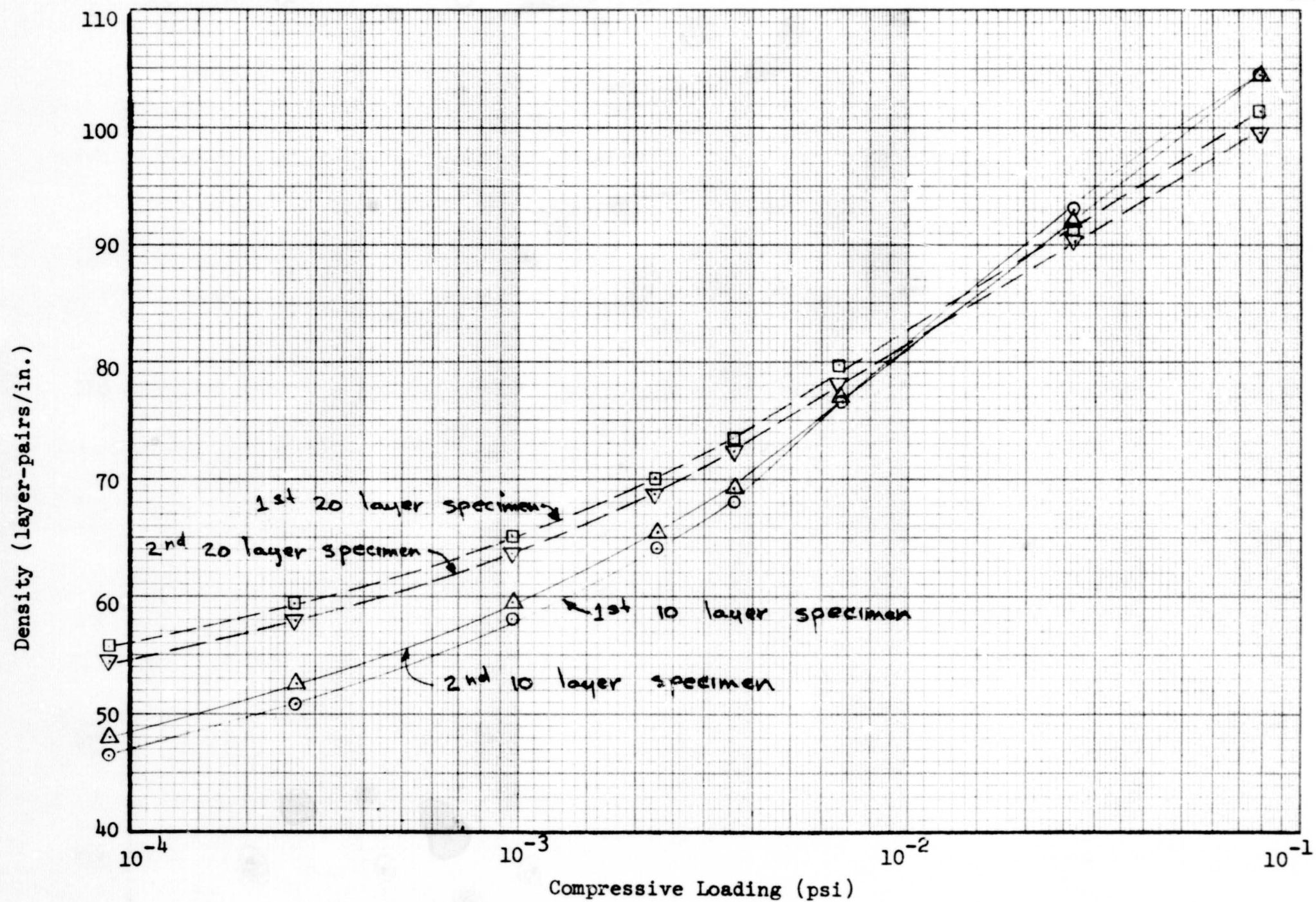


Figure 3-63. Effect of Compressive Loading on Layer Density of 10 and 20 Layer-Pairs of DAK/Nomex HT-287—First Loading Cycle

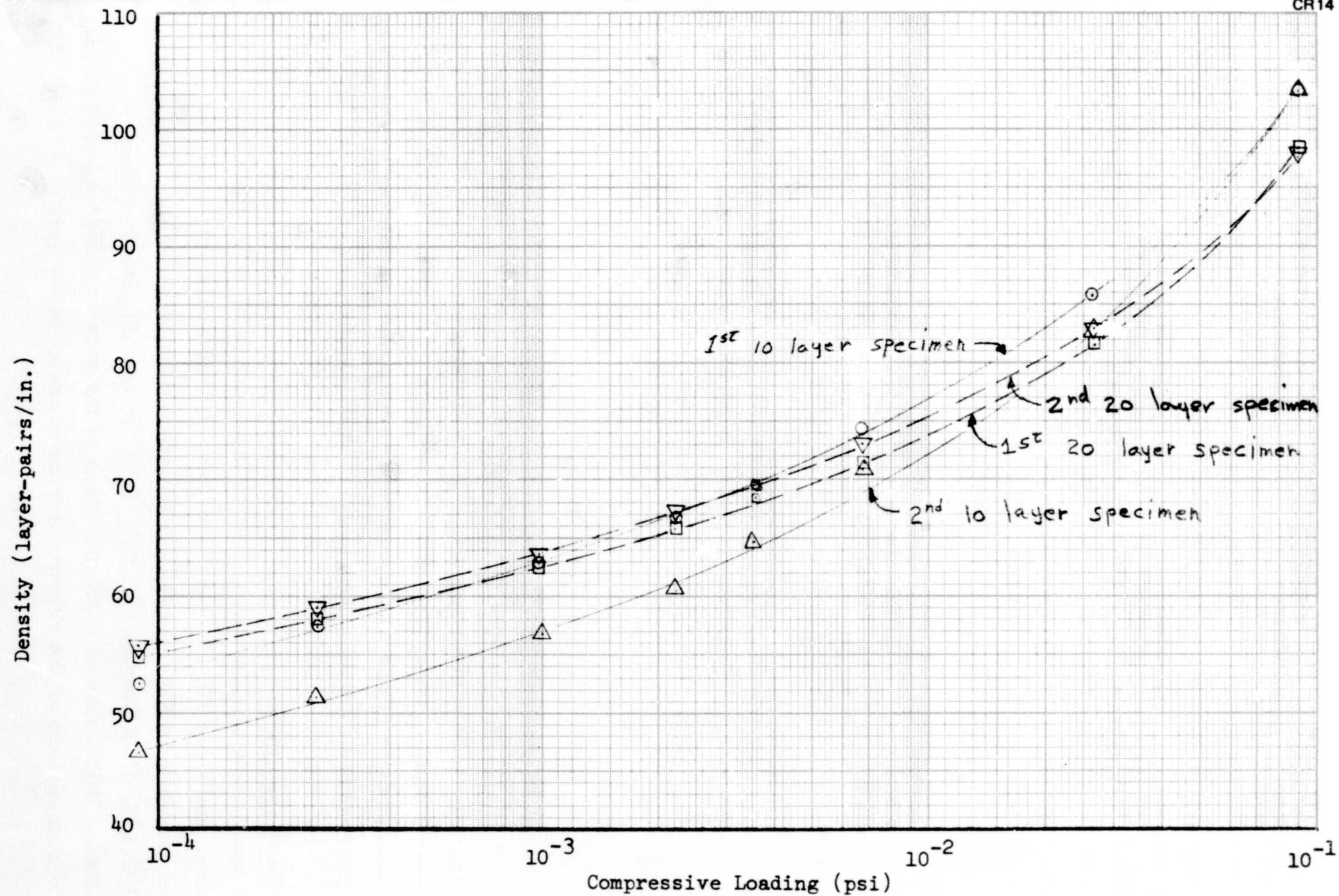


Figure 3-64. Effect of Compressive Loading on Layer Density of 10 and 20 Layer-Pairs of DAK/Nomex HT-96—First Loading Cycle

3.9.3 Compression Cycling Tests – Conclusions and Recommendations

An indication of the maximum expected increase in MLI layer density due to 100 compressive loading cycles from zero to 0.15 psi was obtained for six candidate composites. Of these, the DAK/Dacron B4A composite will sustain the lowest increase. The layer density increase of composites subjected to loads from zero to 15 psi would be significant but would not completely degrade performance. It was also concluded that the layer densities obtained at 10^{-4} psi, after 100 compressive load cycles from zero to 0.15 psi, are a conservative prediction of the in-space layer density.

Further testing of the effects of compression cycling on the layer density does not appear to be required for the six composites considered in this study. Compression cycle testing and the test procedure used in this study are, however, recommended for composites identified in future studies. Testing to a high compressive load of 15 psi is not recommended in future tests unless this loading is a definite possibility for the application being considered.

3.10 FLAT-PLATE CALORIMETER TESTS

Thermal performance data are required for selection of composite materials and thermal analyses. To obtain these data, an effective thermal conductivity was obtained for four composites while in a vacuum of less than 10^{-6} Torr and at several compressive loadings. In addition to these tests, the effective thermal conductivity of one of the composites with interstitial gas in the specimen at pressures of 1×10^{-3} and 1 torr was obtained.

3.10.1 Test Specimens

The test specimens were composed of 10 layer-pairs of reflectors and separators, and were 20.4 in. in diameter. A typical flat-plate calorimeter specimen is shown in Figure 3-65. The composites tested were DAK/Nomex HT-287, DGK/Nomex HT-287, DGK/Nomex HT-96, and DGK/Dacron B4A. Utilization of DGK with each of the three candidate separators allowed a comparison of the relative performance of these separators. The

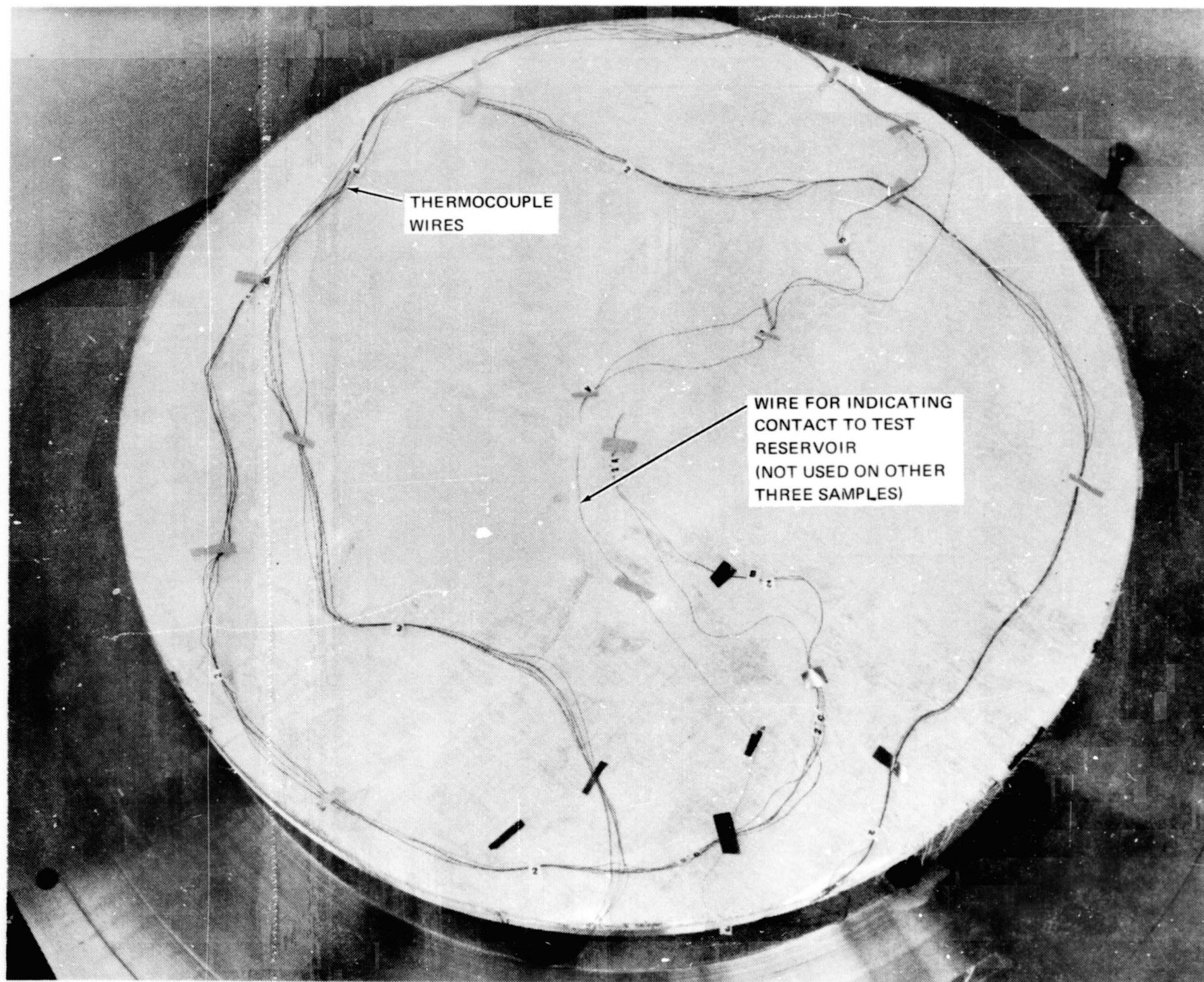


Figure 3-65. DAK/Nomex HT-287 Flat Plate Calorimeter Specimen

DAK/Nomex HT-287 specimen allowed a comparison of the relative performance of the DGK and DAK reflector materials.

3.10.2 Test Apparatus

A flat-plate calorimeter utilizing the boiloff of a cryogenic liquid to measure the heat flux through the test specimen was used to determine the effective thermal conductivity of the composites. Temperatures on the cold face side of the specimen can be controlled by various cryogenic liquids, depending upon the temperature range desired and the heat flux through the specimen. In this test, liquid nitrogen was used to obtain a cold face temperature of -320°F . The hot side of the specimen was controlled to maintain a temperature of 75°F by the use of a temperature controller attached to a 20.5-in.-dia specimen heater. The temperatures were monitored by two sets (four thermocouples per set) of iron-constantan thermocouples attached to the cold face of the specimen and one set attached to the heater.

The calorimeter is shown schematically in Figure 3-66, and a photograph of the calorimeter test setup and instrumentation is shown in Figure 3-67. The calorimeter consists of a central test reservoir surrounded by two guard reservoirs. The central test reservoir has an effective area of 754 cm^2 . A 4-in.-wide inner guard reservoir containing the same cryogen as that in the test reservoir surrounds the inner test reservoir. The outer guard, which surrounds both inner reservoirs, has two functions: it reduces the heat leak down the fill and vent tubes and it reduces the boiloff in the inner guard by preventing radiation exchange between the calorimeter wall and the wall of the inner guard.

Attached to the outer guard is a copper curtain that extends down past the inner guard and past the specimen. The copper curtain, cooled by conduction, establishes a cold wall for radiation exchange between the outer edge of the specimen and the calorimeter. The result is a significant reduction in lateral heat transfer in the specimen, improvement of one-dimensional heat transfer normal to the specimen under steady-state conditions, and an increase in the accuracy of the data.

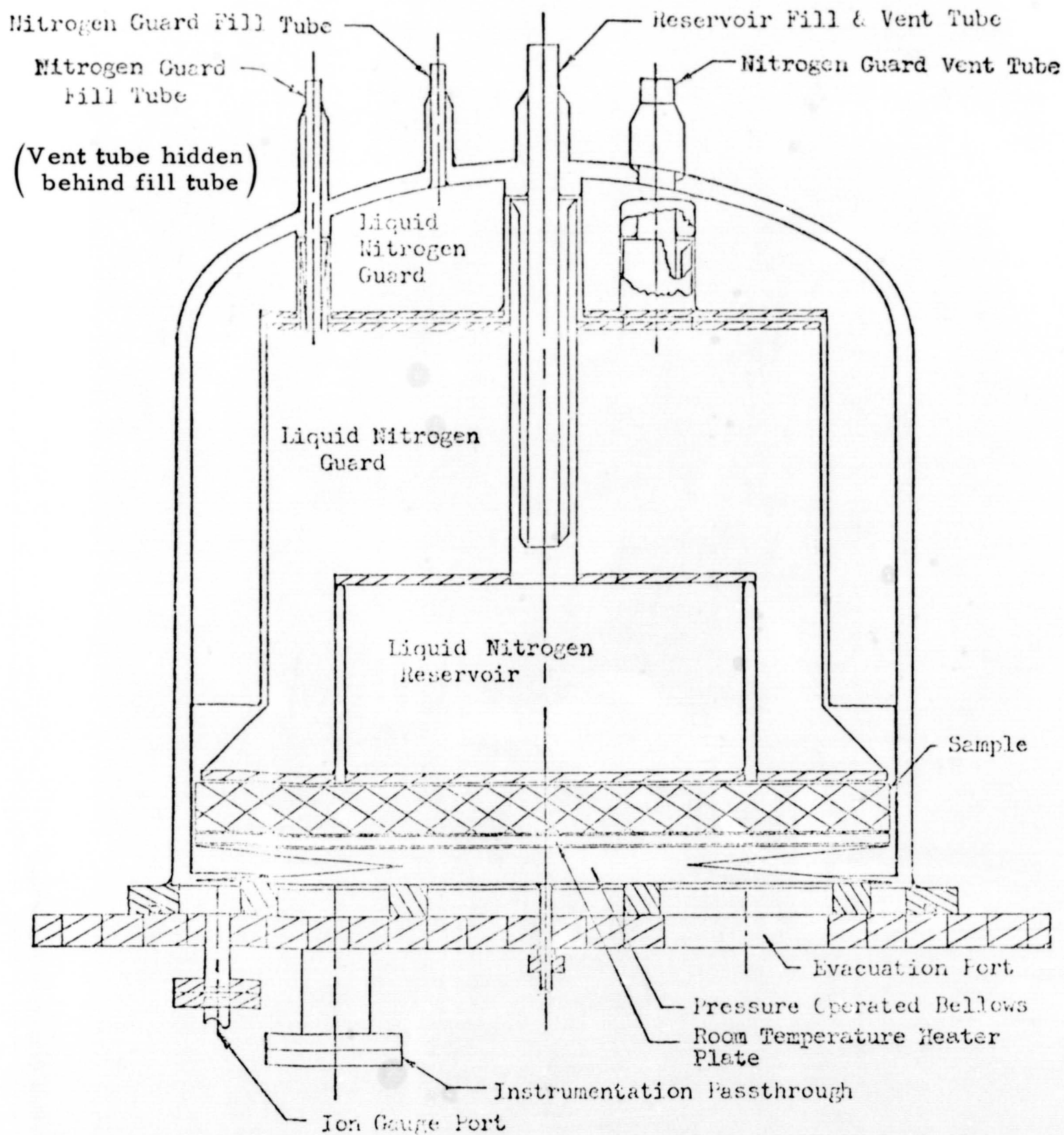


Figure 3-66. Cross-Sectional View of Flat Plate Calorimeter

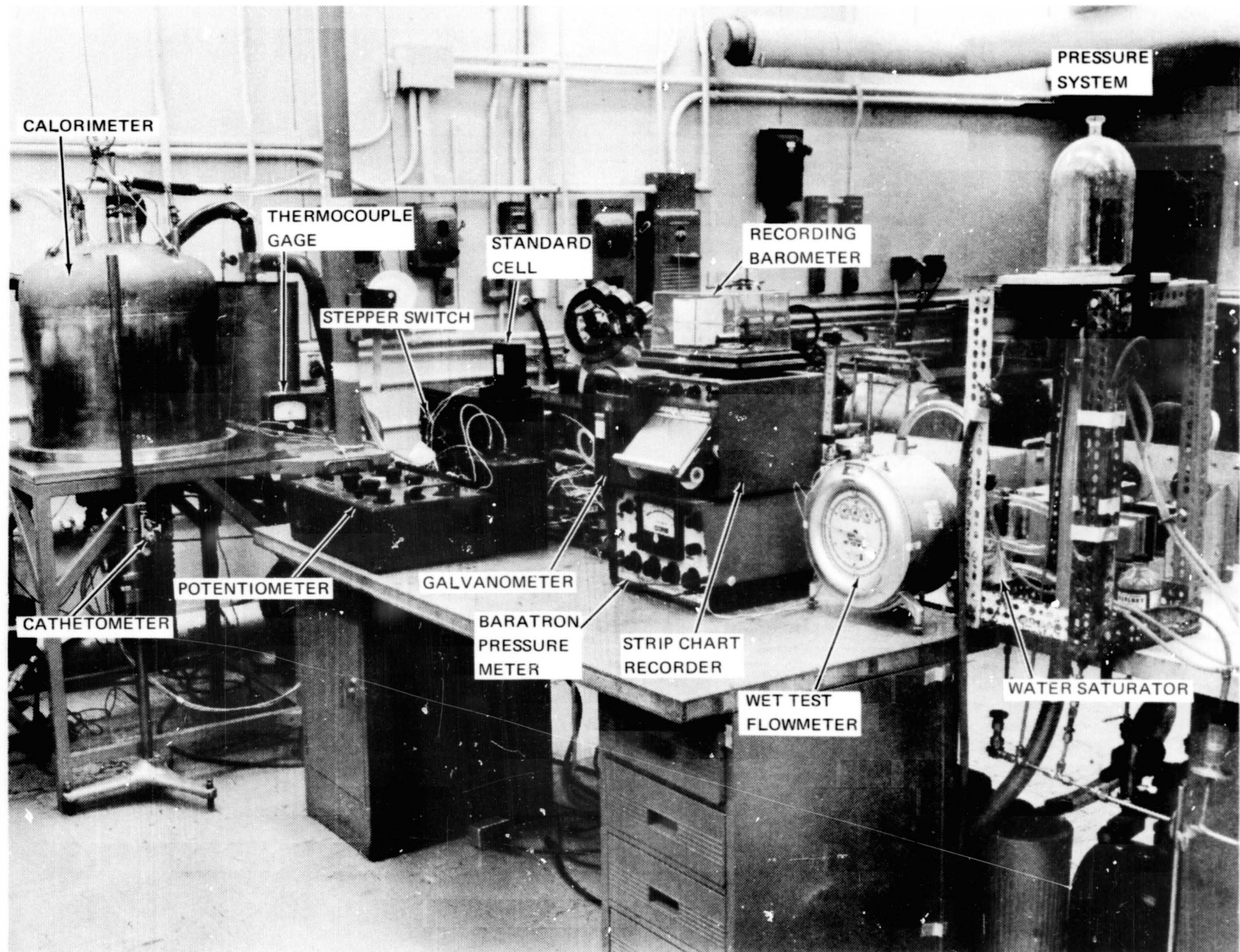
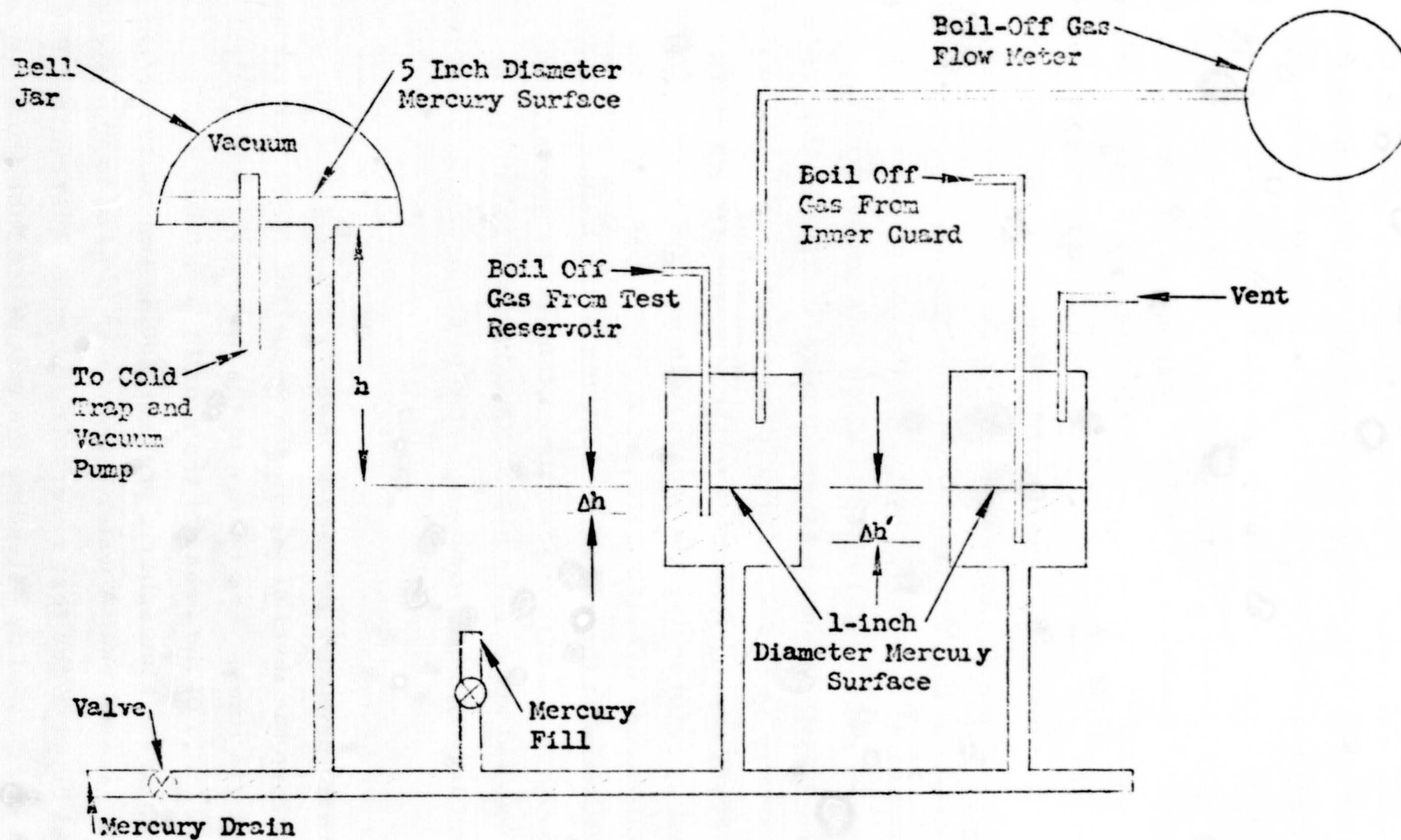


Figure 3-67. Flat Plate Calorimeter Test Setup

High-performance insulations require a long time to establish steady-state heat transfer for small heat fluxes. Therefore, disturbance of the liquid cryogen must be minimized to ensure a constant heat flux through the composite specimen for reliable thermal conductivity data at low compressive loads. Disturbances of the temperatures of the liquid cryogen are caused by atmospheric pressure changes, refilling the reservoir with the cryogenic fluid, and rapid boiloff of the cryogenic liquid. All of these disturbances were minimized in this test. The outer guard significantly reduced the heat leak into the inner guard, thereby permitting tests at all compressive loads to be evaluated without refilling the inner guard. The boiling point of liquid nitrogen changes with variations in atmospheric pressure. Temperature and boiloff variations of the liquid nitrogen due to atmospheric pressure changes were reduced by a factor of 25 by having the gas pressure in the test reservoir and inner guard referenced to a common pressure. The gas pressure control system is shown schematically in Figure 3-68. The device, which is basically an L-shaped tube filled with mercury, maintains a near-constant mercury level. Reduction of the atmospheric pressure variation is achieved by referencing the pressure in the test reservoir and inner guard to the difference in height between the two short legs and the 5-in. -dia mercury surface at the end of the long leg of the L-tube. The exits of the lines carrying the boiloff gases from the test reservoir and inner guard are immersed about 1 in. below the surface of the mercury in the 1-in. -dia short legs of the L-tube subjected to atmospheric pressure variations.

Changes in atmospheric pressure produce changes in the height of the mercury column between the level of the mercury surface in the bell jar and the exit of the boiloff gas lines. The change in the mercury column height is proportional to the ratio of the areas of the small glass tubes and the bell jar, resulting in $1/25$ of the atmospheric pressure being sensed by the gas in the test and guard reservoirs. A water manometer is used to indicate the pressure differential between the test reservoir and guard reservoir. The pressure difference is adjusted by extending the exit of the tube from the inner reservoir about 1 to 2 mm further into the mercury than the tube from the test reservoir. The inner guard is maintained at a slightly higher



Mercury

- h = Height of Mercury column corresponding to atmospheric pressure
 Δh = Height corresponding to positive pressure of test reservoir, ~ 25 mm
 $\Delta h'$ = Height corresponding to positive pressure of inner guard, ~ 27 mm

Figure 3-68. Calorimeter Gas-Pressure Control System

pressure to prevent the recondensation of the boiloff gas in the exhaust tube of the test reservoir. The gas pressure above the liquid nitrogen in the outer guard is at a positive pressure with respect to that in the test reservoir and in the inner guard.

The specimen was mechanically loaded by the use of a pressure-operated bellows placed under the heater. A glass tube in the bellows pressurization line contained a spring-loaded metal pointer which extended into the bellows and reacted against the top of the bellows. This was designed and installed after the first test. Movement of the bellows in the vacuum system was measured by recording the movement of the metal pointer using a cathetometer. The uncertainty of these measurements was less than ± 0.002 in.

The vacuum seal for the calorimeter was obtained with an O-ring. Changes in atmospheric pressure produced changes in the total load exerted on the calorimeter resulting in slightly different O-ring compression values. For very low compressive loads, the movement of the calorimeter produced noticeable changes in pressure of the bellows. These pressure fluctuations with atmospheric pressure variation were reduced significantly by incorporating a Cartesian Manostat (Manostat Corp.) in the bellows pressurization line and maintaining a very small continuous gas flow to the bellows. The bellows pressure was measured using a Baratron pressure gage (MKS Instruments Inc.). Heat flux through the specimen was measured using a flowmeter (Precision Scientific Co.) to monitor the boiloff exhaust gases from the test reservoir.

3.10.3 Test Procedure—Hard Vacuum Tests

The effective thermal conductivity versus compressive load was established by obtaining the heat flux through the insulation at several compressive loadings. At each test point, the compressive load (therefore specimen thickness) was held constant until steady-state heat transfer through the specimen was established. All of these tests were conducted in a vacuum of pressures less than 1×10^{-6} torr. The 10 layer-pair specimens (10 reflectors and 10 separators) were placed in the calorimeter so that a separator was in contact with the cold plate and a reflector was in contact with the hot plate.

Before conducting the tests on the specimens, the inherent heat leak into the test reservoir was measured. This heat leak determination was made under conditions identical to those during evaluation of the test composites, except for an additional cooled plate placed between the test reservoir and the bellows pressurization system. This plate was cooled to liquid nitrogen temperatures to reduce radiation exchange between the test reservoir and the surroundings. Calorimeter pressure during the heat leak evaluation was less than 5×10^{-6} torr.

It was not possible to directly measure the thickness of the insulation in the calorimeter during the test. However, the thickness of the insulation and the distance between the test reservoir (cold plate) and the hot plate was obtained for all but the DAK/Nomex HT-287 specimen by recording the movement of the bellows on which the hot plate rested. The apparatus for this measurement is discussed in the previous section. These bellows displacement measurements were used with a known initial hot-plate-to-test-reservoir spacing to determine the specimen thickness. The initial hot-plate-to-test reservoir spacing was accurately established under temperature and vacuum conditions identical to those encountered during a test.

The compressive load on the test specimen at each test point, except for the DAK/Nomex HT-287 specimen, was obtained by utilizing the measured insulation thickness at that point and the data obtained in the compression tests reported in Section 3.9. The insulation thickness and the fact that there were 10 layer-pairs provided a layer density which was used in the appropriate curve in Figure 3-62, 3-63, or 3-64 to yield the anticipated compressive load. An average of the two curves for 10-layer-pair specimens shown in Figures 3-62, 3-63, and 3-64 was used. It was assumed that DGK and DAK would have an identical layer density versus compressive loading relationship.

The test procedure for the first test (DAK/Nomex HT-287) was different from that for the other three composites as there was no measurement of the insulation thickness. In this test, the point of zero compressive load on the specimen was established by an electrical contact between the test

reservoir and a fine wire placed on top of the test specimen. The pressure to the bellows was then increased to the desired compressive load. Several problems were encountered with this procedure. The fine wire used for establishing the point of contact between the insulation and the test reservoir produced an unacceptable uncertainty in determining the point of zero load on the insulation. This was due to the difficulty in making the wire lie coplanar with the specimen surface, resulting in the insulated wire contacting the reservoir at points other than the center. When this occurred, the wire was compressed into the insulation, necessitating a higher compressive load to make an electrical contact at the center of the specimen. Another problem encountered was the uncertainty in the compressive loading values because the bellows pressure includes both the specimen compressive loading and a loading due to friction within the system. After installation of the bellows deflection measurement apparatus, a curve showing the relationship between the position of the bellows and the bellows pressure with no specimen in the apparatus was established. The difference between the bellows pressure with a specimen installed and with no specimen was the compressive loading. Unfortunately, the magnitude of the friction was such that it negated obtaining compressive loads of less than 2×10^{-3} psi and resulted in uncertainties of approximately 25 percent at a compressive load of 1×10^{-2} psi. In order to utilize the data obtained from the DAK/Nomex HT-287, it was assumed that the bellows pressure would be identical between the DAK/Nomex HT-287 and DGK/Nomex HT-287 at a given specimen thickness; this assumption that DGK and DAK would have an identical layer-density-versus-compressive-load relationship was used throughout this study. Thus, the compressive loading and specimen thickness were determined for the DAK/Nomex HT-287 by using the bellows-pressure data for this specimen and the bellows-pressures-versus-bellows-deflection curve for the DGK/Nomex HT-287 specimen.

3.10.4 Test Results—Hard Vacuum Tests

The effective thermal conductivity (k), obtained as a function of compressive load for each of the composites tested, is shown in Figure 3-69 and Tables 3-25 through 3-28. As shown, the Dacron B4A separator provides

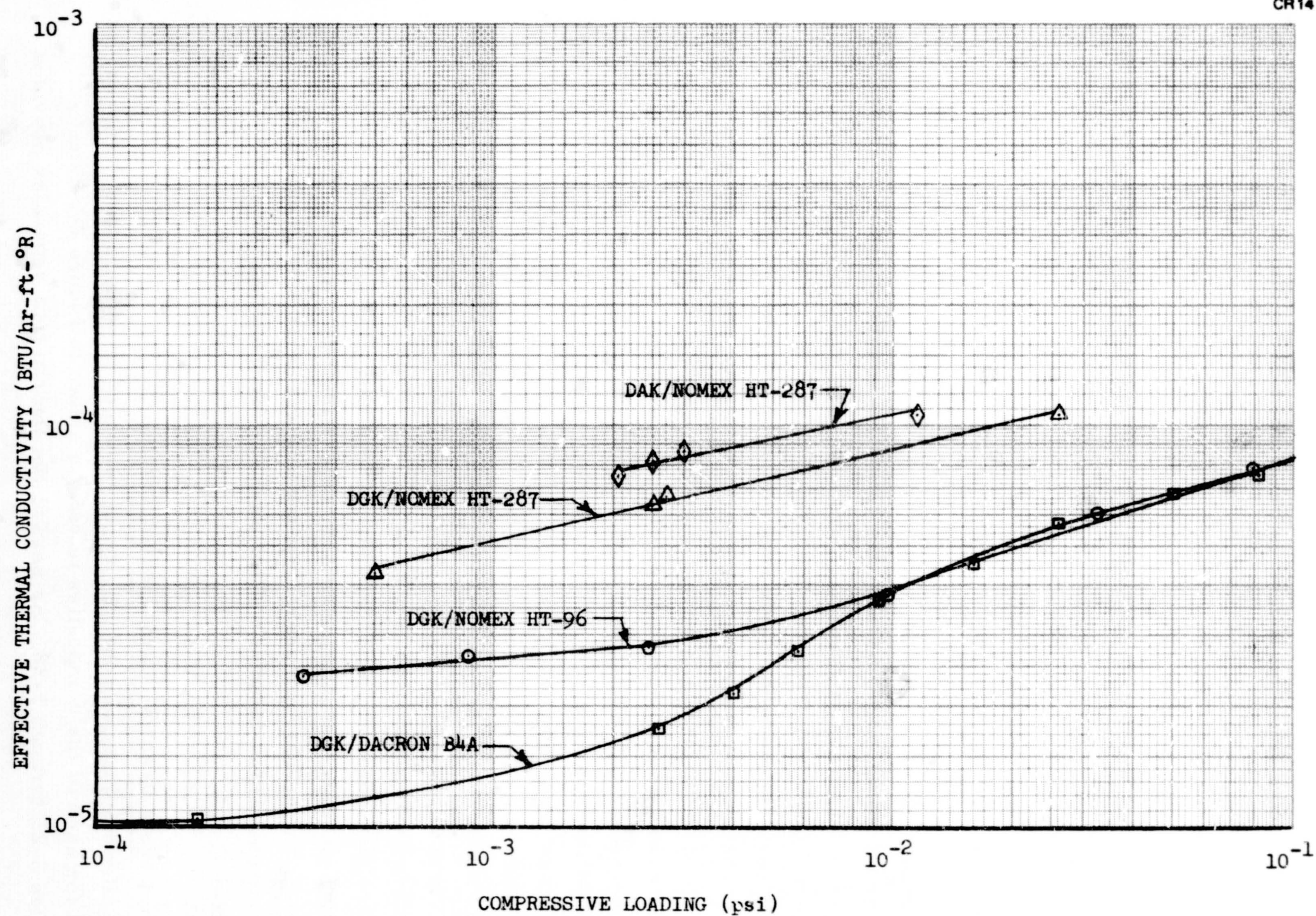


Figure 3-69. Effective Thermal Conductivity—Flat Plate Calorimeter Data

Table 3-25
DAK/NOMEX HT-287 FLAT-PLATE CALORIMETER DATA

Layer Density (layer pairs/inch)	Specimen Thickness (ft)	Compressive Load (psi)	Weight Density (lb/ft ³)	Effective Thermal Conductivity (k) (Btu/ft-hr-°R)	$k\rho$ (Btu-lb/ft ⁴ -hr-°R)
64.1	0.013	2.06×10^{-3}	7.46	7.49×10^{-5}	5.58×10^{-4}
65.4	0.01275	2.5×10^{-3}	7.60	8.13×10^{-5}	6.18×10^{-4}
67.1	0.0124	3.0×10^{-3}	7.81	8.64×10^{-5}	6.74×10^{-4}
84.0	0.00992	1.15×10^{-2}	9.78	1.068×10^{-4}	1.043×10^{-3}

Table 3-26
DGK/NCMEX HT-287 FLAT-PLATE CALORIMETER DATA

Layer Density (layer pairs/inch)	Specimen Thickness (ft)	Compressive Load (psi)	Weight Density (lb/ft ³)	Effective Thermal Conductivity (k) (Btu/ft-hr-°R)	$k\rho$ (Btu-lb/ft ⁴ -hr-°R)
55.2	0.0151	5.0×10^{-4}	6.42	4.22×10^{-5}	2.705×10^{-4}
65.4	0.01275	2.5×10^{-3}	7.60	6.31×10^{-5}	4.78×10^{-4}
66.2	0.0126	2.7×10^{-3}	7.70	6.68×10^{-5}	5.14×10^{-4}
92.6	0.009	2.6×10^{-2}	11.78	1.057×10^{-4}	1.243×10^{-3}

Table 3-27

DGF/NOMEX HT-96 FLAT-PLATE CALORIMETER DATA

Layer Density (layer pairs/inch)	Specimen Thickness (ft)	Compressive Load (psi)	Weight Density (lb/ft ³)	Effective Thermal Conductivity (k) (Btu/ft-hr-°R)	k_p (Btu-lb/ft ⁴ -hr-°R)
54.9	0.0152	3.3×10^{-4}	5.46	2.36×10^{-5}	1.29×10^{-4}
59.5	0.014	8.6×10^{-4}	5.93	2.66×10^{-5}	1.575×10^{-4}
65.0	0.0128	2.45×10^{-3}	6.48	2.78×10^{-5}	1.8×10^{-4}
74.7	0.01118	9.7×10^{-3}	7.43	3.77×10^{-5}	2.8×10^{-4}
87.0	0.00958	3.25×10^{-2}	8.66	6.02×10^{-5}	5.21×10^{-4}
101.0	0.00825	7.9×10^{-2}	10.08	7.89×10^{-5}	7.95×10^{-4}
118.0	0.00709	1.5×10^{-1}	11.70	9.53×10^{-5}	11.14×10^{-4}
126.5	0.00659		12.60	1.04×10^{-4}	13.1×10^{-4}

Table 3-28

DGK/DACRON B4A FLAT-PLATE CALORIMETER DATA

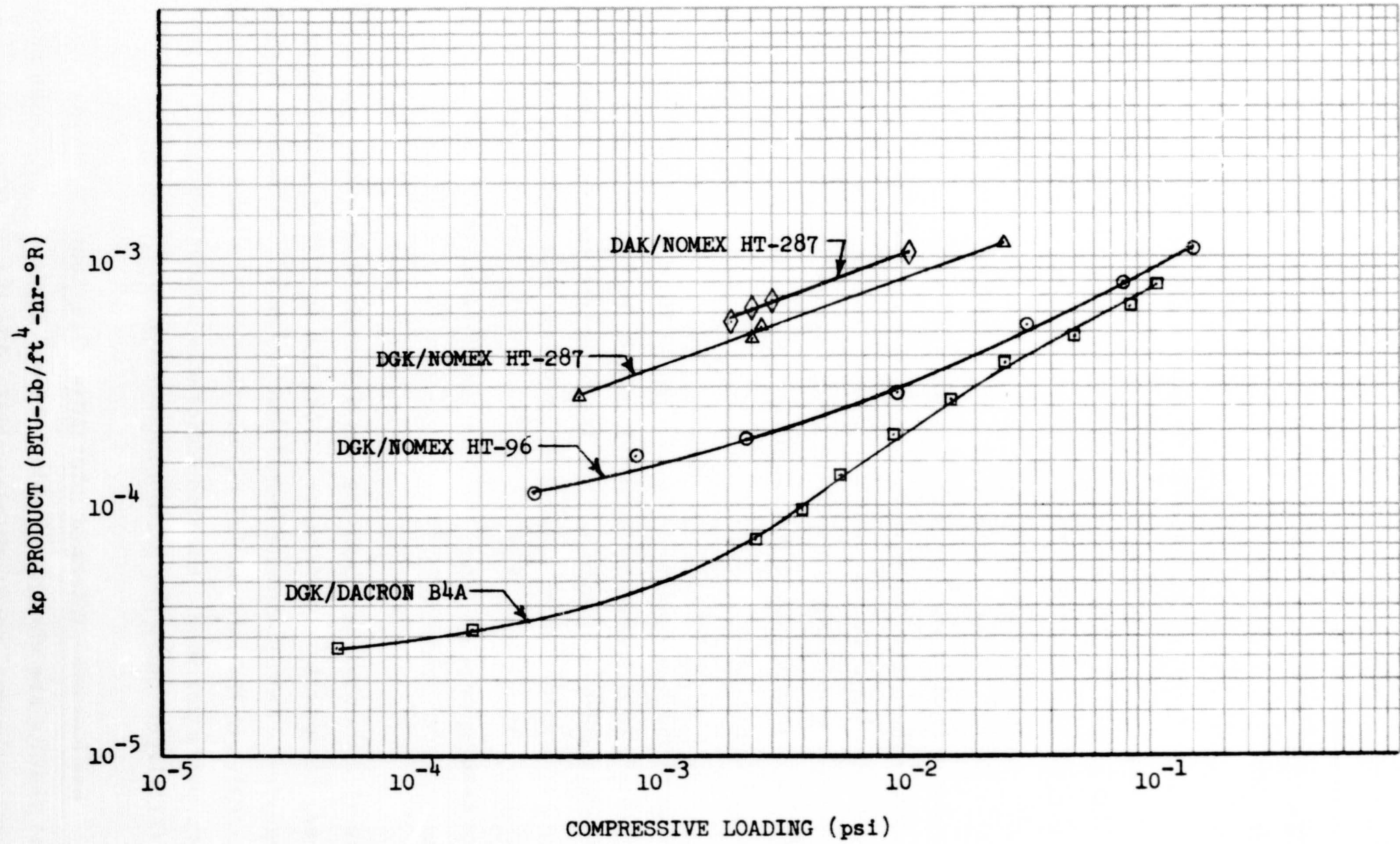
Layer Density (layer pairs/inch)	Specimen Thickness (ft)	Compressive Load (psi)	Weight Density (lb/ft ³)	Effective Thermal Conductivity (k) (Btu/ft-hr-°R)	$k\rho$ (Btu-lb/ft ⁴ -hr-°R)
65.8	0.01266	4.6×10^{-5}	2.61	1.02×10^{-5}	2.66×10^{-5}
78.2	0.01067	1.8×10^{-4}	3.09	1.04×10^{-5}	3.21×10^{-5}
103.1	0.00809	2.6×10^{-3}	4.08	1.76×10^{-5}	7.18×10^{-5}
113.7	0.00734	4.0×10^{-3}	4.49	2.12×10^{-5}	9.52×10^{-5}
123.5	0.00676	5.8×10^{-3}	4.88	2.71×10^{-5}	1.322×10^{-4}
137.0	0.00609	9.2×10^{-3}	5.41	3.53×10^{-5}	1.91×10^{-4}
151.5	0.0055	1.6×10^{-2}	6.0	4.43×10^{-5}	2.66×10^{-4}
164.0	0.00508	2.6×10^{-2}	6.49	5.73×10^{-5}	3.72×10^{-4}
185.0	0.0045	5.0×10^{-2}	7.33	6.72×10^{-5}	4.91×10^{-4}
208.5	0.0040	8.2×10^{-2}	8.25	7.57×10^{-5}	6.24×10^{-4}
232.5	0.00359	1.18×10^{-1}	9.20	8.49×10^{-5}	7.81×10^{-4}

the lowest k values for the compressive loads of most interest ($<10^{-3}$ psi). Of the two Nomex separators tested, the Nomex HT-96 has a lower k than the Nomex HT-287. A comparison of the k values for DGK/Nomex HT-287 and DAK/Nomex HT-287 indicates that use of a goldized reflector (DGK) will result in a slightly lower effective thermal conductivity than will an aluminized reflector. This was expected because the emissivity of the goldized surface is slightly less than that of the aluminized surface. Because of the problems encountered in the first test (DAK/Nomex HT-287) as discussed previously, k values of less than 2×10^{-3} were not obtained. However, the relative performance of the DGK and DAK composites is expected to follow the same trend at compressive loadings of less than 10^{-3} psi.

Since the separators do not have the same weight, a comparison of the composite weights required to provide equivalent thermal performance is needed for ranking purposes. This type of comparison is called a $k\rho$ comparison where k is the effective thermal conductivity (Btu/hr ft $^{\circ}$ R) and ρ is the composite density (lb/ft 3). It can be shown that if two composites are sized to give an equal steady-state thermal performance, the ratio of the $k\rho$ product for the two composites is equal to the ratio of their composite weights. The $k\rho$ values obtained from the calorimeter test data are shown in Figure 3-70 and Tables 3-25 through 3-28. The Dacron B4A separator clearly provides the lowest system weight and therefore the best thermal performance of the three separators tested. The Nomex HT-96 has a lower $k\rho$ product than the Nomex HT-287, but a significantly higher one than the Dacron B4A at the compressive loads of most interest.

3.10.5 Test Apparatus and Procedures—Effect of Interstitial Gas Tests

The 10 layer-pair double-goldized Kapton/Dacron B4A specimen used in the previously discussed hard vacuum calorimeter tests was also used in these tests. The test setup and apparatus were, with one exception, identical to those used previously, (refer to Section 3.10.2). This exception was a 1/4-mil Mylar sheet placed over the sample and sealed with RTV Silastic 140 adhesive to the aluminum plate upon which the sample rested. This was

Figure 3-70. $k\rho$ - Flat Plate Calorimeter Data

required to obtain the interstitial gas pressures of 1×10^{-3} and 1 torr within the specimen. Helium was used as the interstitial gas. A temperature of -320°F was maintained on the cold surface of the specimen. The hot surface of the specimen had temperatures ranging from 36° to 85°F , depending on the interstitial gas pressure.

The layer density of the test specimen had apparently been increased in the earlier tests, because micrometer measurements of the specimen prior to installation in the calorimeter showed a specimen thickness of 0.105 in. for a nearly-no-load condition. This corresponds to a layer density of approximately 95 layer-pairs per inch as compared to a layer density of 72 (or less) layer pairs per inch as shown in Figure 3-62 for a specimen being subjected to a load of 10^{-4} psi (or less) on the first compressive load cycle. Since the layer density vs. compressive load relationship no longer corresponds to the data obtained in the compression tests reported in Figure 3-62, a good indication of the compressive load at each test point could not be obtained. Data were also taken at a layer density of approximately 118 layer-pairs per inch.

In addition to the test points at 1×10^{-3} and 1 torr interstitial gas pressures, a steady-state heat transfer was obtained for the minimum interstitial pressure which could be obtained. Since the pressure gage used had a minimum capability of 1×10^{-3} torr, the actual minimum interstitial pressure obtained is not known but was less than 1×10^{-3} torr. Data at the minimum interstitial pressure were obtained for only the 95 layer-pairs-per inch layer density.

The effective thermal conductivity was determined from the specimen thickness, temperature difference across the specimen, and steady-state heat transfer. Test personnel noted that the steady-state heat transfer was very sensitive to the interstitial gas pressure at the lower compressive load (95 layer-pairs per inch), but this effect was almost negligible at the higher (118 layer-pairs per inch) compressive load.

3.10.6 Test Results—Effect of Interstitial Gas Tests

The test results are shown in Table 3-29 and Figure 3-71. Also shown are the effective thermal conductivities obtained in the previous tests for

Table 3-29

EFFECT OF INTERSTITIAL GAS PRESSURE ON EFFECTIVE
THERMAL CONDUCTIVITY OF DGK/DACRON B4A

Interstitial Helium Gas Pressure (torr)	Layer Density (Layer-Pairs per Inch)	Effective Thermal Conductivity (Btu/hr/ft ² ° R)
(1×10^{-6})	95	* 1.4×10^{-5}
(1×10^{-3})	95	2.8×10^{-5}
1×10^{-3}	95	4.0×10^{-5}
1.0	95	1.2×10^{-3}
(1×10^{-6})	118	* 2.4×10^{-5}
1×10^{-3}	118	1.7×10^{-4}
1.0	118	1.2×10^{-3}

*Interpolated from Table 3-28.

interstitial pressures less than 1×10^{-6} torr. Data for DAM/Dexiglas paper and aluminum foil/fiber glass paper composites, taken from Reference 8 and shown in Figure 3-71, indicate that the test data are consistent with the results of similar previous tests. Based on the effective thermal conductivities obtained, it appears that the minimum interstitial pressure which was obtained with the Mylar sheet installed was somewhere between 1×10^{-4} and 5×10^{-4} psi.

3.10.7 Flat Plate Calorimeter Tests—Conclusions and Recommendations

Of the three separators tested, the data indicate that the Dacron B4A will provide the best thermal performance. The Nomex HT-96 separator will provide a better thermal performance than Nomex HT-287, but both are associated with a significantly higher $k\rho$ product than is the Dacron B4A. As anticipated (gold has a lower emissivity), a goldized reflector appears to have a slight advantage over an aluminized reflector.

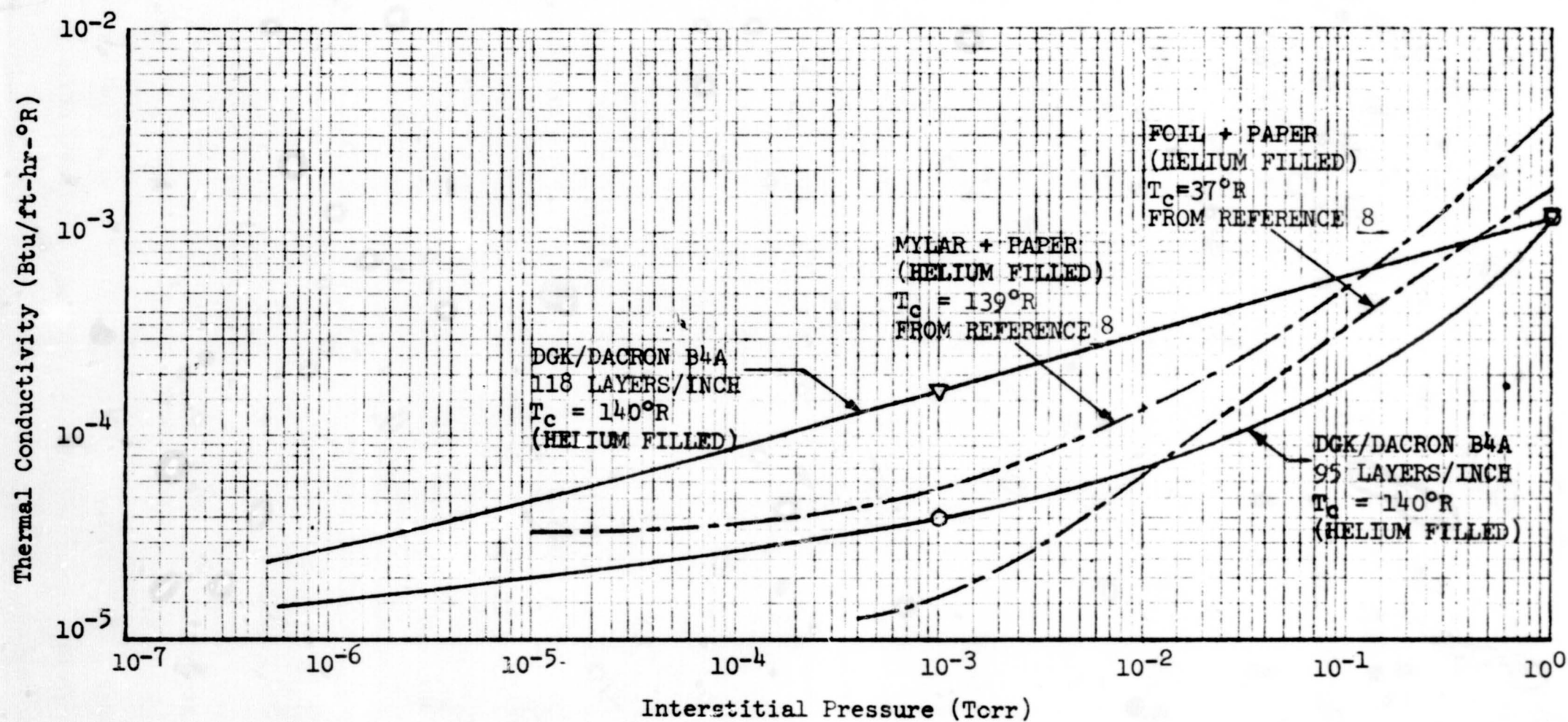


Figure 3-71. Effect of Interstitial Gas Pressure on Effective Thermal Conductivity of DGK/Dacron B4A

Section 4

DEFINITION OF ENVIRONMENT, TOOLING, AND DESIGN VERIFICATION TESTS-TASK 2

The objectives of Task 2 were to: (1) define the environmental parameters to be used in the study; (2) define the MLI manufacturing tooling and fixture requirements; and (3) delineate tests for composite survivability and verification testing.

4.1 ENVIRONMENT

The environmental parameters required for this study were defined in the early part of the contract. These environmental parameters included the temperature, pressure, and acceleration loading histories and the acoustic environment. The environments defined are those anticipated in the vicinity of the cryogenic storage tanks in a typical low-cross-range ILRV orbiter vehicle. The low-cross-range vehicle was selected because it was the basic vehicle configuration at that time.

4.1.1 Thermal Environment

In order to obtain a thermal environment for use in this study, analyses were accomplished which predicted the low-cross-range (LCR) orbiter vehicle side-wall skin-temperature histories at the locations of the secondary liquid hydrogen and liquid oxygen tanks. Because these temperatures exceeded the maximum allowable internal structural temperatures (300°F), it was assumed that a high-temperature insulation would be utilized on the inner surface of the vehicle skin to reduce these maximum temperatures to the allowable level. The resultant internal surface temperature histories are shown in Figure 4-1 through 4-4. An average temperature of 50°F was assumed for the structure surrounding the tanks while in orbit.

The skin-temperature histories were generated using the MDAC MINIVER (MINIature VERsion of the JA70) computer program (Reference 9). Using

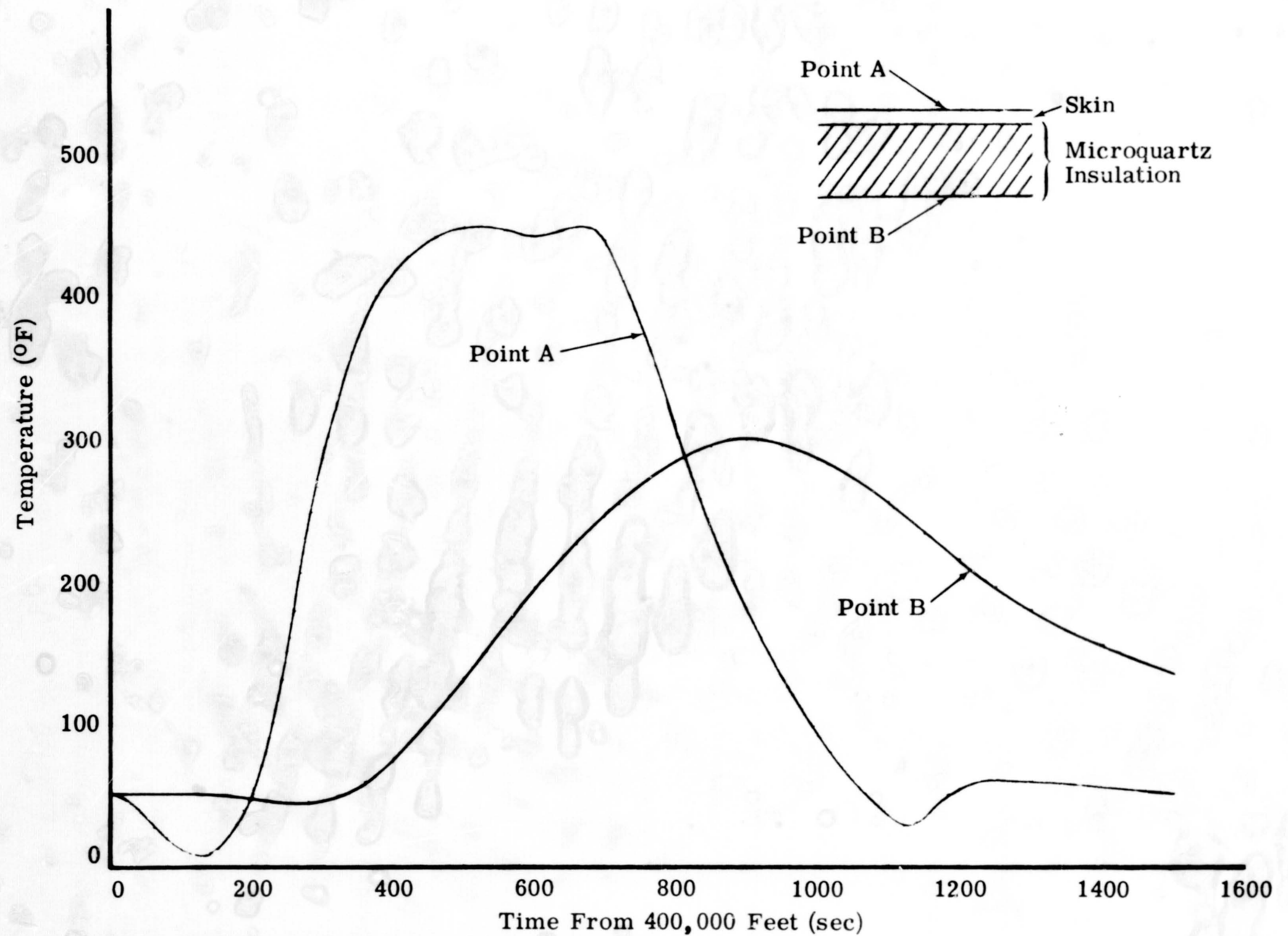


Figure 4-1. Temperature Histories During Reentry—Vicinity of LH₂ Tank

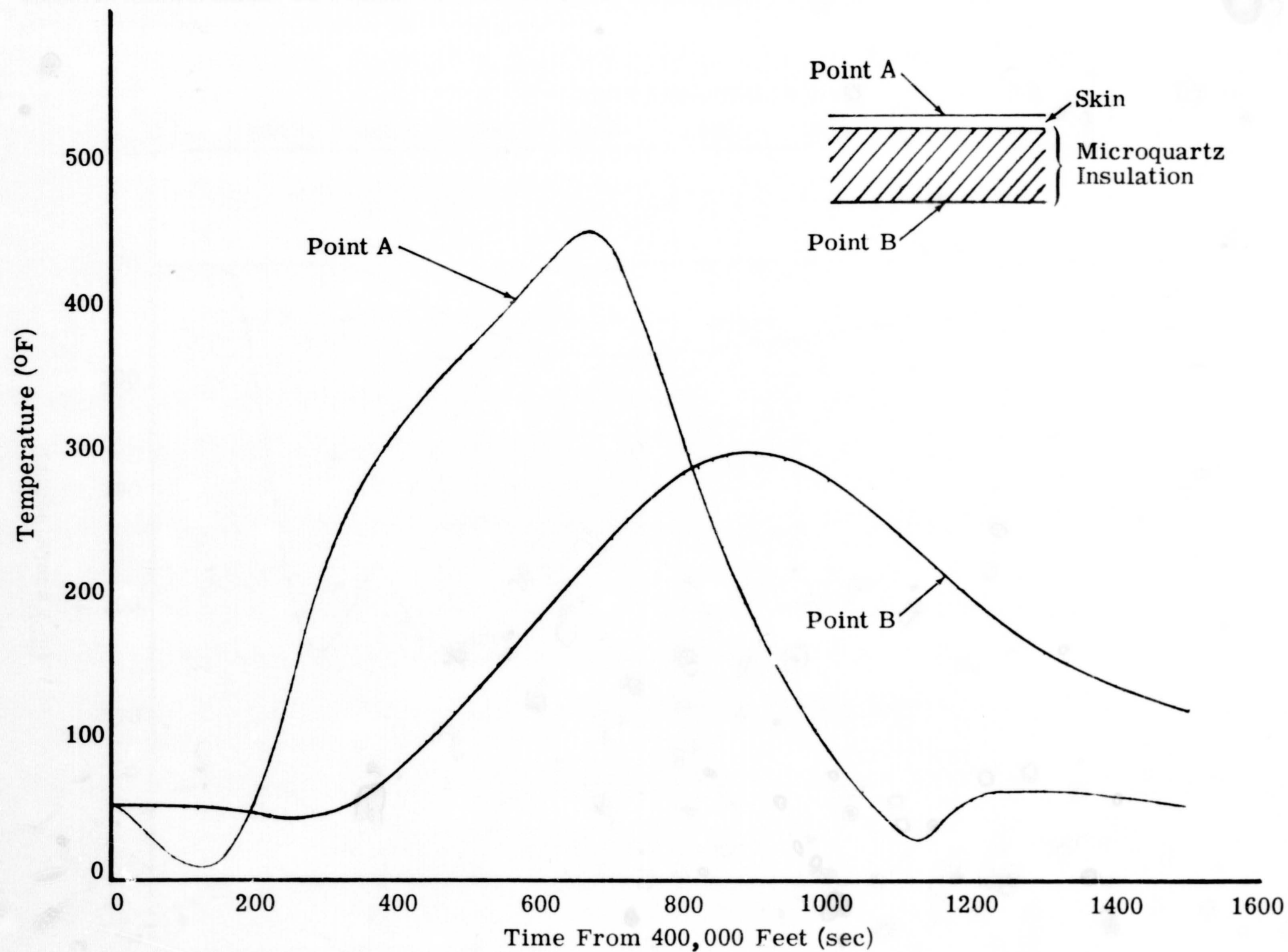


Figure 4-2. Temperature Histories During Reentry—Vicinity of LO₂ Tank

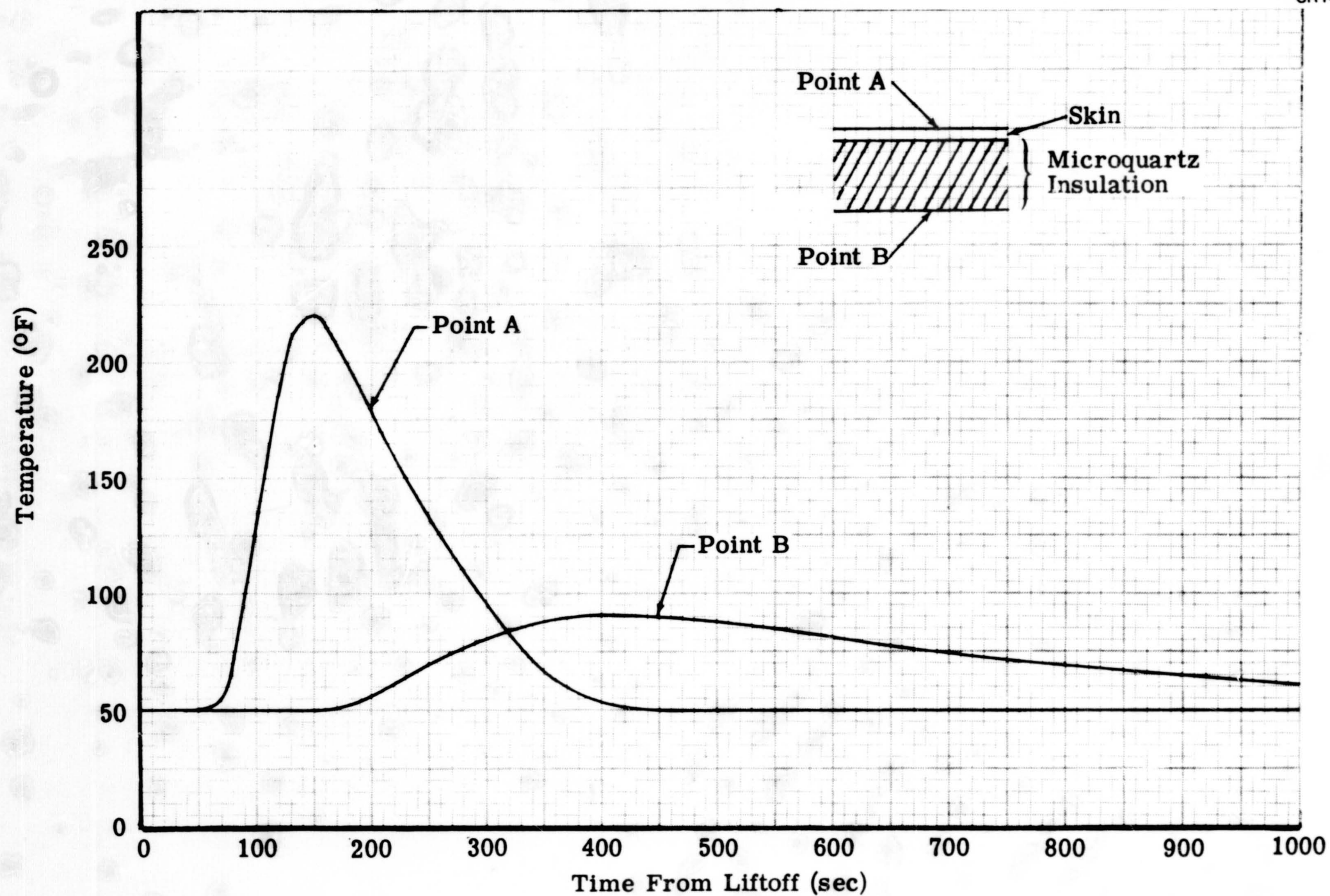


Figure 4-3. Temperature Histories During Ascent—Vicinity of LH₂ Tank

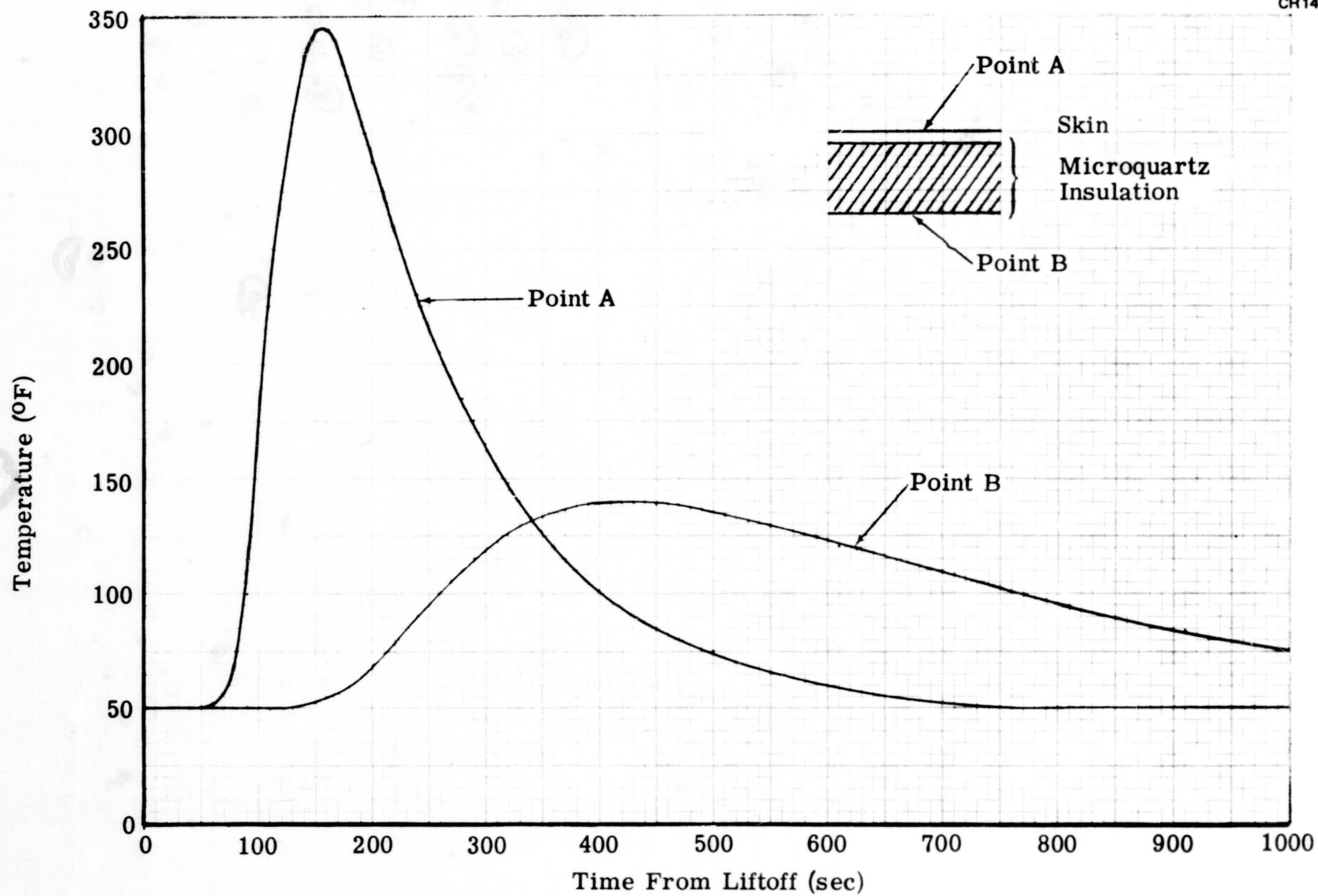


Figure 4-4. Temperature Histories During Ascent—Vicinity of LO₂ Tank

an input trajectory, the program calculates the local boundary layer edge properties using a real gas shock traverse and an isentropic expansion or compression to the desired surface pressure. Heat transfer is calculated using one of eight aerodynamic heating methods and a decision regarding transition is made. A thin skin temperature response is determined, along with the radiation equilibrium temperature. It is possible to obtain estimates of heating at locations whose flow fields are unknown by utilizing ratios to known environments. For the analysis presented, a typical LCR orbiter trajectory was used.

Reentry heating to the side of the orbiter was calculated using a ratio of 0.025 to the bottom centerline heat-transfer coefficient, a number derived from MACH 10 phase-change-paint data on the LCR orbiter. The bottom centerline aerodynamic heating was calculated assuming a shock parallel to the vehicle bottom using Eckert's reference enthalpy method for laminar flow and Spaulding and Chi's method for turbulent flow; the latter method incorporates the von Karman Reynolds analogy. Transition onset was calculated using the parameter

$$\left[\frac{Re_{\theta}}{M_e \left(\frac{\rho_e U_e}{\mu_e} \right)^{0.2}} \right]_{\text{onset}} = 20$$

where Re_{θ} is a compressible flat-plate momentum thickness Reynolds number. Fully turbulent flow was attained when the parameter value reached 80. Crossflow for the flat bottom of the LCR orbiter was accounted for by using a real gas equivalent of the method of Baranowski.

The ascent boundary layer edge properties were calculated assuming sharp plate flow (plus a Prandtl Meyer expansion for the liquid hydrogen tank location). Aerodynamic heating was calculated using the Eckert reference enthalpy method for laminar and Spaulding and Chi method for turbulent flow. Transition was assumed to occur at a boundary layer edge Reynolds number of 1 million.

The modified structural temperature histories resulting from the addition of insulation on the interior of the vehicle skin as shown in Figures 4-1 through 4-4 were obtained from a one-dimensional solution of a segment of the skin using the MDAC JA03 computer program. The temperature history of the skin which was generated with the use of the MINIVER program was used as a driving function to obtain the thermal response history for the inside surface of various thicknesses of microquartz insulation. That insulation thickness which effectively limited the temperature to 300°F at the inside surface was chosen. The same insulation thickness which is required during reentry to limit the maximum temperature to 300°F was also used to establish the ascent temperature histories.

The assumptions which were used in these analyses to define the thermal environment will result in conservative heat-transfer values for the secondary tankage; that is, the warmest conditions presently envisioned were used in order to assure values of heat transfer to the secondary tankage which are higher than nominal.

4.1.2 Pressure Environment

Pressure histories in the vicinity of the secondary liquid hydrogen and liquid oxygen tanks during ascent and reentry were obtained and are presented in Figures 4-5 and 4-6. The pressure histories shown are for a typical trajectory of the LCR orbiter. The ascent pressure histories were obtained from the output of the MINIVER program calculations discussed in Subsection 4.1.1. The predicted pressures are those on the sides of the vehicle at the desired locations. Because of the high angle of attack (60 degrees) during reentry, this computer program could not be used to predict the side-wall pressures during reentry. However, these pressures should not differ significantly from ambient pressures. The reentry pressures shown are ambient pressures obtained by using trajectory data and the 1962 US standard atmosphere.

4.1.3 Acceleration Loading Histories

Acceleration loading histories for both ascent and reentry were obtained for a typical LCR orbiter trajectory and are shown in Figures 4-7 and 4-8. A

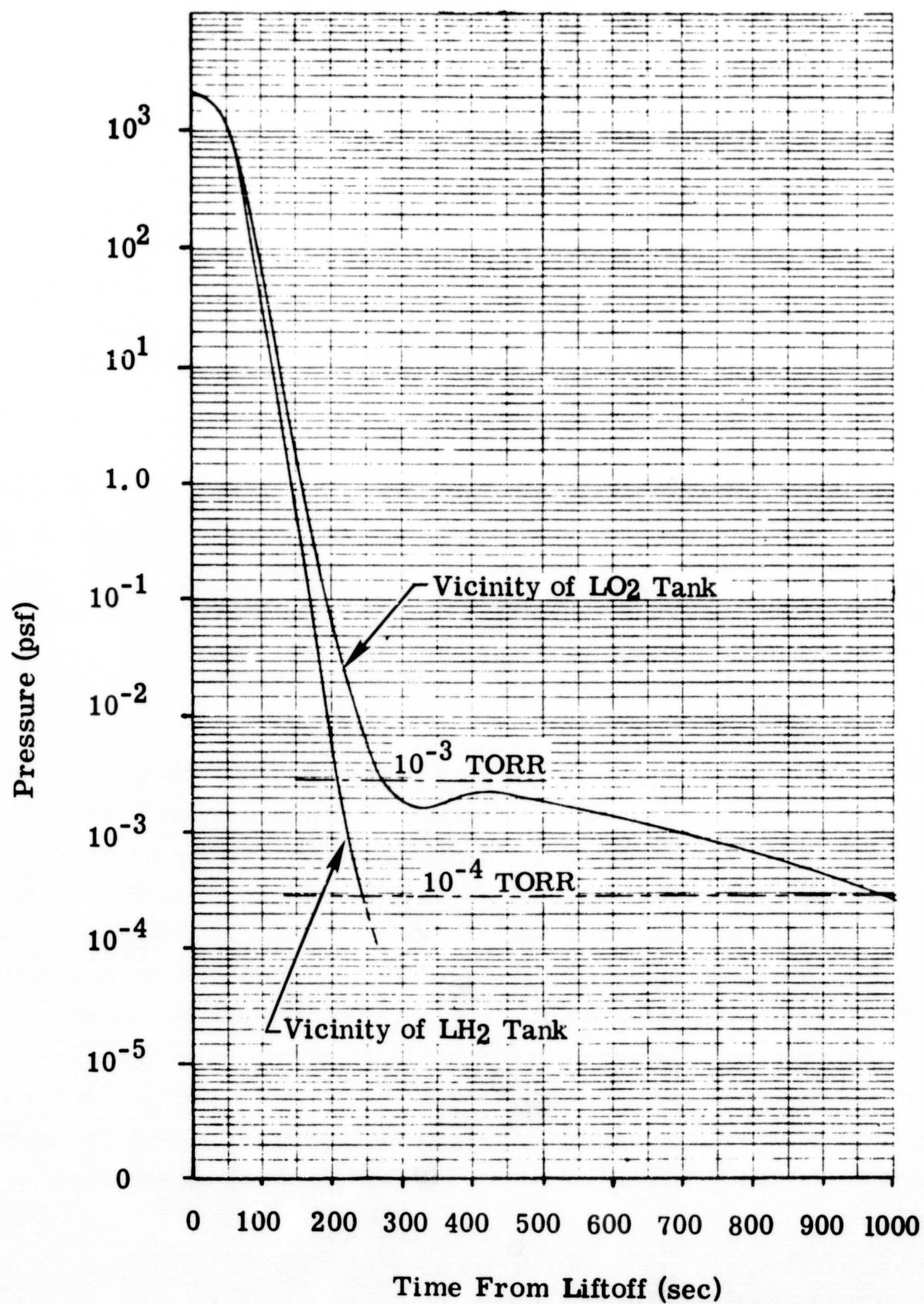


Figure 4-5. Pressure Histories During Ascent

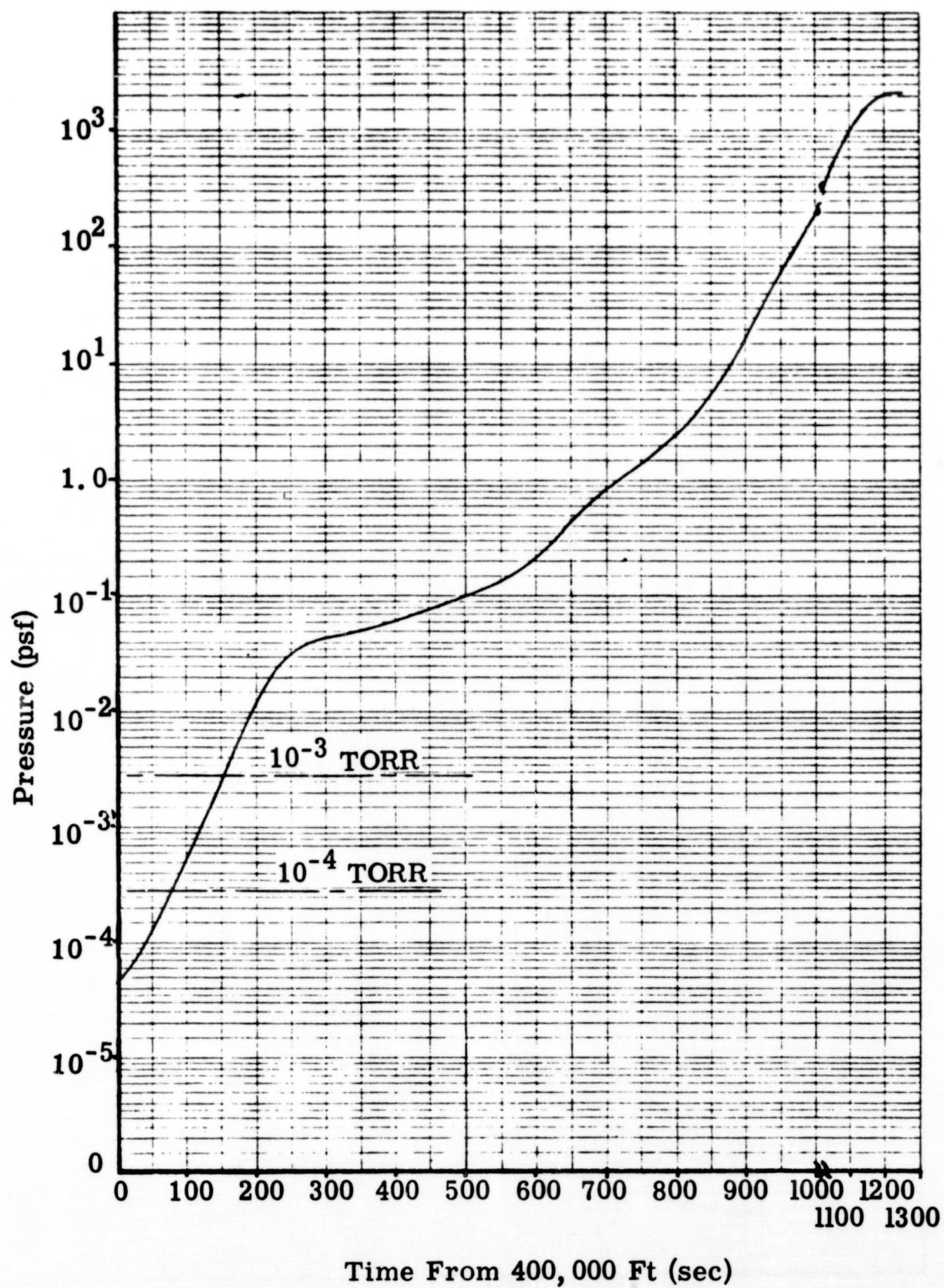


Figure 4-6. Pressure History During Reentry for Both LH₂ and LO₂ Secondary Tanks

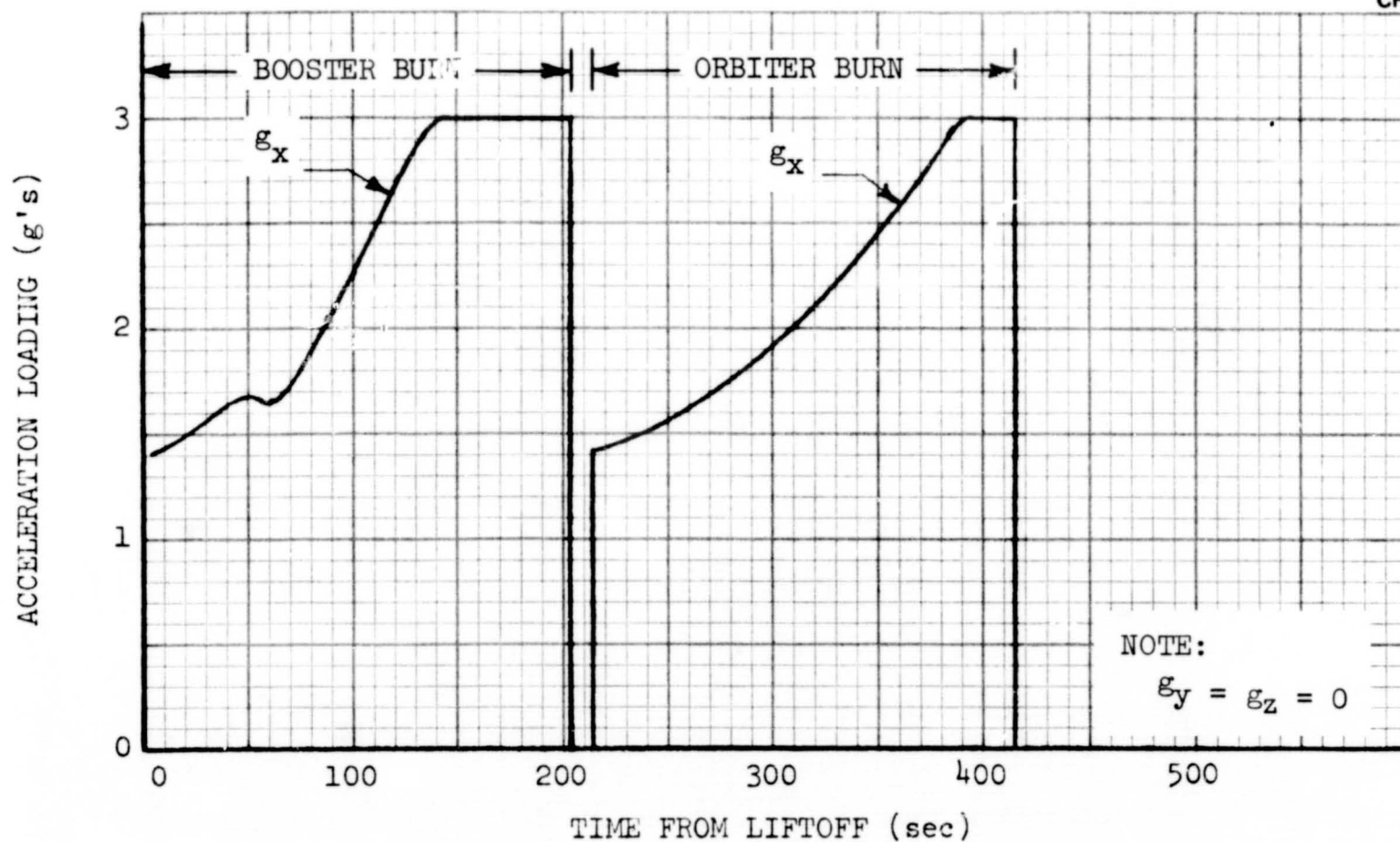


Figure 4-7. Acceleration Loading History During Ascent

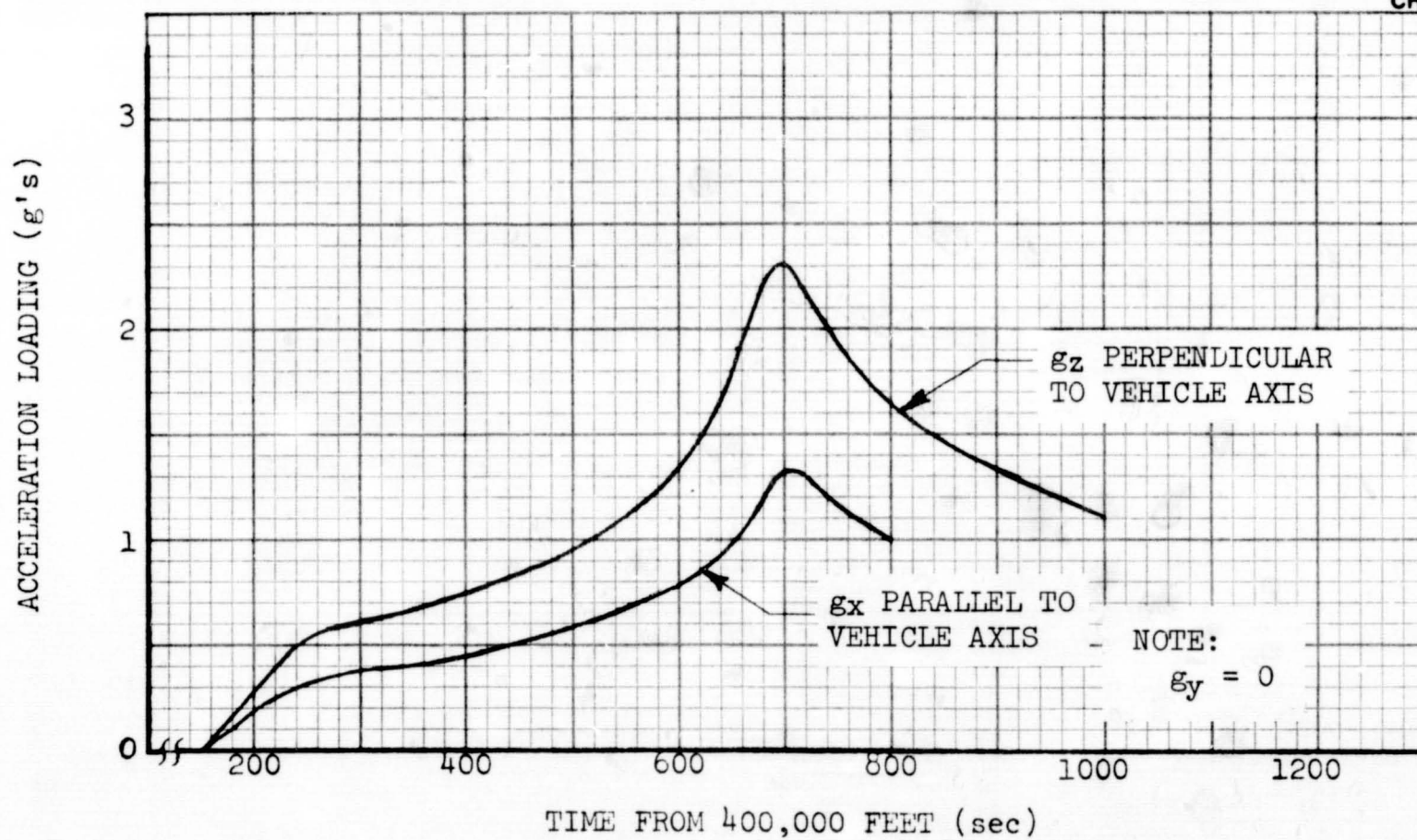


Figure 4-8. Acceleration Loading History During Reentry

short-time transient acceleration loading occurring immediately after clamp-down release at liftoff is not shown since it is expected that it will be significantly attenuated prior to reaching the vicinity of either the secondary liquid hydrogen or liquid oxygen tanks.

The loading will be parallel (g_x) to the vehicle axis during boost engine burn. The loading will also be essentially parallel (g_x) to the vehicle axis for the orbiter ascent burn period since the angle of attack during this period is 12 degrees or less and is less than 5 degrees during the peak acceleration loading.

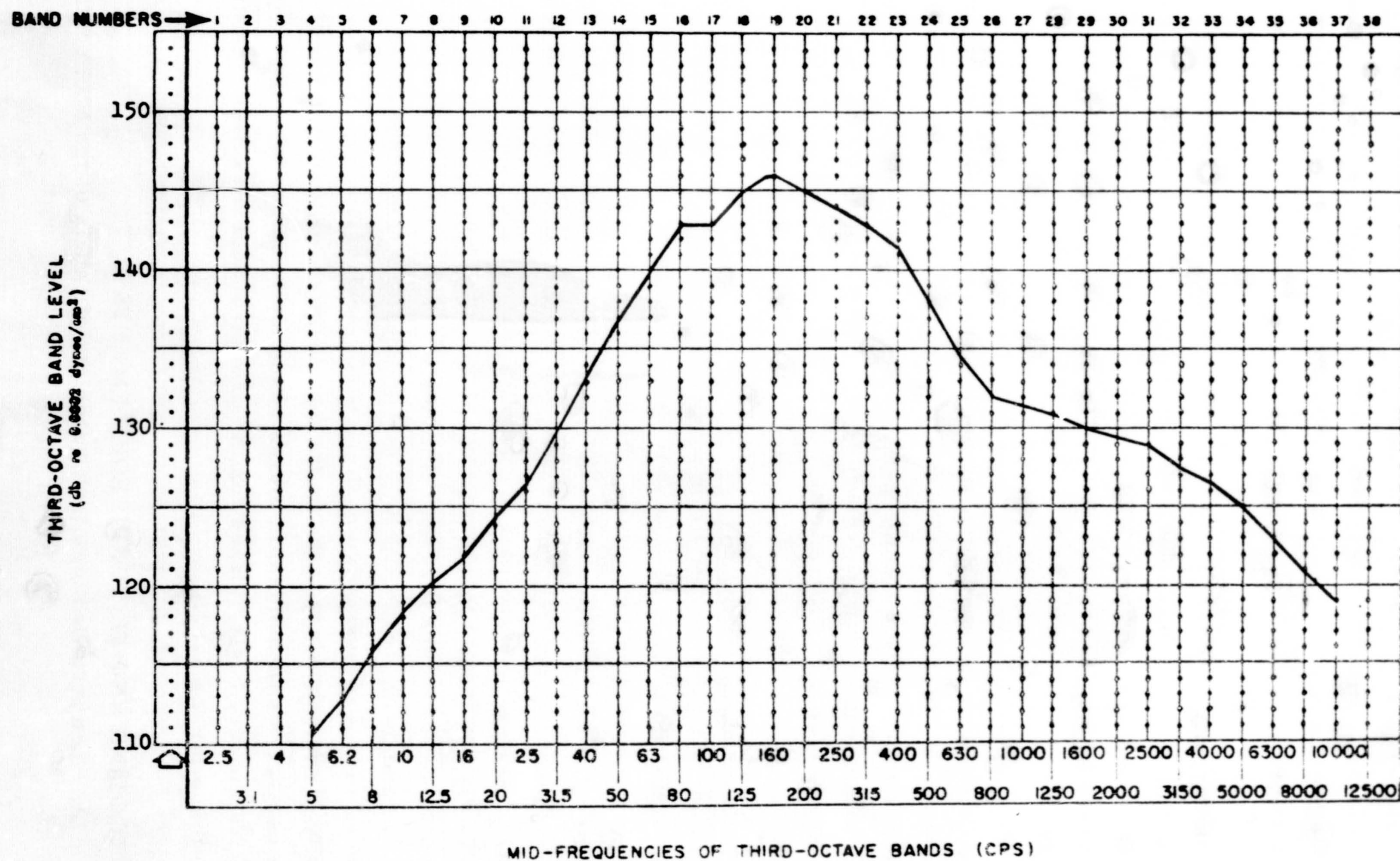
The acceleration loading data available for reentry were normal (perpendicular to vehicle axis) (g_z) values. These values were used to obtain an indication of the peak acceleration loading parallel to the vehicle axis (g_x). The lateral acceleration loading during reentry (g_y), as well as during ascent, is expected to be negligible.

4.1.4 Acoustic Environment

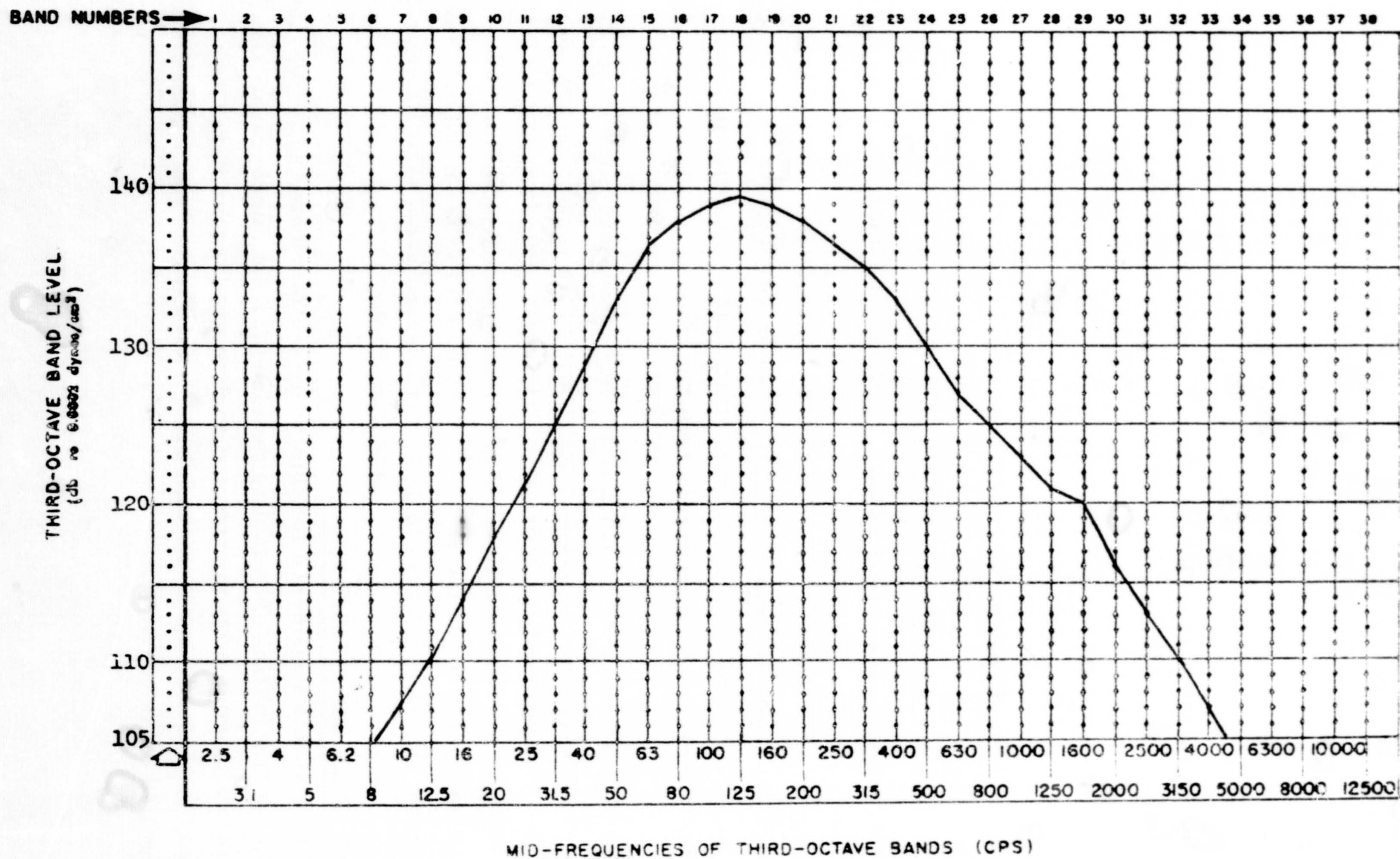
Preliminary Shuttle Booster liftoff acoustic criteria have been provided by NASA-MSFC (Reference 10) for stations every 600 in. along the booster, assuming station 0 at the engines. These data have been linearly interpolated to estimate liftoff acoustic environments for a S-IVB mounted on the Shuttle Booster in contract NAS 7-101, Saturn S-IVB/Alternate Launch Vehicle Analyses (Reference 11). The internal vehicle acoustic sound pressure levels obtained in this study for vehicle locations corresponding to the LCR orbiter secondary LH_2 and LO_2 tank locations are presented in Figures 4-9 and 4-10, respectively. These acoustic sound pressure levels are assumed to be representative of the acoustic environments anticipated in the vicinity of the secondary tanks on the LCR orbiter. Although these levels were derived for transmission losses based on S-IVB structural parameters, on a preliminary basis, losses for the orbiter should not differ significantly from those for the S-IVB.

4.2 TOOLING AND FIXTURE REQUIREMENTS

The MLI, when installed on a tank, consists of panels of the MLI composite

Figure 4-9. Acoustic Sound Pressure Level—Vicinity of LH₂ Tank

145

Figure 4-10. Acoustic Sound Pressure Level—Vicinity of LO₂ Tank

which are fastened together so that the MLI completely covers the surface of the tank. Each panel of MLI is fabricated to a shape which matches the specific contour of the tank in the area where it will be finally installed. Tooling is required for each of the basic steps involved in the fabrication of a typical panel: (1) precutting material; (2) face sheet fabrication; (3) layup of composite material stack; (4) assembly of stack with fasteners; and (5) cutting to final dimensions. The finished panel then undergoes storage or immediate tank installation. Fixtures are also required for these operations.

4.2.1 Precutting Material

In this operation, reflector and separator materials are drawn from the as-received rolls and alternately stacked on a table to the total number of sheets required in a finished panel. The stack is then rough cut to size.

The primary tooling item required is a device which will hold the material rolls on constant-tension spindles at one end of the table. The device should also incorporate provisions for removing residual static electricity from the material as it is drawn from the rolls.

A flat-pattern template, which may be made from thin-gage aluminum, is needed for placement on top of the stack to serve as a guide for the cutting tool for the rough cutting operation. This cutting tool may be either a simple knife or a powered cutter. The flat-pattern template must have the exact configuration for the required contour cuts in the materials for proper layup and should be several inches over finished panel size all around.

4.2.2 Face-Sheet Fabrication

The face sheets considered for this study are fabricated by impregnating straps onto a fabric. The tooling required for the impregnation and cure of the resin includes a layup form and such miscellaneous items as curing forms, rubber squeegees, vacuum bags, caul sheets, and a temperature-controlled oven.

A layup form, which can be thin fiber glass configured to the exact contour of the finished face sheet, is required for the layup and impregnation operations. This form should be scribed to show the outline of the finished face-sheet straps or reinforced areas in the finished part.

A flat-pattern template is needed to cut the primary sheet of fabric material. This can be the same template used for the composite material precut (Subsection 4.2.1). Other templates, which may be thin plastic, are necessary to cut (knife) the second layer of fabric used in the strap areas.

The scribe marks on the layup form serve as locators for positioning the two layers of fabric and the resin. Therefore, no additional tooling other than the resin applicator (a rubber squeegee) is required for face sheet preparation.

A simple form of the same contour as the layup form is required to hold the face sheet during cure. Vacuum bags and caul sheets are also needed for the cure process (see Appendix B of Reference 3).

4.2.3 Panel Composite Layup

A layup surface is the principal tool required, and two of these, one for the inner panel and one for the outer panel are required for each panel configuration. The insulation design, panel configuration, and fabrication details are presented in Section 10. The panel configurations are gore, end cap, manhole cover, plumbing shroud, and one each of three strut types. The strut panels are each different because the struts intersect the surface of the tank at three slightly different angles. Consequently, a total of 14 layup tools are required.

The layup tool (typically, reinforced fiber glass) must have the contour of the final part and include provisions for aligning the face sheet, reflector, and separator materials used to form the panel. The face sheet layup tool (Subsection 4.2.2) could be used as the foundation part for this tooling with scribe marks used as component indexing guides. Lacing button locations must also be defined; again scribe marks could suffice.

Provisions must also be made in the layup tool for indexing with other tools; trim templates, locating fastener jigs, and handling and storage fixtures. Examples of layup tools for a compound curvature and a single curvature panel are shown in Figures 4-11 and 4-12 respectively. The holes in the tool in Figures 4-11 and 4-12 are for the jigs used to locate the fasteners. Figure 4-13 shows an assembled panel on the compound curvature tool. Figures 4-11 through 4-13 were taken from Reference 7.

Lacing buttons are installed on the face sheets at locations scribed into the layup tool. These buttons are stamped out of sheet stock and, therefore, require a die. The grommets are purchased. Tools required to install the lacing buttons are a leather punch to form the hole in the face-sheet strap for the grommet and a grommet pliers to install the grommet.

No special tooling is necessary for stacking the components on the layup tool. After stacking, a tool is required to clamp the components into position for fastener insertion. This can be done with the final trim templates.

CR14



Figure 4-11. Typical Layup Tool for Compound Curvature Panel

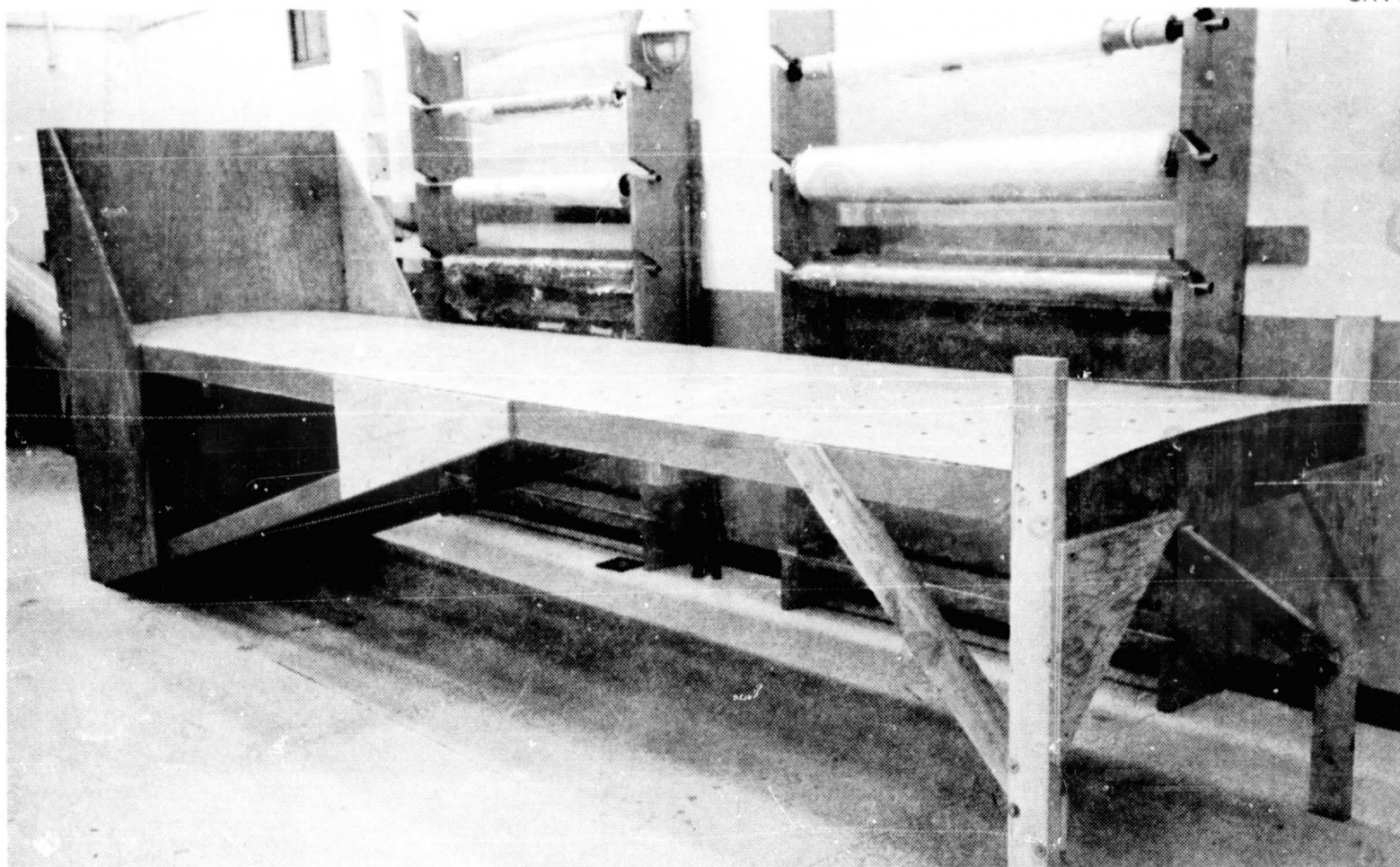


Figure 4-12. Typical Layup Tool for Single Curvature Panel



Figure 4-13. Assembled Panel on a Layup Tool

The final trim templates, one on each panel edge, serve as a guide for a cutting tool holder and must also be designed so that they are clamped securely in position for this purpose. The cutting tool holder which accurately positions a knife or power cutting tool can be guided by a rail built into the trim templates.

After trim template installation and prior to final cutting, the fasteners are inserted through the panel and assembled. Accessory tools used in installing the fasteners include: (1) the jig which is placed in the holes in the layup tool to guide a drill used to form the hole through the panel for the fastener, (2) a foam backing block used when drilling the hole, and (3) a radiant heater used to form a head on the fastener shank to retain the fastener button. A special hollow drill bit is required. The tooling required for fabricating the fasteners includes an injection mold to form the fasteners and a die to stamp the fastener buttons out of sheet stock.

Tooling requirements for the next operation, cutting to final dimensions, has been defined above. The last operation, installing the Velco fasteners on the inner edges of the panel, requires no special tooling.

4.2.4 Storage and Installation

Handling and storage fixtures are necessary for each manufactured panel. Provisions for attaching and support of completed panels during handling and storage are required of this tool.

The storage fixtures may be simple fiber glass structures similar to the layup tools, but they must conform to the contour of the part being stored. At most, one is required for each panel stored. However, there is some experience which shows that more than one panel of the same configuration may be stacked on the same storage fixture without deleterious effects upon the insulation composite.

Handling fixtures will be required for the large gore panels. This is due to the highly curved panel's tendency to straighten out and tear if picked up without some means of panel support. Again a fiber glass fixture can be used. However, in this case, it must be contoured to fit the outer surface

of the panel. Typically, the finished panel is held to the storage fixture as it is inverted and then the panel lowered into the handling fixture. Thin plastic strips can then be used to clamp it in place. The handling fixture is lifted to the proper location of the panel on the tank, plastic strips are removed, and the panel is firmly attached in place.

4.3 COMPOSITE SURVIVABILITY VERIFICATION TESTING

Testing to verify the ability of the MLI materials to survive the anticipated ILRV environment was accomplished in Task 1 of this study. In addition, testing of the fasteners and some testing of the assembled composite were accomplished in Task 6. However, further testing of the assembled composite's performance in the anticipated environment is needed. The tests suggested for consideration in future studies are delineated in the following paragraphs.

4.3.1 Static Tensile Loading of MLI Panel Joint

Because of the high angle of attack of the ILRV orbiter vehicle during reentry, structural tensile loads, both parallel and perpendicular to the joints, will be sustained during a complete mission. The objective of the static tensile loading tests would be to verify the ability of the lacing thread, Velcro, and fasteners to hold adjacent panels together at the joint when the tensile loading is perpendicular to the joint. This would be a comparatively simple test requiring no instrumentation. A visual observation of the joint as the load is applied should be adequate.

A sketch of the test setup is shown in Figure 4-14. A full scale, 40-in.-wide panel is suggested to obtain the maximum sagging, if any occurs, of the reflectors at the joint. An 8-in.-wide panel is suggested for simulating an upper panel. Full thickness panels of 35 to 45 layer pairs of MLI are recommended. The joint is held together with Velcro between the inner face sheets and lacing thread between the outer face sheets in a configuration identical to that proposed in the system design (Section 10). Face sheet straps on the inner face sheet, not shown, would run vertically, as well as horizontally. This is also consistent with the conceptual design discussed in Section 10.

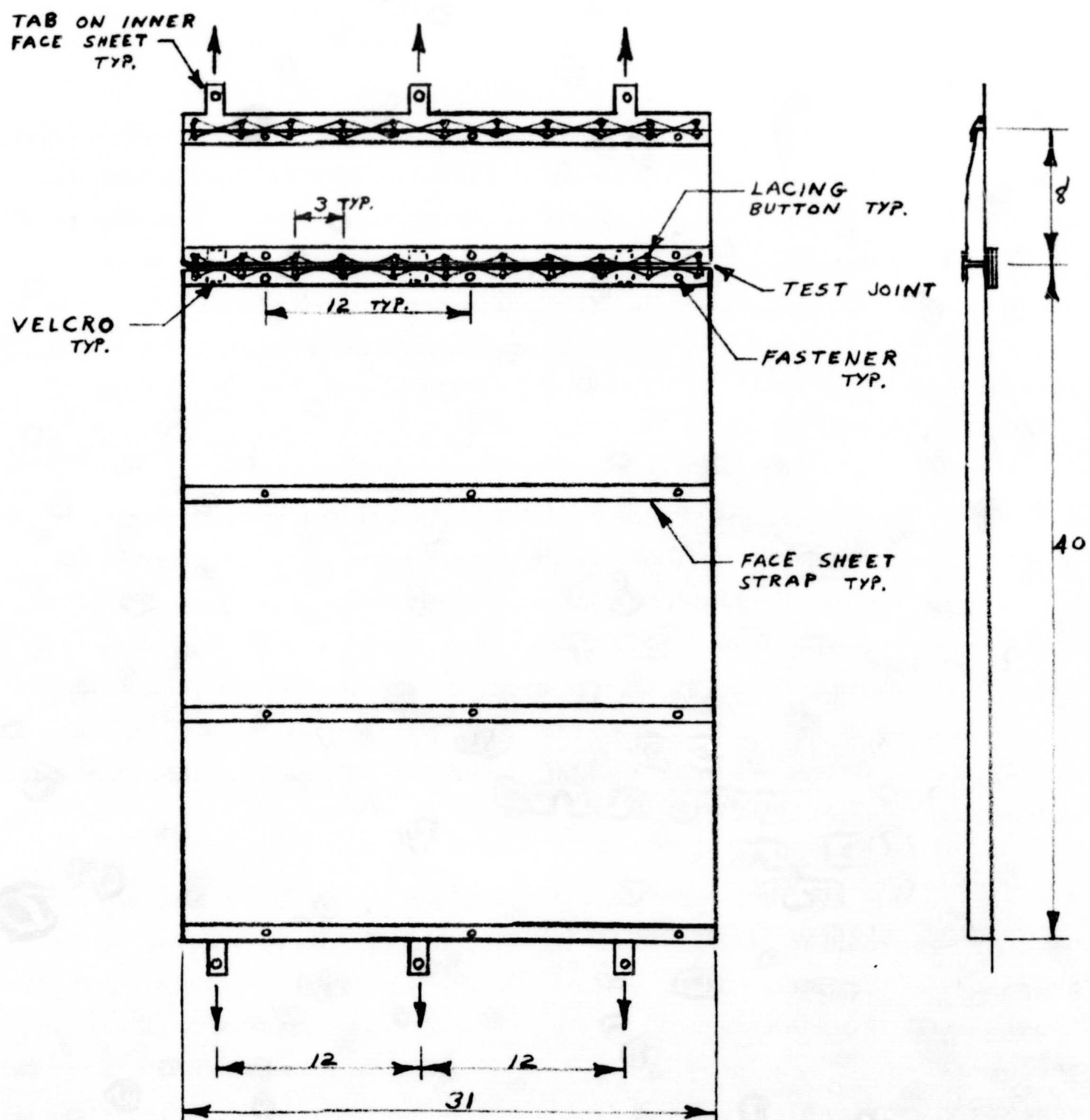


Figure 4-14. Loading of MLI Panel Joint—Test Setup

The test specimen would be hung vertically from three tabs on the inner face-sheet of the upper panel. These tabs are extensions of the face-sheet straps which would be carrying the load in an actual application. The test load to the inner face sheet would be applied by attaching weights to the tabs on the bottom of the inner face sheet of the lower panel. The loading on the reflectors and separators could be obtained by applying tape to these components.

The visual inspection of the joint after the loading has been applied should verify the adequacy of the design. Questions of interest will be: (1) does sagging occur between the Velcro patches holding the inner face sheets together?, (2) do the fasteners sufficiently hold the reflectors and separators in place and thereby prevent a gap at the joint?, and (3) does any component fail by breaking or tearing?

4.3.2 Dynamic Loading of MLI Penetration Panel

Most of the previous dynamic loading testing of MLI panels has been on the basic panels, such as that reported in Section 3.8 and Reference 7. Consequently, dynamic loading testing of a typical MLI panel at a penetration such as a tank support strut is needed. This test would verify the capability of these strut panels to maintain the desired positioning and structural integrity during the dynamic loading in an ILRV orbiter mission.

A full-scale specimen on a fixture simulating the tank-end of a strut and the attachment area of the strut to the tank, is recommended. The proposed configuration of the MLI in this area is discussed in Section 10 and shown in Figure 10-4 of Section 10. The preparation of this specimen would also serve to check fabrication procedures and configuration aspects of this panel.

Dynamic loading induced by both acoustic and vibration environments should be considered. However, a study of the anticipated environments may show the acoustic environment to be more severe than the vibration and only an acoustic test is required. The same specimen could be used for both tests. Initially, both of the tests could be conducted at room temperature. Instrumentation

of the specimen is not essential. A visual inspection of the specimen subsequent to the loading will reveal the effects, if any, of the dynamic loading.

4.3.3 Dynamic Loading of Support Ring and Basic Panel

The ends of the MLI panels that cover the tank are attached to a support ring. This ring is attached to the tank and, therefore, provides a means of both supporting and positioning the panels. The objective of this test is to verify the ability of the support ring and face-sheet tabs, which attach to the support ring, to sustain the anticipated dynamic loading. A further objective, which can be accomplished in the same test, is to verify the ability of the face-sheet straps to withstand the dynamic loading at cryogenic temperatures. This is of interest since the face-sheet straps tend to become more brittle at the cryogenic temperatures.

The test specimen should consist of a full-scale segment of the support ring and attached panels. The proposed MLI design in this area of the tank is discussed in Section 10. The cryogenic temperature on the inner face sheet would be obtained with cooling coils attached to the test fixture. Temperatures as low as 37°R (LH₂) should be obtained if feasible.

Instrumentation of the test specimen is not considered essential. A visual inspection of the specimen subsequent to the loading will reveal any significant effects of the loading.

4.3.4 Large Scale Thermal Performance Tests

Prior to finalization of an MLI system design, a full-scale or, at least, a large-scale test of the system's thermal performance will be required to qualify the system for flight. This test would be designed to include all phases of an ILRV orbiter mission: ground hold, ascent, in-space, and reentry. In addition to data on the thermal performance throughout a mission, the test would provide for a verification of the purge, evacuation, and repressurization system design.

The test configuration should be that of the actual flight hardware. This includes the tank support struts and tank plumbing penetrations. These

penetrations through the MLI could be simulated on a large tank such as the 105-in. tank being used in the MLI tests planned on contract NAS 8-21400, if a full-scale ILRV orbiter tank is not available. The MLI, purge bag, purge evacuation, and repressurization system design is discussed in Sections 6 and 10.

In addition to the test tank, the test hardware required would include a vacuum chamber capable of containing the tank and evacuating at a rate which will simulate the early part of a typical ILRV ascent pressure history. The test should be conducted using LH_2 as the cryogen in the tank and gaseous helium as the purge gas. Consequently, storage and transfer capability for LH_2 and GHe would be required at the test facility. The test hardware would also include the valves, pressure controllers, and plumbing used in the purge and repressurization system. A pressure guard would be required to attenuate fluctuations in the tank pressure due to slight changes in atmospheric pressure.

The instrumentation would include hot wire anemometers to monitor the boiloff from the tank, pressure gages to record the pressure history in the chamber and within the purge bag, and thermocouples to measure temperature histories on the penetrations, chamber walls, tank, and MLI. Flow meters would be required to measure purge and repressurization flow rates and a mass spectrometer would be used to measure the concentration of condensibles during the purging of the MLI.

The overall test procedure would involve measuring the thermal performance of the system while simulating the pressure history of an actual ILRV orbiter mission. Simulation of the anticipated ambient temperature history is not considered necessary and would significantly complicate the test. The major steps in the test procedure would be: (1) purge MLI, (2) fill tank with LH_2 , (3) evacuate chamber simulating ascent pressure history, (4) hold chamber in evacuated condition (pressure less than 10^{-5} torr) until steady-state boiloff is reached, and (5) repressurize chamber simulating reentry pressure history. Purge, evacuation, and repressurization system valves would be actuated at the predetermined times during the simulated mission. Data from all of the instrumentation would be taken throughout all phases of the simulated mission.

Section 5

MLI DESIGN CONCEPTS AND HARDWARE DEFINITION—TASK 3

The objectives of Task 3 were to: (1) define the insulation system concepts which are applicable to the ILRV design and which were to be considered in this study; and (2) define the materials, configurations, and dimensions of the liquid oxygen and liquid hydrogen tanks and associated hardware to be used in this study.

5.1 INSULATION SYSTEM CONCEPTS

Four insulation composite configurations were selected for consideration with concurrence of NASA-MSFC. These were tank-mounted insulation with or without a substrate (foam) and non-tank-mounted insulation with or without a substrate. A purge bag would be used with all of these configurations.

In either non-tank-mounted configuration, the MLI can be mounted on the surrounding compartment walls or structure of the vehicle, or on a shroud which envelops the tank. Of these, a shroud-mounted system appears to be more feasible and optimum than a wall-mounted system for the following reasons:

- A. Serious weight penalties would be incurred with a wall-mounted system because of the increased purge-gas requirements, increased insulation weight (due to the increased surface area), and additional mounting structure requirements. The increased weight due to higher purge-gas requirements would include the increased weight of the storage bottles as well as the additional reentry purge gas. The additional mounting structure would be required in many areas because of the presence of other equipment and apparatus and because the existing structure and bulkheads would not provide the reasonably smooth contoured surface area required for efficient MLI installation and performance. In addition, it may not be

feasible, due to thermal and attachment problems to attach the MLI directly to the inside of the vehicle skin.

- B. The potential ease of installing rectangular panels on the walls of a compartment for the wall-mounted system instead of installing gore segments on a sphere is offset by the greatly increased problem of supporting the MLI panels against the g-forces acting normal to the surface. On the exterior of a sphere, because the panels are tied together and completely envelop the sphere, the panels are evenly supported against the g-forces without the need for attachment to the underlying structure. However, a flat panel mounted on the structure would need to be fastened to the structure at several discrete points to prevent significant sagging. This would present thermal and mounting problems.
- C. One of the potential advantages of either of the non-tank-mounted systems is a reduction in the heat transfer to the tank. This can be obtained because the conduction path between the tank and the inside reflector sheet has been broken. At the low temperature of the tank, radiation is very small and conduction is the primary heat-transfer mode between the inside sheet and the tank. However, as the insulation is removed farther from the tank, the insulation area becomes larger which results in an increase in the total heat transfer. Folkman and Lee (Reference 12) showed that the insulation-to-tank surface area ratio must remain small, less than approximately 1.2, if any increase in thermal efficiency is to be realized. Consequently, a wall-mounted system would not be optimum.
- D. A shroud which has a configuration and size such that the shroud-to-tank surface area ratio is very small is feasible. For example, a shroud can be designed which is located 0.65 inch from the hydrogen tank surface and results in a shroud-to-tank ratio of only approximately 1.02. In addition, the weight penalty with this type of shroud would be principally the weight of the shroud since the increase in insulation weight and reentry purge-gas requirements would not be significant.

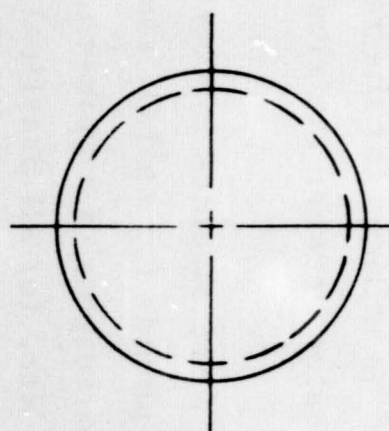
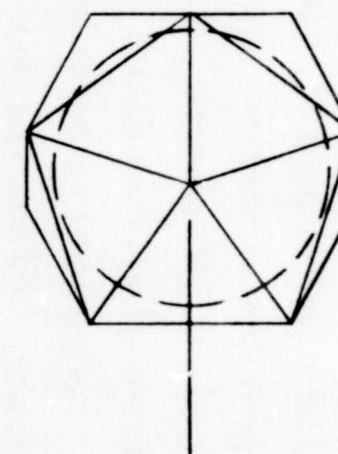
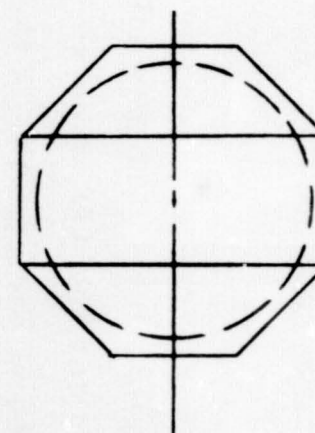
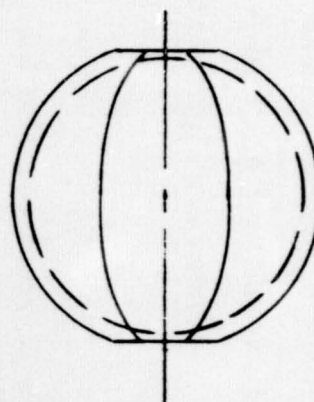
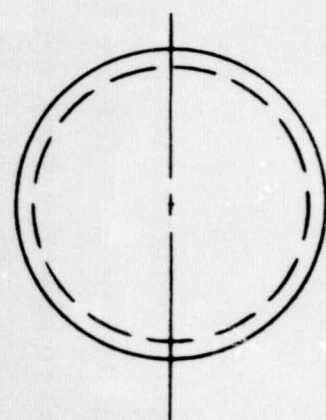
For these reasons, a wall-mounted system was rejected from any further consideration in favor of a tank-mounted shroud and a detailed study of the

tank-mounted shroud system was initiated. Several configurations for the tank-mounted shroud were considered and are shown in Figure 5-1. Of these, the tank-configuration shroud offers the lowest possible shroud-to-tank area ratio, and the lowest possible increase in purge-gas requirements. The single-curvature gore-segment-configuration shroud should facilitate insulation layup by reducing or eliminating the contour cuts required in the reflector sheets. The truncated-cone, dome-and-cylinder, and the regular-polyhedron shroud configurations do not appear to offer any advantages which might outweigh those of the tank-configuration or single-curvature gore-segment-configuration shrouds. Consequently, further investigation of the tank-mounted shroud systems was directed to the tank-configuration shroud and the single-curvature shroud.

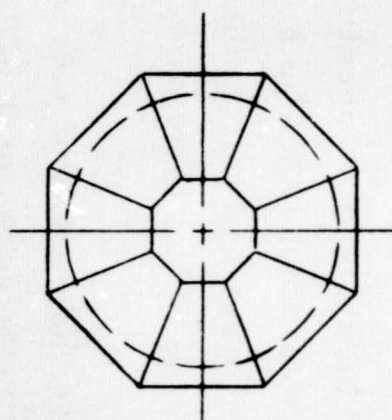
Both the tank-configuration shroud and the single-curvature shroud would be fabricated from fiber glass in gore segments; eight for the LO_2 tank and twelve for the LH_2 tank. The gores would be joined at the equator of the tank and supported off the surface of the tank at the equator and ends of the tank by fiber glass rings. At one end of the tank, the shroud would be fabricated to provide clearance for the manhole cover. For the tank-configuration shroud, this would be a circular opening while for the single-curvature shroud, the opening would be a polygon. The gore segments for either shroud would require ribs for stiffness and lightening holes to both remove weight and to allow efficient purging of the insulation.

Figure 5-2 presents the design of a single-curvature shroud for the LO_2 tank. It would consist of eight gores of 0.020-inch-thick fiber glass which would be located at a minimum distance from the tank surface of 0.65 inch. The greater distance from the tank off the centerline of the gores and at the ends of the gores would be utilized for the required stiffening ribs. The lightening holes would be located between the ribs.

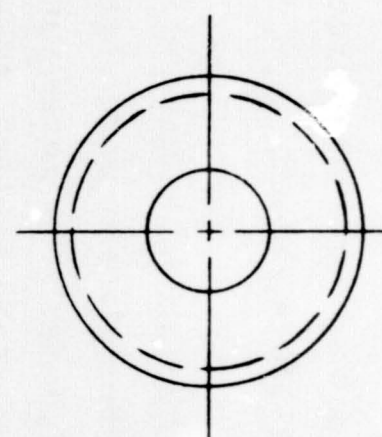
Weight estimates were obtained for both of the shroud configurations. These estimates are 80 pounds for an LO_2 tank shroud and 181 pounds for an LH_2 tank shroud. The weights of a tank-configuration shroud and a single-curvature shroud are, for all practical purposes, equal. There would be a



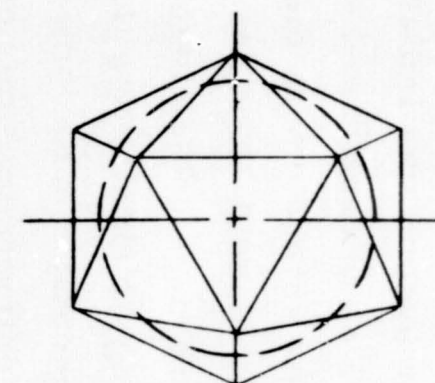
REGULAR
POLYHEDRON



TRUNCATED CONE
DOME AND CYLINDER



SINGLE CURVATURE
GORE SEGMENT



SAME CONFIGURATION
AS TANK

Figure 5-1. Shroud Configurations

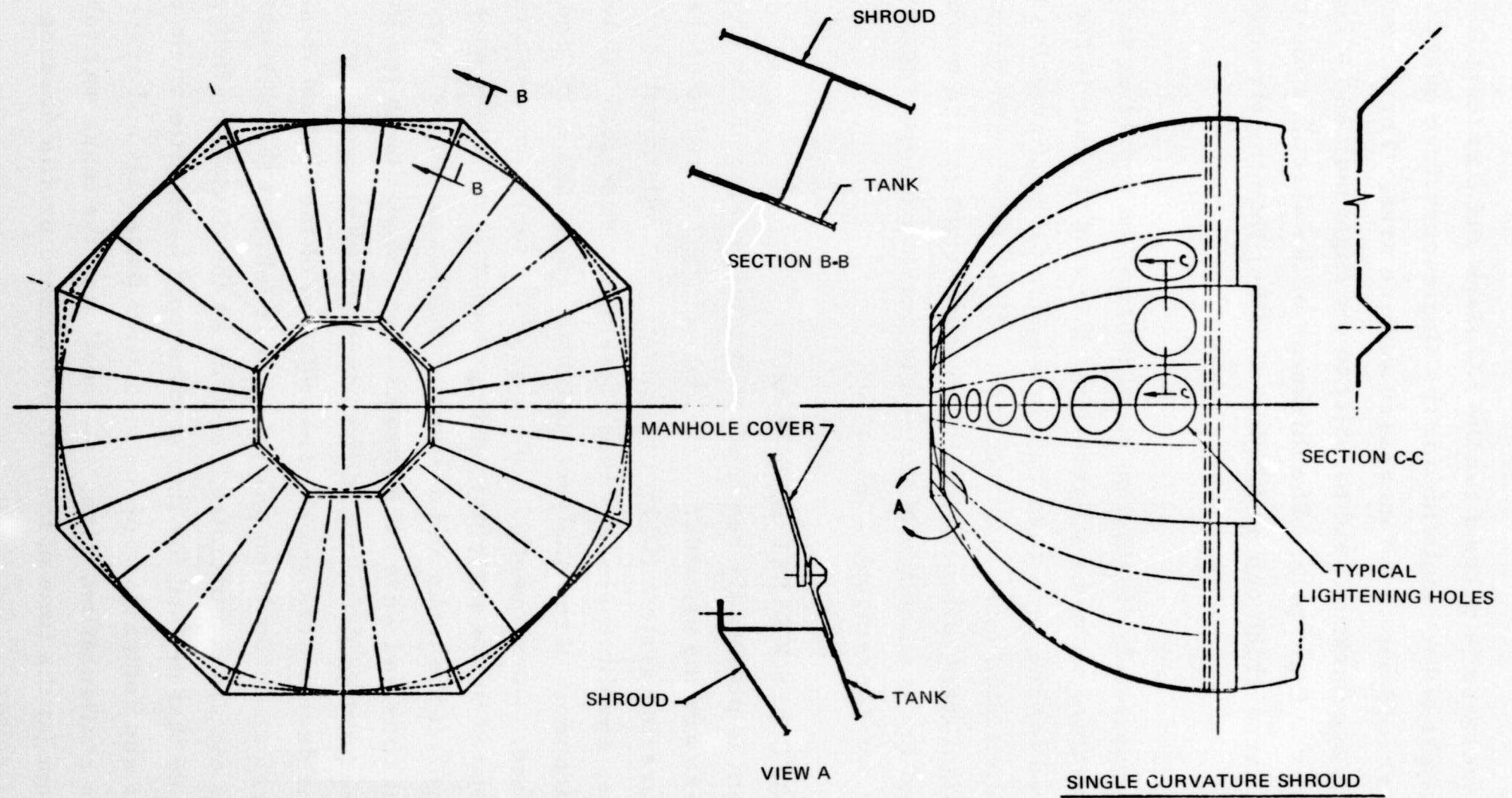


Figure 5-2. Single Curvature Shroud Configuration

slight weight increase (4 percent for the LO_2 tank and 2 percent for the LH_2 tank) in the weight of the insulation for the single-curvature over the tank-configuration shroud due to the increased surface area. The shrouds were sized for a 4-g acceleration load parallel to the flight path and a 1-g lateral acceleration to the flight path. The thickness of the shroud is dictated by the minimum thickness which can be fabricated rather than the strength requirements.

As mentioned previously, insulation panel fabrication should be facilitated by the single-curvature shroud configuration. The contour cuts in the reflector sheets required for the gore segments in a spherical configuration layup can probably be eliminated or at least reduced. This, plus the fact that there would be no significant difference in the shroud weight for the two configurations, resulted in the selection of the single-curvature gore-segment configuration for non-tank-mounted insulation.

5.2 TANKS AND ASSOCIATED HARDWARE

An MLI system is potentially required on two large tanks in the Orbiter vehicle. These are the secondary LH_2 and LO_2 tanks used to store the orbital maneuvering system (OMS) propellant. Establishment of the materials, configurations, and dimensions of these tanks and associated hardware was required before most of the analyses and design in Tasks 4, 5, and 8 could be accomplished. Consequently, definition of the tanks and associated hardware was initiated in the early part of the contract. A survey showed that detailed designs of the tanks and associated hardware had not been accomplished at that time and were not scheduled for completion in the immediate future. Consequently, definition of the hardware to be used in this contract required some design work and the assimilation of the current thinking of the ILRV designers and propulsion analysts. It is felt that the lack of final design details did not compromise the study as the deviations between the final design and that defined for this study should have little or no effect on the evaluation and comparison of the insulation materials and systems considered. The configuration, size, and location of the tanks was taken from the most recent (at the time of the survey) inboard profile drawing of the low cross-range Orbiter.

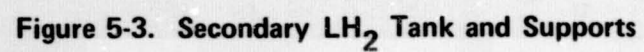
5.2.1 Liquid Hydrogen Tank and Hardware

The liquid hydrogen (LH_2) tank used in this study is 208 inches long and 190 inches in diameter with 95-inch radius hemispherical end domes and an 18-inch-long cylindrical center section as shown in Figure 5-3. The tank material would be either 2014-T6 or 2219-T87 aluminum alloy. The current vehicle designs did not show the method of tank support. Therefore, an equatorial reinforcing frame was designed on the interior tank wall for the tank support attachments. Locating the frame on the interior of the tank provides a tank outer surface which is relatively free of obstructions and simplifies both the design and fabrication of the MLI system. Potential interference between the structure near the tank and an external tank frame is also eliminated. The configuration of the frame was sized for a 4-g acceleration load parallel to the flight path and a 1-g acceleration lateral to the flight path. The approximate dimensions of the frame are shown in Figure 5-4.

The tank contains a 36-inch-diameter manhole. The manhole cover dimensions of interest for the application of the MLI at the manhole cover are shown in Figure 5-5. The electrical feedthrough and the plumbing feedthrough fittings (not shown) are welded into reinforced sections of the tank wall.

5.2.1.1 LH_2 Tank Supports

A tank support design was unavailable. Therefore, a design study was accomplished to define this critical component. Several alternatives were formulated and simple models built. A design utilizing six struts was selected. These struts (Figure 5-6) are constructed of fiber glass and attached to the tank surface at three points, as shown in Figure 5-3. The struts are assumed to be attached to reinforced points in the vehicle framework on the aft side of the end bulkhead in the cargo compartment. The lengths of the struts are shown in Figure 5-3. The struts are 6 inches in diameter and are fabricated from collimated fiber glass tape. Approximately 12 to 16 longitudinal layers and 4 to 5 peripheral layers of tape would be required. An average strut wall thickness of 90 mils was assumed.



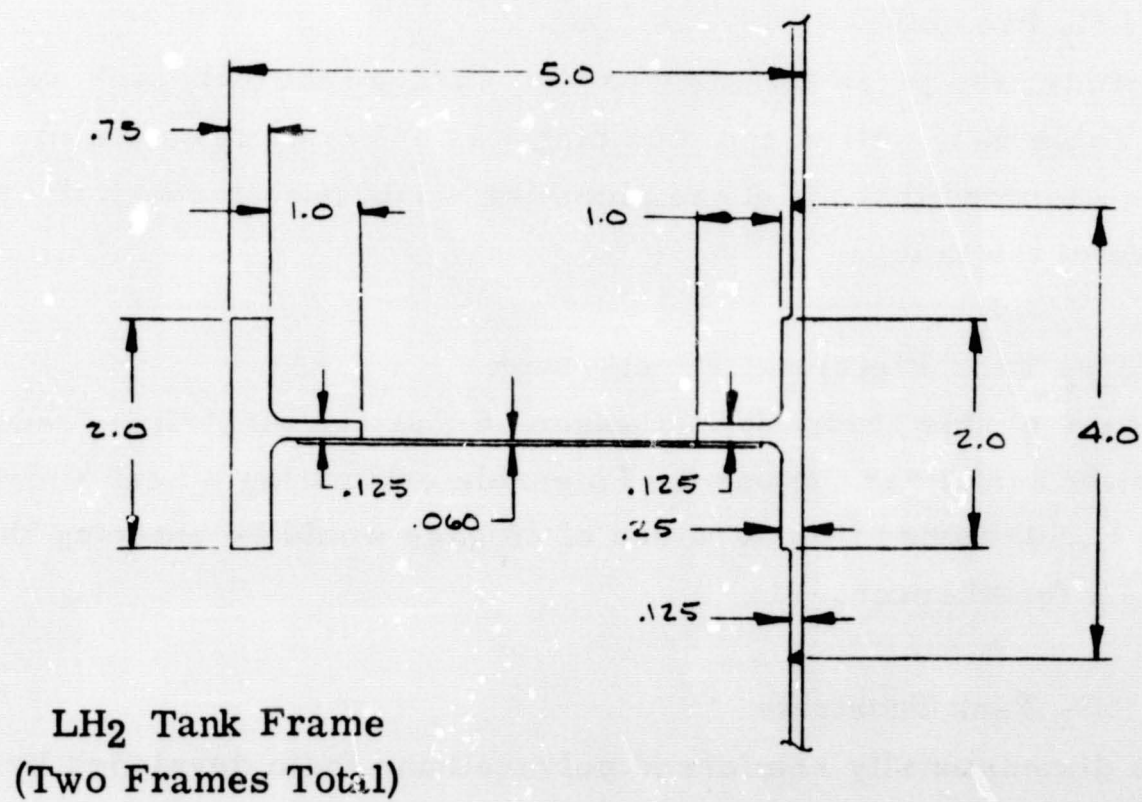
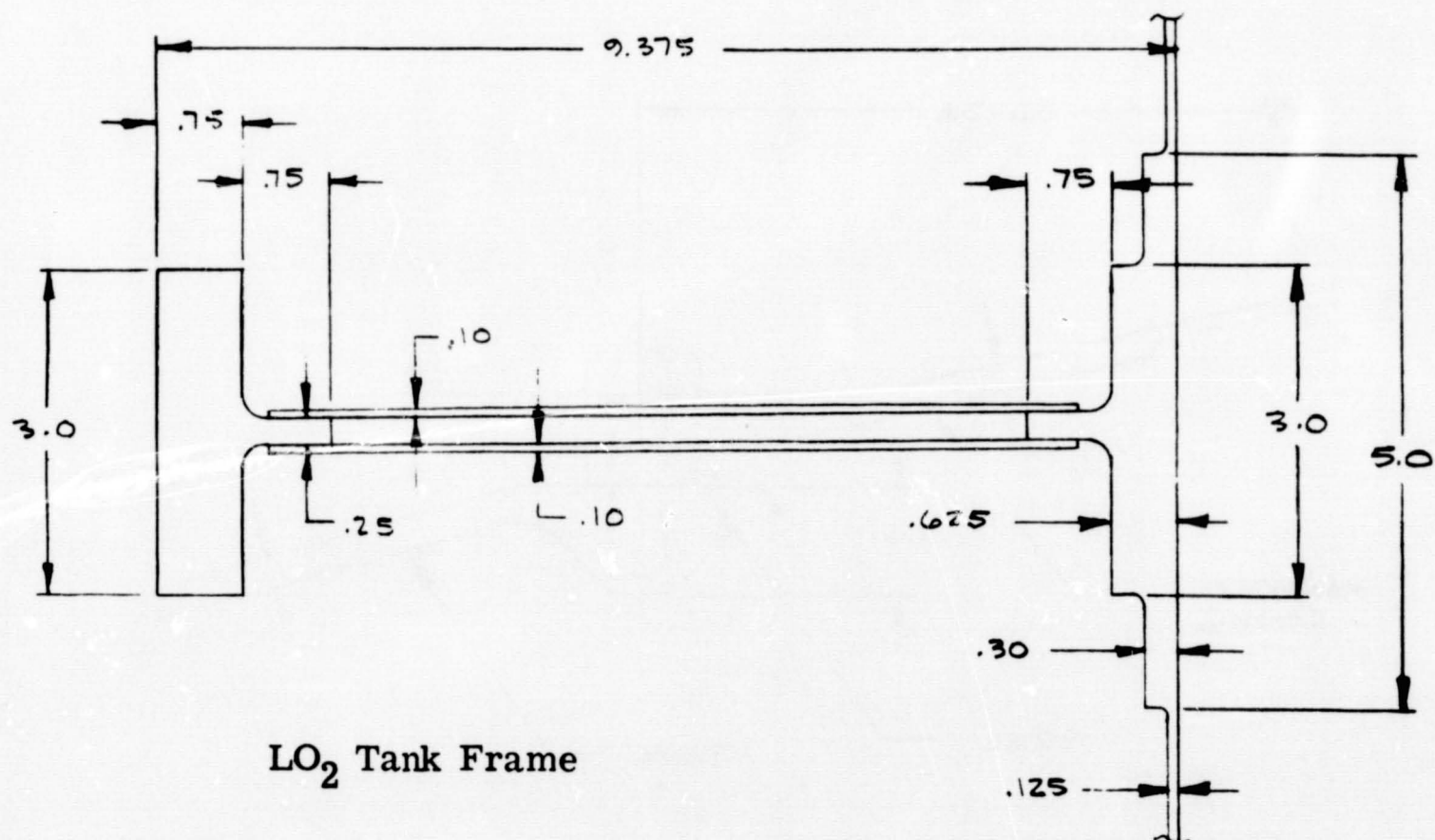


Figure 5-4. Tank Equatorial Reinforcing Frames

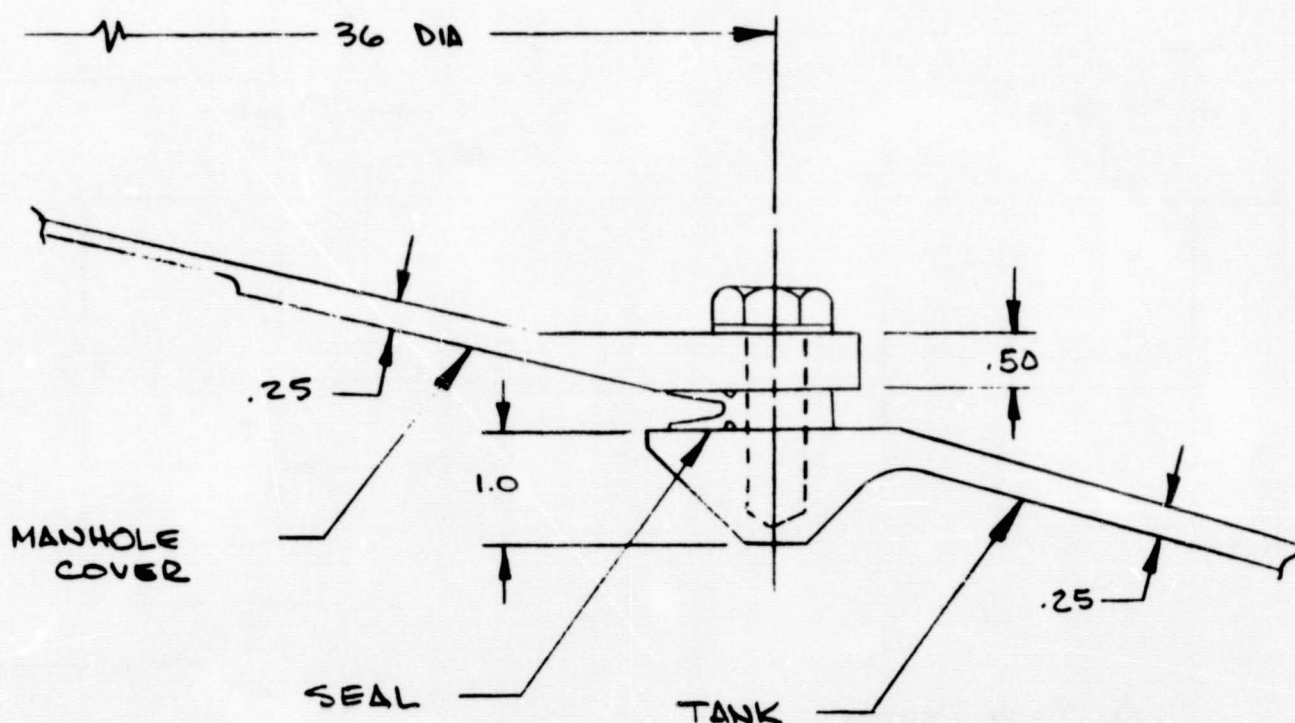


Figure 5-5. Manhole Cover Attachment

5.2.1.2 LH₂ Plumbing

For this study, the pipes assumed to pass through the LH₂ tank wall are shown in Table 5-1. All of the plumbing was assumed to be stainless steel and it was assumed that all of the plumbing would pass through the tank wall at the base of the tank.

5.2.1.3 LH₂ Tank Electrical Feedthrough

For purposes of this study, it was assumed that one electrical feedthrough is located in the tank near the base. To enable estimating a heat short due to the wires, it was assumed that 36 wires of 26 gage would be entering the tank through this feedthrough.

5.2.1.4 LH₂ Tank Substrate

The three dimensionally reinforced polyurethane foam developed by MDAC for use on the interior surface of the Saturn S-IVB LH₂ tank was used as the candidate substrate material in this study. The required thickness of a substrate was studied in Task 4, Section 6.

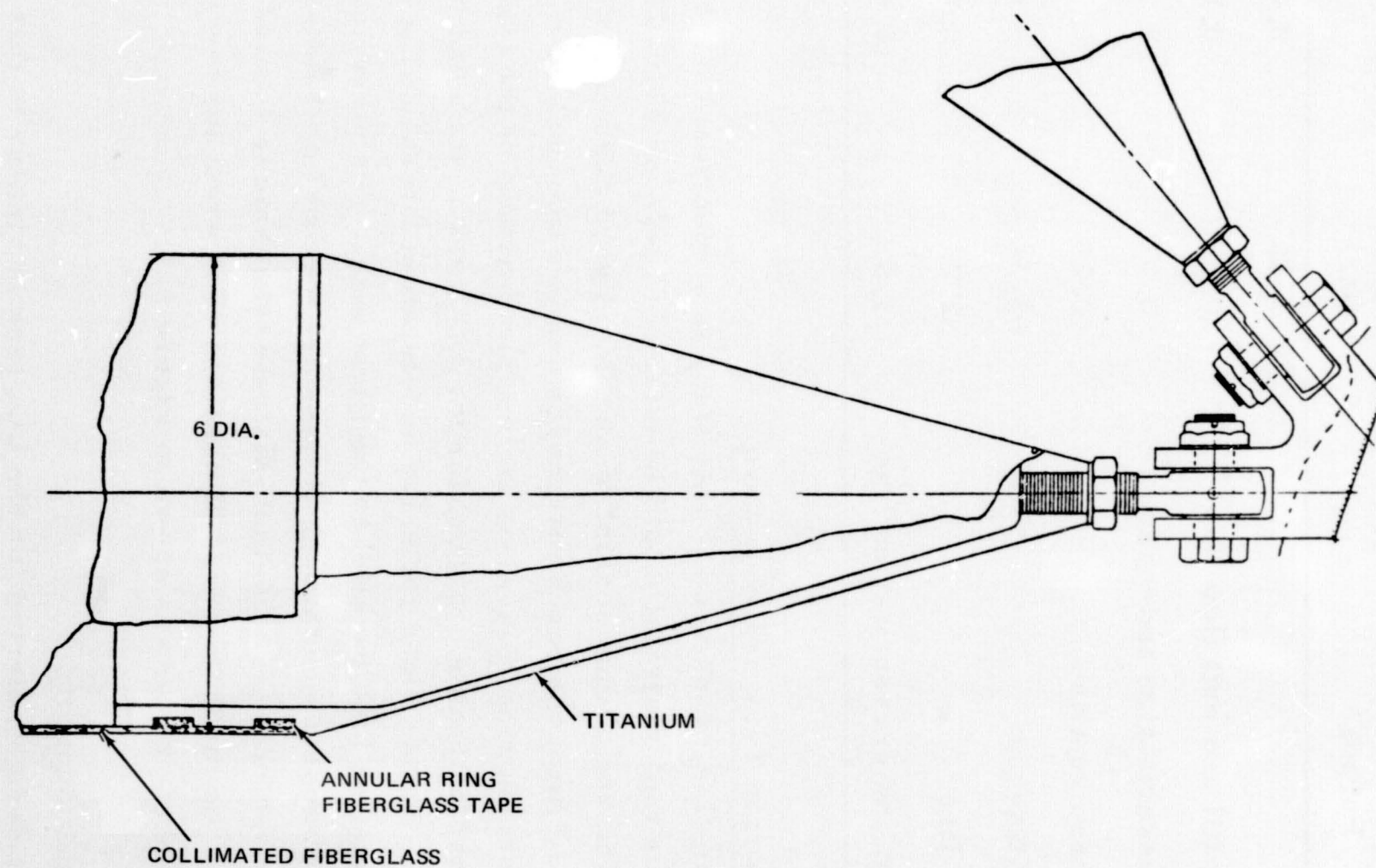


Figure 5-6. Typical Tank Support Strut

Table 5-1
LH₂ TANK PLUMBING

Purpose	Diameter (in.)	Wall Thickness (in.)
Feedline	2.25	0.012
Helium bottle fill and exit flow line	0.25	0.020
Start tank pressurization and ventline	0.75	0.035
Start tank screen ventline	0.25	0.020
Main tank fill line	2.25	0.012
Start tank fill line	2.25	0.012
Main tank vent and pressurization line	1.0	0.012

5.2.2 Liquid Oxygen Tank and Hardware

The liquid oxygen (LO₂) tank used in this study is a spherical tank 127 inches in diameter. The tank material would be either 2014-T6 or 2210-T87 aluminum alloy. The end domes consist of aluminum gore segments which are welded together to form the two hemispheres and are then welded to an equatorial reinforcing ring located on the interior surface of the tank. The equatorial reinforcing frame designed for the LO₂ tank is included in Figure 5-4. The frame was sized for a 1-g acceleration lateral to the flight path and a 4-g acceleration load parallel to the flight path. The electrical feedthrough and the plumbing feedthrough fittings are welded into reinforced sections of the gore segments. A 36-inch-diameter manhole is located in one end of the tank. The manhole cover dimensions of interest for the application of MLI at the manhole cover are shown in Figure 5-5.

5.2.2.1 LO₂ Tank Supports

The tank support design selected for the LO₂ tank is similar to that selected for the LH₂ tank, see Subsection 5.2.1.1. The design features six struts which are fixed to the spherical tank at three attachment points over the interior equatorial reinforcing ring. The other ends of the support struts are located at structural hardpoints on the crew and cargo compartments of the

baseline vehicle as shown in Figure 5-7. The strut diameters and wall thicknesses shown in Figure 5-7 are those required for loadings resulting from a 4-g acceleration parallel to the flight path and a 1-g acceleration lateral to the flight path. As in the design for the hydrogen tank, the support struts would be fabricated from collimated fiber glass tape and would incorporate titanium end fittings.

5.2.2.2 LO₂ Plumbing

The pipes assumed to pass through the LO₂ tank wall in this study are shown in Table 5-2. All of the plumbing was assumed to be stainless steel and it was assumed that all of the plumbing would pass through the tank wall at the base of the tank.

5.2.2.3 LO₂ Tank Electrical Feedthrough

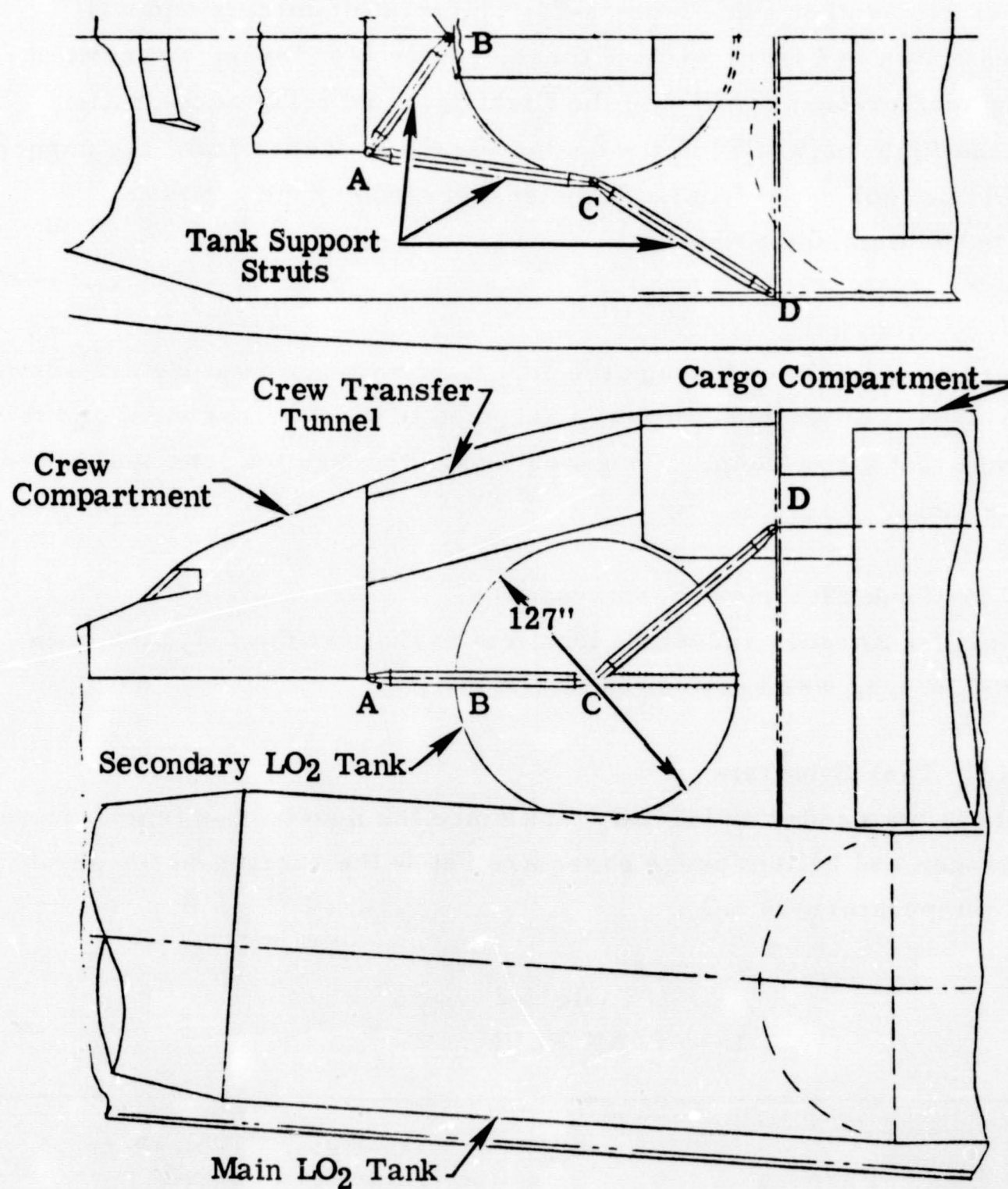
An electrical feedthrough and wires identical to that for the LH₂ tank, see Subsection 5.2.1.3, was assumed in this study.

5.2.2.4 LO₂ Tank Substrate

A substrate is not needed on the LO₂ tank since the liquefaction temperature of both nitrogen and helium purge gases are below the saturation temperature (tank wall temperature) of LO₂.

Table 5-2
LO₂ TANK PLUMBING

Purpose	Diameter (in.)	Thickness (in.)
Feedline	2.25	0.012
Start tank pressurization and vent line	0.75	0.035
Start tank screen vent line	0.25	0.020
Main tank fill line	2.25	0.012
Start tank fill line	2.25	0.012
Main tank vent and pressurization line	1.0	0.012



Strut	Length (inch)	Dia- meter (inch)	Wall Thickness (inch)
A-B	62	6.0	0.035
A-C	102	6.0	0.055
C-D	116	4.5	0.045

Figure 5-7. Secondary LO₂ Tank and Supports

Section 6

THERMAL ANALYSES—TASK 4

The objectives of Task 4 were as follows: (1) to conduct parametric heat transfer analyses for the ground hold, ascent, in-space, and reentry phases of an ILRV mission; (2) to determine an optimized number of layer-pairs for the insulation system; and (3) to determine purge, evacuation, and repressurization requirements. Extensive parametric and optimization analyses were accomplished in a related IRAD program designed to consider MLI systems for the OMS propellant tanks in an orbiter vehicle. The results which are pertinent to this study are included herein.

6.1 LH₂ TANK THERMAL ANALYSES

Three different MLI system concepts for the LH₂ tank were investigated in detail: (1) helium purge of the MLI during ground hold and helium repressurization during reentry, with no foam substrate; (2) helium purge and repressurization as in No. 1, but with 0.5 in. of foam substrate; and (3) nitrogen purge of MLI during ground hold, helium repressurization during reentry, and with sufficient foam substrate to preclude liquefaction of nitrogen purge gas during ground hold. All the systems analyzed in detail were configured so that the MLI was located on the tank surface since a cursory comparison of the weight of a shroud to hold the insulation off the tank, with the corresponding anticipated reduction in LH₂ boiloff indicated that the lowest-weight system was a tank-mounted one.

6.1.1 Ground-Hold Phase—LH₂ Tank

The ground-hold period is an important consideration for several practical reasons, which include the boiloff penalty during lockup prior to launch, the constraints on system concepts resulting from the temperature

distribution throughout the system during ground hold, and the necessity for realistic initial temperatures for the ascent-period thermal analysis.

The ground-hold heat transfer analyses were conducted using the MDAC JA03 Three-Dimensional Heat Transfer computer program. This program has the capability to calculate the three-dimensional heat transfer and temperature distribution within a system which has been defined by a number of small sections called nodes. The JA03 uses standard equations for the calculation of conduction, convection, and radiation. The incremental temperature change of a node is defined as the net heat exchange at the node divided by the heat capacitance.

A cross-sectional segment of the tank and insulation system (Figure 6-1) was used in the analyses. A one-dimensional solution with heat flow normal to the surface was assumed. The thermal properties used for the foam substrate are presented in Reference 4. The thermal model shown in

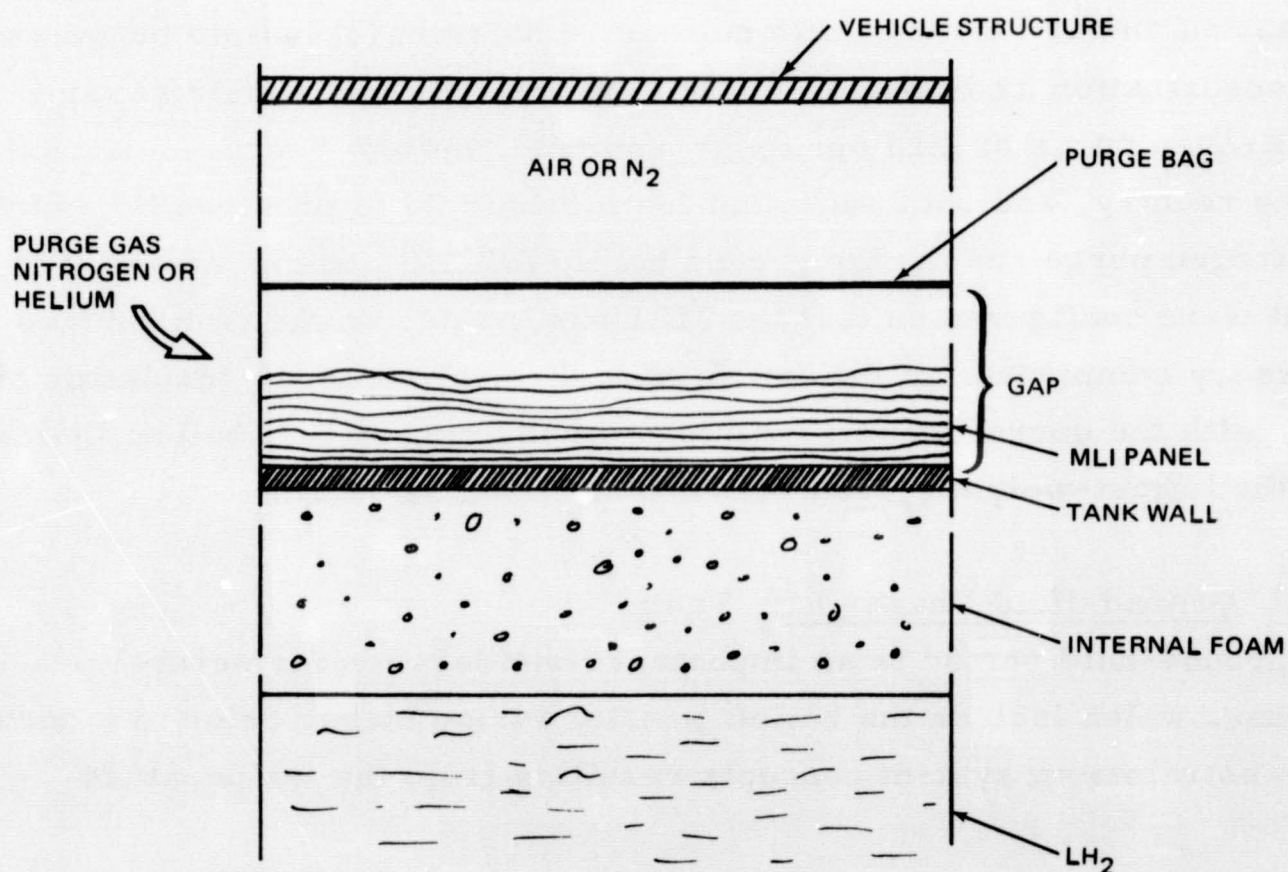


Figure 6-1. Thermal Model--Ground Hold

Figure 6-1 was modified to exclude the foam substrate for the no-foam cases. The distance between the purge bag and outer surface of the MLI was assumed to be 0.25 in.

A convection heat transfer coefficient of one, representing natural convection between the ambient gas (gas external to purge bag) and the exterior of the purge bag, was assumed. The temperature of the ambient gas (assumed to be air in this case) was held constant at 70, 100, and 150°F to determine the effect of this parameter on purge-bag temperature, tank wall temperature, and ground-hold heating rate. A radiation interchange factor of one was assumed between the purge bag and the vehicle structure. Heat transfer between the purge bag and the tank was assumed to be due solely to conduction through the purge gas. Convection between individual insulation sheets or between the outer layer of insulation and the purge bag was not considered. With the aid of information on free convection between flat plates obtained from Reference 13, calculations have shown that for small gaps (≤ 0.25 in.) between the outer layer of insulation and the purge bag, the effects of convection are small in comparison with conduction. For large gaps between the insulation and the purge bag (> 0.25 in.) the contribution from convection is significant, and the effective insulating purge-gas layer thickness is equal to the thickness of the insulation.

The steady-state purge-bag temperature, tank temperature, and heat flux for the secondary LH₂ tank during ground hold for the systems using a foam substrate are shown in Figures 6-2 through 6-5. Temperatures and heat fluxes were predicted for foam thickness up to 3 in. and purge-bag-to-tank spacings of 0.5, 1.0, and 1.5 inches. Both He and N₂ were considered for the purge gas. The steady-state purge-bag temperatures and heat fluxes for a system using no foam and helium as the purge gas are shown in Figures 6-6 and 6-7. The curves in Figure 6-7 are identical to those for helium in Figure 6-5 except that they have been extended to include the no-foam configuration. The results show that, as expected, the critical requirement for sizing of a foam substrate, when using He as the purge gas (Figure 6-2), is the prevention of ice formation on the exterior of the

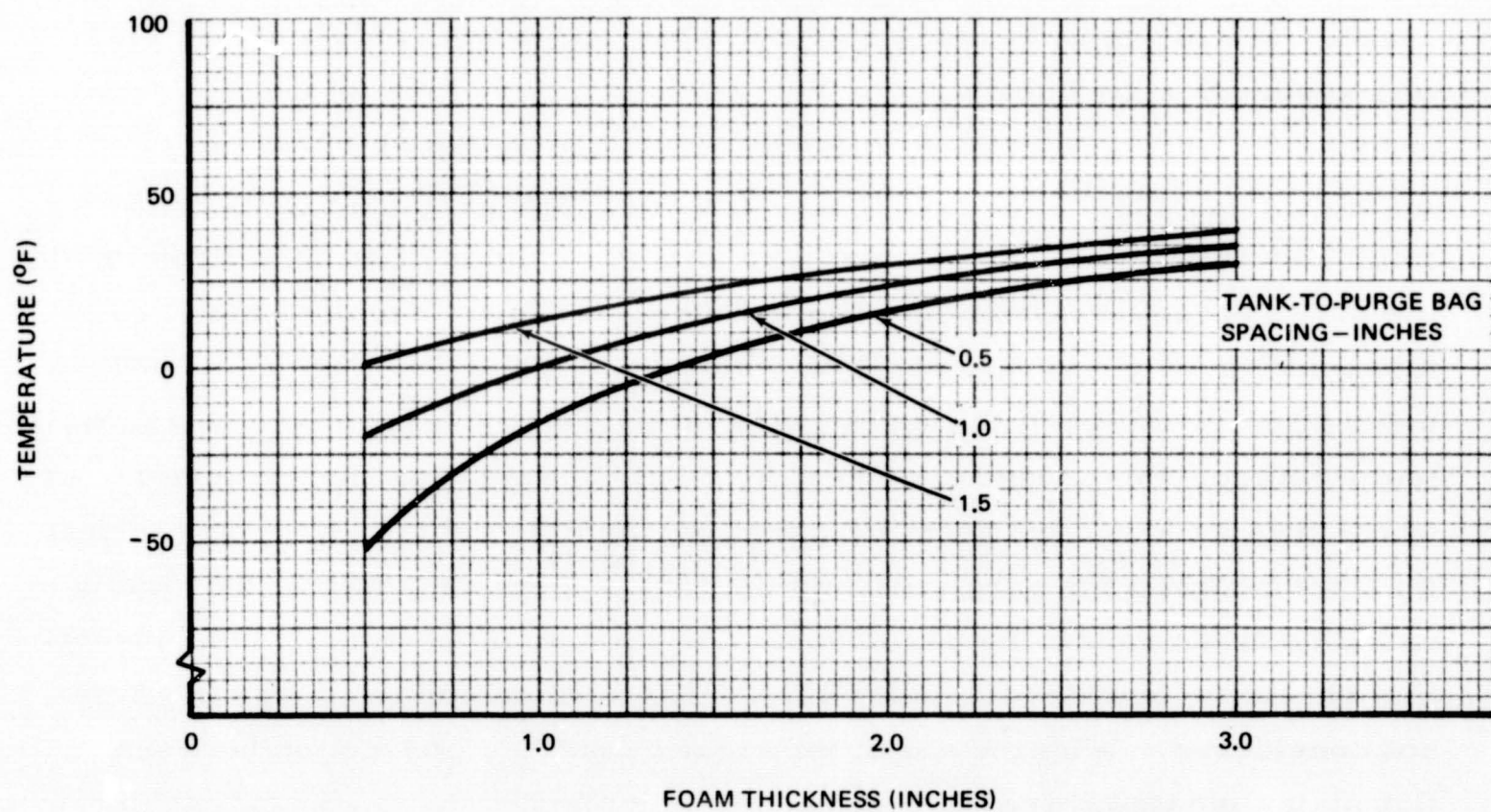


Figure 6-2. LH₂ Tank Purge Bag Surface Temperatures--Helium Purge

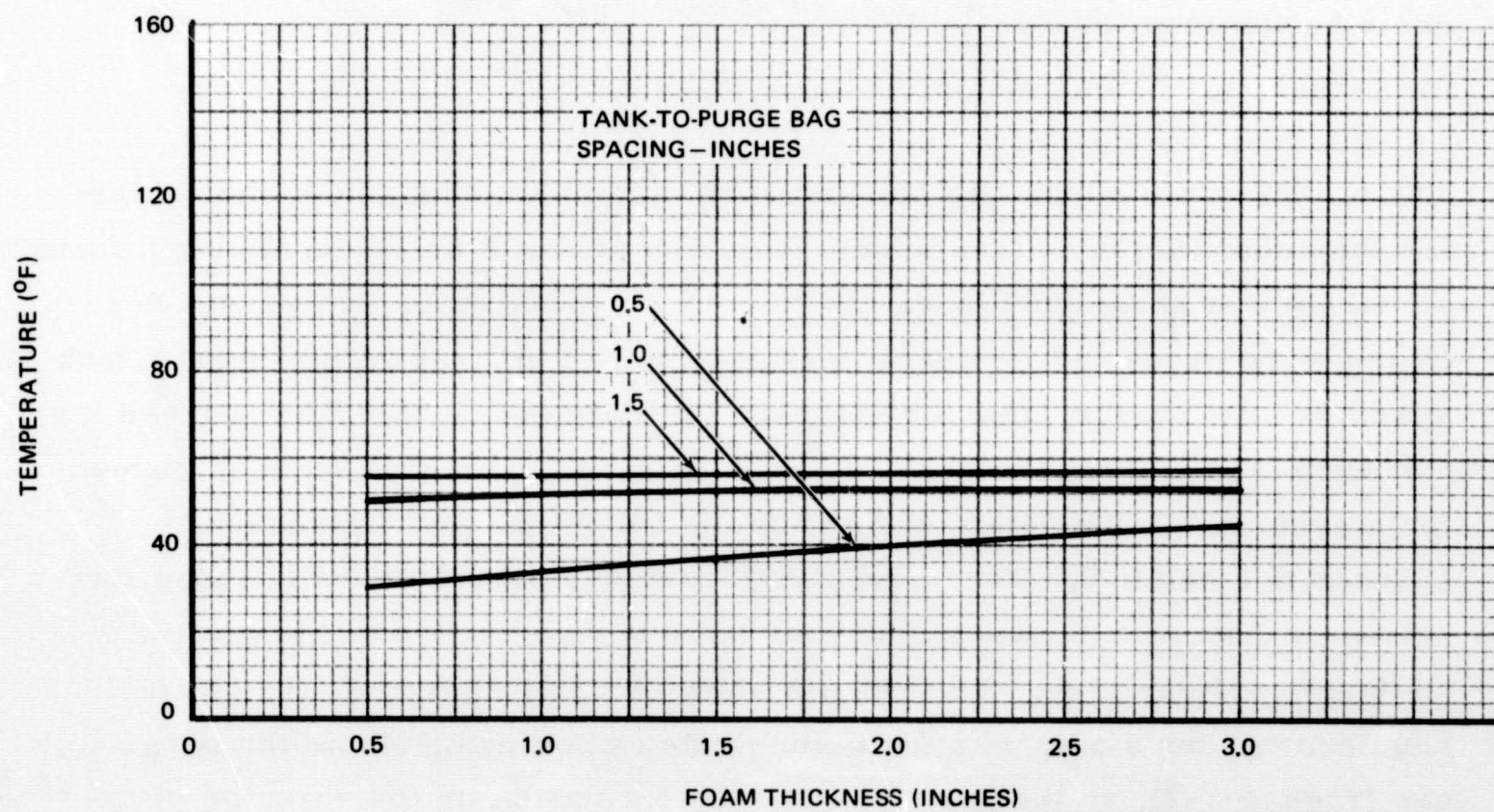


Figure 6-3. LH₂ Tank Purge Bag Surface Temperatures--Nitrogen Purge

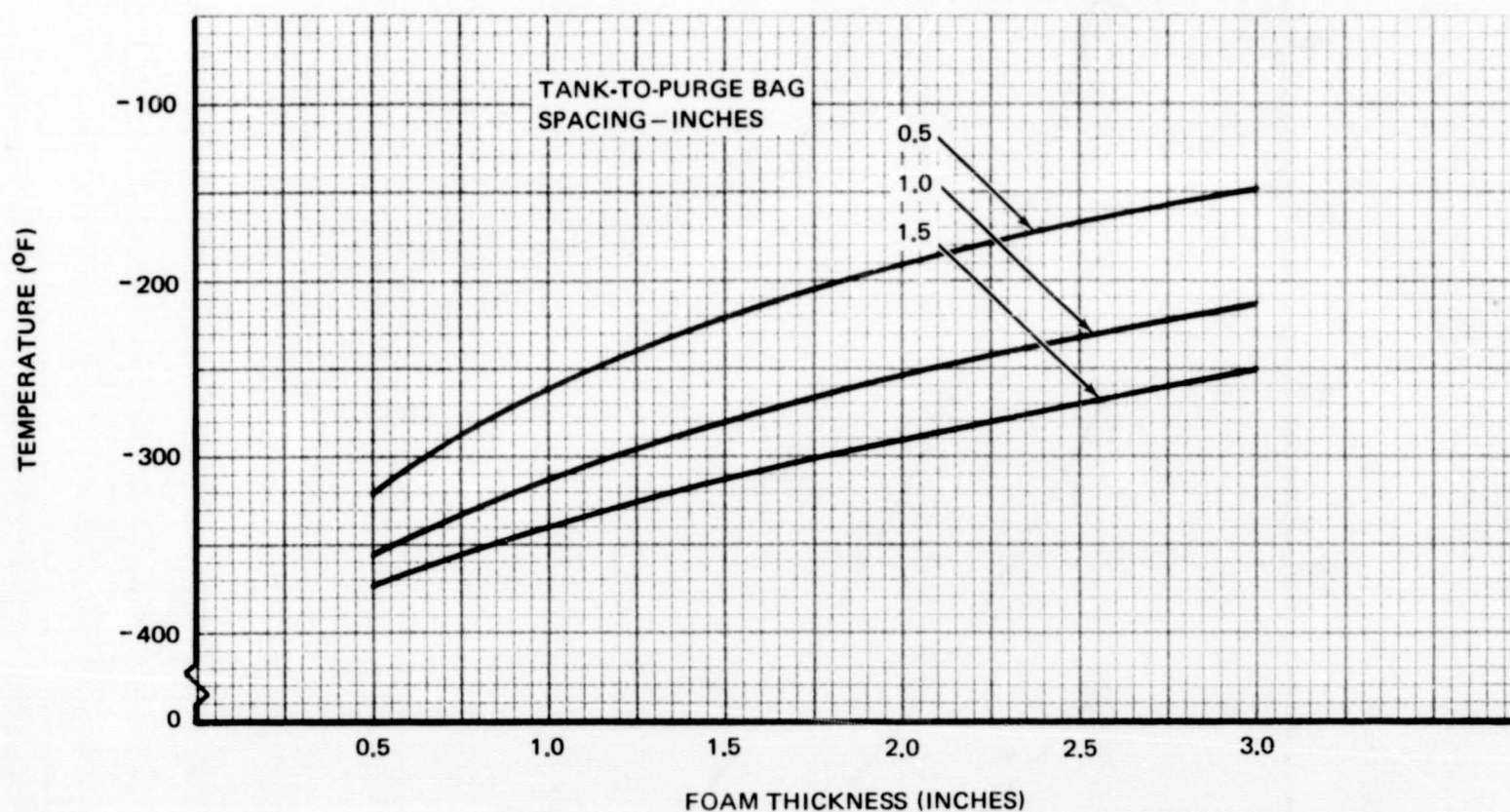


Figure 6-4. LH₂ Tank Wall Temperatures--Nitrogen Purge

purge bag (assuming a surrounding environment of air); the critical requirement for sizing of the foam substrate when using N₂ as the purge gas (Figures 6-3 and 6-4) is the prevention of liquefaction of the N₂ on the tank. If the surrounding environment outside the purge bag is nitrogen instead of air, ice prevention on the exterior of the purge bag will not be possible. The results also show that, as expected, the higher thermal conductivity of helium results in higher heat fluxes relative to those for nitrogen (Figure 6-5).

In addition to the above results, the effect of the temperature of the gas external to the purge bag on the ground-hold heating rate was studied for the secondary LH₂ tank. These data are of interest if the interior of the vehicle is purged with an ambient or hot gas to prevent frost formation on the main tanks. The results shown in Figure 6-8 were obtained assuming a tank-to-purge-bag spacing of 0.5 in. This is the minimum spacing anticipated and therefore results in the maximum heat flux to the tanks. A nitrogen purge was assumed in this case.

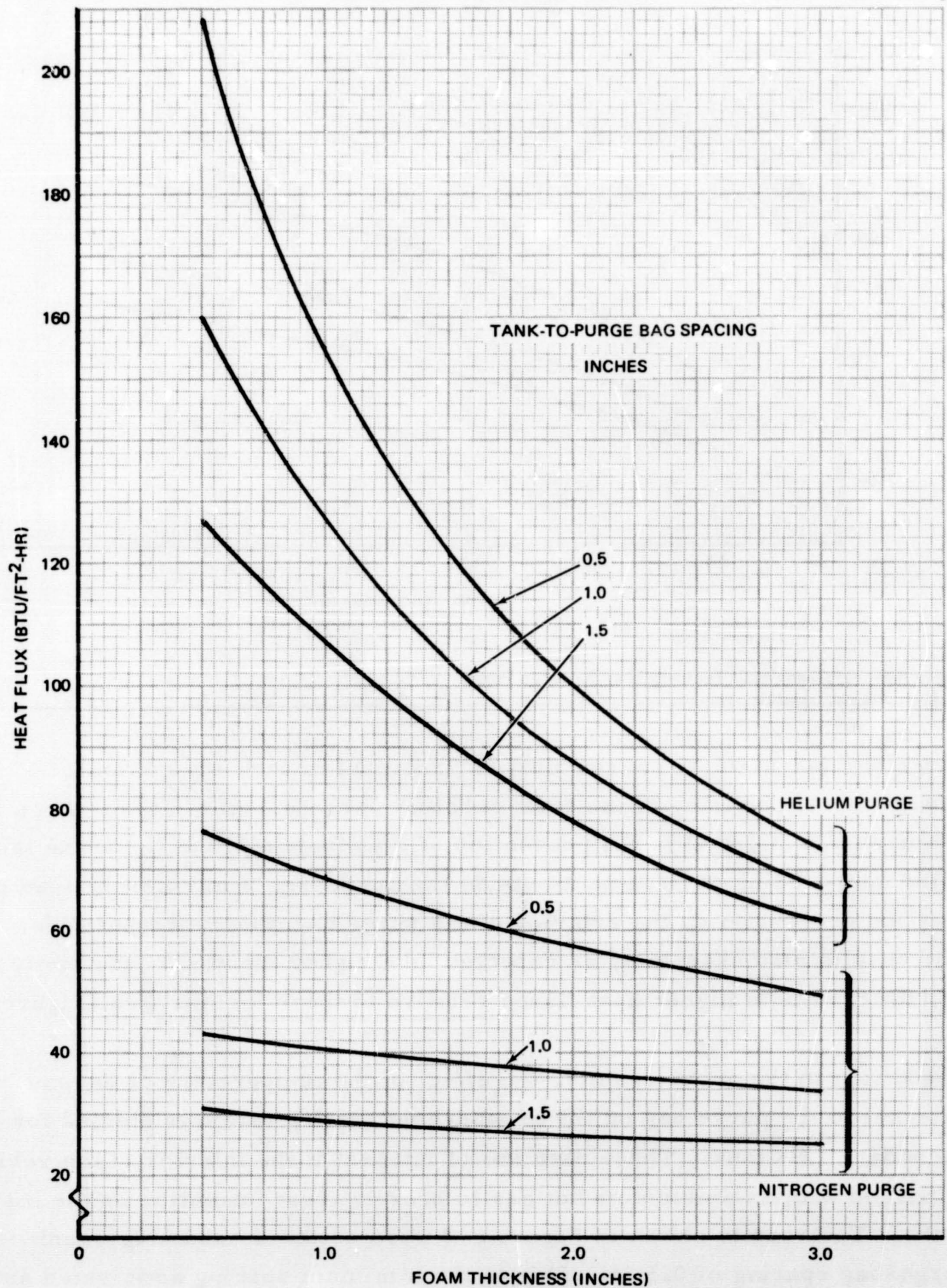


Figure 6-5. LH₂ Tank Ground Hold Heat Transfer Rates

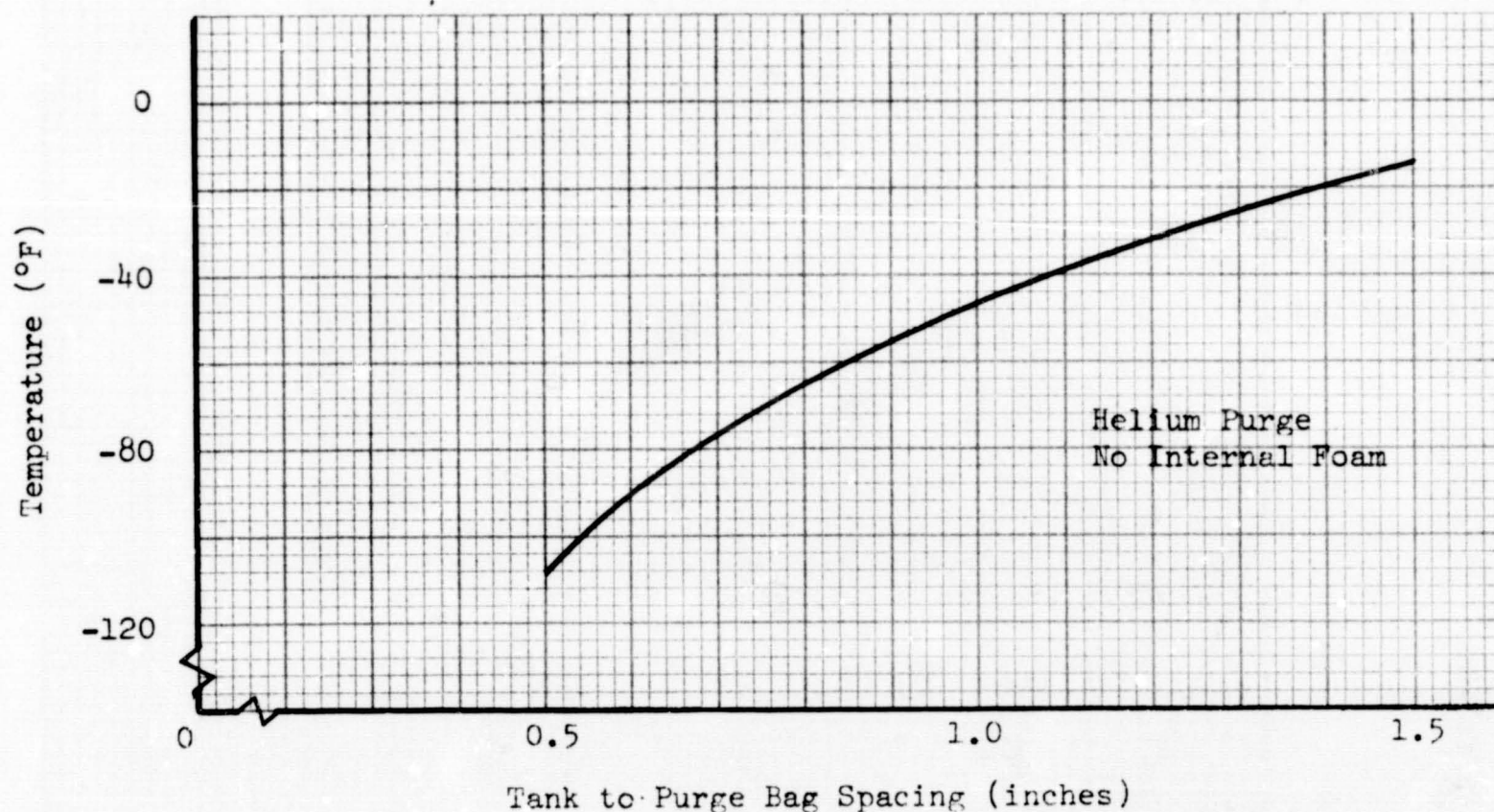


Figure 6-6. LH₂ Tank Purge Bag Temperature--Ground Hold, No Foam

The LH₂ boiloff penalty associated with ground hold is a result of the prelaunch lockup period. Prior to launch, the tanks will be topped continuously except for this short period just before liftoff. It has been assumed that a constant pressure will be maintained within the tank during this time by venting hydrogen, and replacement of the liquid will not be possible. For the Saturn S-IVB stage, this interval is just under 3 minutes. Consequently, in order to estimate the boiloff loss during lockup, a 3-minute period has been assumed in this study. The boiloff weight associated with the lockup period is given in Figure 6-9 for the system using no internal tank foam and helium purge gas. The lockup period boiloff weights for the helium purge with 0.5 in. of internal tank foam and for the nitrogen purge with internal tank foam are shown in Figures 6-10 and 6-11, respectively. The 0.5-in. foam thickness used with the helium purge represents a minimum practical thickness for the application of the foam material. The foam thicknesses used with the nitrogen purge gas represent the minimum thickness which must be used to prevent liquefaction of nitrogen on the tank (see Figure 6-4).

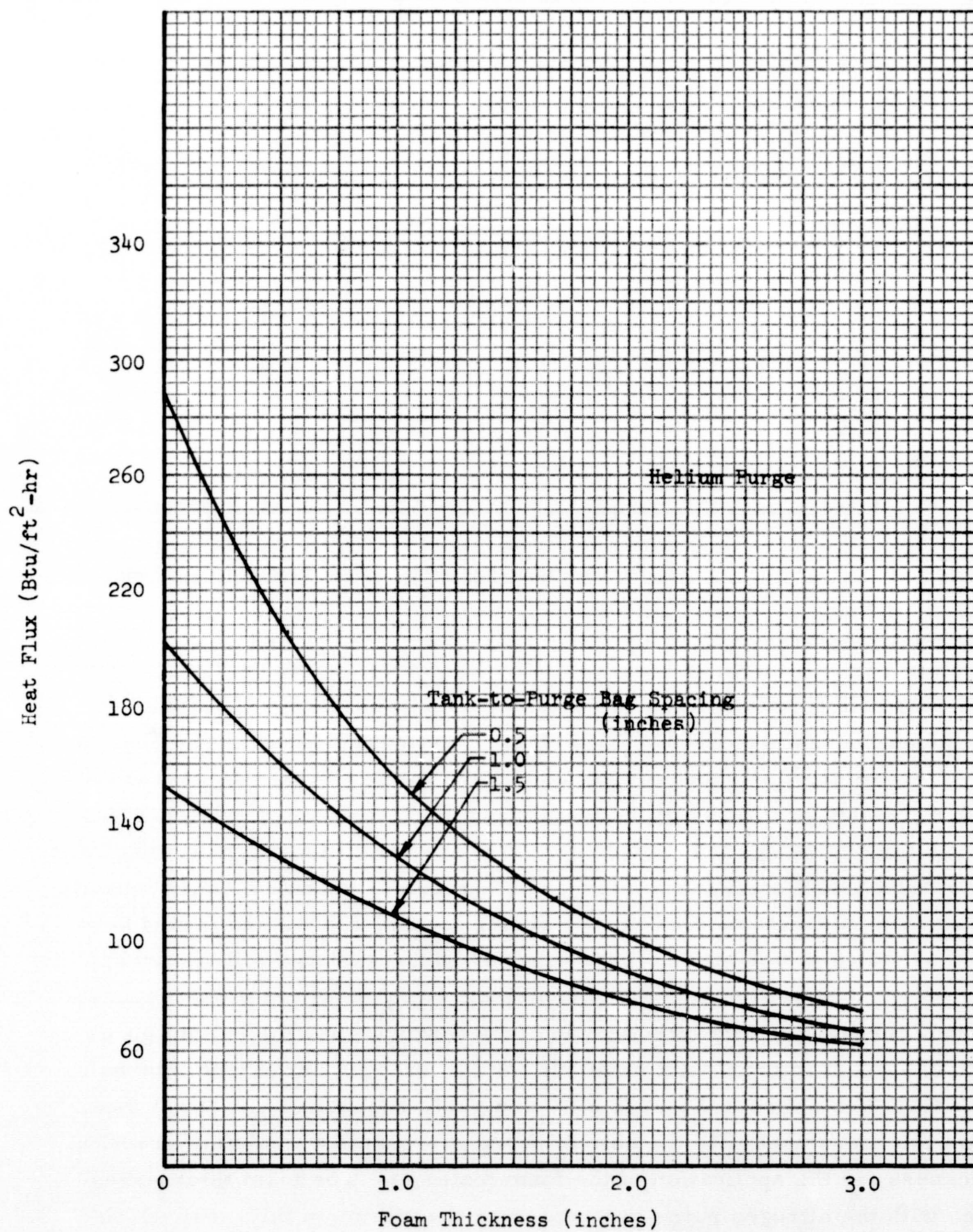


Figure 6-7. LH₂ Tank Ground Hold Heat Transfer--Helium Purge

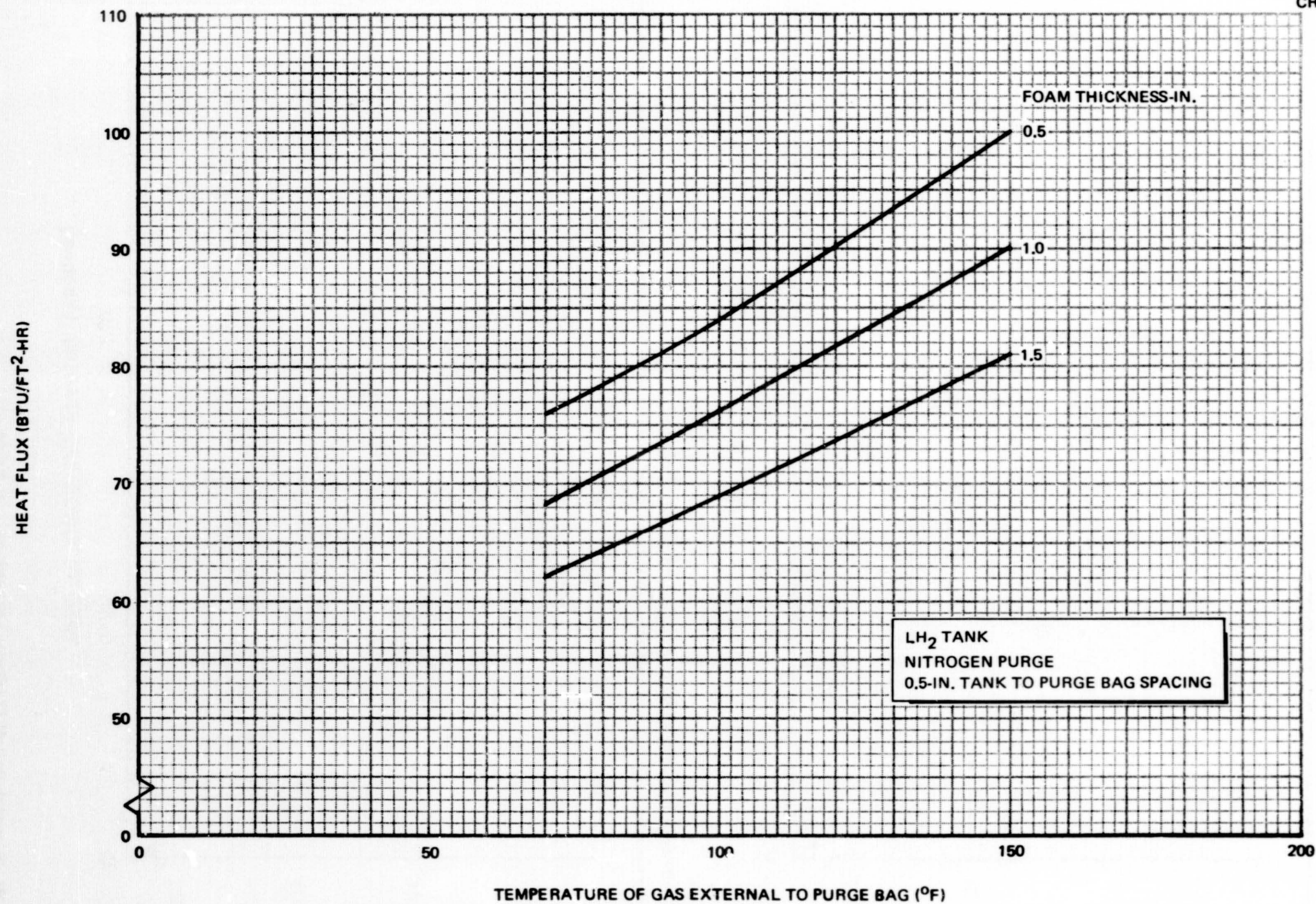


Figure 6-8. Effect of Ambient Gas Temperature on LH₂ Tank Ground Hold Heating Rate

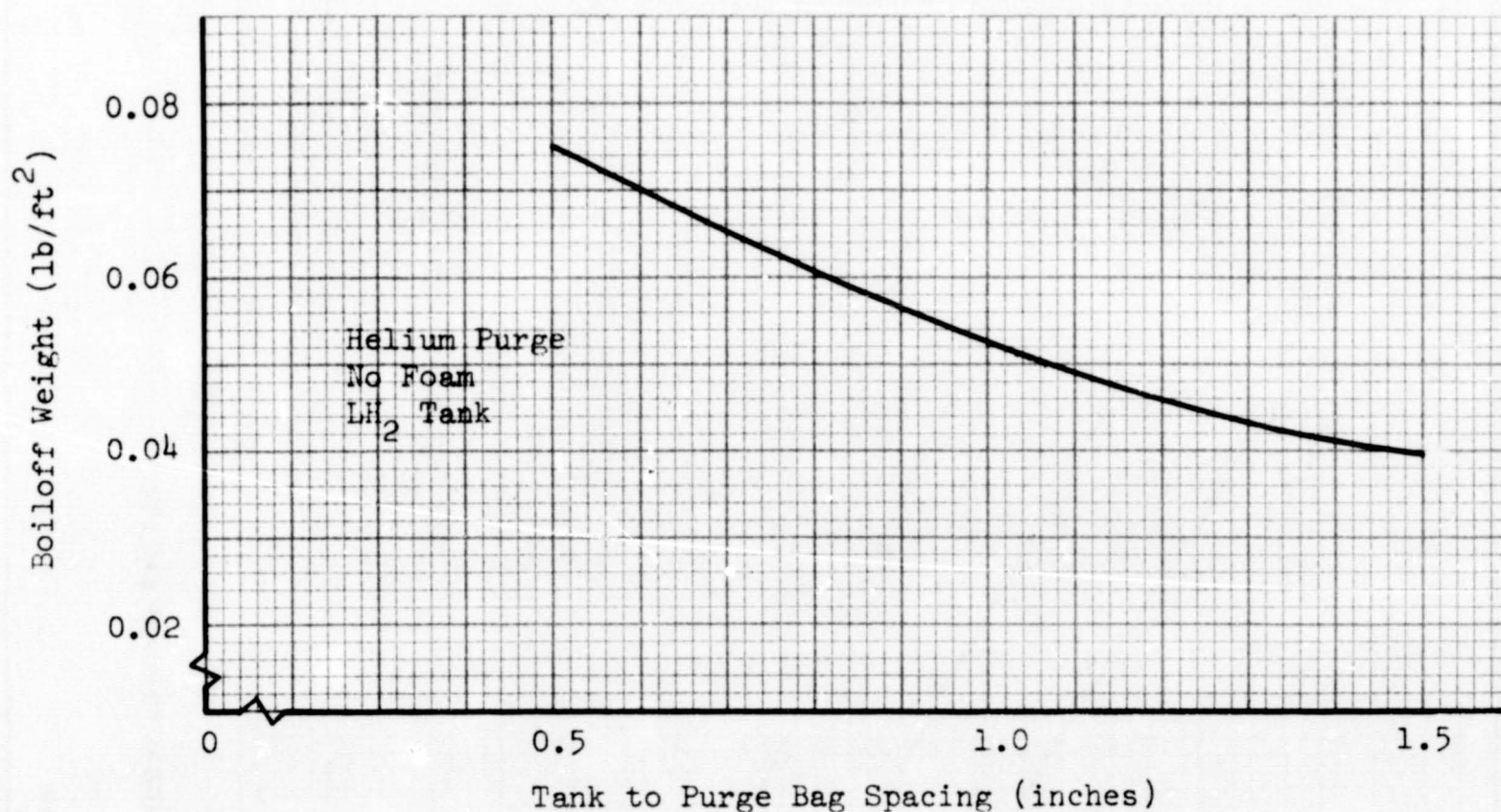


Figure 6-9. Prelaunch Boiloff (3-Minute Lockup)--Helium, No Foam

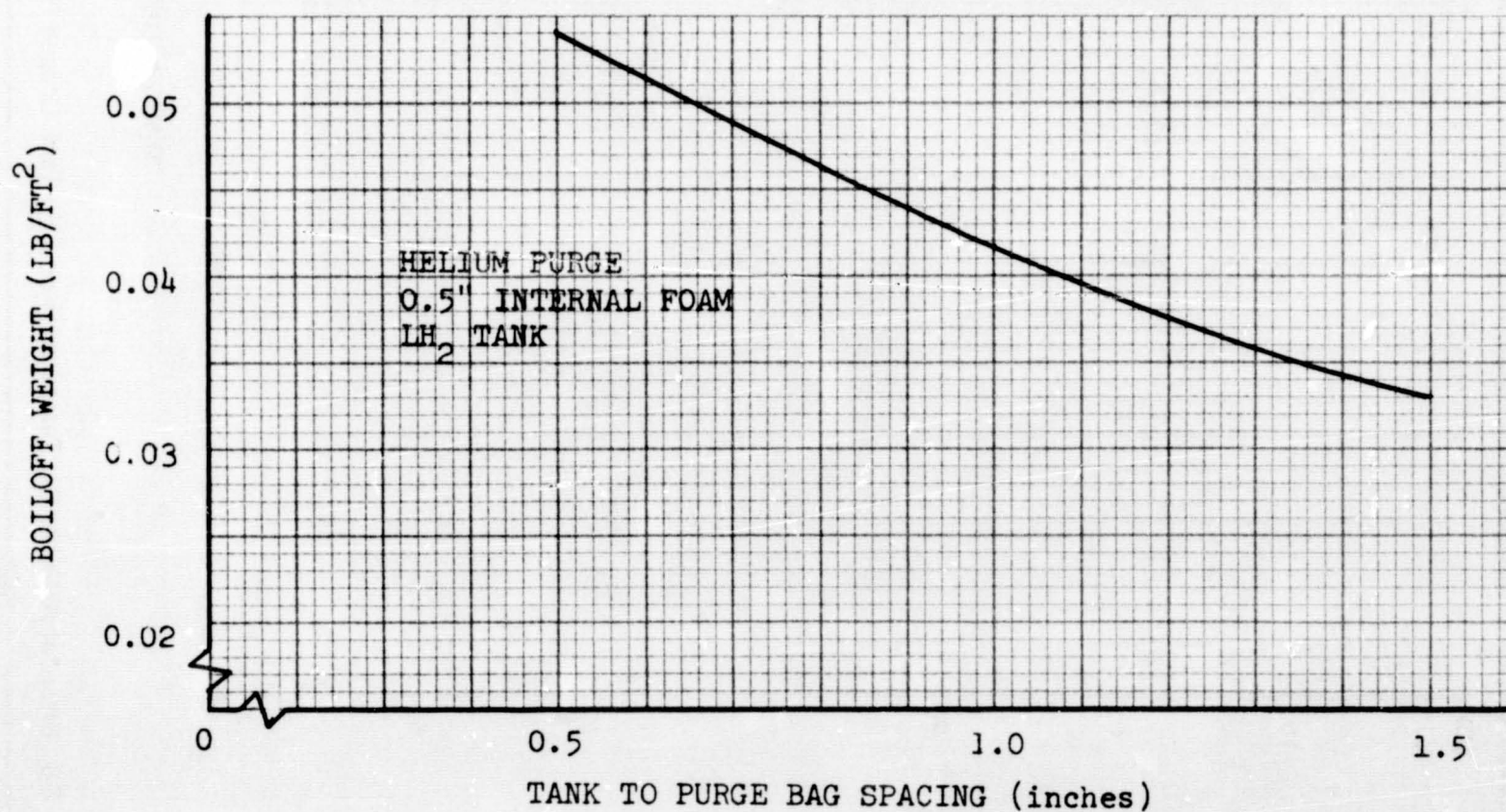


Figure 6-10. Prelaunch Boiloff (3-Minute Lockup)--Helium, Foam

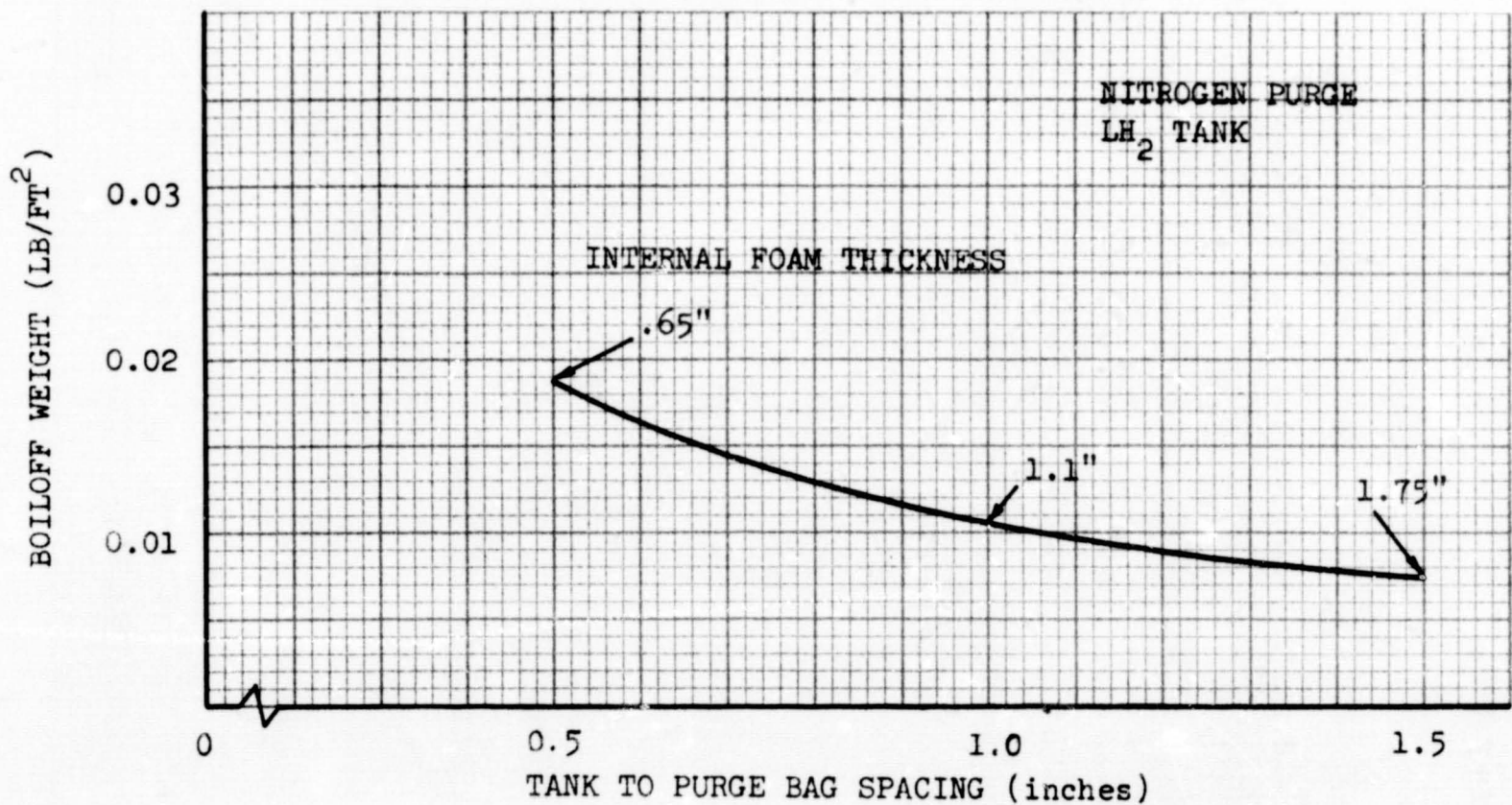


Figure 6-11. Prelaunch Boiloff (3-Minute Lockup)--Nitrogen, Foam

The ground-hold temperature distribution affects the amount of thermal energy which will soak into the LH₂ during the ascent phase. Consequently, the proper distribution must be obtained. Typical steady-state temperature profiles for the ground-hold period are shown in Figure 6-12.

6.1.2 Ascent Phase—LH₂ Tank

A thermal analysis was performed on each of the three previously described insulation system concepts to determine the heat flow into the LH₂ tank during the ascent phase. The thermal model and JA03 computer program discussed previously were used. In order to perform a realistic analysis of the ascent phase, which is a transient condition, a number of considerations and assumptions were necessary. In each case, regardless of the purge gas, an air (or nitrogen) environment between the vehicle structure and the purge bag was assumed. This region is vented to the atmosphere during ascent and was assumed to follow the ascent pressure profile shown as Curve A in Figure 6-13. The MLI interstitial gas pressure was assumed

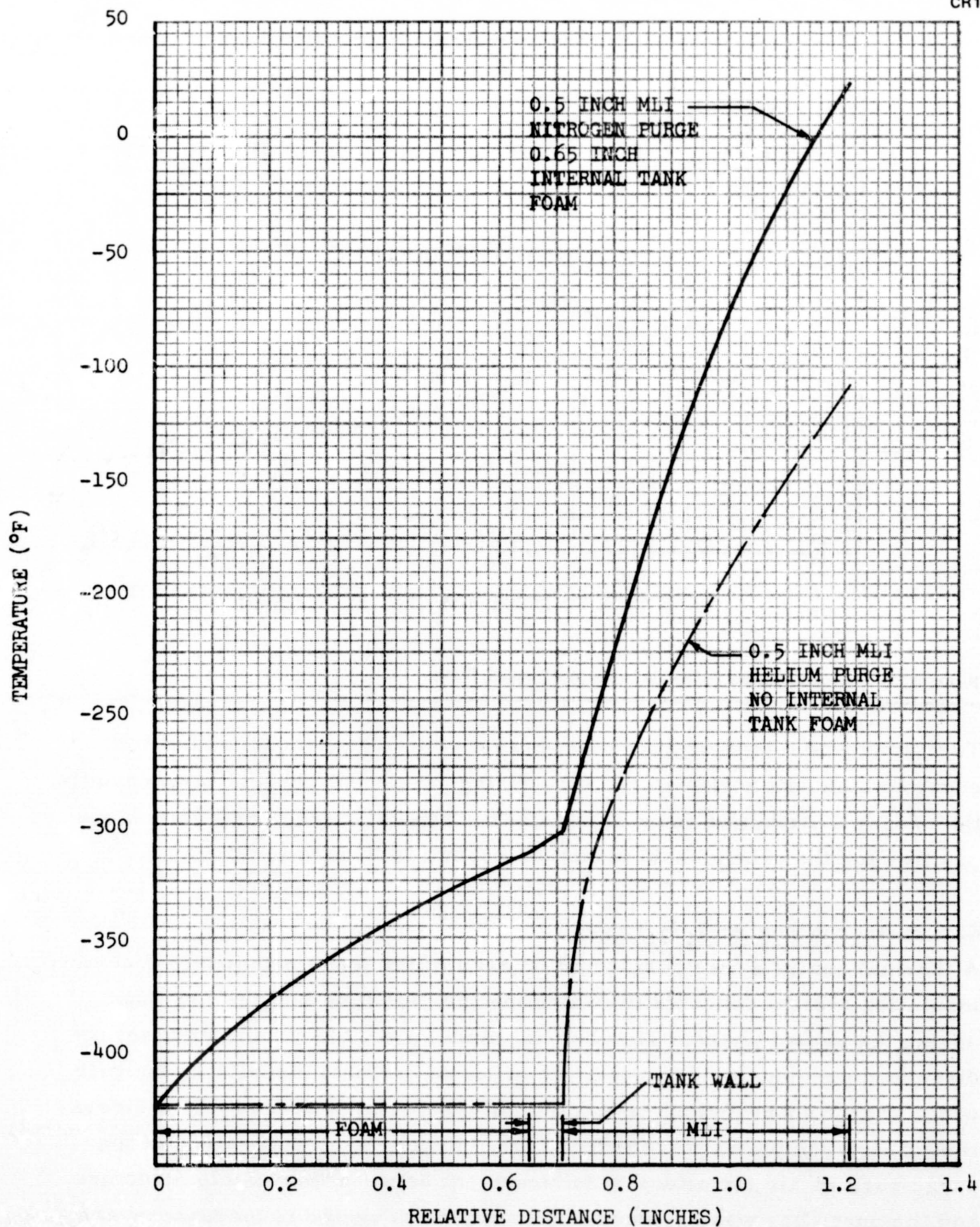


Figure 6-12. Typical Ground Hold Temperature Distributions--LH₂ Tank

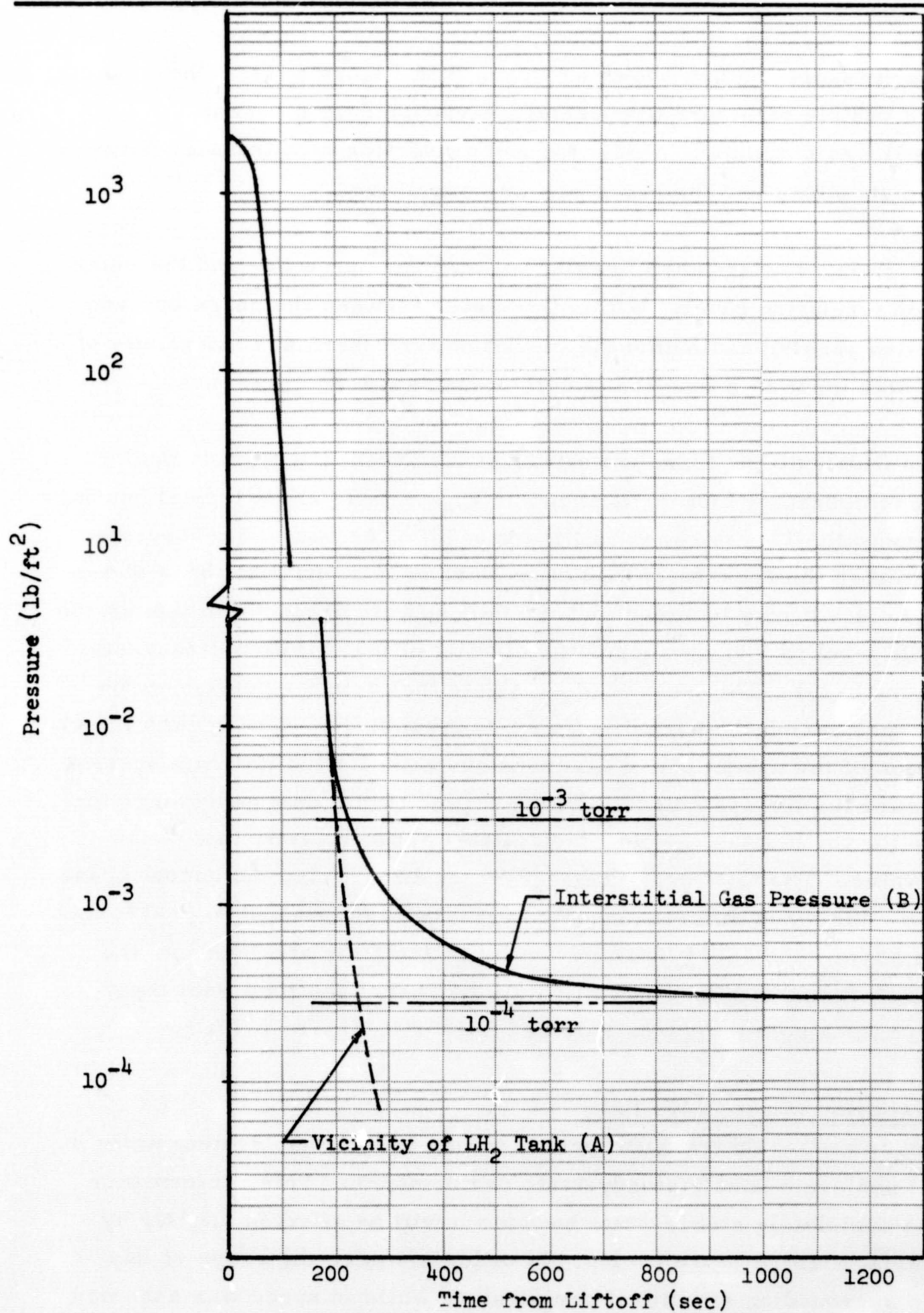


Figure 6-13. Pressure History Assumed During Ascent--LH₂ Tank

to follow a pressure history shown as Curve B in Figure 6-13. The anticipated vehicle structure temperature variation during ascent (Figure 4-3) was simulated. Radiation and convection heat transfer between the vehicle structure and the purge bag was considered.

A gap of 0.25 in. was assumed to exist between the purge bag and the outer layer of the insulation panel. Within this space between the purge bag and the insulation panels, and within the insulation, the thermal conductivity of purge gas was input as a function of both temperature and pressure.

In order to illustrate the transient nature of the ascent phase, a typical purge-bag temperature history is shown in Figure 6-14 and a typical heating rate history to the LH_2 is shown in Figure 6-15. The purge-bag temperatures for other thicknesses of insulation were very similar to those shown in Figure 6-14. It may be noted that the heating rate drops rapidly from the ground-hold level to a value approximately that of the in-space steady-state level (Figure 6-15). This serves to illustrate that a major portion of the heating occurs during the period in which continuum flow venting is in effect. The duration of the ascent phase used was one hour for the no-foam system and two hours for the systems with internal tank foam, thus providing sufficient time for the heating rate to reach a level approximately that of the in-space value. The total heat absorbed by the LH_2 during the ascent phase is shown for the three different system concepts in Figures 6-16, 6-17, and 6-18. As shown, the energy transferred from the foam and tank into the LH_2 in the systems with foam significantly increases the total heat input during ascent; compare Figures 6-16 and 6-18 with Figure 6-17.

6.1.3 Evacuated Phase— LH_2 Tank

Subsequent to the highly transient period during ascent, the system while in space will achieve a nearly steady-state performance. This performance will not be completely steady-state because it will be affected slightly by vehicle surface temperature cycles. In order to match the scope of this study, the surrounding structural temperature while in space was assumed nominally to be a constant 50°F.

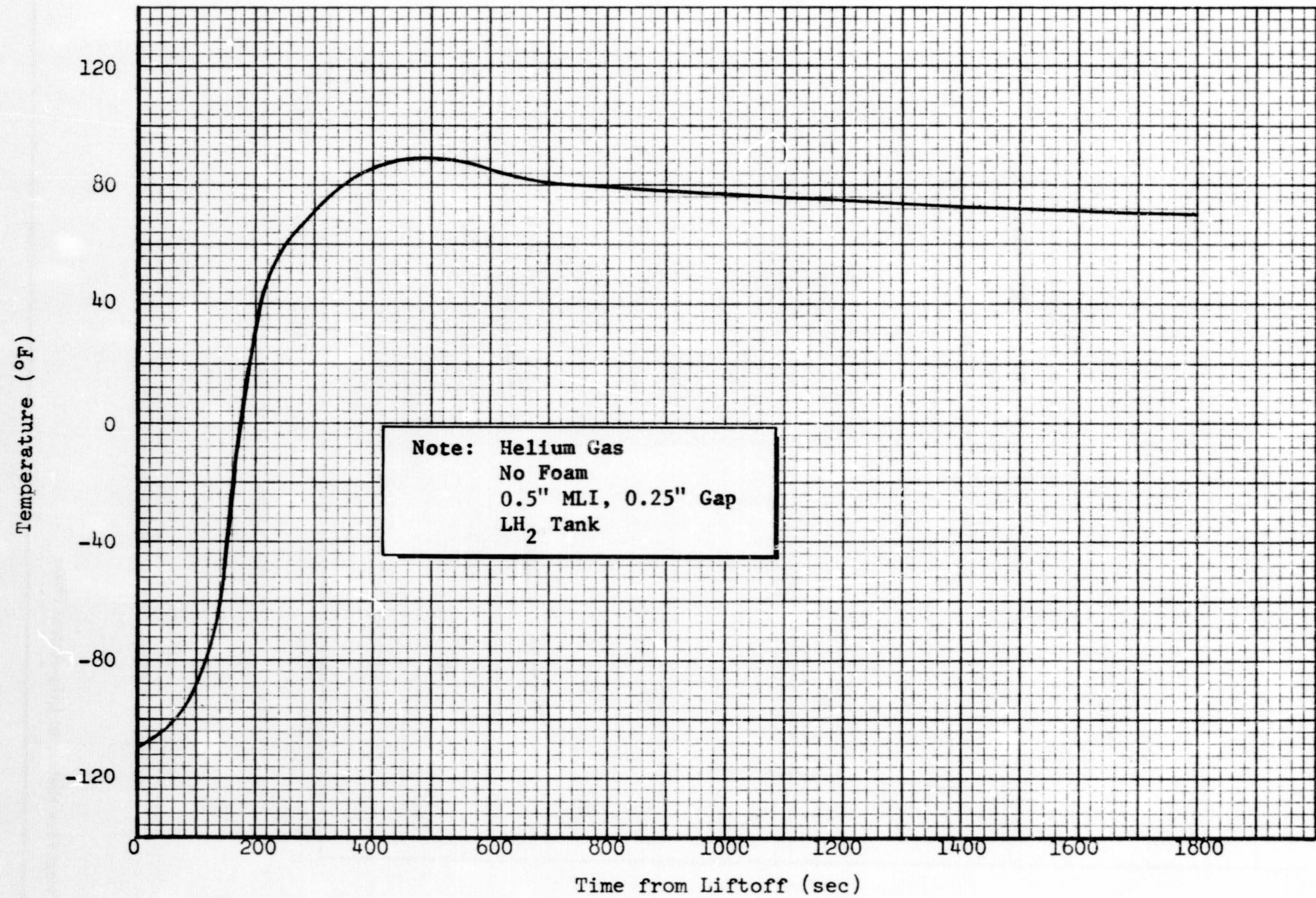


Figure 6-14. Purge Bag Temperature History During Ascent--LH₂ Tank

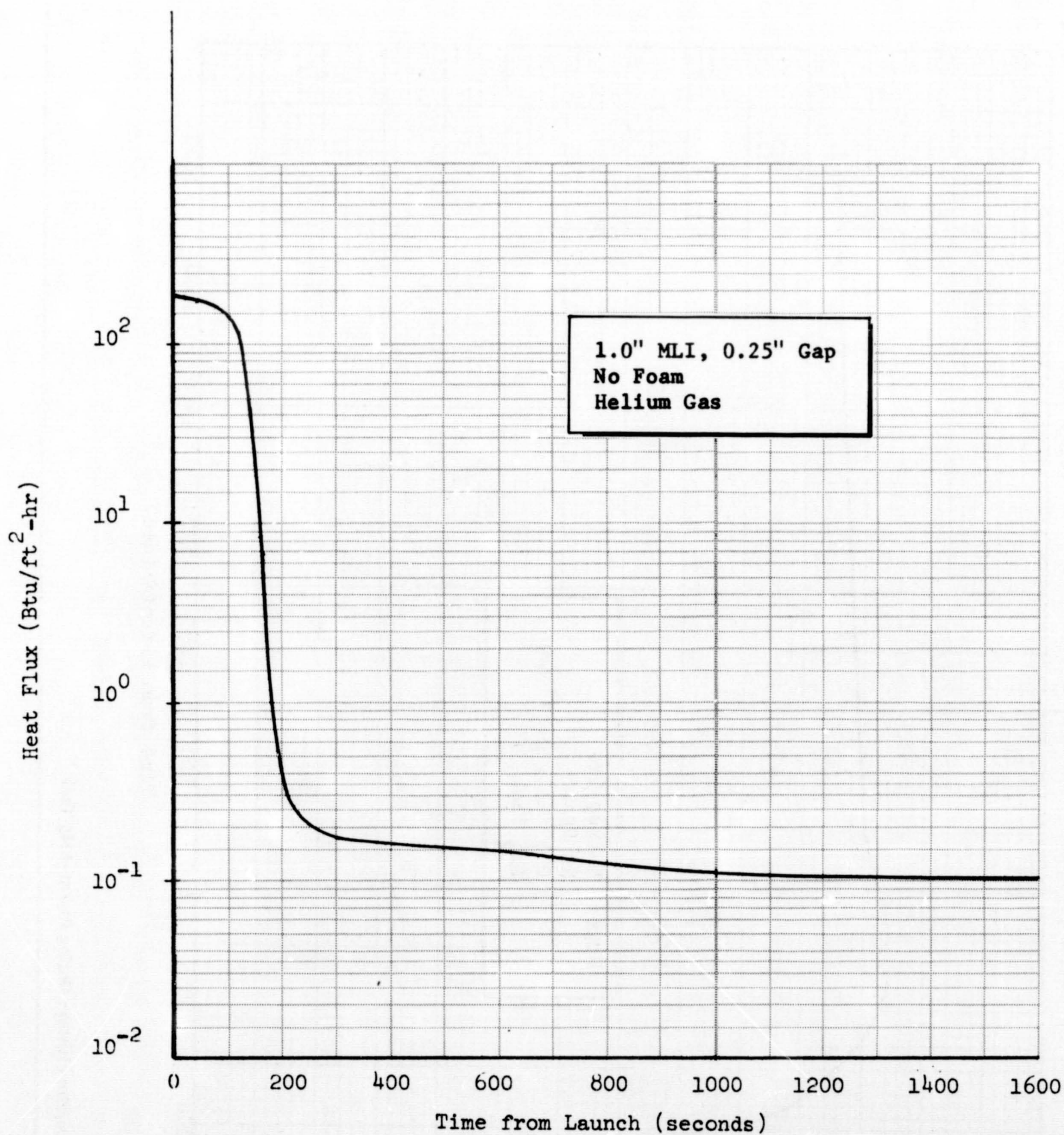
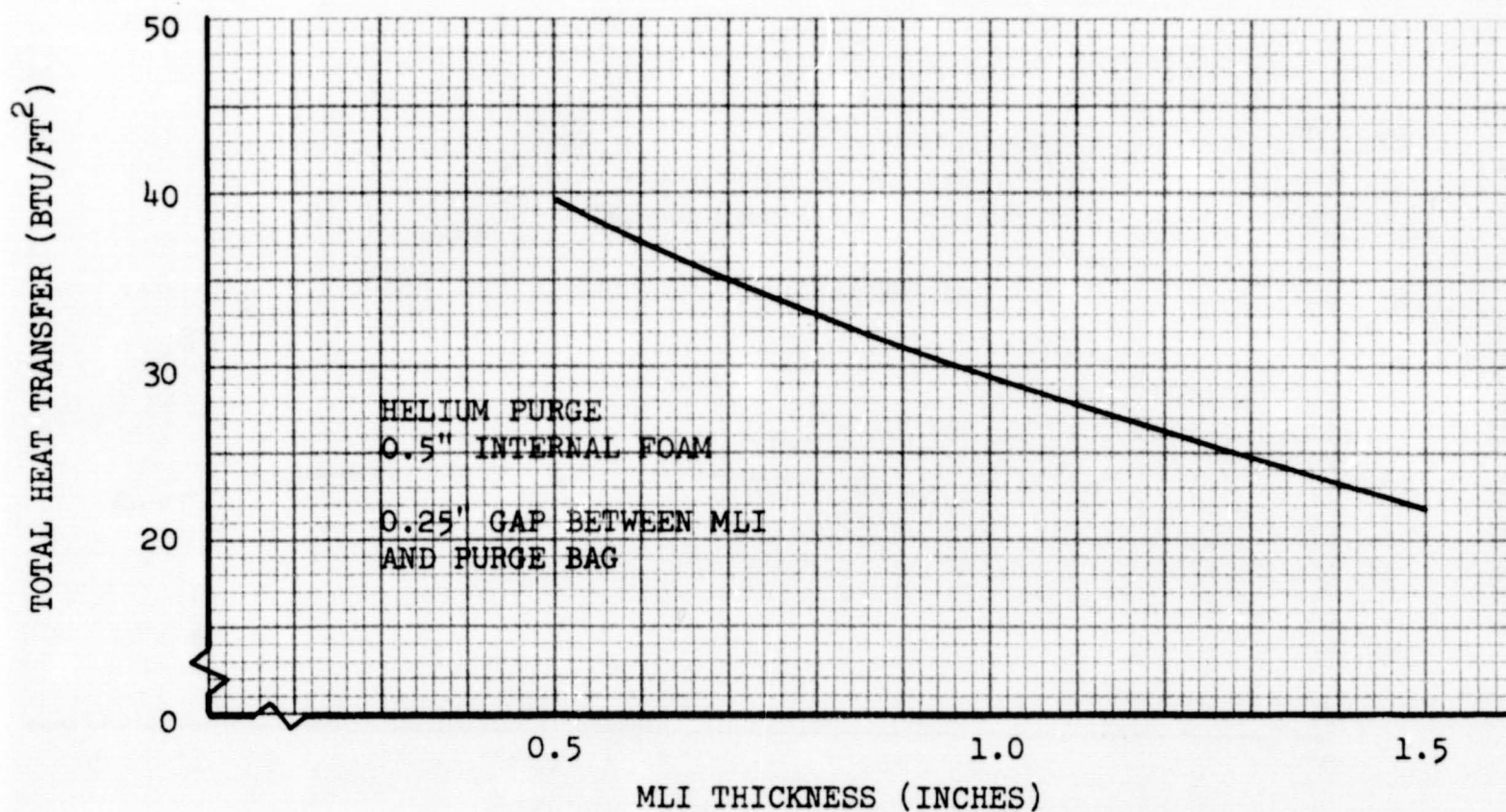
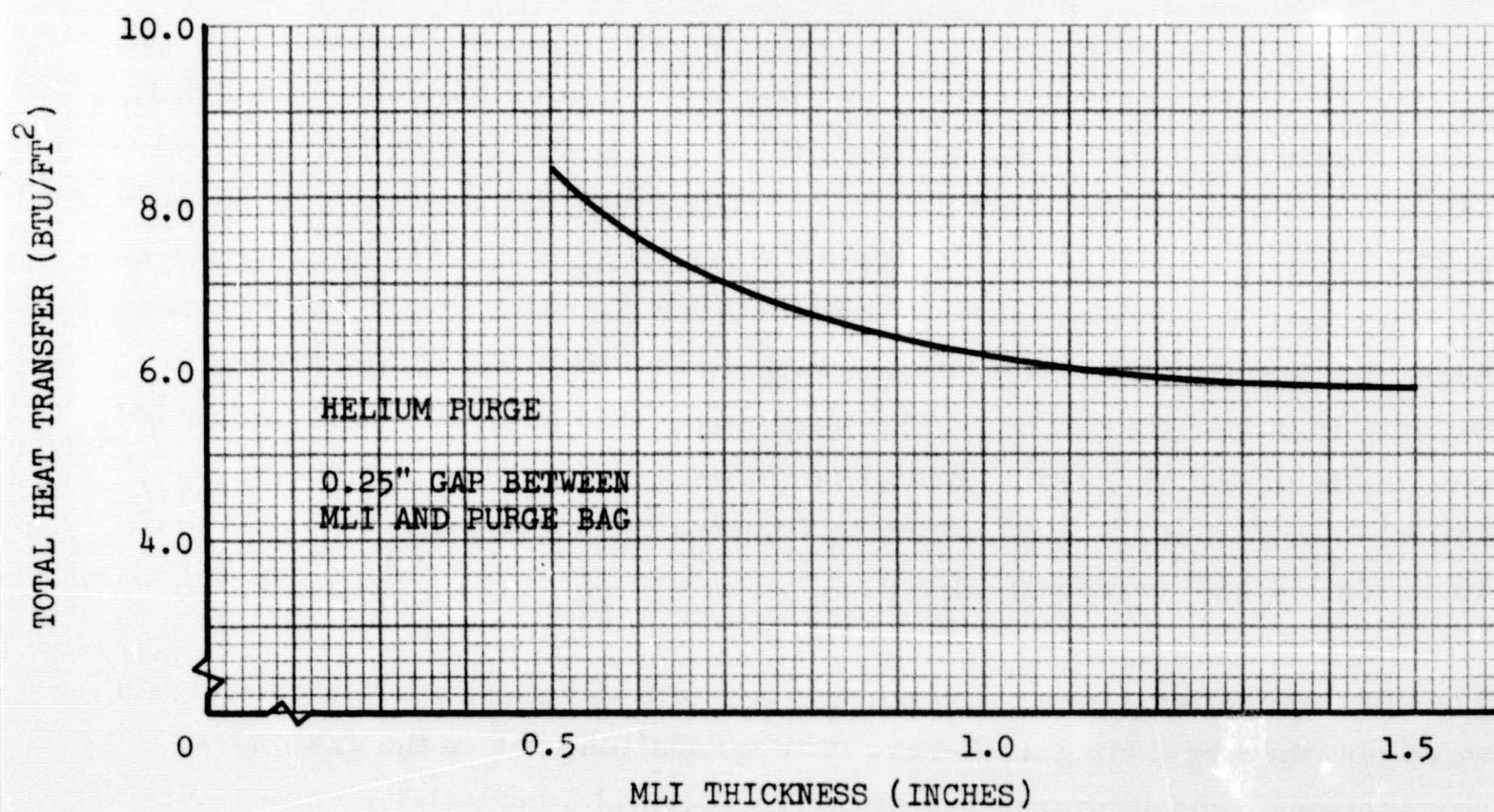


Figure 6-15. Heat Flux History to LH₂--Ascent Phase

Figure 6-16. Heat Transfer to LH₂ During Ascent—Helium, FoamFigure 6-17. Heat Transfer to LH₂ During Ascent--Helium, No Foam

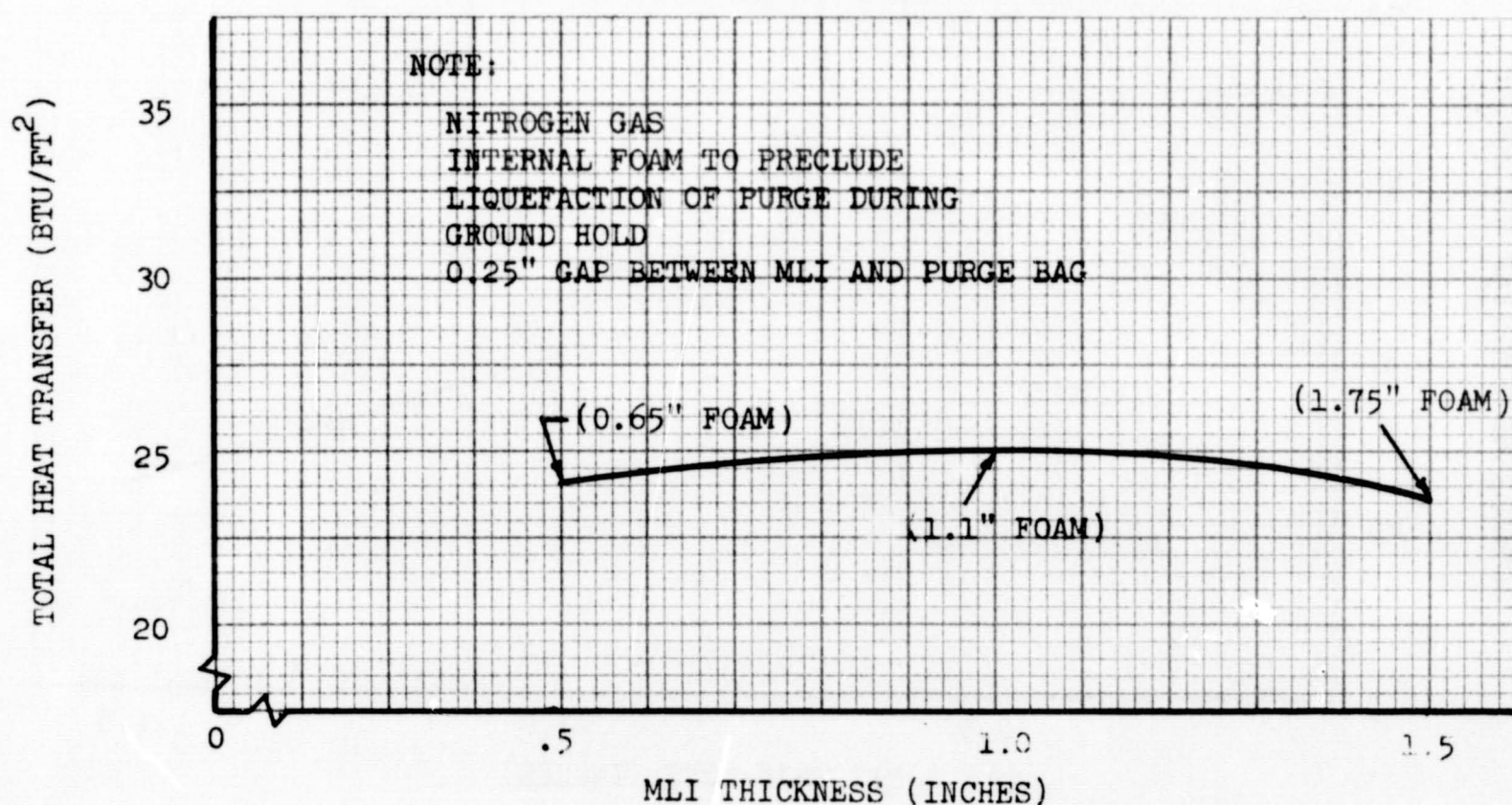
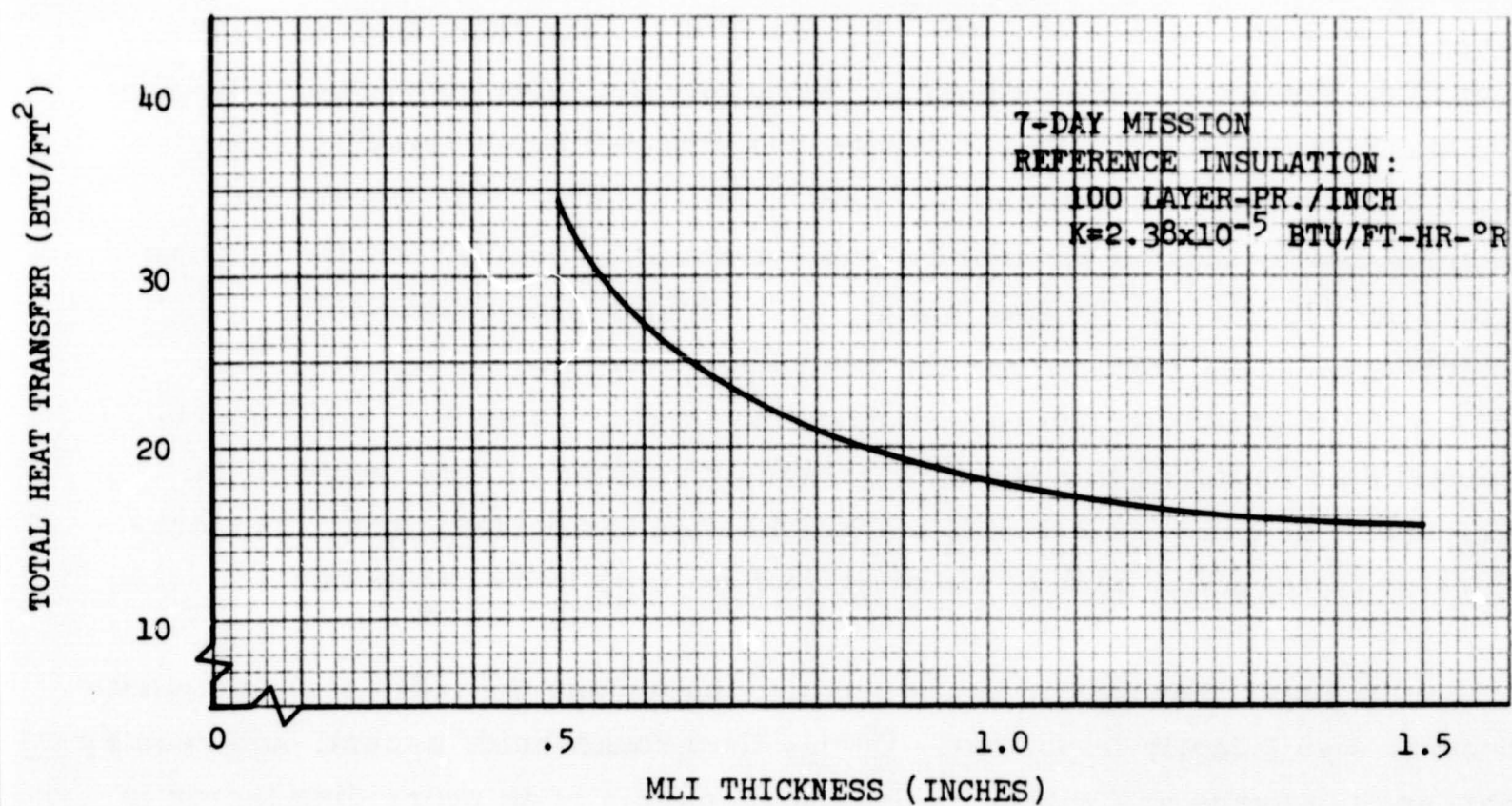
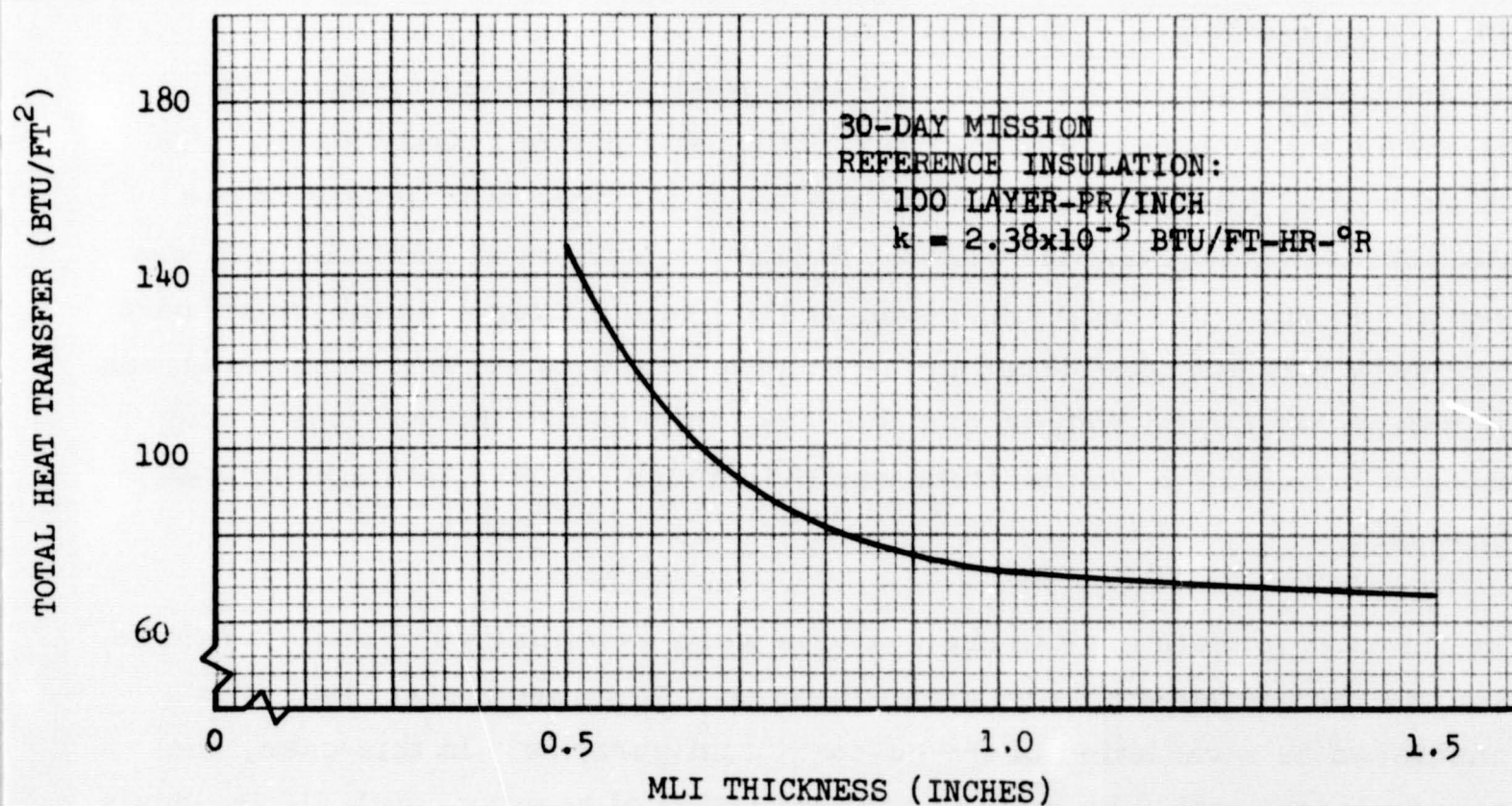


Figure 6-18. Heat Transfer to LH₂ During Ascent--Nitrogen, Foam

At the time of the initiation of this analysis, experimental conductivity and composite density data on the composites were not available. As a result, for analysis purposes, a typical insulation composite having a density of 100 layer-pairs per inch and a fully degraded thermal conductivity (k) of 2.38×10^{-5} Btu/hr ft °R was assumed. Later experimental information has been utilized by ratioing with respect to this reference composite performance; the resulting in-space boiloff weights are included in the system weights in Subsection 6.1.5. The total integrated heat absorbed by the LH₂ tank utilizing the reference insulation composite (100 layer-pairs/inch, and $k = 2.38 \times 10^{-5}$) is provided in Figures 6-19 and 6-20 for 7-day and 30-day missions, respectively.

The thermal conductivity values used to obtain the in-space boiloff weights were obtained by adding a 50-percent degradation (due to the fasteners, perforations, and joints) to the effective thermal conductivity values obtained in the calorimeter tests (Figure 3-69) at a compressive loading of 1×10^{-4} psi. The degraded effective thermal conductivity (k) values used

Figure 6-19. Total Heat Transfer During Evacuated Period--7-Day Mission, LH₂ TankFigure 6-20. Total Heat Transfer During Evacuated Period--30-Day Mission, LH₂ Tank

were 1.55×10^{-5} and 3.45×10^{-5} Btu/hr ft²R for the DGK/Dacron B4A and DGK/Nomex HT-96 composites, respectively. The nondegraded k value for the DGK/Nomex HT-96 composite was obtained by extrapolating the calorimeter data to a value of 2.3×10^{-5} Btu/hr ft²R. The 50-percent degradation included 8 percent for the fasteners, 7 percent for the perforations, and 35 percent for the joints. Calorimeter data reported in Reference 14 was adjusted for the secondary LH₂ tank system design to obtain the degradation due to fasteners and joints. Analytical and experimental data reported in Reference 12 and experimental data reported in Reference 14 were used to obtain a degradation for perforations. Perforations of 1 percent or less of the total surface area were assumed.

It may be noted that only in the evacuated phase does the individual composite become significantly important. During the ground-hold, ascent, and reentry phases, the purge gas within the insulation panels is an overriding factor in the total contribution of heat to the LH₂, and the MLI composite materials have very little effect.

6.1.4 Reentry Phase—LH₂ Tank

The insulation system concepts were analyzed for the reentry phase to determine the heat flow into the tank during this period. Only helium was considered as the repressurization gas since nitrogen will liquefy on the tank surface at LH₂ temperatures. A dual gas system in which helium was used at the start of reentry followed by the use of nitrogen at the latter part of reentry was not considered in the final analyses as results of the analyses for helium with foam showed that the tank temperature did not rise to the nitrogen liquefaction temperature rapidly enough to make this a practical approach.

The thermal models used in the analysis were essentially the same as those used for the ground-hold and ascent phases. An internal start tank was considered as a variation of the no-foam configuration. In this case, the secondary tank would be empty at the initiation of reentry, with all residuals having been transferred to the start tank. As a result, the temperature of the secondary tank wall will rise during reentry. It may be noted that the

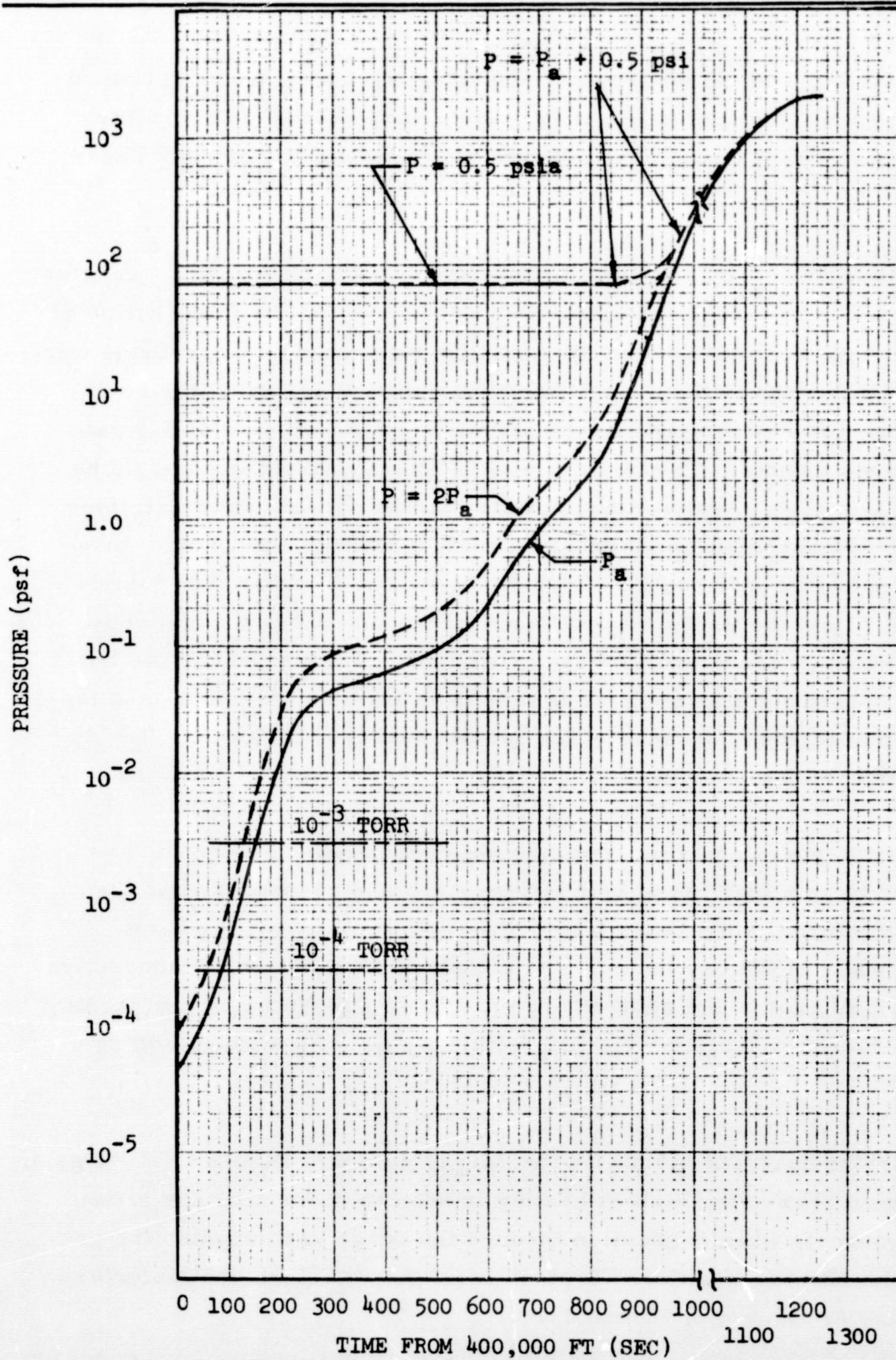
effect of a start tank would be nonexistent during the ascent phase, because the secondary tank is full of LH_2 during that period. The JA03 computer program used in the previous analyses was also used for the reentry phase analyses.

In order to assess the effect of the repressurization process on heat transfer to the tank, it was necessary to establish a procedure for the introduction of gas into the purge volume between the tank and purge bag. Two methods were considered. The first method consisted of introducing helium at the beginning of reentry to immediately develop and maintain a pressure of 0.5 psi within the purge volume. This pressure of 0.5 psi above ambient would be maintained throughout reentry. The second method consists of maintaining the pressure within the purge volume at a level two times the ambient pressure until a pressure differential of 0.5 psi is reached. After that point, the pressure within the purge volume would be maintained at 0.5 psi above ambient. These pressure profiles are presented in Figure 6-21. The latter method was chosen for this study as it results in less heat transfer than the other method described, because of the lower pressures involved. This is discussed further in Subsection 6.5.

As in the ascent-phase analysis, the thermal conductivity through the gas was assumed to be a function of both temperature and pressure. For the case with the internal start tank, free convection was assumed to exist between the walls of the two tanks. The results indicated that the convective process is significant to the point where very little attenuation of the reentry heating is obtained by isolating the LH_2 within a start tank without adding a foam.

A typical reentry heat flux history to the LH_2 is shown in Figure 6-22. Again, as in the ascent phase, the highest heating is seen to occur near the ground (higher pressures), when conduction through the purge gas becomes the predominant mode of heat transfer. Typical purge-bag temperature histories during reentry are shown in Figure 6-23.

The total heat transfer to the LH_2 during the reentry phase is provided for each system concept in Figures 6-24, 6-25, and 6-26. As shown, and as

Figure 6-21. Pressure History During Reentry--LH₂ and LO₂ Tanks

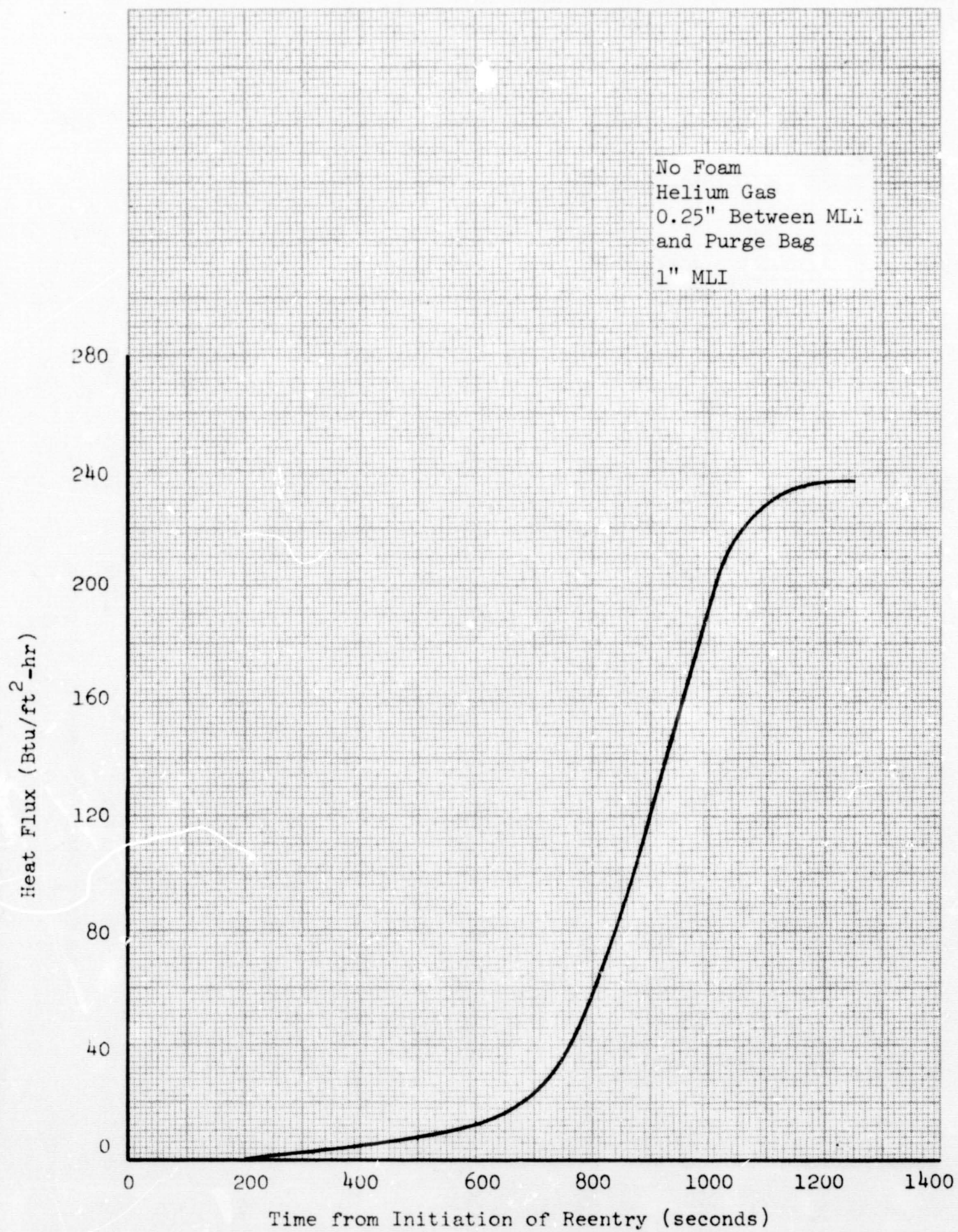


Figure 6-22. Heat Flux History to LH₂-Reentry Phase

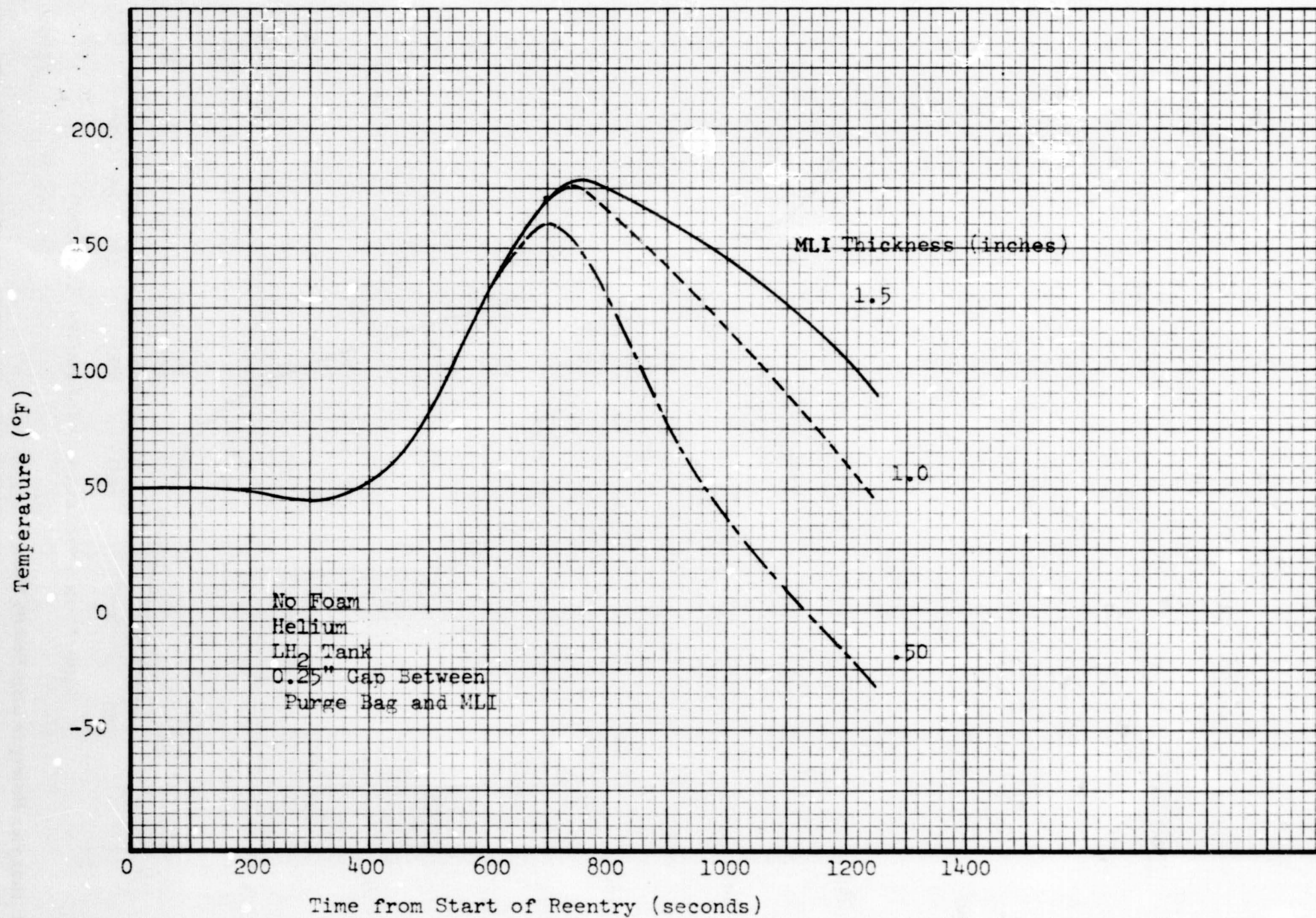
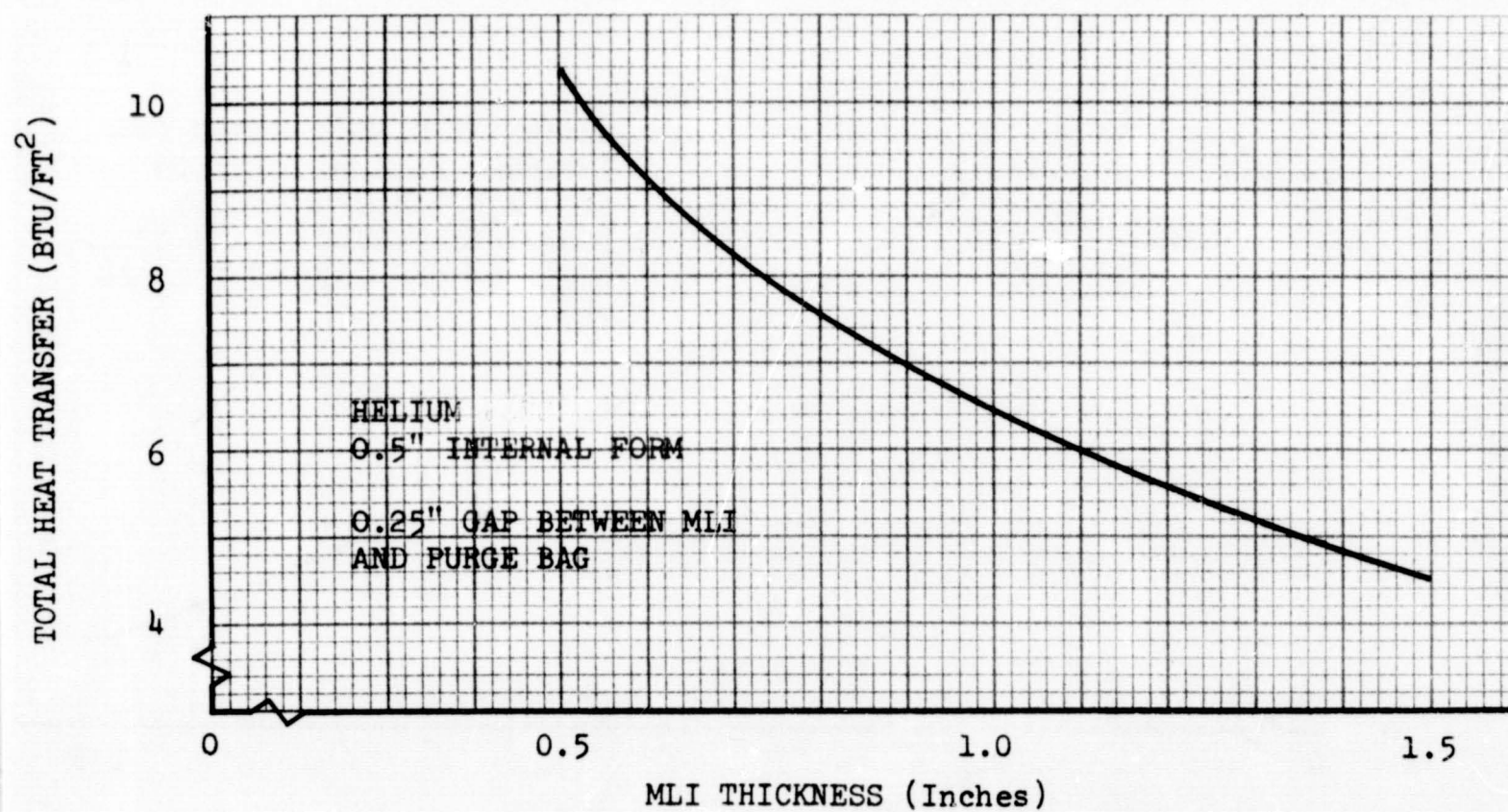
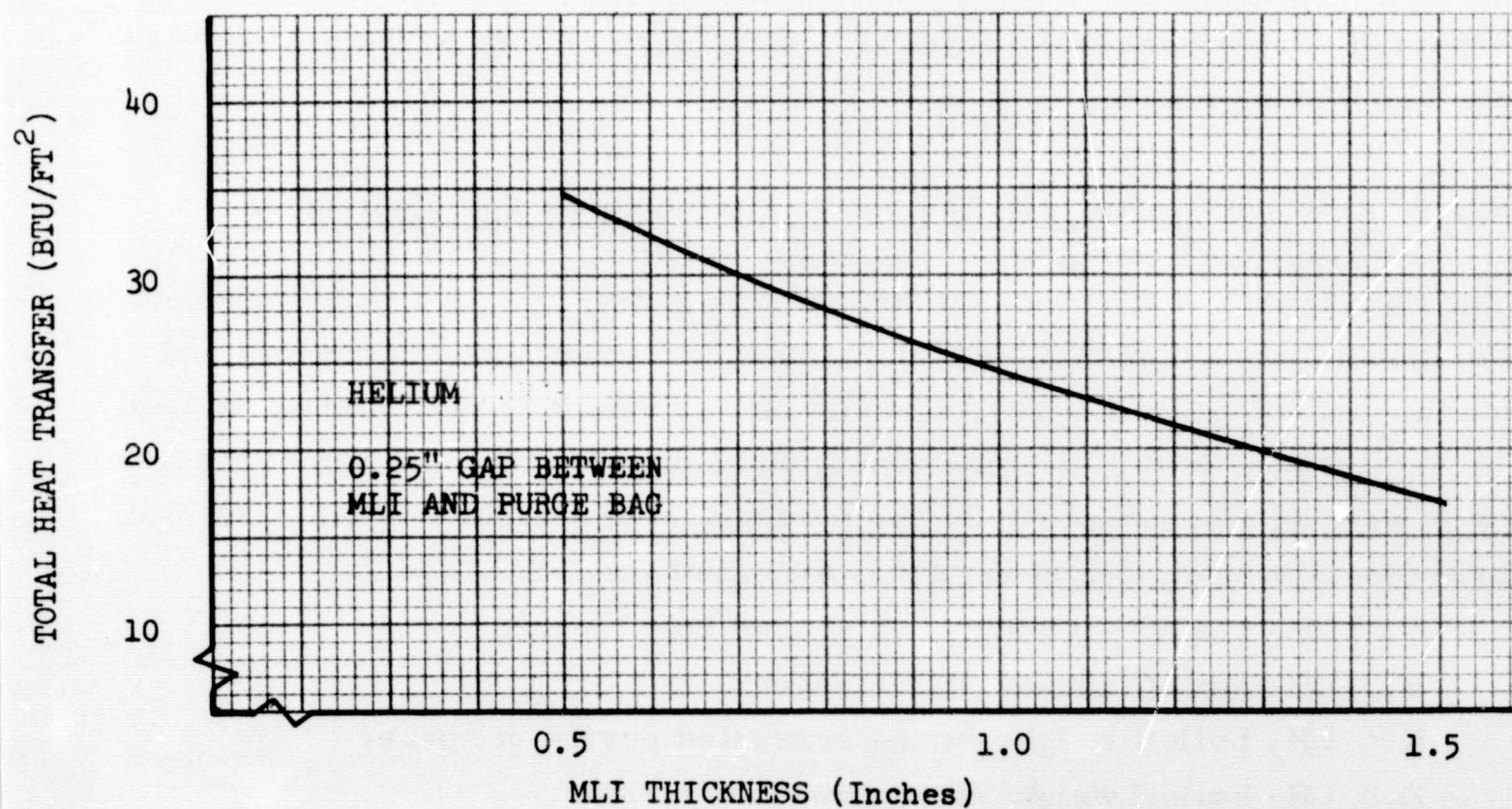


Figure 6-23. Purge Bag Temperature History--Reentry Phase

Figure 6-24. Heat Transfer to LH₂ During Reentry—Helium, FoamFigure 6-25. Heat Transfer to LH₂ During Reentry—Helium, No Foam

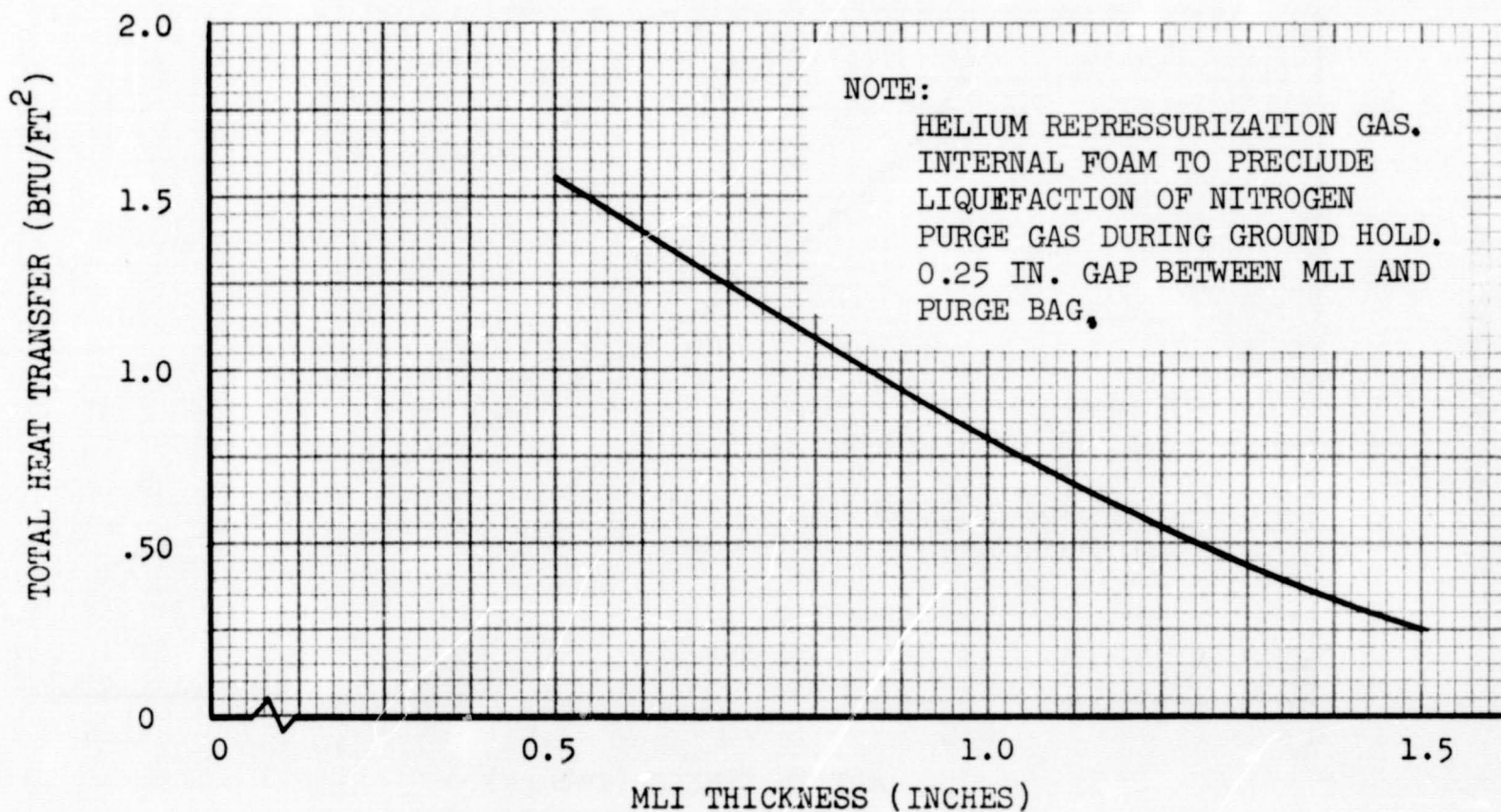


Figure 6-26. Heat Transfer to LH₂ During Reentry--Nitrogen Purge, Helium Repressurization, Foam

expected, the internal tank foam is beneficial in retarding the heat flow to the LH₂ during reentry.

6.1.5 Relative System and Composite Performance and Optimum Number of Layers for LH₂ Tank

The data from the analyses for the various phases of a mission described in the preceding paragraphs were utilized in the selection, from a thermal standpoint, of an MLI system concept and a composite material to be used in that system, and in the determination of the optimum number of layers to be used in that composite. The lowest system weight was the selection criterion. System weight used was a total of the following:

- A. LH₂ boiloff weight during ground hold lockup.
- B. LH₂ boiloff weight during ascent.
- C. LH₂ boiloff weight during evacuated period in space.
- D. LH₂ boiloff weight during reentry period.
- E. MLI composite weight.
- F. Foam weight, where applicable.

The boiloff due to the plumbing, tank supports, and wiring bundle was not included in the system weight because it was assumed to be similar regardless of the system or composite being considered. However, the in-space degradation due to fasteners, joints, and perforations was included. It should be noted that the boiloff weight loss values were determined assuming a continuously venting tank to maintain a constant tank pressure. This does not take advantage of the reduction in boiloff due to tank pressure reduction by propellant utilization. The inclusion of the effect of propellant utilization was beyond the scope of these analyses.

During the ground-hold, lockup, ascent, and reentry periods, the heat transfer is governed primarily by conduction through the gas within the MLI. As a result, the boiloff weights associated with these periods did not vary with composite material. However, a significant variation in boiloff weights did occur during the ascent and reentry periods for the different systems (Tables 6-1 and 6-2; Figures 6-27 and 6-28). As shown, the increased boiloff during ascent due to the energy stored in the foam and tank wall and

Table 6-1
TYPICAL HELIUM/NO-FOAM SYSTEM
WEIGHT (LB/FT²)

	7-Day Mission	30-Day Mission
Prelaunch lockup boiloff	0.0446	0.0446
Ascent-period boiloff	0.0321	0.0321
In-space-period boiloff	0.1307	0.5590
Reentry-period boiloff	0.1274	0.1274
Insulation	0.2970	0.2970
Foam	0.0	0.0
Total	0.6318	1.0601

He purge, He repressurization.

No internal tank foam.

1.0-inch DGK/Dacron B4A (90 layer-pair/inch).

Table 6-2
TYPICAL HELIUM/FOAM SYSTEM
WEIGHT (LB/FT²)

	7-Day Mission	30-Day Mission
Prelaunch lockup boiloff	0.0367	0.0367
Ascent-period boiloff	0.1525	0.1525
In-space-period boiloff	0.1307	0.5590
Reentry-period boiloff	0.0336	0.0336
Insulation	0.2970	0.2970
Foam	0.2165	0.2165
Total	0.8660	1.2953

He purge, He repressurization.

0.5-inch internal tank foam.

1.0-inch DGK/Dacron B4A (90 layer-pair/inch).

transmitted to the LH₂ is greater than the reduction in boiloff which the foam provides during reentry (for the trajectory used in this study). Consequently, a system utilizing internal tank foam has a higher system weight than a no-foam system. Of the three systems considered, the system utilizing helium as the purge and repressurization gas and having no internal tank foam appears to offer the lowest system weight. It should be noted that selection of this system assumes that the interior of the vehicle in the vicinity of the LH₂ tank is purged with a dry gas to prevent condensation or freezing on the purge bag's exterior surface.

As noted above, the selection of a system is influenced by the reentry trajectory. If the reentry trajectory is altered to include a longer period at the high heating rates in the lower atmosphere, it is anticipated that the use of internal tank foam would become more desirable. With long cruise periods at low altitudes, the reduction in boiloff resulting from using the foam could be greater than the increase in ascent boiloff and foam weight. An even better approach would consist of placing the foam on the start tank. In this configuration, the only penalty to overcome would be the foam weight, since all of it would be cooled to LH₂ temperature during the ground hold and would, therefore, not transmit any energy to the LH₂ during the ascent period.

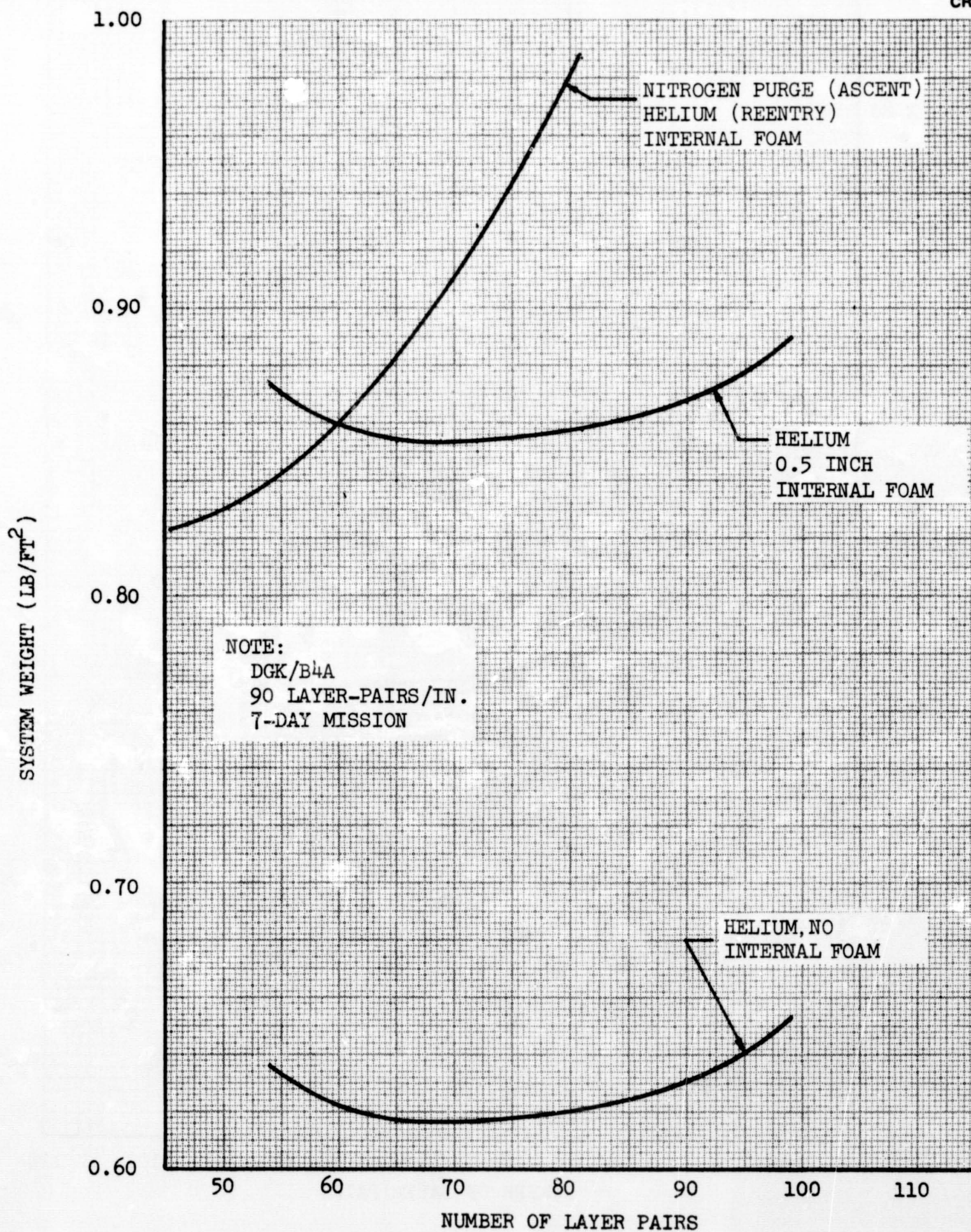


Figure 6-27. Effect of System Concept on System Weight--7-Day Mission, LH₂ Tank

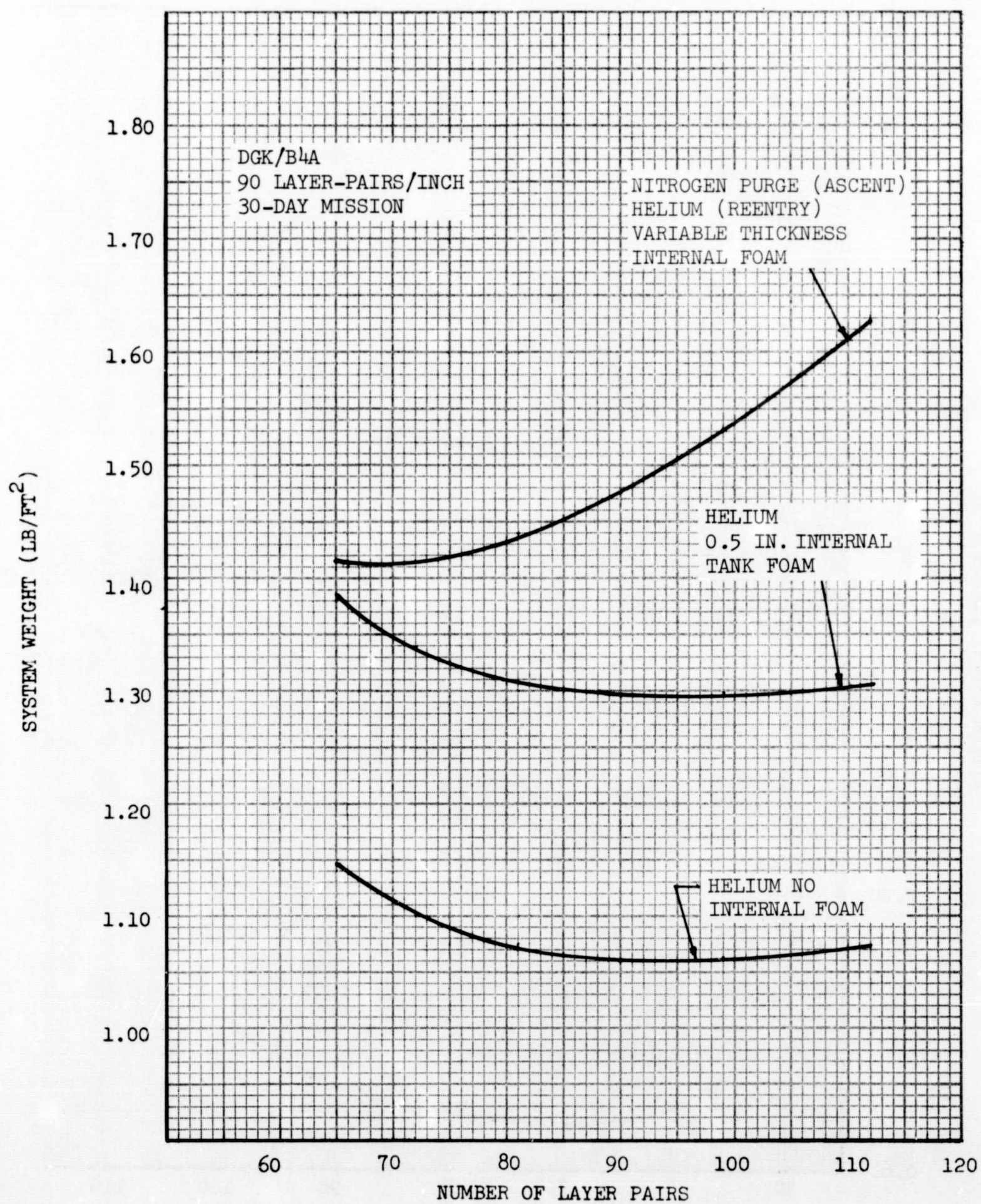


Figure 6-28. Effect of System Concept on System Weight--30-Day Mission, LH₂ Tank

A cursory comparison of the anticipated reduction in reentry boiloff and the corresponding weight of foam on a start tank revealed that, for the trajectory being considered, the use of foam on a start tank was probably not advantageous. However, a reduction in the size of the start tank or an increase in reentry time could quickly change this result.

The candidate composite which provides the lowest system weight is DGK/Dacron B4A (Figures 6-29 and 6-30). The DGK/Nomex HT-287 candidate composite was not considered in detail since it has both higher effective thermal conductivity and higher layer density than the DGK/Nomex HT-96 (Subsections 3.10 and 3.9). Composites utilizing DAK reflectors were not considered in detail since the test data reported in Subsection 3.10 shows that the DAK composites would have a higher system weight than the corresponding DGK composite.

An additional comparison of composites (Figures 6-31 and 6-32) revealed that some reduction in system weight could be obtained if the environmental design constraints were reduced to permit using the 15-gage DAM reflector material instead of the 25-gage candidate reflector materials being considered in this study.

The optimum number of layer pairs for the DGK/Dacron B4A composite is indicated in Figures 6-31 and 6-32. A total of 68 layer pairs appears to be optimum for a 7-day mission and approximately 94 layer pairs for a 30-day mission. At a layer density of 90 layer pairs/inch, the optimum total thickness of the MLI would be approximately 3/4 inch for a 7-day mission and 1 inch for a 30-day mission. The layer density assumed for each composite in the analyses corresponded to the density at 1×10^{-4} psi compressive loading after 100 cycles of compression (Subsection 3.9). The effect of layer density on the system weight is shown in Figures 6-33 and 6-34.

6.2 LO₂ TANK THERMAL ANALYSES

The following two systems were investigated in the thermal analyses for the LO₂ tank: (1) helium purge and repressurization, with no foam; and (2) nitrogen purge and repressurization with no foam. The insulation system concept

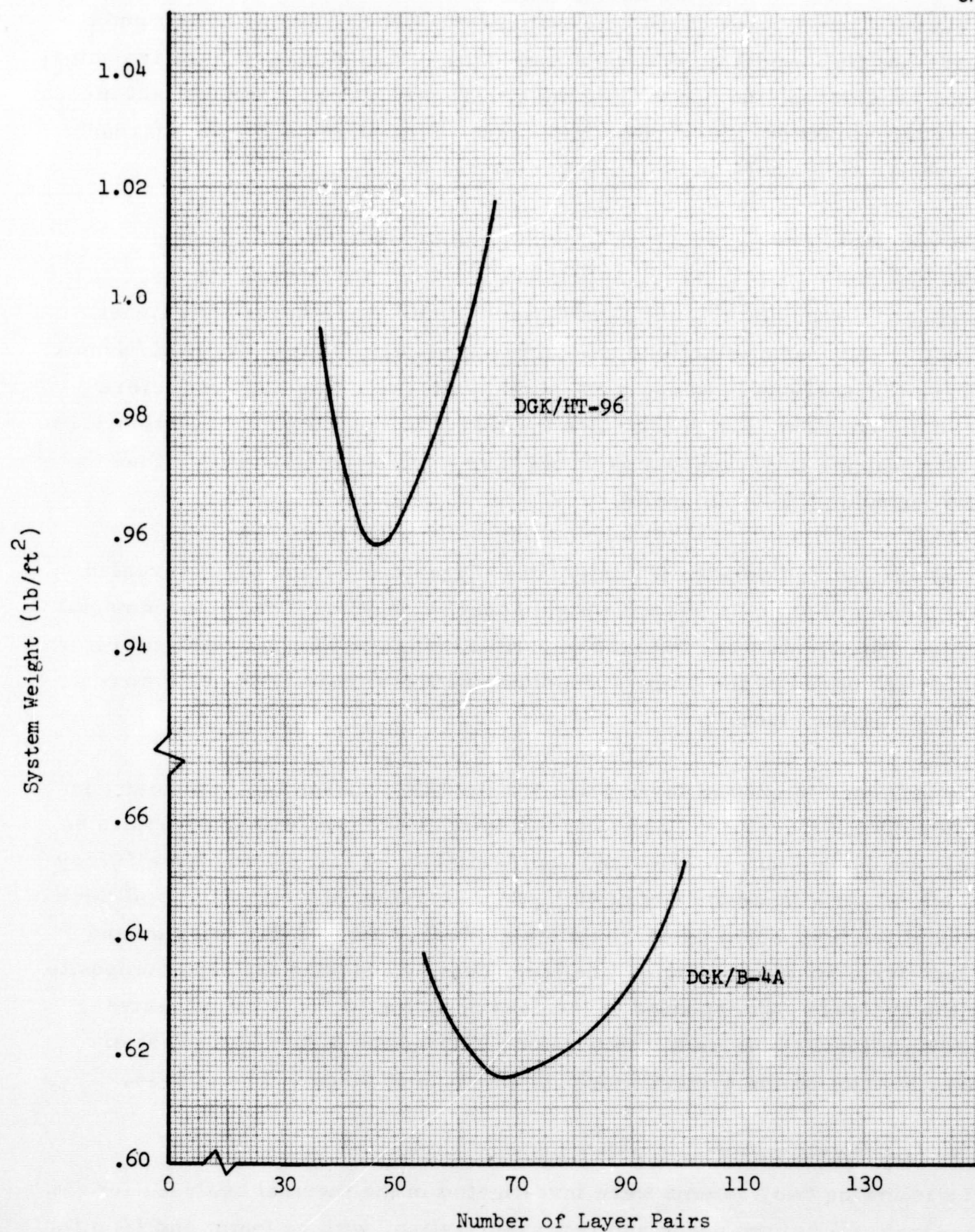


Figure 6-29. MLI Composite Comparison—7-Day Mission, LH₂ Tank

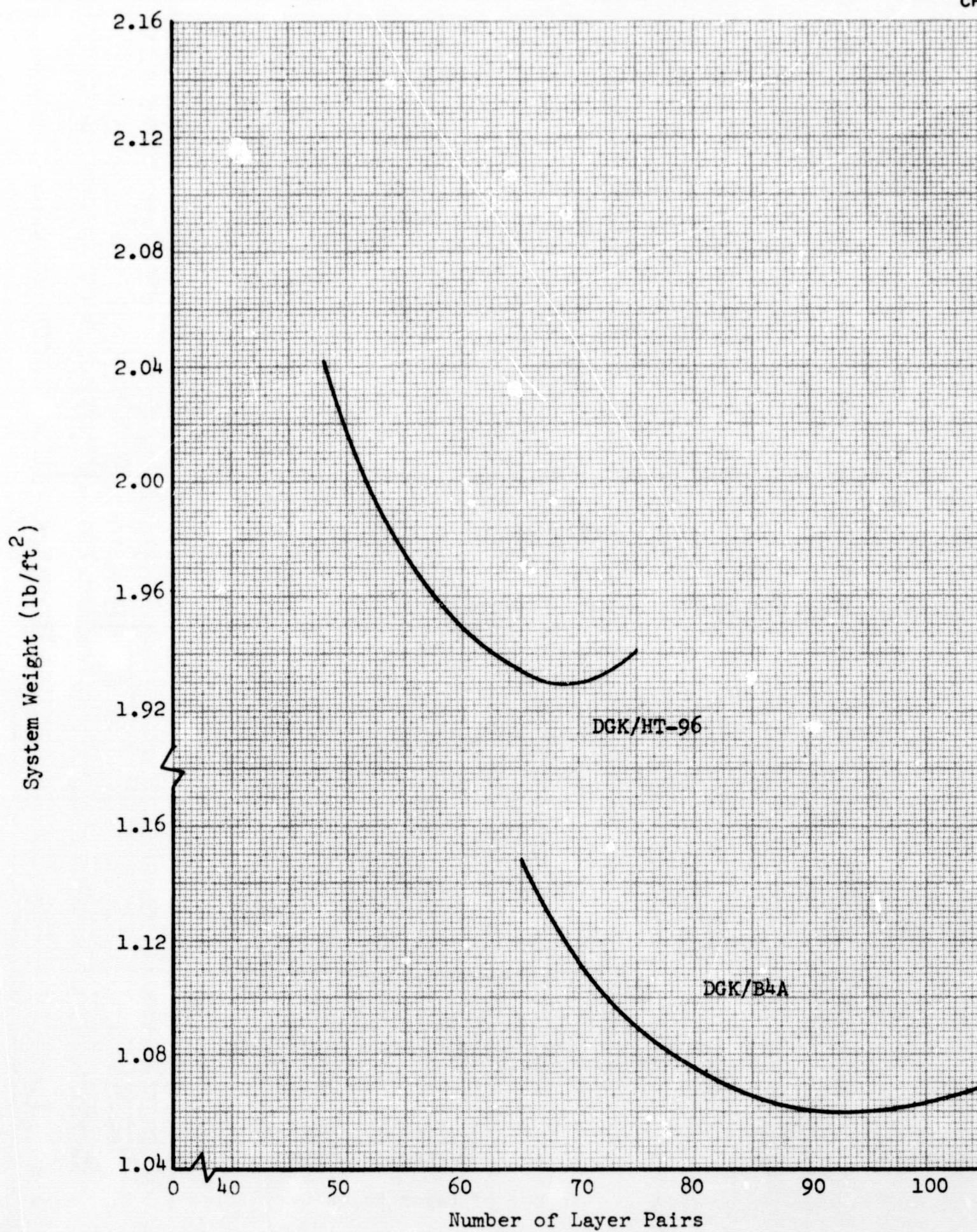


Figure 6-30. MLI Composite Comparison—30-Day Mission, LH₂ Tank

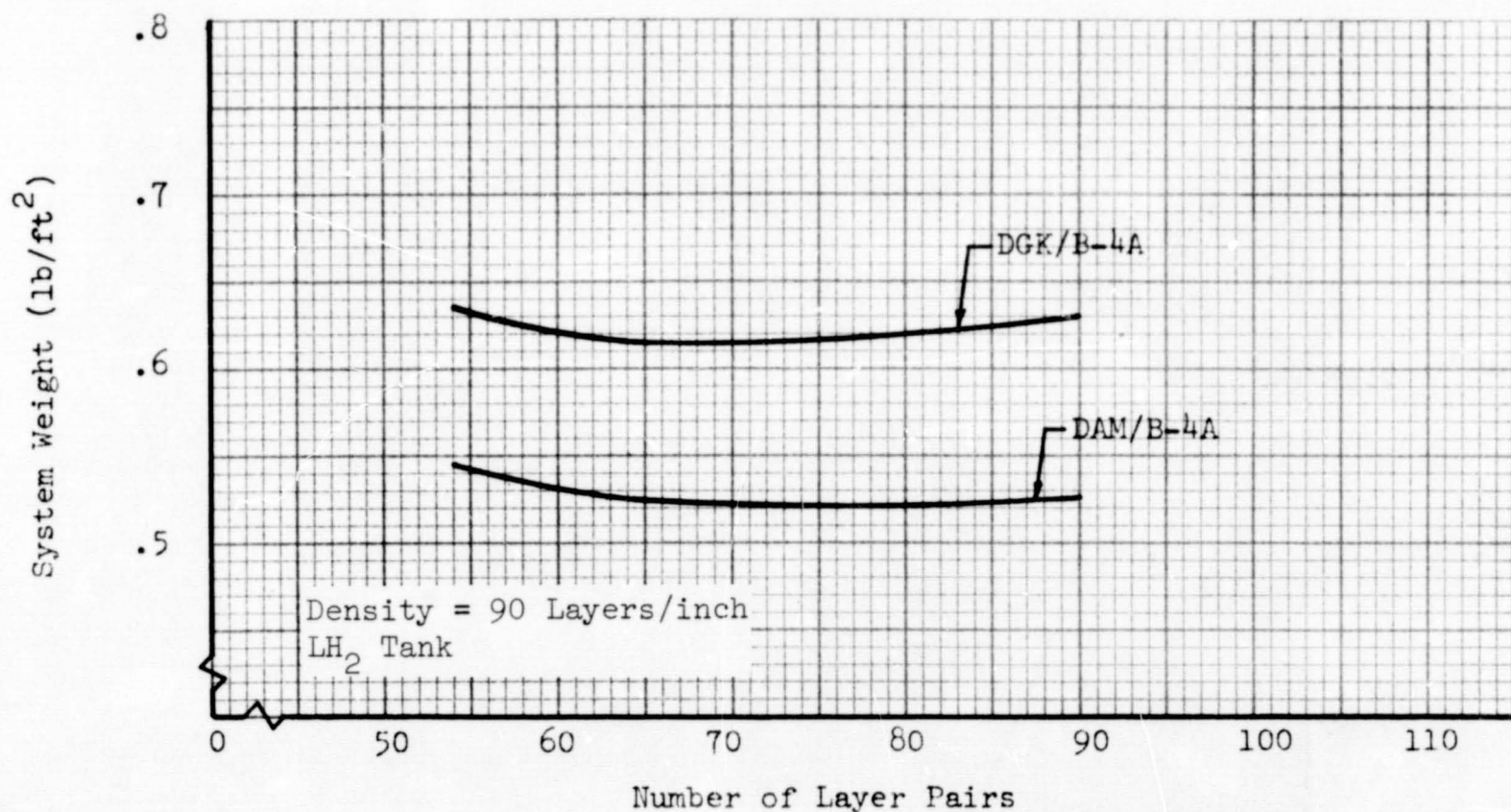


Figure 6-31. Comparison of DGK and DAM Composites--7-Day Mission

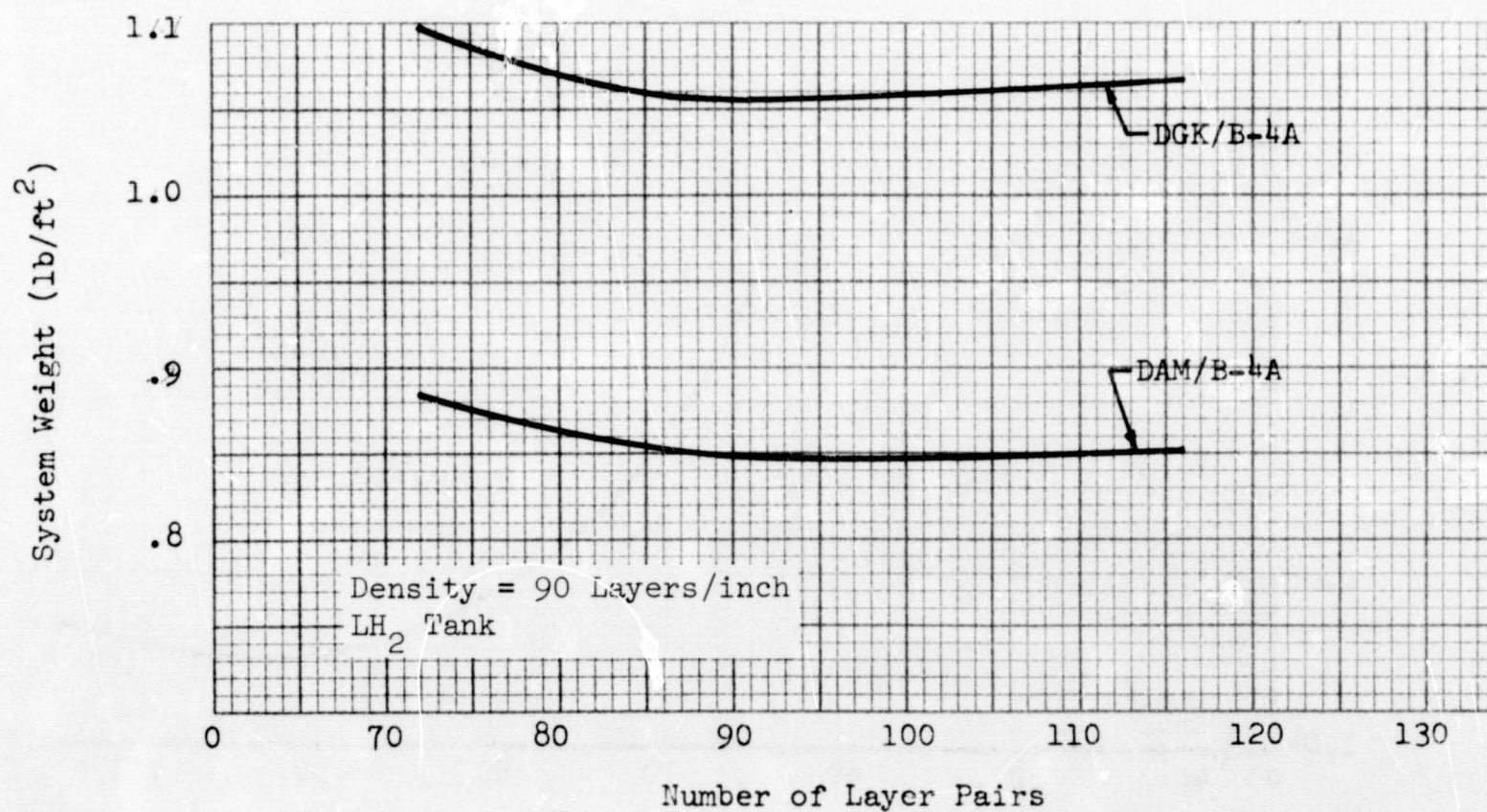


Figure 6-32. Comparison of DGK and DAM Composites--30-Day Mission

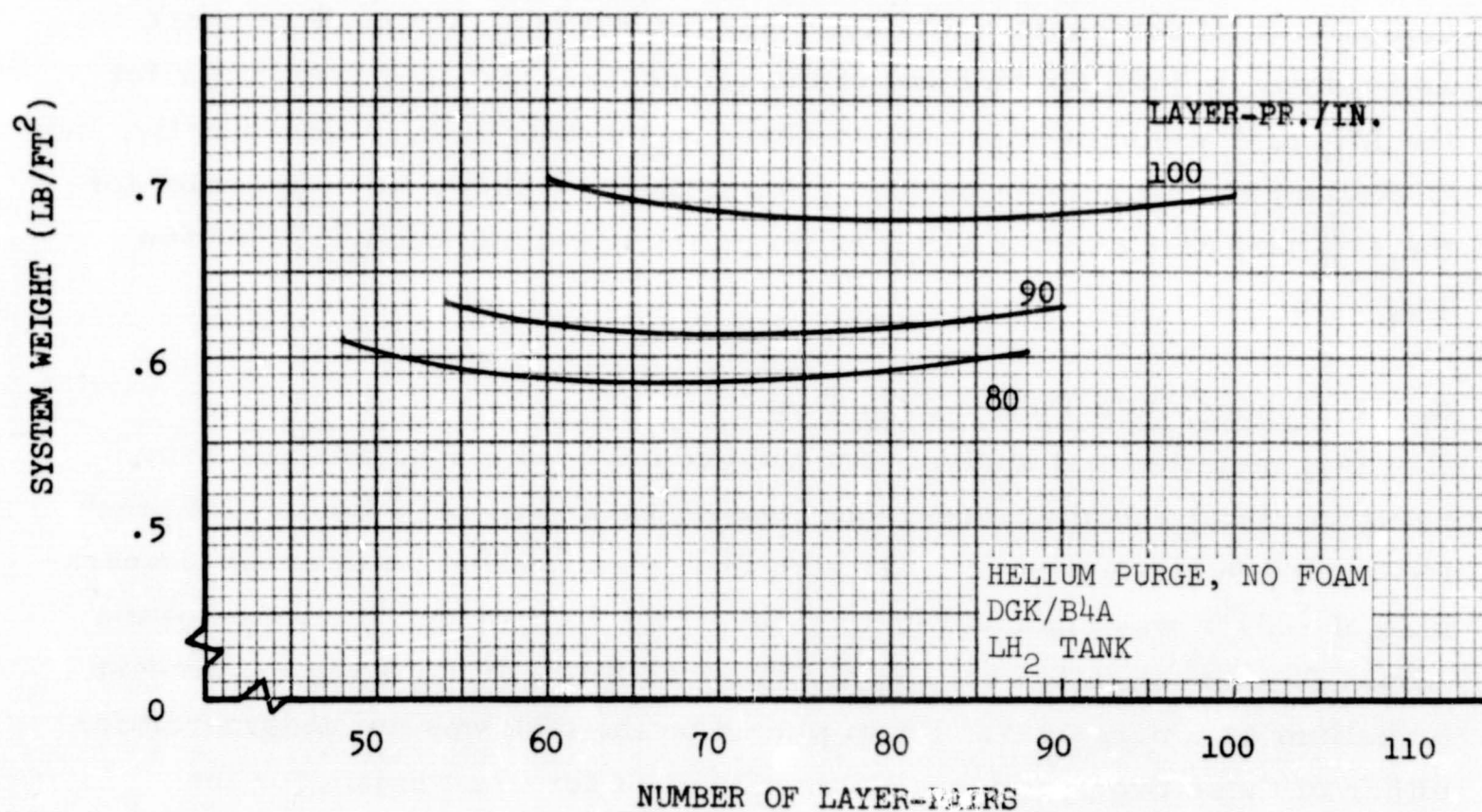


Figure 6-33. Effect of Layer Density on System Weight--7-Day Mission

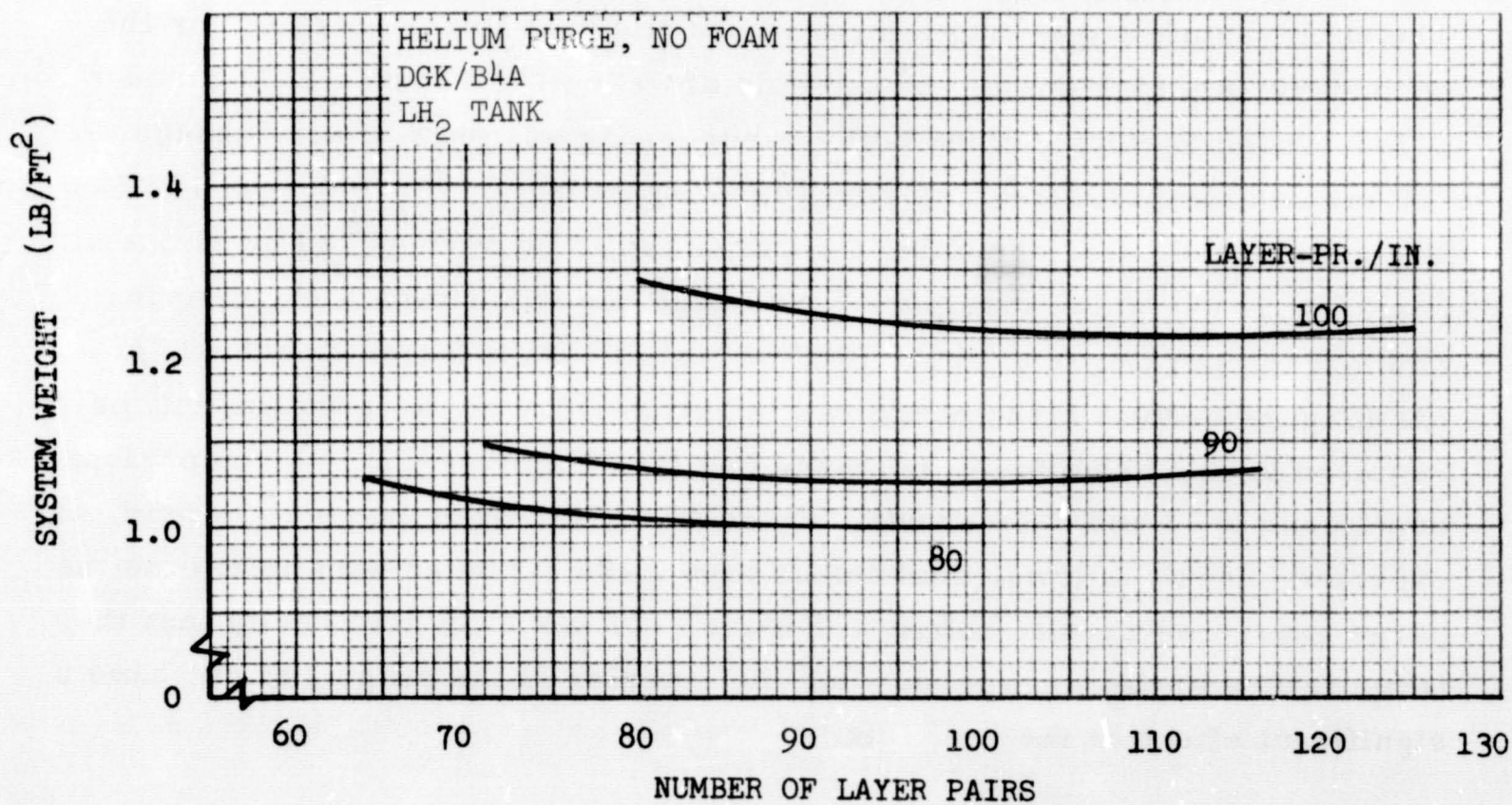


Figure 6-34. Effect of Layer Density on System Weight--30-Day Mission

was configured so that the MLI is located on the tank surface. A detailed comparison of composites was not made for the LO₂ tank because there is no evidence to indicate that any of the candidates evaluated previously for the LH₂ tank would be more competitive on the LO₂ tank. Consequently, the DGK/Dacron B4A composite insulation which was shown to be optimum for the LH₂ tank was carried along as the most promising candidate for the LO₂ tank.

6.2.1 Ground-Hold Phase—LO₂ Tank

The LO₂ tank thermal analysis for the ground-hold period was performed using the same thermal model and approach that was used for the LH₂ tank (described in Subsection 6.1.1), with the exception that an internal temperature of -281°F was assumed instead of -423°F to provide simulation of the LO₂. The investigation considered the possibility of using either nitrogen or helium as a purge gas. Foam placed on the tank was not considered for either of these two systems. No requirement for foam exists for the secondary LO₂ tank since the temperature of the LO₂ is above the condensation temperature of nitrogen.

The steady-state purge-bag temperatures and heat fluxes obtained for the secondary LO₂ tank during ground hold are shown in Figures 6-35 through 6-38. These results include tank-to-purge-bag spacings of 0.5 through 2.0 in. and temperatures external to the purge bag of 70, 100, and 150°F. The results indicate, assuming the purge bag to be surrounded by air, that frost formation on the exterior of the purge bag will not be a problem for ambient temperatures of about 70°F or higher with nitrogen as the purge gas (Figure 6-36). If the purge gas is helium, dry air or nitrogen will be required on the exterior of the purge bag (see Figure 6-35). A comparison of Figures 6-37 and 6-38 shows that the use of nitrogen purge gas would, as expected, result in lower heat fluxes than those expected with helium as the purge gas. The results shown in Figure 6-37 and 6-38 also verify that the temperature of the gas surrounding the exterior of the purge bag can have a significant effect on the heat flux.

The weight loss due to boiloff which is expected during a prelaunch lockup period of 3-minute duration is shown in Figures 6-39 and 6-40 for varying

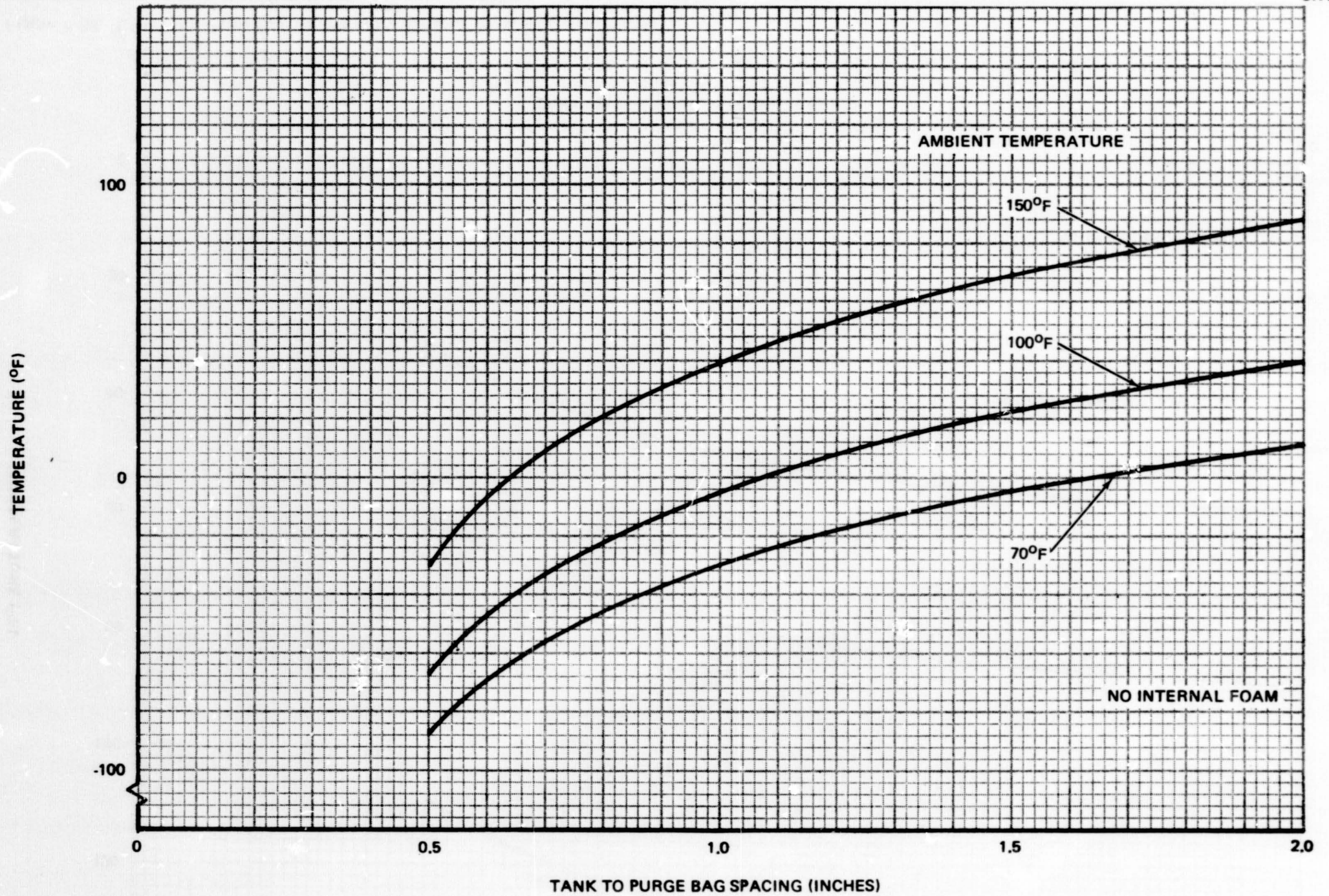


Figure 6-35. LO₂ Tank Purge Bag Temperature--Ground Hold (Helium Purge)

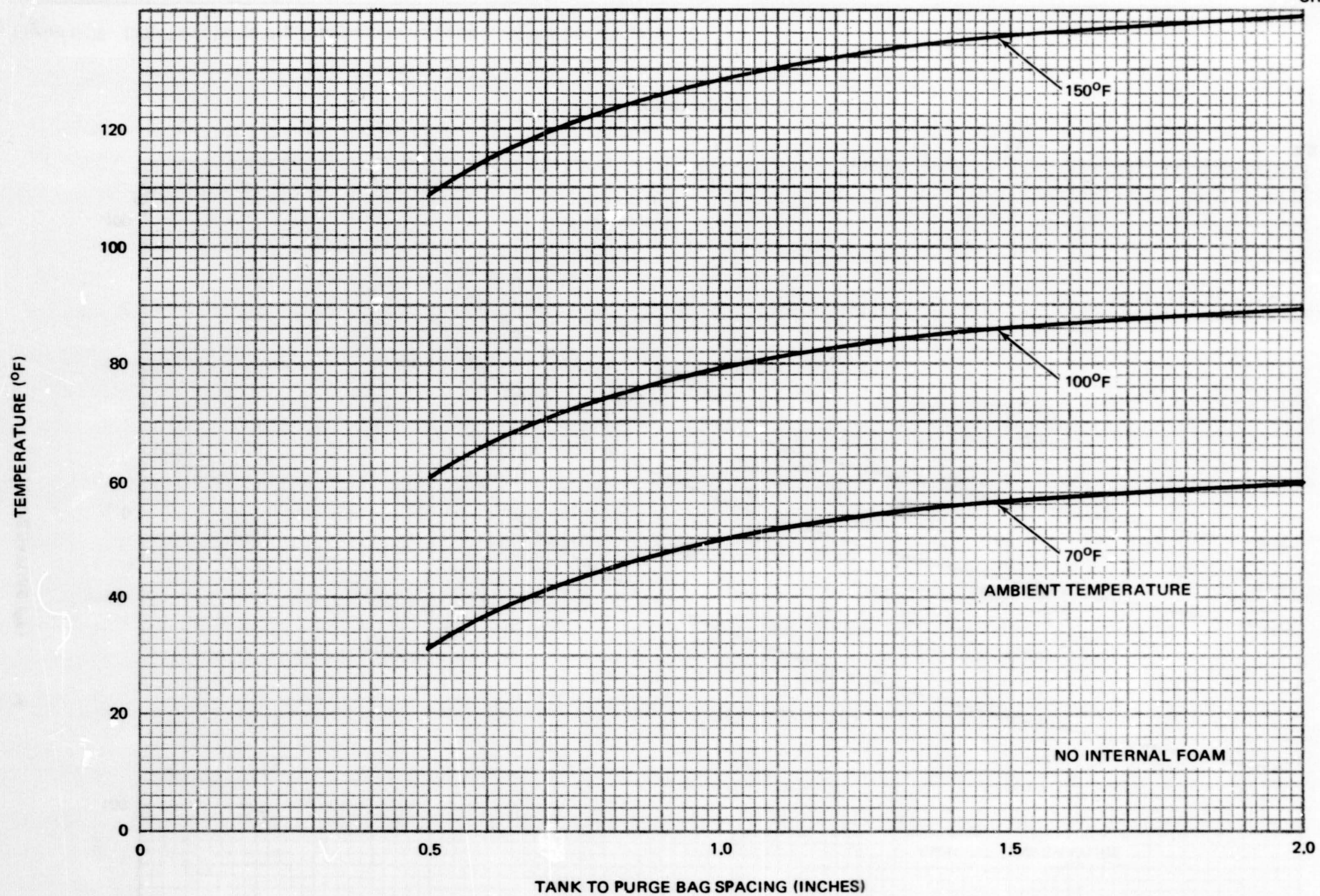


Figure 6-36. LO₂ Tank Purge Bag Temperature--Ground Hold (Nitrogen Purge)

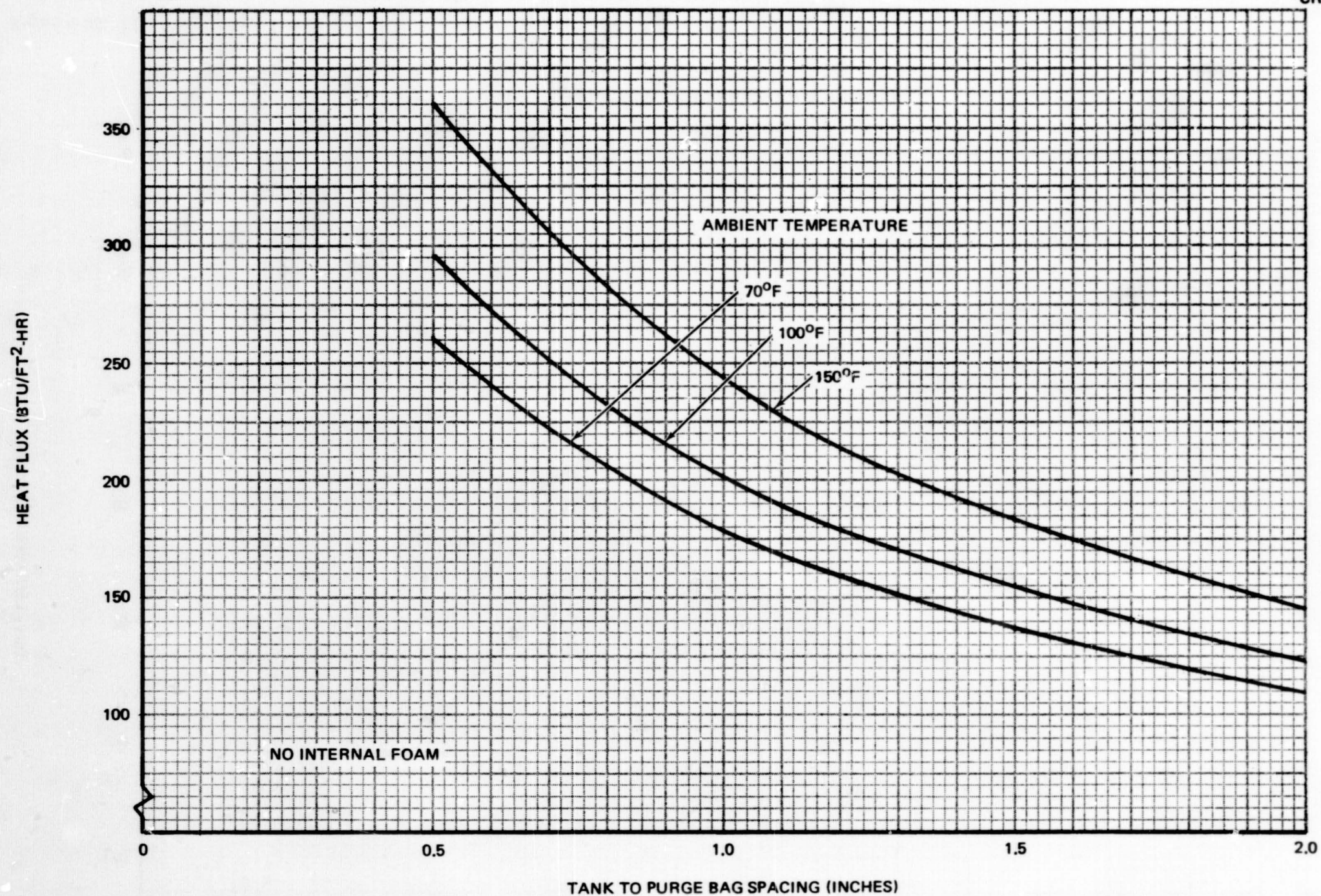


Figure 6-37. LO₂ Tank Ground Hold Heat Flux (Helium Purge)

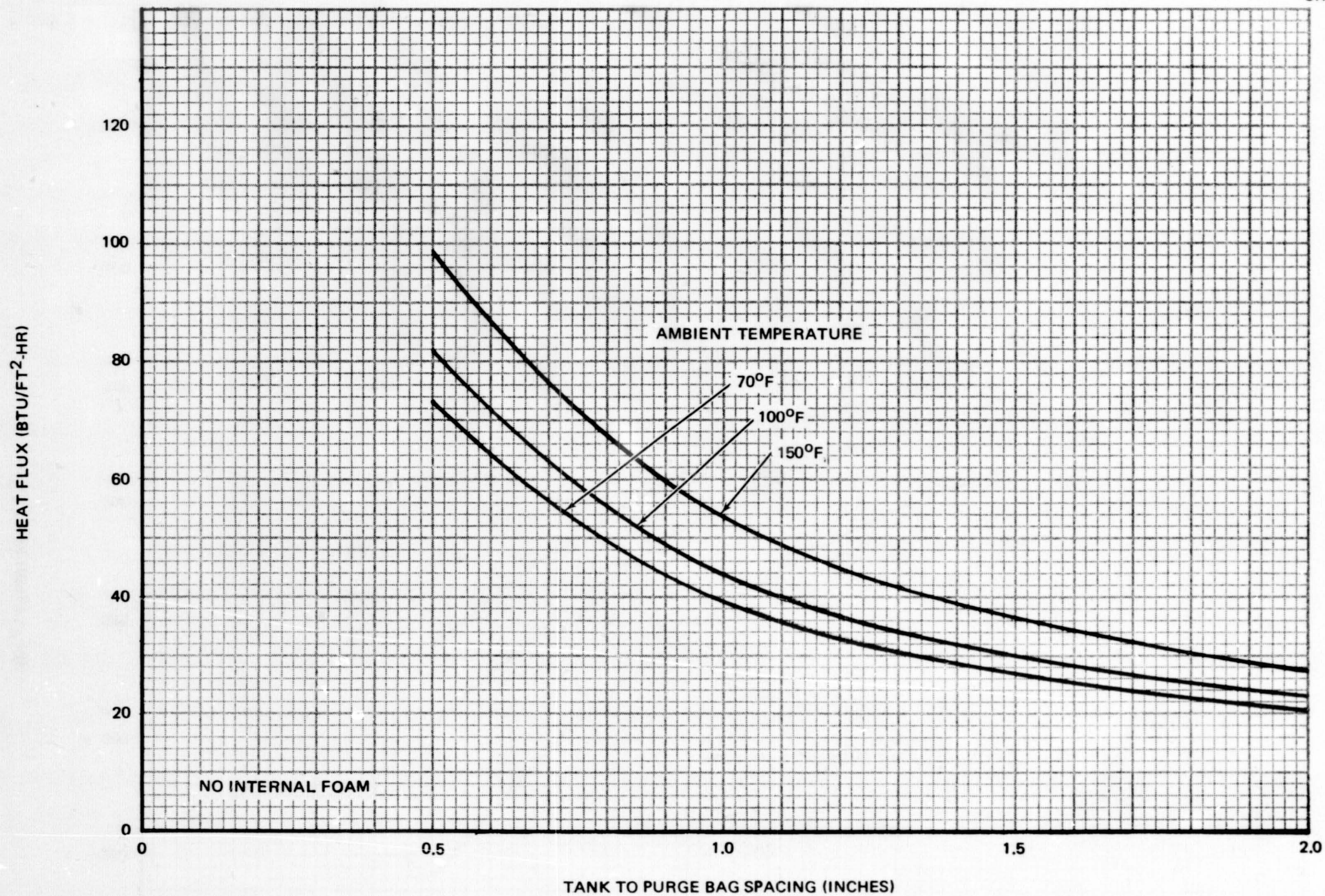
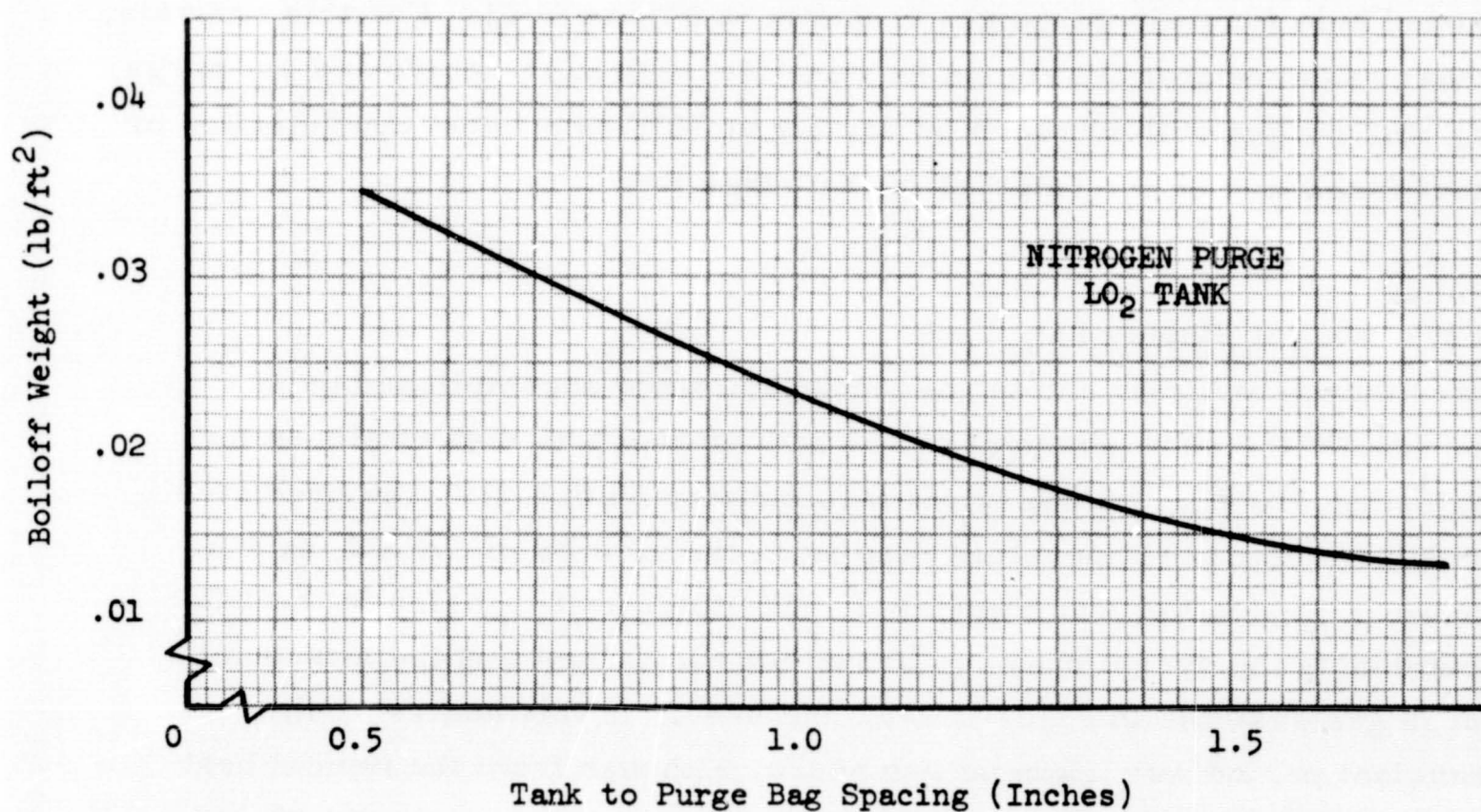
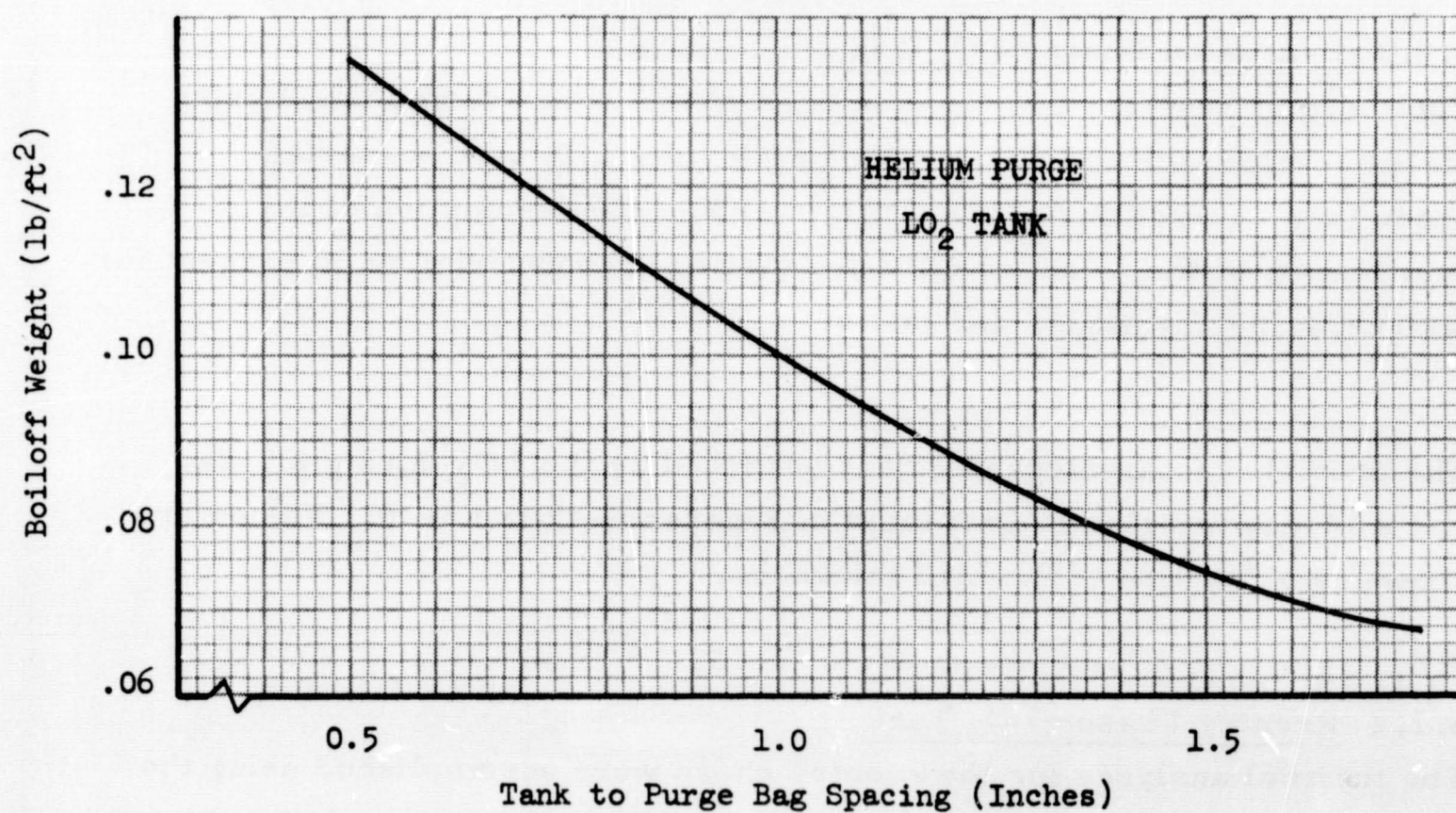


Figure 6-38. LO₂ Tank Ground Hold Heat Flux (Nitrogen Purge)

Figure 6-39. LO₂ Tank Prelaunch Boiloff (3-Minute Lockup)—NitrogenFigure 6-40. LO₂ Tank Prelaunch Boiloff (3-Minute Lockup)—Helium

tank-to-purge-bag spacings. A typical temperature distribution during ground hold for each purge gas is shown in Figure 6-41. For this analysis, it was assumed that the region between the vehicle structure and the purge bag was purged with nitrogen or dry air at 70°F to prevent condensation or frost formation on the exterior of the purge bag.

6.2.2 Ascent Phase—LO₂ Tank

The thermal analyses for the ascent phase were accomplished using essentially the same thermal model and approach as that employed for the secondary LH₂ tank analysis (see Subsection 6.1.2). The predicted vehicle structure temperature history in the vicinity of the LO₂ tank as shown in Figure 4-4 was simulated. The total heat transfer to the LO₂ tank during the ascent phase is shown for the helium and the nitrogen purge gas systems in Figures 6-42 and 6-43. In this analysis, the transient period was taken as two hours, although from the typical heat flux history shown in Figure 6-44 it can be seen that a majority of the heating occurs during the first few minutes after launch.

6.2.3 Evacuated Phase—LO₂ Tank

The thermal analyses for the evacuated phase were accomplished using the same approach and assumptions as for the LH₂ tank evacuated phase (see Subsection 6.1.3). This included the assumption of the degradation of the in-space effective thermal conductivity by 50 percent for fasteners, perforations, and joints.

The predicted total integrated heat absorbed by the LO₂ during a 7-day and a 30-day mission is presented in Figures 6-45 and 6-46. Values are shown as a function of the MLI thickness.

6.2.4 Reentry Phase—LO₂ Tank

The thermal analyses for the reentry phase were accomplished using the same approach and assumptions as for the LH₂ tank reentry phase

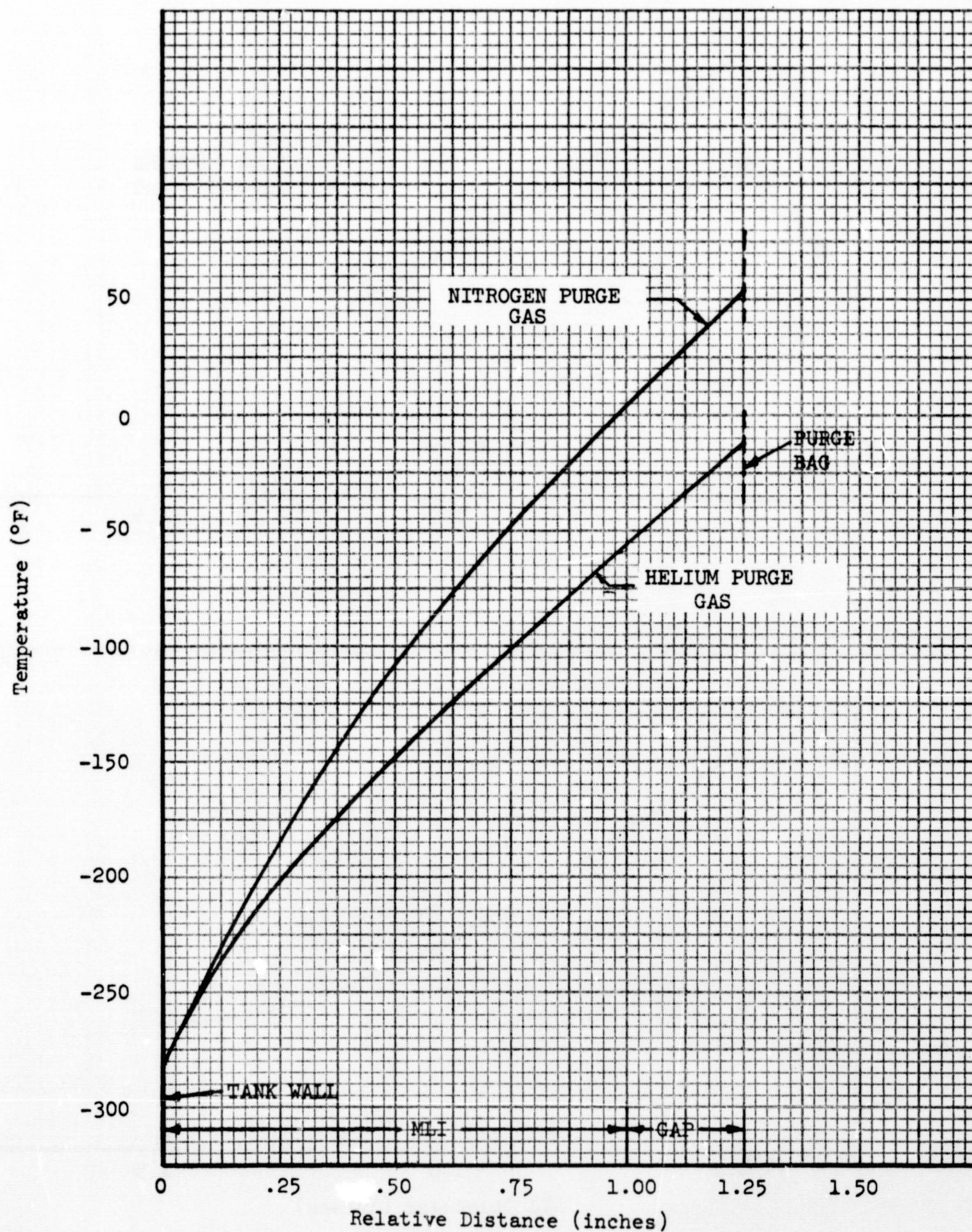
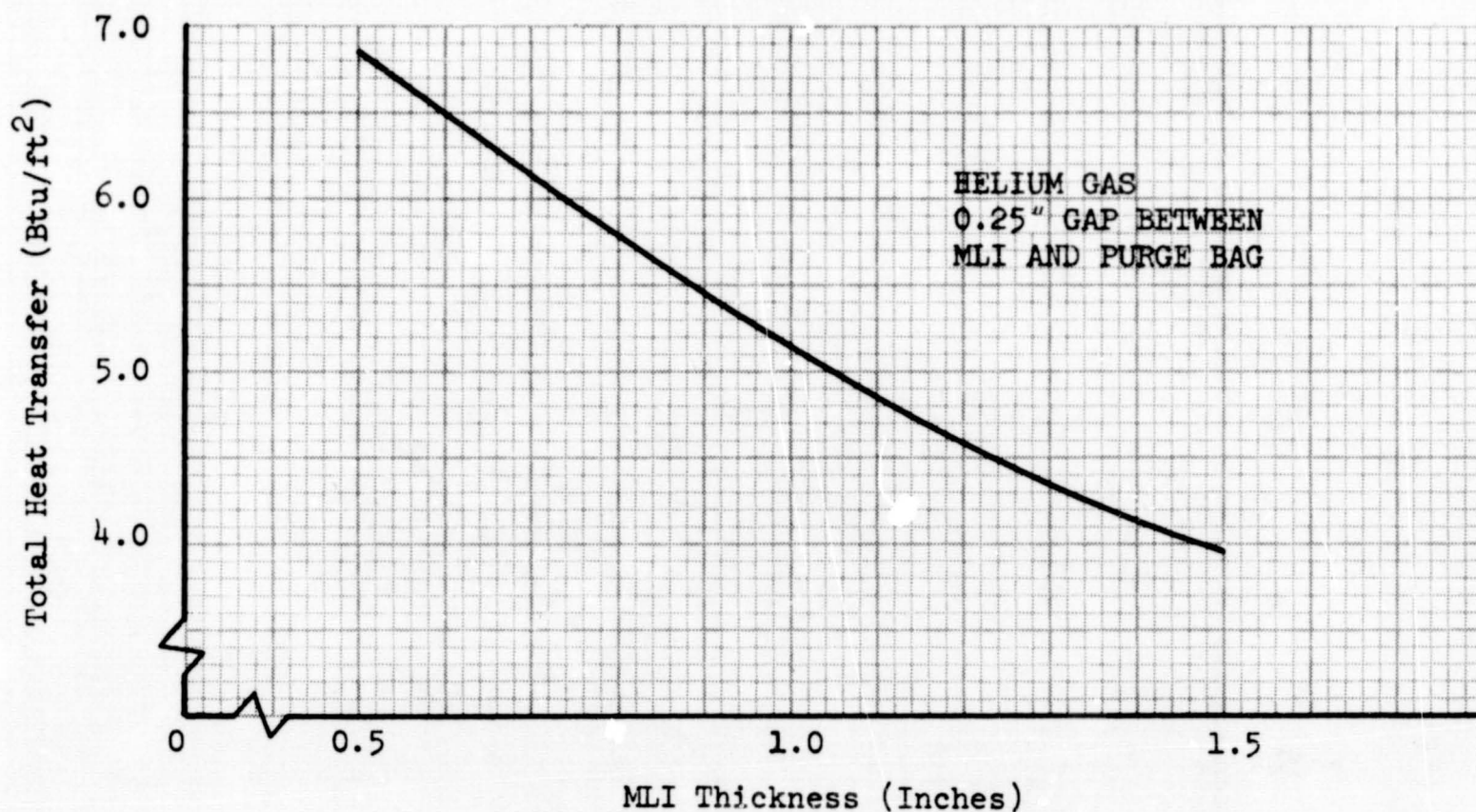
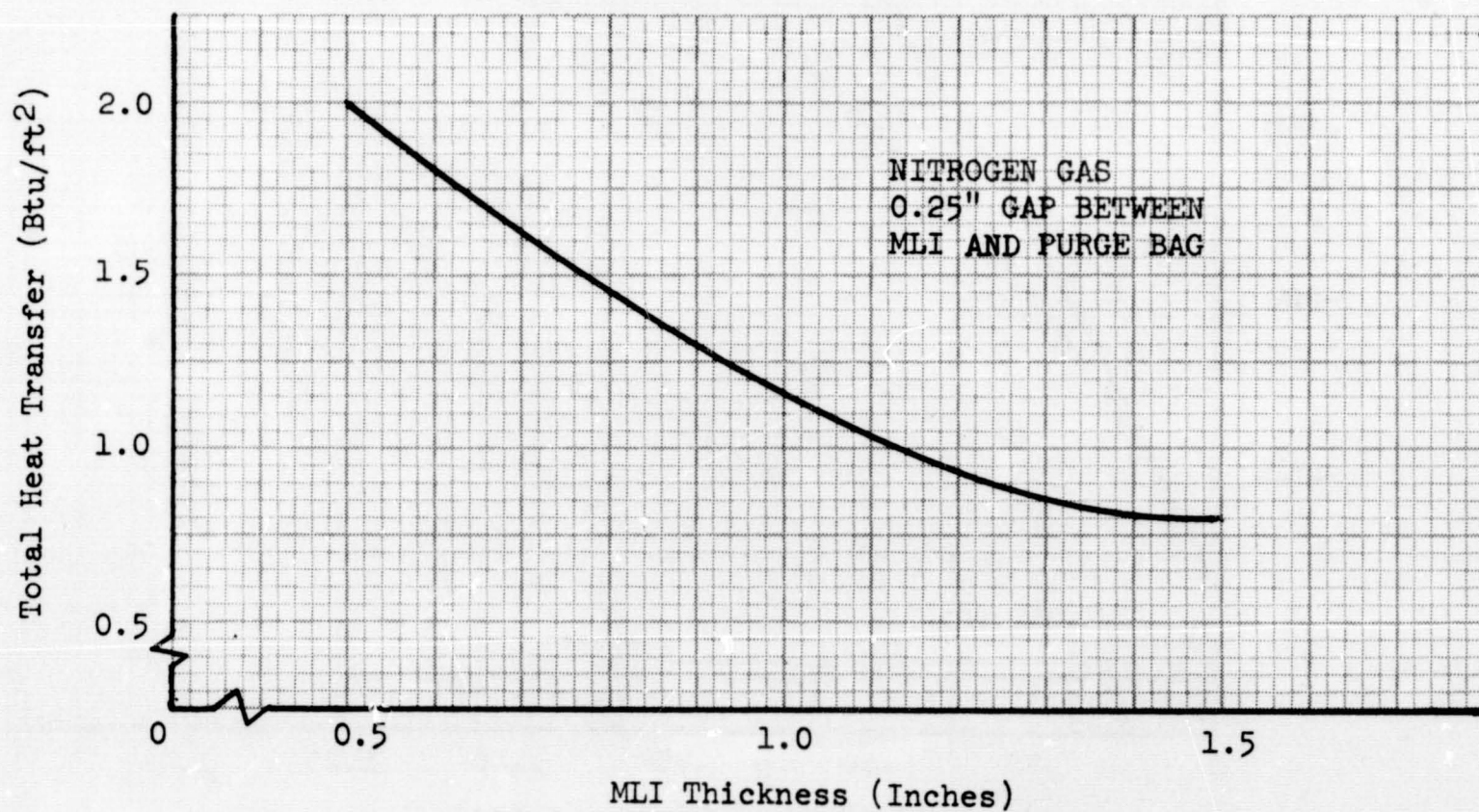
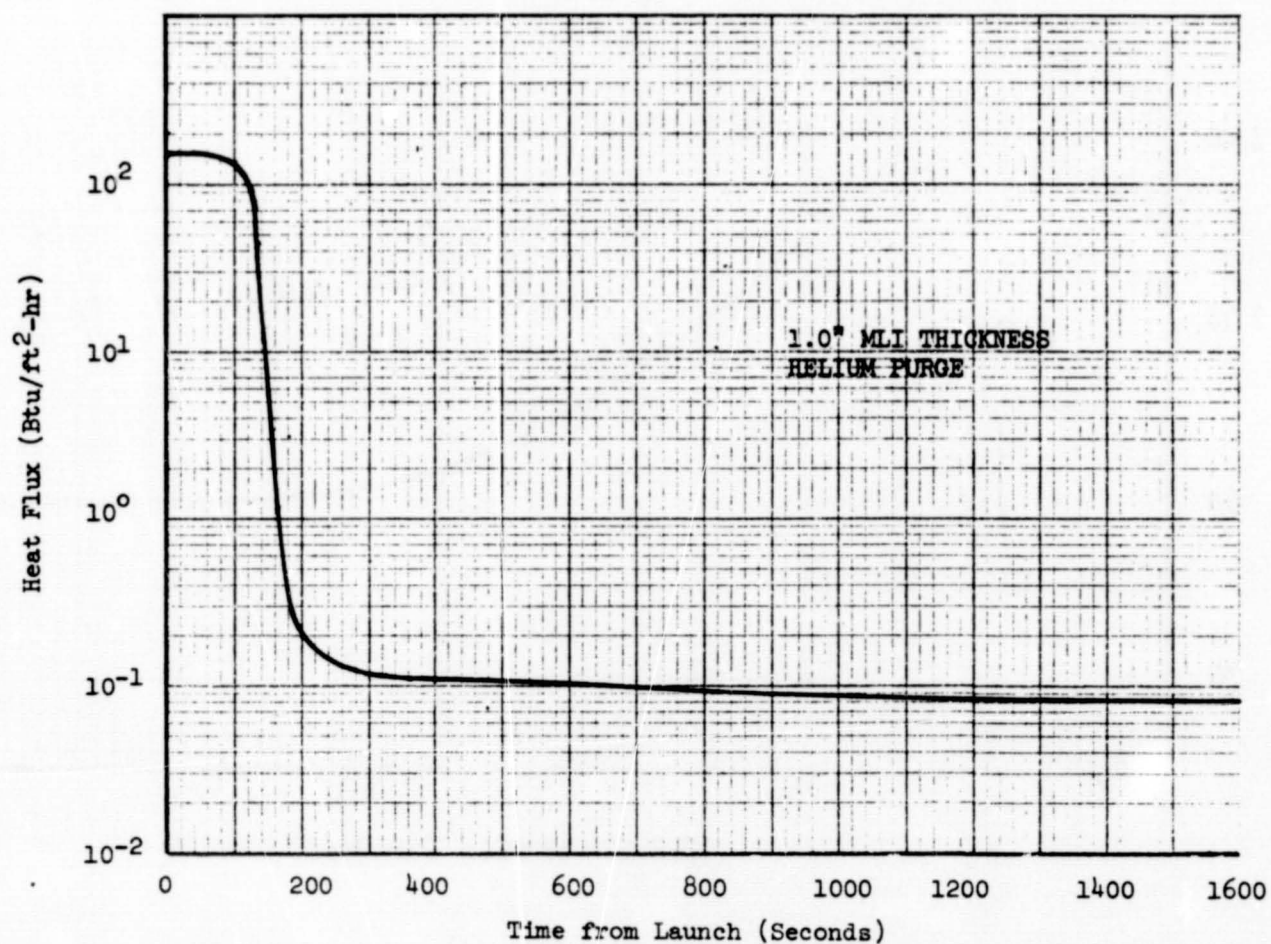
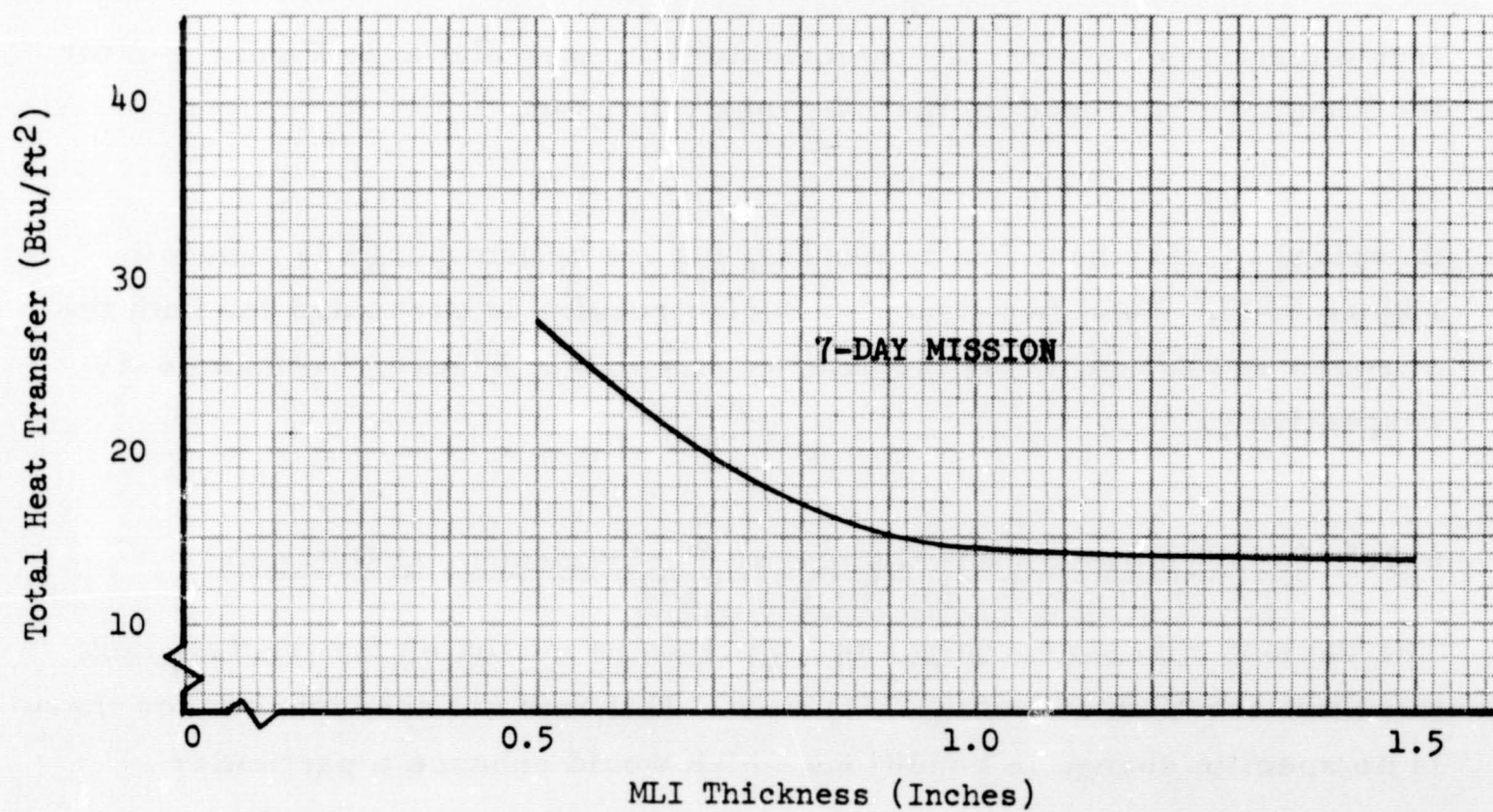


Figure 6-41. Typical Ground Hold Temperature Distributions—LO₂ Tank

Figure 6-42. Heat Transfer to LO₂ During Ascent—Helium Purge GasFigure 6-43. Heat Transfer to LO₂ During Ascent—Nitrogen Purge Gas

Figure 6-44. Heat Flux History to LO₂--Ascent PhaseFigure 6-45. Total Heat Transfer to LO₂ During Evacuated Period--7-Day Mission

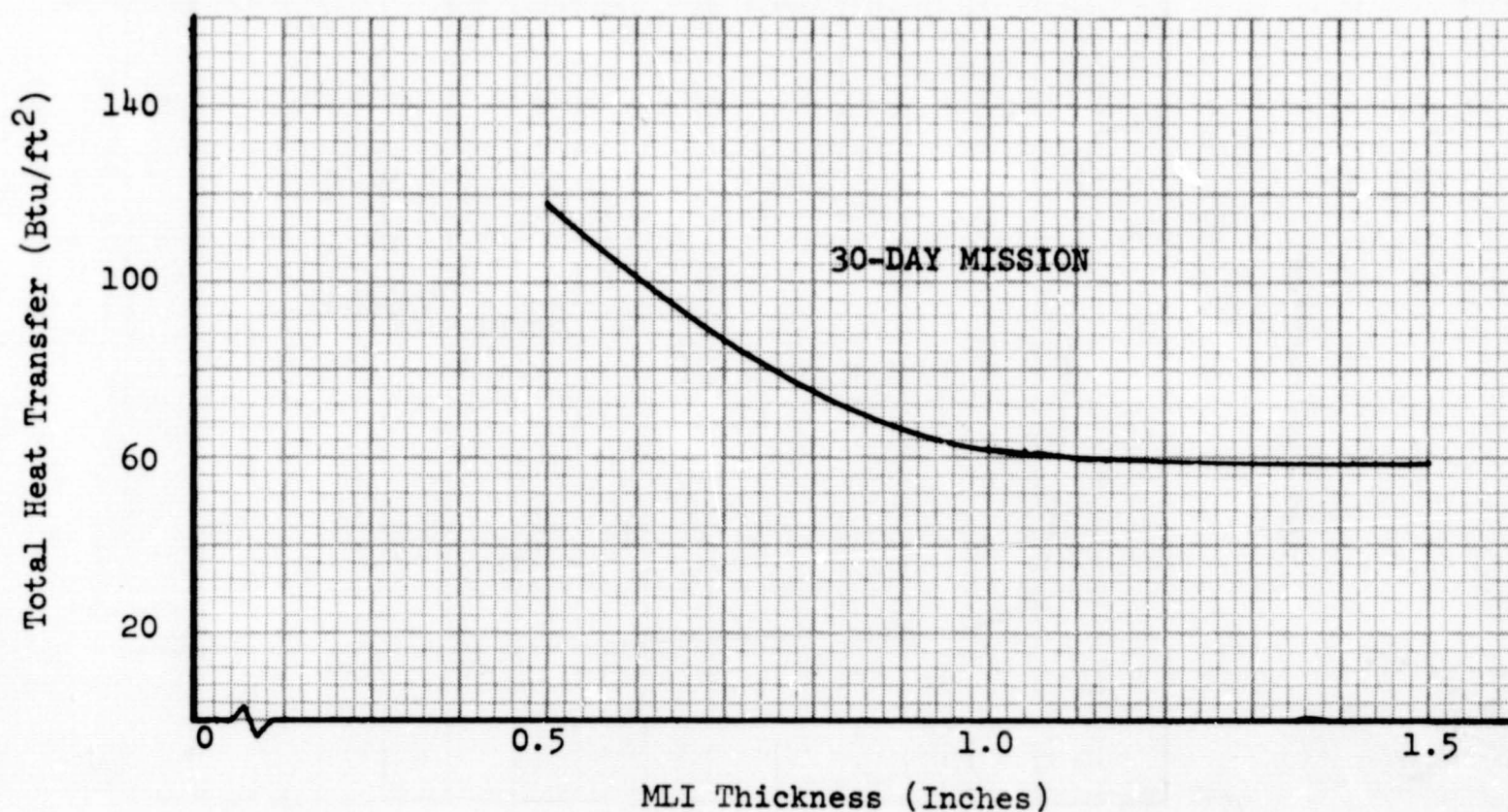


Figure 6-46. Total Heat Transfer to LO₂ During Evacuated Period—30-Day Mission

(see Subsection 6.1.4). The temperature history shown in Figure 4-2 for the structure surrounding the LO₂ tank was used.

A typical reentry heat flux to the LO₂ for the helium purge is shown in Figure 6-47. Total heat transfer during reentry is presented for both the nitrogen and helium repressurization concepts in Figures 6-48 and 6-49, respectively.

6.2.5 Relative System and Composite Performance and Optimum Number of Layers for the LO₂ Tank

The various candidate composites which were evaluated for the LH₂ tank were not reevaluated for the LO₂ tank. This was not necessary since there is no specific change in conditions which would enhance a particular

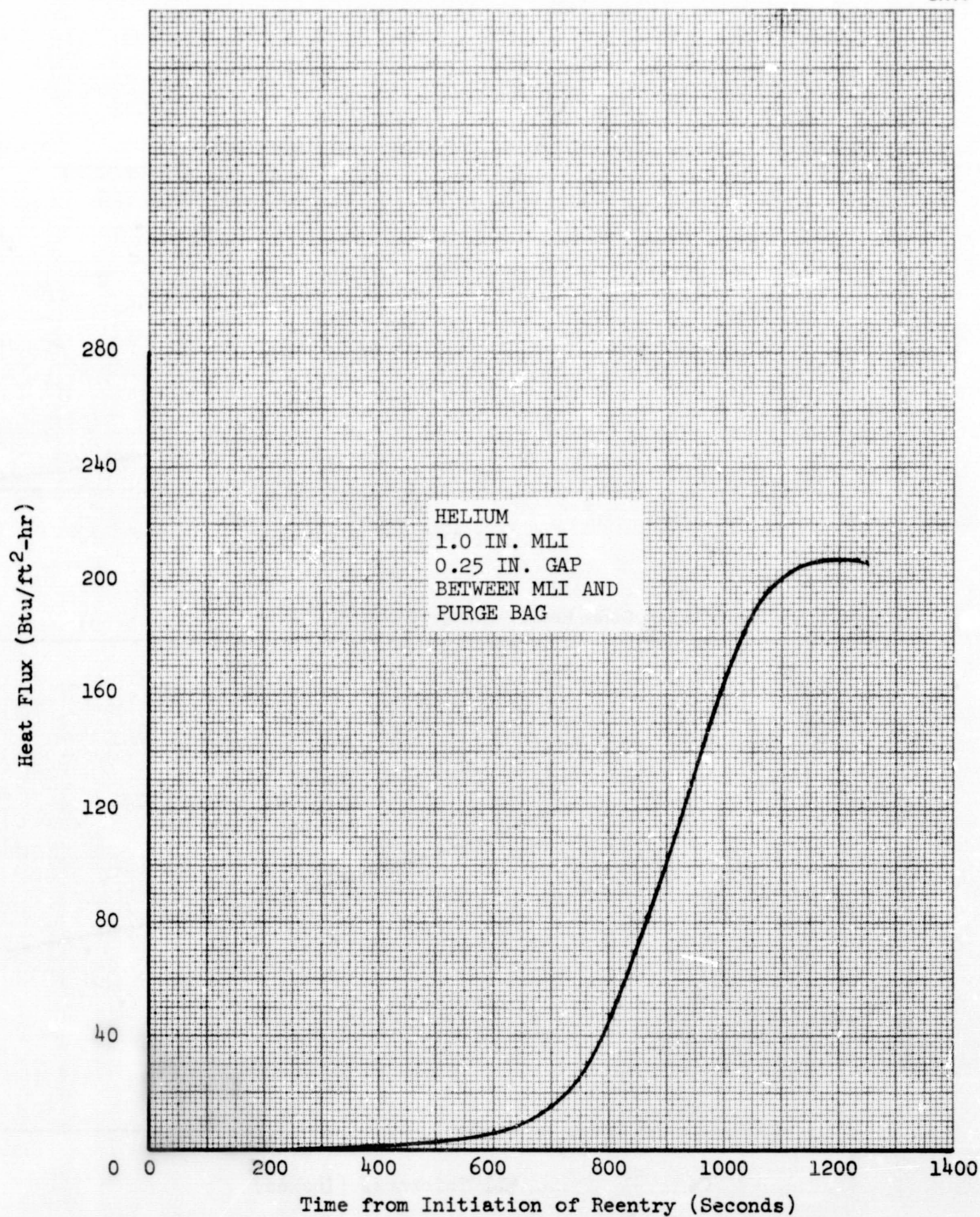


Figure 6-47. Heat Flux History to LO₂-Reentry Phase

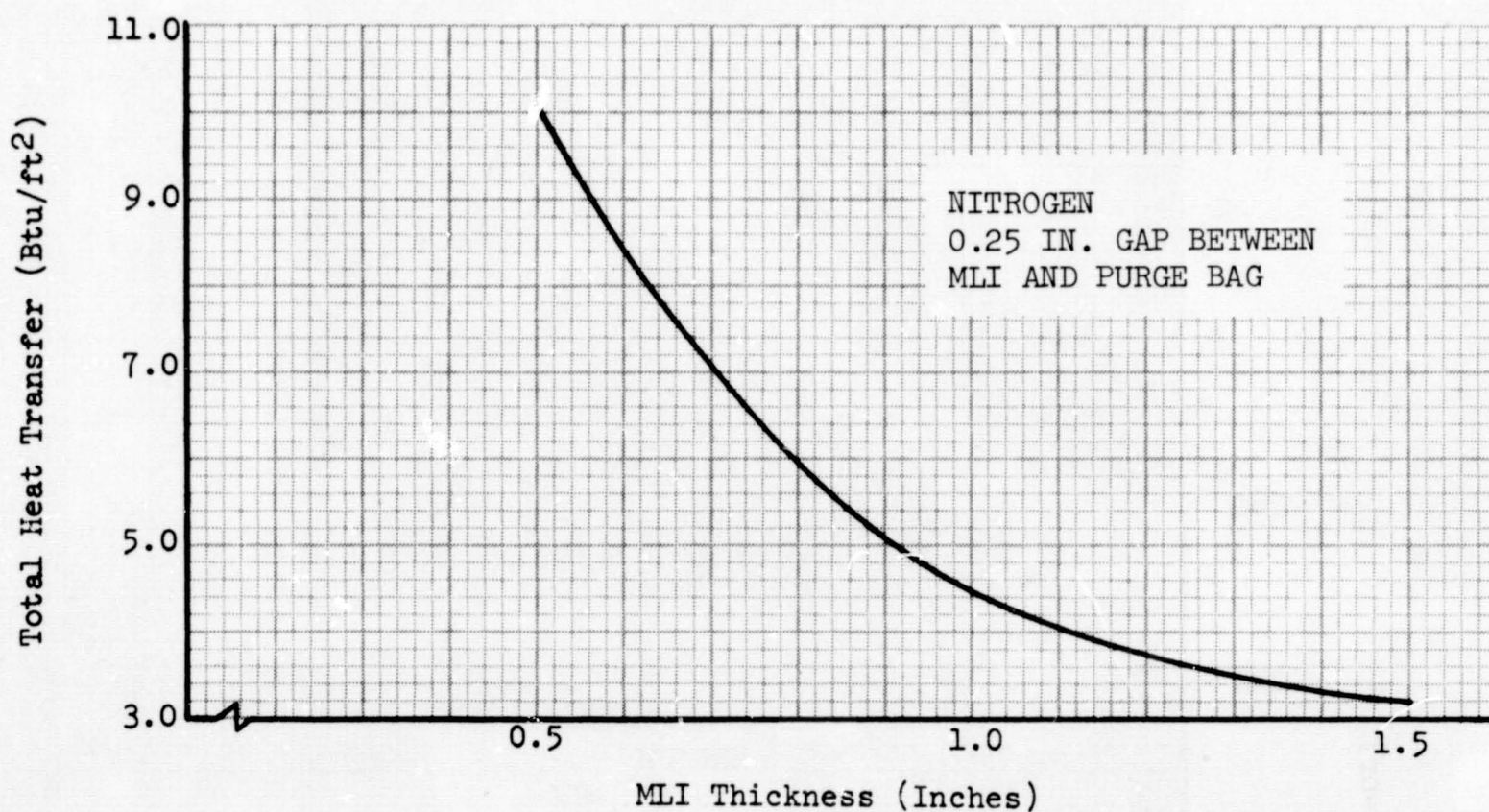


Figure 6-48. Heat Transfer to LO₂ During Reentry—Nitrogen Repressurization Gas

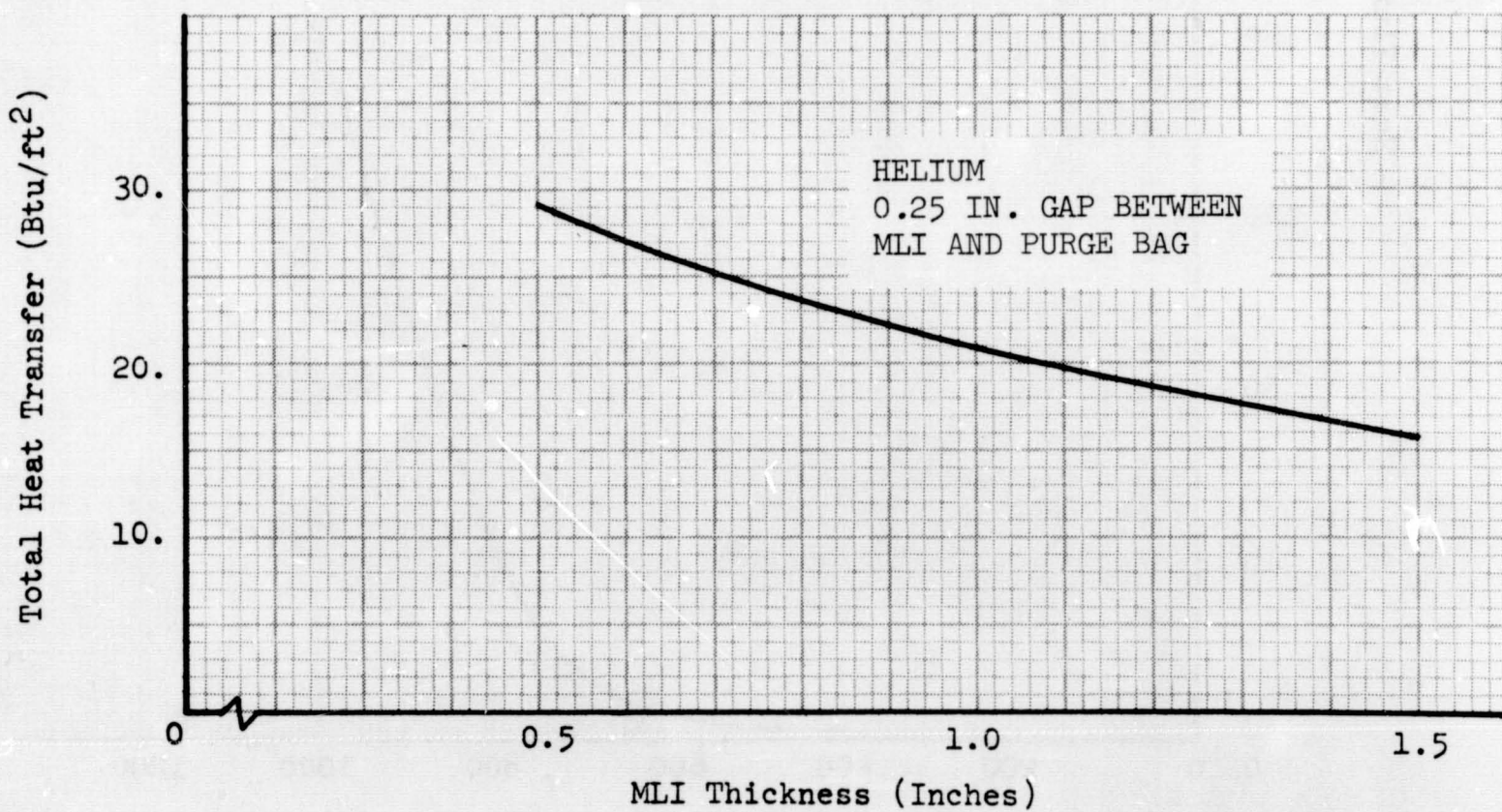


Figure 6-49. Heat Transfer to LO₂ During Reentry—Helium Repressurization Gas

composite to make it more competitive. As a result, the DGK/Dacron B4A composite was considered the most attractive for use on the LO₂ as well as on the LH₂ tank.

As in the analysis of the secondary LH₂ tank (see Subsection 6.1.5), the lowest system weight was used as a criteria for selection of the purge and repressurization gas and in determining the optimum number of layers in the MLI composite. The system weight was a total of the following:

- A. LO₂ boiloff weight during ground-hold lockup.
- B. LO₂ boiloff weight during ascent.
- C. LO₂ boiloff weight during evacuated period in space.
- D. LO₂ boiloff weight during reentry period.
- E. MLI composite weight.

The DGK/Dacron B4A composite was investigated with both a nitrogen purge/repressurization and a helium purge/repressurization system. As shown in Figures 6-50 and 6-51, the nitrogen purge/repressurization system results in the lowest weight for both the 7- and 30-day missions. There are, however, other factors which were not included in these analyses and which must be considered in the selection of the purge and repressurization gas for the LO₂ tank MLI. These include the reduction in weight and system complexity if a common repressurization system (common gas supply) is used for both tanks and the reduction in ground hold facility requirements which would result from using the same kind of purge gas for both tanks. Thus, utilization of helium for the LO₂ tank as well as the LH₂ tank may be optimum. This is discussed further in Subsection 6.5 and in the Summary, Section 2.

Determination of the optimum number of layers was made by obtaining the system weight as a function of the number of layers (insulation thickness) and finding the minimum weight. The layer density which was assumed (90 layers/inch) corresponded to the density at 1×10^{-4} psi compressive loading after 100 cycles of compression (see Subsection 3.9). The optimum number of layer-pairs for the DGK/Dacron B4A composite on the LO₂ tank is indicated in Figures 6-50 and 6-51. A total of 83 layer-pairs appears to be optimum for a 7-day mission. Similarly, a total of 92 layer-pairs appears optimum for a 30-day mission. At a layer density of 90 layers/inch, the above requirements correspond to insulation thicknesses of 0.92 and 1.02 in., respectively.

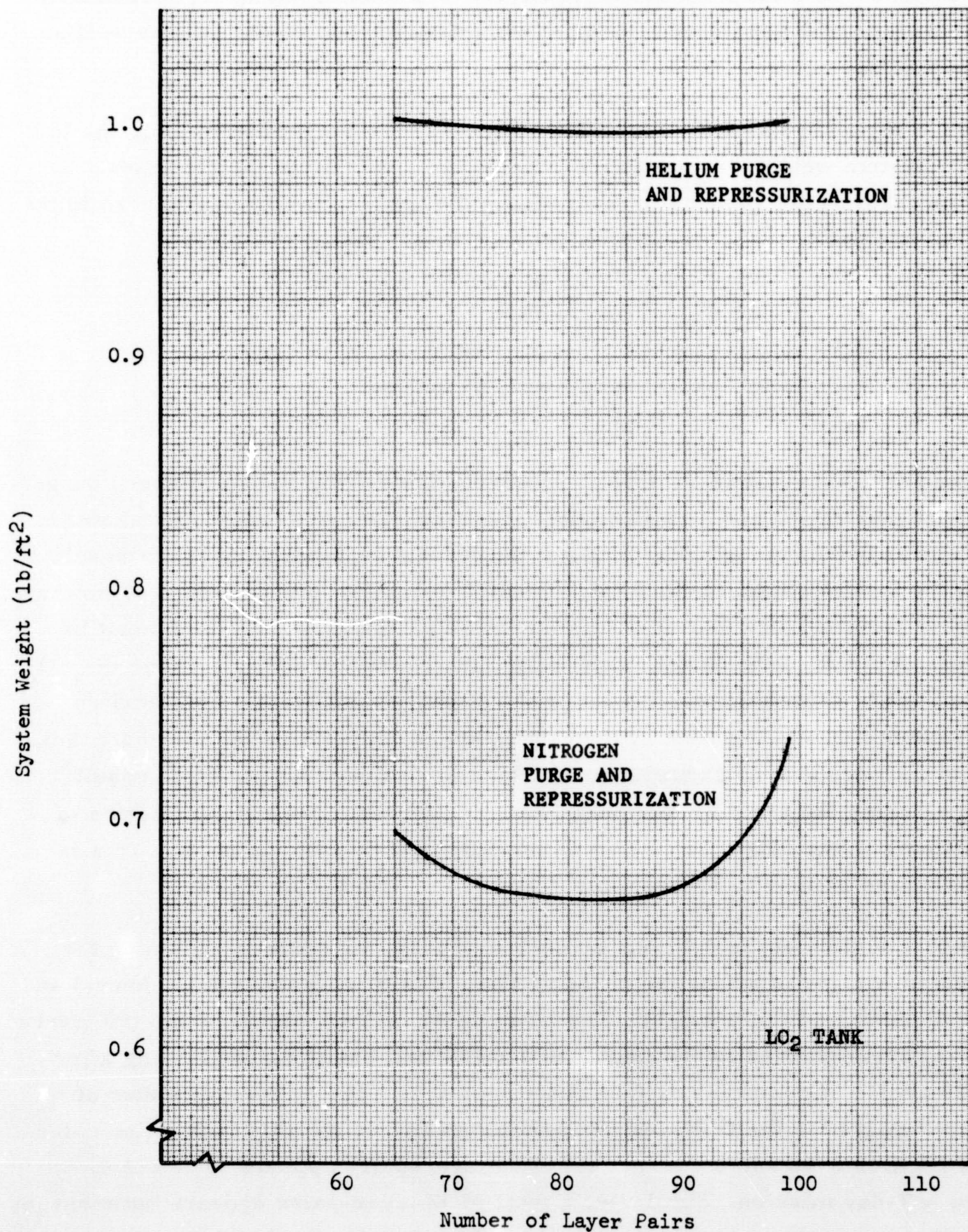


Figure 6-50. Effect of Purge and Repressurization Gas on System Weight—7-Day Mission

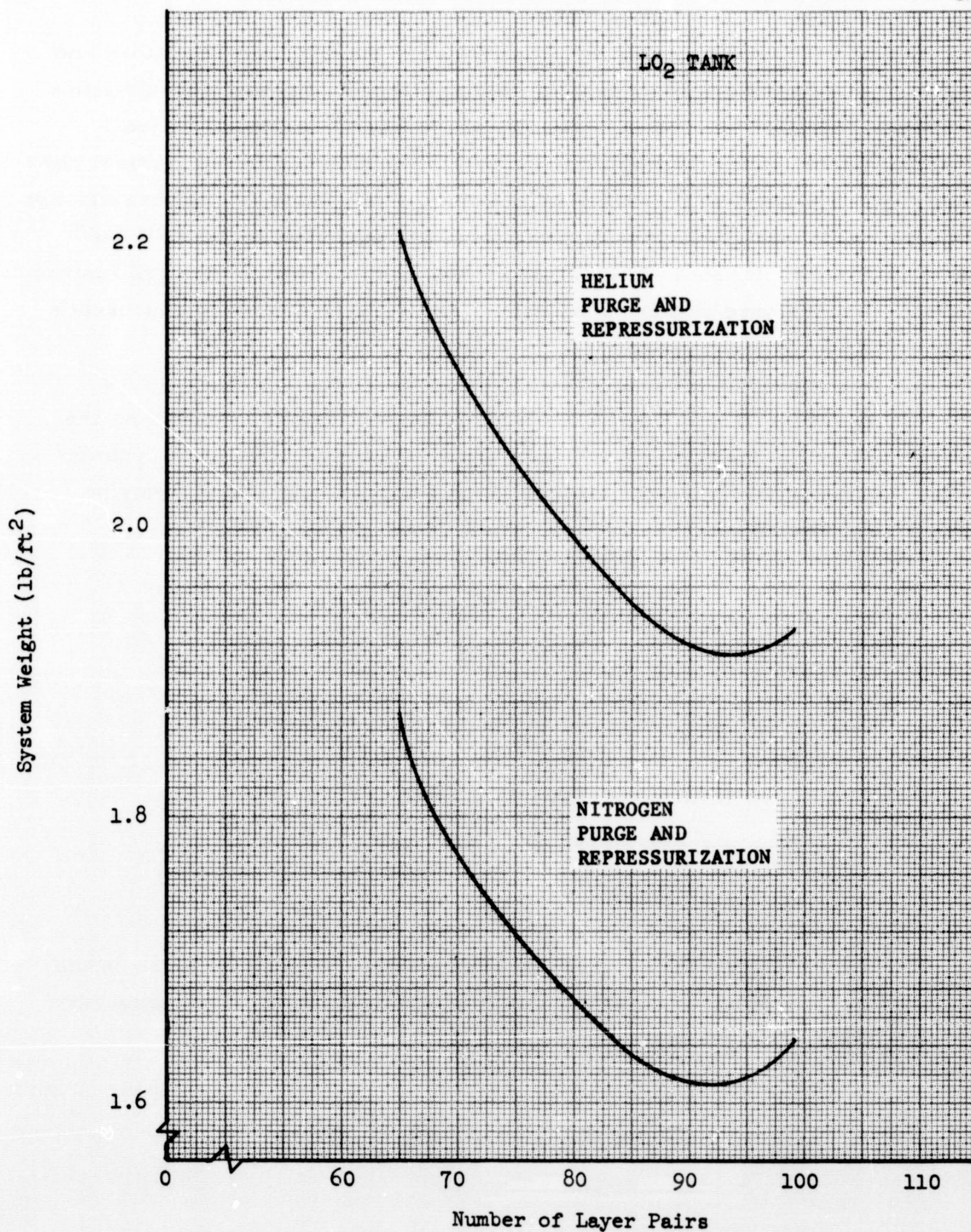


Figure 6-51. Effect of Purge and Repressurization Gas on System Weight—30-Day Mission

6.3 PARAMETRIC STUDY OF EFFECT OF MLI THERMAL PERFORMANCE DEGRADATION

The detailed thermal analyses accomplished for the LH₂ and LO₂ tanks and reported in Subsections 6.1 and 6.2 utilized effective thermal conductivities and layer densities based on the results of the Task 1 testing, Section 3. Thermal performance degradations beyond those included in the thermal conductivity and layer density values selected for these detailed analyses are not anticipated. However, a parametric study, as requested in the RFP and presented in the proposal, was accomplished on the possible effect of further thermal performance degradations if they occur. The following approaches were utilized for these parametric analyses:

- A. A simple percent degradation resulting from each environment cycle (vehicle missions). This is accomplished by increasing the effective thermal conductivity of the insulation after each cycle by a fixed percentage of the initial conductivity. The above may be expressed by

$$K_N = K_O (1 + NA)$$

where

K_N = Effective conductivity after Nth cycle

K_O = Initial effective conductivity

N = Percent degradation per cycle

A = Number of cycles

- B. A degradation that decreases in percentage with an increase in the number of environment cycles (vehicle missions). This procedure takes the form of

$$K_N = K_{N-1} \left[1 + A \left(\frac{B-N}{B} \right)^2 \right]$$

where

- K_N = Effective conductivity after the Nth cycle
 K_{N-1} = Effective conductivity for previous cycle
A = Percent degradation
B = Number of cycles after which no degradation occurs
N = Number of cycles ($N \leq B$)

The effect of degradation such as that noted above was evaluated for percentage degradations of 1 percent and 5 percent and for 100 cycles. The values of effective thermal conductivity resulting from the above calculation procedures are provided in increments of 20 cycles in Tables 6-3 and 6-4.

The amount of propellant lost due to boiloff during the evacuated period was determined for both the LH_2 and LO_2 tanks using the degraded thermal performances obtained from methods A and B. An insulation thickness of 1.0 in. and surface areas of 800 ft^2 and 300 ft^2 for the LH_2 and LO_2 tanks, respectively, were assumed. The results are shown in Figures 6-52 through 6-55.

Table 6-3
DEGRADATION OF EFFECTIVE THERMAL CONDUCTIVITY
USING METHOD A

1% Degradation		5% Degradation	
Cycle No.	K_N	Cycle No.	K_N
0	1.545×10^{-5}	0	1.545×10^{-5}
20	1.851×10^{-5}	20	3.090×10^{-5}
40	2.160×10^{-5}	40	4.635×10^{-5}
60	2.470×10^{-5}	60	6.180×10^{-5}
80	2.775×10^{-5}	80	7.725×10^{-5}
100	3.090×10^{-5}	100	9.270×10^{-5}

Table 6-4
DEGRADATION OF EFFECTIVE THERMAL CONDUCTIVITY
USING METHOD B

1% Degradation		5% Degradation	
Cycle No.	K_N	Cycle No.	K_N
0	1.545×10^{-5}	0	1.545×10^{-5}
20	1.831×10^{-5}	20	3.679×10^{-5}
40	2.018×10^{-5}	40	5.769×10^{-5}
60	2.119×10^{-5}	60	7.383×10^{-5}
80	2.157×10^{-5}	80	8.080×10^{-5}
100	2.165×10^{-5}	100	8.180×10^{-5}

6.4 HEAT SHORTS DUE TO TANK PENETRATIONS

The heat input due to the tank penetrations was estimated for both the LH₂ and LO₂ tanks. The tank penetrations which contribute to this additional heat input into the cryogen include the tank support struts, the plumbing, an MLI support shroud around the plumbing, and instrumentation wires. The Fourier steady-state equation was used to determine heating rates due to the plumbing and instrumentation wiring. Data from Reference 15 were extrapolated and/or modified to obtain a prediction of the rate of heat flow through the tank support struts and the shroud around the plumbing. The data in Reference 15 were found to be directly applicable for the LH₂ tank design. The Reference 15 data were modified for the LO₂ tank design to compensate for the difference in temperature between LO₂ and LH₂.

The plumbing was assumed to extend from the base of each tank in a cluster, and is insulated as a single unit. The insulation for the cluster will be supported by a fiber glass shroud. The shroud and insulation around the cluster of pipes were assumed to extend four feet from the tank. It was also assumed that the wiring to a single electrical penetration will be included in the cluster of plumbing. This wiring was assumed to consist of 36 wires of

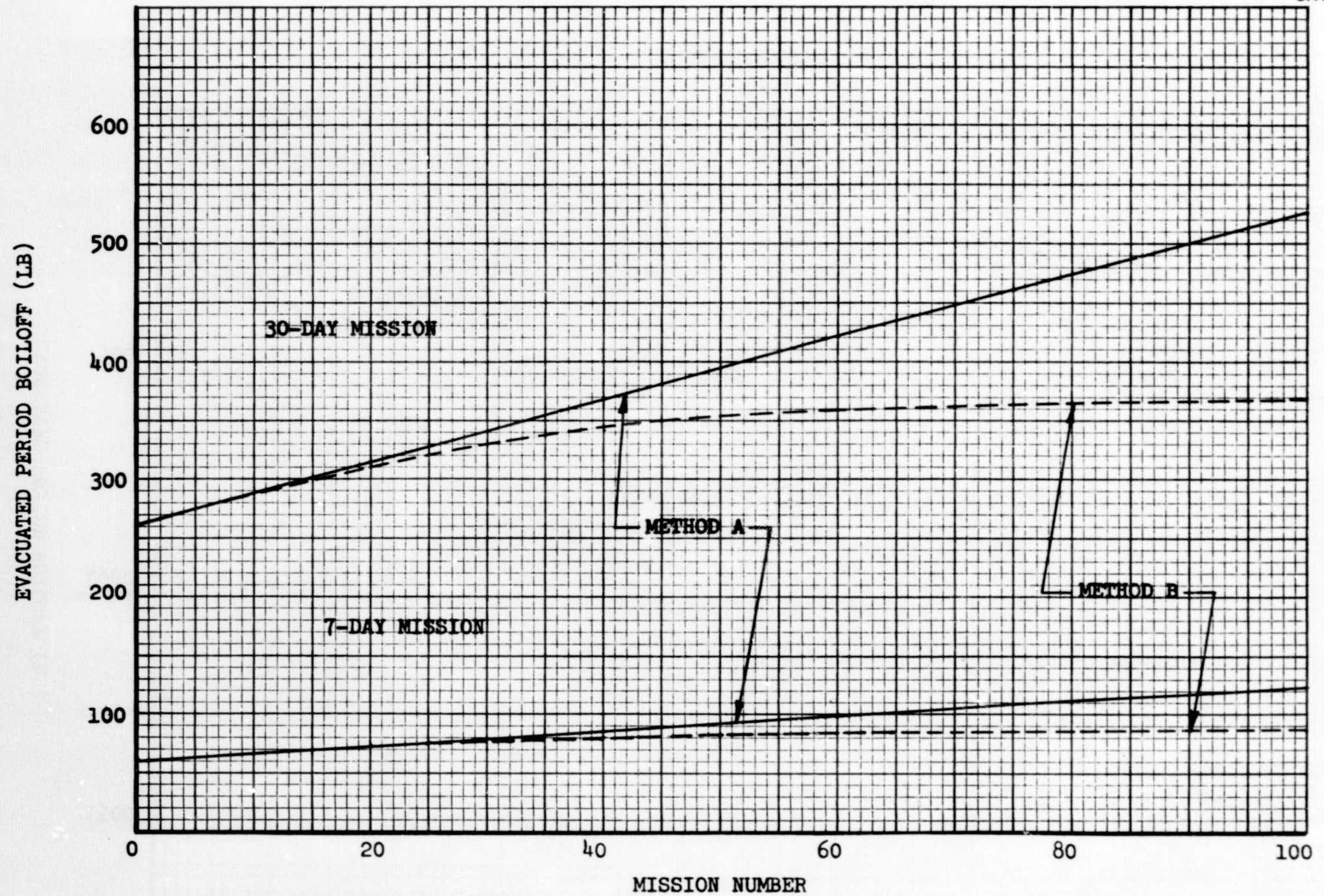


Figure 6-52. Effect of 1% Thermal Performance Degradation on LH₂ Tank Boiloff

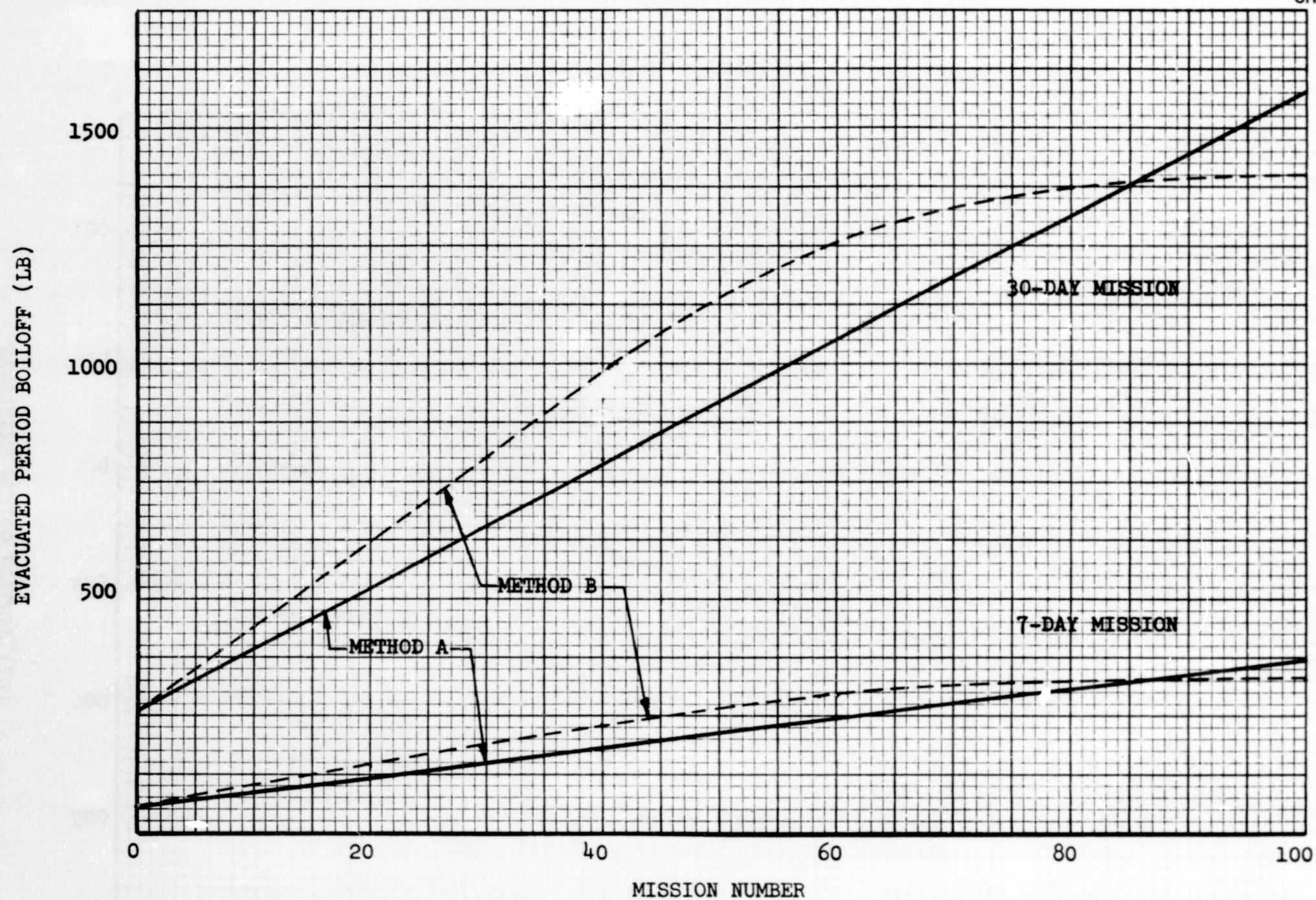


Figure 6-53. Effect of 5% Thermal Performance Degradation on LH_2 Tank Boiloff

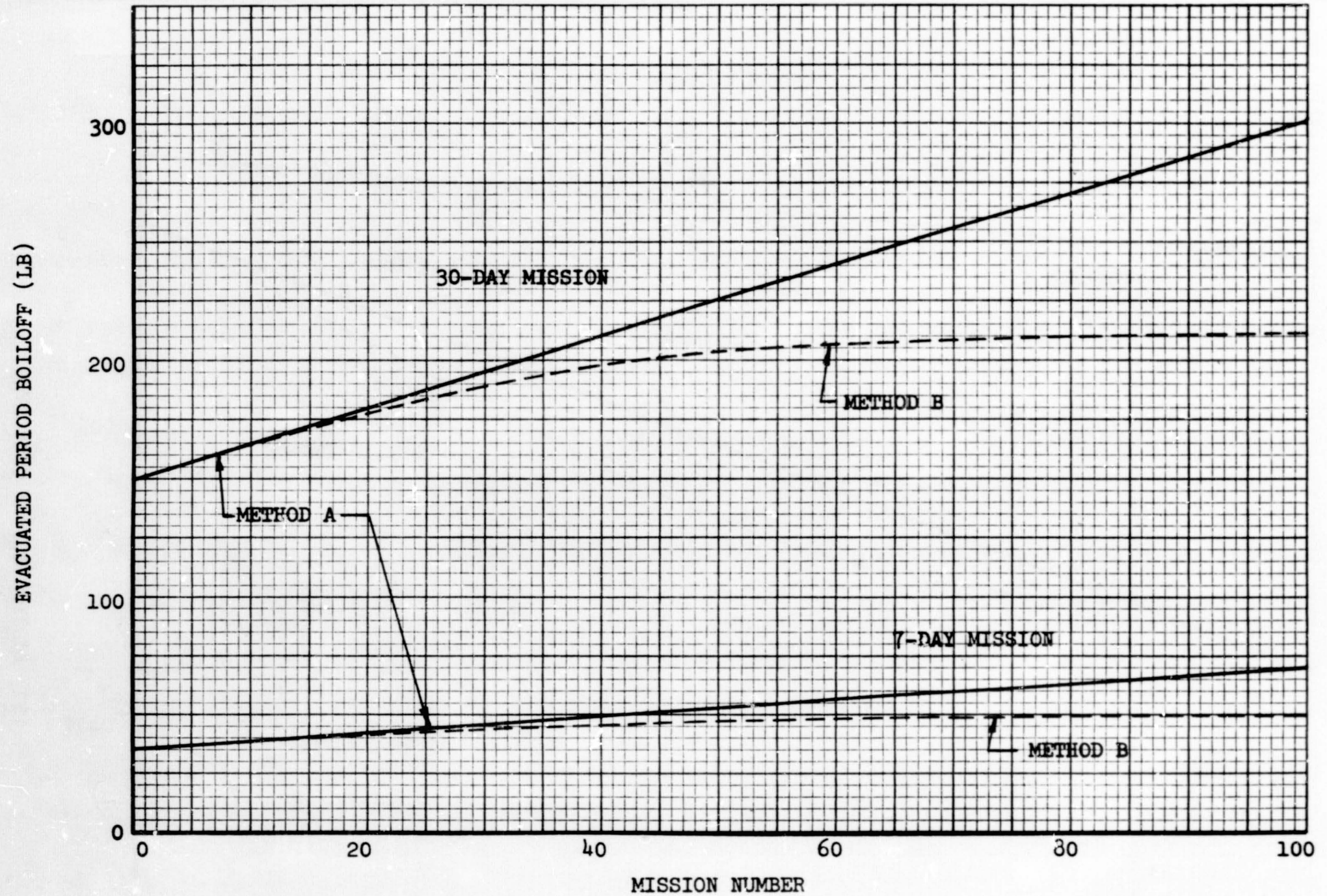


Figure 6-54. Effect of 1% Thermal Performance Degradation on LO₂ Tank Boiloff

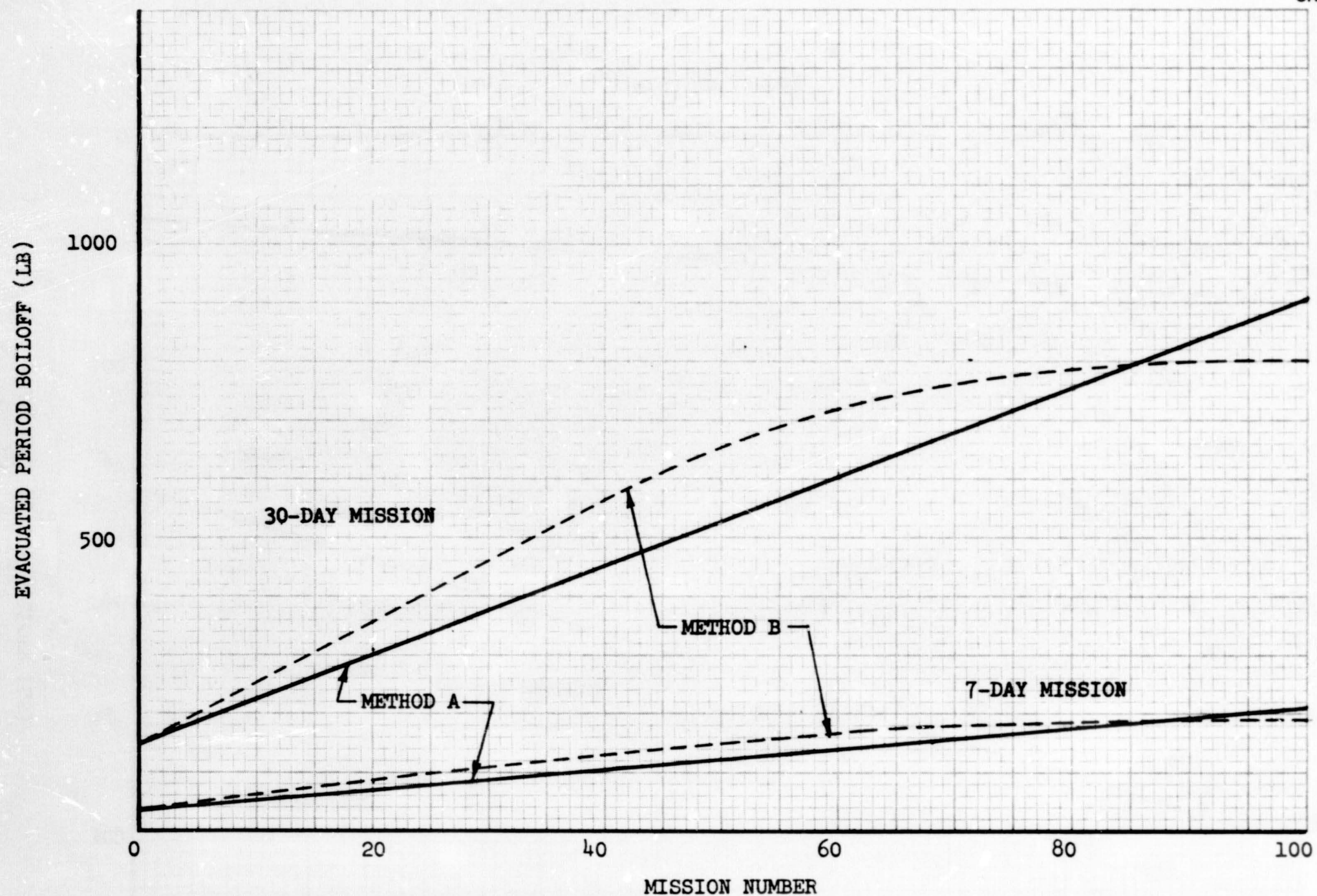


Figure 6-55. Effect of 5% Thermal Performance Degradation on LO₂ Tank Boiloff

26 gage (AWG). The insulation on the tank support struts was assumed to extend out on the struts two feet from the tank. Details of the insulation design are presented in Section 10.

A summary of the estimated heat input due to the tank penetrations is shown for the LH_2 and LO_2 tanks in Tables 6-5 and 6-6. These results show a total of 11.45 Btu/hr heating rate to the LH_2 tank and a total of 6.59 Btu/hr to the LO_2 tank.

Table 6-5

TOTAL HEATING RATE DUE TO TANK PENETRATIONS — LH_2 TANK

Item	Heating Rate (Btu/hr)
Plumbing	2.81
Plumbing Shroud	0.62
Instrumentation Wires	0.52
Tank Support Struts (6)	7.50
Total	11.45

Table 6-6

TOTAL HEATING RATE DUE TO TANK PENETRATIONS — LO_2 TANK

Item	Heating Rate (Btu/hr)
Plumbing	1.97
Plumbing Shroud	0.90
Instrumentation Wires	0.52
Tank Support Struts (6)	3.20
Total	6.59

6.5 PURGE, EVACUATION, AND REPRESSURIZATION REQUIREMENTS

To obtain efficient in-space performance as well as to prevent degradation of the MLI composite, the design of the MLI system must include the means for preventing condensation and freezing of condensibles on the layers of MLI. This protection is provided by purging the MLI with a dry inert gas such as helium or nitrogen during ground hold and repressurizing the MLI with one of these gasses during reentry. A purge bag which completely envelops the tank is used to contain these gasses.

An additional requirement for efficient in-space thermal performance is the rapid evacuation of the purge gas from the MLI during the ascent and initial in-space periods. This is obtained by opening valves to allow evacuation of the purge bag and by placing perforations in the MLI reflector layers to facilitate rapid evacuation of the composite.

The rationale and analyses used in defining a conceptual design for the purge, evacuation, and repressurization systems are contained in the following subsections. A summary of the purge, evacuation, and repressurization conceptual design is also presented in this section rather than in Section 10 (Insulation System Configuration) to aid the reader in following the subsequent discussion.

6.5.1 Purge, Evacuation, and Repressurization System Design Summary

A schematic of the conceptual purge, evacuation, and repressurization system design applicable for both the LH_2 and LO_2 tanks is shown in Figure 6-56. For the ground-hold purge, helium gas is inlet into the vehicle through valve Number 2, flows through the six tubular tank support struts, and then flows into the MLI at the ends of the tank support struts, see Figure 10-4 in Section 10. The purge gases then diffuse through the MLI, and the flushed gases leave the purge volume through an exit tube located at the aft end of the tank, see Figure 10-3. The flushed gas flows through valve Number 5 to the vehicle wall where it is dumped overboard. Valves Numbers 2 and 5 are of the umbilical disconnect type that close (and remain closed) at liftoff.

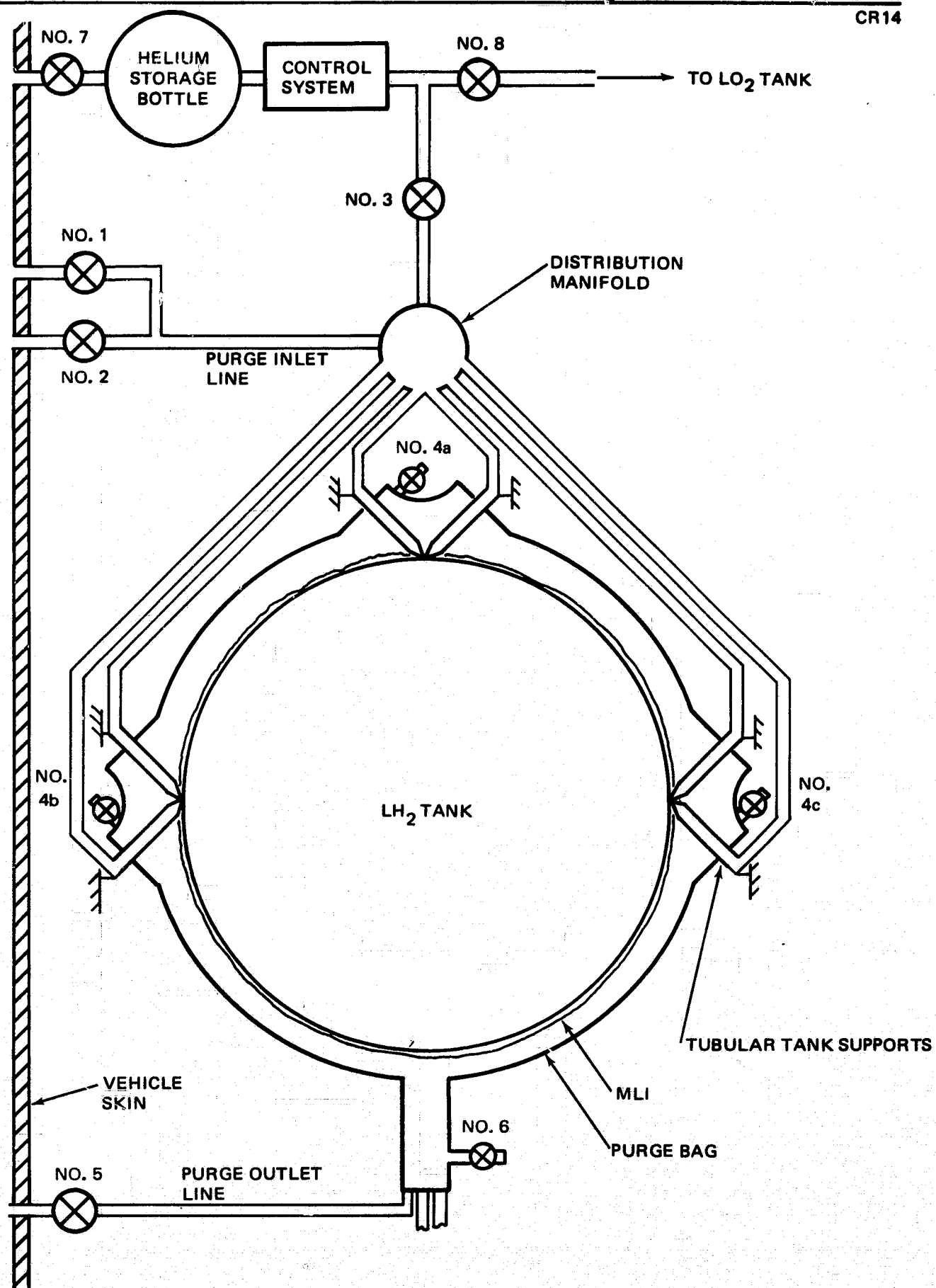


Figure 6-56. Schematic of Conceptual Purge, Evacuation, and Repressurization System Design

At liftoff, valves Number 1, 4a, 4b, 4c, and 6 are opened to allow the trapped gases to escape. Valve Number 1 is used to evacuate the purge inlet lines. Valves 6, 4a, 4b, and 4c are all used to evacuate the gas within the purge bag. Valve 6 is a motor-operated butterfly valve and is located at the aft end of the tank on the MLI support shroud around the plumbing, see Figure 10-3. Valves 4a, 4b, and 4c are mounted on the tank supports (Figure 10-4) close to the tank so that the flow resistance paths are minimized. These are also motor-operated butterfly valves and are located so that one valve is near each of the three tank support attachment points, see Figure 6-56.

Upon reentry, all valves are closed and valve Numbers 3 and 8 are opened to allow helium stored on the vehicle to enter the purge bags and thereby prevent condensible gases from entering the purge bags and damaging the insulation. The repressurization gas is introduced through the tank supports in a fashion similar to the groundhold purge gas. A control system regulates the flow of gas into the purge volume. For the system in which helium repressurization gas is used for the MLI on both the LH_2 and LO_2 tank, the control system and storage bottle shown in Figure 6-56 are common to both the LH_2 and LO_2 tank systems. Valve Number 7 is used to fill the helium storage bottle prior to a mission. The valve event sequence is summarized in Table 6-7 for the entire mission.

6.5.2 Ground-Hold Purge System

A satisfactory purge system for any cryogenic propellant tank must accomplish two objectives. First, the condensible gases initially trapped inside the purge volume must be removed prior to loading the tank with the cryogen. Second, these gases must be prevented from reentering afterward. Once the condensible gas in the purge volume has been depleted, a typical vehicle will go through a propellant loading phase and possibly two hold periods. As a consequence, it is convenient to treat the purging operation as four separate phases:

- A. Reduction of condensible gas concentration within the purge volume to an acceptable minimum.
- B. Maintaining the low-level concentration prior to loading of the tank with the cryogenic propellant.

Table 6-7
VALVE EVENT SEQUENCE - PURGE, EVACUATION, AND
REPRESSURIZATION SYSTEM

Event	Valve Number/Condition							
	1	2	3	4a, b, c	5	6	7	8
Ground-Hold Purge								
(a) Reduction of Condensibles	C	O	C	C	O	C	C	C
(b) Hold	C	O	C	C	C*	C	C	C
(c) Chillydown	C	O	C	C	C*	C	C	C
Ascent Evacuation	O	C	C	O	C	O	C	C
Reentry (Repressurization)	C	C	O	C	C	C	C	O

O = OPEN

C = CLOSED

*A valve downstream from No. 5 would be closed for these events and thereby prevent flow in the line of valve No. 5.

- C. Makeup of the purge gas collapse during tank loading chillydown, preventing back diffusion and cryopumping.
- D. Maintaining the low-level concentration for a chilled, fully loaded tank prior to vehicle lifeoff.

6.5.2.1 Purge System Design Considerations and Equations

The problem of designing a ground-hold purge system for a cryogenic storage tank utilizing MLI has been previously investigated by MDAC. The design equations previously developed (Reference 16) are applicable to the secondary propellant tanks being considered in this study and were, therefore, used in the present design. Since purge system design is covered in detail in Reference 16, only a review of the various operational phases, which must be considered for the design, and the design computational techniques are included herein.

Reduction of Condensibles

The first operation, reduction of condensibles, will most likely be initiated well in advance of propellant loading. It consists of removing from within the purge volume essentially all the air and moisture that might condense as the tank is cooled by the cryogen. For liquid oxygen whose saturation temperature is above 140°R , nitrogen is suitable as a purge gas. With liquid hydrogen, helium must be used for the purge unless an insulative substrate is placed beneath the MLI to increase its temperature during ground hold to above 140°R . In any case, however, the purge-gas liquefaction point must be sufficiently low to prevent any chance of it condensing.

The treatment of the purge-gas concentration reduction process must consider back diffusion of condensible gases into the purge volume as the purging operation proceeds. Back diffusion, both through the purge exit tube and purge-bag leakage points, becomes increasingly important as the condensible gas concentration within the purge volume decreases. As a result of back diffusion, the concentration of condensible gases can never be reduced to exactly zero. The higher the purge flow rate through the purged volume, the lower the concentration level achievable. Since a low condensible concentration level is desirable to prevent MLI damage but a low purge flow rate is desirable to conserve purge gases, a compromise must be made. Consequently, it is desirable to know the maximum amount of residual concentration that must not be exceeded if damage is to be prevented.

Unfortunately, the degree to which the condensible gases must be removed to prevent MLI damage is not firmly fixed. Some investigations have suggested that a volume is sufficiently purged when the concentration of residuals is 5 percent of its initial concentration. Others have suggested that a 1-percent value is required. At present there does not appear to be any definitive set of data to uphold or reject either claim. Consequently, it is felt that the lowest concentration suggested, 1 percent, is better for conservative design purposes. Should studies later prove that 5 percent (or some other value) is indeed sufficient, relaxation of design constraints will be a simple matter.

Prefill Hold

Once the condensible concentration has been reduced to an acceptable level in the desired time period, it may be necessary to hold this concentration level while other vehicle prelaunch operations are being completed before loading the propellant. Should this hold period be required, the purge flow rate should be reduced to a value just great enough to maintain the condensable concentration level. This would most likely consist of closing all purge-bag exit-line valves and providing purge gas inlet flow just sufficient to restrict back diffusion through leaks around penetrations, pinholes, and zippered seams in the purge bag.

Chiltdown and Fill

As the tank is being prepared to load the cryogenic propellant, a chiltdown of the components is necessary. During the chiltdown period, the gas within the purge volume is cooled and thereby contracts. As a result, the purge-gas flow rate must be increased to make up for the gas collapse. If the purge rate is not sufficient, the pressure inside the purge volume will decrease, allowing condensibles to reenter the volume, and/or will cause the purge bag to bear on the MLI. The rate at which the purge gas must be supplied depends on the chill rate of the tank as well as the chill rate of the purge gas and insulation.

Post-Fill Hold

Once the MLI has been purged and the tank filled with cryogen, another hold period may be necessary while other systems are being checked out. This additional hold period can be treated in the same fashion as the hold period prior to tank chiltdown.

Purge System Design Equations

The equations that are used to calculate the purge-gas flow rates and thereby size many of the plumbing components are summarized in Table 6-8.

6.5.2.2 LH₂ and LO₂ Purge System Design

For the detailed computation of ground-hold purge-gas requirements, a number of baseline purge parameters must be defined. The parameters

Table 6-8
SUMMARY OF PURGE SYSTEM DESIGN
EQUATIONS (REFERENCE 16)

Purge Phase	Design Equation	Remarks
1.	$\frac{\rho}{\rho_o} = 1 - \left(\frac{1}{1 + \frac{D_o}{v_e L_e}} \right) \left[1 - \exp \left[- \frac{A'_e D_o}{V L_e} \left(\frac{v_e L_e}{D_o} + 1 \right) t \right] \right]$	Concentration of condensible gas within the purge volume, ρ , as a function of time, t .
2.	$\dot{m}_{He} = \rho_{He} A'_e \frac{D_o}{L_e} \left(\frac{\rho_o}{\rho} - 1 \right)$	Mass flow rate of helium required to maintain the concentration of condensibles at the ratio ρ/ρ_o .
3.	$\frac{dM_{He}}{dt} = - \frac{P_{He} V_S}{R_{He}} \left\{ \frac{T_S - T_H - T_H \ln (T_S/T_H)}{T_H (T_S - T_H)^2} \right\}$ $\left\{ \frac{\dot{m}_{H_1} h_{H_1} - \dot{m}_{H_1} C_{P_H} T_H}{(MC_P)_{TNK} + \frac{MC_P}{2} INS + \frac{P_H V_{TNK}}{R_H T_H} C_{P_H} + \frac{P_{He} V_S}{R_{He}} C_{P_{He}} \frac{T_S \ln (T_S/T_H)}{(T_S - T_H)^2} \left[\frac{T_S - T_H}{T_H \ln (T_S/T_H)} - 1 \right]} \right\}$	The solution to this differential equation gives the mass in the purge volume as a function of time. The increase in mass must be provided by the purge system in order to prevent purge volume collapse.
4. (post-fill hold)	Same as 2.	Same as 2.

chosen for this study are summarized in Table 6-9. It is acknowledged that some of these parameters may vary from launch to launch, namely the hold periods, causing modifications in the total helium usage. However, the hardware has been designed to allow for increased flow conditions and can therefore meet reasonable excursions from the design conditions.

The ground-hold purge system chosen for both the LO₂ and LH₂ tanks does not utilize ducting beneath the MLI to flush the condensible gases from the insulation. At the present time, purging of perforated MLI is thought to be dominated by gaseous diffusion. Testing planned on the 105-in. tank on NAS 8-21400 will provide data to verify this design assumption. Should testing show that flow channels under the MLI are necessary, these could be included without changing the inlet or outlet flow locations. Techniques for providing flow channels are available and can be included in the purge system design if required.

Table 6-9
GROUND-HOLD PURGE DESIGN PARAMETERS

	LH ₂ Tank	LO ₂ Tank
Concentration Reduction Time Period (hr)	1.0	1.0
Chiltdown Time Period (hr)	0.33	0.33
Hold-Time Period (hr)	1.0	1.0
Purge Volume (ft ³)*	123	59
Chiltdown Effective Volume (ft ³)*	108	44
Residual Condensible Concentration after Purge Period	1%	1%

*The purge volume includes the volume within the tank support struts as they must be purged. The chiltdown volume includes only the bag volume surrounding the insulations.

Helium purge gas was selected for both the LH₂ and LO₂ propellant tanks. The results of the thermal analysis (Subsection 6.1) show that helium is clearly the optimum purge gas for the LH₂ tank. For the LO₂ tank, a nitrogen purge is optimum thermally. However, it is felt that a helium groundhold purge may result in a lower overall cost since the same ground support components can be used for both the LO₂ and LH₂ tanks.

Reduction of Condensibles

As noted in Table 6-9, a 1-hour time interval was selected for the concentration reduction period for both tanks. The helium mass flow rate is plotted parametrically in Figure 6-57, as a function of the purge volume and the condensible concentration after a period of 1 hour. Although a 1-percent residual was taken as the design point, several other curves are presented for comparison. To achieve a 1-percent residual in the LH₂ tank in 1-hour, a constant helium flow rate of 1.7×10^{-3} lbm/sec is required. For the same conditions, the LO₂ tank purge-gas flow rate is 8.4×10^{-4} lbm/sec. These flow rates are used to size the purge exit lines (the inlet lines are sized by either the chilldown or the repressurization requirements) and the spacing between the MLI and the purge bag.

The principal requirement in sizing the purge exit tubes and the MLI purge-bag separation is to maintain a moderately low pressure in the purge bag so that it will not burst. A maximum pressure differential of 0.5 psi was considered reasonable. The minimum practical MLI/purge-bag separation that was considered reasonable from an assembly standpoint was 0.5 in. As a consequence, calculations showed that the major pressure drop would occur in the exit tube. The pressure drop along the annulus between the MLI and purge bag was several orders of magnitude lower than that in the tubing and was therefore neglected.

In order to size the purge lines, the pressure drop (per foot of tube) as a function of the helium mass flow rate is required. Figure 6-58 shows these friction losses for laminar and turbulent flow in smooth pipes. For both

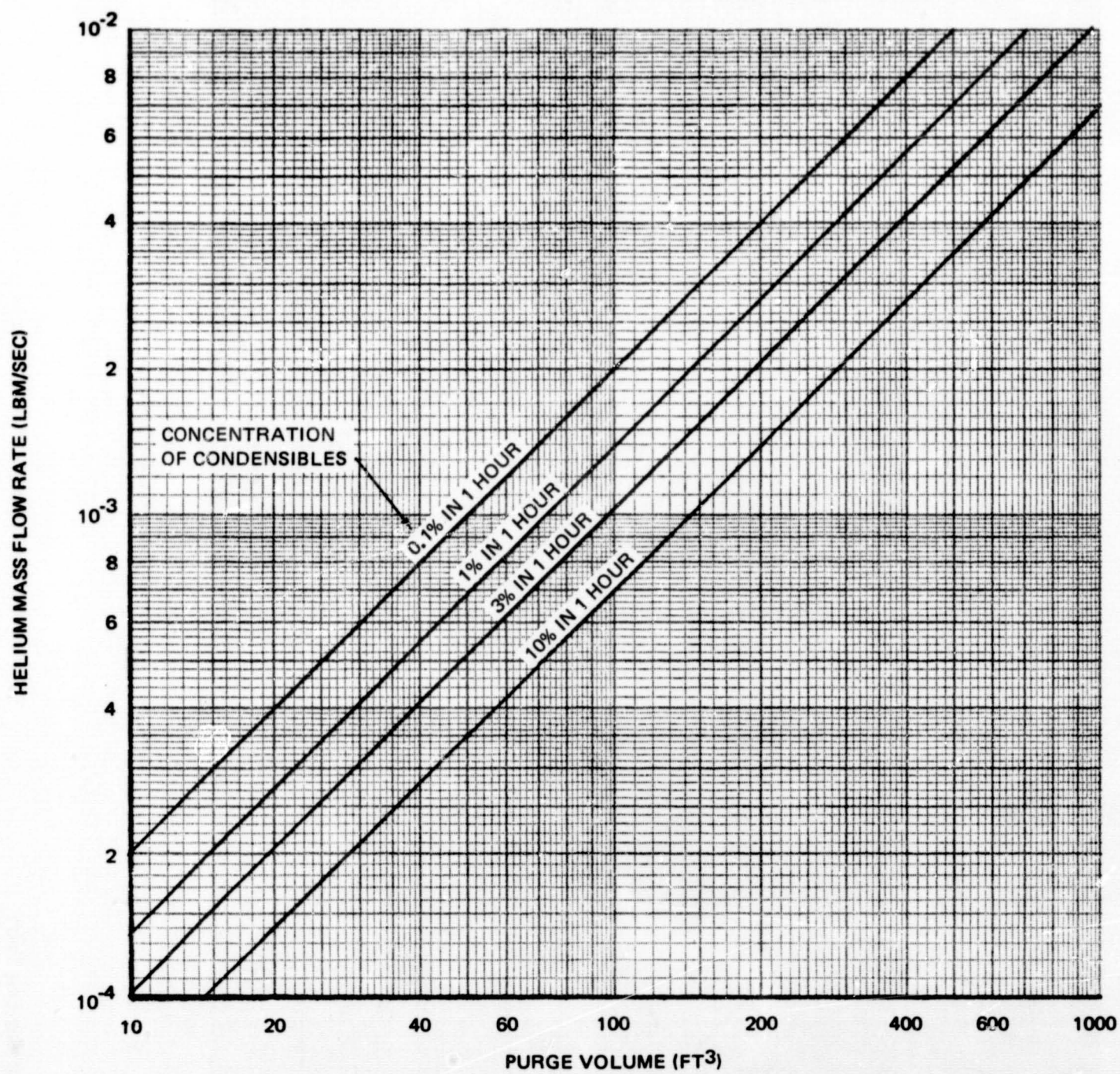


Figure 6-57. Effect of Purge Volume and Concentration of Condensibles on Purge Gas Flow Requirements

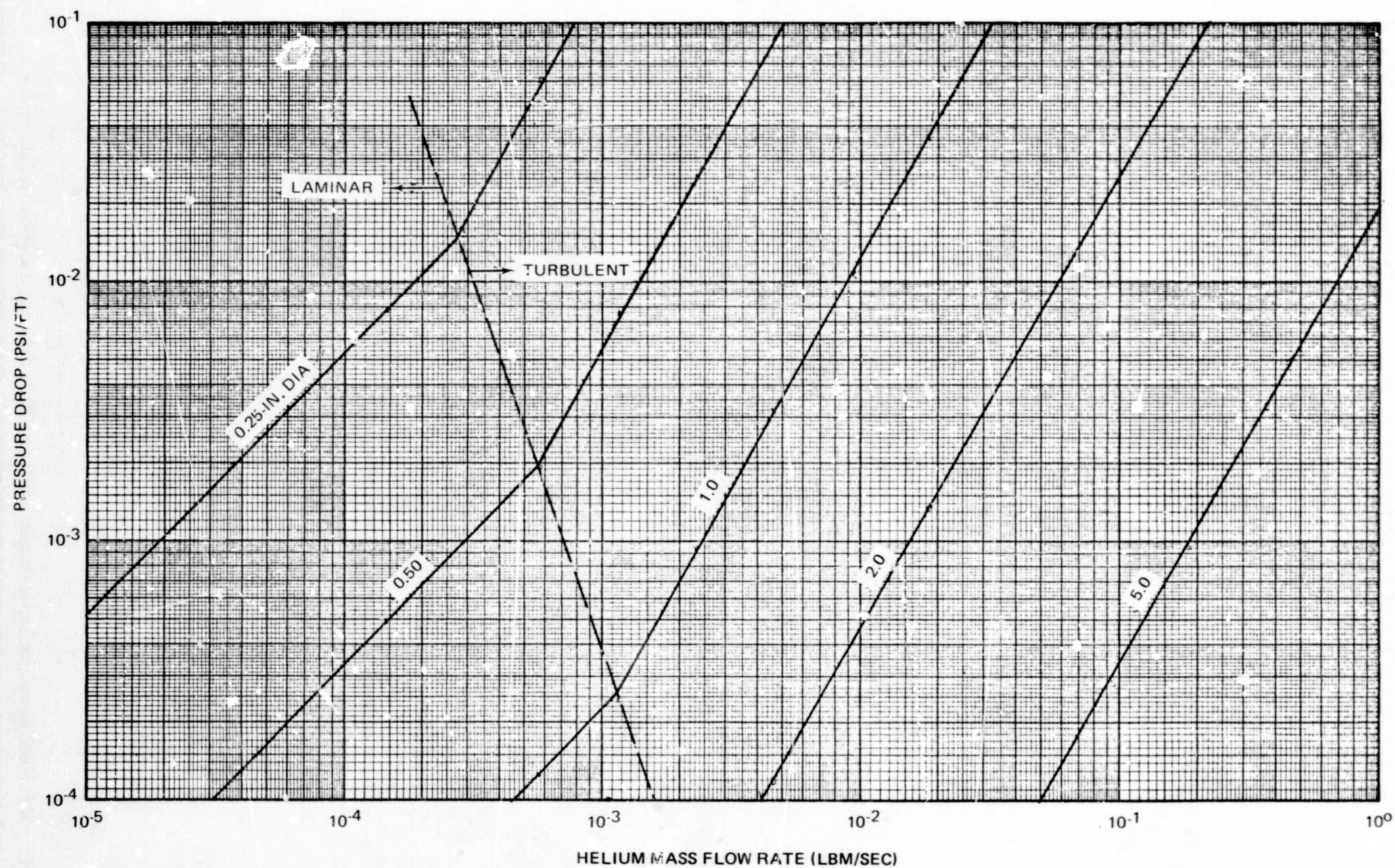


Figure 6-58. Friction Losses in Purge Gas Exit Tube

the LH₂ and LO₂ tanks, it was assumed that the purge-gas exit flow path would be approximately equivalent to 13 ft of straight tubing. A 1/2-in. line was selected for both tanks. For the LH₂ tank, the pressure drop in the exit line will be approximately 1.4×10^{-2} psi per foot of line or 0.18 psi.

For the LO₂ tank, the pressure drop will be 4×10^{-3} psi per foot of line or 0.05 psi for a 13-ft line. Although both pressure drops will be considerably below the 0.5-psi design drop, the larger lines will allow much more flexibility on line routing (as the flow resistance is a function of bends) and will allow more rapid purging if necessary.

Chilldown

The chilldown time period for both the LH₂ and LO₂ tanks was assumed to be 20 minutes. This time period is consistent with the chilldown time periods for current cryogenic stages. The computed helium flow rates required to prevent purge pressure collapse during chilldown are presented in Figures 6-59 and 6-60 for the LH₂ and LO₂ tanks, respectively. For the LH₂ purge volume, the maximum helium flow rate required is 5.5×10^{-3} lbm/sec (2.1 lb of helium is needed to prevent collapse). For the LO₂ purge volume, a maximum helium flow rate of 9.4×10^{-4} lbm/sec (0.32 lb of helium is required to prevent collapse) is required. These flow rates are used to size the inlet purge lines (if consistent with reentry repressurization requirements).

The pressure drop for the inlet purge lines is not as significant as that for the exit lines. The high pressure at the upstream location bears only on the purge inlet line and not the purge bag. A 1/2-in. line was selected as the purge inlet lines for both the LH₂ and LO₂ tanks. Assuming that an equivalent 13-ft of straight 1/2-in. tubing is typical, the maximum pressure drop for the LH₂ inlet line will be 1.5 psi, and for the LO₂ inlet line it will be 0.07 psi. Both these pressure drops are very acceptable considering the line pressure and the maximum strength of thin-walled aluminum tubing. The pressure drop within the tubular tank supports is negligible, as they are nearly 6-in. in diameter. The pressure drop across the orifice outlets is also negligible compared to the line losses. The purge system inlet lines for both the LH₂ and LO₂ allow for significantly increased flow rates if required and therefore maintain the conservative nature of the design.

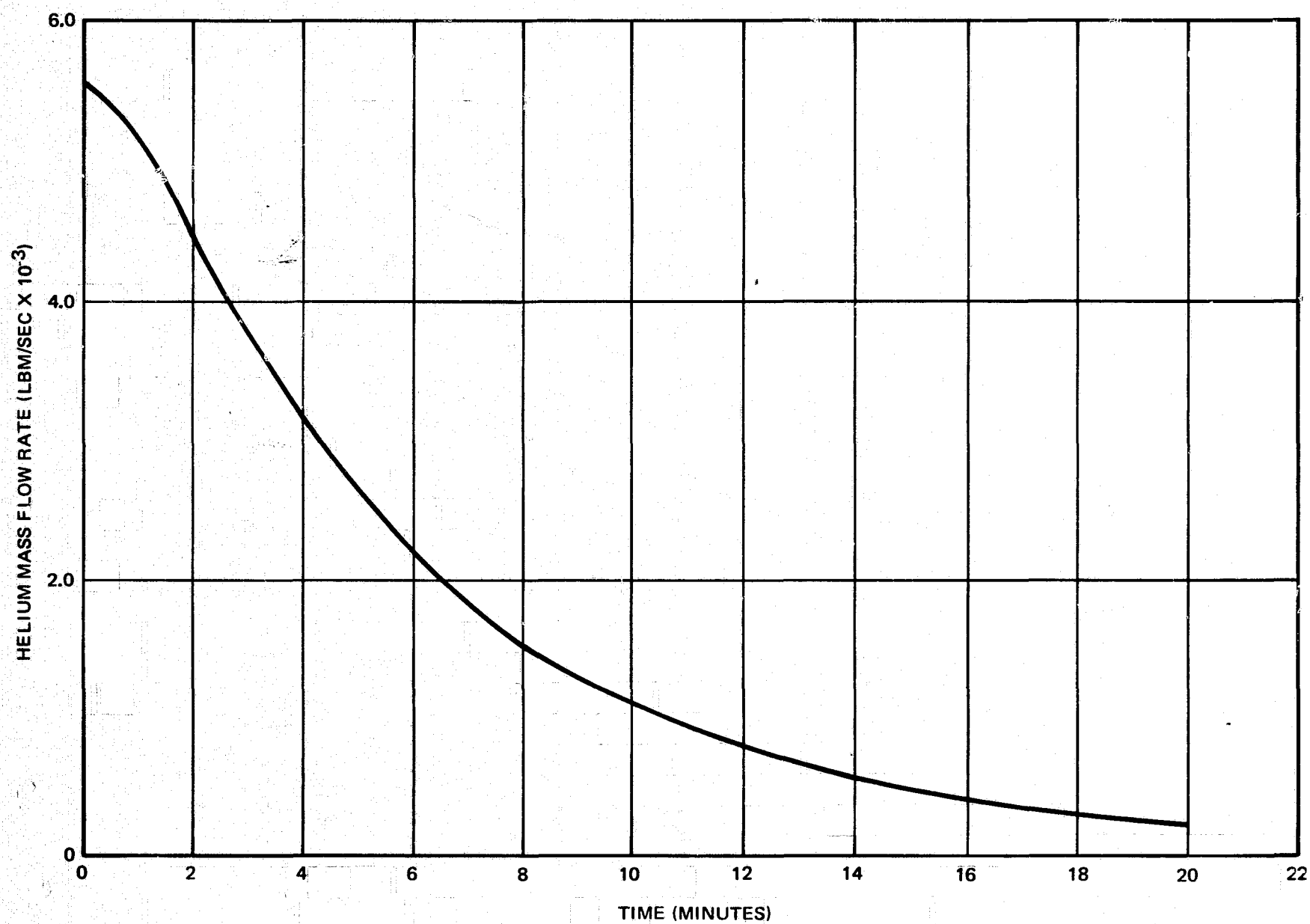


Figure 6-59. Helium Mass Flow Rates Required During Chilldown--LH₂ Tank

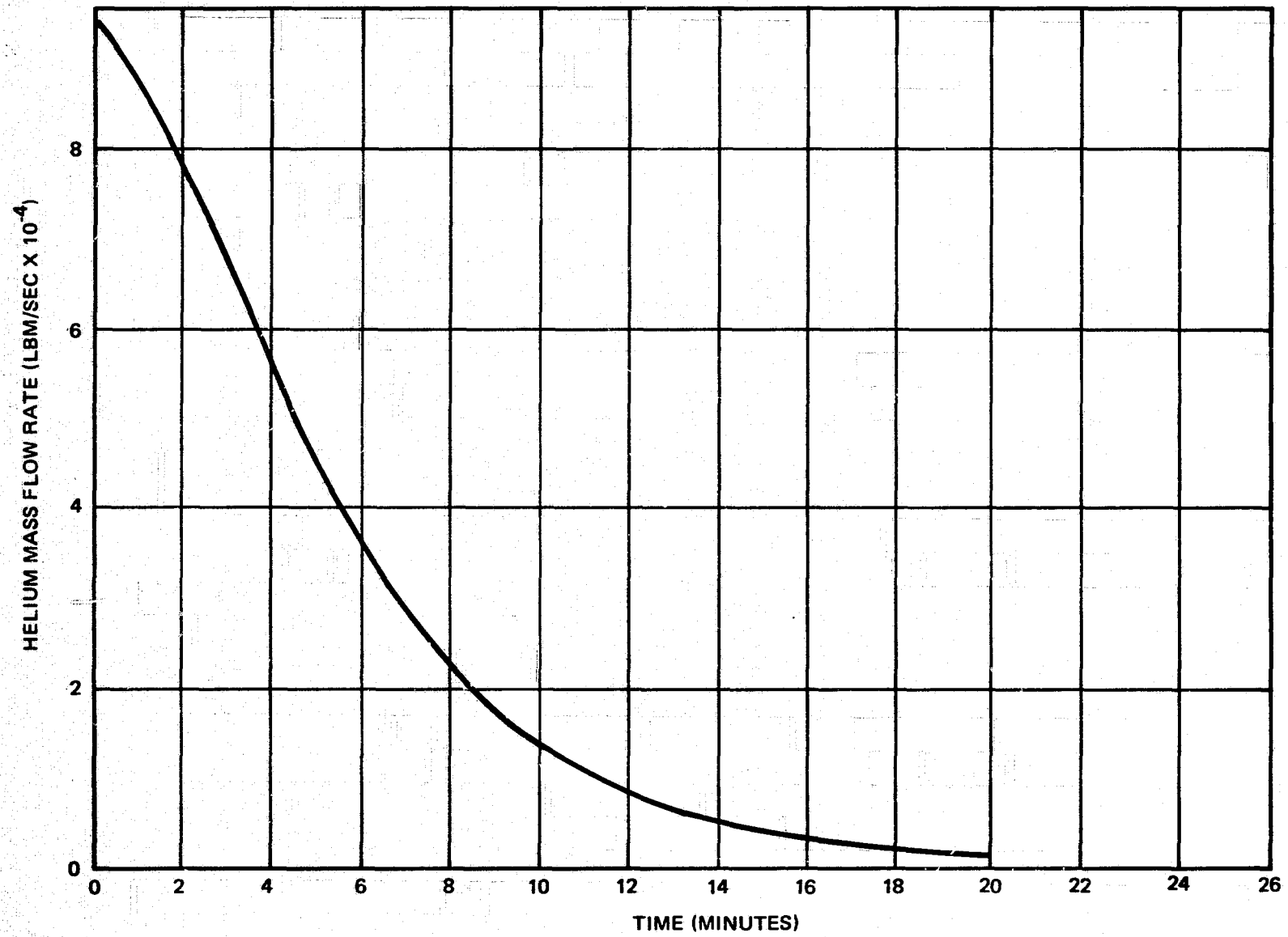


Figure 6-60. Helium Mass-Flow Rates Required During Chillydown--LO₂ Tank

Purge Gas Requirements

The helium used for the ground-hold purge operational phase is summarized in Table 6-10. The total amount of helium required for the ground-hold phases for both the LH₂ and LO₂ tanks is 11.57 lb. The helium used during the reduction-of-condensables and chilldown phases were obtained by using the mass flow rates previously discussed.

The amount of helium used during the hold periods is primarily a function of the amount of leakage in the bag. Since the flexible purge-bag material is relatively free of pinholes, the principal leak path will be through the zippers in the bag. To estimate the leakage through the zippers, water leakage data from B. F. Goodrich (Reference 17) was converted to helium leakage by ratioing, using their dynamic viscosities. For a pressure differential of 0.5 psig, the helium leakage was calculated to be 1.7×10^{-8} lbm/sec per foot of zipper. For the LH₂ tank the total zipper length is 110 ft and the leakage flow is 1.87×10^{-6} lbm/sec. The LO₂ tank has 81 ft of zipper, giving a flow rate of 1.38×10^{-6} lbm/sec. These leakage rates are applied to the tanks during the hold periods. However, as may be noted, they were insignificant.

Table 6-10
GROUND-HOLD PURGE HELIUM USAGE

Helium Usage Period	LH ₂ Tank (lb)	LO ₂ Tank (lb)
Concentration Reduction Period	6.12	3.03
Chilldown Period	2.10	0.32
Hold Period	5.15×10^{-3}	3.82×10^{-3}
Totals	8.22	3.35

6.5.3 MLI Evacuation

From the time the vehicle lifts off until reentry is initiated, the region surrounding the MLI should be as open to space as is reasonably possible. The system design must allow the pressure to drop rapidly within the purge bag for the system to achieve high thermal performance. Purge gases, gases adsorbed on the surfaces of the MLI, and gases leaked from the tankage must pass through the insulation, flow along the annulus between the MLI and the purge bag, and then flow out an exit port in the purge bag. If this path is too tortuous, the gases will not evacuate rapidly, resulting in an increase in the total heat transfer to the propellant. If the path is too open, as with highly perforated MLI, the evacuated thermal performance will be degraded. If the path is too open, as with a wide spacing between the purge bag and MLI, the purging and repressurization operations will be more costly because of the larger purge volume. As a consequence, analyses were conducted to provide guidance to the compromises that must be made to establish a workable solution. At best, because of the severe unknown nature of portions of the problem, the solution must be considered preliminary. Many answers were analytically computed from mathematical models that have not been experimentally verified.

A key assumption made with regard to the launch period is that the purge bag remains at least 1/2 in. from the MLI at all times. As a consequence, it is assumed that the gas exit paths during evacuation will not be blocked due to purge-bag sagging. Computations indicate that the pressure differential during the continuum regime of evacuation will guarantee adequate flow paths. In the free molecular flow regime, however, the pressure differentials may not be adequate to "balloon" out the bag and, therefore, form an evacuation gas flow channel. It is apparent that in some locations on the upper tank hemisphere, the purge bag will be forced down onto the MLI surface by the boost acceleration loading. However, it is felt that the excess bag material (the purge-bag surface area is larger than that of the MLI), the stiffness of the bag material, the fixed positioning of the bag at all tank support and plumbing locations, and the inertia forces at engine cutoff will prevent a

complete blockage of the annulus between the MLI and the purge bag. If future analyses and testing show that steps must be taken to provide flow channels between the MLI and the purge bag, several techniques are possible. These include the following:

- A. A purge-bag support frame
- B. Localized supports between the purge bag and the vehicle structure
- C. Pressurized ribs in the purge bag
- D. Standoffs attached either to the MLI face sheet or the purge bag

6.5.3.1 MLI Perforations

Uncertainties at the present time concerning: outgassing of adsorbed gases on the MLI, leakage rates of relatively large cryogenic tankage, and evacuation computational methods make it prudent to select an MLI system for the secondary propellant tanks that has perforated reflectors. Perforations allow relatively easy broadside evacuation and outgassing to take place and thereby significantly reduce (or essentially eliminate) pressure buildup behind the MLI blankets. Consequently, a perforated MLI system was selected for both the LH_2 and LO_2 tanks.

The most efficient perforation pattern is one with the smallest perforation spacing, as this minimizes the resistance to gas outflow and results in the minimum evacuation period. By using a shorter perforation spacing, it is possible to reduce the percentage of open area required and thereby increase the system thermal performance while in space. The choice of a perforation configuration represents a compromise between manufacturing limitations and the desire for minimum perforation spacing and minimum perforation area fraction. At the present time, the smallest perforation which can be cut into the reflector material by the vendor is 0.046 in. in diameter. Given a fixed perforation spacing, the smaller the perforation holes, the smaller the perforation area fraction will be. Conversely, with a fixed area fraction, the smaller the hole is, the closer the spacing will be. Therefore, it follows that the smallest perforation size should be chosen.

The configuration chosen has 0.85-percent open area, five holes per square inch, and 0.046-in. hole diameter. The perforations are placed in a triangular pattern, as illustrated in Figure 10-5. This configuration has the highest perforation density (closest perforation spacing) of the patterns currently available from the vendor which have less than 1-percent perforation area fraction.

6.5.3.2 MLI Pressure History

Two computational models were used in predicting the MLI pressure history. First, outgassing was neglected and the pressure history during the initial phase of evacuation was studied. Then the long-term effects of outgassing on the pressure and heat-transfer history were studied.

MLI Pressure History with Negligible Outgassing

In order to predict the performance of the evacuation system without outgassing, the MDAC Perforated HPI Evacuation/Pressurization (PHEP) computer code was used to calculate the pressure history within the MLI. For this computation, the only path available to the trapped gases was through the perforations. Flow along the insulation and out the blanket seams was neglected, thus giving conservative results. The input conditions for calculating the pressure history for the LH₂ tank were:

Perforation Size	= 0.046-in. diameter
Perforation Pattern	= Triangular
Perforation Area Fraction	= 0.85 percent
Layer Density	= 90 Layer-pairs/inch
Total Layers	= 70
Interstitial Gas	= Helium
Temperature Profile	= Linear from 60°R to 460°R

The predicted maximum pressure history in the MLI panel for the LH₂ tank is shown in Figure 6-61. The anticipated ambient pressure history is also shown. The maximum pressure is seen to reach 10^{-4} psf only about 5 sec after the ambient pressure had reached this value.

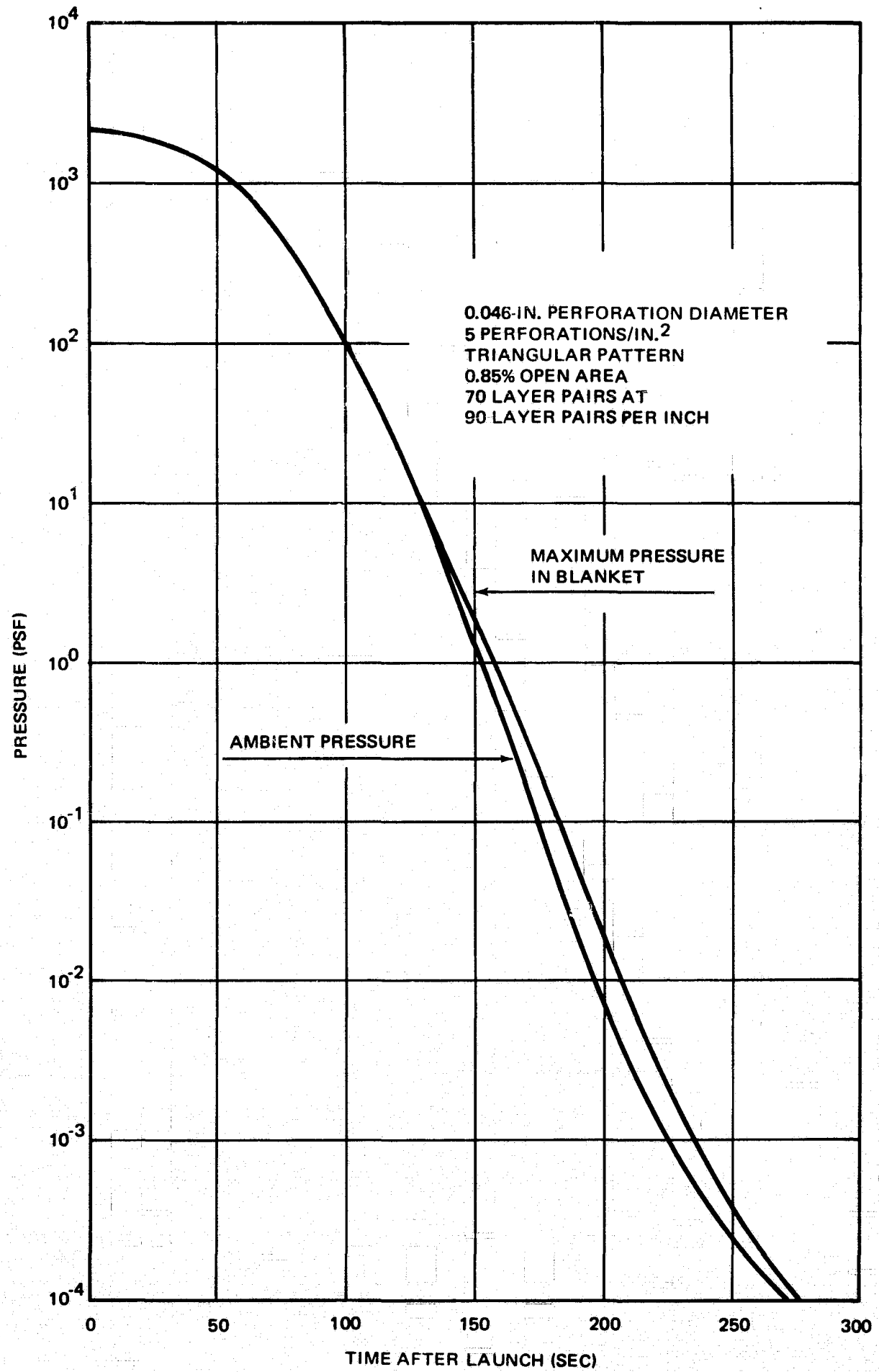


Figure 6-61. Ascent Pressure History in MLI Panel--No Outgassing

Figure 6-62 shows the predicted history of the pressure drop across the MLI blanket where the pressure drop is defined as the difference between the maximum pressure in the blanket and the ambient pressure. The maximum pressure drop of about 1 psf is insufficient to cause an appreciable change in the layer density during evacuation, see Figure 3-52.

Figure 6-63 shows pressure profiles through the blanket at 120 sec (the time of the maximum pressure drop) and at 200 sec (the time at which the ratio of pressure drop to ambient pressure is a maximum). The 120-sec profile is still in the parabolic shape typical of continuum flow, while effects of temperature distribution are apparent in the free molecular flow dominated profile at 200 sec. Clearly, if the outgassing is neglected, the pressure history within the MLI is essentially that of the ambient pressure.

MLI Pressure History with Outgassing

When outgassing is considered, a different picture is presented. The gases that evolve from the surfaces of the MLI alter the pressure history significantly in the free molecular flow regime. Analyses were conducted to evaluate the effects of outgassing and the resulting tradeoffs in the purge bag vent system design.

During this contract, samples of MLI materials were weighed continuously during purging and evacuation, see Subsection 3.6. These data indicated two important features of outgassing for these particular samples. First, there was an unexpectedly large mass loss from the reflector specimen. The sample of double goldized Kapton, a material combination whose performance is not substantially degraded by exposure to moisture, lost 2.3×10^{-7} slugs/ft² of surface area. If this weight were surface adsorbed water vapor, it would correspond to a layer of water with an average thickness of about 700 Angstroms, or about 830 molecular layers thick. Second, the weight loss rate was nearly constant in time during evacuation until virtually all the gas had evolved. These results suggest that the customary assumption of an Arrhenius relationship to govern outgassing may not be appropriate for MLI. Consequently, the outgassing rate for each layer was

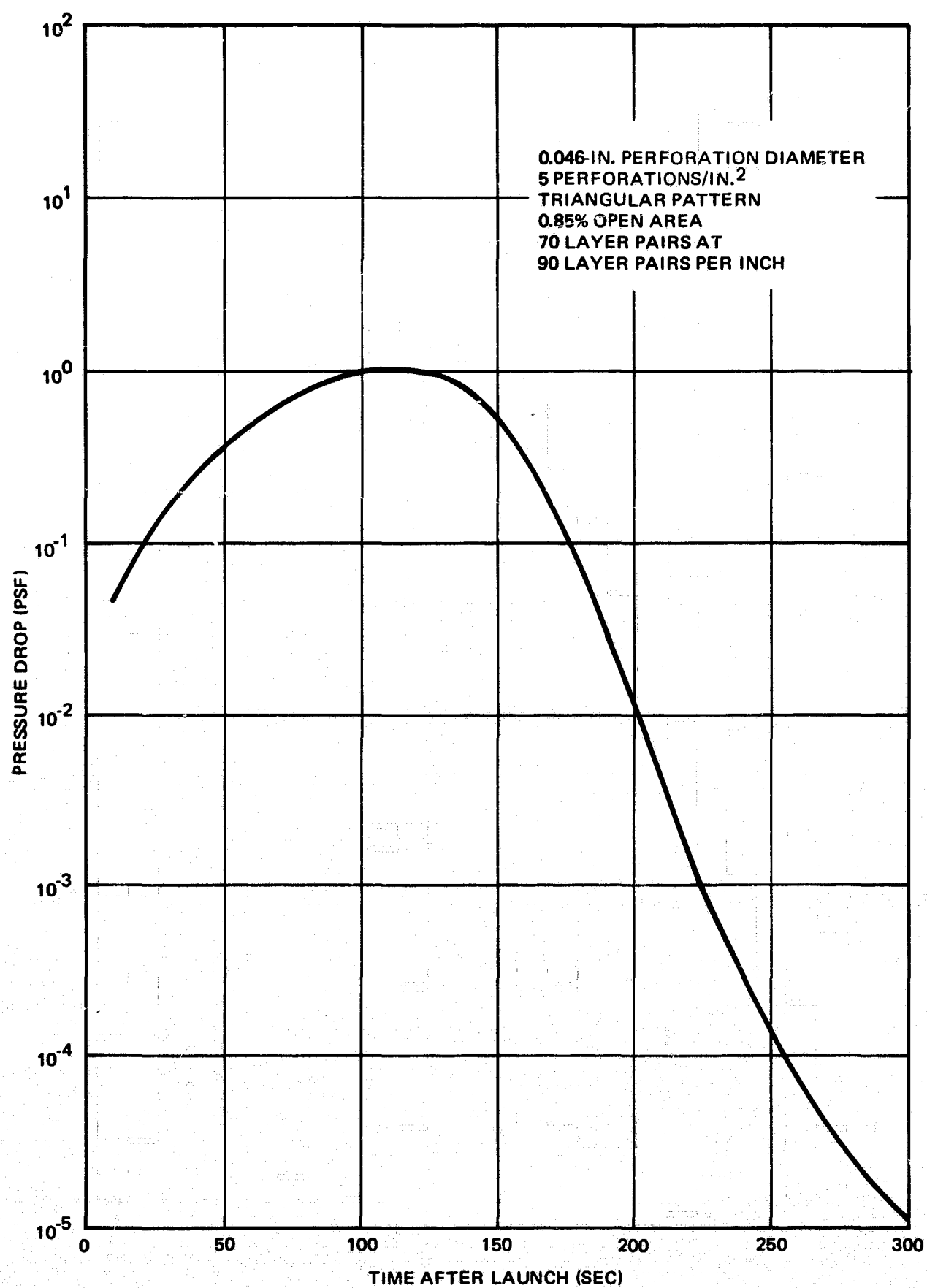


Figure 6-62. History of Pressure Drop Across MLI Panel--No Outgassing

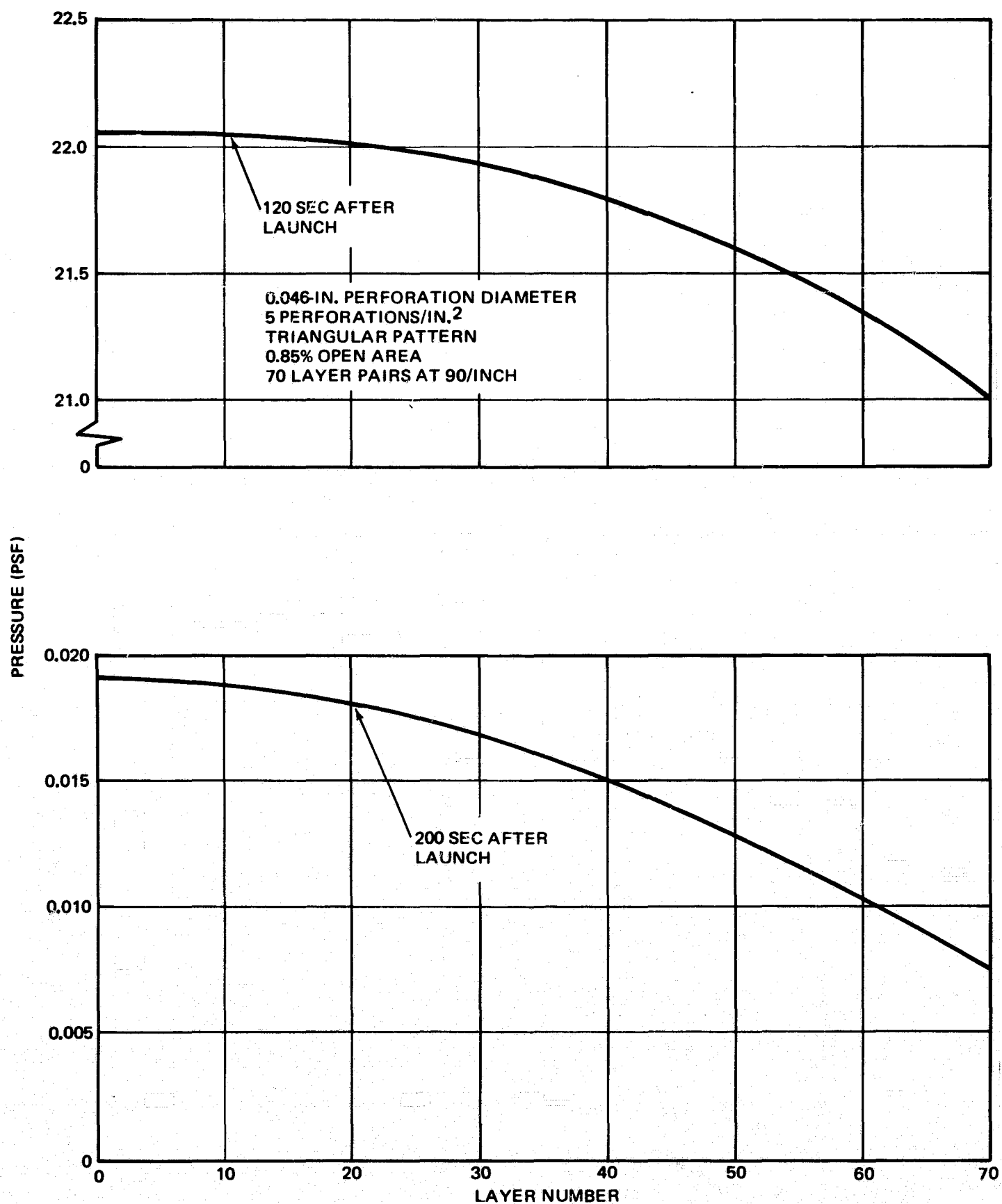


Figure 6-63. Pressure Profiles in MLI During Evacuation--No Outgassing

assumed to be constant until all the condensible gases had been volatilized. The total weight loss for each layer pair, including the measured weight loss of a Dacron B4A net spacer, was assumed to be 5.1×10^{-7} slugs/ft²/layer pair, counting both sides of the radiation shield. Since the vapor pressure is directly related to the rate of escape of molecules from a free surface, it was assumed that the outgassing rate is proportional to the vapor pressure of water. It is conceded that the physics of outgassing may not be correctly represented by this assumption. However, if there is indeed a relatively thick film (compared to the thickness of a molecular layer) the evaporation rate, in the absence of appreciable back pressure, should be approximately the outgassing rate.

Two further assumptions were made. First, MLI layers whose temperature is less than 336°R were assumed not to outgas. This temperature corresponds to a vapor pressure of 10^{-4} psf. Pressures this low will not affect the MLI heat transfer significantly. Second, it was assumed that the colder MLI layers do not remove gas evolved from the warmer layers by cryopumping.

With the above assumptions, the distribution of outgassing rate through the MLI may be calculated. This predicted rate is shown in Figure 6-64. Note, of course, that the outgassing rate for any layer drops to zero as soon as the originally present gas has volatilized. In actual practice the outgassing rate will not drop suddenly to zero, because there will always be a regime dominated by surface adsorption thermodynamics. However, this tail-off is a trivial part of the total outgassing according to the test results.

Summing the outgassing rates of Figure 6-64 gives the total assumed MLI outgassing rate history shown in Figure 6-65. The curve has been smoothed, rather than leaving it as the sequence of step functions used to calculate the curve.

As previously shown in Figure 6-61, the transient evacuation of the purge bag proceeds very rapidly in the absence of outgassing. Outgassing, as shown in Figure 6-65, takes place over a much longer period of time than does evacuation of the original purge gas.

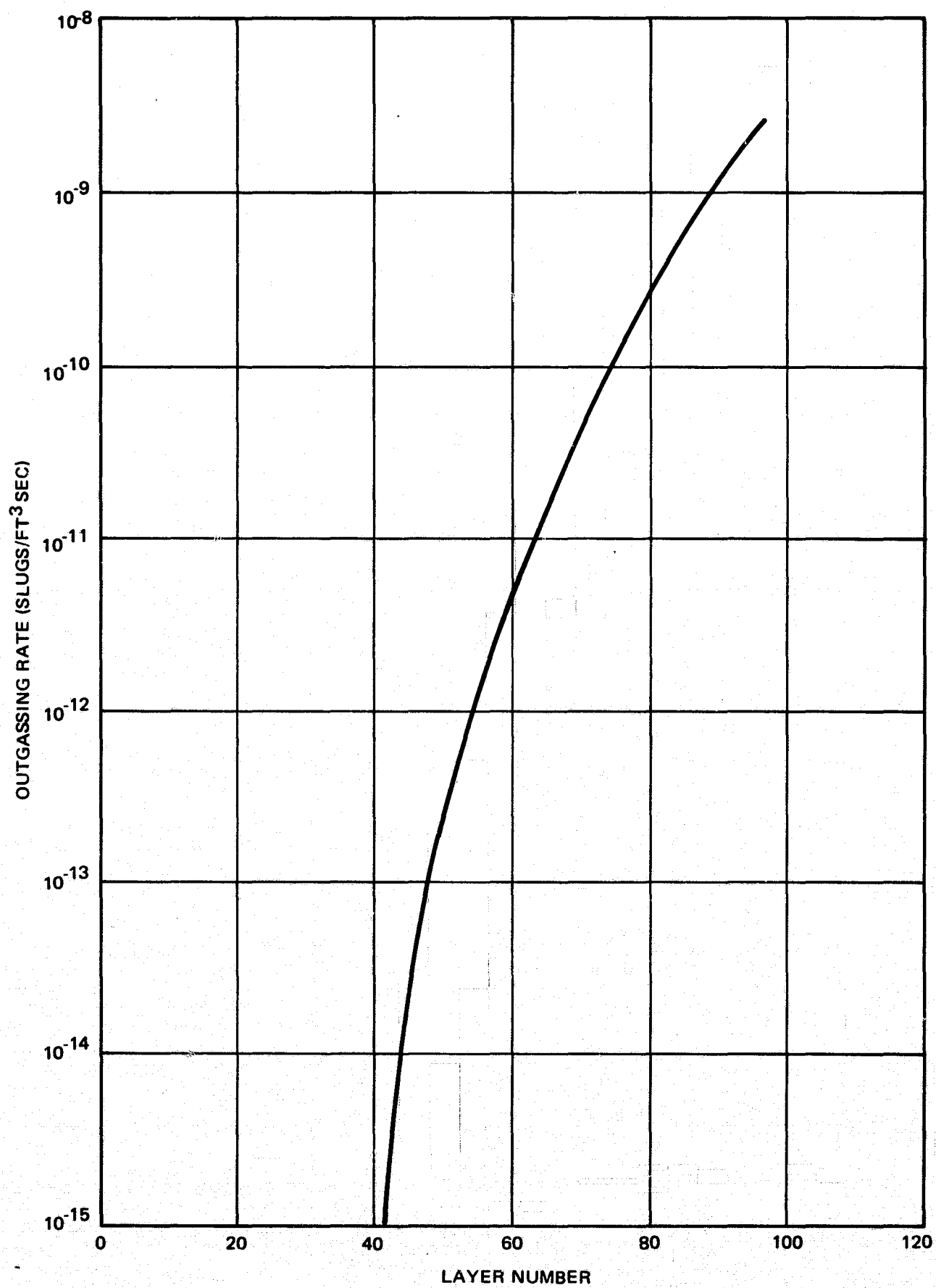


Figure 6-64. Distribution of Outgassing Rate Through the MLI

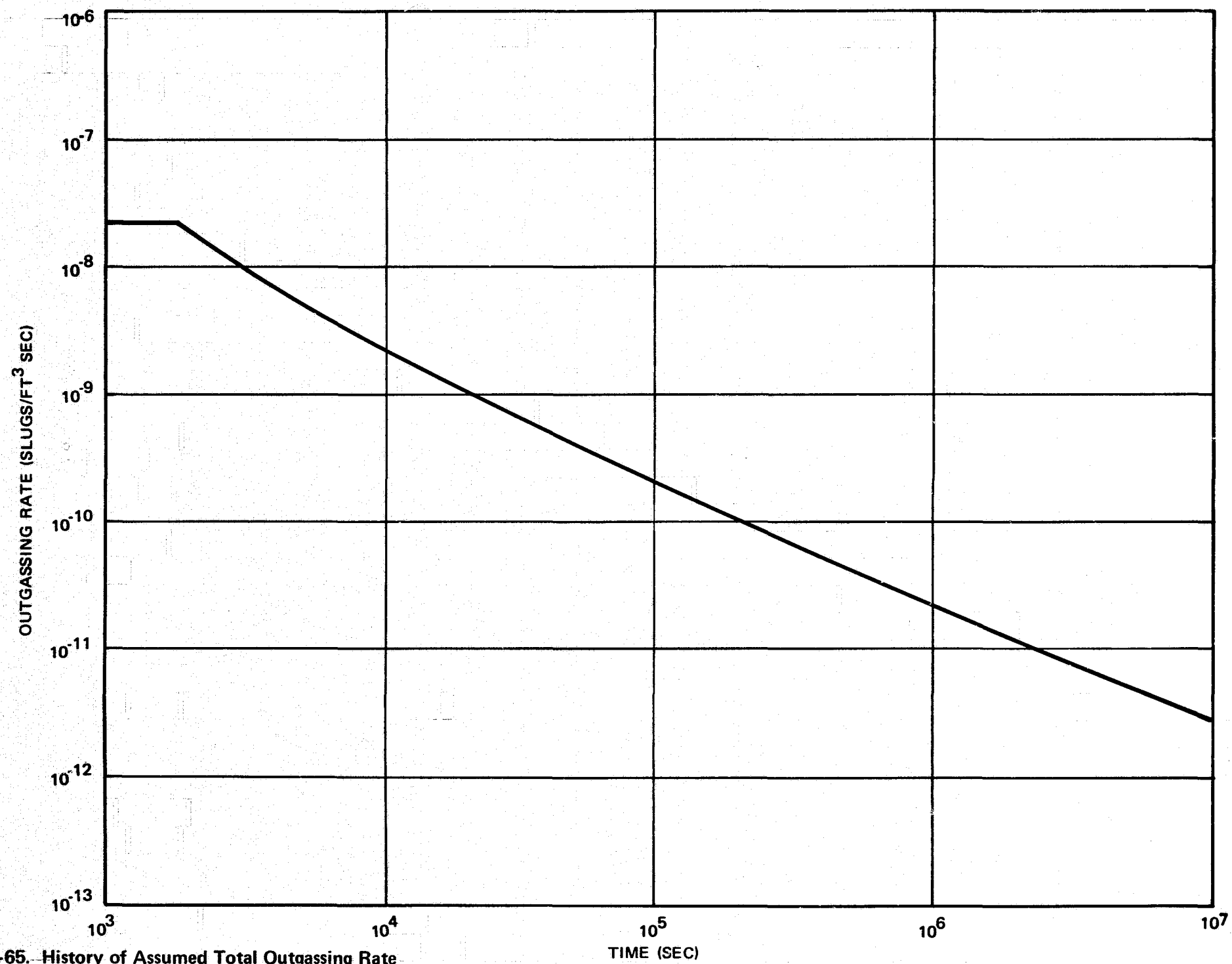


Figure 6-65. History of Assumed Total Outgassing Rate

Some typical pressure histories obtained with the assumed outgassing are shown in Figure 6-66. The solid lines refer to pressure histories utilizing tank support struts for venting as well as other vents. For the broken lines, the struts are not used to help vent the purge bag. The two curves (with and without strut venting) are indistinguishable when there are two 12-in. vents in the purge bag. Note that two 3-in. vents are more effective in venting the purge bag than the six struts. Since the six 6-in. valves assumed for the six struts would surely be much heavier than the two 3-in. vents, it is rather clear from Figure 6-66 that venting through the struts is undesirable.

6.5.3.3 Selection of Evacuation Valves

Decisions which must be made to define an efficient evacuation system obviously include the number and size of the valves. Boiloff weight penalties associated with different vent sizes and number of vents is shown in Figure 6-67. Evacuation through the struts was not included in the values in Figure 6-67. However, the effect of strut venting would be negligible in the lower weight penalty portion of the curve. The boiloff weight penalty presented in Figure 6-67 is the total boiloff less the boiloff which would have occurred had the purge bag always been at ambient pressure.

Note that the boiloff weight penalty for two 12-in. valves is about 7 lb (Figure 6-67). Thus, the maximum weight savings possible for vent systems achieving 10^{-4} torr in 1 hour (Figure 6-66) is 7 lb. The valves required to achieve this goal would be expected to be much heavier than the potential savings. Thus, it is clear that if outgassing is present, the criteria for purge-bag venting design must be based on minimum weight rather than on some arbitrary time to reach optimum MLI performance by reducing pressure.

The primary weight of the vent system will be in the valves and actuators. The valves will never be required to work under large differential pressure loads because the maximum pressure load is estimated to be about 0.5 psi. Under this load, the valves can be made of very light-weight construction, and the

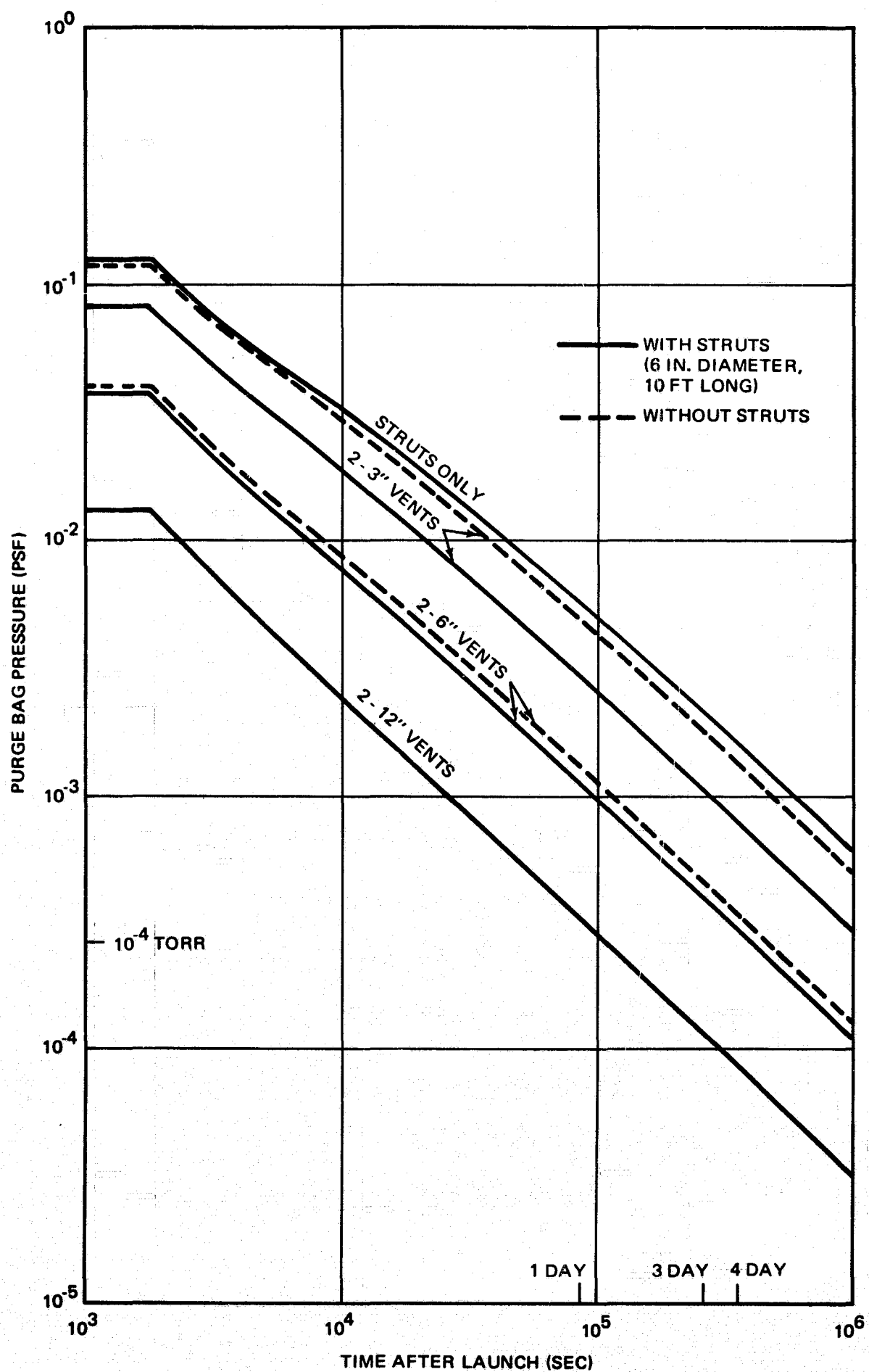


Figure 6-66. Effect of Vents on Purge Bag Pressure History

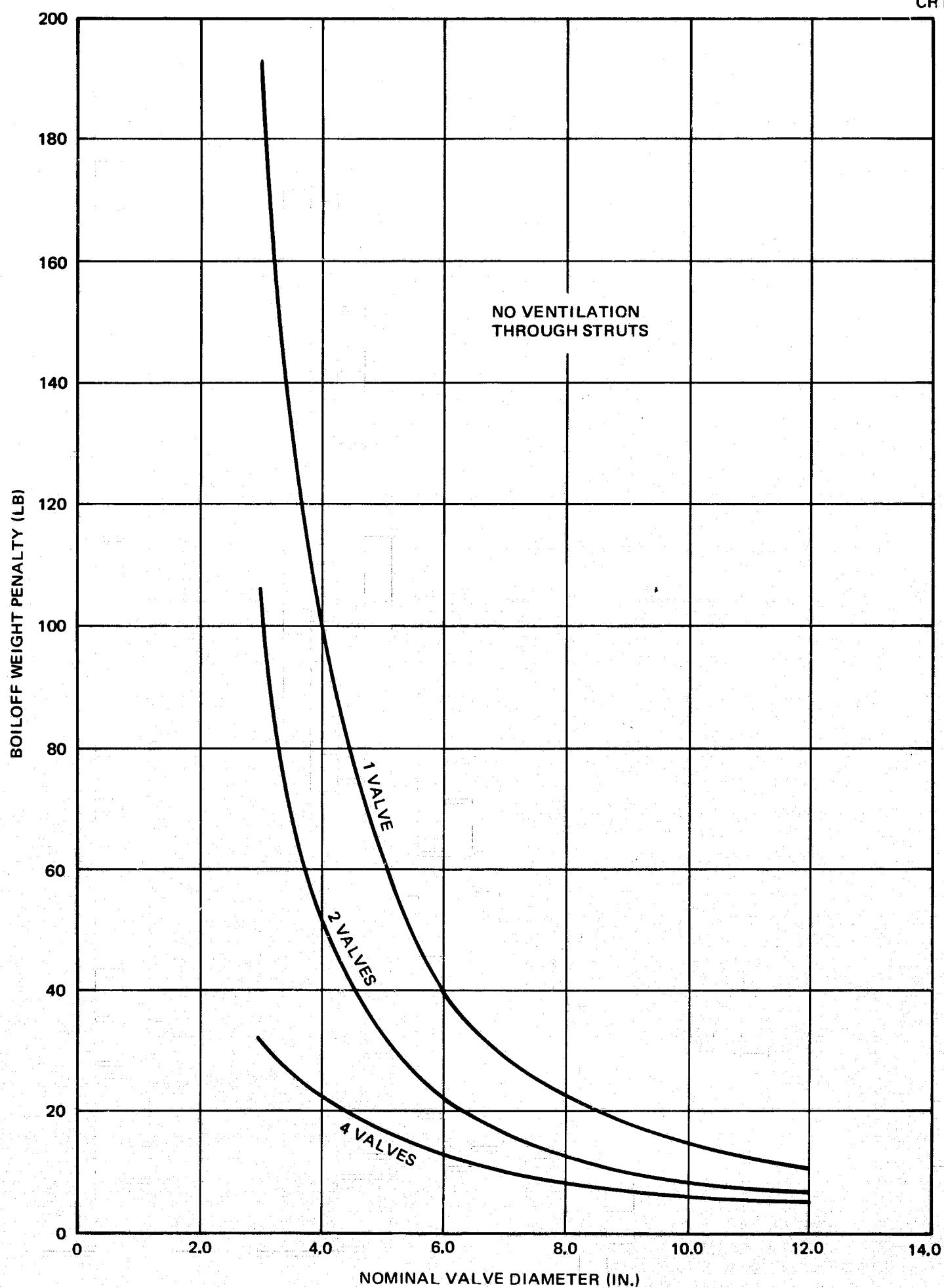


Figure 6-67. Effect of Evacuation Valves on Boiloff Weight Penalty

actuators can also be quite light. Figure 6-68 shows valve weights for two types of valves. The upper curve is the basic design curve for pneumatically actuated, thin-flange butterfly, cryogen valves for the Space Shuttle (Reference 18). These valves are designed for a 200-psi operating pressure in a liquid hydrogen environment. Redesigning the valves to the less severe environment and pressures of the purge-bag vent will achieve a substantial weight reduction. This weight reduction was estimated by allowing 20 percent of the valve weight for the actuator, dividing the remainder by two, and adding back the actuator weight. The net effect is a 40-percent reduction in valve weight. There is substantial justification for a weight reduction of 40 percent in that some valve designs are in this weight range, i. e., 40 percent less than a least squares fit of valve weights.

A still lighter valve design can be made using an electrical torque motor actuator. The J. C. Carter Company quotes the two points indicated in Figure 6-68. Using these points, a line parallel to the previous valve weight line was drawn to represent the torque motor actuated valve design.

Both the light-weight pneumatic valve and the torque motor design were used to perform an optimization analyses to select the size and number of valves. Figure 6-69 shows the optimization curves for the pneumatic valves. The minimum weight penalty would be one 8-in. valve, at a total weight penalty of 51 lb. This weight results from 23 lb of boiloff and 28 lb estimated for the valve. However, the minimum weight is seen to be rather insensitive to the number of valves. It is important to note that a rather severe outgassing environment has been assumed, resulting in larger boiloff weights than will probably be encountered. If four 3-in. valves were used, the valve weight would be 26 lb and the total weight penalty for the venting system, with a lower boiloff, could easily be less than it was for a single 8-in. valve.

The total weight penalties for electrical torque-motor-actuated valves are shown in Figure 6-70. Here, the weight difference among the minimum of the one-, two-, and four-valve curves is less than the probable accuracy of the calculations. The argument regarding outgassing will again bias the

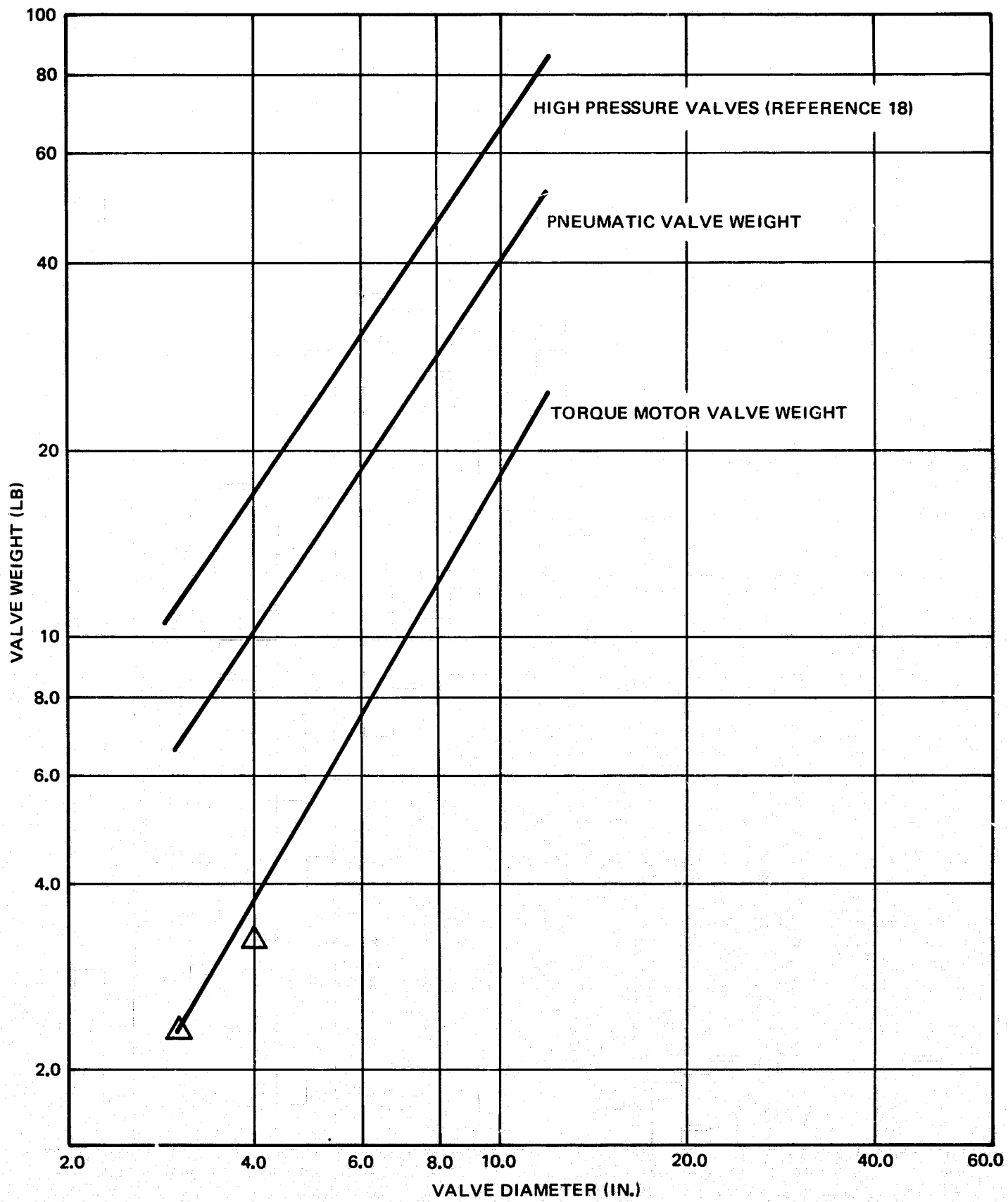


Figure 6-68. Valve Weights

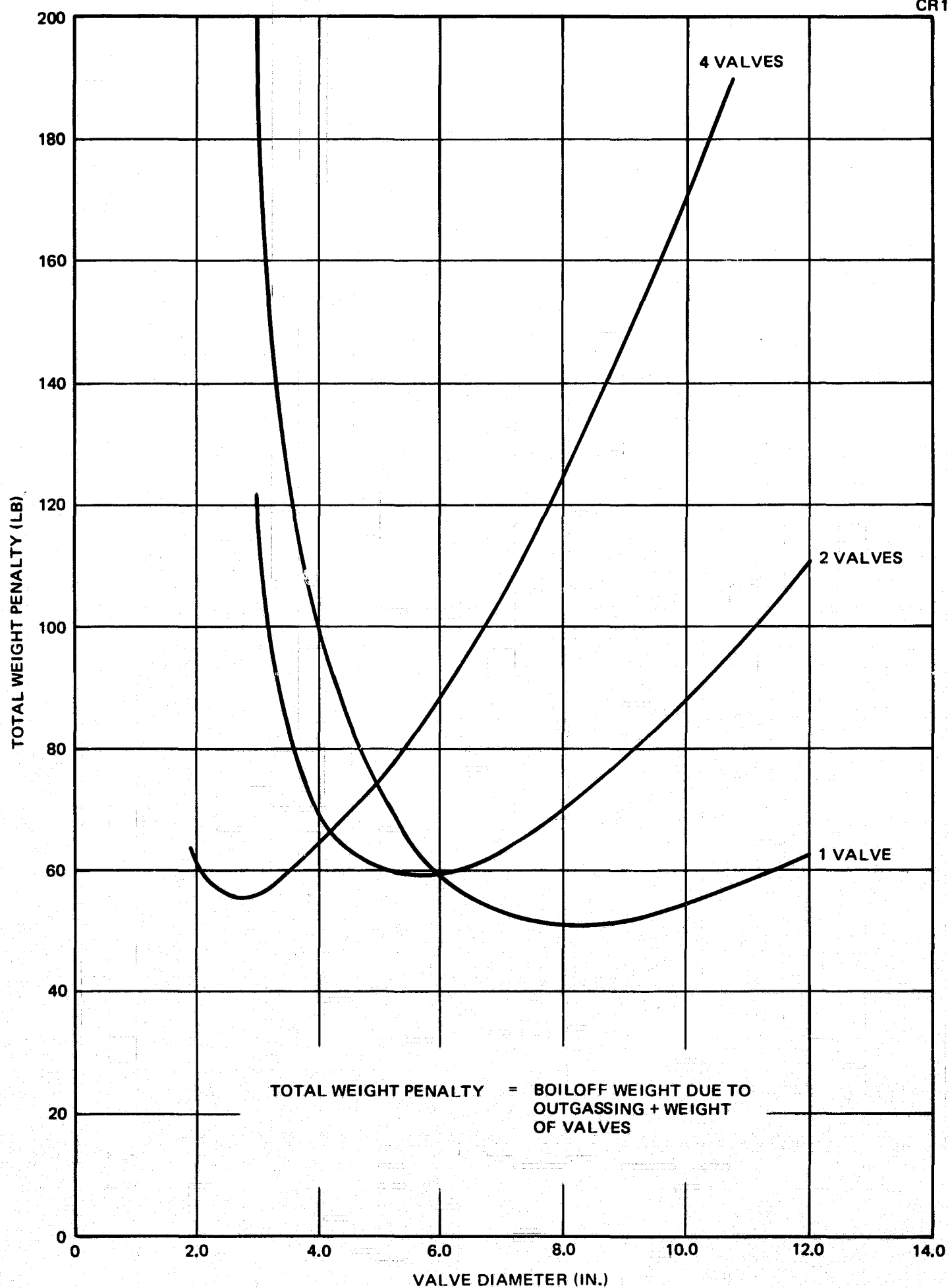


Figure 6-69. Total Weight Penalty with Pneumatically Actuated Evacuation Valves

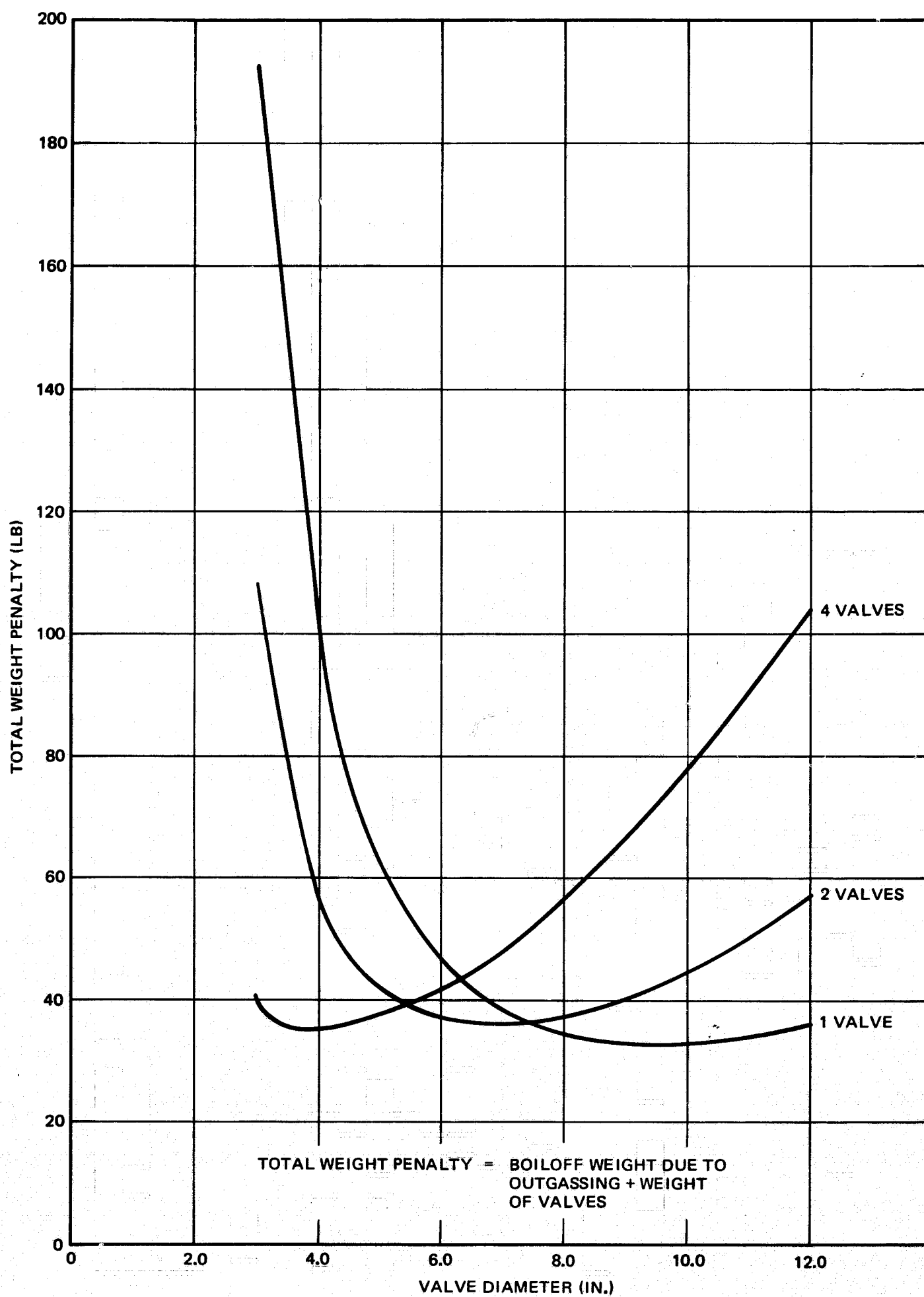


Figure 6-70. Total Weight Penalty with Torque Motor Actuated Valves

selection of the vent system toward choosing four 4-in. valves. There is a more important argument also favoring the 4-in. valves. Valves of this type and size are presently used in aircraft. Hence, the development cost would be minimized.

As previously discussed, all the optimum valving schemes, as defined by Figures 6-69 and 6-70, maintain a pressure greater than 10^{-4} torr for times ranging from 3 to 6 days. While these long time periods at greater than 10^{-4} torr may cause some trepidation, the potential weight savings show clearly that, if outgassing is present, a boiloff weight in excess of the minimum should be accepted in order to minimize the total weight of the system.

The above evacuation and outgassing calculations were made only for the LH₂ tank. If four 4-in. valves are also used for the LO₂ tank evacuation system, it can be expected that the pressure will drop more rapidly than for the LH₂ tank. As a result, the LH₂ tank evacuation valve design, as applied to the LO₂ tank, provides a conservative system design.

6.5.4 Reentry Repressurization

During reentry, it is necessary to prevent atmospheric gases from entering the MLI and subsequently condensing. For a purge-bag system, this is accomplished by repressurizing the volume within the purge bag with dry helium or nitrogen gas. Helium was selected as the repressurization gas for the MLI systems on both the LH₂ and LO₂ tanks. For the LH₂ tank MLI system, helium is the only suitable gas for repressurization. However, nitrogen, as well as helium, could be used for the LO₂ tank MLI system and was shown to be thermally better than helium in the thermal analyses, Subsection 6.2. Helium was selected for the LO₂ MLI system because it was anticipated that the overall system could be better with a single repressurization system. With a single repressurization gas, only one supply bottle and one control system need be carried on board the vehicle. This results in a reduction in repressurization system complexity and weight.

The final decision as to the optimal choice between using nitrogen or helium to repressurize the LO₂ tank MLI will depend on numerous factors beyond the scope of this study. For example, the vehicle design may utilize nitrogen to repressurize the storage bay. If this system could also be used to repressurize the purge bag on the LO₂ tank, nitrogen would probably be the more desirable repressurization gas. It should be noted that the selection of nitrogen in future studies would not significantly alter the study results reported herein. Only the repressurization system hardware design for the LO₂ tank would be changed, since the thermal analyses were conducted for both gases (Subsection 6.2), and the MLI materials and configuration are not affected by the purge and repressurization gas selected.

6.5.4.1 Repressurization Pressure History

Two repressurization schemes were considered for the LH₂ and LO₂ tanks. The first assumed that the pressure in the purge bag was maintained at 0.5 psi above ambient for the entire reentry period (see Figure 6-21). This pressure history had the advantage of providing choked flow at the bag leakage points during the free molecular flow and transition regimes. This would help prevent entry of condensibles into the MLI. However, the amount of heat transferred into the LH₂ and LO₂ tanks during reentry would be significantly increased by the high purge-bag pressure. The second repressurization scheme (see Figure 6-21) assumed that the purge-bag pressure was approximately twice the ambient pressure up to an ambient pressure of 0.5 psi. After this point, the purge-bag pressure was maintained at 0.5 psi above ambient. This scheme had the advantages of a reduced total heat transfer during reentry because of the lower overall purge-bag pressure. A repressurant gas outflow would occur at all leakage points and would inhibit condensable entry into the purge bag. This scheme has the disadvantage of requiring a more complex flow control system to provide the proper purge-bag pressure history.

The integrated heat transfer to the LH₂ tank is shown for the two pressure-history schemes in Figure 6-71. The difference in the heat transfer between the two pressure schemes represents 113 lb of hydrogen boiloff. Since this is

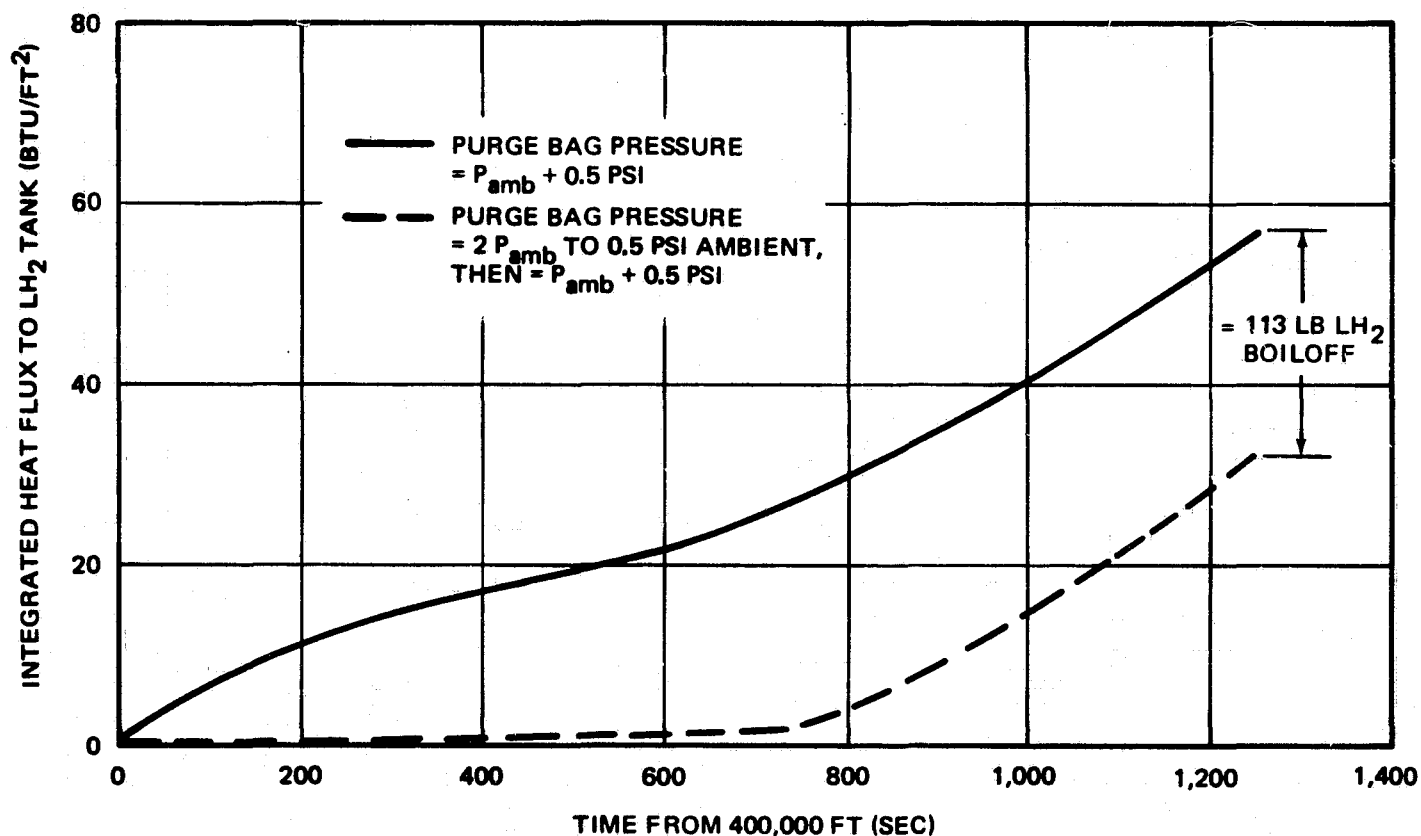


Figure 6-71. Effect of Purge Bag Pressure History on Reentry Heat Transfer

a very significant increase, the scheme with the lower overall pressure was selected for reentry repressurization. This pressure history choice would, however, require the design of a sensitive control system that will operate over a pressure range of several orders of magnitude. Although the design of such a device was out of the scope of this contract, the results of a cursory study of its feasibility seemed promising enough to warrant assuming this lower reentry pressure history for the thermal analyses reported in Subsection 6.2.

6.5.4.2 MLI Compression Due to Repressurization

To establish whether or not the repressurization gas would compress the MLI during reentry, computations were made using the PHEP computer code. Figure 6-72 shows the minimum predicted pressure in the MLI on the LH₂ tank during reentry. The external pressure shown is the pressure in the area between the MLI and purge bag. The pressure differential across the MLI Panel as a function of the reentry time is shown in Figure 6-73. Note

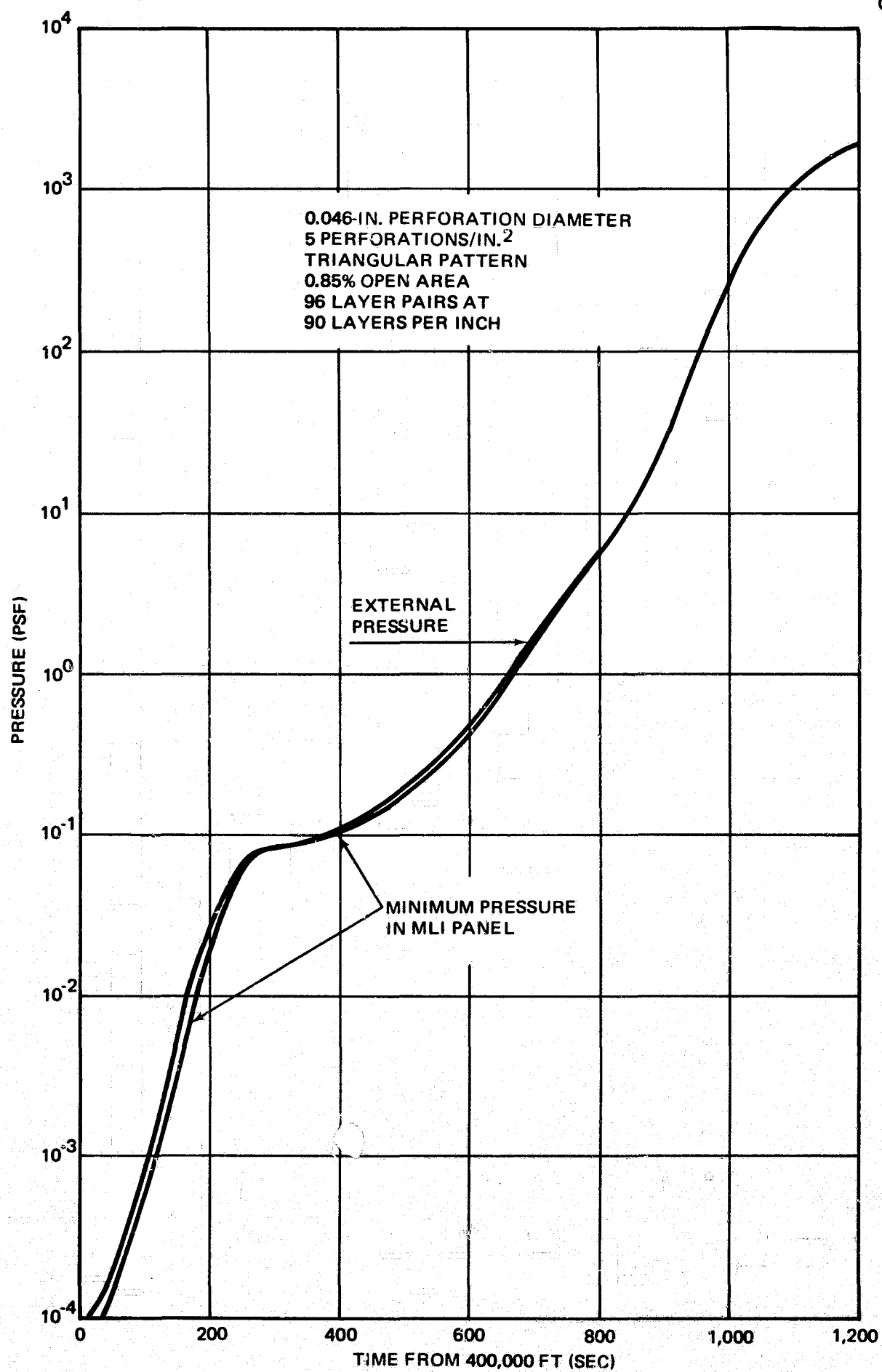


Figure 6-72. Pressure History in MLI Panel During Reentry

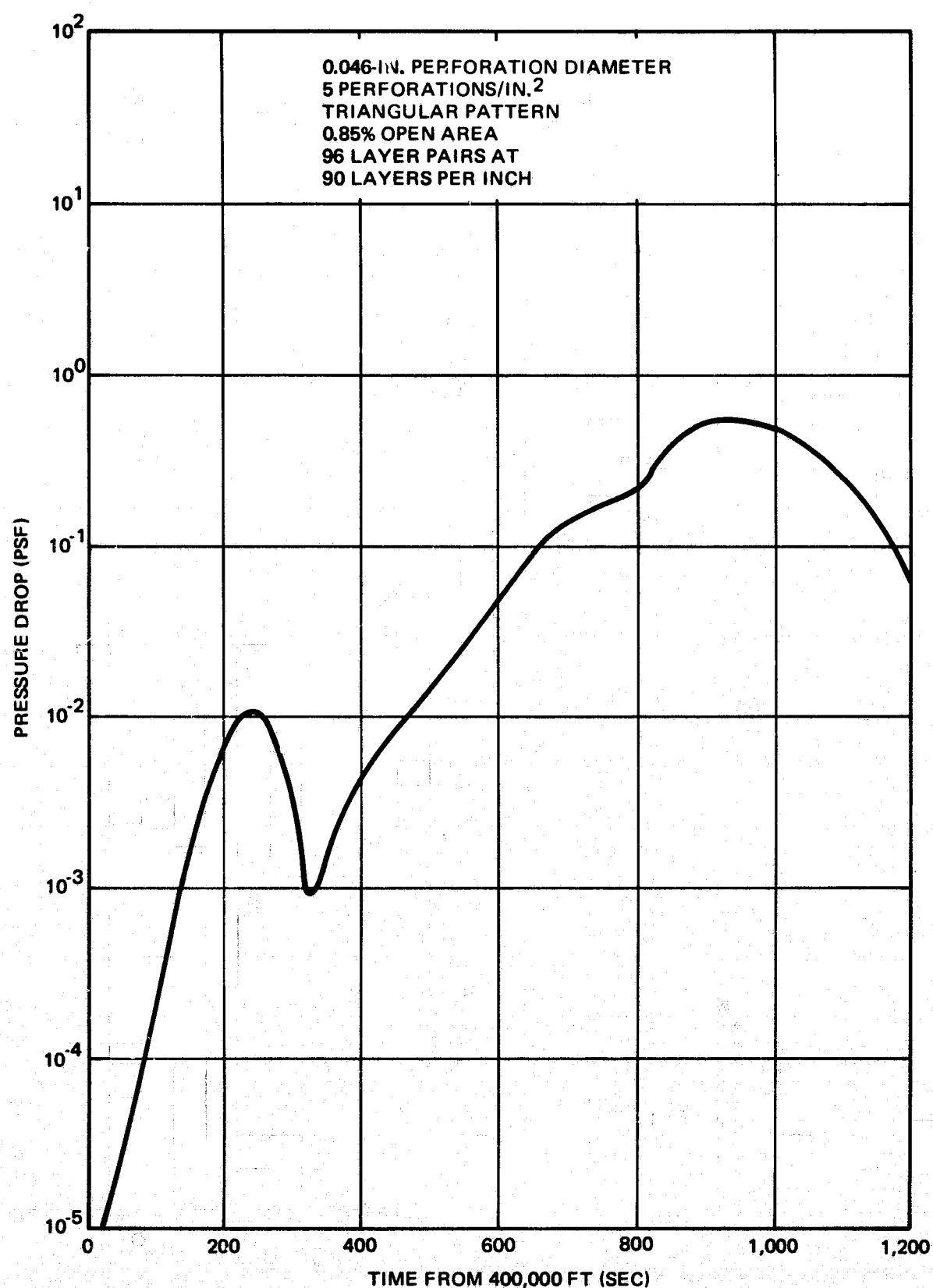


Figure 6-73. Pressure Differential Across MLI Panel During Reentry

that a maximum pressure differential of 0.55 psf (3.82×10^{-3} psi) occurs at approximately 940 sec in the continuum flow regime. In the free molecular flow regime, the maximum pressure differential is 1.1×10^{-2} psf (7.6×10^{-5} psi) at 240 sec. The pressure profiles for these two time points are shown in Figure 6-74.

Because of the very low computed pressure drops across the insulation coupled with the MLI compression test results (Section 3), the compressive effects of the repressurization gas are considered negligible for the LH₂ tank. Similarly, it can be shown that repressurization gas compression effects on the LO₂ tank MLI will be negligible.

6.5.4.3 Repressurization Gas Usage

The repressurization gas used will consist of the gas required to increase the pressure within the purge bag and the gas leakage through the zippers and any small holes in the purge bag. It is anticipated that the zipper and pinhole leakage rates will be negligible (see Subsection 6.5.2.2) and can be omitted. The pressurization gas flow rates required to increase the bag pressure for the two tanks are plotted in Figure 6-75. The total helium mass used during the reentry repressurization is 2.3 lb (assuming an average gas temperature of 300°R) for the LH₂ tank and 0.9 lb (assuming an average temperature of 350°R) for the LO₂ tank.

6.5.4.4 Line Sizes Required for Repressurization

The repressurization gases must flow from the helium storage bottle to the supports, through the supports, and out the orifices at the junction of the tank and the supports. Of interest is the pressure drop from the control system to the volume within the purge bag. Unless the pressure in the line and supports is nearly equal to the purge-bag pressure, the volume within the tank supports and line (approximately 15 ft³) will act as an accumulator and will continue to supply repressurization gas to the purge bag for some time after the control valve is closed. This condition, if allowed to exist, might cause the purge bag to rupture due to overpressure. Consequently, it

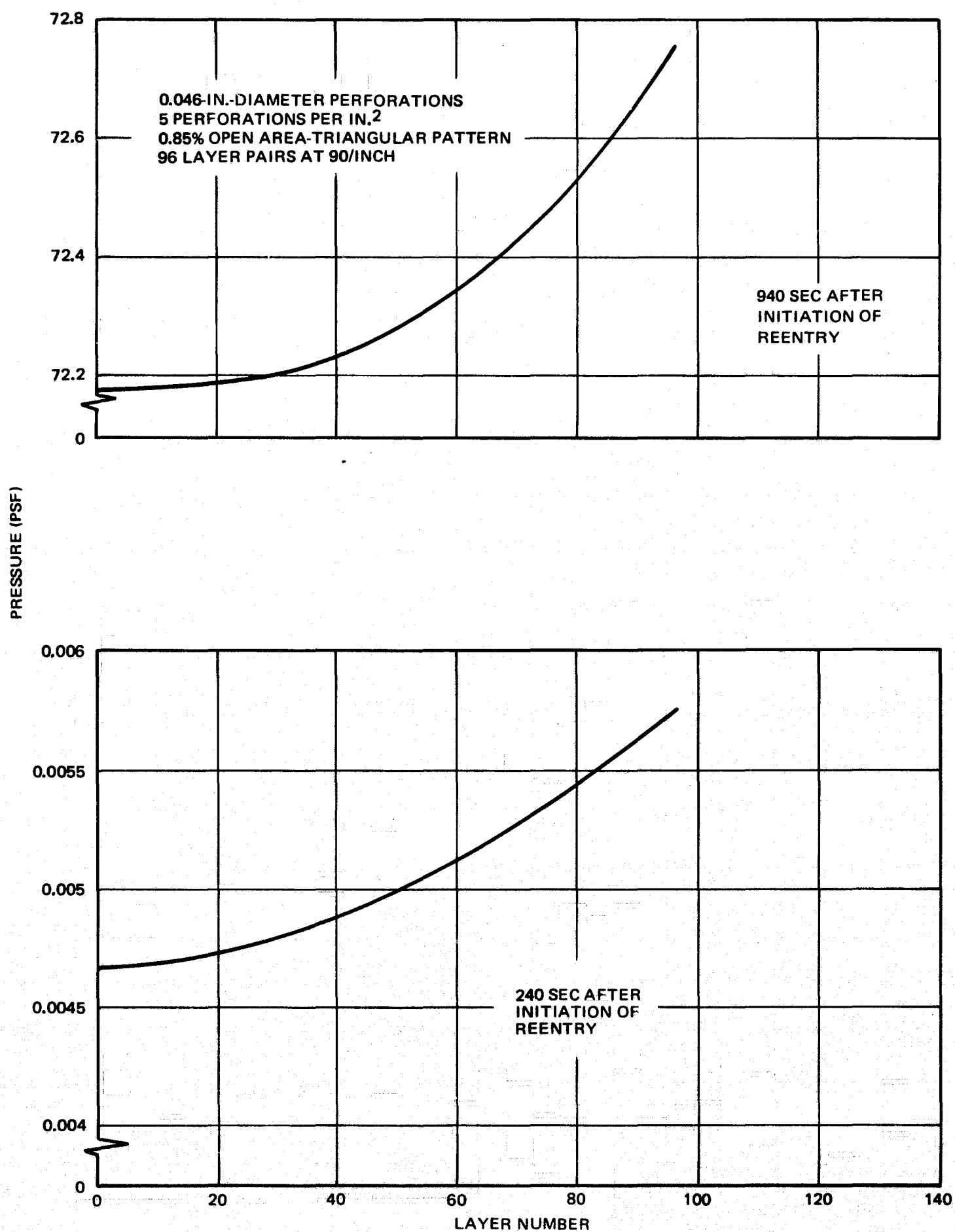


Figure 6-74. Pressure Profiles in MLI During Repressurization

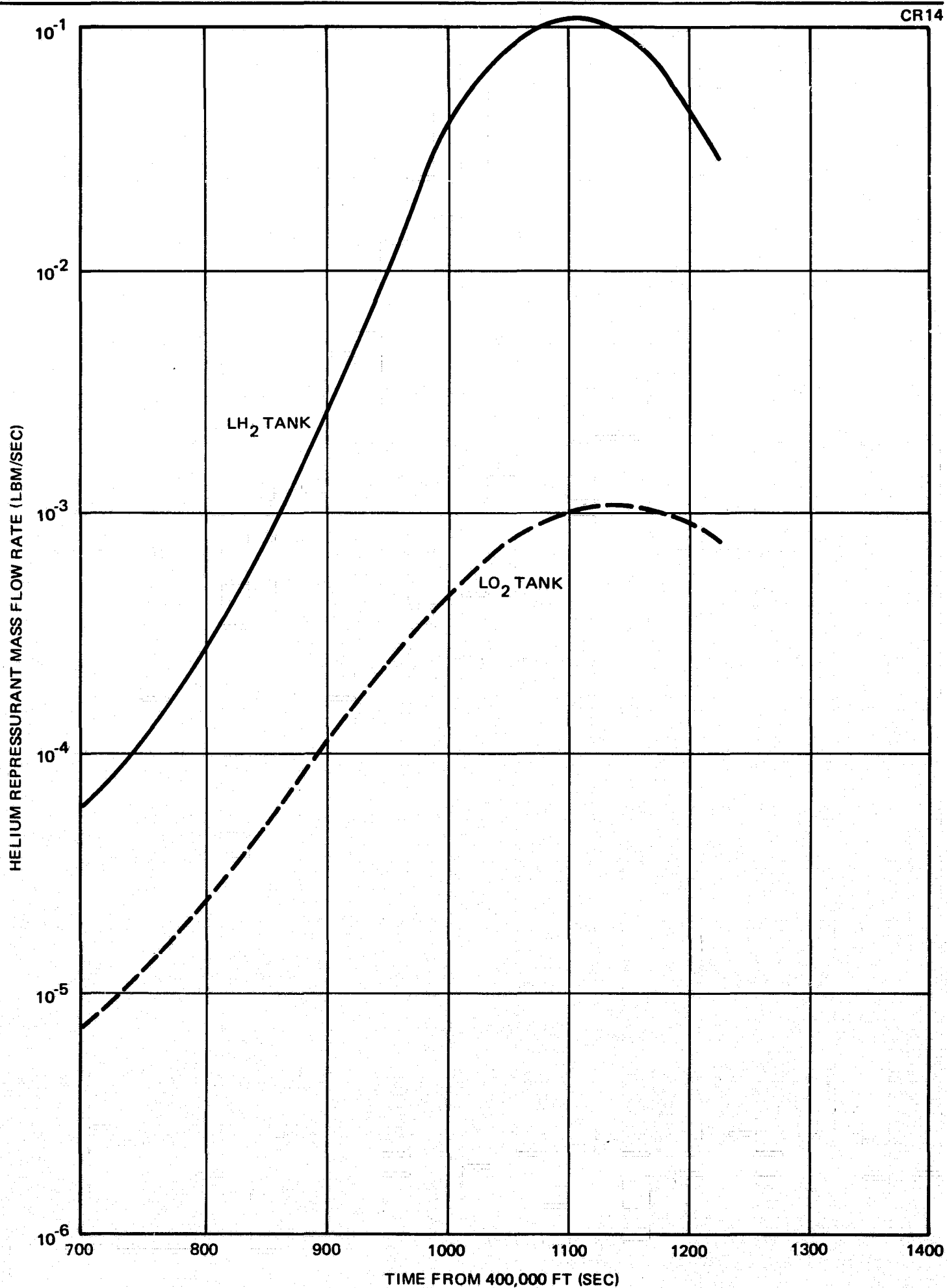


Figure 6-75. Repressurization Gas Flow Rates

is necessary to ensure that the total pressure drop down the supports and across the outlet orifices is small. Because of the large diameter of the supports, the principal pressure drop occurs at the orifice. This drop was calculated to be approximately 0.7 psi for the LH₂ tank and 0.7×10^{-4} psi for the LO₂ tank at the maximum flow rates. These pressure drops will not allow the struts to function as accumulators.

The maximum pressure drop from the distribution manifold to the struts for each of the 13-ft-long, 1-in. lines will be 0.6 psi for the LH₂ tank MLI system. A 3-ft-long, 2-in. line from the control system to the distribution manifold will add an estimated 0.1 psi, giving a total of 0.7-psi maximum pressure drop from the control system to the struts on the LH₂ tank. The maximum pressure drop from the LO₂ tank MLI system distribution manifold to the struts for each of the assumed 20-ft-long, 1/4-in. lines will be 0.2 psi. An assumed 60-ft-long, 1/2-in. line from the control system to the LO₂ tank distribution manifold will add an additional 0.4 psi, giving a total of 0.6-psi pressure drop from the control system to the struts on the LO₂ tank. Since the volume of gas within the tubing is small compared to the strut and purge bag volume, all these pressure drops are acceptable and will not cause the tubing to act as an accumulator.

6.6 CONCLUSIONS AND RECOMMENDATIONS

As a result of the thermal analyses, it was concluded that, of the system configurations considered, a tank-mounted MLI composite which did not include foam on the inner wall of the tank was the best. It should be noted, however, that a reentry trajectory with a longer reentry period could result in the need for including foam. This will be particularly true if a cruise period at low altitude is added to the reentry trajectory. All of this assumes, of course, that the storage of the cryogen is required during the reentry and cruise periods. It is recommended that future studies for longer reentry periods also include a consideration of foam mounted on the exterior surface of the tank. This configuration could prove to be competitive to the internal foam if effective and reliable sealing of the foam can be assured.

The thermal analyses showed that the Dacron B4A separator material was clearly the most desirable of those considered. It was concluded that, for the LH₂ tank, a total of approximately 68 layer pairs of DGK/Dacron B4A would be optimum for a 7-day mission and approximately 94 layer pairs of DGK/Dacron B4A would be optimum for a 30-day mission. For the LO₂ tank, it was concluded that a total of approximately 83 layer pairs would be optimum for a 7-day mission and approximately 92 layer pairs would be optimum for a 30-day mission.

Helium was selected as the purge and repressurization gas for both the LH₂ and the LO₂ tank. The analyses showed clearly that helium with no foam was the optimum system for the LH₂ tank. However, the optimum purge and repressurization gases for the LO₂ tank are not as clear. The final selection of these gases for the LO₂ tank will involve additional tradeoff studies. It is recommended that these additional studies be accomplished but that they await a better definition of other vehicle parameters.

Helium flow rates of 1.7×10^{-3} lbm/sec and 8.4×10^{-4} lbm/sec were selected for the LH₂ and LO₂ tank purge volumes, respectively, to reduce the condensibles to 1 percent or less within 1 hour. The maximum helium flow rates required during the chilldown period are 5.5×10^{-3} lbm/sec for the LH₂ tank purge volume and 9.4×10^{-4} lbm/sec for the LO₂ tank purge volume. The total helium usage predicted for the ground-hold period was 8.22 lb for the LH₂ tank and 3.35 lb for the LO₂ tank. The total helium usage for repressurization was predicted to be 2.3 lb for the LH₂ tank and 0.9 lb for the LO₂ tank. Additional conclusions reached as a result of the purge, evacuation, and repressurization analyses included the selection of four 4-inch butterfly valves for evacuation of the purge volume and the line sizes required for the system.

The purge, evacuation, and repressurization analyses must be considered somewhat preliminary because of the mathematical model and gas property assumptions which were required. Experimental evaluation of these models and properties is recommended. This includes testing designed to determine

such things as diffusion coefficients as a function of temperature and pressure, environmental effects on outgassing, outgassing rates of the component materials in the MLI system, and evaluation of mathematical models. Future testing should also include the evaluation of a full-scale purge, evacuation, and repressurization system.

The thermal analyses showed that the repressurization pressure history can have a significant impact on the overall performance of the system. Further studies regarding the selection and design of the control system for regulating the repressurization pressure history are recommended.

Section 7

STRUCTURAL ANALYSES—TASK 5

The objective of Task 5 was to verify, analytically, the capability of the MLI system design to withstand the structural loading during a typical ILRV Orbiter mission. This included analyses of the tensile and compressive loads on an MLI panel, the tensile loads on the purge bag, and the thermal contraction compatibility of the system components.

7.1 MLI STRENGTH ANALYSES

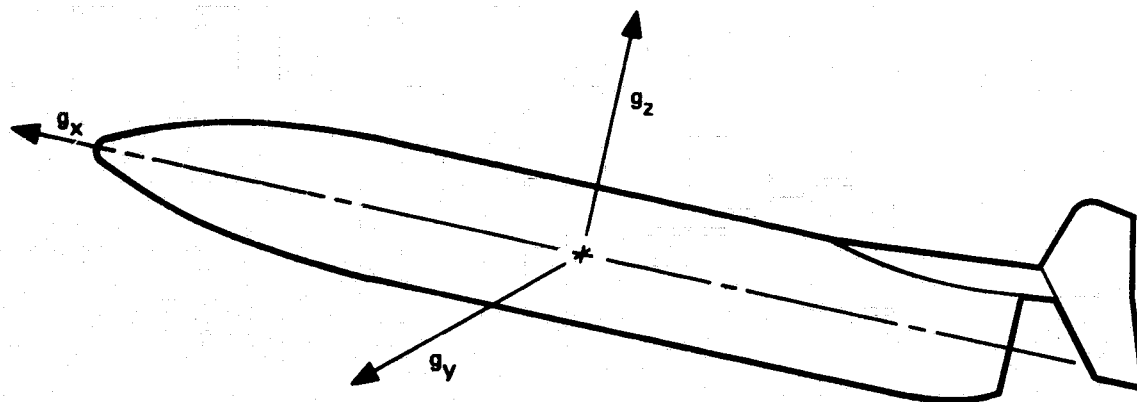
The quasi-static loads that affect the MLI panels are produced by the vehicle accelerations during ascent and reentry. These anticipated acceleration loading histories are presented in Figures 4-7 and 4-8, Section 4, and the most severe loadings are summarized in Table 7-1. As indicated, the maximum loading during both Booster and Orbiter burn is 3 g's acting parallel to the vehicle axis. During reentry, the components parallel and perpendicular to the vehicle axis are 1.32 and 2.3 g's, respectively. Since the lateral acceleration (g_y) during both ascent and reentry is negligible, it was not considered.

The MLI design consists of gore-shaped panels which are held together with lacing thread and Velcro in a butt joint configuration. Two layers of MLI panels are used to obtain the desired MLI thickness. Each panel consists of the reflectors and separators sandwiched between face sheets on the outer surfaces of the panel. The panel is held together with fasteners. The face sheets consist of a fabric with resin-impregnated areas (straps) fabricated onto the fabric. These 1-inch-wide straps provide bearing areas for the fasteners as well as providing load-carrying capability for the panel. The resin-impregnated areas are continuous on the inner face sheet of both the inner and outer panel because these face sheets are the primary load-carrying members of the MLI system. Due to the location of the tank-support

Table 7-1
MAXIMUM VEHICLE G LOADS

	g_x	g_y	g_z	Time
Ascent				
Booster burn	3	~ 0	~ 0	$140 < t < 200$ sec
Orbiter burn	3	~ 0	~ 0	$390 < t < 420$ sec
Reentry	-1.32	~ 0	2, 3	$t = 700$ sec*

*Time from 400,000 ft



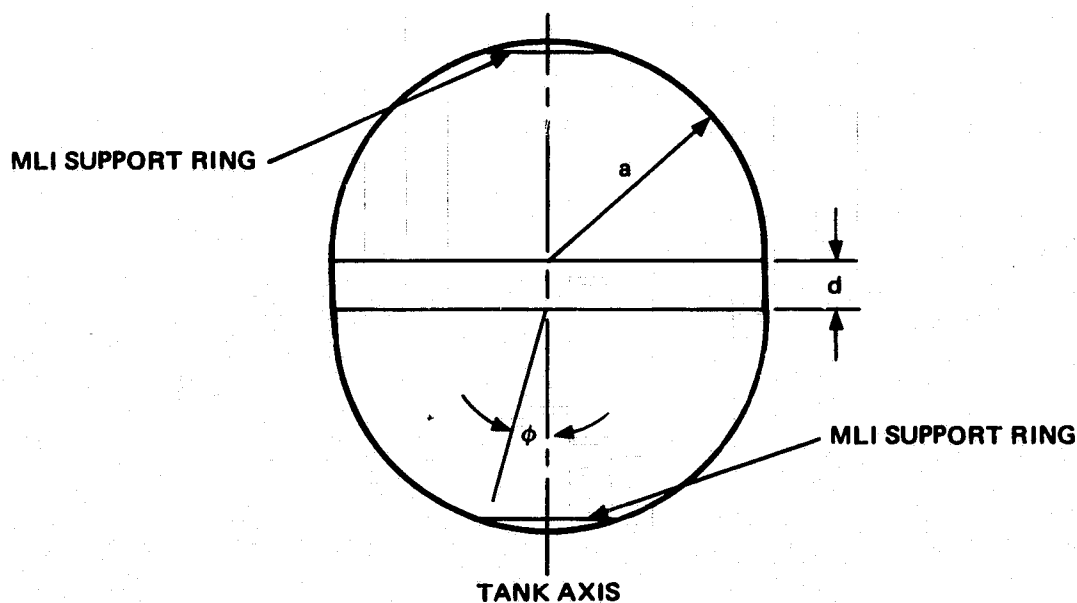
attachment points in the vehicle, the LO_2 tank axis is normal to the axis of the vehicle while the LH_2 tank axis is parallel to the vehicle axis. The tank axis is that axis perpendicular to the plane of the interior equatorial reinforcing ring. The resin impregnated straps on the inner face sheets are oriented in both the tank-axis and perpendicular-to-the-tank-axis directions forming a "waffle" pattern on the face sheet.

Resin impregnated tabs are also located on the ends of the inner face sheet of each gore panel. These tabs are fastened to an MLI support ring, which is fastened to the tank, and therefore, carry the load between the support ring and the MLI panel. Both the LO_2 and the LH_2 tanks have these MLI support

Table 7-2

LH₂ AND LO₂ TANK DIMENSIONS

	LH ₂	LO ₂
a	95 inches	63.5 inches
d	18 inches	0 inches
ϕ_o	11.5 degrees	17.4 degrees



rings to which the gore panels are attached. The LO₂ tank is completely spherical while the LH₂ tank has spherical end domes with a cylindrical center section, see Table 7-2.

7.1.1 Analyses for Loading Parallel to Tank Axis

Acceleration loads parallel to the tank axis are the significant loads for the LH₂ tank during ascent and for the LO₂ tank during reentry. During loading parallel to the tank axis, the MLI panels are hanging from the upper support ring, are draped over the upper half of the tank, and hang free around the lower half of the tank, see Figure 7-1. Because of tank symmetry and since

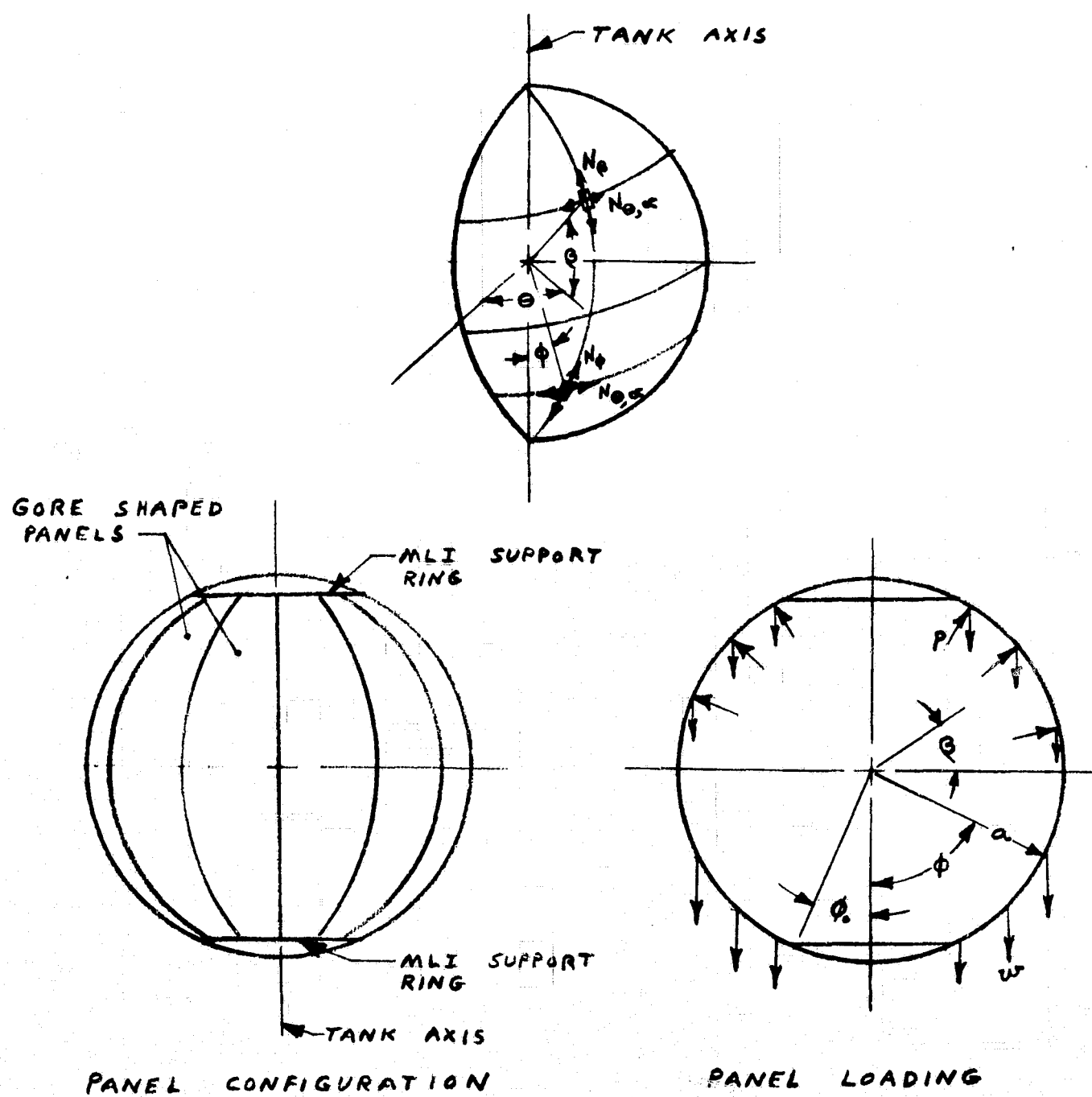


Figure 7-1. Loading Model When Acceleration is Parallel to Tank Axis

the face sheet straps carrying these loads follow the contour lines of the gore segments, $N_{\theta, \alpha}$ loads need not be considered for acceleration loading parallel to the tank axis.

The tensile loads in the face sheet straps on the lower tank dome due to a 1-g axial loading are given by the equation:

$$N_{\phi} = \frac{w a}{\sin^2 \phi} (\cos \phi_0 - \cos \phi)$$

where:

N_{ϕ} = the tensile load in lb/inch of circumferential distance at the location defined by the angle ϕ .

ϕ = the angle measured from the lower part of the tank axis, see Figure 7-1.

ϕ_0 = the angle from the tank axis to the MLI support ring.

w = the weight density of the MLI panel in lb/inch²

a = the tank radius

The tensile load (N_1) in the face sheet straps at $\phi = 90$ degrees is:

$$N_1 = w a \cos \phi_0$$

For the LH₂ tank, the tensile load in the face sheet straps over the cylindrical section will be:

$$N = N_1 + w x$$

where:

x = the distance up from the base of the cylindrical section.

The tensile load at the top of the cylindrical section (N_2) will be:

$$N_2 = N_1 + w d$$

where:

d = the length of the cylindrical section

The tensile loads in the face sheet straps on the upper tank dome due to a 1-g axial loading are given by the equation:

$$N = \frac{w a \sin \beta + N_{1, 2}}{\cos^2 \beta + \frac{\sin^3 \beta \cos \beta}{(\sin \beta \cos \beta + \beta)}}$$

where:

N_{β} = the tensile load in lb/inch of circumferential distance at the location defined by the angle β .

β = the angle measured from a plane through the base of the upper dome, see Figure 7-1.

Friction between the tank and MLI panels was conservatively not considered.

The maximum load in the face sheet straps will occur at the upper end of the gore panels near the upper support ring. The angle β at this point is $90 - \phi = 78.5$ and 72.6 degrees for the LH_2 and LO_2 tanks, respectively (see Table 7-2). The values of a and d are also shown in Table 7-2. A conservative (slightly high) value for the weight density (w) of a panel is 1.32×10^{-3} lb/inch². The circumferential dimension at the end of a gore panel (at $\beta = 78.5$ degrees and 72.6 degrees) is 7.93 and 11.93 inches for the LH_2 and LO_2 tanks, respectively. Using these values, the total loads to be supported at the upper end of a gore panel in a 1-g field are 13.35 and 7.45 pounds for the LH_2 and LO_2 tanks, respectively. There are three face-sheet straps to support the load at this point. These straps are 1 inch wide and 0.012 inch thick. Also, from Table 7-1, the maximum acceleration parallel to the tank axis is 3 g's for the LH_2 and 2.3 g's for the LO_2 tank. Therefore, the maximum stresses in the face-sheet straps resulting from loading parallel to the tank axis are 1,110 and 475 psi for the LH_2 and LO_2 tank MLI systems, respectively. These results are included in Table 7-3.

Table 7-3
MAXIMUM STRESSES ON MLI
LOAD-CARRYING COMPONENTS

	Maximum Stress (psi)	
	Acceleration Loading Parallel to Tank Axis	Acceleration Loading Perpendicular to Tank Axis
LH₂ Tank MLI System		
Face-Sheet Straps	708	740
Velcro	Negligible	5.9
Lacing Thread	Negligible	< 1.2 lb/thread
LO₂ Tank MLI System		
Face-Sheet Straps	313	648
Velcro	Negligible	5.2
Lacing Thread	Negligible	<1 lb/thread

The tensile strength of the Silicone/Nomex HT-287 face sheet straps was determined in Task 1, Section 3, after the material had been cycled 100 times from -320 to 650°F. In the Orbiter application, the temperature of these inner face-sheet straps will vary between the cryogenic temperature of the tank and ambient temperature. The test results showed strengths of 3,000 to 3,600 psi for the Silicone/Nomex HT-287 material in this temperature range, see Table 3-14 of Section 3. Consequently, the face-sheet straps have strength margins over 2.5 times that required.

The tabs on the end of the gore panels are similar in size and number (3) to the face-sheet straps except that the tabs contain three layers of fabric instead of the two layers present in the face-sheet straps. Consequently, the tabs also have adequate strength.

7.1.2 Analyses for Loading Perpendicular to Tank Axis

Acceleration loads perpendicular to the tank axis will be applied to the LO_2 tank MLI system during ascent and to the LH_2 tank MLI system during reentry. These loads are carried within the MLI panel by the integral straps on the inner face sheet and between panels by Velcro. Since the face-sheet straps oriented perpendicular to the tank axis are parallel to each other instead of following the contour lines of a gore segment, a series of rings were used as the loading model, see Figure 7-2. The N_ϕ reactions between rings were conservatively not considered. The $N_{\phi,\beta}$ loadings in the face sheet straps parallel to the tank axis would be less than those calculated previously for acceleration loading parallel to the tank axis, so were not calculated for accelerations perpendicular to the tank axis. The MLI support rings were conservatively considered to have no effect on the $N_{\theta,\alpha}$ loads.

The MLI on one side of the tank hangs away from the tank. The tensile loads in the face sheet straps, in a 1-g field, on this side of the tank are given by the equation:

$$N_\theta = \frac{w r \theta}{\sin \theta}$$

where

N_θ = the tensile load in lb/inch width of panel segment at the location defined by the angle θ .

θ = the angle as defined in Figure 7-2.

r = the radius of the segment under consideration, see Figure 7-2.

w = the weight density of the MLI panel in lb/in.^2 .

The tensile load (N_1) at $\theta = 90$ degrees = $\frac{w r \pi}{2}$

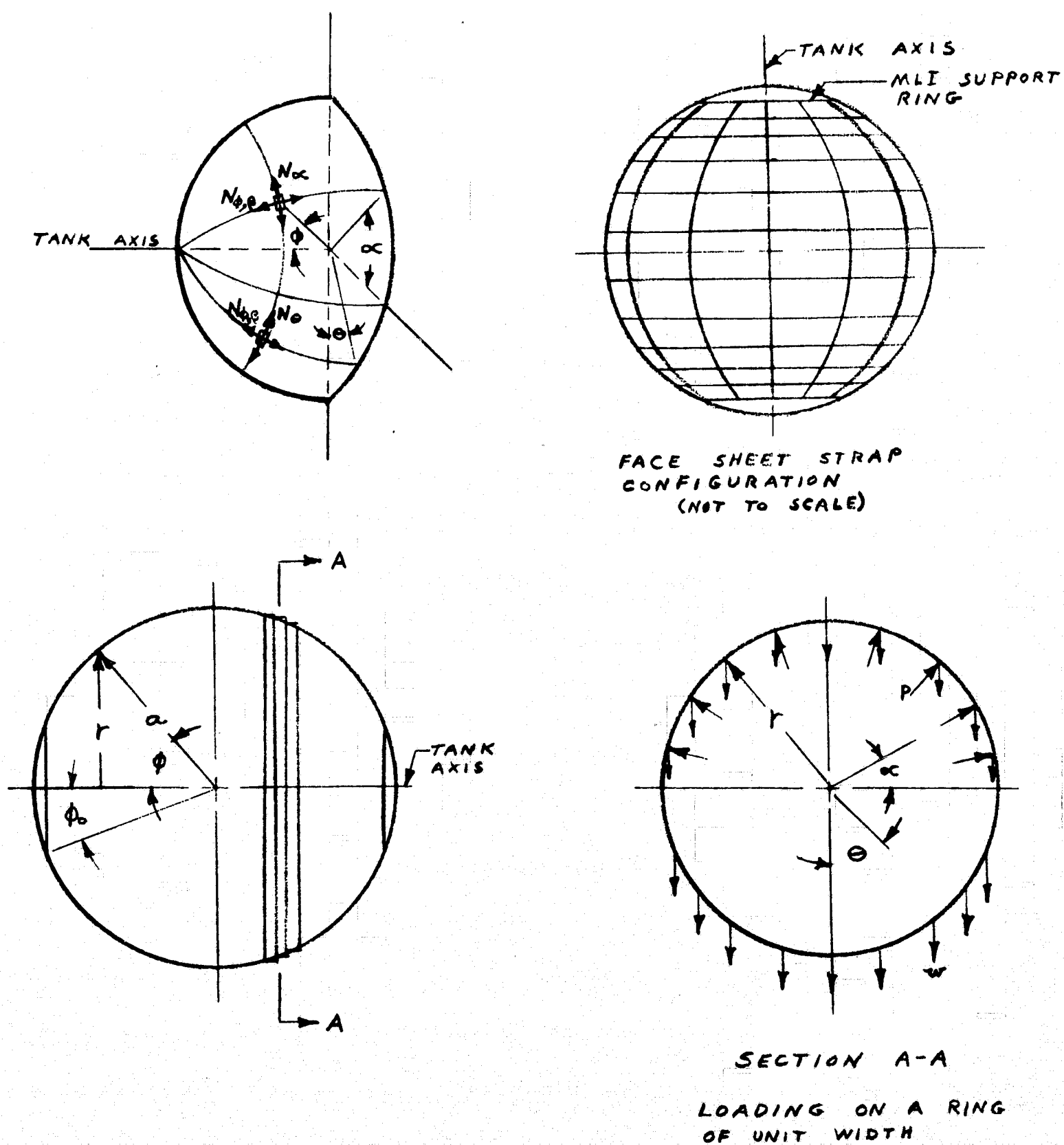


Figure 7-2. Loading Model When Acceleration is Perpendicular to Tank Axis

Both a tensile and a compressive load are produced on the other side of the tank, see Figure 7-2. The tensile loads N_α in this part of the MLI, in a 1-g field, are given by the equation

$$N_\alpha = w r \sin \alpha + N_1 = w r \sin \alpha + \frac{w r \pi}{2}$$

Friction between the tank and MLI panels was conservatively not considered.

The maximum loading in the face-sheet straps and in the Velcro between gore segments will occur in the center of the tank ($\phi = 90$ degrees) and at $\alpha = 90$ degrees, see Figure 7-2. A conservative value for the weight density (w) of the panel is 1.32×10^{-3} lb/in.² and the radii at $\phi = 90$ degrees are 95 and 63.5 inches for the LH₂ and LO₂ tanks, respectively. Using these values, N loadings for the LH₂ tank of 0.322 lb/in. and for the LO₂ tank of 0.216 lb/in. were obtained. The face-sheet straps oriented perpendicular to the tank axis are 12 inches apart and the maximum acceleration perpendicular to the tank axis is 2.3 g's for the LH₂ tank and 3.0 g's for the LO₂ tank. Consequently, the maximum load in these straps are 8.87 and 7.77 pounds. The straps are 1 inch wide and 0.012 inch thick. Therefore, the maximum stress is 740 and 648 psi for the straps on the LH₂ and LO₂ tanks, respectively. These results are included in Table 7-3. Based on a minimum strength of 3,000 psi, these straps have strength margins over four times that required.

The Velcro patches which carry the load between the inner face sheets of two adjacent panels are spaced 12 inches apart and have a surface area on each face sheet of 1.5 in.², see Section 10. Therefore, the maximum load carried is the same as that for the straps, 8.87 and 7.77 pounds (see above paragraph). This results in a lap shear load of 5.9 psi for the 8.87 pound load. The average ultimate lap shear for Velcro, as reported in Reference 6, is 54 psi. Consequently, the Velcro design should be adequate to carry the anticipated loads.

The maximum load on the lacing yarn would occur if the Velcro were not present or properly hooked together. The lacing buttons are 3 inches apart and two lacing threads are present to carry the load between each set of

lacing buttons. Consequently, the maximum load per thread would be less than 1.2 lb for the LH_2 tank MLI system and less than 1 lb for the LO_2 MLI system. The Tefglas, No. 18, lacing thread used has a breaking strength of 12 lb. Therefore, the strength of the thread is also very adequate.

7.2 COMPRESSIVE LOAD ON MLI

The MLI panels will be placed under a compressive load resulting from vehicle accelerations. Purge-gas evacuation and repressurization will also result in forces normal to the MLI panels but these forces will be less than those from vehicle accelerations and will be in the opposite direction since the repressurization gas is introduced under the MLI and the principal evacuation is through the MLI from the inside to the outside of the panels.

An indication of the maximum compressive loads (P) anticipated were obtained by using the equation:

$$P = \frac{2w \sin \beta \cos \beta}{(\sin \beta \cos \beta + \beta)} \left[\frac{\sin \beta + \cos \phi_o + d/a}{\cos^2 \beta + \frac{\sin^3 \beta \cos \beta}{(\sin \beta \cos \beta + \beta)}} \right]$$

where

w = panel weight density in lb/in.^2

β = the angle measured from a plane through the base of the upper dome, see Figure 7-2.

ϕ_o = the angle from the tank axis to the MLI support ring.

d = the length of a cylindrical section.

a = the tank radius.

The acceleration loading parallel to the LH_2 tank axis, the ascent period, and a location near the upper support ring ($\beta = 78.5$ degrees) were selected for the analyses because these should be the conditions and location for maximum compressive loading. Values for a, d, and ϕ_o are shown in Table 7-2. A value of $1.65 \times 10^{-3} \text{ lb/in.}^2$ was used for w. This includes the weight of the

purge bag. The resulting compressive load is 5.57×10^{-3} psi in a 1-g field. The maximum anticipated compressive load in a 3-g field is, therefore, 1.67×10^{-2} psi. This is the compressive loading which the outer MLI panel will place on the inner MLI panel. This should be conservatively higher than actual compressive loads sustained because of conservative assumptions made in the value of w and in the analytical model.

The MLI has demonstrated the capability of withstanding compressive loads nearly an order of magnitude greater than 1.67×10^{-2} psi without a significant change in layer density when the load was removed, see subsection 3.9. The capability of the fasteners to withstand this load was demonstrated by a test included in Task 6, see Section 8. Consequently, the MLI design appears adequate for the maximum anticipated compressive loads.

7.3 PURGE-BAG STRENGTH ANALYSES

The principal loading of the purge-bag material will be due to a pressure differential across the bag. The purge and repressurization gas system design includes a pressure controller which will control this pressure differential to a maximum of 0.5 psi. A detailed structural analyses of the ability of the purge bag to sustain this loading was beyond the scope of this study. However, a cursory analyses was accomplished to preliminarily size the purge-bag material and to verify the feasibility of the conceptual purge-bag design.

The hoop stress in a sphere is given by the equation:

$$\sigma = \frac{P r}{2 t}$$

Using a pressure (P) of 0.5 psi, bag radii (r) of 97 inches for the LH_2 tank and 65.5 inches for the LO_2 tank, and bag material thickness of 6 mils and 5 mils for the LH_2 and LO_2 tanks respectively, the predicted maximum hoop stresses (σ) are 4,040 psi for the LH_2 tank purge bag and 3,280 psi for the LO_2 tank purge bag.

Teflon coated Kapton (polyimide film type F) has been selected as the purge-bag material. The materials selected and their properties are summarized

in Table 7-4. This data was taken from Reference 19. Kapton with Teflon coating on both sides was selected for the LO_2 tank purge bag to ensure LO_2 compatibility for both faces of this bag. As shown, the calculated stresses are well below the ultimate tensile strengths. This should provide an adequate design margin for any stress concentration points such as a joint between gore segments. It should also be noted that the predicted maximum purge-bag temperature is less than 200°F , see Section 6. Consequently the ultimate tensile strength of the material will be between that shown at 392 and 77°F . The yield point data at 3-percent elongation in Table 7-4 indicates that the maximum elongation will be less than 3 percent.

7.4 THERMAL CONTRACTION COMPATIBILITY ANALYSES

To ensure thermal contraction compatibility between the components within the MLI system and between the MLI system and the tank, the following conditions must be satisfied.

- A. The load-carrying inner face sheet of each MLI panel must contract more during cooling and expand less during heating than do the reflector and separator materials in that panel. This ensures that the reflectors and separators will never be placed under load. The reflector and spacer materials (DGK and Dacron B4A) have been previously selected based on their thermal efficiency and their ability to withstand an ILRV environment. Consequently, the face-sheet systems are the MLI components selected to provide the proper thermal contraction and expansion compatibility within the MLI panels.
- B. Contraction (and expansion) of the reflector and separator materials should match, reasonably well, that of the face sheets to prevent excessive bulging of the separators and reflectors.
- C. The MLI system must be sized to allow for any relative thermal contraction between the MLI components and that of the tank. This ensures that the MLI panel dimensions will be adequate at the cryogenic temperature of the tank.

7.4.1 Selection of Face-Sheet Systems for LH_2 Tank MLI

Since any of the candidate face-sheet systems could be sized to fit the tank at the tank operating temperature and pressure, the major criteria for

Table 7-4
PURGE BAG MATERIALS

	LH ₂ Tank	LO ₂ Tank
Du Pont order code	600F051	500F131
Nominal thickness	6 mils	5 mils
Teflon thickness, face 1	0 mils	1 mil
Kapton thickness	5 mils	3 mils
Teflon thickness, face 2	1 mil	1 mil
Weight	0.0476 lb/ft ²	0.0435 lb/ft ²
Ultimate tensile strength at 392°F	14,000 psi	10,000 psi
Ultimate tensile strength at 77°F	21,000 psi	16,000 psi
Yield point, 3 percent elongation, at 392°F	5,000 psi	3,600 psi
Yield point, 3 percent elongation, at 77°F	8,600 psi	6,700 psi

selection of the face-sheet systems is to ensure the proper relative thermal contractions within the MLI composite. The operating temperature band at various points within the MLI was predicted in the Task 4 thermal analyses (Section 6) and is summarized for the LH₂ tank in Table 7-5. Using these operating temperature bands and the thermal contraction data shown in Figures 3-40 and 3-41, Section 3, it can be seen that only three face-sheet systems, Teflon/Nomex HT-287, Viton/Nomex HT-287, and Silicone/Nomex HT-287 can be considered for the inner face sheet of the inner MLI panel. Of these, the Silicone/Nomex HT-287 has the lightest weight, Table 7-6, and has a total thermal contraction closest to that of the DGK and Dacron B4A materials. Consequently, the Silicone/Nomex HT-287 system was selected for this face sheet.

Table 7-5
OPERATING TEMPERATURE BANDS - LH₂ TANK MLI

Face-Sheet Location	Minimum Temperature (°F)	Maximum Temperature (°F)
Inner Panel		
Inner Face Sheet	-423	+70
Outer Face Sheet	-200	+70
Outer Panel		
Inner Face Sheet	-200	+70
Outer Face Sheet	0	+90

Table 7-6
PHYSICAL PROPERTIES OF FACE-SHEET SYSTEMS

Composite	Weight (lb/ft ²)	Thickness (mils)
Polyimide/Nomex HT-287	0.0316	11-12
Silicone/Nomex HT-287	0.0489	12-14
Polyimide/Beta Glass 81677	0.0562	8-10
Silicone/Beta Glass 81677	0.0660	9-11
Teflon/Nomex HT-287	0.0873	16-18
Teflon/Betaglass 81677	0.0916	12-13
Viton/Betaglass 81677	0.0966	8-10
Viton/Nomex HT-287	0.1310	15-16

Silicone/Nomex HT-287 is also the most suitable system for the outer face sheet of the inner MLI panel and the inner face sheet of the outer MLI panel. For the operating temperature band of these face sheets (see Table 7-5), the same three face-sheet systems can be considered as for the inner face sheet of the inner panel. The Silicone/Nomex HT-287 again offers the lowest weight and best match of thermal contraction characteristics.

During reentry, the outer face sheet of the outer MLI panel will reach 90°F, see Table 7-5. Figures 3-40 and 3-41 indicate that only the Polyimide/Nomex HT-287 system has the proper thermal contraction and expansion characteristics relative to that of the DGK for the temperature band of this face sheet. The Polyimide/Beta Glass, Teflon/Beta Glass, Silicone/Beta Glass, and Viton/Beta Glass systems all provide acceptable thermal expansion values at 90°F but are somewhat questionable at the lower end of the temperature band, 0°F. Of these latter systems, the Teflon/Beta Glass system has the best match of contraction and expansion characteristics to the DGK and Dacron B4A. The Polyimide/Nomex HT-287 system was chosen because of its better match to the thermal contraction of DGK and Dacron B4A at 0°F and because its weight is only approximately 1/3 that of the Teflon/Beta Glass system, see Table 7-6.

7.4.2 Selection of Face-Sheet Systems for LO₂ Tank MLI

The MLI panels for the LO₂ tank will be of the same general construction and will use the same reflector and spacer materials as used for the LH₂ tank MLI panels. The major criteria for selection of the face-sheet materials is again the proper relative thermal contractions within the MLI composite. The anticipated operating temperature bands at the locations of the LO₂ tank MLI face sheets are presented in Table 7-7. A comparison of these temperature bands, with the thermal contraction and expansion data shown in Figures 3-40 and 3-41, shows that the same face-sheet systems can be considered for the LO₂ tank as were considered for the LH₂ tank. Of these face-sheet systems, the Silicone/Nomex HT-287 and Polyimide/Nomex HT-287 systems were again selected for the same reasons as discussed previously for the LH₂ tank. A summary of the face-sheet systems selected for both the LO₂ and LH₂ tank is shown in Table 7-8.

Table 7-7
OPERATING TEMPERATURE BANDS - LO₂ TANK MLI

Face-Sheet Location	Minimum Temperature (°F)	Maximum Temperature (°F)
Inner Panel		
Inner Face Sheet	-281	+70
Outer Face Sheet	-126	+70
Outer Panel		
Inner Face Sheet	-126	+70
Outer Face Sheet	-4	+176

Table 7-8
FACE-SHEET SYSTEMS SELECTED FOR
LH₂ AND LO₂ TANK MLI PANELS

	Inner Face Sheet	Outer Face Sheet
Inner Panel	Silicone/Nomex HT-287	Silicone/Nomex HT-287
Outer Panel	Silicone/Nomex HT-287	Polyimide/Nomex HT-287

7.4.3 Required MLI Oversizing Caused by Relative Contraction Between Tank and Inner Face Sheet

To insure that the MLI panel dimensions will be adequate at the cryogenic temperature of the tank, an analyses was accomplished to determine the required oversizing of the MLI panels. The MLI panels will be mounted directly on the exterior surface of the tanks. Consequently, changes in tank geometry caused by cooling by the cryogen, tank pressurization, and vehicle acceleration during ascent must all be considered in the analyses. If the net contraction in tank circumference is greater than the contraction of the MLI panel, the panels can be sized to fit the tank snugly at ambient temperature.

If the net contraction in tank circumference is less than the contraction of the MLI panels, the panels must be oversized when assembled at ambient temperature.

The ILRV Orbiter secondary LO₂ and LH₂ tank design parameters used in the analyses are shown in Table 7-9.

7.4.3.1 MLI Oversizing for LH₂ Tank

The greater circumference (circumference in plane containing tank axis) of the LH₂ tank at ambient temperature is:

$$\Delta C = 2\pi r + 2h = 632.98 \text{ inches}$$

where the values for r and h are shown in Table 7-9. This is also the greater circumference dimension for the inner layer of the assembled MLI composite. The change in the greater circumference of the LH₂ tank caused by cooling of the tank is:

$$\Delta C = C \left(\frac{L_{-423^\circ\text{F}} - L_{70^\circ\text{F}}}{L_{-423^\circ\text{F}}} \right) = -2.63 \text{ inch}$$

where the total fractional contraction of the tank at -423°F used was -4.15×10^{-3} in./in. (Reference 20, Figure A.5.t). The contraction in the greater circumference dimension of the inner face sheet is:

$$\Delta C = C \left(\frac{L_{-423^\circ\text{F}} - L_{70^\circ\text{F}}}{L_{-423^\circ\text{F}}} \right) = -3.42 \text{ inch}$$

where the total fractional contraction

$$\left(\frac{L_{-423^\circ\text{F}} - L_{70^\circ\text{F}}}{L_{-423^\circ\text{F}}} \right)$$

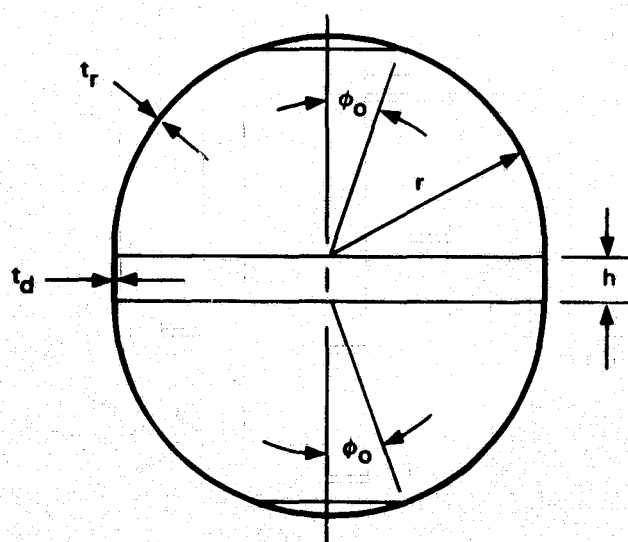
value of -5.4×10^{-3} was taken from Figure 3-40.

Table 7-9
 LH_2 AND LO_2 TANK DESIGN PARAMETERS

	LO_2	LH_2
Material	2219 Al	2219 Al
T^*	-297°F	-423°F
P^{**}	40 psi	40 psi
ϕ_o	17.4°	11.5°
r	63.5 inches	95 inches
h	0	18 inches
t_r	0.05 inch	0.06 inch
t_d	0	0.10 inch

* T = Saturation temperature at 1 atm pressure

** P = Maximum tank operating pressure



To outline a method for sizing the MLI, a worst-case LH_2 tank pressure differential of 41.9 psia was assumed. This includes an assumed initial tank pressurization of 40 psia plus an additional 1.9 psia caused by a vehicle acceleration of 3 g's. The resulting stress in the hemispherical dome is:

$$\sigma = \frac{P r}{2 t_r} = 33,170 \text{ psi}$$

where r and t_r are shown in Table 7-9.

The change in the radius of the dome is

$$\Delta r = \frac{r \sigma}{E} (1-u) = +0.19 \text{ inch}$$

where $E = 11.7 \times 10^{-6}$ psi at -423°F (Reference 20, Figure A.5.i), and $u = 0.3$. The increase in the radius of the cylindrical section was assumed to be the same as that of the domes ($\Delta r = +0.19$ inch). The resulting increase in circumference of the domes or the cylindrical section (minor circumference) will be:

$$\Delta C = 2\pi (\Delta r) = 1.19 \text{ inches}$$

The change in length of the cylindrical section is:

$$\Delta h = \frac{Fh}{AE} = +0.030 \text{ inch}$$

where:

$$A = 2 \pi r t_d = 59.69 \text{ in.}^2$$

$$F = \pi r^2 P = 1.178 \times 10^6 \text{ lb}$$

$$E = 11.7 \times 10^{-6} \text{ psi}$$

and r , t_d , and h are shown in Table 7-9.

The net change in the greater circumference of the LH_2 tank is, therefore, $-2.63 + 1.19 + 0.03 + 0.03 = -1.38$ inches. The analyses for the changes in LH_2 tank minor circumference were accomplished in the same way and the results for the changes in both the greater and minor circumferences are summarized in Table 7-10. Since the contraction of the inner face sheets of -3.42 inches is greater than the contraction of the tank (-1.38 inches), the total oversizing required on the face sheets in the greater circumference direction is 2.04 inches. The oversizing required in the minor circumference direction is 1.83 inches. The results are summarized in Table 7-11.

7.4.3.2 MLI Oversizing for LO_2 Tank

The circumference of the LO_2 tank at ambient temperature is:

$$C = 2\pi r = 398.97 \text{ inches}$$

where the radius r is 63.5 inches, see Table 7-9. This is also the circumference dimension for the inner layer of the assembled MLI composite. The change in the LO_2 tank circumference due to cooling of the tank is:

$$\Delta C = C \left(\frac{L_{-281^\circ\text{F}} - L_{70^\circ\text{F}}}{L_{-281^\circ\text{F}}} \right) = -1.36 \text{ inches}$$

where the total fractional contraction of the tank at -281°F used was -3.4×10^{-3} in./in. (Reference 20, Figure A.5.t).

The contraction of the inner layer of the assembled MLI composite (inner face sheets) is:

$$\Delta C = C \left(\frac{L_{-281^\circ\text{F}} - L_{70^\circ\text{F}}}{L_{-281^\circ\text{F}}} \right) = -1.92 \text{ inches}$$

where the total fractional contraction value of -4.8×10^{-3} was taken from Figure 3-40.

As with the LH_2 tank, an initial tank pressurization of 40 psi was assumed. The pressure at the aft end of the tank will increase by an additional 15.7 psi

Table 7-10

CHANGES IN TANK GEOMETRY DUE TO FILLING,
PRESSURIZATION, AND ACCELERATION

	Initially		After Filling with Cryogen		After Pressurization and at Maximum Acceleration		Net Geometry Change	
	LO ₂	LH ₂	LO ₂	LH ₂	LO ₂	LH ₂	LO ₂	LH ₂
T (°F)	70	70	-281	-423	-281	-423		
P (psi)	0	0	0	0	55.7	45		
Greater radius (in.)	63.5	NA	63.28	NA	63.42	NA	-0.08	NA
Greater circum- ference (in.)	398.97	632.98	397.61	630.35	398.47	631.60	-0.5	-1.38
Minor radius (in.)	NA	95	NA	94.60	NA	94.79	NA	-0.21
Minor circumference (in.)	NA	596.88	NA	594.40	NA	595.59	NA	-1.29

Table 7-11
REQUIRED OVERSIZING OF INNER FACE
SHEETS OF INNER BLANKETS

	Face-Sheet Contraction due to Loading the Cryogen (in.)		Net Tank Geometry Change (in.)		Required Oversizing (in.)	
	LO ₂	LH ₂	LO ₂	LH ₂	LO ₂	LH ₂
Greater radius (in.)	-0.3	NA	-0.08	NA	+0.22	NA
Greater circumference (in.)	-1.92	-3.42	-0.5	-1.38	+1.42	+2.04
Minor radius (in.)	NA	-0.5	NA	-0.21	NA	+0.29
Minor circumference (in.)	NA	-3.12	NA	-1.29	NA	+1.83

due to an acceleration of 3 g's during ascent. Consequently, a worst-case LO₂ tank pressure differential of 55.7 psia was assumed to calculate the net change in tank circumference. The resulting stress in the hemisphere is:

$$\sigma = \frac{P r}{2 t_r} = 35,370 \text{ psi}$$

where r and t_r are shown in Table 7-9.

The change in the radius of the dome is:

$$\Delta r = \frac{r \sigma}{E} (1-u) = +0.14 \text{ inch}$$

where $E = 11.5 \times 10^6$ psi at -281°F (Reference 20, Figure A.5.i), and $u = 0.3$. The resulting change in circumference is +0.88 inch.

The net change in the circumference of the LO₂ tank is, therefore, $-1.36 + 0.88 = -0.48$ inch. The total oversizing required on the inner face sheets is $1.92 - 0.48 = 1.44$ inches. These results are summarized in Tables 7-10 and 7-11.

Section 8

FASTENER STRUCTURAL TESTS AND THERMAL DEGRADATION TESTS—TASK 6

The objective of Task 6 was to accomplish testing that would assist in verifying the performance capability of the MLI system for an ILRV Orbiter vehicle application. This included structural tests of the fastener and thermal degradation testing of the MLI composite.

8.1 FASTENER TESTS

The MLI system uses fasteners to hold the layers together to form an integral unit (panel). These fasteners consist of a small diameter shank, which passes through the layers in an MLI panel, and a button on each end of the shank to contain the layers. The shank and the button on one end of the shank are normally a single piece which has been formed by molding. The button on the other end of the shank is installed after the shank has been passed through the layers and is retained by a head formed by heating the end of the shank. For the tests reported herein, molded Astrel 360 fasteners, which were selected for the system (Section 9), were not available and the buttons were retained on both ends of an Astrel 360 shank by a heat formed head. Since the button material was not of importance to the tests, available Nylon buttons were used. The shanks were cut from 0.026-inch Astrel 360 sheet-stock.

Three test series were conducted to verify the capability of the fasteners to withstand the structural loads anticipated in an ILRV application. These tests determined the load limit of the fasteners in both the tensile and shear directions and the ability of the fasteners to withstand cyclical compressive loads. All of the tests were run at room temperature.

8.1.1 Load Limit of Fasteners in Tensile Direction

The load limit of the fasteners in the tensile direction was determined by loading the fastener specimens in an Instron testing machine as shown in

Figure 8-1. As shown in Table 8-1, the tensile load at specimen failure varied from 1.6 to 1.8 pounds. All of the specimen failures were due to the button retaining head, formed by heating, popping off. There was no failure of the fastener shank.

The maximum load in the tensile direction is expected to be caused by the pressure differential across the MLI panel during purge gas evacuation. Since the fasteners are one foot or less apart in an MLI panel and since the peak anticipated pressure differential across the panel is 1 lb/ft^2 , the maximum load expected on the fasteners in the tensile direction is one pound. Thus, the fastener design appears to be adequate for this application.

8.1.2 Load Limit of Fasteners in Shear Direction

The load limit of the fasteners in the shear direction (see Figure 8-2) was also determined by loading the specimens in an Instron testing machine. Significant deflection of the shanks was sustained when the load was applied but all of the specimens failed because of the heat-sealed head popping off.

CR14

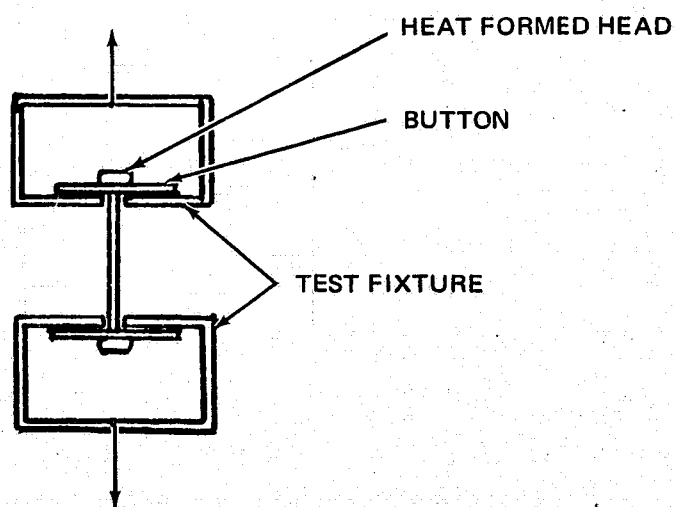


Figure 8-1. Specimen Configuration for Loads in Tension Direction - Fastener Tests

Table 8-1
TENSILE LOAD LIMIT OF FASTENERS

Test Specimen Number	Cross Sectional Area of Shank (in. ²)	Tensile Load at Failure* (lb)
T1	7.75×10^{-4}	1.6
T2	7.28×10^{-4}	1.8
T3	8.1×10^{-4}	1.62

*All specimens failed by heat formed head popping off.

There was no shear or tensile failure of the shank. The load at specimen failure varied from 2.8 to 3.87 lb, see Table 8-2.

Since the inner face sheet carries the load from each fastener to the end of the panel, the load on a fastener in the shear direction is caused by the

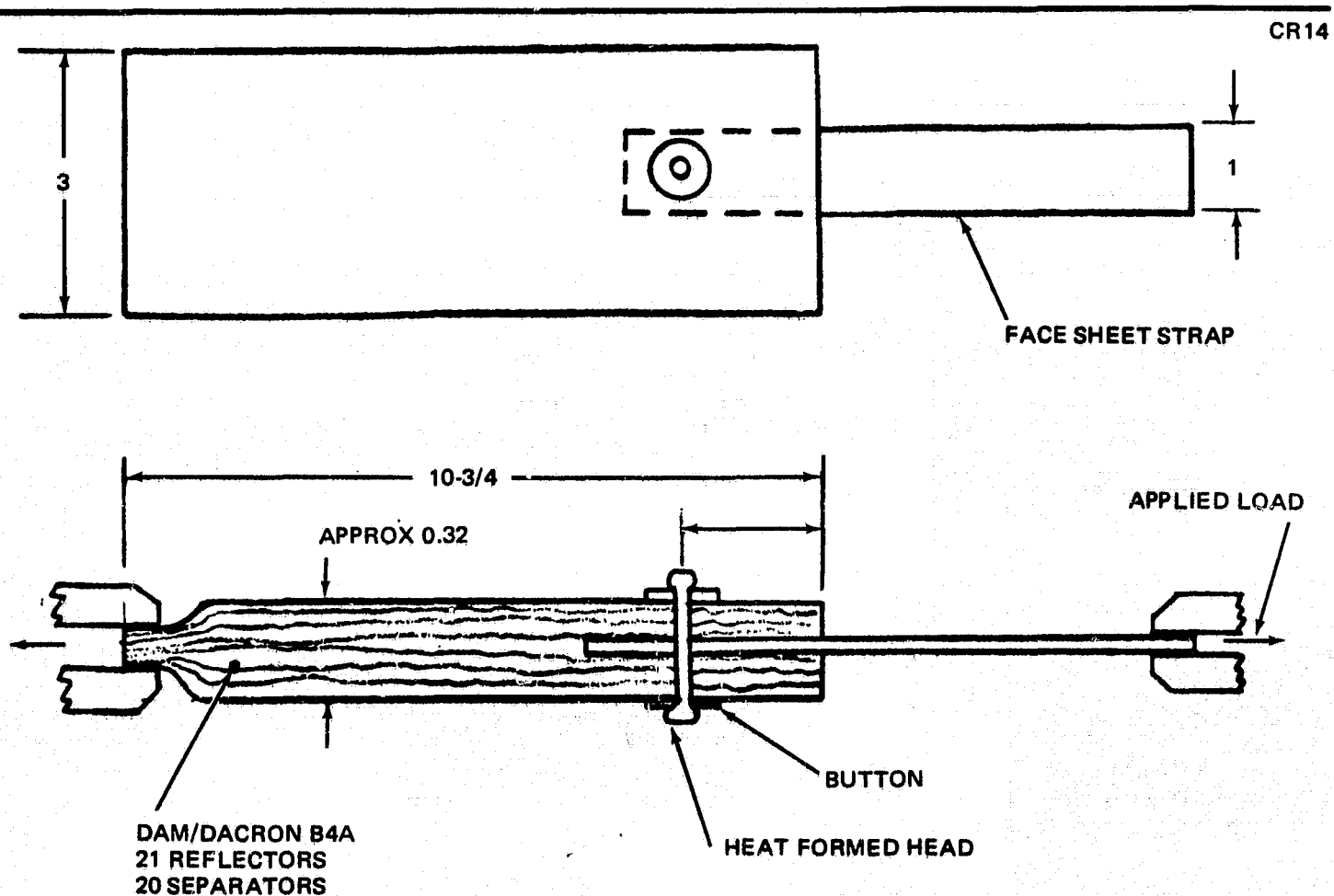


Figure 8-2. Specimen Configuration for Loads in Shear Direction - Fastener Tests

Table 8-2
LOAD LIMIT OF FASTENERS IN SHEAR DIRECTION

Test Specimen Number	Cross Sectional Area of Shank (in. ²)	Load at Failure* (lb)
S1	8.84×10^{-4}	2.8
S2	8.06×10^{-4}	3.87
S3	7.5×10^{-4}	3.52

*All specimens failed by heat formed head popping off.

weight of the panel in the vicinity of the fastener. The fasteners are one foot or less apart in an MLI panel and a conservative (slightly high) value for the weight density of a panel is 0.19 lb/ft^2 . Consequently, in a 3-g field, the maximum load anticipated in the shear direction is 0.57 lb which is much less than the 2.8-lb minimum load capability of a fastener (Table 8-2).

8.1.3 Cyclic Compression Test

The ability of the fasteners to withstand cyclical compressive loads was tested by placing an MLI specimen containing a fastener between two plates which were mounted in an Instron testing machine. The machine was set to cycle the load on the specimen with a total cycle time of approximately two minutes. The cycles were repeated 100 times with an inspection for specimen damage every 10 cycles. Two test series were accomplished on the same specimen. The first cycled the compressive load from zero to 1.15 lb and the second cycled the compressive load from zero to 3.5 lb.

The MLI specimen was 15 by 15 inches and contained a fastener through 20 layer-pairs of DGK/Dacron B4A. The fastener was located in the center of the specimen. The fastener shank was Astrel 360 and had a cross-sectional area of $7.56 \times 10^{-4} \text{ in.}^2$. The buttons were 0.5-inch diameter and 0.01-inch-thick Nylon. The buttons were held on the shank by a heat-formed head on each end of the shank.

The inspection of the test specimen after both test series revealed that there was no damage to the fastener or to the MLI layers. The peak compressive load of 3.5 lb is approximately 45 percent higher than the maximum anticipated compressive load in a 3-g field. Consequently, the cyclic compressive tests indicate that the Astrel 360 material and the fastener design are adequate for the anticipated compressive cycling.

8.2 THERMAL DEGRADATION TEST

The reuseability of the MLI system in a ILRV application results in environments not encountered heretofore in single launch applications. One of these is the cyclical pressure environment within the MLI. The effects of this phenomena were investigated on a MDAC IRAD program which included a test to determine if any degradation of the MLI thermal performance occurs as a result of numerous evacuation-repressurization cycles. The test objective was met through the use of an MDAC-conceived and sponsored new calorimeter which uses heat-flux gages. The test included insulating the calorimeter with a representative MLI composite, and evacuating and repressurizing the MLI 101 times in a vacuum chamber. The results of this study which are pertinent are reported herein for reference.

8.2.1 Test Calorimeter

The heat flux gage calorimeter designed and fabricated for these tests is shown in Figures 8-3 and 8-4. This tank is 4 feet long, 2 feet wide, and 5 inches deep and is constructed of aluminum. The heat flux gages are located on the top surface of the tank as shown in Figure 8-3. Heat flowing through these gages causes a very small temperature difference across the gages which is directly proportional to the heat flux to be measured. Multiplication of the effect of this very small temperature difference by means of a miniature thermopile within each gage makes it possible to measure the voltage output without amplification, thereby maintaining high accuracy. The gages are thin (approximately 80 mils) and have a negligible effect on the total thermal resistance of the system being tested. The gages selected have a very thin copper cladding on the top and bottom surface which automatically averages fluxes that are not uniform in the area contacted by the gage. Four of these heat flux gages were used and were connected in series

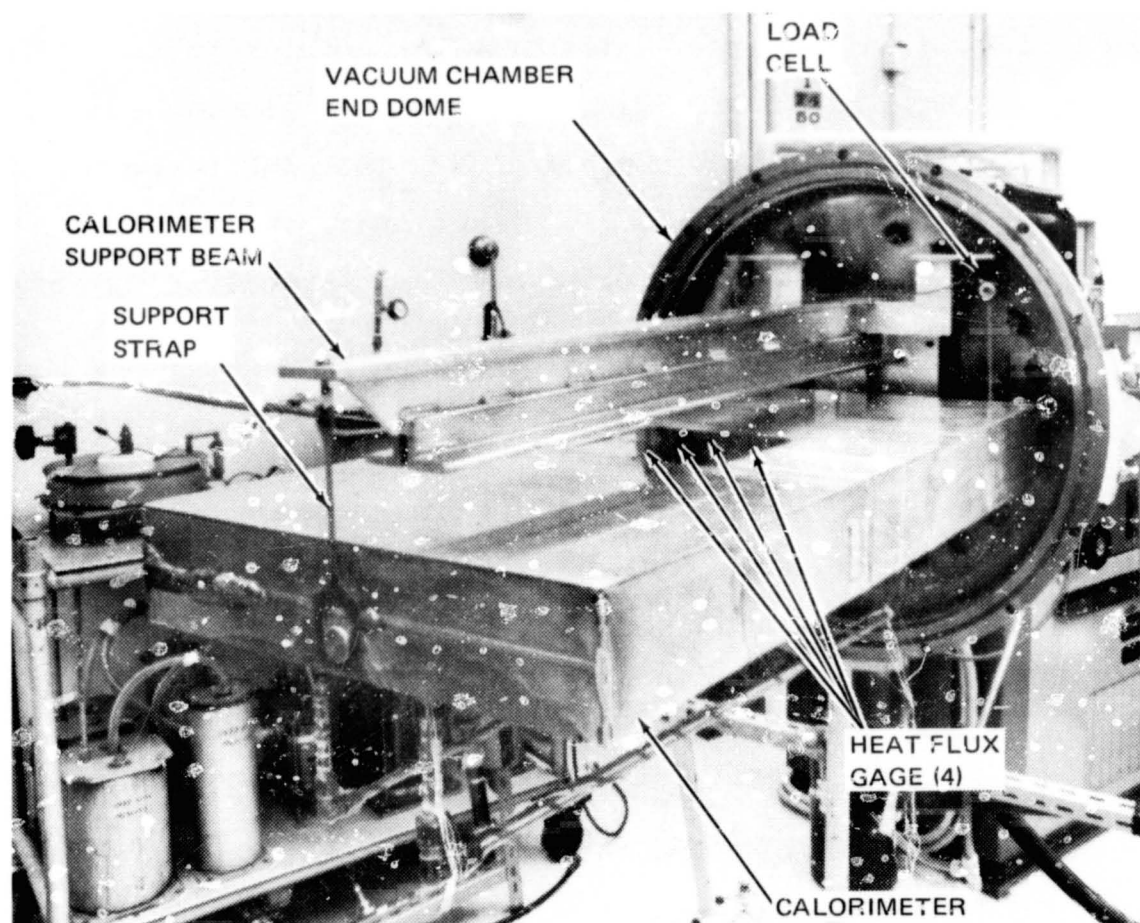


Figure 8-3. Heat Flux Gage Calorimeter - Top View

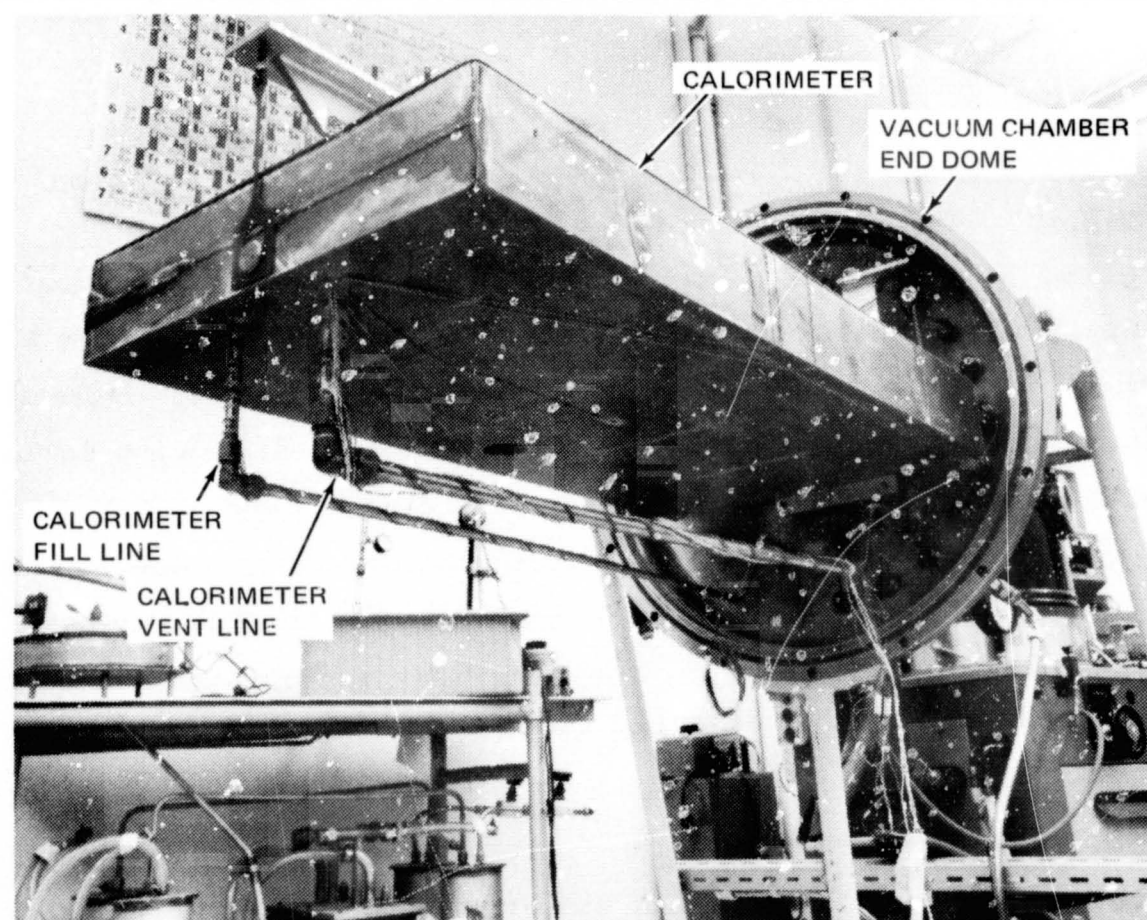


Figure 8-4. Heat Flux Gage Calorimeter - Bottom View

to provide a microvolt output sufficient for measurement at the low heat fluxes. Each of the gages measures 4.5 by 4.5 inches giving a total surface area of 81 in.² for the four gages.

The tank is supported in the vacuum chamber by a support beam cantilevered off of the end dome of the chamber, see Figure 8-3. Three vertical straps support the tank from this beam. The support straps are constructed of epoxy-glass and have a small cross-sectional area to minimize heat flow to the tank through these supports.

A fill line and a vent line are located as shown in Figure 8-4. These plumbing lines are located at the tank end farthest from the plumbing pass-throughs in the end dome. This allows insulating these lines for a length sufficient to minimize the heat flow to the tank through the plumbing lines. The wiring from the heat flux gages and from thermocouples on the tank are fastened to the plumbing. This minimized the heat flow to the tank through the wiring.

8.2.2 Test Specimen

The test panels of MLI were fabricated in a basic panel configuration consistent with the design discussed in Section 10. This included face sheets, fasteners, and lacing buttons. The reflector material was 25-gage DAM and contained the perforation pattern selected in Task 4, Section 6; 0.046-in. -diameter holes, 5 holes/in.², 0.85 percent open area. The separator material was Dacron B4A net. The face sheet material was Dacron 15413 net with Nylon straps. Two panels of MLI were used to obtain the desired thickness. Each panel contains 35 layer pairs giving a total thickness of 70 layer pairs. The average thickness of the MLI over the heat flux gages was 0.69 inches.

The ends of the calorimeter were covered with MLI as shown in Figures 8-5 and 8-6. These end caps were fabricated in-place on the calorimeter. The MLI layers on the support straps and plumbing lines were installed at the same time as the end caps and the reflector layers were interleaved at the junction of a strap or plumbing line with the tank. Velcro was used to help

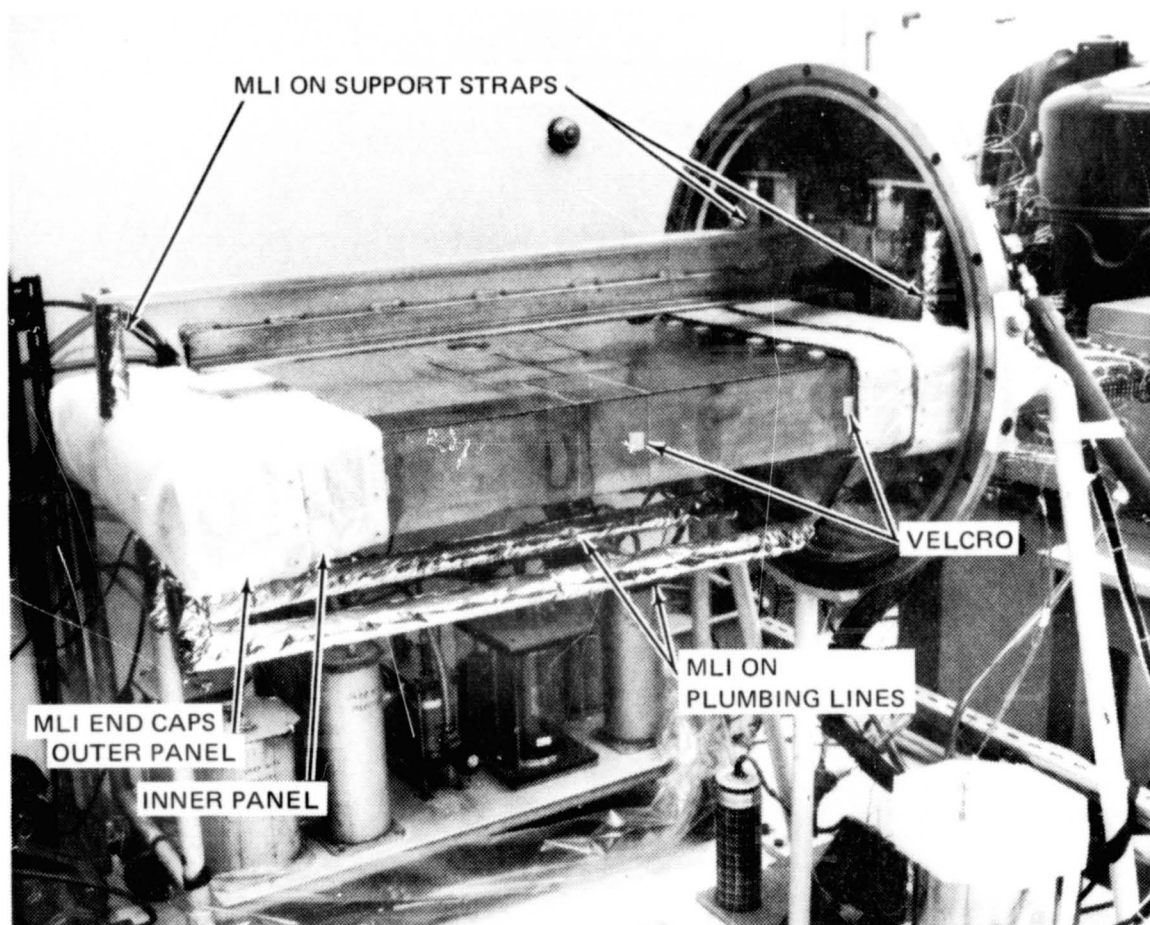


Figure 8-5. Heat Flux Gage Calorimeter With MLI End Caps - Top View

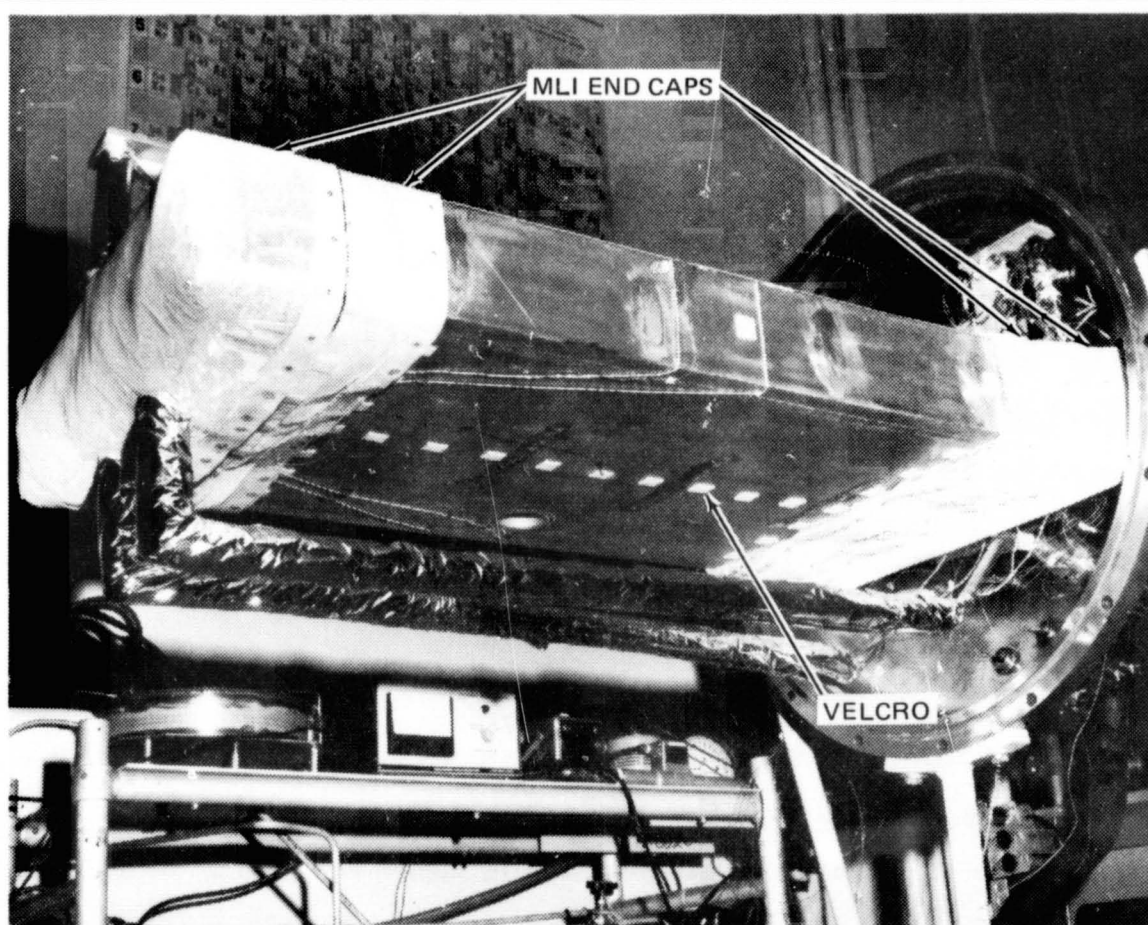


Figure 8-6. Heat Flux Gage Calorimeter With MLI End Caps - Bottom View

position and hold the panels in place. The Velcro at the joints also served to tie the inner face sheet of a panel to the adjacent inner face sheet.

The installation of the inner MLI test panel is shown in Figure 8-7. This panel wraps around the tank with the ends of the panel forming a joint across the bottom. The joint across the bottom between the ends of the test panel and the joints between the test panel and the end caps were held together with lacing thread between the outer face sheets and with Velcro between the inner face sheets.

The outer MLI test panel was installed in a manner similar to that of the inner panel. The location of the joint across the bottom formed by the outer panel was offset from the corresponding joint for the inner panel by four inches. The offset between the joint formed by the outer test panel and an end cap and the joint formed by the inner test panel and an end cap was also four inches. The width of the inner panel is 30 inches. The outer panel is 38 inches wide. The MLI, completely installed on the calorimeter, is shown in Figures 8-8 and 8-9.

8.2.3 Test Apparatus and Procedure

The vacuum chamber used is an ultrahigh vacuum system manufactured by the Ilikon Corporation (Model 120). This chamber has an internal diameter of 30 inches and a length of approximately 50 inches plus the end domes. Numerous electrical and plumbing pass-throughs are available in one of the end domes, see Figure 8-10. A window is located in the other end dome. The system, see schematic in Figure 8-11, normally includes a forepump ($15 \text{ ft}^3/\text{min}$), a 10-inch diffusion pump, and a 2 inch diffusion pump. An additional forepump ($15 \text{ ft}^3/\text{min}$) was added for these tests to obtain a faster chamber evacuation rate.

The pressure history in the chamber was measured with an NRC Model 530 alphasatron gage and a CEC Model G1C-100 hot cathode ionization gage. The alphasatron gage provides pressure data from 1 atm to approximately 5×10^{-4} torr. The ionization gage provides pressure data below 10^{-3} torr.



Figure 8-7. Installation of Inner MLI Test Panel

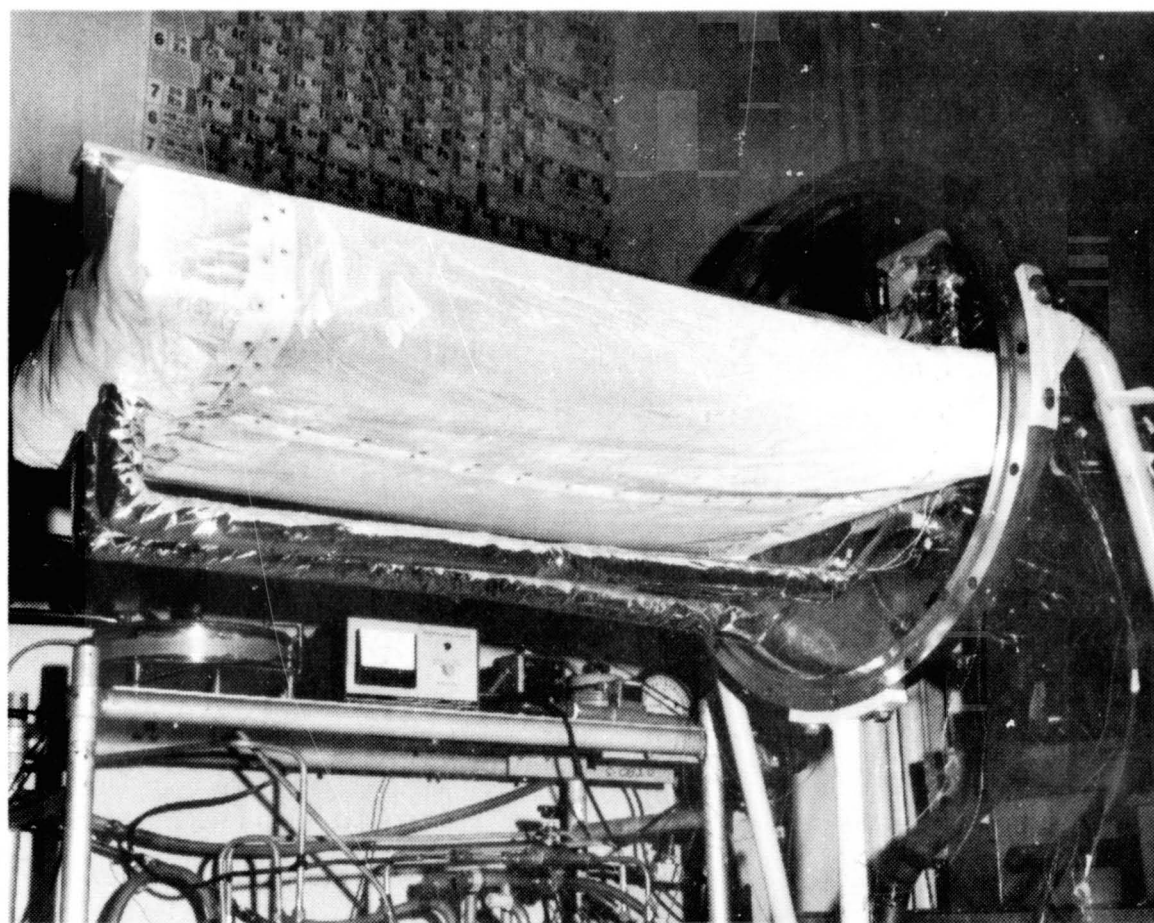


Figure 8-8. MLI Installed on Heat Flux Gage Calorimeter - Bottom View

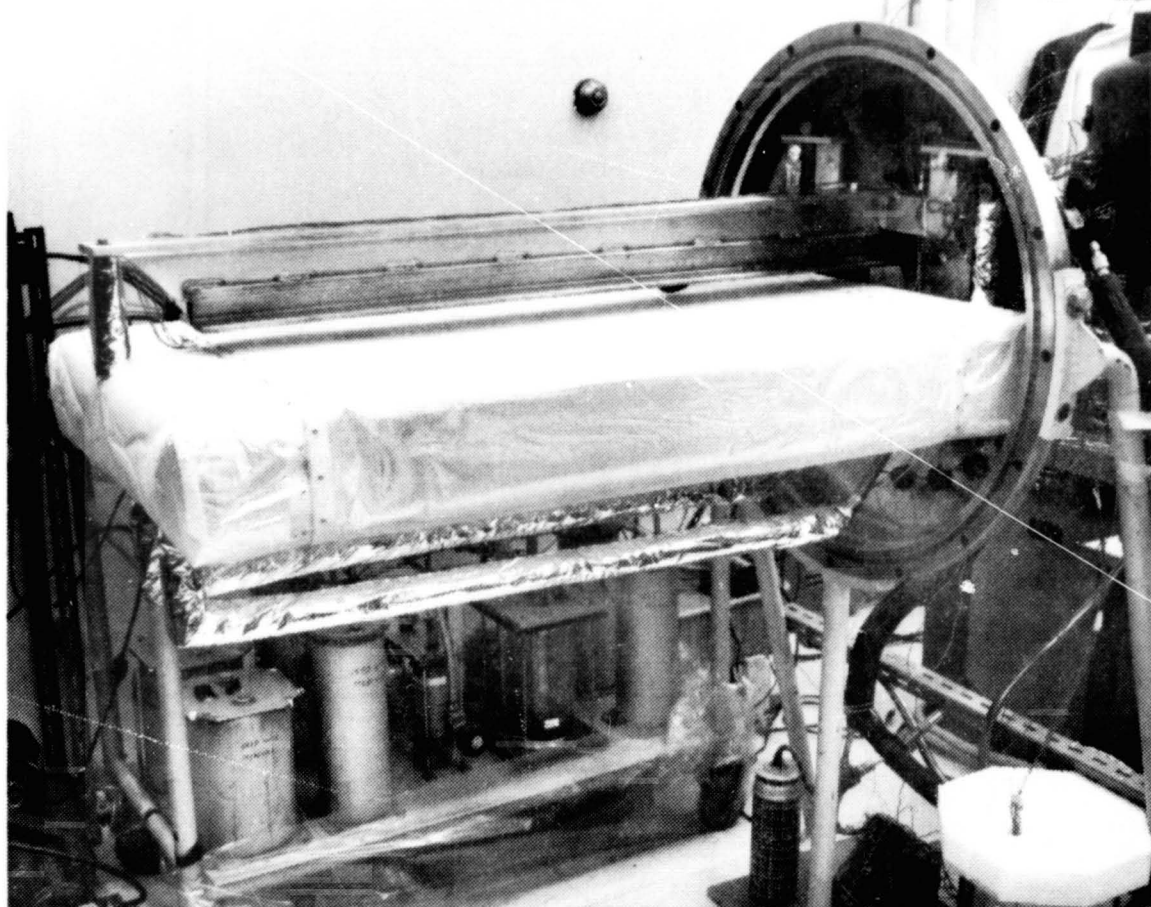


Figure 8-9. MLI Installed on Heat Flux Gage Calorimeter - Top View

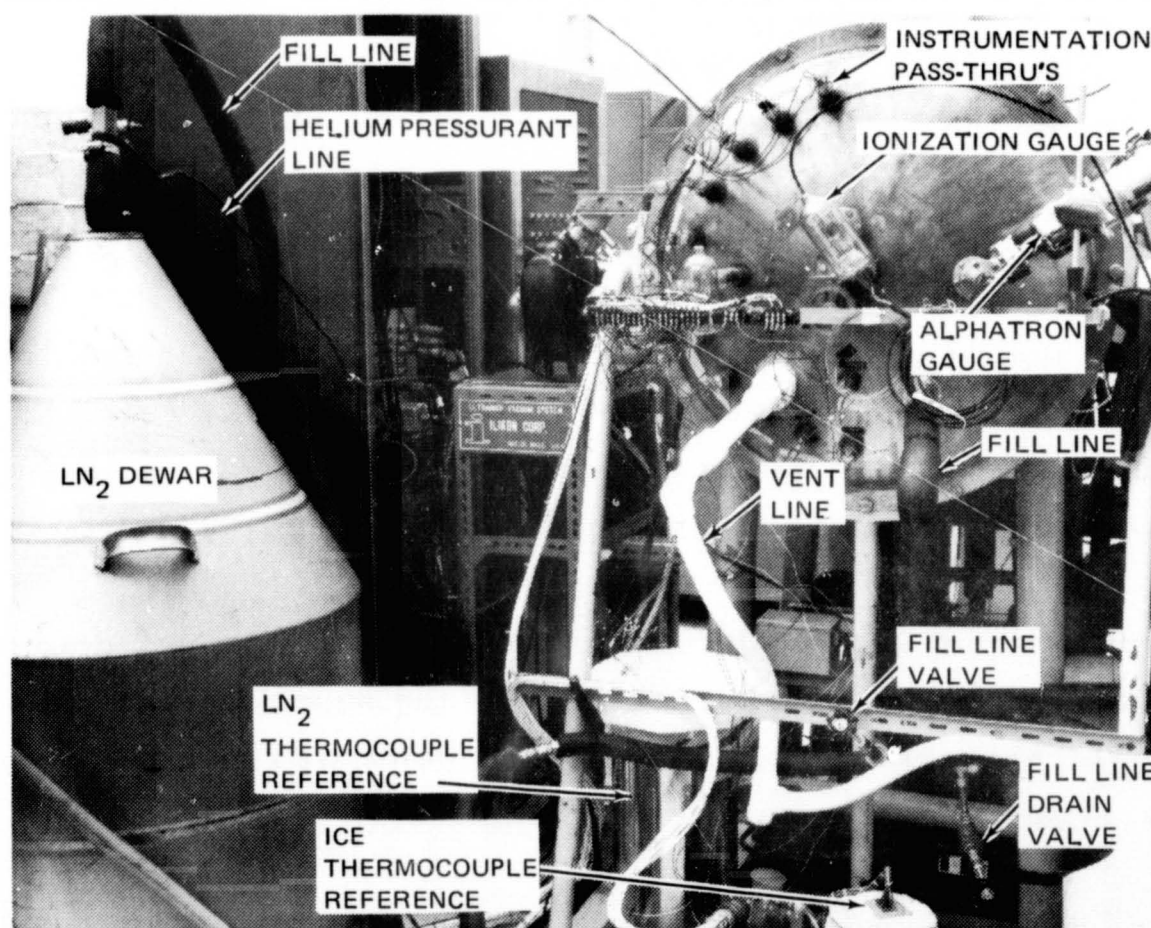


Figure 8-10. Test Setup, Heat Flux Gage Calorimeter

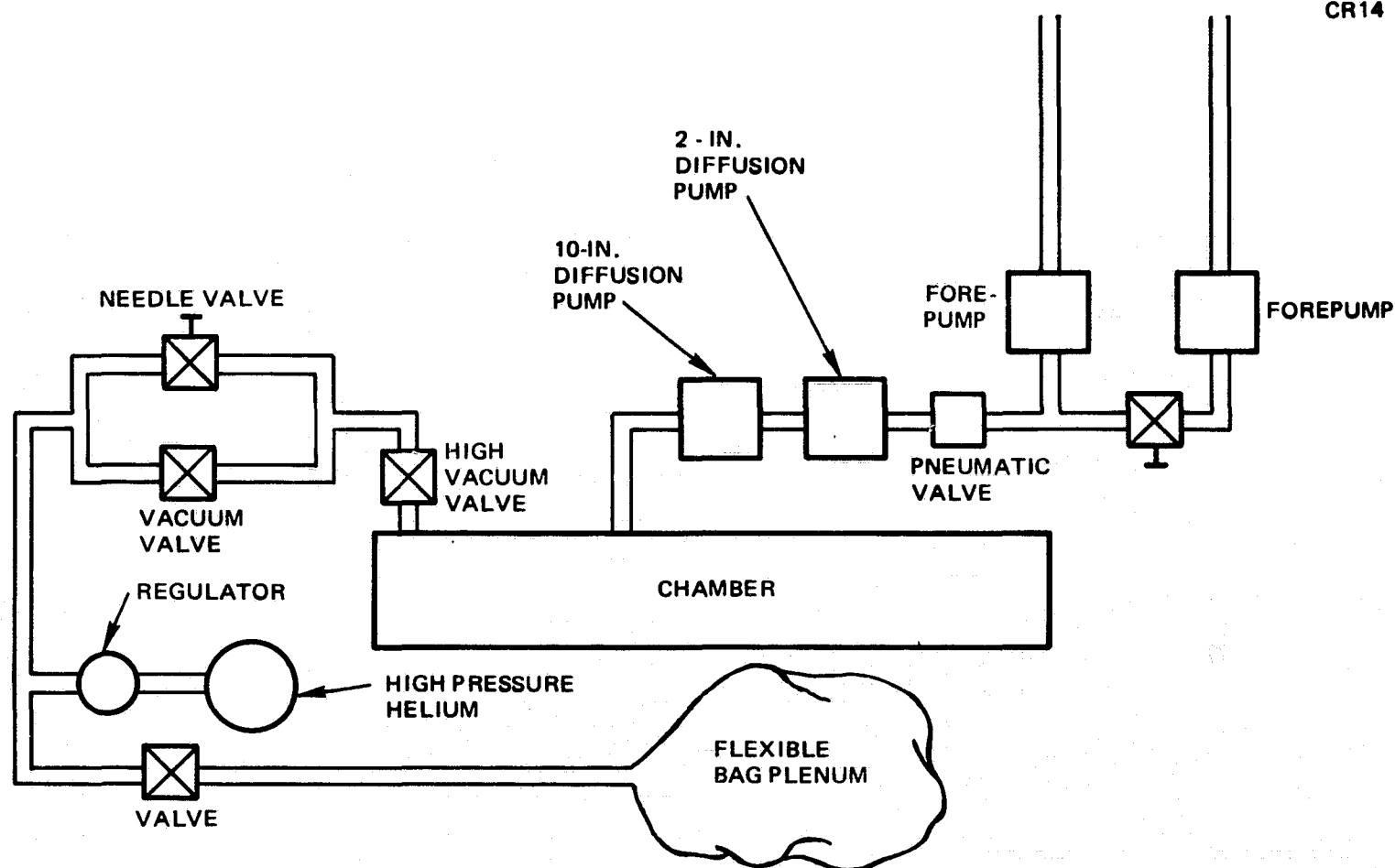


Figure 8-11. Evacuation and Repressurization System Schematic

Copper constantan thermocouples were located on the calorimeter, within the MLI, and on the outer surface of the MLI. The thermocouples and their locations are shown in Table 8-3. Further details of the location of the thermocouples within the MLI are presented in Figure 8-12. The wires for the thermocouples on the calorimeter and the thermocouple in the heat flux gage were brought out under the MLI along the fill and vent lines, see Figure 8-4. The wires for the thermocouples within the MLI were located for a distance on an isotherm within the MLI and then brought out through the joint between the test panels and an end cap.

The amount of liquid in the calorimeter was monitored by using a load cell placed between one of the support straps and the support beam, see Figure 8-3. The pressure history in the calorimeter was monitored with a 0 to 15 psi strain-gage-type pressure transducer.

All of these data were recorded on computer tape with an NLS Model 126220 data acquisition system, see Figure 8-13. The data were also recorded on

Table 8-3
THERMOCOUPLES - THERMAL DEGRADATION TEST

T/C Number	Location
1	Vent line near tank - Differential T/C, 4.2-in. spacing
2	Outer surface of vacuum chamber, South side
3	Fill line near tank - Differential T/C, 4.3-in. spacing
4	Fill line near tank - Differential T/C, 2.25-in. spacing
5	Vent line near tank
6	Fill line near tank
7	Bottom of tank
8	Support strap
9	Support strap
10	Outside layer of MLI, top of tank
11	In MLI, 35 layers from tank
12	In MLI, 20 layers from tank
13	In MLI, 10 layers from tank
14	At joint between outer test panel and end cap, 35 layers from tank
15	2-in. from joint between outer test panel and end cap, 35 layers from tank
16	4-in. from joint between outer test panel and end cap, 35 layers from tank
17	Outside layer of MLI, end of tank
18	In one of heat flux gages

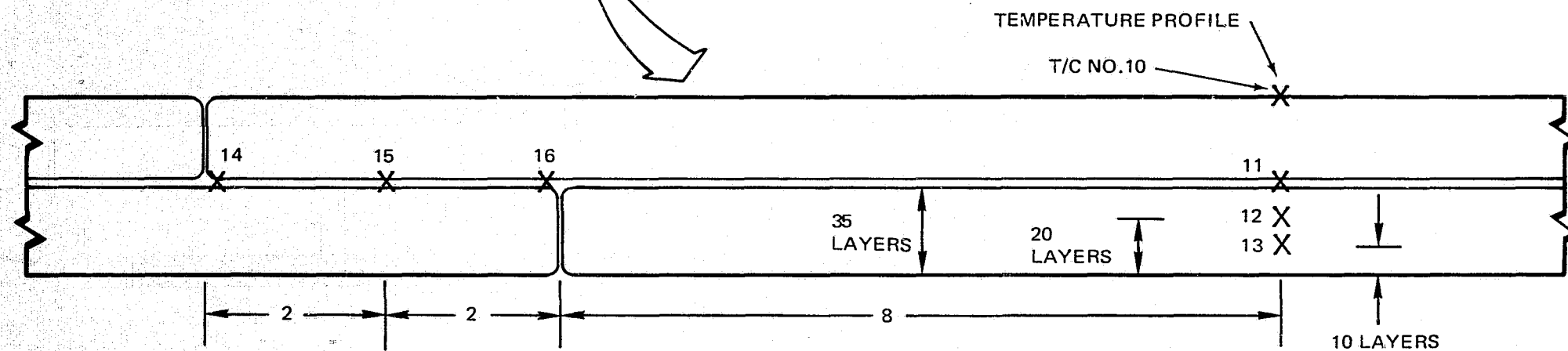
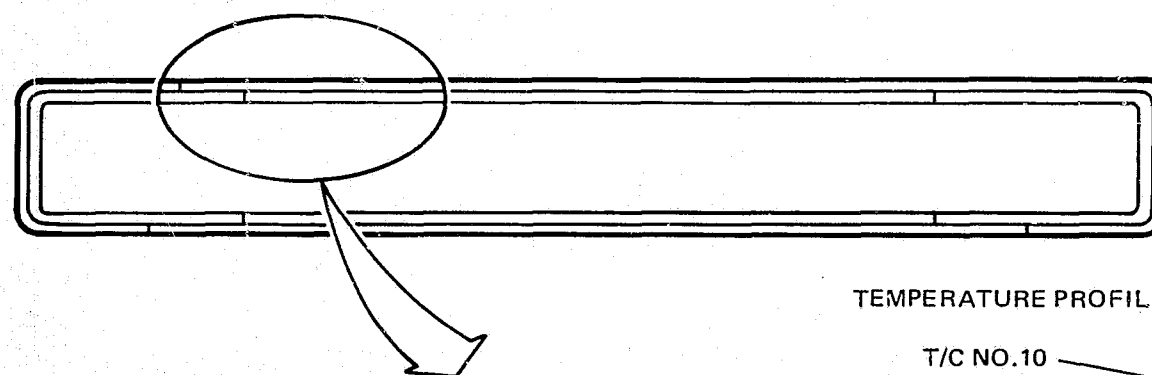
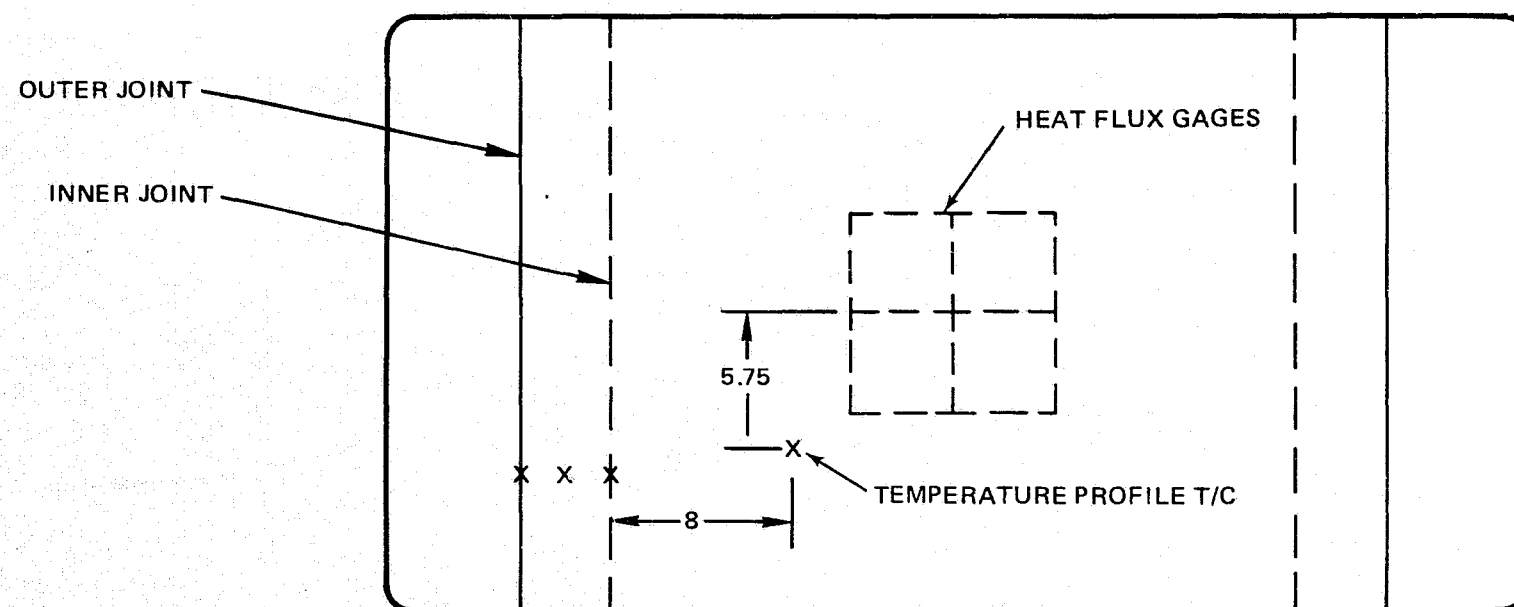


Figure 8-12. MLI Thermocouple Locations

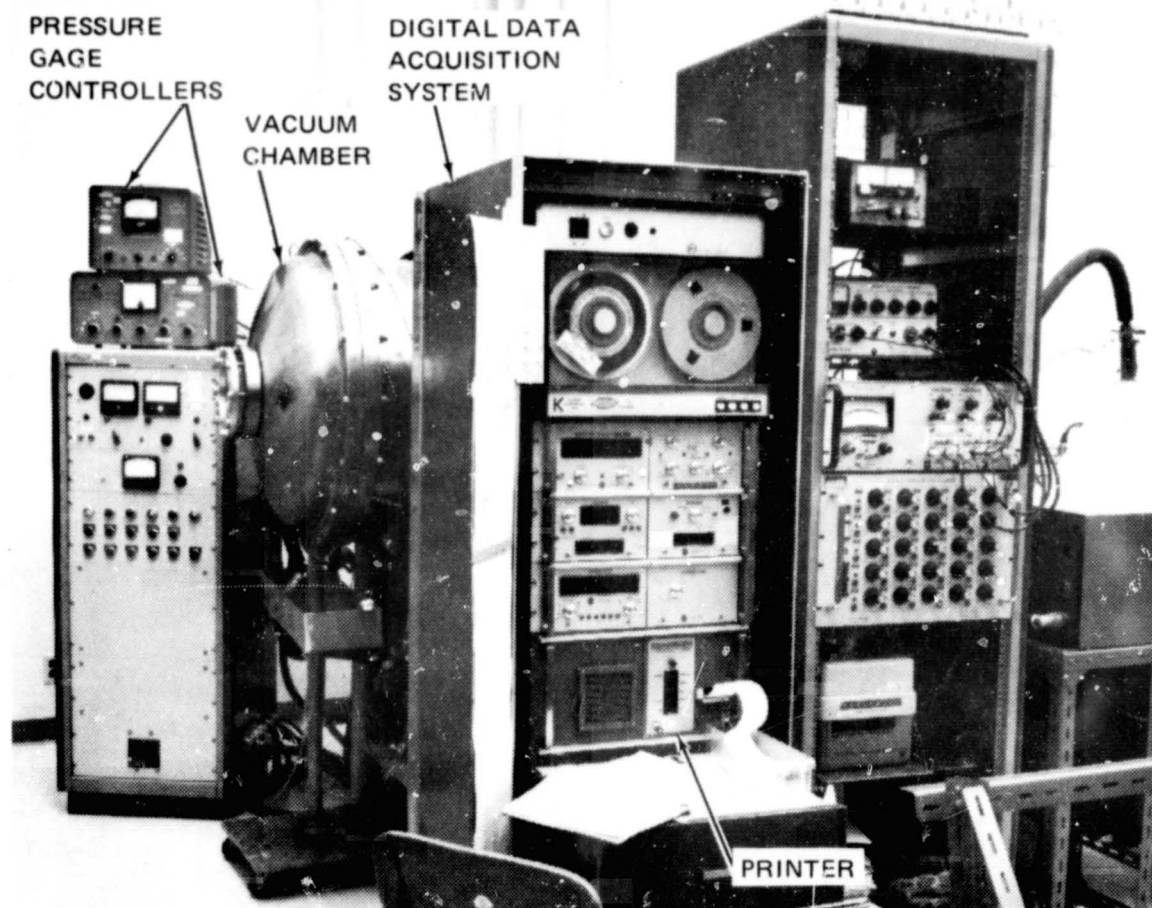


Figure 8-13. Data Acquisition System, Heat Flux Gage Calorimeter

a "printout" with a Franklin Electronics printer. The data acquisition system includes a digital clock. This time is recorded at the start of each data scan. A reference zero and reference voltages were also recorded as part of each data scan.

The calorimeter was filled with LN_2 from a 100-liter dewar (Figure 8-10). The LN_2 was forced out of the dewar and into the calorimeter by pressurizing the dewar with helium. During the filling operation, the fill-line valve was opened and the fill-line drain valve was closed, see schematic in Figure 8-14. After the calorimeter was full, the fill-line drain valve was opened to ensure that no liquid remained in the fill line. Both valves were then closed, forcing the nitrogen boiloff out the vent line.

The evacuation of the chamber was initiated by opening the pneumatic valve, see schematic in Figure 8-11; both of the forepumps were operating at all times. After reaching a pressure of 0.4 torr or less, the 10-inch diffusion pump was turned on. The 2-inch diffusion pump was not normally used

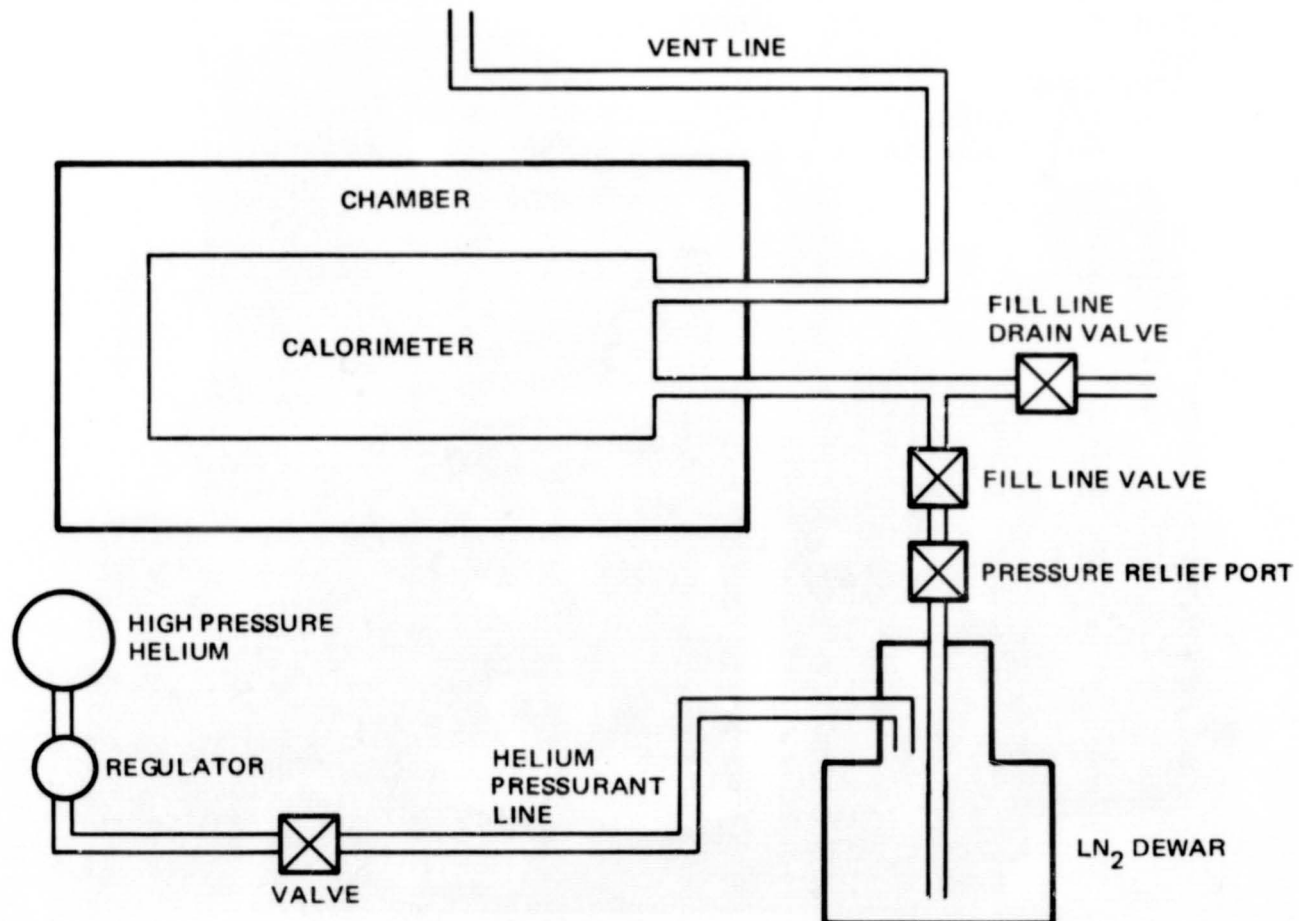


Figure 8-14. Calorimeter Fill and Vent System Schematic

because it was of little benefit in the pressure ranges of interest. An evacuation pressure history, cycle 50, is shown in Figure 8-15. The anticipated ambient pressure history during ascent for an ILRV is also shown (see Figure 4-5). Because of the long periods required to reach pressures of 10^{-5} to 10^{-6} torr, only a few of the cycles were allowed to reach pressures this low. For most of the cycles, the diffusion pumps were not turned on and repressurization of the chamber was initiated when the evacuation had reached a pressure of approximately 0.02 torr. This pressure of 0.02 torr is well below that which would create a significant pressure differential across the MLI.

Evacuation was normally begun shortly after the pressure in the chamber had reached one atm. However, on those cycles where the chamber pressure was allowed to drop to the 10^{-6} torr range, (those cycles of special interest such as number 1, 50, and 101) the chamber pressure was maintained at one atmosphere pressure until a nearly steady-state heat flux condition had been reached.

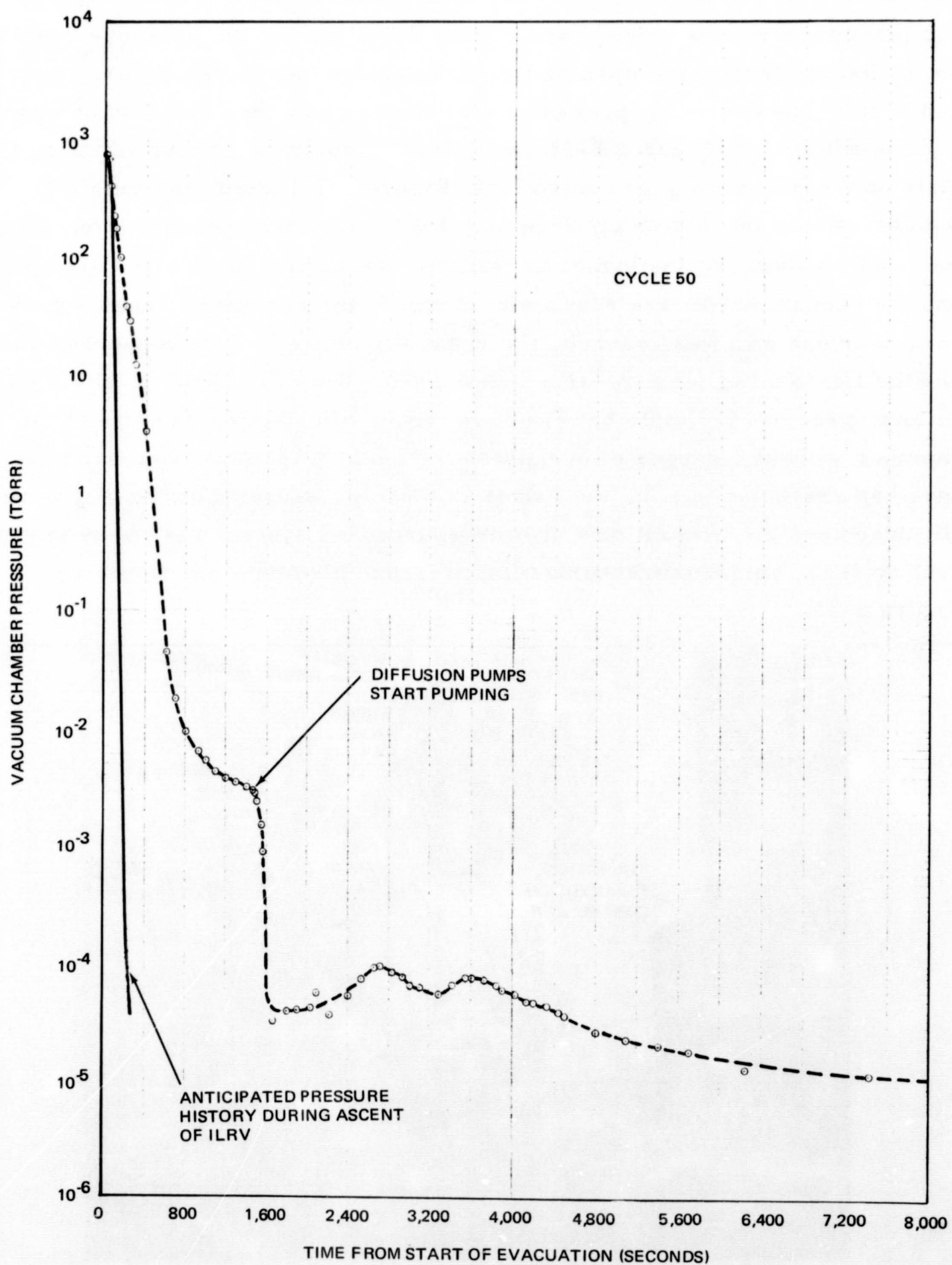


Figure 8-15. Evacuation Pressure History

The initial steps involved in the repressurization consisted of: closing the pneumatic valve in the chamber evacuation line; verifying that the flexible bag plenum valve was closed, see Figure 8-11; setting the pressure regulator on the helium bottle; and opening the high vacuum valve, see Figures 8-11 and 8-16. The desired repressurization history was then obtained by opening a needle valve (Figures 8-11 and 8-16) as required. A stop watch and dials on the pressure gage controllers (Figure 8-16) were used with a plot of the desired pressure history (Figure 8-16) to guide the operator in opening the needle valve. At the higher pressures, the needle valve was fully opened and the vacuum valve (see Figures 8-11 and 8-16) was used. When a pressure near one atm was reached, the regulator on the helium bottle was closed and the flexible bag plenum valve was opened. This flexible bag, filled with helium, provided a simple but effective means of obtaining one atm in the chamber without a danger of overpressurization. When the chamber pressure had reached one atm, the valves in the repressurization system were all closed and the evacuation and repressurization system was ready for the next cycle. Typical repressurization pressure histories are shown in Figure 8-17.

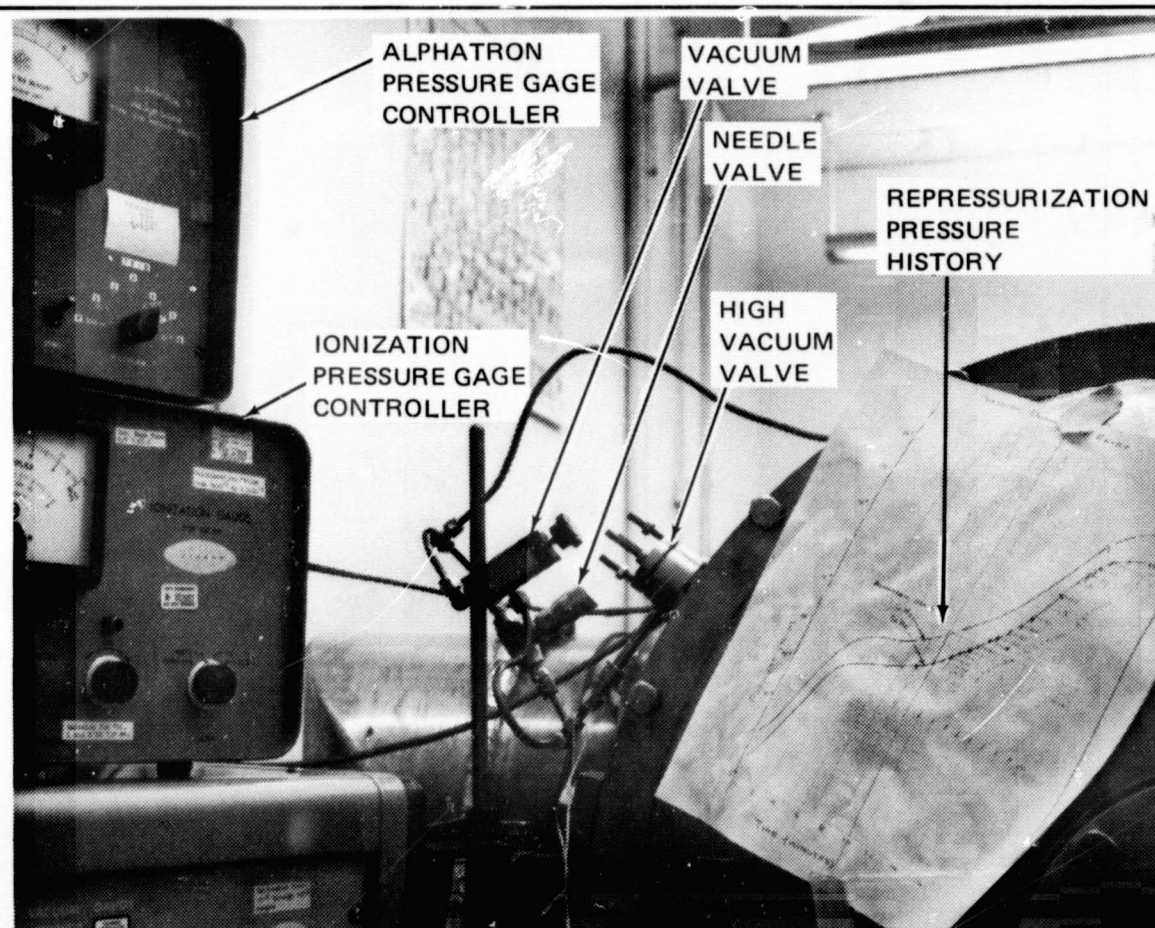


Figure 8-16. Repressurization System

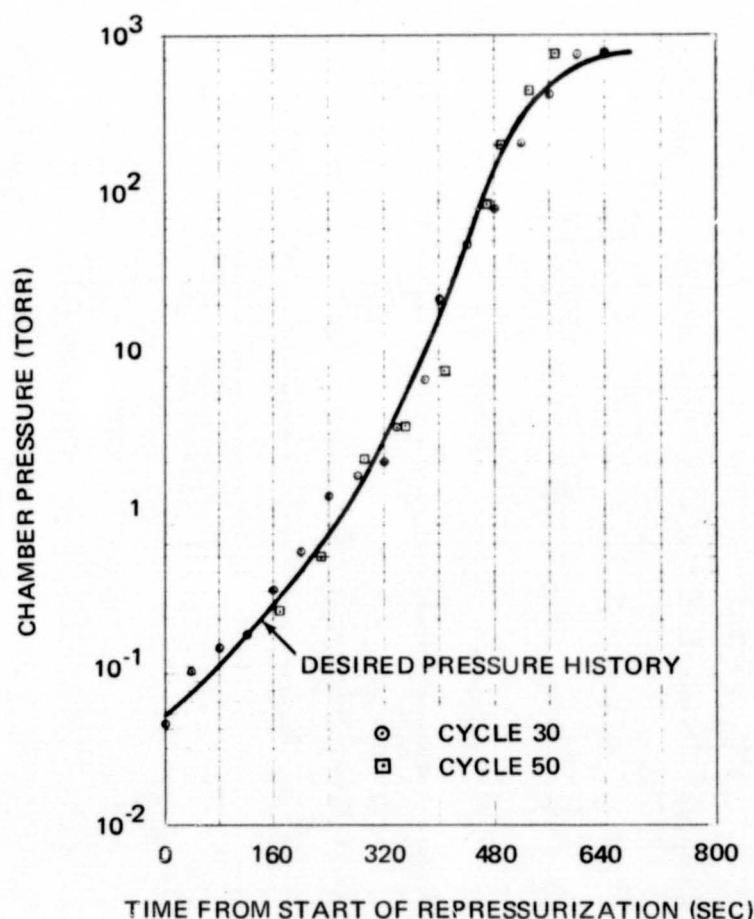


Figure 8-17. Typical Repressurization Pressure Histories

Liquid nitrogen (LN_2) was used as the cryogen in the calorimeter and helium was used as the repressurization gas for all of the cycles. The MLI and vacuum chamber were purged with helium prior to evacuation on the first cycle. After purging the MLI, the calorimeter was filled with LN_2 while the chamber contained helium at one atm. This simulated the ground-hold phase of an actual vehicle launch. The calorimeter was refilled during the cycles whenever needed and at times which did not interfere with obtaining significant data. The calorimeter was never allowed to be completely emptied of LN_2 .

8.2.4 Test Results

The heat flux histories obtained for cycles 1, 50, and 101 are shown in Figures 8-18 and 8-19. The steady-state heat flux for cycles 50 and 101 are in good agreement with each other, showing heat fluxes of approximately 0.14 to 0.15 Btu/hr ft^2 . The steady-state heat flux for cycle 1 was a little over twice as high, with a value of approximately 0.34 Btu/hr ft^2 . It is felt that the higher heat flux for cycle 1 was probably due primarily to a higher

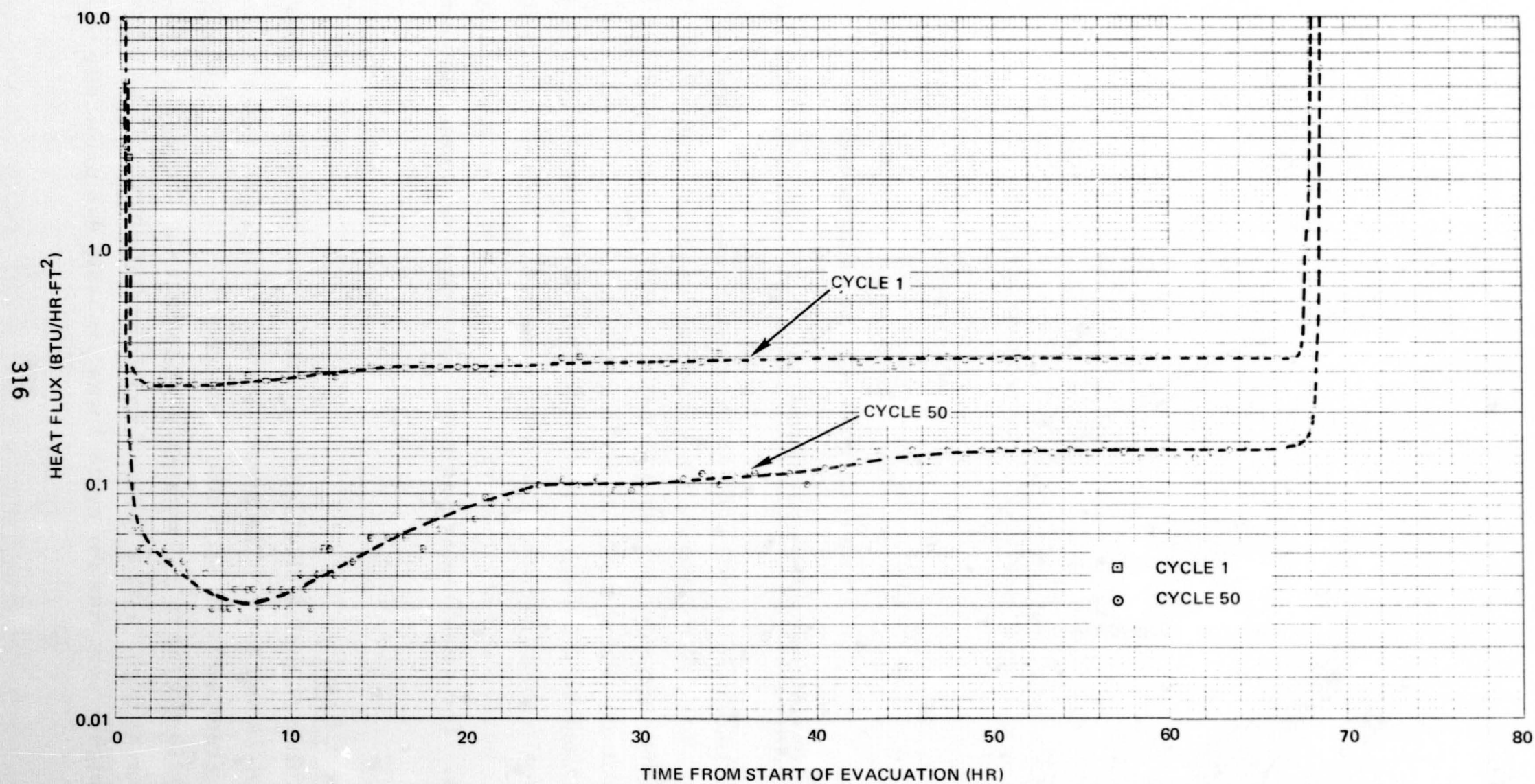


Figure 8-18. Heat Flux History - Cycle 1 and 50

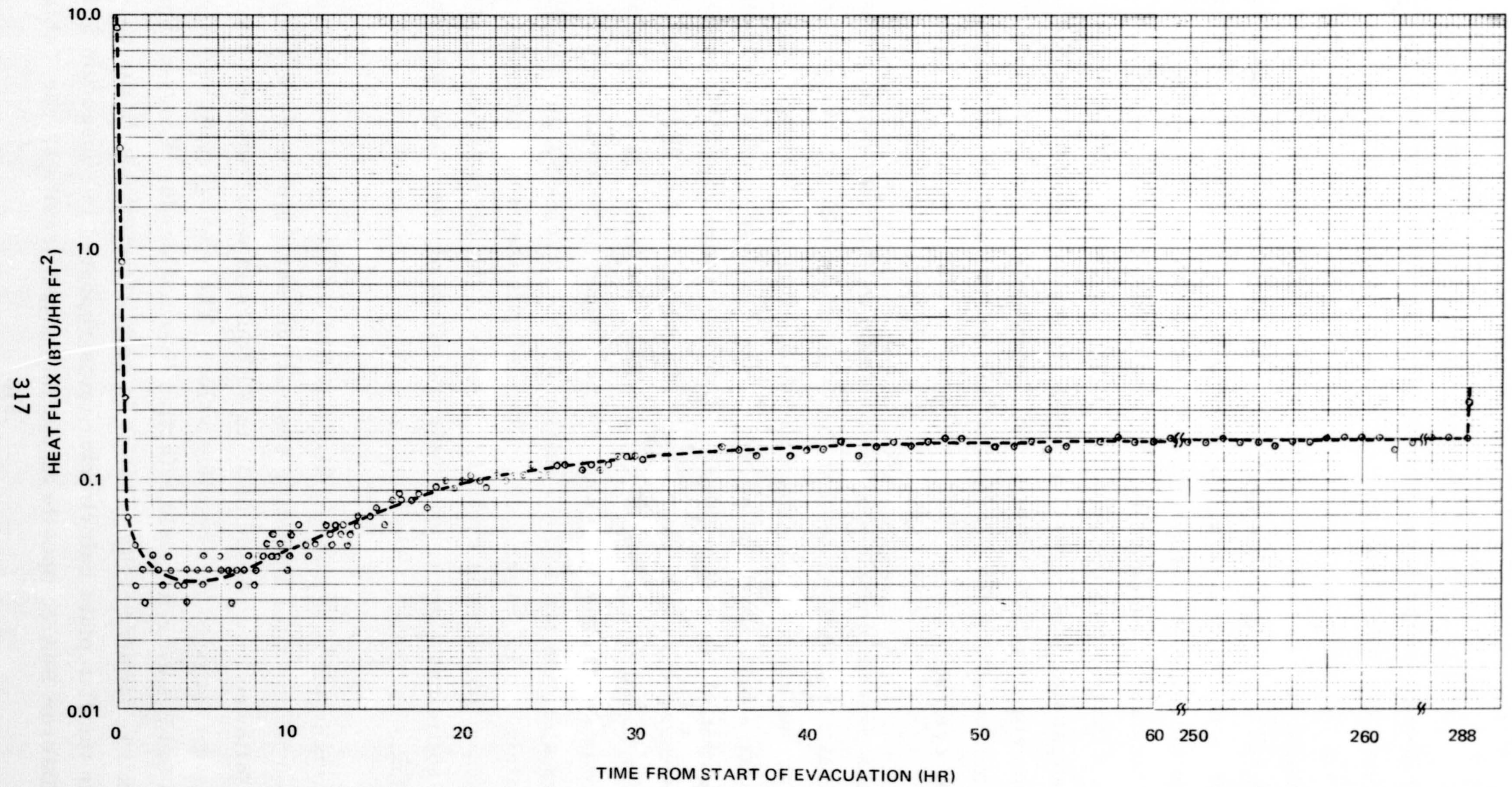


Figure 8-19. Heat Flux History - Cycle 101

layer density for this cycle. The repressurization and evacuation of the MLI apparently decreased the layer density resulting in a lower heat flux for the evacuated periods in the later cycles.

The dip in heat flux immediately after evacuation to values of 0.03 to 0.04 Btu/hr ft², as shown for cycles 50 and 101, is consistent with expected results and is due to the storage of energy by the MLI layers. The energy required to increase the temperature of the layers after evacuation does not reach the tank and, consequently, the heat flux to the tank is reduced. The absence of a large dip in the heat flux for cycle 1 is thought to be an indication that outgassing was occurring. This would tend to increase the heat flux and thereby offset the effect of storing energy in the layers. Pressure data also indicated that the evacuation was not as rapid as that experienced in the later cycles.

Although the evacuation rate was not as rapid on the first cycle, it is not apparent that the steady-state heat flux was affected by a higher interstitial gas pressure within the MLI. Unfortunately, this conclusion is somewhat tenuous since a large part of the cycle 1 steady-state chamber pressure data were not obtained due to a problem with the pressure gage. However, some steady-state pressure data were obtained near the end of the cycle. For example, at 66 hours after the start of evacuation on cycle 1, the chamber pressure was approximately $3 \text{ to } 3.5 \times 10^{-6}$ torr. The chamber pressure at 66 hours after the start of evacuation for both cycles 50 and 101 was approximately 9×10^{-7} torr. This may indicate that some outgassing was still present at 66 hours in cycle 1. However, the pressure of 3.5×10^{-6} torr should be sufficiently low to eliminate the effect of interstitial pressure on the heat flux.

The heat flux in all of the cycles had reached its steady-state evacuated value in less than 1 hour after initiating evacuation, see Figures 8-18 and 8-19. This was followed by a period of 30 to 40 hours in which the heat flux was less than the evacuated steady-state value. The steady-state heat flux values of 0.14 to 0.15 Btu/hr ft² yield effective thermal conductivities of approximately 2×10^{-5} Btu/hr ft°R. This is in good agreement with the data obtained in the flat-plate calorimeter tests reported in Subsection 3.10 for the DGK/Dacron B4A composite at similar layer densities, see Table 3-28.

The heat flux history during an evacuation and a repressurization are shown in Figures 8-20 and 8-21, respectively. Both curves are data obtained on cycle 50. A typical steady-state heat flux in helium at one atmosphere pressure is also shown in Figure 8-20.

A typical steady-state temperature profile through the MLI, when in a vacuum, is shown in Figure 8-22. A typical temperature profile within the MLI layup at a joint is shown in Figure 8-23. The thermocouples for the data shown in Figure 8-23 were all located on a face sheet between the inner and outer panels (layer number 35). The temperature effect of the joint was less than had been expected. As shown, a temperature difference of only approximately 12°F was recorded.

CR14

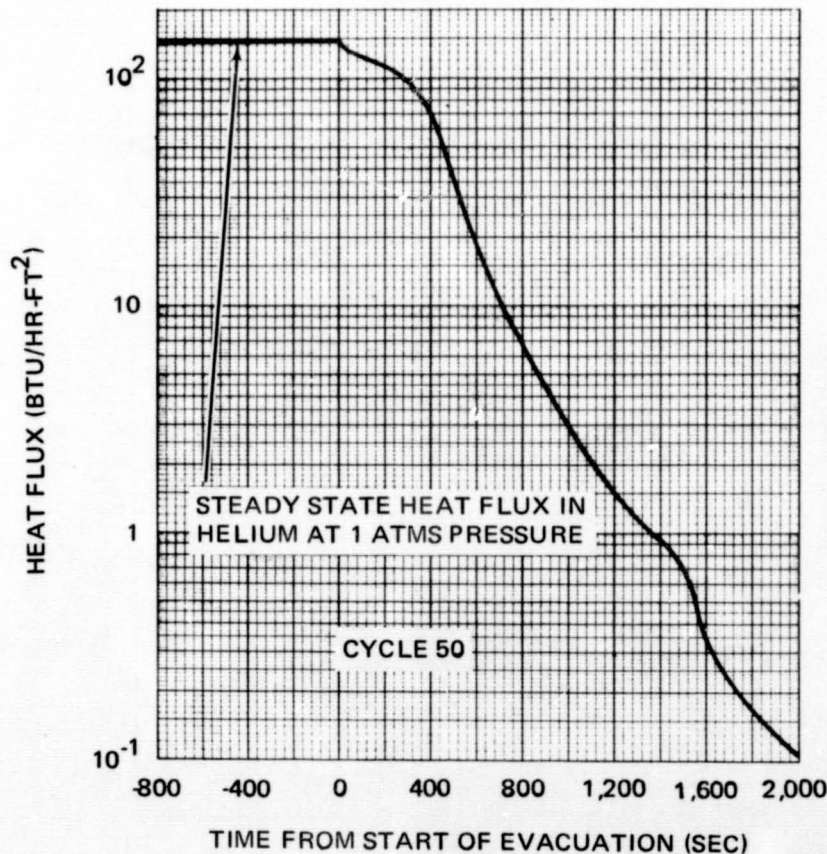


Figure 8-20. Heat Flux History During Evacuation

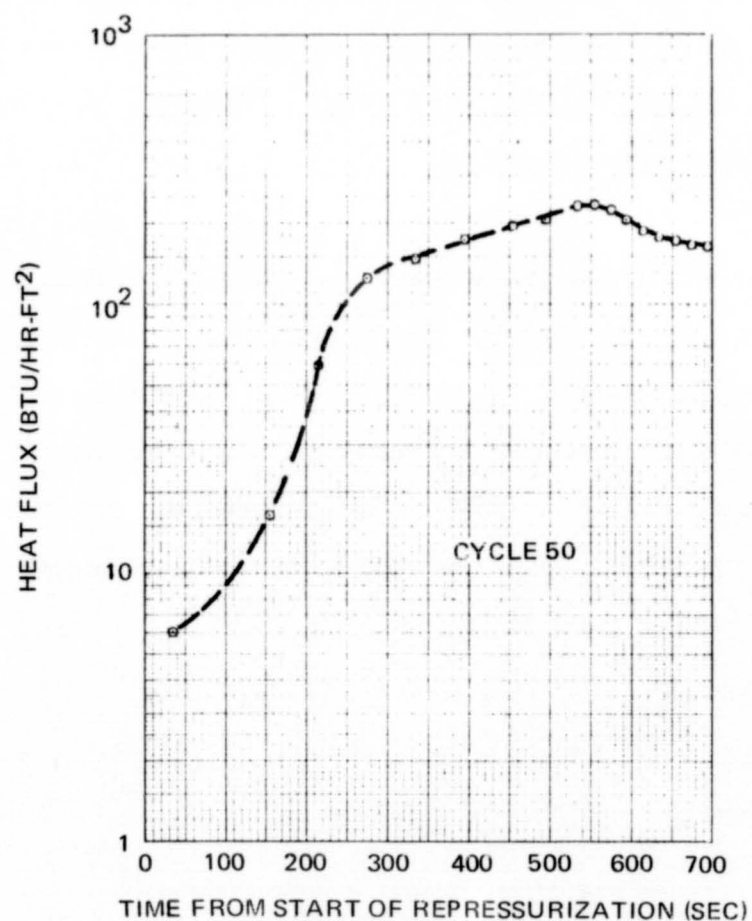


Figure 8-21. Heat Flux History During Repressurization

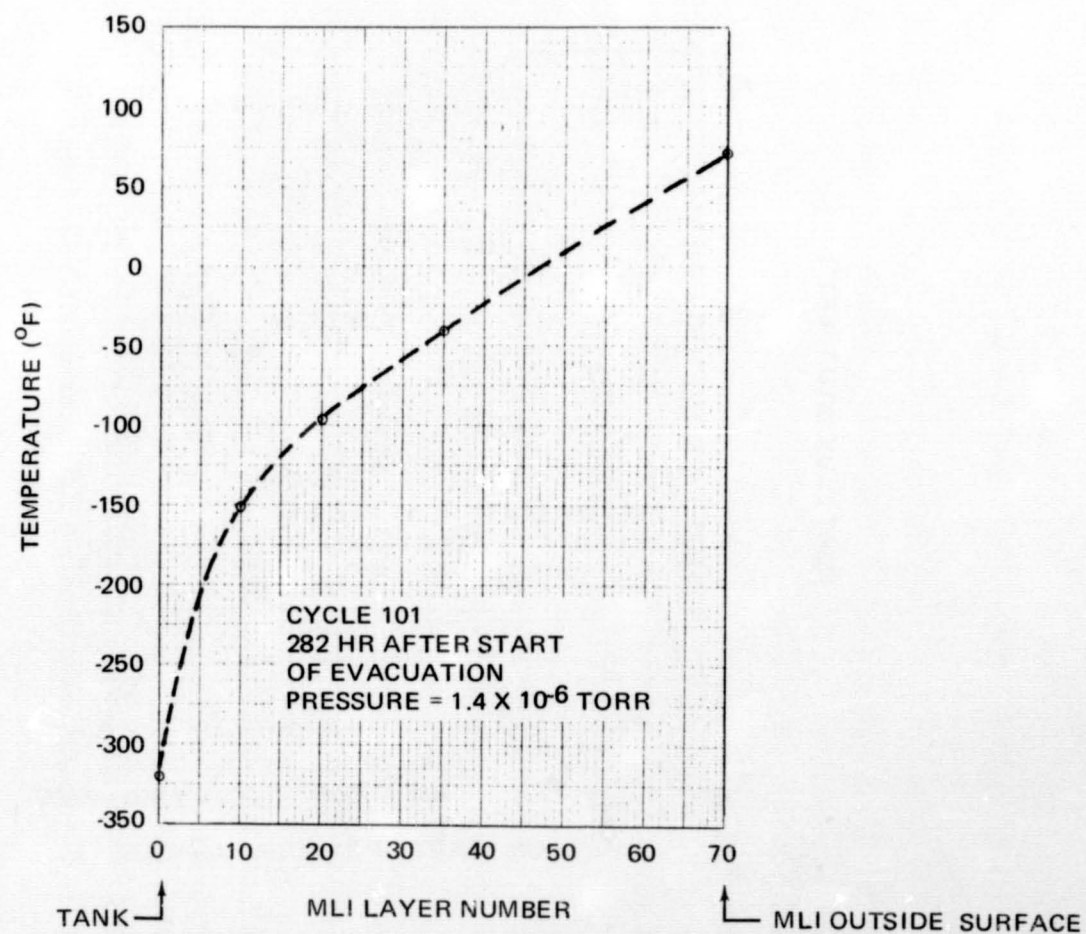


Figure 8-22. Typical Evacuated Steady State Temperature Profile Through MLI

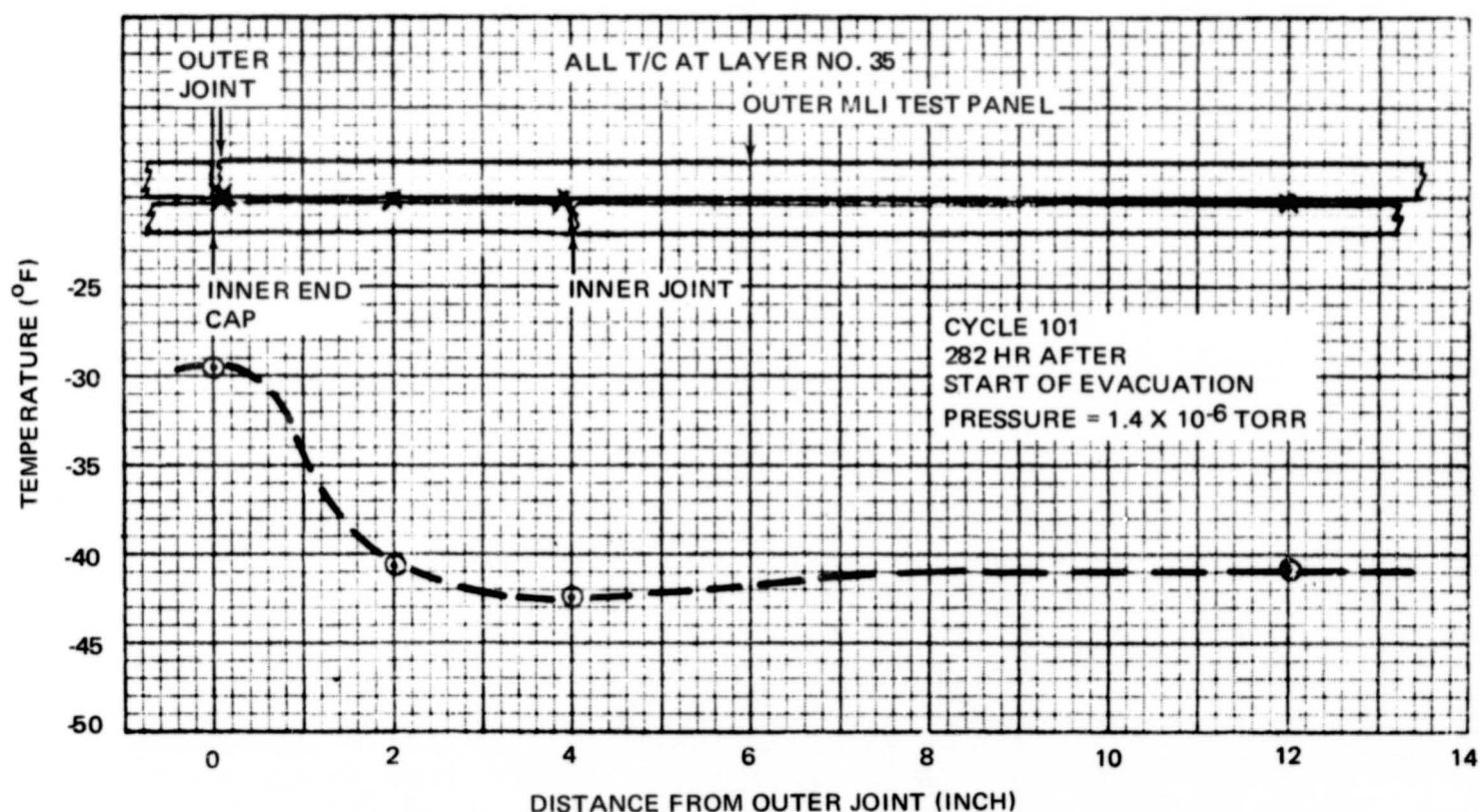


Figure 8-23. Typical Temperature Profile at a Joint

8.2.5 Conclusions and Recommendations—Thermal Degradation Test

The thermal degradation tests showed that an improvement, not a degradation, may be expected in the thermal performance of the MLI as a result of repeated evacuation and repressurization cycling. It was concluded that some outgassing was present on the first cycle, but the evacuation of the MLI was quite rapid for all of the cycles. The evacuated steady-state heat flux value was reached in less than one hour.

The heat-flux gage calorimeter has proven to be a very useful tool. It appears to have great potential for studies on MLI evacuation, effects of outgassing, effects of joints, effects of system configuration, purging, chilldown, and effects of environmental cycling, as well as the thermal performance of full thickness MLI candidate composites. Further studies in these areas using the heat-flux gage calorimeter are strongly recommended.

Section 9

SELECTION OF MLI SYSTEM AND MATERIALS-TASK 7

The objective of Task 7 was to select an MLI system and the materials for the components in that system based on the test data and analytical results obtained in other tasks within this contract.

9.1 SYSTEM SELECTION

Four insulation system configurations were considered in this study. These were tank-mounted insulation with or without foam on the interior surface of the tank wall and non-tank-mounted insulation with or without foam on the interior surface of the tank wall. Purging of the insulation and the associated purge bag and plumbing hardware are included as part of each of the systems considered. For the non-tank-mounted insulation systems, a single-curvature gore segment shroud which envelops the tank was selected to support the insulation, see Section 5. The weight of this shroud was estimated to be 80 and 181 lb for the LO_2 and LH_2 tanks, respectively. Although this weight is relatively small considering the large size of these shrouds, the reduction in boiloff does not appear to be sufficient to offset the weight of the shroud. As shown in Table 9-1, a complete elimination of the in-space boiloff would not offset the weight of the shroud for a 7-day mission. A reduction in boiloff of 35 to 38 percent would be required to offset the weight of a shroud on a 30-day mission. This is slightly more than the theoretical maximum anticipated reduction of 20 to 30 percent. Since the shroud was designed to fit as closely as possible over the tank, the net effect on the system weight of any changes in the weights of such things as the MLI, purge bag, fasteners, lacing buttons, attachment hardware, plumbing, and repressurization bottle, resulting from placing the MLI on the shroud, should be negligible. Consequently, a tank-mounted insulation system appears to be a better configuration for this application when used in missions of 30 days or less duration.

Table 9-1
IN-SPACE BOILOFF VS SHROUD WEIGHT

Tank	Tank Surface Area (ft ²)	7-Day Mission		30-Day Mission		MLI Shroud Weight (lb)
		In-Space Boiloff (lb/ft ²)	Total In-Space Boiloff (lb)	In-Space Boiloff (lb/ft ²)	Total In-Space Boiloff (lb)	
LH ₂	863	*0.1307	113	*0.559	482	181
LO ₂	352	**0.1645	58	**0.665	234	80

*Taken from Table 6-1.

**Obtained from Figures 6-45 and 6-46.

Three different system concepts were investigated in detail for MLI mounted on the LH₂ tank: (1) helium purge of the MLI during ground hold and helium repressurization during reentry, with no internal tank foam; (2) helium purge and repressurization as in (1), but with the minimum practical thickness (0.5 inch) of internal tank foam; and (3) nitrogen purge of MLI during ground hold, helium repressurization during reentry, and with sufficient internal tank foam to preclude liquefaction of nitrogen purge gas during ground hold. The analyses showed that the helium purge and helium repressurization with no foam system provides the lowest system weight and was, therefore, selected for the LH₂ tank, see Section 6.

Two different system concepts were investigated in detail for MLI mounted on the LO₂ tank: (1) helium purge and repressurization, with no tank foam; and (2) nitrogen purge and repressurization, with no tank foam. The results of the analyses (Section 6) show that the nitrogen purged system concept offers the lowest system weight and was, therefore, selected for the LO₂ tank.

9.2 REFLECTOR MATERIAL

Four candidate reflector materials were considered after a preliminary evaluation and material survey. These were double goldized Kapton (DGK),

double aluminized Kapton (DAK), double goldized Mylar (DGM), and double aluminized Mylar (DAM). From these candidates, the DGK material was chosen. One of the significant advantages of the goldized material over the aluminized material is its high resistance to moisture degradation. This was verified in tests (Section 3.5) which indicated that control of the condensibles within the MLI while the vehicle is on the ground between flights will not be required to prevent moisture degradation if DGK is used. An aluminized reflector would require control of the condensibles within the MLI. The goldized materials also have a lower surface emissivity than do the aluminized materials. Consequently, a slightly higher thermal performance can be obtained with a goldized reflector. This was verified in the calorimeter tests reported in Subsection 3.10. Testing also indicated that the gold will not be removed by abrasion from the separator when subjected to the acoustic environment (Subsection 3.8) and that the DGK material is capable of withstanding the temperature cycling in an orbiter application (Subsection 3.3).

DGK was chosen over DGM because Kapton has the capability of withstanding much higher temperatures. Also the supplier has experienced difficulty in manufacturing the DGM and this material will probably only be available in much thicker (therefore heavier) sheets in the future.

Should future studies show that control of the condensibles within the MLI while the vehicle and tankage are being serviced and inspected between flights is not a significant problem in terms of system complexity, reliability, and operating costs, and the in-flight temperature environment is low enough to permit using Mylar, the DAM material could be considered. The DAM is available in 15-gage material and is, therefore, lighter than the 25-gage DGK material. The DAM also has a lower material cost.

9.3 SEPARATOR MATERIAL

Numerous candidate separator materials were considered in this study. These included: Nomex nets (styles HT-96, HT-289, and HT-58); Dacron net (style B4A); Beta glass nets (styles 1653 and 1659); Nomex fabric (style HT-287); Durette fabric (style 6632-27-2); and Beta glass fabric (style 81677). From the separators considered, the Dacron B4A has been selected. The

combination of light weight and high thermal insulation performance provided by the Dacron B4A net is the principal reason for its selection. Testing that was accomplished to evaluate the separator candidates has included thermal-resistance screening (Section 3.2), flat-plate calorimeter (Subsection 3.10), outgassing (Section 3.6), cyclical temperature (Subsection 3.3), strength after cyclical temperature (Section 3.3), effect of separator volatiles on reflector emissivity (Section 3.4), thermal expansion (Subsection 3.7), compression effects on layer density (Subsection 3.9), and acoustic tests (Subsection 3.8). The results indicated that the Dacron B4A net would provide the highest thermal performance, the lowest outgassing, and would meet the current cyclical temperature design criteria (maximum temperature of 350°F). The strength of all of the separator materials tested was degraded by the temperature cycles, but all retained adequate strength to support the minimal loads to which the separators are subjected. No degradation in reflector emissivity due to separator volatiles could be detected for any of the separator materials tested. The thermal expansion characteristics of the Dacron B4A are satisfactory. The use of Dacron B4A results in relatively higher layer densities but the increase in layer density resulting from 100 compressive load cycles was lowest (approximately 5 percent) for the DGK/Dacron B4A composite. The Dacron B4A withstood the acoustic environment tests without degradation. The Nomex HT-96 and HT-287 separator materials which were also included in the acoustic environment tests sustained some unraveling.

Should future requirements necessitate a material with the capability for withstanding higher temperatures than possible with Dacron, the Nomex HT-96 net or Nomex HT-287 fabric could be considered because these materials withstood temperature cycles to 650°F. These materials also are lighter weight and indicated better thermal performance, except for Dacron B4A, than the other separator materials considered. Nomex HT-96 has the lowest weight and exhibited the highest thermal insulation performance of the Nomex materials considered; however, it is difficult to handle in fabrication of composite panels as it has a tendency to unravel. The Nomex HT-287 fabric is slightly less desirable from a weight and thermal performance consideration but is much more resistant to unraveling. Both Nomex materials would require further evaluation in an acoustic environment. B4A can be readily fabricated and has no tendency to unravel.

9.4 FACE-SHEET SYSTEM

The face-sheet system consists of a basic material with a load-carrying strap fabricated onto this basic material by impregnating the strap area with a resin. A Nomex fabric (style HT-287) and a Beta glass fabric (style 81677) were considered for the basic material. Viton, Silicone, Polyimide, and Teflon were considered as the resin. Thus, a total of eight face-sheet systems were considered. Of these, the Polyimide/Nomex HT-287 and Silicone/Nomex HT-287 systems have been selected, as shown in Table 9-2.

An important consideration in the selection of a face sheet system is its thermal expansion characteristics. To ensure that the load is being carried by the face sheet strap and not the reflectors or separators, the face sheet must always have a contraction greater than that of the reflector and separator material at a cold temperature and an expansion less than that of the reflector or separator at a hot temperature. The thermal expansion characteristics of the face-sheet systems considered were obtained and are reported in Section 3.7. The results indicated that the Silicone/Nomex HT-287,

Table 9-2
MLI COMPOSITE MATERIALS SELECTED

Component	Material	Supplier
Reflector	Double goldized Kapton (25 to 30 gage)	National Metallizing
Separator	Dacron net (Style B4A)	Apex Mills
Face-Sheet System		
Outer surface of MLI	Nomex fabric (Style HT-287) and Polyimide resin	Fabric: Stern and Stern
Center of MLI	Nomex fabric (Style HT-287) and Silicone resin	
Inner surface of MLI	Nomex fabric (Style HT-287) and Silicone resin	
Fastener	Polysulfone—Astrel 360	

Viton/Nomex HT-287, and Teflon/Nomex HT-287 systems could all be considered for the face sheet on the inner (cold) surface of the MLI. Of these systems, the Silicone/Nomex HT-287 system has the lightest weight and the best match of thermal contraction characteristics to that of the DGK and Dacron B4A. Therefore, Silicone/Nomex HT-287 has been chosen for use in the cold portion of the MLI composite. The strength of the Silicone/Nomex system was shown to be adequate after temperature cycling and no brittleness problem at cryogenic temperatures was apparent (Subsection 3.3).

Silicone/Nomex HT-287 has also been selected for the outer face sheet of the inner MLI panel and the inner face sheet of the outer MLI panel. For the temperature operating band at the location of these face sheets in the center of the MLI composite, the same face-sheet systems can be considered as for the inner, cold, surface with the Silicone/Nomex HT-287 again offering the lowest weight and best match of thermal contraction characteristics.

The thermal expansion test results indicated that the Polyimide/Nomex HT-287, Polyimide/Beta glass, Teflon/Beta glass, Silicone/Beta glass, and Viton/Beta glass systems could all be considered for the face sheet on the outer (hot) surface of the MLI composite. Of these, the thermal expansion characteristics for the Polyimide/Nomex HT-287 and Teflon/Beta glass, at the temperatures of the outer face sheet, appeared to have the best match to the thermal expansion characteristics of the DGK and Dacron B4A. The Polyimide/Nomex HT-287 was chosen since its weight is only approximately 1/3 that of the Teflon/Beta glass system. The weight of the Polyimide/Nomex HT-287 system is also less than that of the other face-sheet systems considered. The strength of the Polyimide/Nomex was shown to be adequate (Subsection 3.3) at the operating temperatures of the outer face sheet. A more detailed discussion of the selection of the face sheet systems is contained in Subsection 7.4.

9.5 FASTENER MATERIAL

The candidate materials considered for the fastener were Polyimide, Teflon, Nylon, and Polysulfone (Astrel 360). The Polyimide materials can be expected to be too brittle in the thin sections required for fastener design. A

difficult joining problem of fastener shank and button would be anticipated with Teflon materials. The Nylon material has been used in the past but does not have high temperature capability. Only the Astrel 360 material has both a high temperature capability and lends itself to fabrication. Consequently, Astrel 360 has been chosen. The Astrel 360 material successfully withstood temperature cycles to 400°F, which is within present design requirements, with a minimal loss of strength (Subsection 3.3). This material, however, did not survive temperature cycles to 650°F and could not, therefore, be used at temperatures above 400°F without further evaluation.

9.6 PURGE BAG MATERIAL

Teflon-coated Kapton was selected for the purge bag material. Other possible materials which would meet the temperature requirements and which were considered were a Beta glass or Nomex fabric impregnated with a silicone, Viton, or Teflon coating. In this application, the resin serves to greatly reduce the permeability of the fabric. The Teflon-coated Kapton was chosen because it appears to offer the lowest weight and permeability of those materials considered. The purge bag materials selected and their properties are summarized in Table 7-4.

PRECEDING PAGE BLANK NOT FILMED

Section 10

INSULATION SYSTEM CONFIGURATION-TASK 8

The principal objective of Task 8 was to define a conceptual design for the MLI system selected. To accomplish this objective, sketches were prepared showing how the insulation system could be assembled and applied to a typical ILRV cryogenic tank. The LH_2 tank defined in Task 3 (see Section 5) was used. The approach taken was to start with the basic gore panel design outlined in NAS 8-21400 (Ref. 1) changing it where justified, and adding elements where necessary to complete the design. The resulting conceptual design includes sketches showing assembly configurations for all regions of interest. This includes the area around the tank manhole and MLI gore panel support ring, tank support struts, and plumbing. It also includes a sketch of a typical gore panel, gore reflector sheet, purge bag, fastener, and lacing button. Evacuation valves and purge and repressurization gas inlet and outlet ports are included in the sketches. The plumbing schematic and further details of the purge and repressurization system conceptual design are included with the analyses and discussion of the purge and repressurization system in Subsection 6.5.

10.1 MLI COMPOSITE ASSEMBLY CONFIGURATION

In the system design selected, the layers of reflectors and separators are fabricated into panels which are then attached to the tank. Two panels, an inner and outer panel, are used to obtain the desired insulation thickness. Use of 2 panels for the thickness allows offsetting the joints between panels to form what is termed a staggered butt-joint configuration. An indication of the orientation and location of the staggered butt joints is included in Figure 10-1 (Sketch No. SK 710511). The main MLI panels are gore shaped to conform to the compound curvature of the tank. These gore panels extend from one end of the tank to the other except for a circular, disk-shaped panel located at each end of the tank (Figure 10-1). All of the tank plumbing is located at one end of the tank and insulation is placed around this plumbing. Insulation is

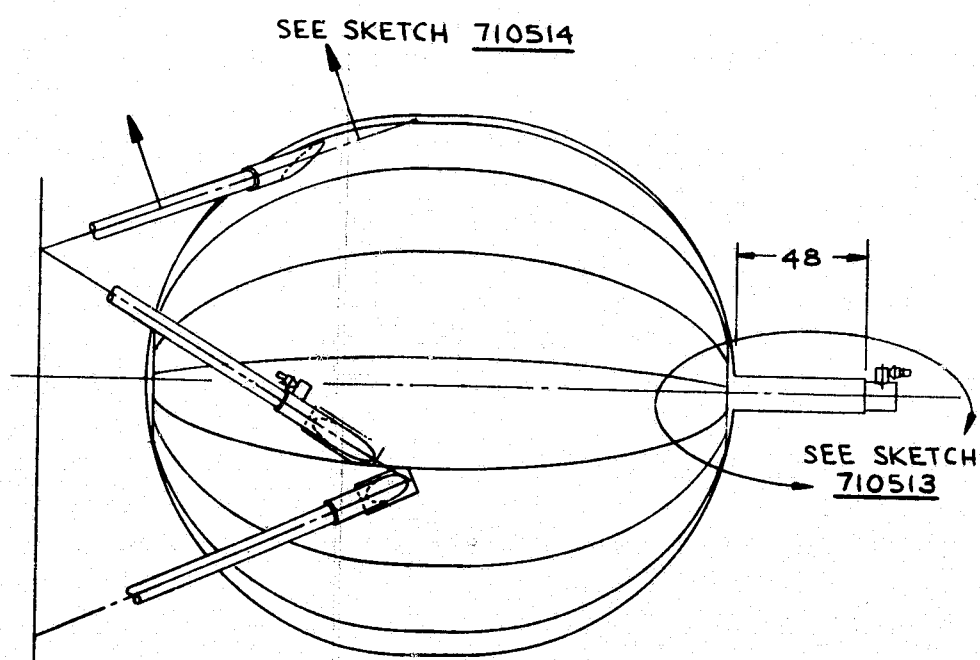
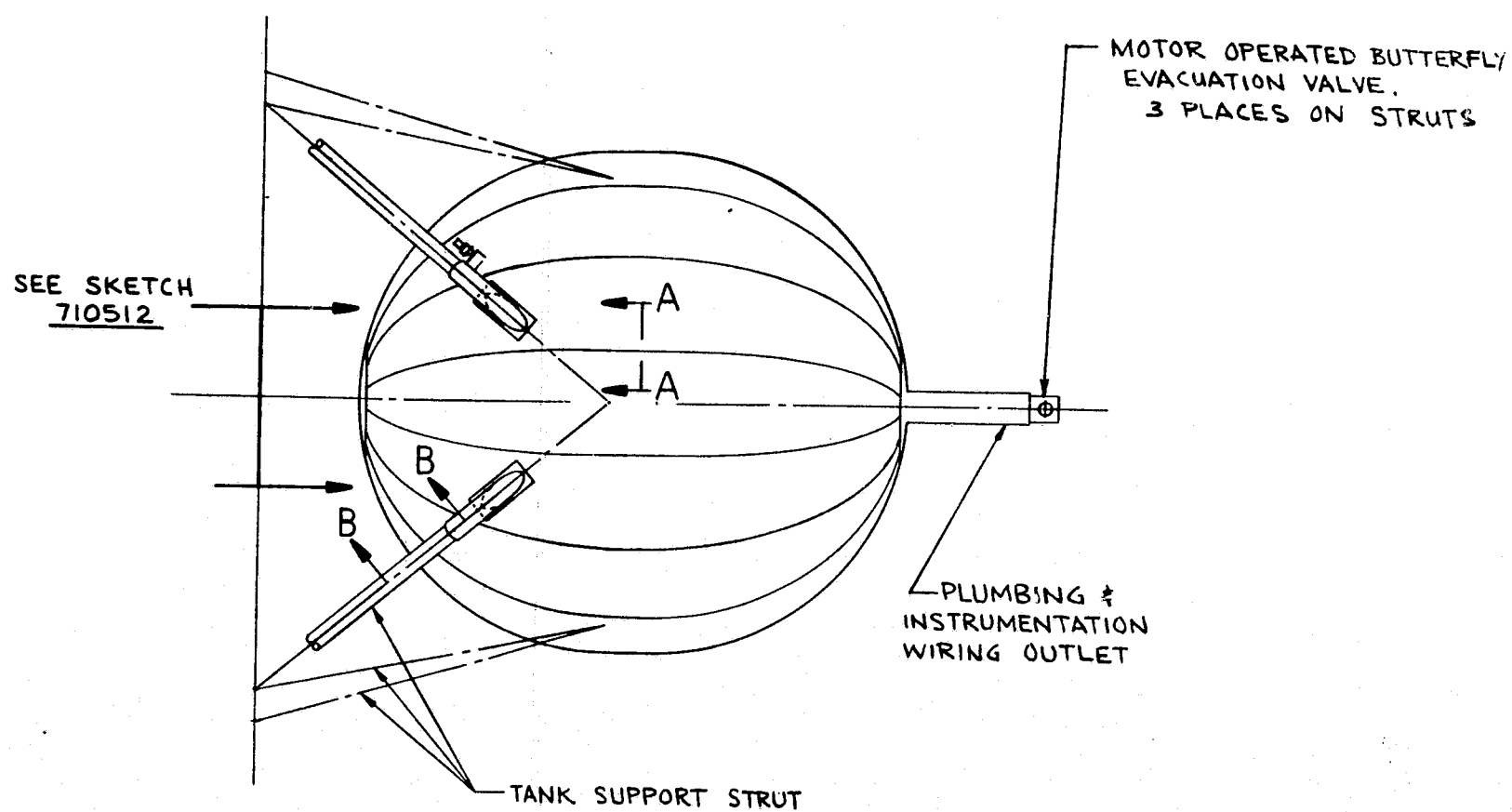
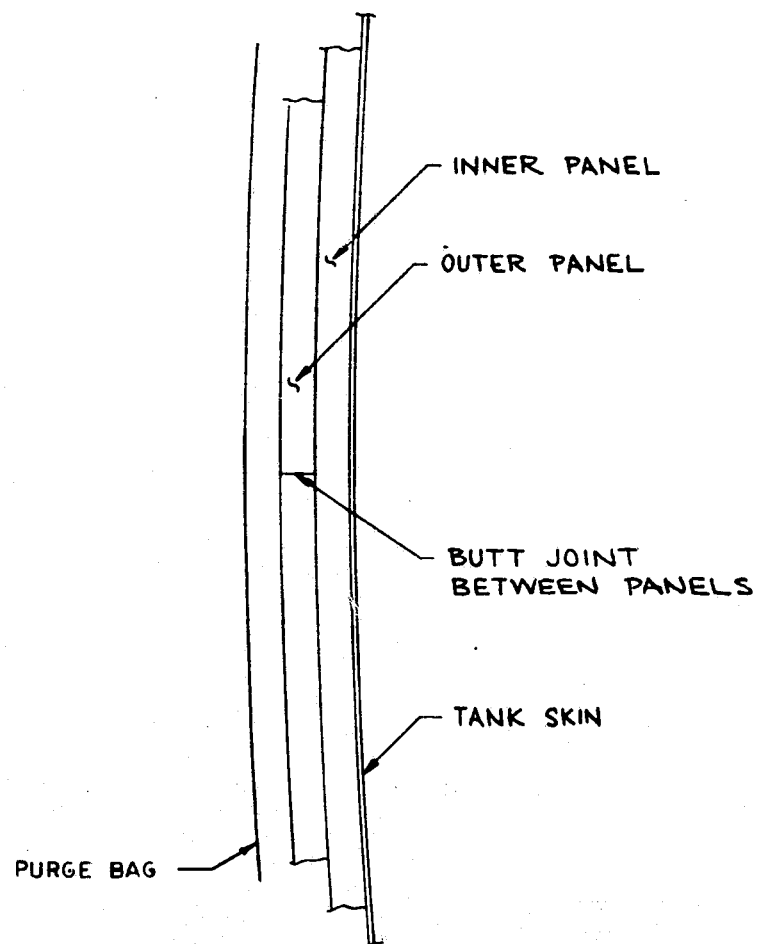


Figure 10-1. Conceptual Insulation Installation for Secondary LH₂ Tank—SK 710511

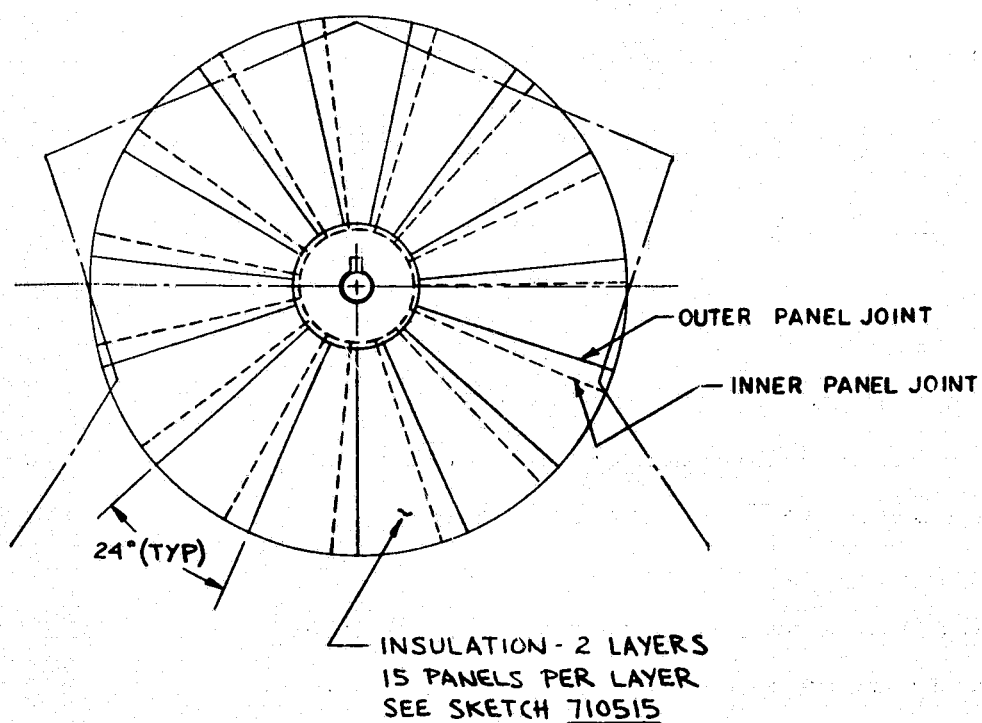
FOLDOUT FRAME 2

CR14

RATED BUTTERFLY
N VALVE.
S ON STRUTS



SECTION A-A
SCALE 1/2



VIEW WITH PURGE BAG REMOVED SHOWING
LOCATION OF STAGGERED BUTT JOINTS
BETWEEN PANELS

also placed around the six tank-support struts. Details of the configuration of the MLI panels and assembly are discussed in the following sections.

10.1.1 MLI Attachment to Tank

The MLI gore panels are supported by being attached to the tank through a fiber glass support ring at each end of the tank. This ring, shown in Figure 10-2 (SK 710512), is secured to the tank by three aluminum attachment brackets. Tabs on the end of the inner face sheet of the gore panels are secured to the support ring with screws. Localized areas on this support ring are raised to provide an attachment surface for the tabs on the outer MLI gore panels. Adjacent gore panels are held together with lacing thread and Velcro. Further details of the gore panels and their assembly are discussed in Subsection 10.1.4.

The end of the tank under consideration in Figure 10-2 contains a manhole. Circular, disk-shaped, inner and outer MLI panels are used to cover this manhole area. The manhole MLI panels are supported by being attached to the ends of the gorepanels with Velcro and lacing thread. The Velcro connecting the inner face sheet of the inner panels is bonded to the support ring. The design allows access to the manhole and tank interior without removal of the gore panels. This access can be readily accomplished by removing the lacing between the manhole and gore panels and lifting off the manhole panels.

10.1.2 MLI Configuration at Tank Aft End—Plumbing Penetration Area

In the tank design under consideration, all of the plumbing and the wiring bundle for instrumentation in the tank, or under the MLI, are located at one end of the tank. This allows the placement of a fiber glass shroud around the cluster of pipes and wires to support the MLI, see Figure 10-3 (SK 710513). This shroud is supported at the tank end by three aluminum clips which are welded to the tank. The shroud is supported at the outer end by a fiber glass disk which is bolted to the shroud and clamped to the fill line. Three foam blocks which fit around the pipes are bonded to the disk and provide a sealing surface around the pipes. Polyurethane is used to provide a leak-tight seal between the pipes and foam. In assembly, the foam blocks would be sealed to the pipes with the polyurethane. The fiber glass disk would then be slid down over the pipes to the foam (the holes in the disk are

oversize), clamped to the fill line, and bonded to the foam. The shroud would then be slid down over the disk and bolted to the disk. This design allows removal of the shroud to inspect the plumbing or wiring normally within the shroud. An instrumentation wiring pass through is bonded into one of the foam blocks.

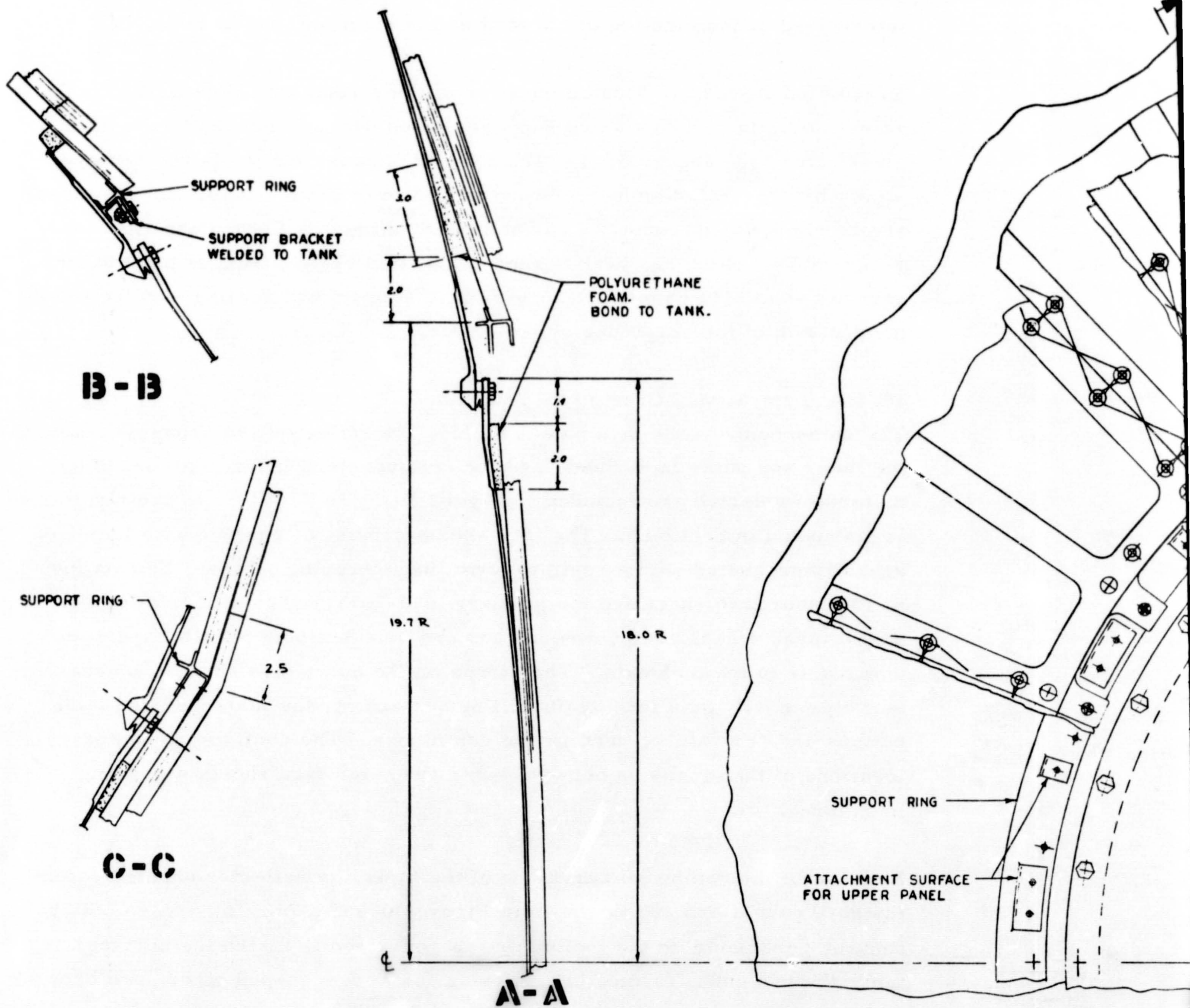
Holes are located in the shroud between the end of the MLI and the MLI support ring. These holes allow gas within the MLI to pass through the shroud and evacuate out through a butterfly valve. The butterfly valve is mounted on the exterior of the shroud as shown in Figure 10-3.

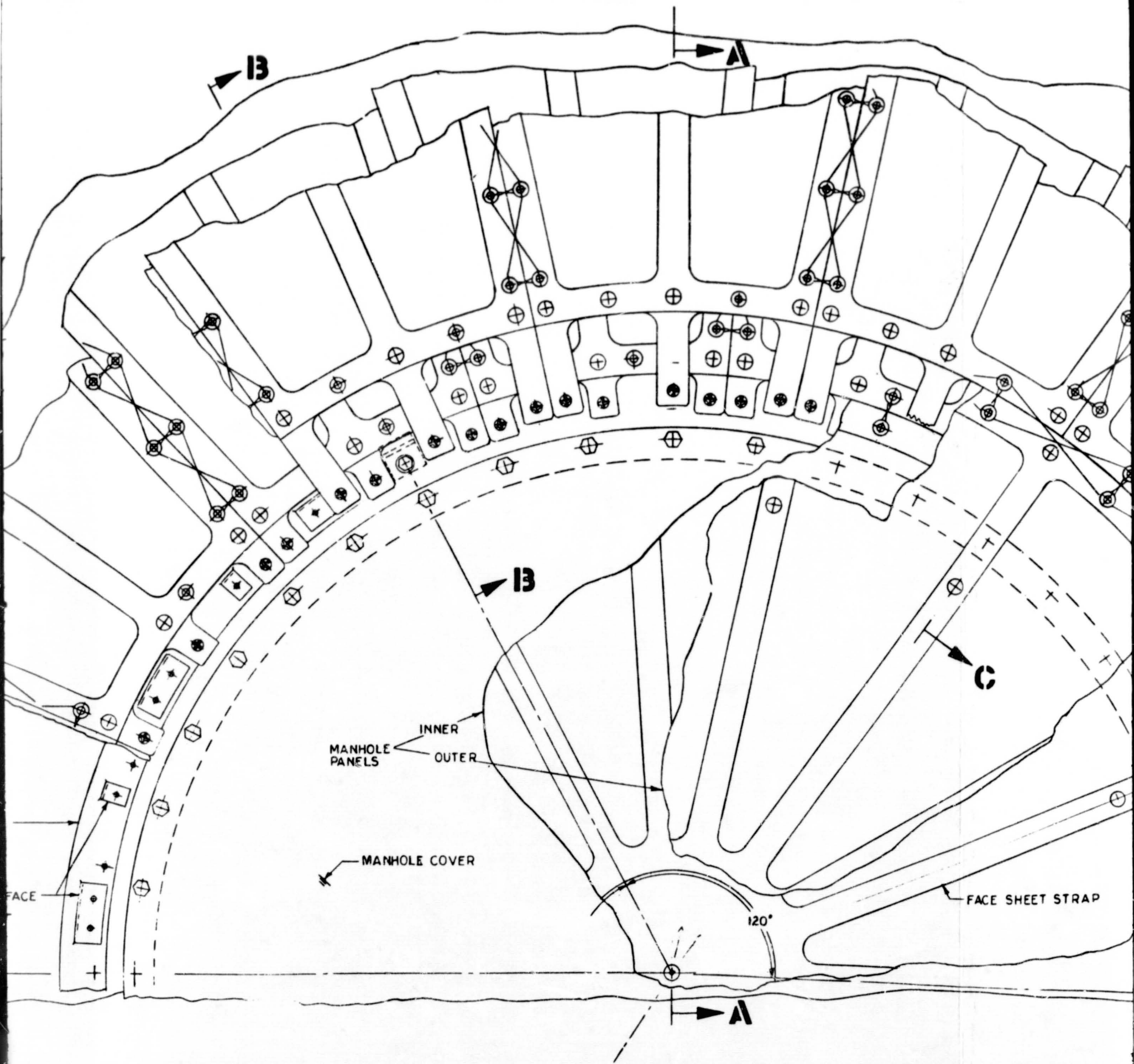
The MLI is placed on the exterior of the shroud for a distance of approximately four feet and is supported by being attached to a ring bonded and sealed to the exterior of the shroud, see Figure 10-3. This ring also provides a surface for supporting and sealing the termination of the purge bag at this point. The plumbing shroud MLI inner and outer panels are both fabricated in two pieces to facilitate installation onto the shroud. The two halves forming each panel layer are joined by lacing thread and Velcro. The reflector sheets are interleaved at the junction of the shroud and tank to provide a thermally efficient corner at this point.

The plumbing MLI panels are attached to the end-dome panels by lacing thread and Velcro as shown in Figure 10-3. The joint between the end-dome and gore panels and the attachment to the support ring is not shown but is identical to that shown for the gore panel to manhole panel joints shown in Figure 10-2.

10.1.3 MLI Configuration at Strut Penetration

Six hollow fiber glass struts are used to support the tank. Each of these struts tangentially intersects the tank as shown in Figures 10-1 and 10-4. A cylindrical fiber glass shroud is placed over the end of the strut and the strut attachment hardware to support the MLI in this area. This shroud facilitates the fabrication of the MLI panel for the strut by maintaining a constant inside diameter on the portion of the panel over the strut. The shroud is positioned after the strut has been attached to the tank by sliding it down over the shroud support. The shroud is then clamped to the strut to hold it in position.





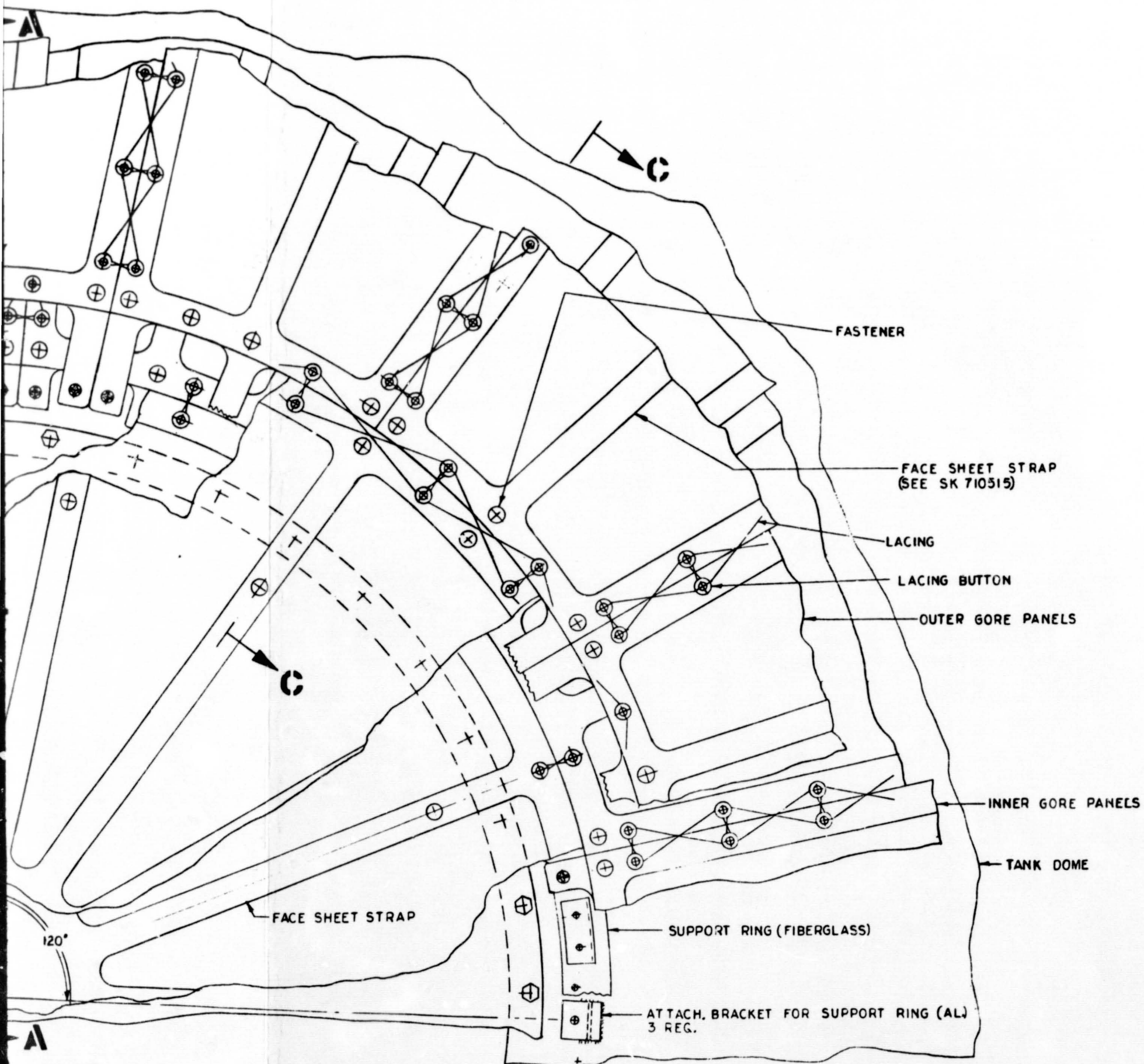


Figure 10-2. Panel Attachment to Tank and Manhole Cover—SK 710512

The strut MLI panels are fabricated in one piece with a joint running parallel to the strut axis which, when opened, allows installation of the panel on the strut. This joint is held closed by lacing thread and Velcro as shown in Figure 10-4. The strut MLI panels and gore panels are also joined with lacing thread and Velcro. The reflector sheets in the strut panel are interleaved at the junction of the MLI on the strut and on the tank.

Evacuation valves are located on three of the struts, see Figure 10-1. These valves are attached to a valve support shroud which is bonded to the fiber glass strut, see Figure 10-4. The strut MLI panel and the purge bag are attached to the valve support shroud as shown in Figure 10-4. On the three struts which do not contain a valve support shroud, a fiber glass ring, see Figure 10-4, which has been bonded and sealed to the strut, is used to support the strut MLI panels and to provide a support and sealing surface for the termination of the purge bag on the struts.

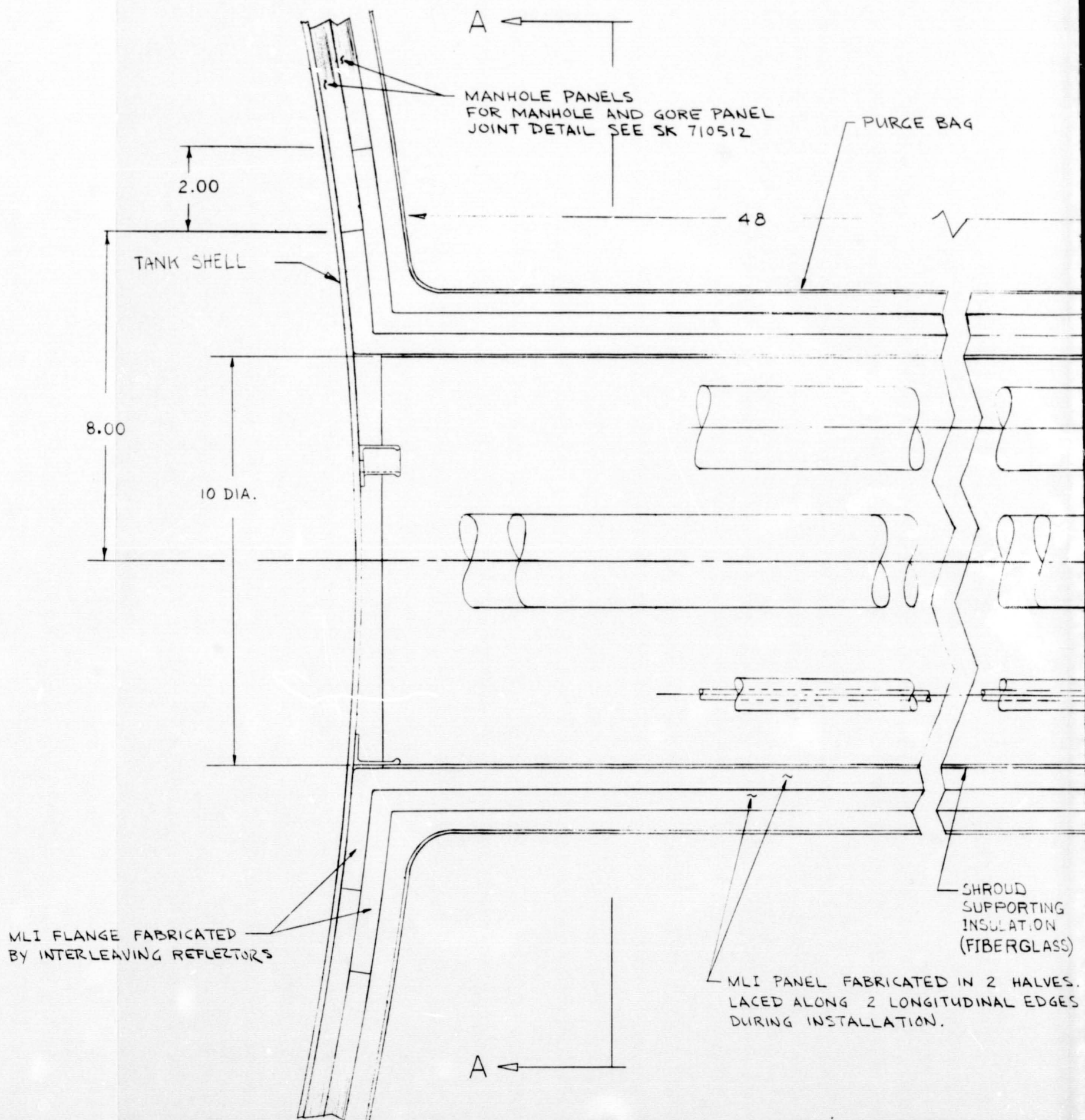
10.1.4 Typical MLI Gore Panel Assembly

The components of the MLI panels include the reflector and separator layers, the inner and outer face sheet, and the fasteners and lacing buttons. The materials selected are included in Figure 10-5 (SK 710515) and their selection is discussed in Section 9. The face sheets consist of a fabric with localized areas impregnated with a resin to form load-carrying straps. The straps on the inner face sheet are the primary load-carrying components for the panel; these straps are continuous and are oriented both parallel and perpendicular to the tank axis. The straps on the outer face sheet of a panel serve primarily as a load-transmitting surface for the fasteners and lacing buttons and, therefore, need not be continuous. The configurations and locations of the straps on both the inner and outer face sheets are shown in Figure 10-5.

Because of the compound curvature of the tank, the reflector sheets used in the gore panels are cut as shown in Figure 10-6 (SK 710516). When fabricating the gore panel on the tooling that is contoured to match the surface of the tank, the two ends, formed by removing the wedge-shaped piece, are brought together and overlapped one inch at the end. This greatly reduces the bulging and rippling along the edge of the sheets due to excess material. The

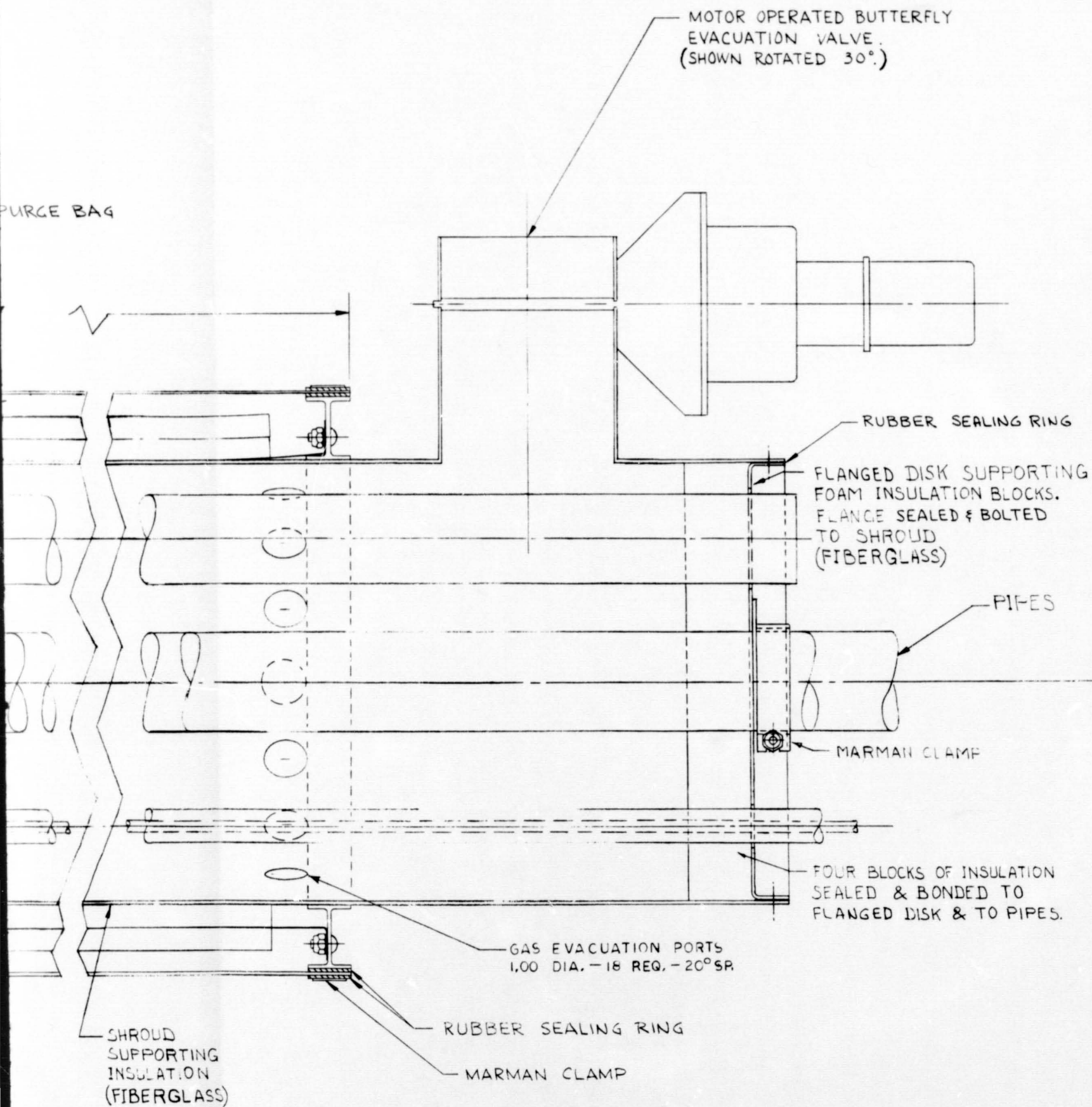
FOLDOUT FRAME

1



FOLDOUT FRAME

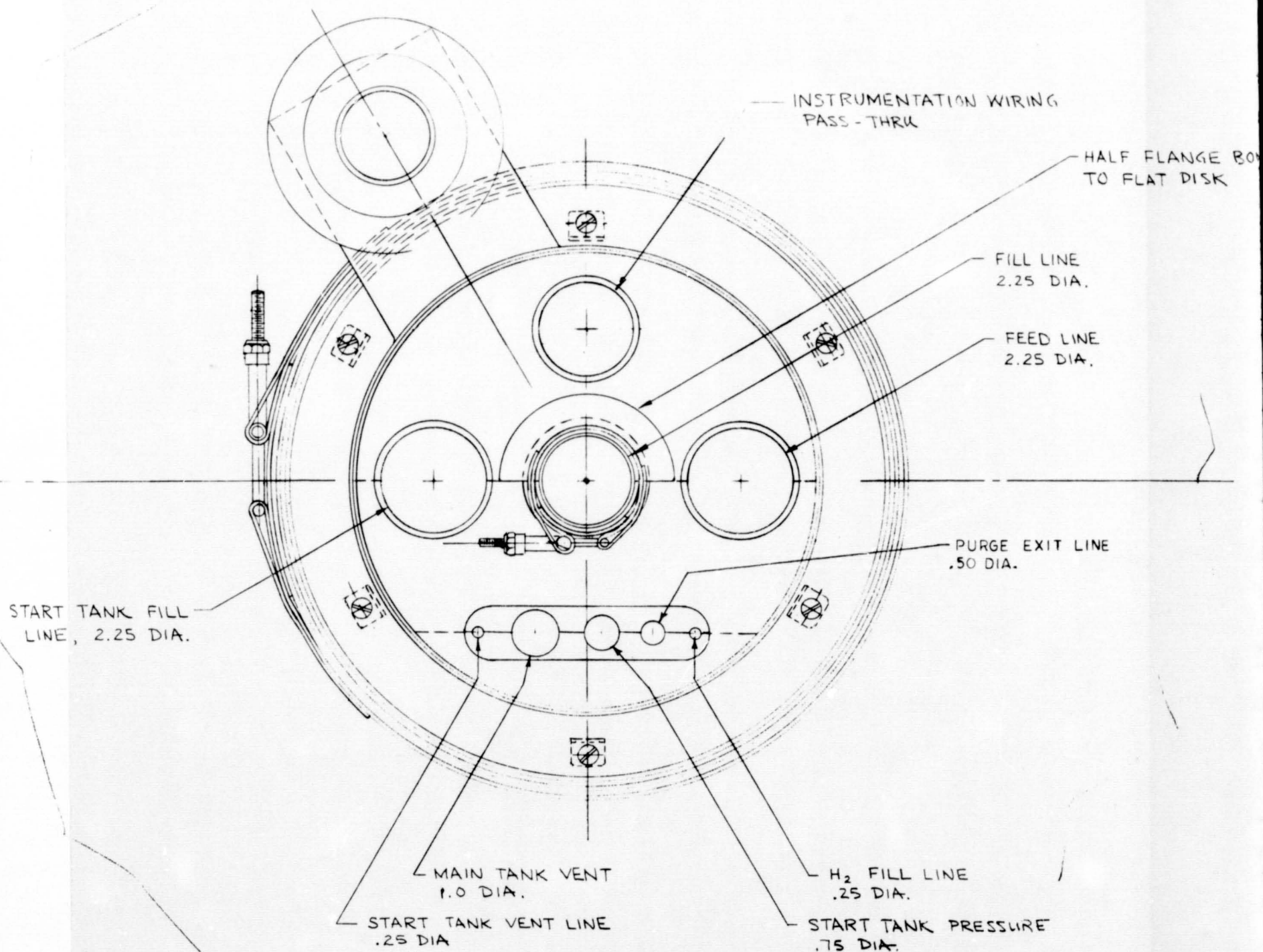
2

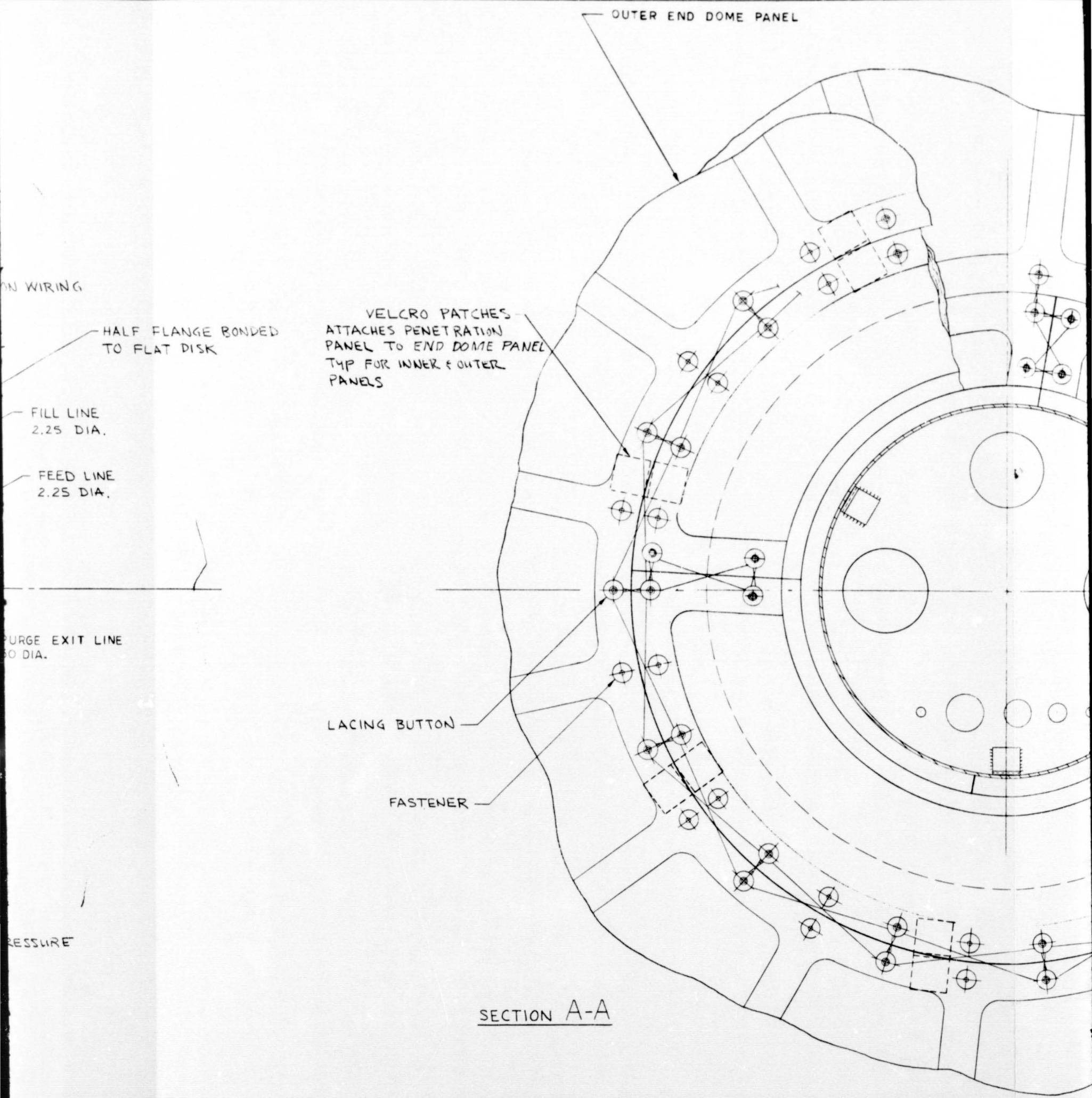


START TANK
LINE, 2.29

RICATED IN 2 HALVES.
LONGITUDINAL EDGES
LATION.

FOLDOUT FRAME 3





DOME PANEL

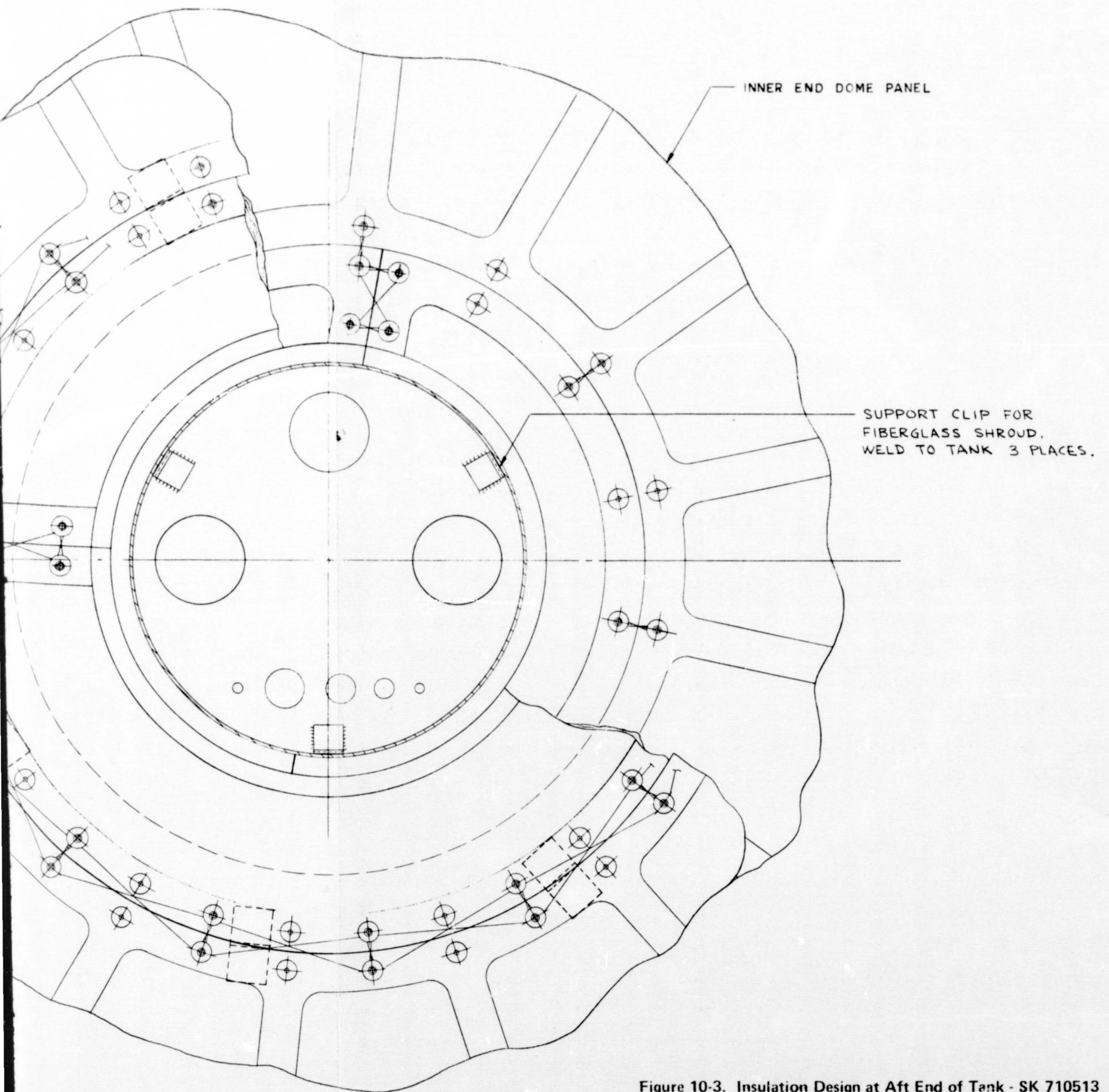
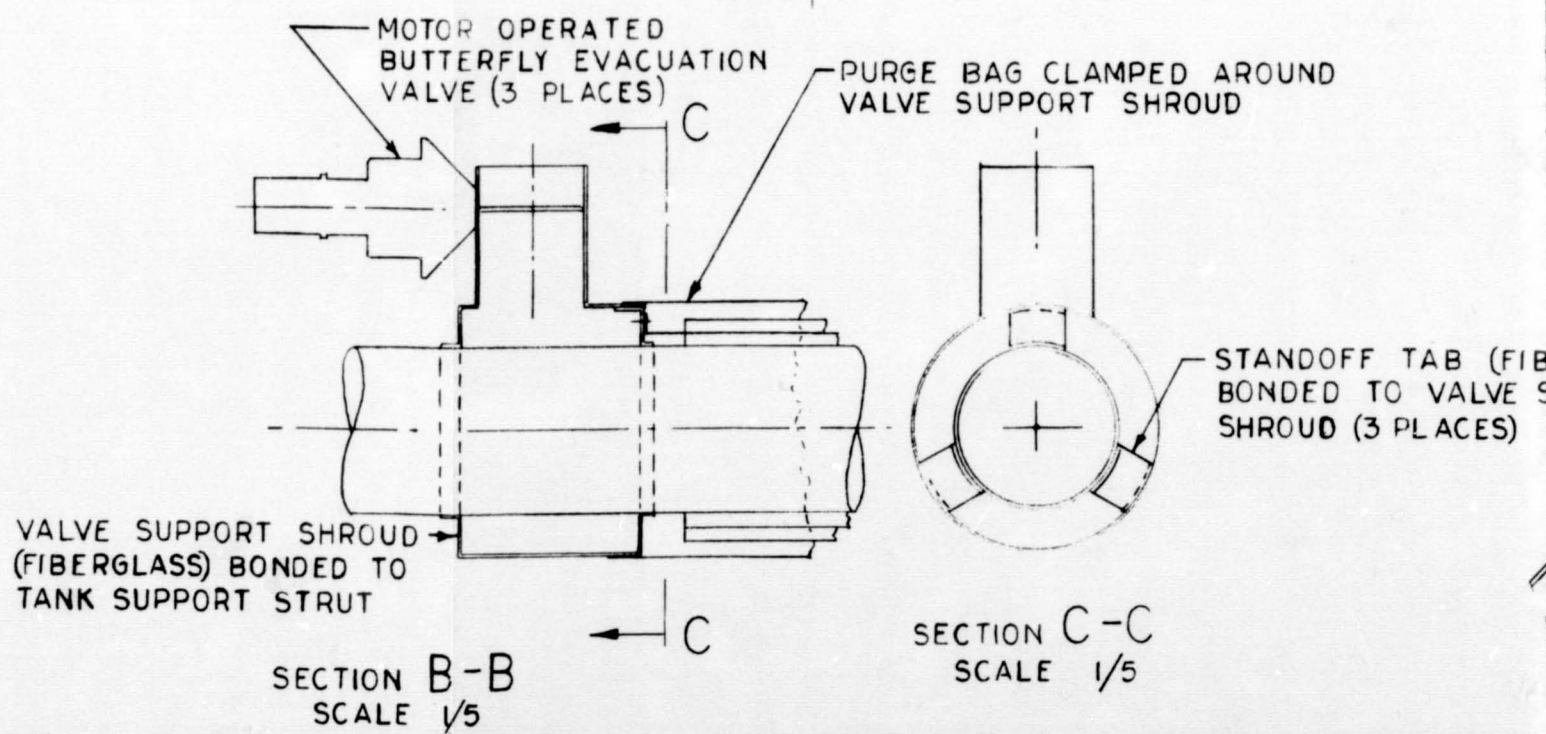
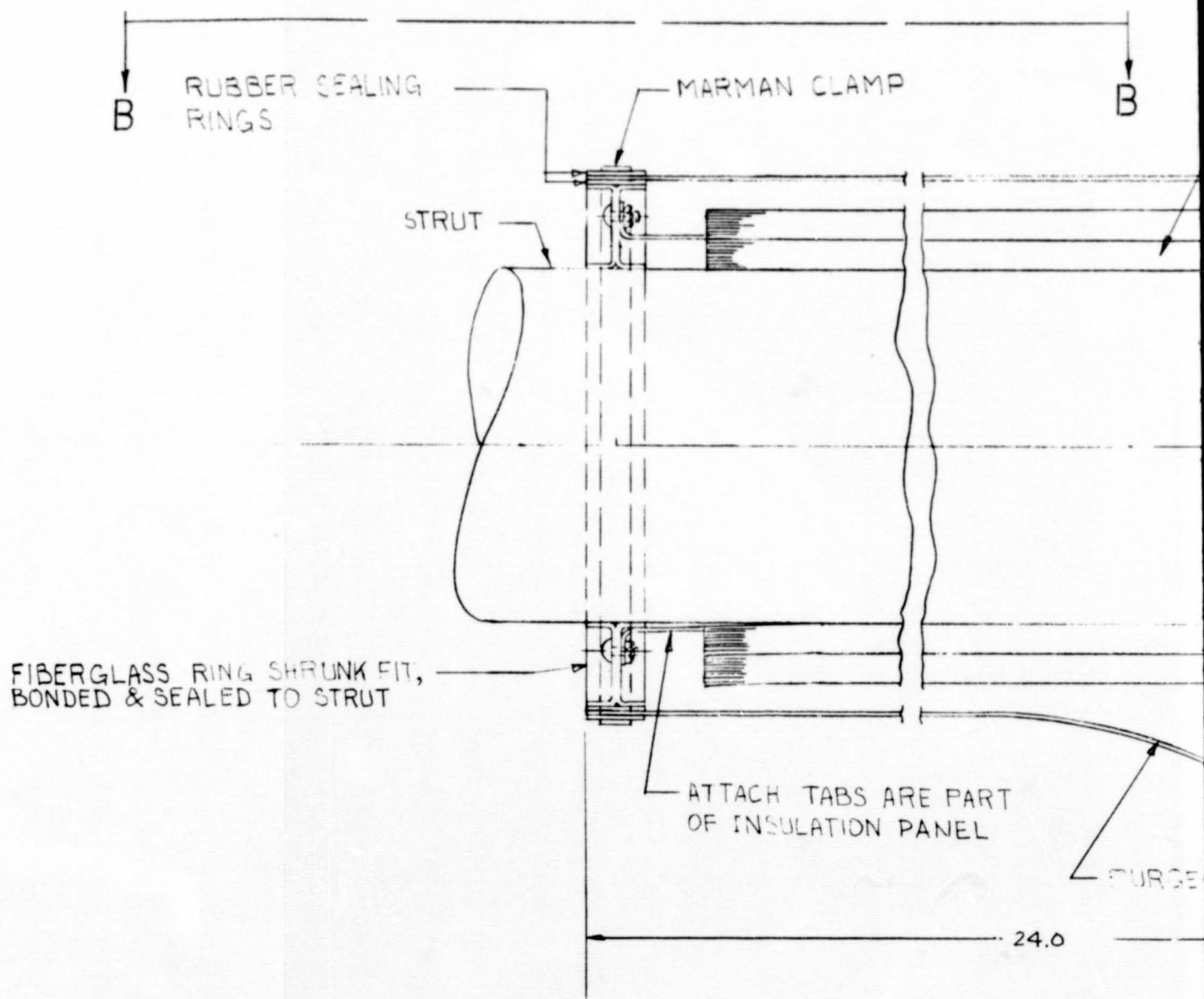


Figure 10-3. Insulation Design at Aft End of Tank - SK 710513

FOLDOUT FRAME

1

STRUT INSULATION PANEL
TO BE LACED ALONG LONGITUDINAL
EDGE DURING INSTALLATION



FOLDOUT FRAME 2

PANEL
G LONGITUDINAL
RING INSTALLATION

B

A

RATCHET CLAMP
HOLDING SHROUD
TO STRUT

0.25 DIA 2 HOLES
FOR PURGE AND REPRESSURIZATION GAS

TUBULAR SHROUD SUPPORTING
INSULATION
(FIBERGLASS)

SHROUD
SUPPORT
(FIBERGLASS)

MLI FLANGES FABRICATED
BY INTERLEAVING REFLECTORS

RE PART
PANEL

PURGE BAG

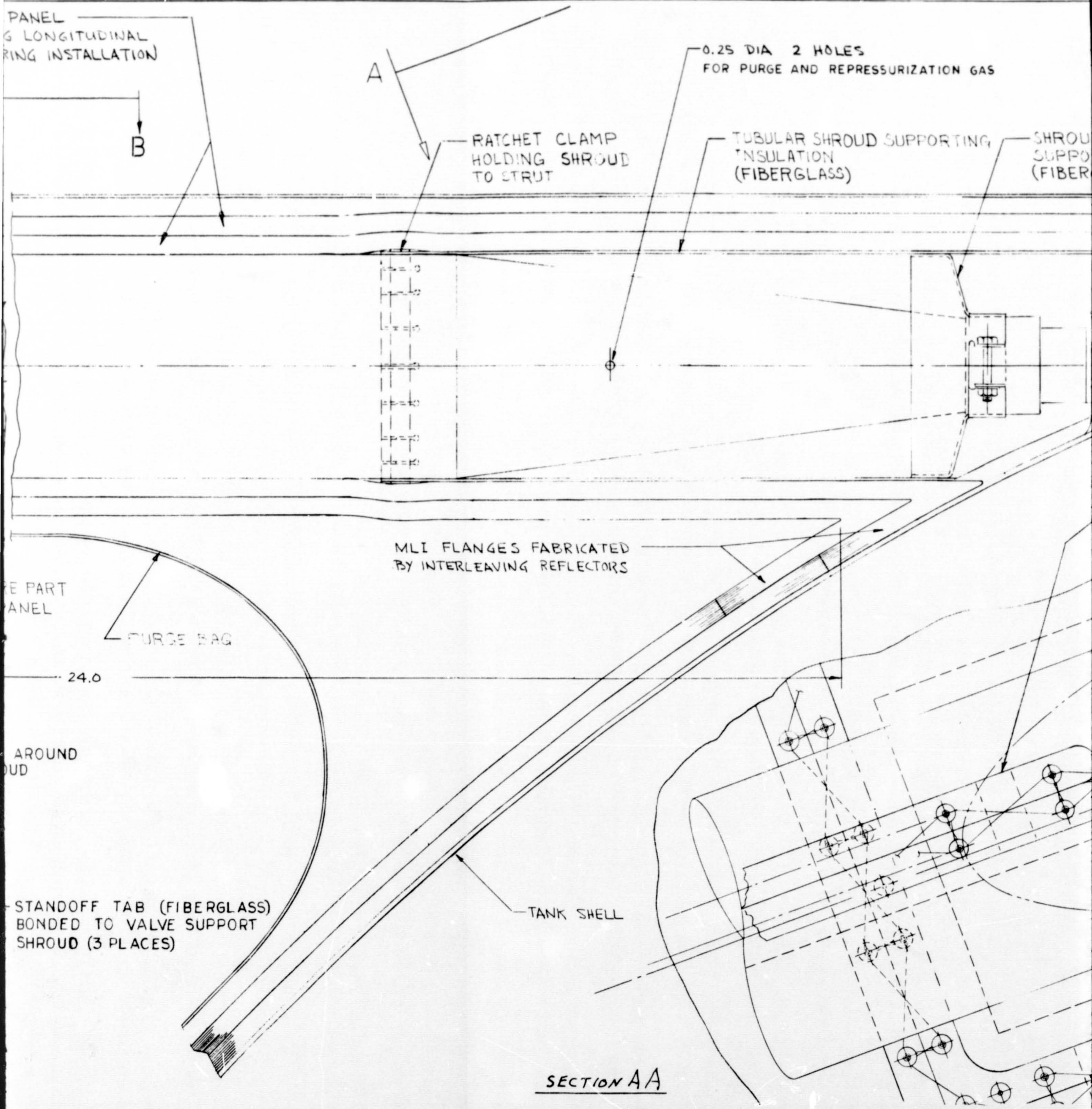
24.0

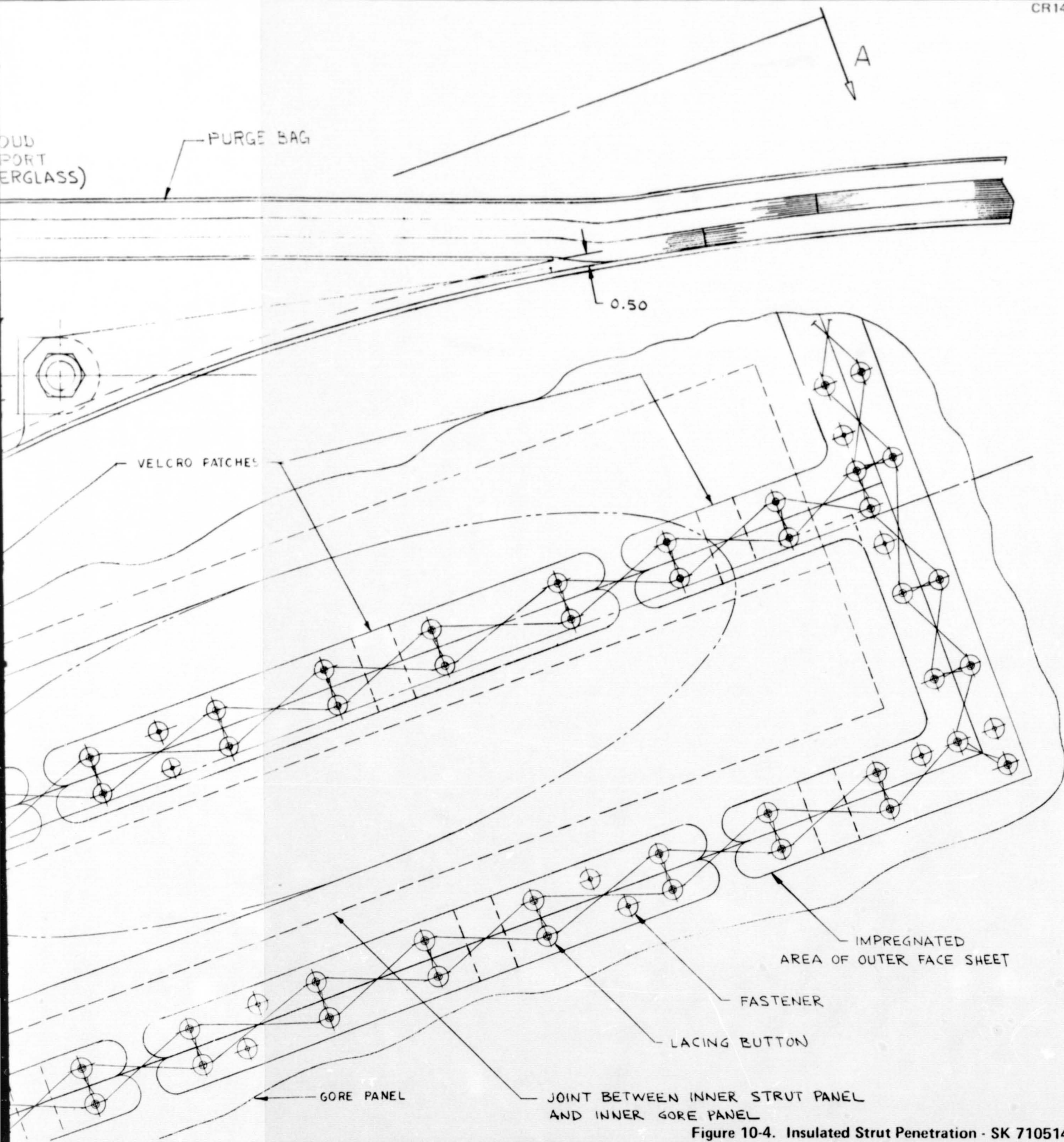
AROUND
SHROUD

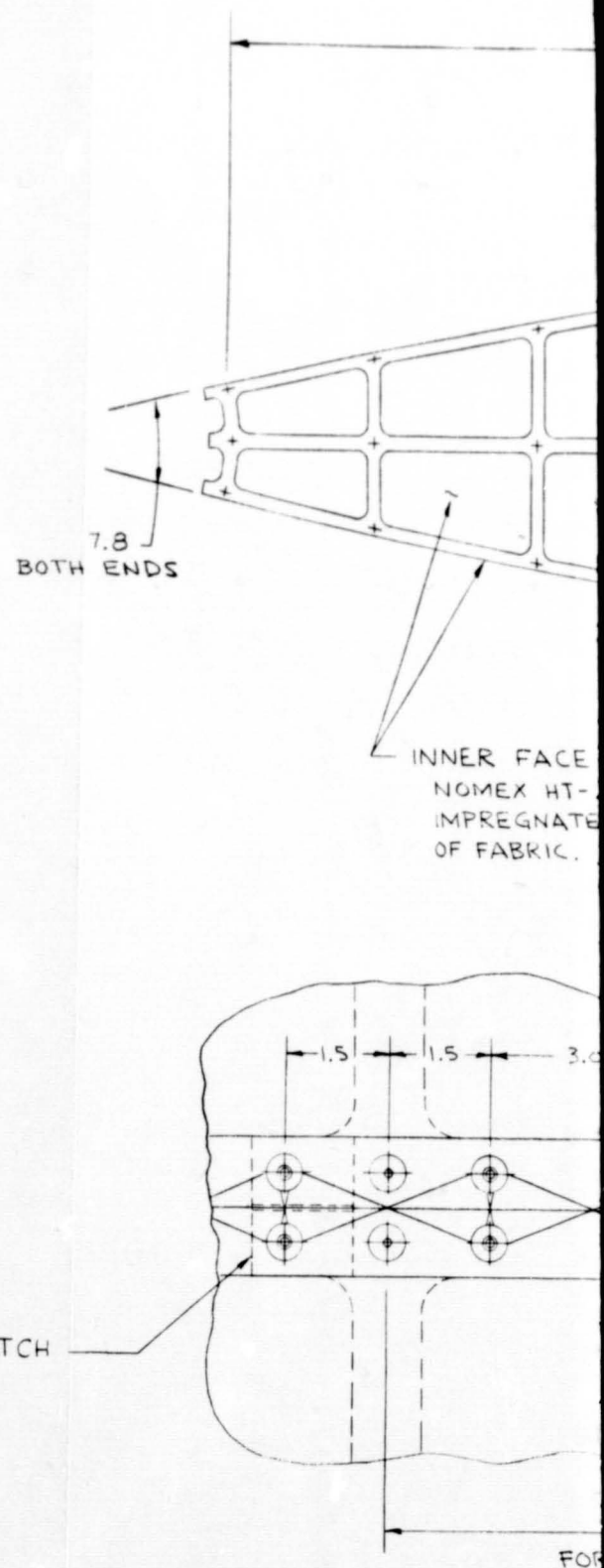
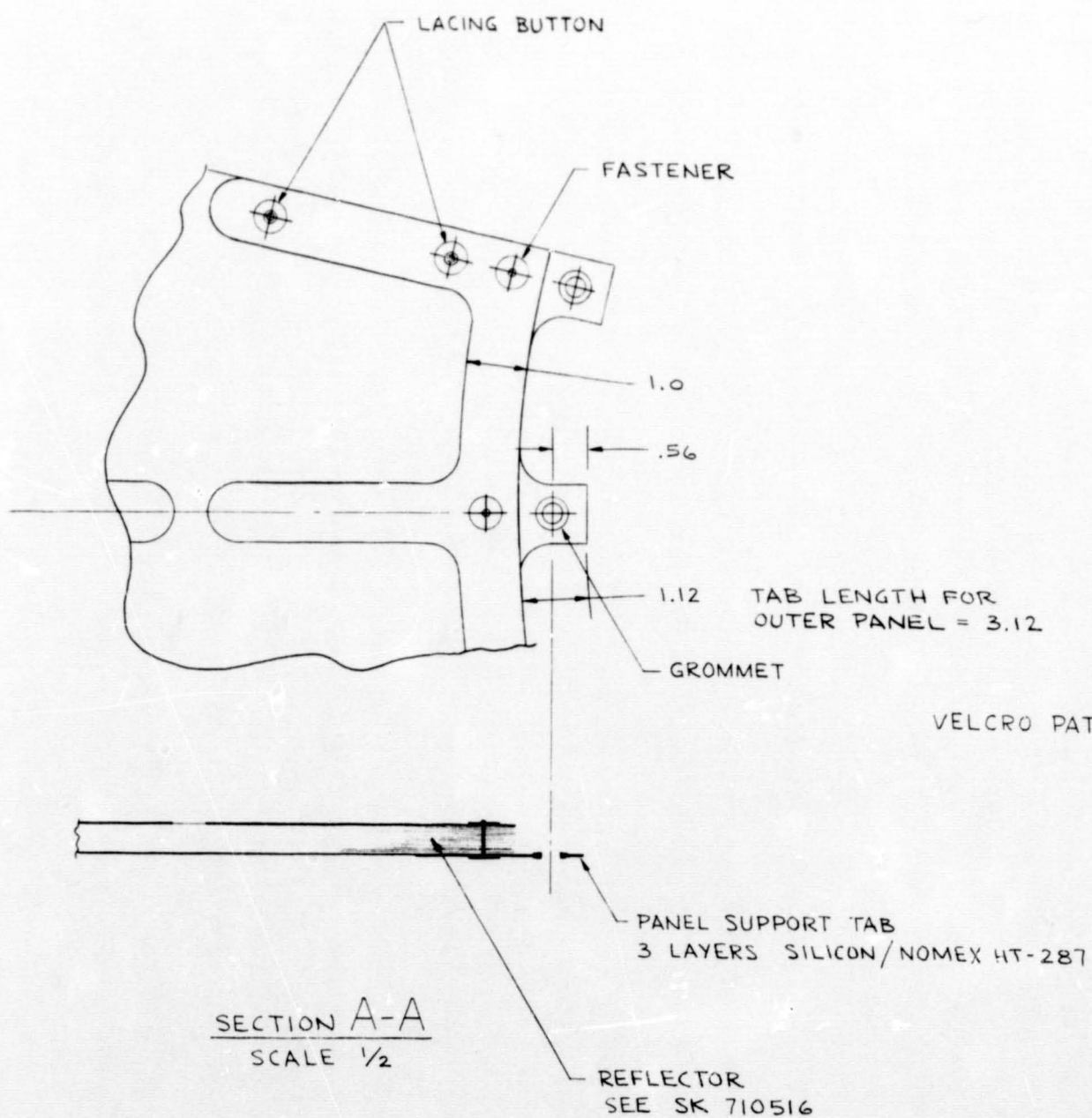
STANDOFF TAB (FIBERGLASS)
BONDED TO VALVE SUPPORT
SHROUD (3 PLACES)

TANK SHELL

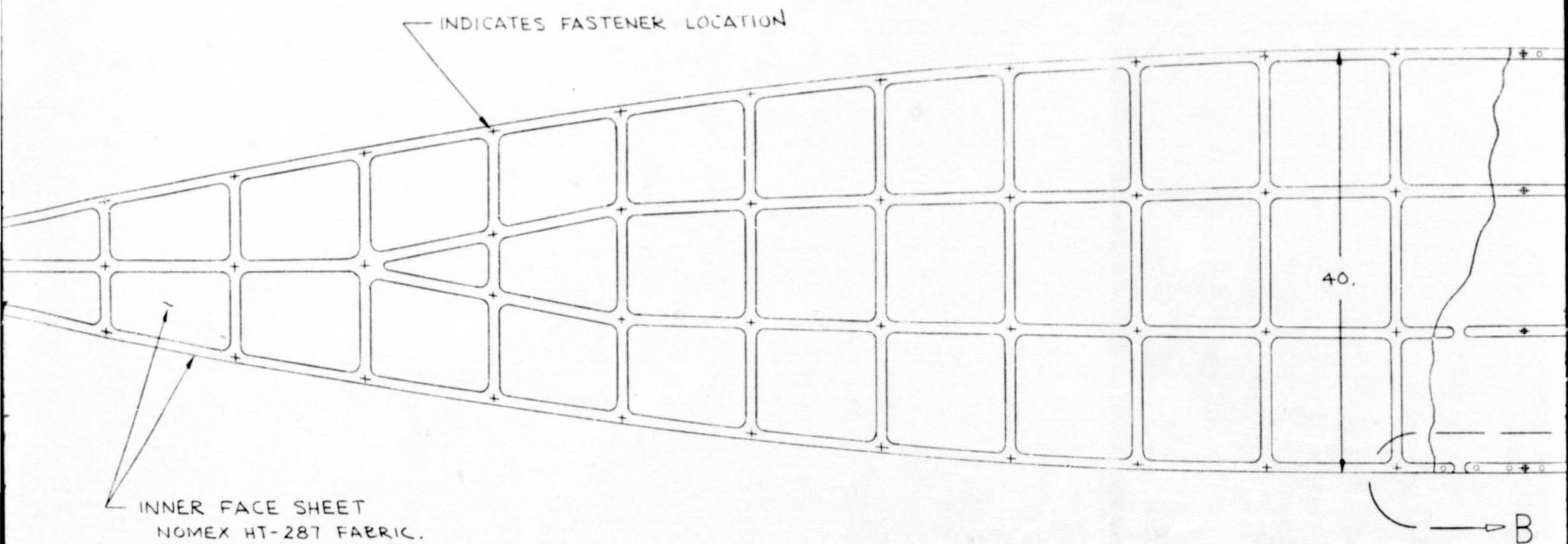
SECTION AA



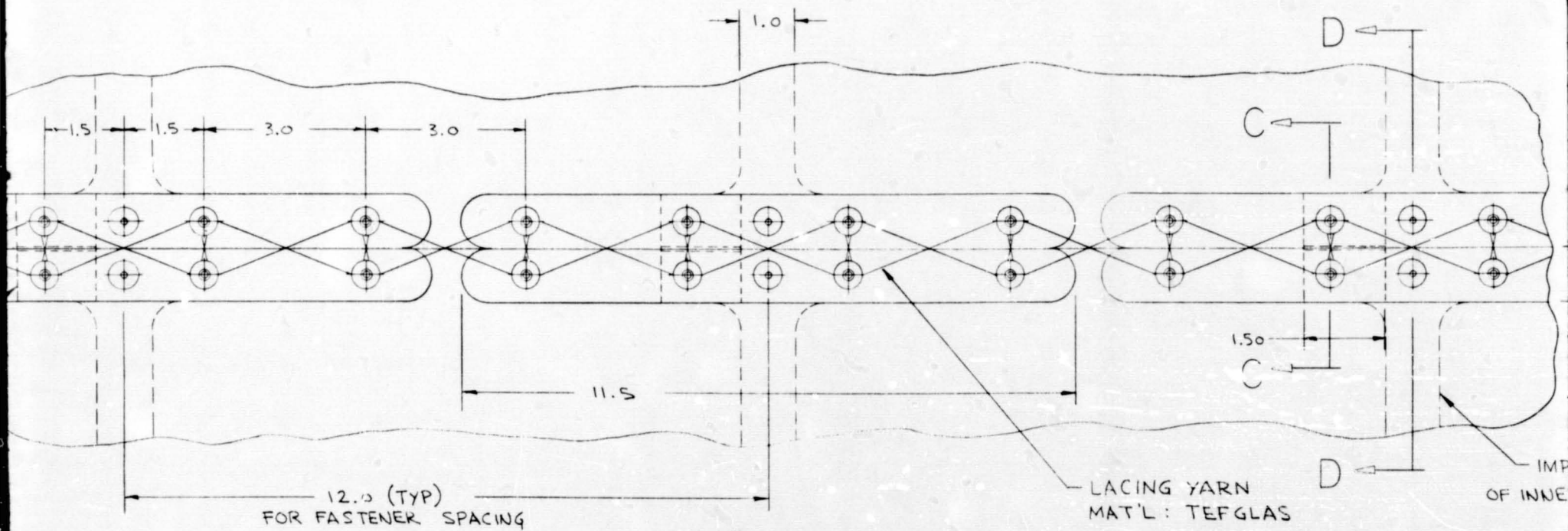




280.

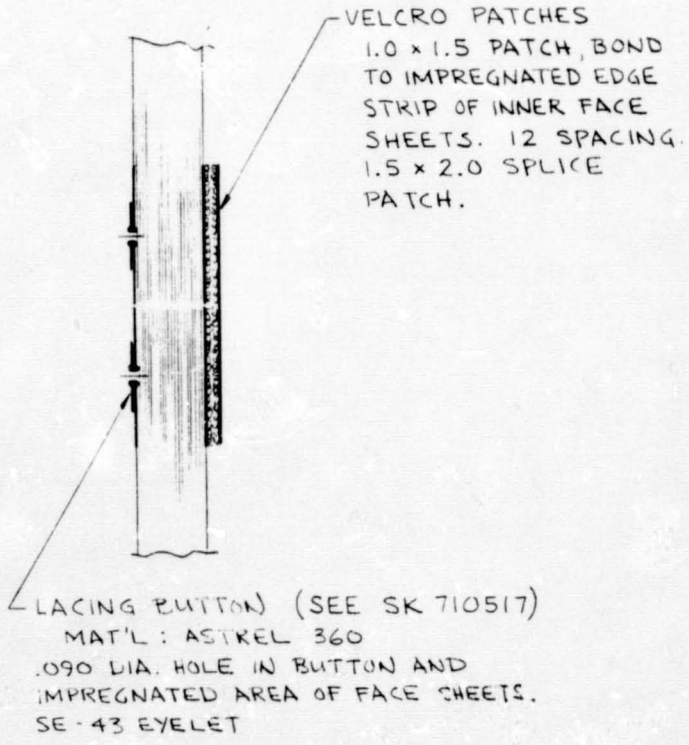
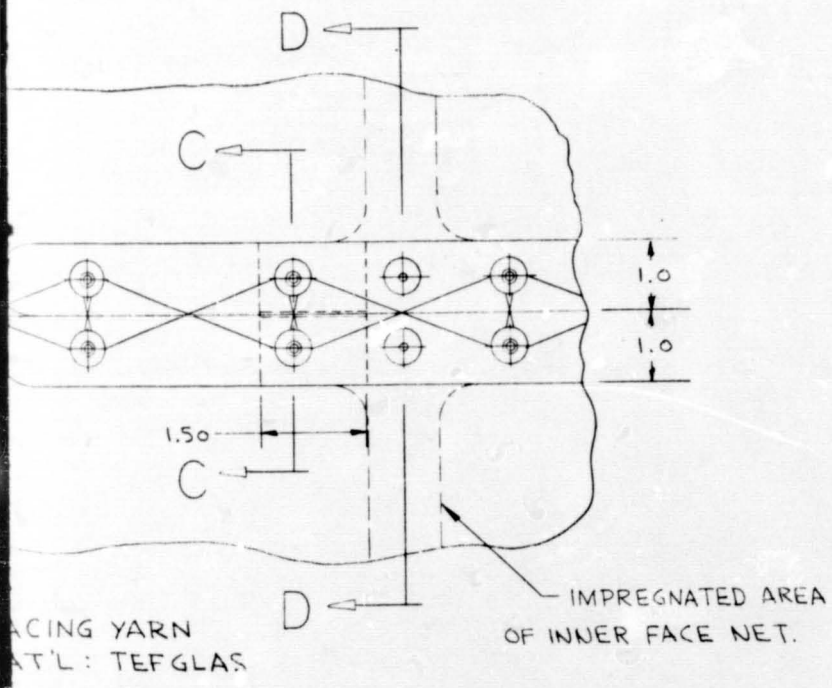
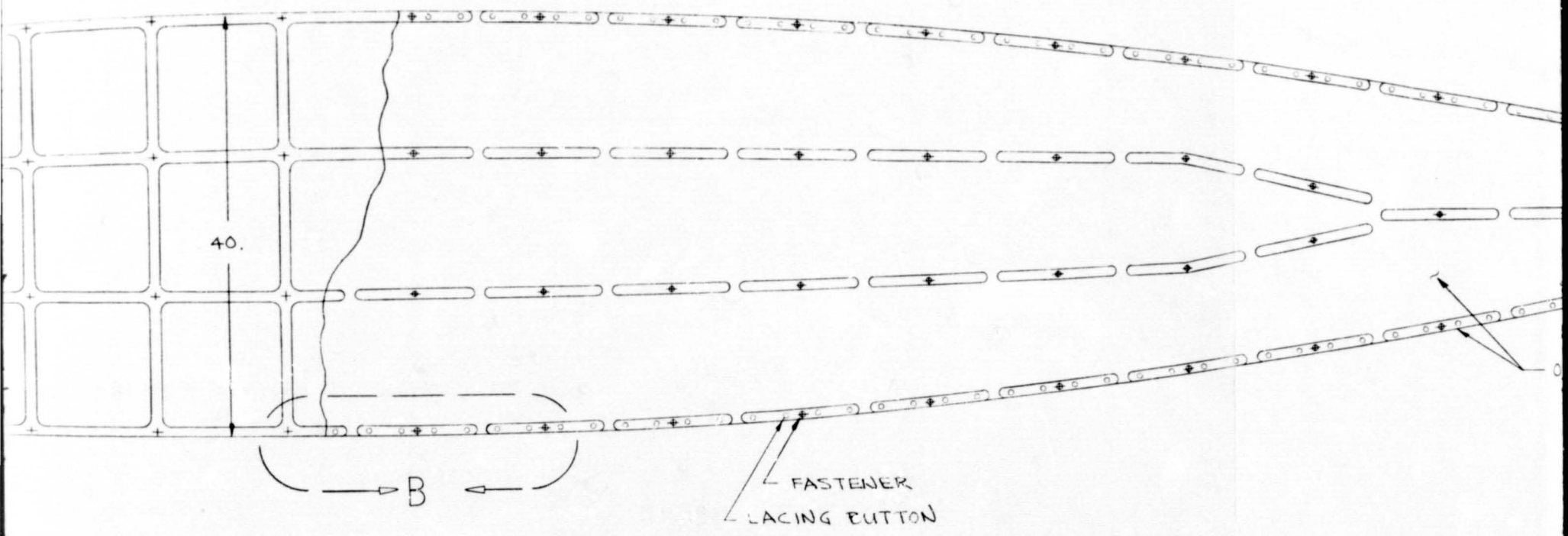


INNER FACE SHEET
NOMEX HT-287 FABRIC.
IMPREGNATED AREA HAS 2 LAYERS
OF FABRIC. SILICONE FILLER.

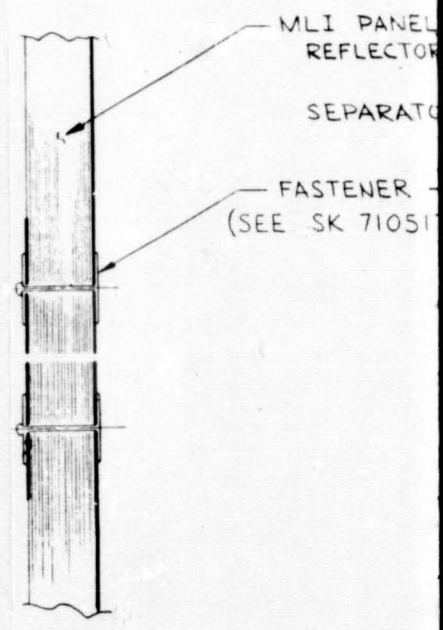


VIEW B

METHOD OF LACING GORE PANELS TOGETHER
SCALE $\frac{1}{2}$

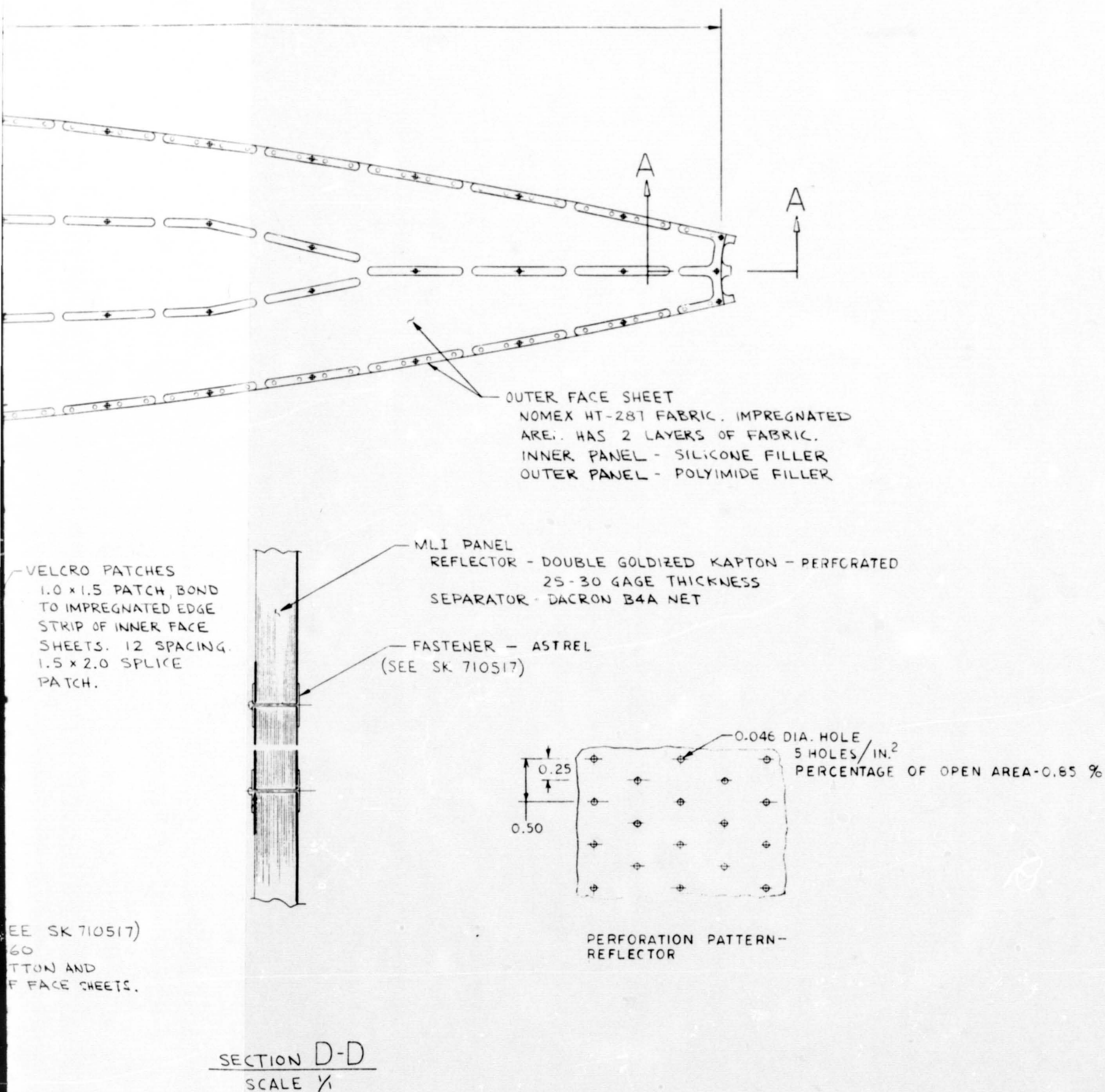


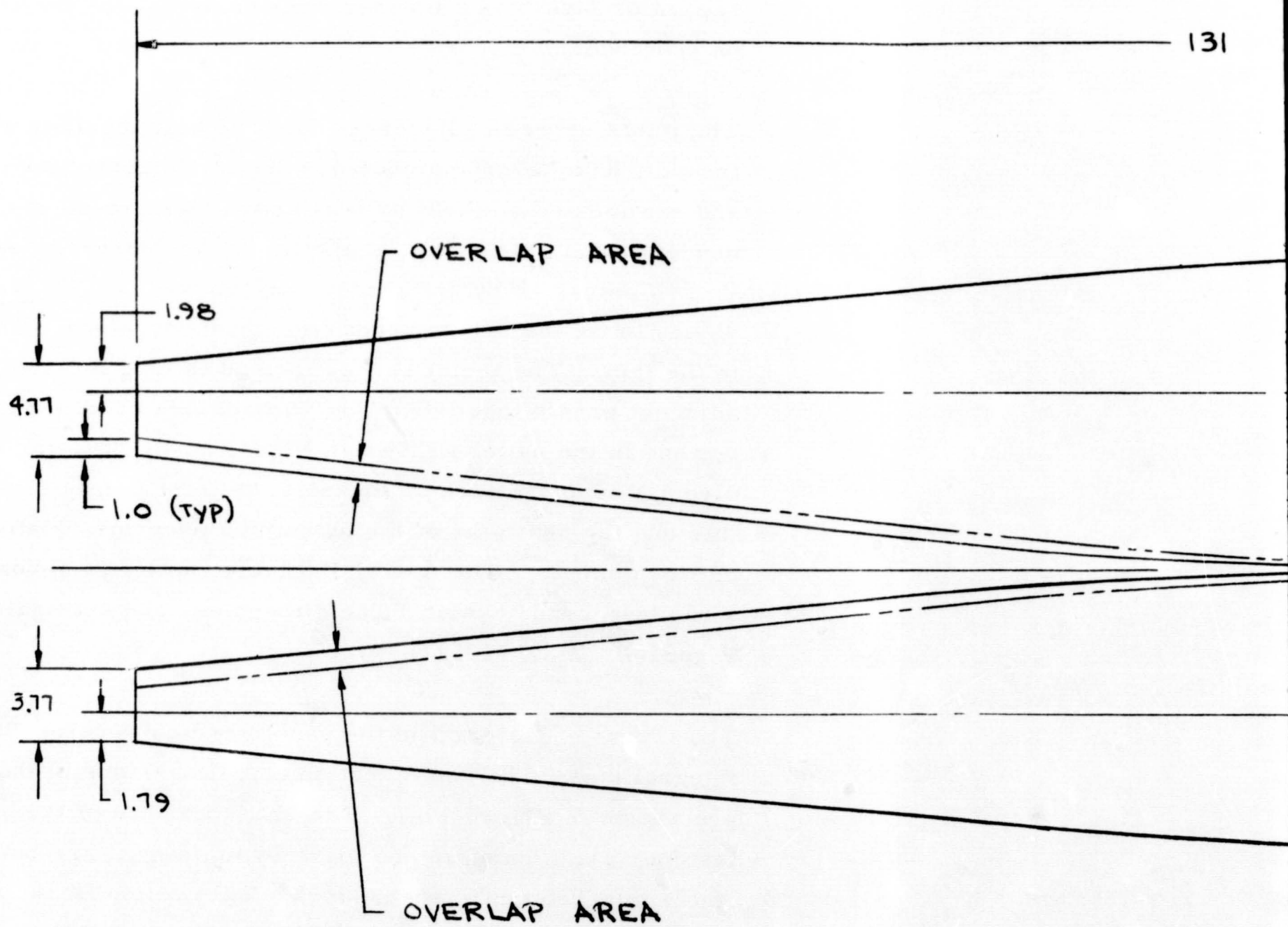
SECTION C-C
SCALE 1/4



SECTION D-D
SCALE 1/4

Figure 10-

Figure 10-5. Typical MLI Gore Panel Assembly - LH₂ Tank Configuration SK 710515



131

39.8

SYM

Figure 10-6. Typ

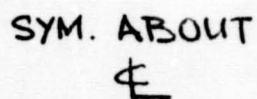


Figure 10-6. Typical Reflector Sheet - SK 710516

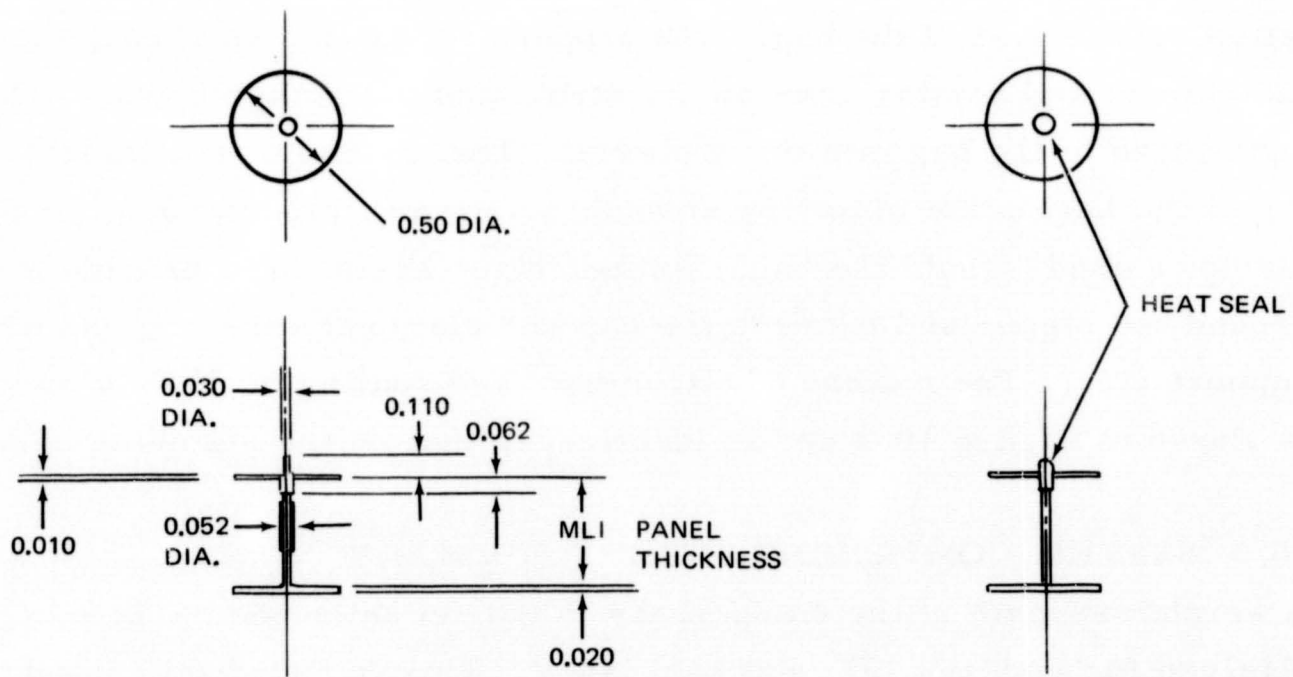
wedge-shaped piece removed from the reflector is not centered in the sheet, see Figure 10-6. This allows a layup wherein the overlap and slit areas on alternate reflector sheets are not directly on top of each other. This is accomplished by turning over every other sheet during layup of the panel. Due to the flexibility and large mesh of the separator net, slitting the separator layers in a manner similar to that for the reflectors should not be required.

The joints between adjacent panels are held together with Velcro and lacing thread. The Velcro patches are used to hold the inner face sheets together and are located one foot or less apart. Velcro pieces, 1 by 15 inches are bonded to the edge straps of the inner face sheets of each of the gore panels. Velcro pieces, 2 by 1.5 inches, are hooked into the Velcro bonded to the face sheets to tie the two adjacent face sheets together. The Velcro is not bonded to the tank. The lacing thread is used to hold the outer face sheets of adjacent panels together. Two threads are used and are wound around lacing buttons in the pattern shown in Figure 10-5. The tie between lacing buttons directly opposite each other holds the joint firmly closed. The tie between this and the next pair of lacing buttons prevents relative lateral motion between panels. The Astrel 360 lacing button is secured to the face-sheet strap by a brass eyelet. The dimensions and configuration are shown in Figure 10-7 (SK 710517).

The layers of material in the panel are held together by fasteners to form an integral unit. The configuration and dimensions of the Astrel 360 fasteners are shown in Figure 10-7. The shank and one of the button ends of the fastener are formed in one piece by molding. The button used on the other end is punched out of sheet stock. This button is put on the shank after the shank has been passed through the layers of reflectors, separators, and face sheets and is held in place by a heat-formed head on the end of the shank.

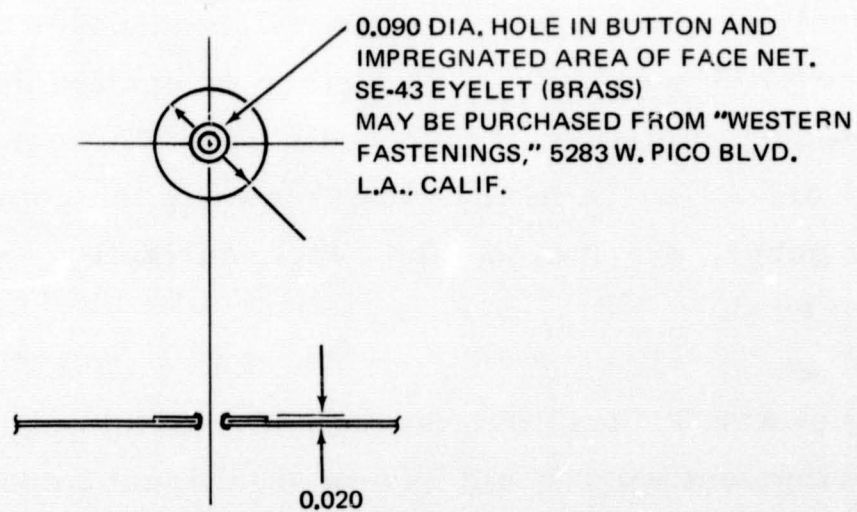
10.2 PURGE BAG

The MLI is protected from condensables during ground hold and reentry by a dry inert gas (helium). This gas is contained by a bag which completely envelops the MLI on the tank. The bag follows the contour of the tank and extends out over the MLI on the tank support struts and the plumbing. The



FASTENER DETAIL

MATERIAL: ASTREL 360



LACING BUTTON DETAIL

MAT'L: ASTREL 360

Figure 10-7. Fastener and Lacing Button Detail—SK 710517

bag for the LH_2 tank is fabricated of 6-mil, Teflon-coated Kapton. The bag consists of gore-shaped pieces joined by heat sealing, see Figure 10-8 (SK 710518). A doubler is used at these joints. Doublers and heat sealing are also used at the joints in the strut and plumbing areas.

Zippers are placed in the bag, as shown in Figure 10-8, to facilitate installation or removal of the bag. The zippers all extend out through the bag attachment and sealing area on the struts and plumbing shroud. This allows separation of the bag into three pieces. The method of attachment and sealing of the bag on the plumbing shroud is shown in Figure 10-3. A Marmon clamp is used to hold the bag. Rubber rings are used to provide a seal around the zipper and between the bag and clamp and the bag and fiber glass support ring. The method of attachment and sealing of the bag on the struts is shown in Figure 10-4 and is identical to that on the plumbing shroud.

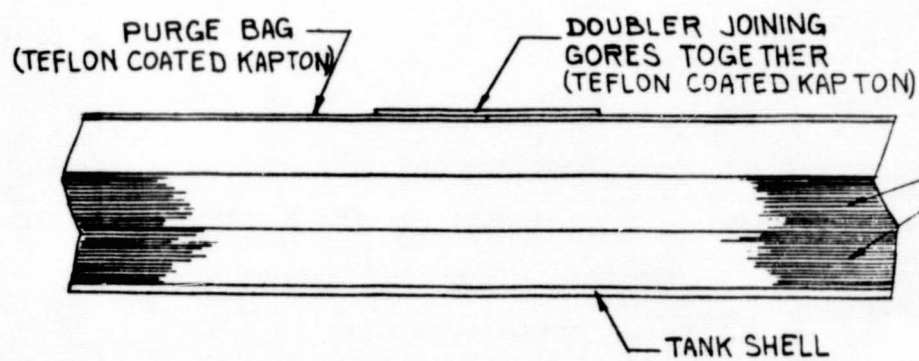
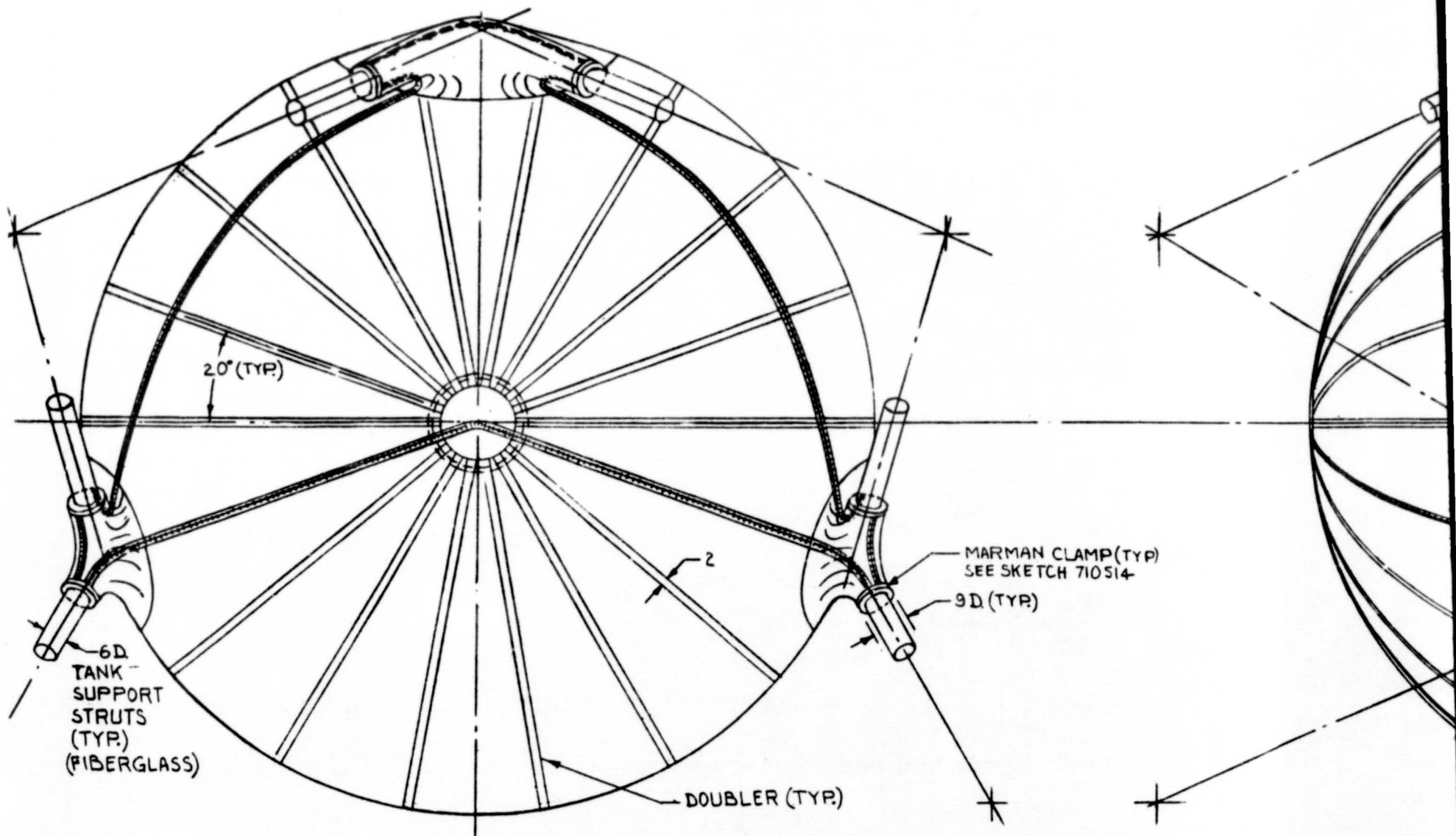
10.3 SYSTEM COMPONENT WEIGHT SUMMARY

A weight estimate of the components in the recommended MLI system was obtained for both the LH_2 and LO_2 tanks. This included all components required for the MLI system except that portion of the vehicle power supply, electronic packages, and wiring required to activate the valves for evacuating and repressurizing the system. The weights obtained are cursory estimates only, but an attempt was made to include estimates of the weights of hardware such as bolts, screws, and clamps. For purposes of the weight summary, a Velcro patch was defined as a piece on each side of the joint plus the splice piece. A summary of the predicted component weights are shown in Tables 10-1 and 10-2. A further breakdown of the component weights needed for the purge, evacuation, and repressurization system hardware are shown in Table 10-3.

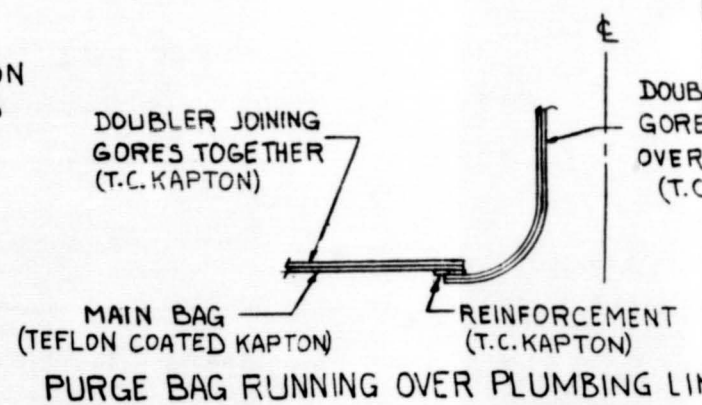
The weights shown in Tables 10-1 through 10-3 point out the areas where additional development work could have a significant impact on the total system weight. All of these areas (reflectors, separators, face sheets, purge bag, and purge and repressurization hardware) have potential for a reduction in weight. For example, a significant portion (22 lb) of the 71-pound LH_2 tank purge bag is due to the zippers. A thorough vendor

FOLDOUT FRAME

1

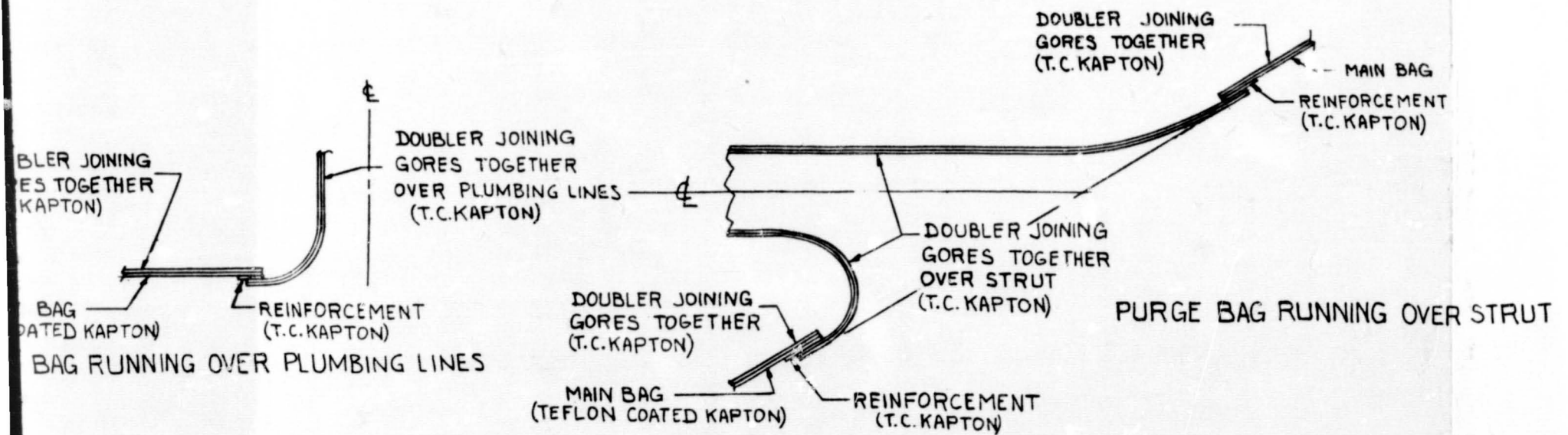
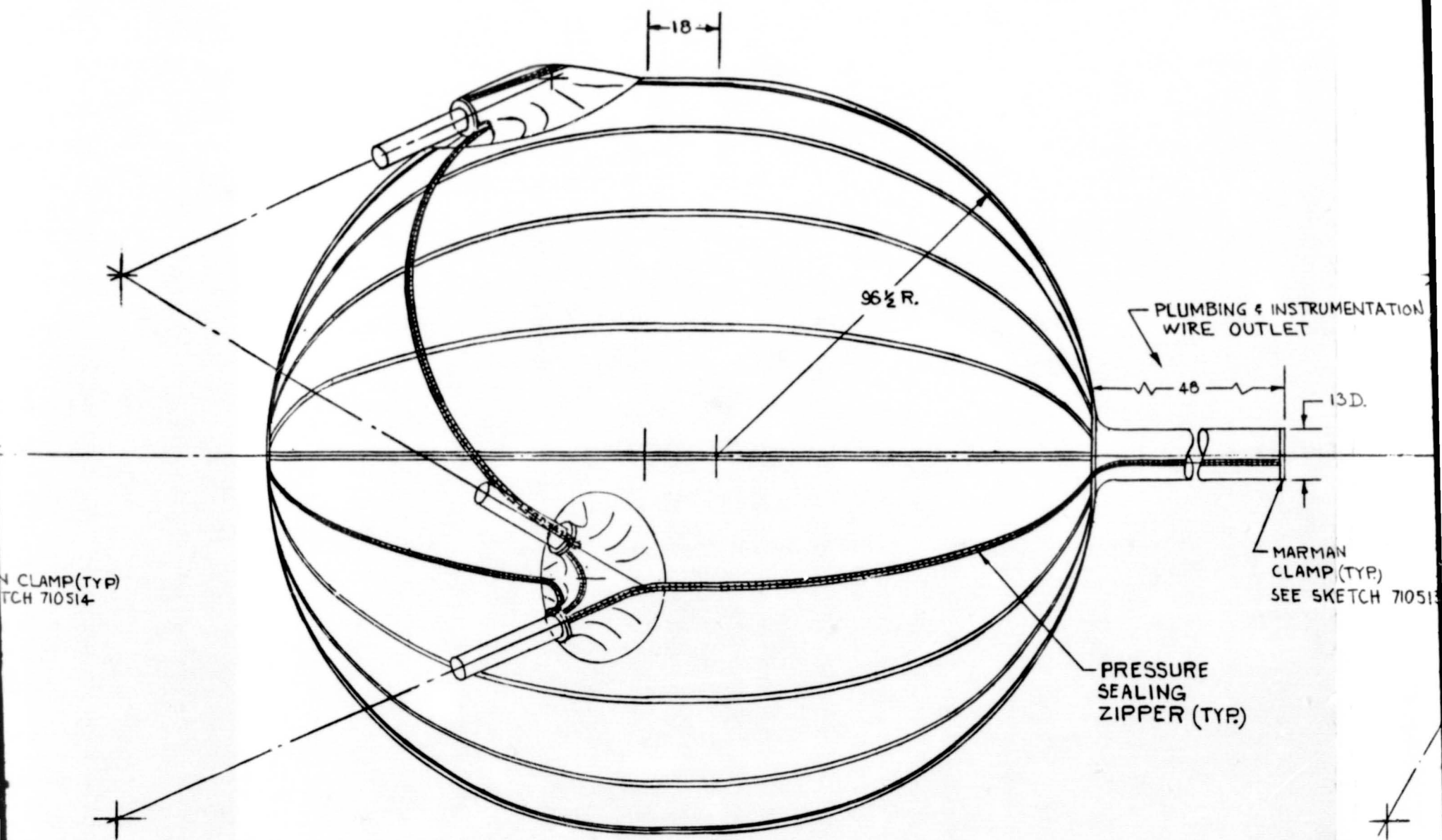


JOINT BETWEEN GORES FORMING PURGE BAG



FOLDOUT FRAME

2



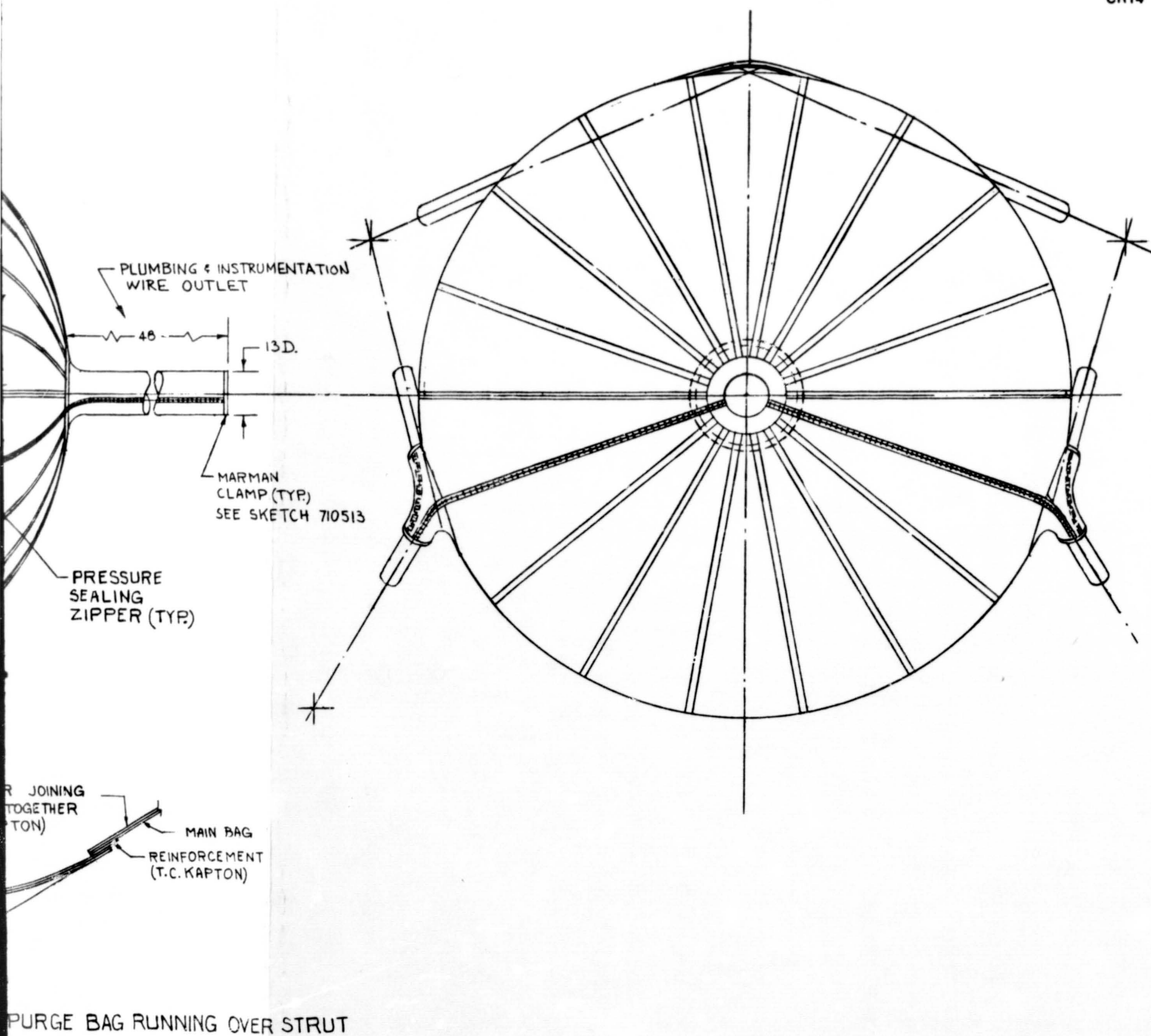


Figure 10-8. Conceptual Purge Bag Design for Secondary LH₂ Tank—SK 710518

Table 10-1
MLI SYSTEM COMPONENT WEIGHT SUMMARY-LH₂ TANK

System Component	Number	Unit Weight (lb)	Total Weight (lb)
DGK Reflectors	94 layers	0.0022 lb/ft ² layer	189
Dacron B4A Separators	93 layers	0.0013 lb/ft ² layer	110
Fasteners	3055	2.44 x 10 ⁻³ lb/fastener	7.5
Lacing Buttons	5983	1.74 x 15 ⁻⁴ lb/grommet and button	1.0
Face Sheets	—	—	52.5
Velcro	776 patches	1.06 x 10 ⁻³ lb/in. ²	2.5
Lacing Thread	3,000 ft	1.72 x 10 ⁻⁴ lb/ft	0.4
Strut Shroud and Hardware	6	1.07 lb/strut	6.4
Plumbing Shroud and Hardware	1	—	3.5
MLI Support Ring and Hardware	2	1.56 lb/ring	3.1
Foam Blocks (near support rings)	4	10 lb/ft ³	3.3
Wiring Pass-Through	1	—	0.4
Purge Bag	1	—	71
Purge and Repressurization System Hardware	See Table 10-3	—	69.6
Repressurization Gas (Helium)	—	—	2.4

Total estimated weight of system components = 522.6 lb

Total estimated weight per area covered = 0.59 lb/ft².

Table 10-2
MLI SYSTEM COMPONENT WEIGHT SUMMARY-LO₂ TANK

System Component	Number	Unit Weight (lb)	Total Weight (lb)
DGK Reflectors	92	2.2×10^3 lb/ft ² layer	80
Dacron B4A Separators	91	1.3×10^{-3} lb/ft ² layer	47
Fasteners	1455	2.44×10^{-3} lb/fastener	3.5
Lacing Buttons	1483	1.74×10^{-4} lb/grommet and button	0.3
Face Sheets	—	—	24
Velcro	356 patches	1.06×10^{-3} lb/in. ²	1.2
Lacing Thread	1,023 ft	1.72×10^{-4} lb/ft	0.2
Strut Shroud and Hardware	6	1.07 lb/strut	6.4
Plumbing Shroud and Hardware	1	—	3.5
MLI Support Ring and Hardware	2	1.56 lb/ring	3.1
Foam Blocks (near support rings)	4	10 lb/ft ³	3.3
Wiring Pass-Through	1	—	0.4
Purge Bag	1	—	38
Purge and Repressurization System Hardware	See Table 10-3	—	47.6
Repressurization Gas (Helium)	—	—	0.9

Total estimated weight of system components = 259.4 lb.
Total estimated weight per area covered = 0.67 lb/ft².

Table 10-3
PURGE AND REPRESSURIZATION SYSTEM
HARDWARE WEIGHT SUMMARY

System Component*	Total Number	Total Weight (lb)	
		LH ₂ Tank	LO ₂ Tank
Evacuation Butterfly Valves (Valve No. 4 _a , 4 _b , 4 _c and 6)	8	12.8	12.8
Umbilical Disconnect Valves (No's. 2 and 5)	2**	1	1
Helium Storage Bottle Fill Valve (No. 7)	1**	1.3	1.3
Inlet Line Vent Valve (No. 1)	1**	0.5	0.5
Repressurization Line Valves (No's. 3 and 8)	2**	1.0	1.0
Helium Storage	1***	31.2	11.7
Pressure Controller	1**	7	7
Tubing and Fittings	—	10.3	7.8
Evacuation Valve Support Shrouds	6	2.5	2.5
Marmon Clamps and Sealing Rings	14, 30	2	2
Total		69.6	47.6

*See Figure 6-56.

**Common to both tanks, weight evenly divided between tanks.

***Common to both tanks, weight divided between tanks based on ratio of helium used by each tank.

survey for zippers was beyond the scope of this study, but it is felt that such a survey might identify zippers with a much lower weight.

The majority of the face-sheet weight is due to the straps. Consequently, a reduction in the strap area would have a significant impact on the total weight. A consideration of the strap requirements in a more detailed analyses and in testing in future studies appears to have potential for a system weight reduction.

A more detailed study would also be expected to show the total weight for the purge and repressurization system hardware to be conservatively high since conservative estimates were made of the weights of several of the components. For example, the weight of the pressure controller could, depending on the control system design selection, be 3 to 4 pounds instead of the 14 pounds assumed.

As shown in Tables 10-1 and 10-2, the weights of all of the components add up to a sizeable total system weight. However, it should be kept in mind that these are large tanks. The surface areas of the LH_2 and LO_2 tanks are approximately 860 and 357 ft^2 respectively. There is, for both tanks, an additional 30 ft^2 of surface area which is covered on the struts and plumbing shroud. This results in a total weight per area covered of 0.59 lb/ft^2 for the LH_2 tank and 0.67 lb/ft^2 for the LO_2 tank.

10.4 CONCLUSIONS AND RECOMMENDATIONS

As a result of the conceptual design configuration study, it was concluded that an efficient and reliable MLI system design which lends itself to fabrication can be accomplished. Certain details of the design such as the optimum way to lay up the MLI layers on the strut panels remain to be considered in the future. A further study of the design details in areas such as this, as well as full-scale fabrication trials, are recommended.

The weight summary assembled for both the LH_2 and LO_2 tanks show that even a small percentage weight reduction in several of the component weights could have a significant effect in reducing the total weight. Components recommended for further study with the objective of reducing the weight include:

purge bag zippers, face sheets, separators, repressurization control system, and the valves for the purge, evacuation, and repressurization system.

Section 11

INSPECTION AND REFURBISHMENT PROCEDURES—TASK 9

The objectives of Task 9 are to: (1) conduct a preliminary evaluation of nondestructive inspection techniques for detecting material degradation within an insulation composite; and (2) define procedures for repair of damaged areas.

11.1 INSPECTION TECHNIQUE EVALUATION

Because of the reusability requirements of the ILRV, a nondestructive inspection technique for assessing the physical condition of the insulation while installed on the tank would be of value. Identification and location of physical changes and defects within the insulation such as corroded areas, compressed areas, or gross tears could be essential to ensure efficient and reliable performance of the insulation system.

Since physical changes and defects within the insulation are usually not detectible by visual inspection of the outer surface of the insulation composite, techniques using electromagnetic waves to penetrate into and through the insulation system were selected for consideration. Infrared, microwave, and radio-frequency techniques were considered in this study. This included technique evaluation tests on current MLI composites.

11.1.1 Infrared Radiation

Infrared radiation was considered as a possible technique for inspecting an insulation composite, but was eliminated because of the excellent reflectivity of the insulation reflector sheets to infrared radiation. Due to this high reflectivity, infrared radiation would only be applicable for inspecting the outermost reflector sheet of the composite, giving no advantage over visual inspection.

Consideration was given to the possibility of detecting composite degradation by detecting a cold spot on the outer sheet. However, inspection is to be accomplished on the ground and this technique would need to be conducted while purging since cryogen would be required in the tank. The conductivity of the purge gas would be expected to eliminate any localized cold spots on the outer sheet.

11.1.2 Microwaves

The use of microwaves as an insulation inspection technique was considered, but was also eliminated because of the high reflectivity of the reflector sheets. The microwaves would not be expected to penetrate beyond the first reflector sheet in the insulation composite. In addition, the microwave measurements would have to be made in a carefully controlled antireflection chamber and the precision of the apparatus would not be expected to detect small amounts of corrosion on the reflector sheets.

11.1.3 Radio-Frequency Techniques

Radio-frequency techniques appear to be more feasible for an inspection tool than the infrared or microwave techniques since the insulation composite will be somewhat transparent to electromagnetic waves of low frequencies. For example, the penetration depth of 3-MHz radiation into aluminum at room temperature is 5.2×10^5 Angstroms which is greater than the total thickness of aluminum in a typical composite containing 50 to 100 aluminized reflector sheets.

Two radio-frequency techniques were selected for experimental feasibility studies. These were a capacitor and an induction coil technique.

11.1.3.1 Capacitor Technique

The capacitor technique utilizes the principle of a parallel plate capacitor wherein the capacitance is a function of the distance between the plates (thickness of the dielectric), cross-sectional area, and the dielectric material. These parameters are related in the form $C = K' KA/d$ where C is the capacitance; K' is a constant relating the units of capacitance, area, and thickness; K is the dielectric constant; A is the cross-sectional area; and d is the thickness of the dielectric.

The application of the capacitor technique is accomplished by placing the insulation composite between capacitor plates connected to a capacitance bridge. Since each of the layers of metal becomes a capacitor plate in this arrangement, an insulation composite would result in a circuit with numerous capacitors in series. For n capacitors in series, the equivalent capacitance of the series is given by:

$$\frac{1}{C_{\text{total}}} = \frac{1}{C_1} + \frac{1}{C_2} + \frac{1}{C_3} + \dots + \frac{1}{C_n}$$

Interpretation of inspection data to determine the condition of the insulation will require noting changes in the capacitance in a given location and the use of calibration curves. Changes in the insulation thickness would result in changes in the capacitance because of the change in the dielectric thickness of some of the capacitors in the series. Removal of the reflector metal by corrosion or a gross tear would change the capacitance because of a reduction in plate surface area. Corrosion could also change the dielectric constant because of the introduction of a metal oxide on the surface of the reflector sheets.

Pilot tests were conducted to determine the feasibility of using a capacitor technique to measure insulation thickness on Project Thermo, Contract NAS 8-18053 (Reference 21). In this study, the outer capacitor plates were formed on the outer reflector sheets by isolating a patch of the reflector metal. This was accomplished by removing a narrow circular band of the metal, leaving an electrically isolated disk-shaped area. A test apparatus was constructed which allowed the insulation thickness to be varied and held at a given thickness while a capacitor reading was taken. The data showed that repeatable results could be obtained and that reasonable accuracy could be expected for insulation when highly compressed. For the specimen configuration tested, however, the uncertainty of a thickness reading for slightly compressed insulation was quite high. This might be alleviated by using larger patches for the capacitor plates. Test data from Reference 21 is shown in Figure 11-1.

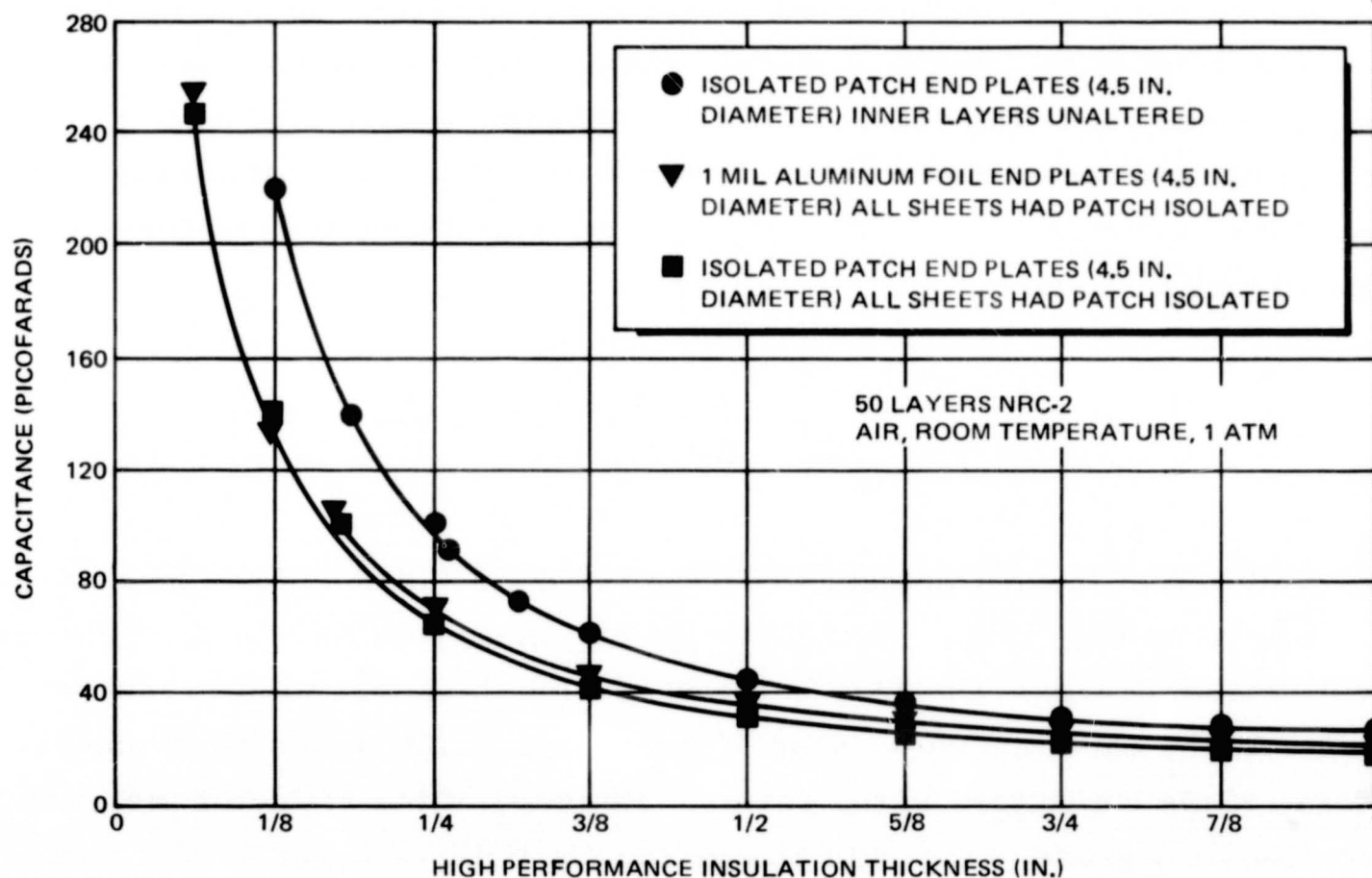


Figure 11-1. HPI Thickness Gage

Two additional problems with the capacitor technique were identified in the MSFC/MDAC Project Thermo work; the significant effect of the external field on the capacitance, and the need to isolate electrically a patch on each of the reflector layers in the composite. In addition, that portion of the sheets surrounding the isolated area would probably need to be electrically shorted since, although isolated from direct conduction, edge effects could be significant. Because the external field was significant, changes in the positions of objects in this field such as repositioning of hardware or the movement of the test operator could not be tolerated. The external field problem did not eliminate the use of the capacitor technique but does mean that the gage would need to be calibrated in its actual inflight physical environment.

In an actual application as an inspection technique for an insulation system on a tank, the Project Thermo insulation thickness gage could only be used

as a check of selected localized areas or as an indication of the average insulation thickness over all of the tank. In the latter case, the outer capacitor plates would simply be the complete outer and inner reflector layers of the insulation composite.

In the current study, a cursory investigation was made to determine if the use of alternating current at a high frequency (~13 megacycles) would reduce the external field problem. A test specimen of MLI was placed between the capacitor plates in a large parallel plate capacitor as shown in Figure 11-2. The 5 by 6 in. aluminum capacitor plates were electrically insulated from the test specimen and connected to an RX meter with a 15-in. length of coaxial cable (RG58C/U). The measured capacitance of the capacitor and coaxial cable was 58 picofarads. A small 0.9-microhenry inductor was connected in parallel with the parallel plate capacitor to form a resonant circuit. This circuit could be tuned to the preselected working frequency of the RX meter by adjusting the input capacitance in the impedance bridge of the RX meter. Changes in the capacitance due to variations in the MLI would be indicated by changes in the value of the RX meter input capacitance required to keep the circuit tuned to the working frequency.

In the course of several measurements, it was observed that the capacitance readings were strongly influenced by the location of the test operator. The effects were significant enough to negate the reliability of the data. Since the results appeared similar to those obtained in the previous study, further evaluation of the capacitor technique was not conducted.

11.1.3.2 Induction Coil Technique

The basic procedure involved in the induction coil inspection technique is to monitor the impedance of an inductor which has been electromagnetically coupled to the MLI by having been placed in close proximity with the MLI surface. When this coupling is present, changes in the MLI layer density or the resistivity of the metallized coating on the reflector sheets, due to corrosion or a tear, will result in changes in the impedance of the coil. This technique has an advantage over the capacitance technique discussed

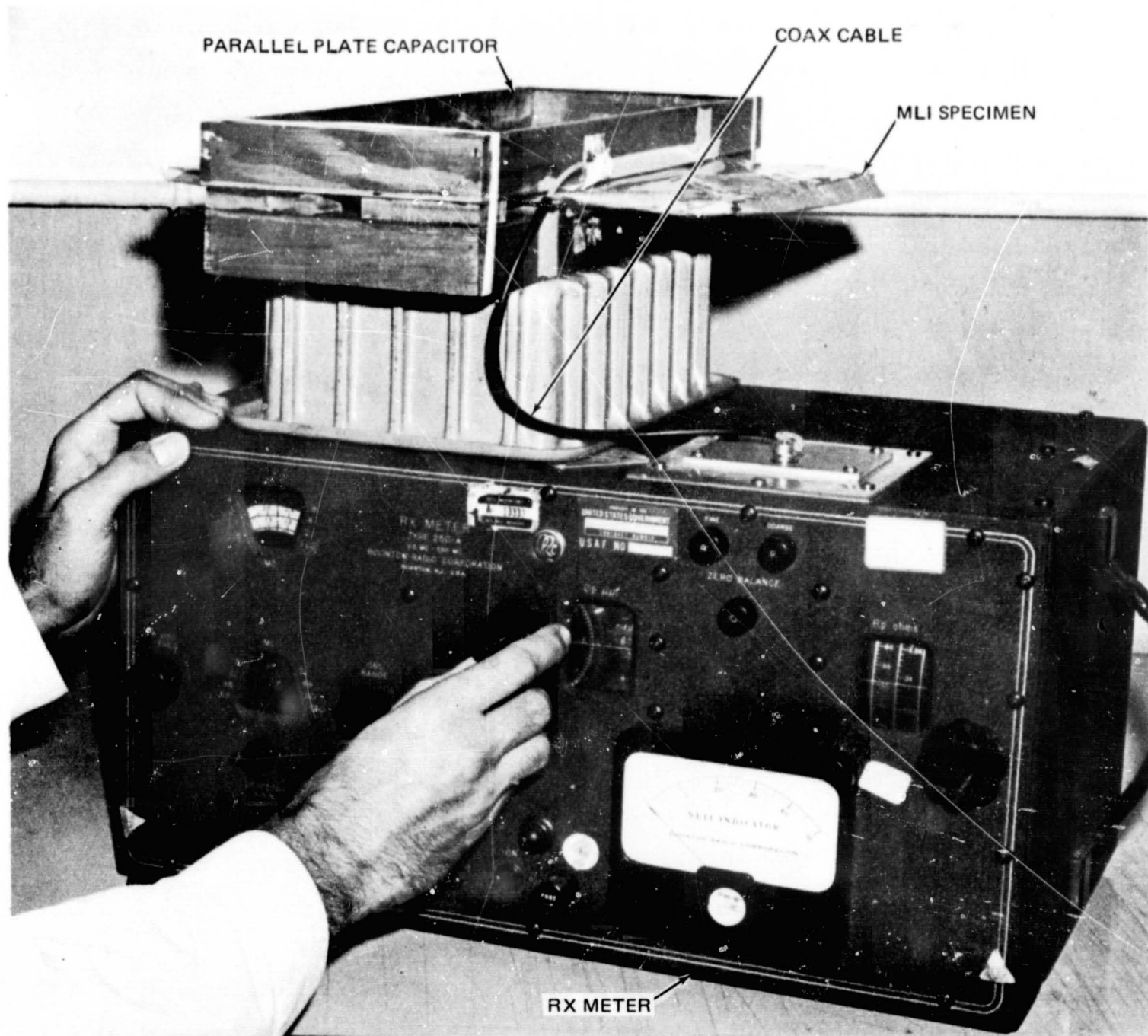


Figure 11-2. Parallel Plate Capacitor Set-up

previously because it provides a means of inspecting the MLI locally since only the insulation in the immediate vicinity of the coil is electromagnetically coupled to the coil. Movements of test personnel have no observed effects on the measurements. In addition, this technique provides a potential method for inspection at randomly selected locations since the apparatus is all on the exterior of the insulation and need not be fastened to the insulation.

The impedance (Z) is a complex quantity which can be expressed as $Z = R_p + iX_p$ where R_p is the equivalent parallel resistance and X_p is the equivalent parallel reactance. The equivalent parallel reactance (X_p) of the tuned circuit is related to the equivalent parallel capacitance (C_p) by the equation $X_p = 1/(2\pi f C_p)$ where f is the frequency. The changes in the impedance of the coil were monitored by using an RX meter to measure the equivalent parallel resistance and equivalent parallel capacitance needed to keep the coil tuned to a preselected frequency.

A ring-shaped induction coil having an outside diameter of 3 in. and an inductance of $112\mu\text{h}$ was used. A nonconducting plate was mounted within the coil so that the coil assembly, when placed on the surface of the MLI uniformly contacted and compressed a 3-in. -diameter area of the MLI. The coil was connected to an RX meter (Boonton model 250A) by 13 in. of coax cable (RG58C/U) as shown in Figure 11-3. This RX meter develops 0.1 to 0.5 volts across its terminals and is a wide-frequency-range impedance meter designed to permit individual determination of the equivalent parallel resistance (R_p) and parallel reactance (X_p) of two terminal networks and components.

In the first, and main, test series, two test specimens of MLI were fabricated and used. Each specimen contained 36 reflector sheets of double aluminized Mylar with each reflector sheet separated by a nylon net. Each of the specimens was encased in a nylon sheet envelope to facilitate handling. One test specimen contained reflectors which had 10 percent, by area, of the reflector metal removed, simulating 10-percent corrosion, and the other specimen contained reflectors that had 2 percent of the reflector metal

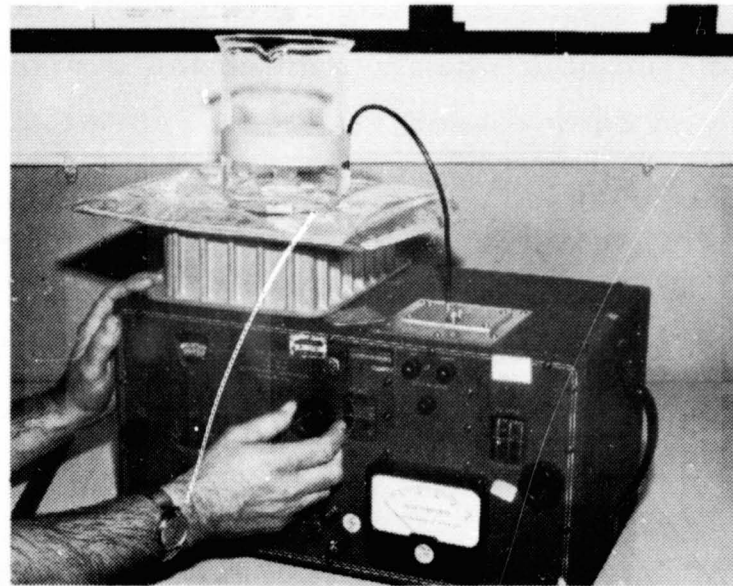
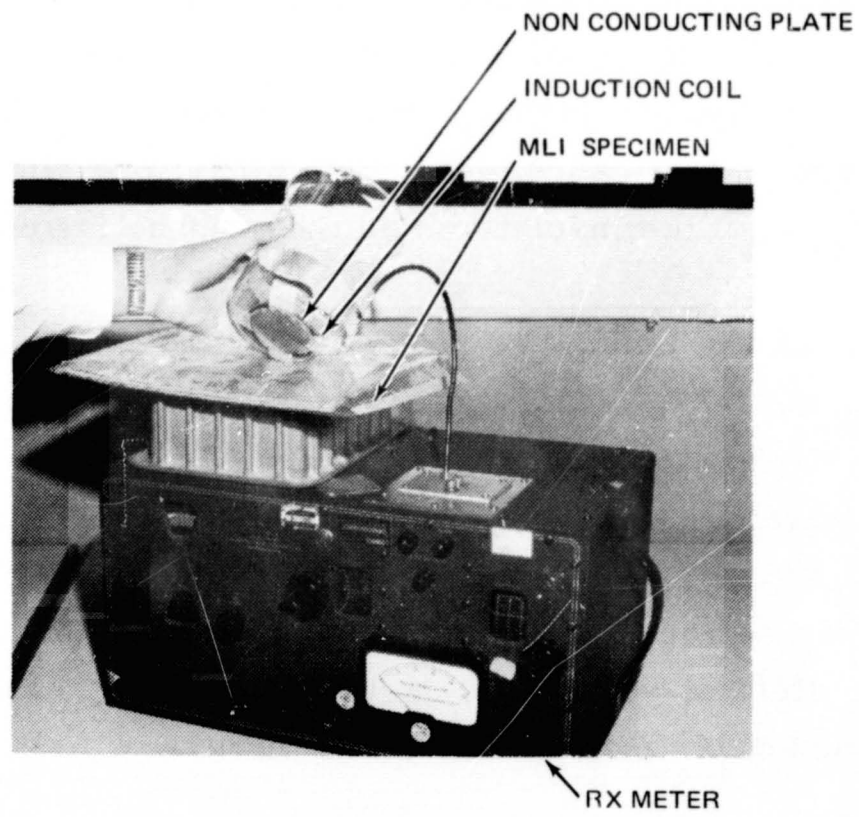


Figure 11-3. Induction Coil Set-up For Corrosion Tests

removed. The specimens were 10 by 11-1/2 in. with the corrosion confined to a 10 by 5 in. portion of the surface area. The corrosion was achieved by brushing concentrated NaOH onto the aluminum coating and then blotting the NaOH area dry. All the aluminum was removed that was contacted by NaOH. The 10 percent corroded area was produced by removing one 1/2-in. -wide strip on both sides of each Mylar sheet in the 5-in. -wide area. The location of the corroded strips on adjacent reflector sheets was varied throughout the panel so that approximately nine sheets of Mylar separated each corroded strip from another one directly above or below it. This corrosion pattern resulted in an average of 10-percent corrosion throughout the 5 by 10 in. surface area of the specimen. The 2 percent corroded area was similarly produced. In this case, two 1/4-in. -wide strips were corroded on every fifth sheet throughout the thickness of the insulation panel. The location of the corroded strips was again staggered throughout the panel.

Induction Coil Tests for Detecting 10-Percent Corrosion

Measurements were taken to determine the feasibility of detecting 10-percent corrosion with the induction coil technique. This was accomplished by obtaining data with the coil placed over the 10 percent corroded area of the specimen and with the coil placed over the adjacent uncorroded area. Two applied pressures of the coil against the MLI were used; 0.11 lb/in.² and 0.51 lb/in.². The working frequency used was 2.5 MHz.

As expected, the results showed good stability throughout the measurements. Movement of the operator or changes in the thickness of the insulation in areas away from the immediate vicinity of the coil had no apparent significant effect on the measurements. The data (shown in Table 11.1) indicated that 10-percent corrosion can be readily detected and that corrosion results in a decrease in the parallel capacitance (Cp) and an increase in the parallel resistance (Rp). Compression of the specimen results in an increase in Cp and a decrease in Rp.

The trends of the data were as expected. Since the metal coatings on the reflector sheets will partially shield the electromagnetic field of the probe

Table 11 1
DETECTION OF 10-PERCENT CORROSION
BY THE INDUCTION COIL TECHNIQUE

Applied Pressure	10 Percent Corroded Area		Noncorroded Area	
0.11 lb/in. ²	C _p *	R _p #	C _p	R _p
	29.7	2.41	39.0	2.33
	28.6	2.45	39.9	2.33
	30.0	2.41	38.0	2.37
	29.9	2.40	38.2	2.35
	28.6	2.45		
	29.8	2.42		
0.51 lb/in. ²	36.2	2.21	44.6	2.21
	35.0	2.24		
	36.1	2.23		

Working frequency = 2.50 MHz

*C_p = Capacitance in picofarads

#R_p = Resistance in ohms x 10³

coil, an increase in the insulation layer density, resulting from compression of the composite, should result in a decrease in the inductance. Decreasing the inductance requires an increase in the capacitance in order to maintain a tuned circuit at the selected frequency since these are related by the equation: $2\pi f = 1/\sqrt{LC}$ where f is the frequency, L is the inductance, and C is the capacitance. Consequently, as was shown in the data, compression of the insulation composite should result in an increase of the capacitance. In addition to a decrease in the inductance, the increase in layer density should, as shown in the data, cause a decrease in the parallel resistance. Since the induction field is more intense near to the coil, the eddy current flux set up in the aluminum layers will be increased because of the increase in the number of layers near to the coil.

Corrosion of the reflector metal is expected to produce effects opposite those for compression. When the amount of metal in the vicinity of the coil is

decreased, there is less conducting material to shield the induction field of the coil and in which to create eddy currents. As a result, the presence of corrosion should cause the inductance of the coil to increase (decrease in parallel capacitance) and approach that of the coil when no MLI is in proximity with it. Also, since there are less eddy currents set up due to less conductor metal in which the currents can exist, the coil should have a higher parallel resistance. Both the decrease in capacitance and the increase in parallel resistance with increasing corrosion were observed.

A gross tear would be expected to produce effects, at the location of the tear, similar to those resulting from corrosion. As with corrosion, a reduction in the number of metallized layers would cause a reduction in the parallel capacitance in the tuned circuit.

Induction Coil Tests for Detecting 2-Percent Corrosion

Measurements were taken with the induction coil technique to determine the feasibility of detecting corrosion as low as 2 percent. The data were obtained by the same procedures used in the 10-percent corrosion detection tests except that a frequency of 2.0 MHz instead of 2.5 MHz was used.

The data (shown in Table 11-2) indicated that a sufficient change was made in the capacitance to allow detection of 2-percent corrosion. The trend of a decrease in capacitance with the presence of corrosion was as expected from the previous test of the 10 percent corroded specimen. No change could be detected in the resistance.

Detection of 2-Percent and 10-Percent Corrosion with Zero Applied Pressure

Measurements were also taken with the induction coil when the coil was suspended above the insulation surface. This provided evaluation of the technique for a zero compaction condition. The test procedures and specimens were those discussed for the previous tests. The test frequency was 2.0 MHz.

Table 11-2
DETECTION OF 2-PERCENT CORROSION
BY THE INDUCTION COIL TECHNIQUE

Noncorroded Area		2 Percent Corroded Area	
C_p^*	$R_p^\#$	C_p^*	R_p
96.7	1.92	93.5	1.91
96.8	1.91	93.1	1.92
96.4	1.92	94.0	1.91
96.4	1.92		

Working frequency: 2.0 MHz

Applied pressure: 0.11 lb/in.²

* C_p Capacitance in picofarads

R_p Resistance in ohms $\times 10^3$

The data (shown in Table 11-3) indicated trends consistent with those in the previous tests. They also indicated that corrosion as low as 2 percent can be detected when the induction coil is positioned so that it is not contacting the insulation surface.

Induction Coil Tests for Detecting Compression

Extensive measurements were taken to evaluate the capability of the induction coil technique for detecting a change in the thickness of the insulation composite. Measurements were performed on six MLI composites in an effort to correlate layer density, for a given applied pressure, with the type of separator in the composite. The six composites tested were: (1) Super-floc, (2) DAM/dacron net (style B3B), (3) DAM/dacron net (style B4A), (4) DAM/nylon net (NN), (5) DAM/Dacron net (style B2A), and (6) DAM/Tissu-glas (Tg). The test specimens fabricated for each of the six insulation composites were 6 in. square and contained 24 reflector sheets of doubly aluminized Mylar (DAM) and 23 separators.

Table 11-3

CORROSION DETECTION BY THE INDUCTION COIL TECHNIQUE
WITH ZERO LOADING OF THE TEST SPECIMEN

10 Percent Corroded Panel				2 Percent Corroded Panel			
Corroded Area		Noncorroded Area		Corroded Area		Noncorroded Area	
C_p^*	$R_p^\#$	C_p	R_p	C_p	R_p	C_p	R_p
67.8	3.02	76.0	3.00	76.0	2.69	76.7	2.70
66.6	3.20	76.1	2.99	76.2	2.68	76.8	2.70

* C_p Capacitance in picofarads

R_p Resistance in ohms $\times 10^3$

Working frequency 2.0 MHz

The experimental setup is shown in Figure 11-4. The coil used was the same 3-in. -diameter coil used in the previous induction measurements and was mounted, as shown, in a platform fixture directly above the RX meter. This arrangement allowed varying pressure to be applied to the insulation test specimen. It also enabled the induction coil to be connected to the RX meter with short leads, which minimized the effects of the connecting cable on the impedance of the coil. The operating frequency for the initial series of measurements was 2.50 MHz which provided good penetration of the MLI specimen. With the specimen in place on top of the probe coil and the RX meter impedance bridge balanced, waving a piece of metal near the insulation surface and over the coil caused a moderate deflection of the RX meter null indicator, indicating penetration of the specimen.

A set of nonmetallic weights was used to vary the pressure. The weights were supported by the entire area of the test specimen. Measurements of the C_p and R_p of the circuit, when tuned, were taken for each panel in the unloaded condition and after the addition of each weight.

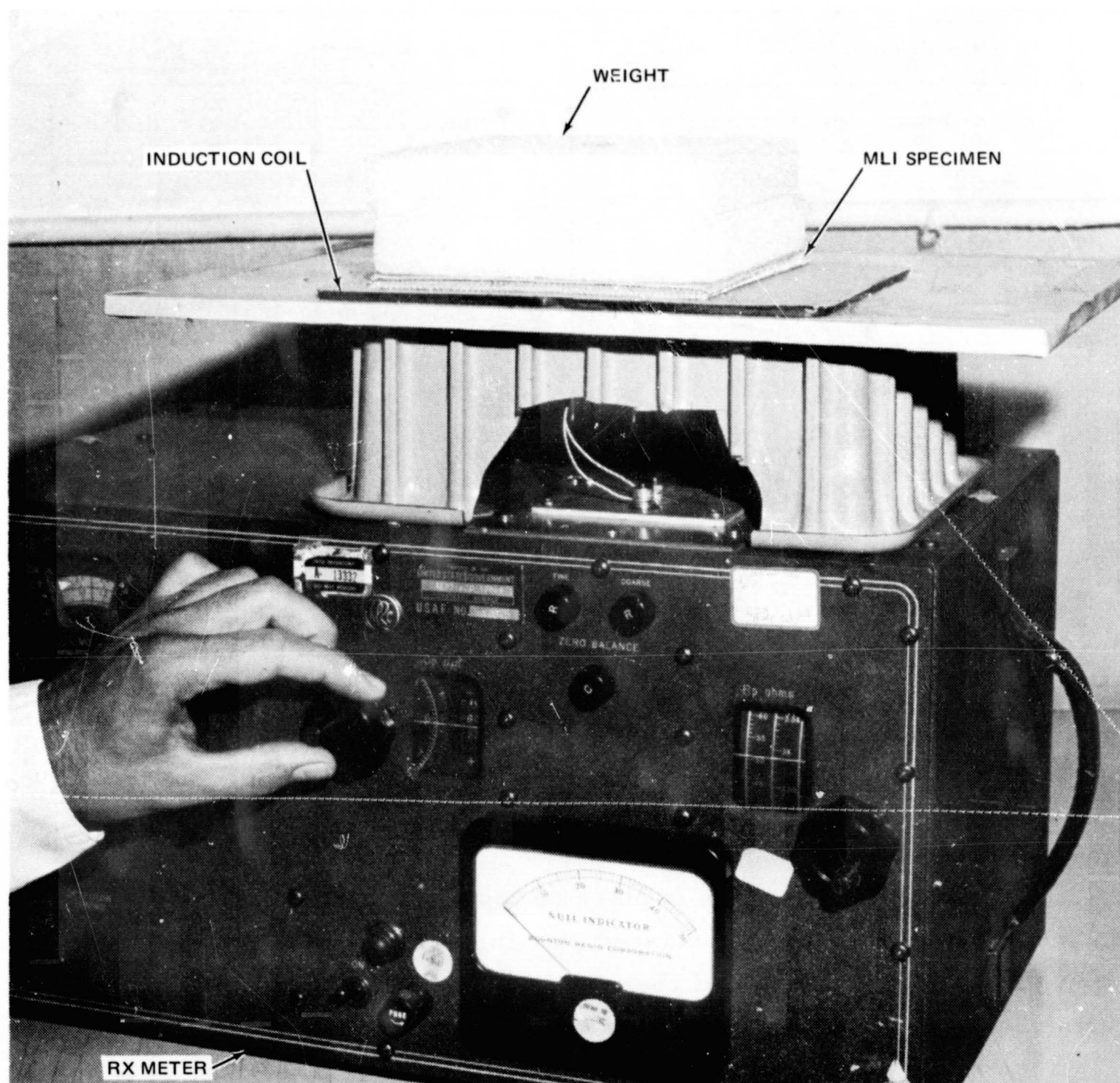


Figure 11-4. Induction Coil Set-up For Compression Tests

The data (Table 11-4 and Figures 11-5 and 11-6) show consistent trends for each of the insulation systems. As expected, the C_p increased with an increase in compression and the R_p decreased. The only exception to this is found in the DAM/NN sample where the R_p increases with compression and then decreases. This behavior was observed repeatedly with this composite.

The data indicate that a good calibration curve for interpreting inspection data is obtainable. A comparison of Figures 11-5 and 11-6 reveals that the use of the C_p data for such a calibration curve will provide more accuracy than the R_p data. It is also important to note that the slopes of the C_p curves at low compression conditions are adequate for good accuracy whereas this was not the case with the capacitor inspection technique (see Figure 11-1).

The data in Table 11-4 indicate that the insulation thickness recovers to nearly its original condition when the load is removed. Figure 11-7 shows a plot of the C_p data for a typical composite. The curves are essentially hysteresis loops indicating that elastic properties can be ascribed to the insulation. These elastic properties are important for predicting the effects of environmental loading on the layer density history and for implementing the induction method as an inspection technique.

Induction Coil Tests for Determining the Effect of Changing the Frequency

Compression measurements were conducted in which the working frequency was changed for each set of measurements in an attempt to determine the optimum frequency to be used. The 6-in. square, 24 reflector, DAM/B2A specimen was used and was fluffed between measurements.

The data (Table 11-5 and Figures 11-8 and 11-9) show that the parallel resistance initially increases and then decreases as the loading is increased for frequencies above 3.0 MHz. The data also show that the range of C_p and R_p values decreases as the frequency is increased. For a fixed value of inductance of the coil, this behavior indicated that the sensitivity of the measurements is decreasing as the frequency is increased.

Table 11-4

COMPRESSION DETECTION WITH THE INDUCTION COIL TECHNIQUE

Incremental Applied Weight (grams)	Applied Pressure (lb/in. ²)	HPI Test Specimens											
		SUPERFLOC		DAM/B3B		DAM/B4A		DAM/NN		DAM/B2A		DAM/Tissuglas	
		C _P *	R _P #	C _P *	R _P #	C _P *	R _P #	C _P *	R _P #	C _P *	R _P #	C _P *	R _P #
0.0	0	39.0	3.62	55.5	3.30	51.6	3.35	48.0	3.06	57.5	3.12	58.0	3.20
10.6	6.50 x 10 ⁻⁴	41.7	3.59	56.3	3.30	52.9	3.36	48.7	3.07	57.7	3.13	60.5	3.21
17.0	1.69 x 10 ⁻³	44.9	3.58	58.1	3.24	55.3	3.35	50.1	3.08	58.8	3.10	63.2	3.18
17.0	2.73 x 10 ⁻³	46.7	3.57	59.1	3.20	56.8	3.34	50.9	3.09	59.6	3.09	64.8	3.13
45.4	5.51 x 10 ⁻³	49.8	3.50	60.1	3.18	58.8	3.31	52.6	3.10	60.3	3.06	66.8	3.07
93	1.12 x 10 ⁻²	53.4	3.41	61.4	3.15	61.2	3.30	54.8	3.10	61.3	3.03	68.4	2.99
96	1.71 x 10 ⁻²	55.8	3.34	62.1	3.13	63.0	3.29	55.7	3.10	61.9	3.00	69.4	2.94
99	2.31 x 10 ⁻²	57.3	3.28	62.6	3.11	64.3	3.27	56.3	3.10	62.3	2.99	70.1	2.91
150	3.13 x 10 ⁻²	59.1	3.19	63.3	3.10	65.6	3.24	57.0	3.10	62.6	2.97	71.0	2.88
153	4.16 x 10 ⁻²	60.3	3.12	63.7	3.00	66.9	3.20	57.5	3.09	63.1	2.95	71.5	2.84
154	5.10 x 10 ⁻²	61.4	3.07	64.3	3.07	67.7	3.18	57.8	3.09	63.3	2.93	71.8	2.80
150	6.03 x 10 ⁻²	62.4	3.00	64.8	3.05	68.3	3.15	58.1	3.08	63.6	2.91	72.2	2.79
300	7.86 x 10 ⁻²	64.4	2.89	65.3	3.02	69.3	3.10	58.4	3.07	63.9	2.90	72.8	2.75
300	9.70 x 10 ⁻²	65.9	2.79	65.9	3.00	70.1	3.07	58.8	3.05	64.1	2.87	73.2	2.71
300	1.16 x 10 ⁻¹	67.3	2.70	66.5	2.96	70.6	3.03	59.2	3.04	64.5	2.86	73.6	2.69
450	1.43 x 10 ⁻¹	68.7	2.61	67.0	2.93	71.5	2.99	59.4	3.03	64.7	2.83	74.0	2.65
450	1.70 x 10 ⁻¹	70.0	2.52	67.3	2.90	72.3	2.95	59.8	3.00	64.9	2.80	74.5	2.62
470	1.99 x 10 ⁻¹	70.9	2.45	67.9	2.89	72.8	2.92	60.1	2.99	65.2	2.79	74.7	2.60
-470	1.70 x 10 ⁻¹	70.9	2.46	67.8	2.90	72.6	2.93	60.0	3.00	64.9	2.79	74.6	2.60
-450	1.43 x 10 ⁻¹	70.7	2.47	67.3	2.90	72.2	2.95	59.6	3.00	64.9	2.80	74.5	2.61
-450	1.16 x 10 ⁻¹	70.2	2.50	66.9	2.92	71.7	2.97	59.4	3.01	64.6	2.80	74.2	2.63
-300	9.70 x 10 ⁻²	69.9	2.53	66.6	2.93	71.3	2.99	59.1	3.02	64.4	2.82	73.8	2.66
-300	7.86 x 10 ⁻²	69.4	2.57	66.2	2.95	70.8	3.01	58.9	3.03	64.1	2.84	73.5	2.67
-300	6.03 x 10 ⁻²	68.6	2.61	65.5	2.97	69.9	3.05	58.5	3.05	63.9	2.85	73.3	2.69
-150	5.10 x 10 ⁻²	68.1	2.65	65.2	2.99	69.5	3.08	58.1	3.05	63.6	2.87	72.9	2.71
-154	4.16 x 10 ⁻²	67.4	2.70	65.1	3.00	68.9	3.10	57.9	3.06	63.5	2.88	72.6	2.73
-153	3.13 x 10 ⁻²	66.5	2.75	64.5	3.00	68.1	3.11	57.5	3.06	63.2	2.90	72.3	2.75
-150	2.31 x 10 ⁻²	65.0	2.82	63.8	3.03	67.1	3.15	57.1	3.07	62.9	2.92	71.7	2.78
-99	1.71 x 10 ⁻²	63.6	2.90	63.4	3.05	65.9	3.18	56.8	3.08	62.5	2.93	71.0	2.81
-96	1.12 x 10 ⁻²	61.6	3.00	62.6	3.07	63.9	3.20	56.0	3.09	61.9	2.95	70.5	2.85
-93	5.51 x 10 ⁻³	58.4	3.13	61.6	3.09	62.1	3.22	54.8	3.09	61.4	2.97	69.2	2.90
-45	2.73 x 10 ⁻³	54.8	3.25	60.4	3.10	59.8	3.24	53.3	3.09	60.5	3.00	67.7	2.95
-17	1.69 x 10 ⁻³	52.3	3.30	59.8	3.12	58.5	3.25	52.0	3.08	60.0	3.01	66.6	2.99
-17	6.50 x 10 ⁻⁴	48.2	3.48	58.0	3.15	56.1	3.25	50.5	3.06	58.6	3.03	63.7	3.05
-10.6	0	42.5	3.49	56.9	3.16	53.8	3.25	49.1	3.03	57.9	3.04	61.0	3.06

Working Frequency = 2.50 mHz.

* C_P Capacitance in picofarads.

R_P Resistance in ohms x 10³.

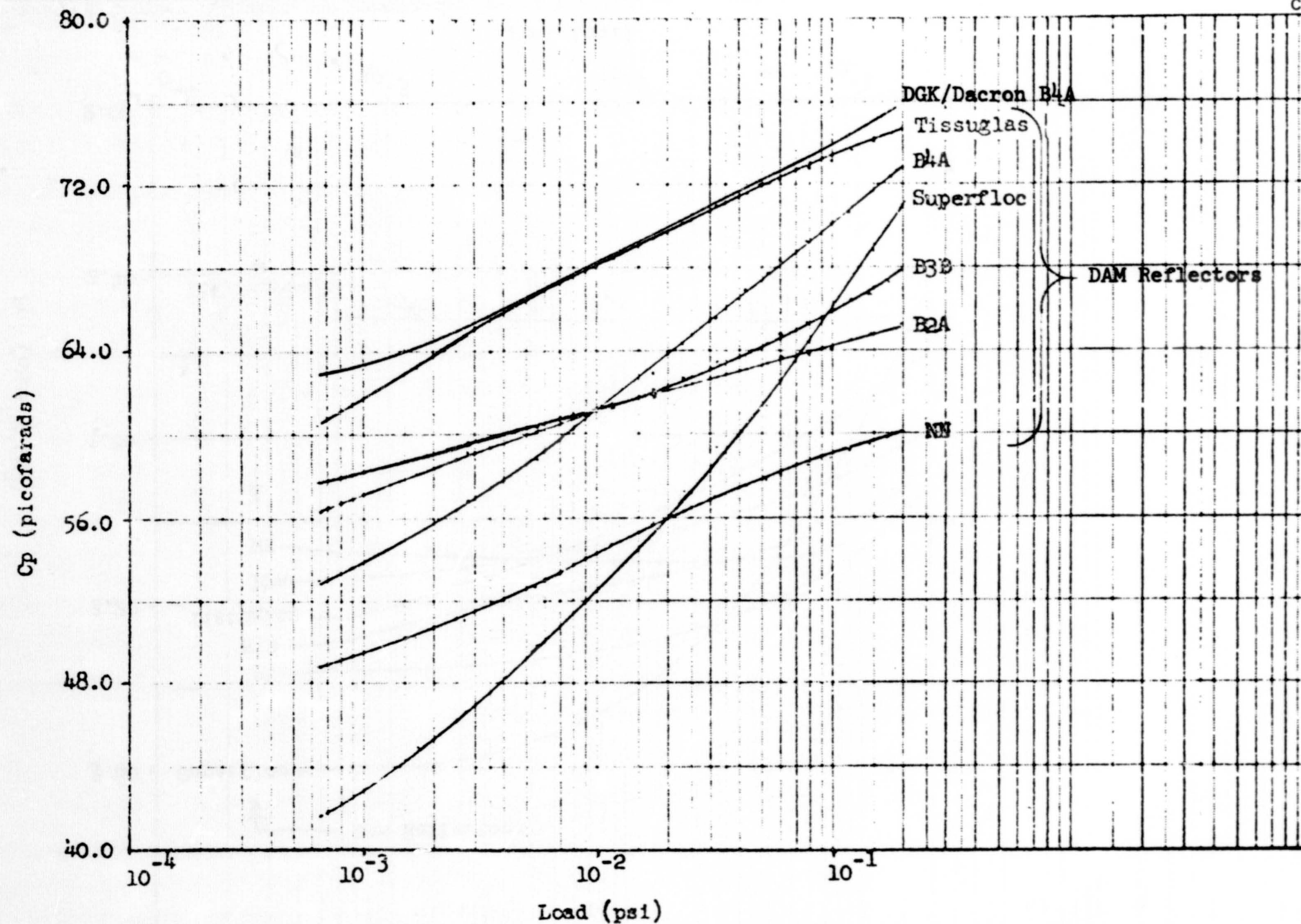


Figure 11-5. Compression Detection with Induction Coil Technique-Cp Data

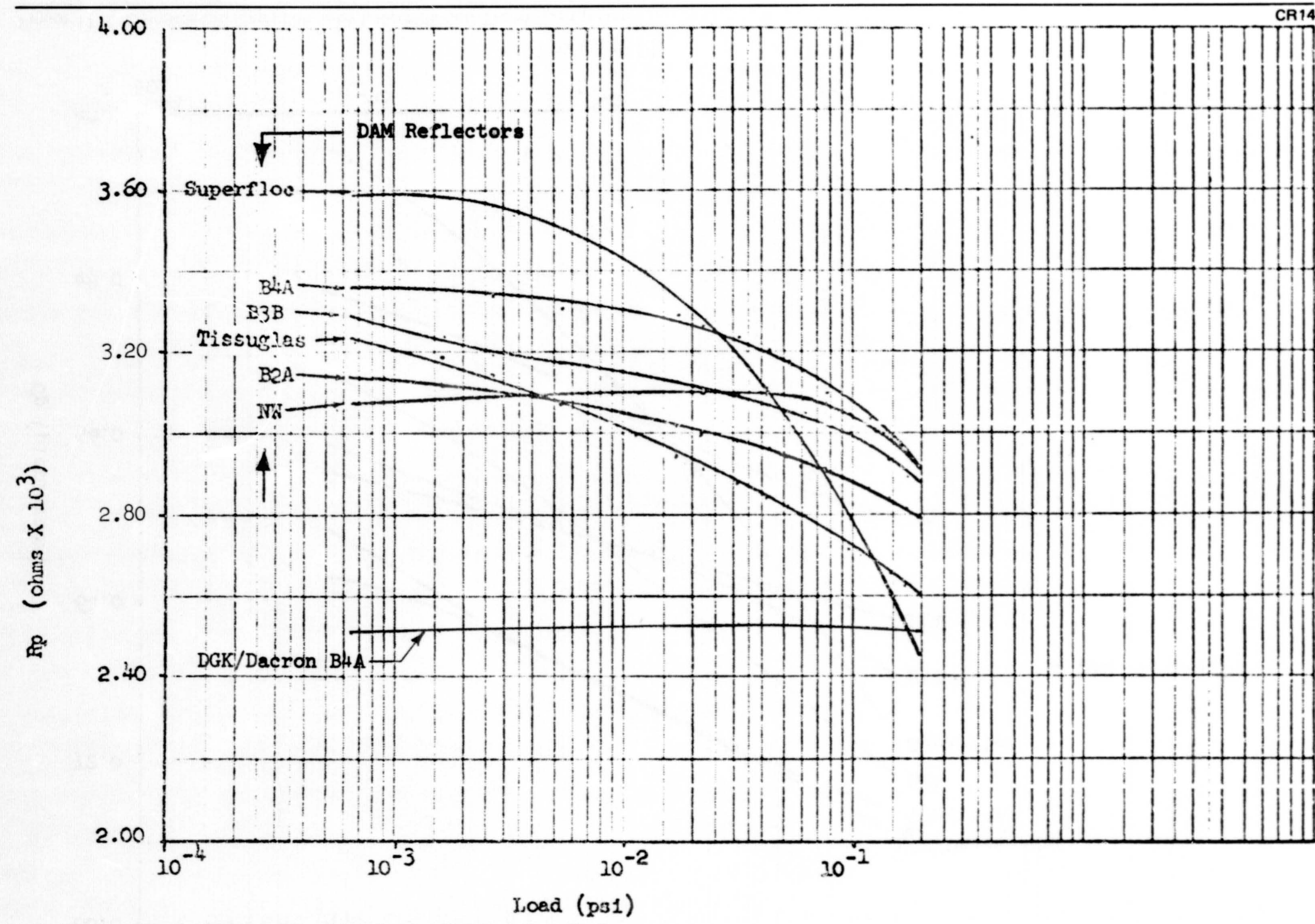


Figure 11-6. Compression Detection with Induction Coil Technique-Rp Data

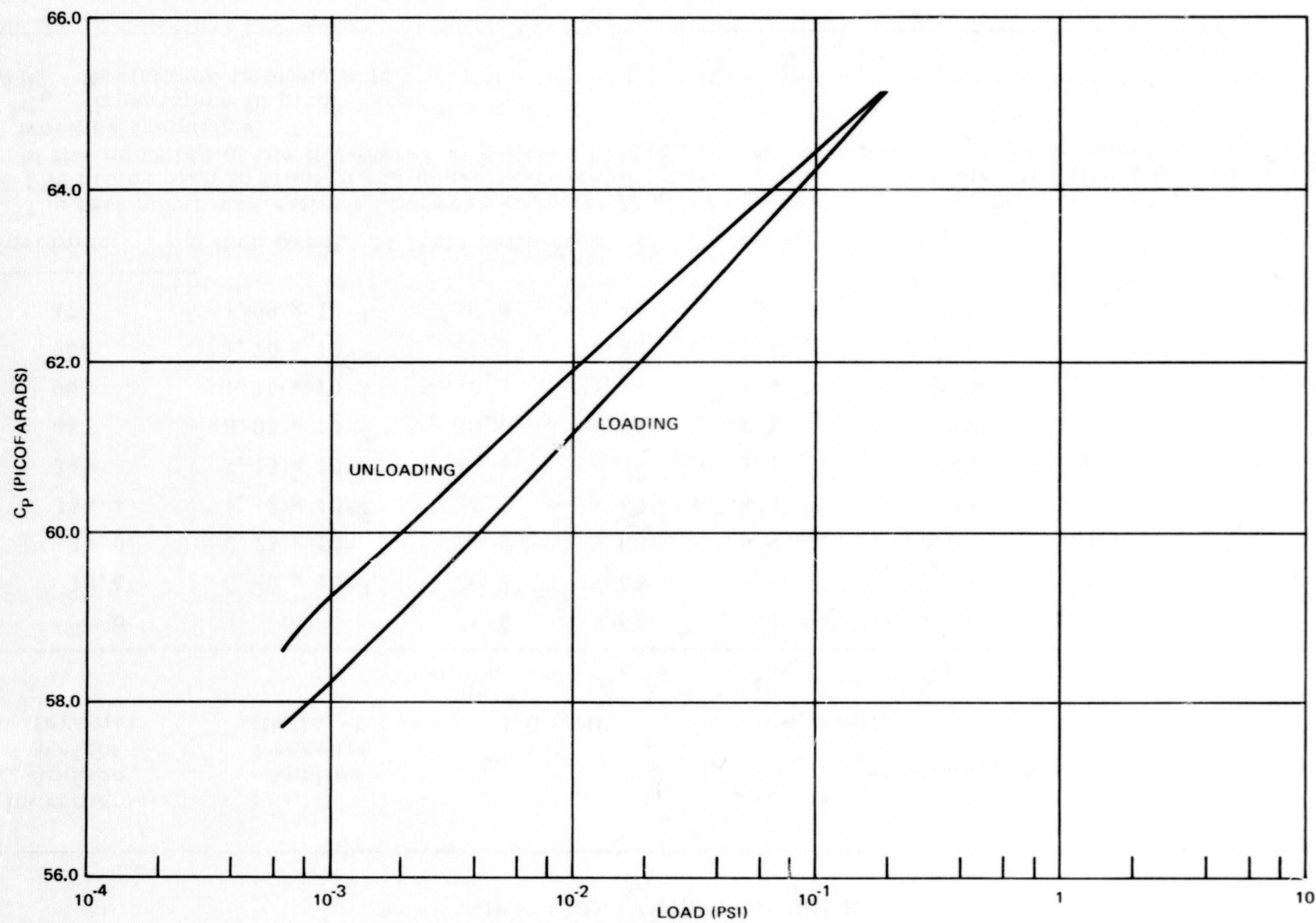


Figure 11-7. DAM/B2A Elastic Behavior- C_p Data

Table 11-5

COMPRESSION MEASUREMENTS ON DAM/B2A MLI AT SEVERAL FREQUENCIES—
INDUCTION COIL TECHNIQUE

Incremental Applied Weight (grams)	Applied Pressure (lb/in. ²)	Frequency**					
		3.0 mHz		4.0 mHz		5.0 mHz	
		C _p [*]	R _p #	C _p	R _p	C _p	R _p
0	0	25.8	3.62	-5.9 ##	4.71	-21.5 ##	5.50
10.6	6.50 x 10 ⁻⁴	26.2	3.63	-5.6	4.75	-21.4	5.52
34.0	2.73 x 10 ⁻³	27.5	3.60	-4.7	4.80	-21.0	5.60
138.4	1.12 x 10 ⁻²	28.7	3.59	-4.1	4.80	-20.6	5.65
345	3.13 x 10 ⁻²	29.6	3.55	-3.7	4.80	-20.4	5.70
457	6.03 x 10 ⁻²	30.0	3.51	-3.5	4.79	-20.3	5.70
900	1.16 x 10 ⁻¹	30.4	3.46	-3.3	4.73	-20.3	5.68
900	1.70 x 10 ⁻¹	30.7	3.42	-3.3	4.71	-20.4	5.65
470	1.99 x 10 ⁻¹	30.8	3.40	-3.2	4.70	-20.5	5.63

Specimen: 6 x 6 inch panel, 24 DAM reflectors, 23 B2A net separators

**The test panel was refluffed between each set of compression measurements.

The minus sign in front of the capacitance values corresponds to decreasing the internal capacitance of the input leg of the RX-meter impedance bridge past its zero-point to tune the induction coil to the working frequency.

*C_p Capacitance in picofarads

#R_p Resistance in ohms x 10³

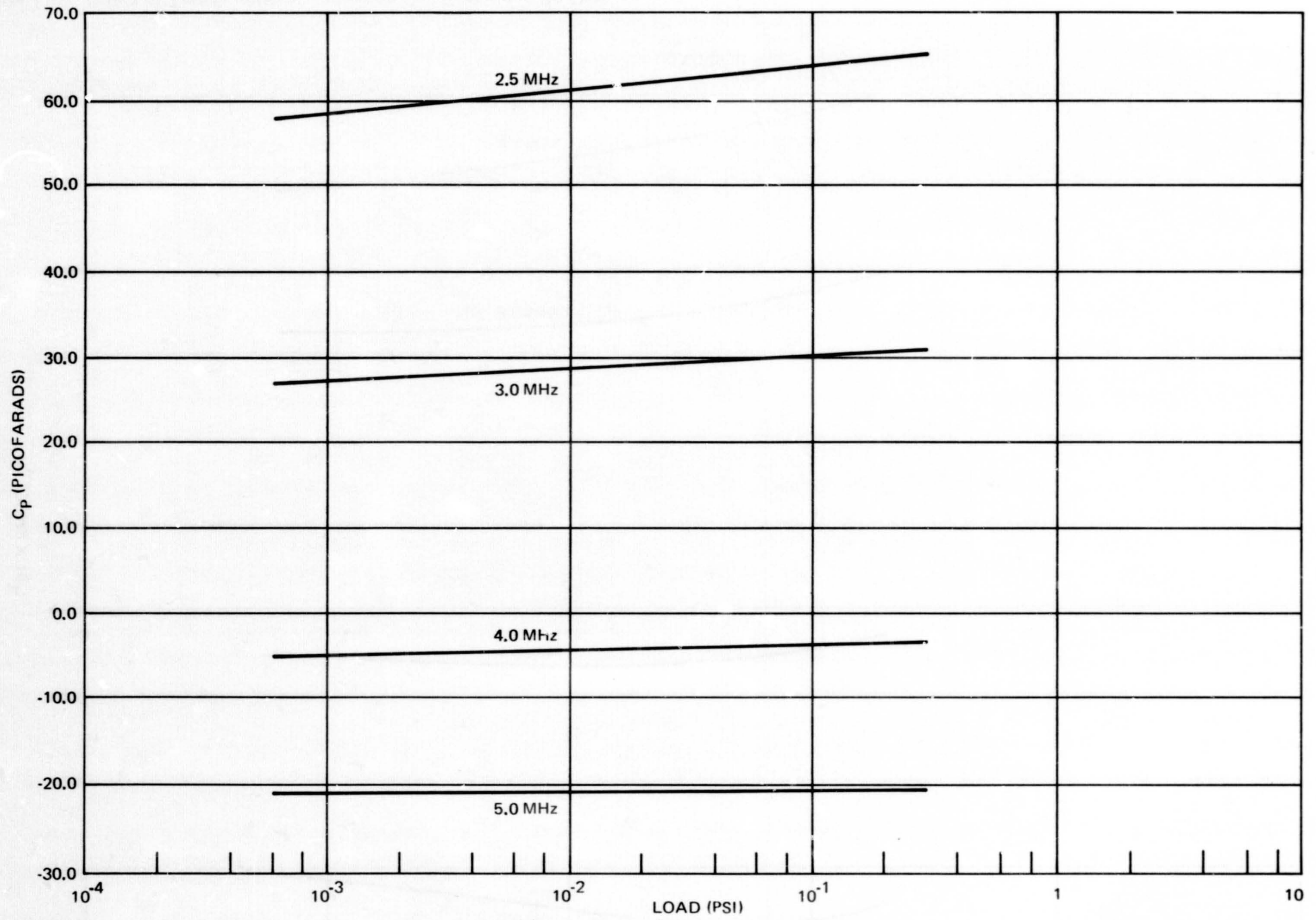
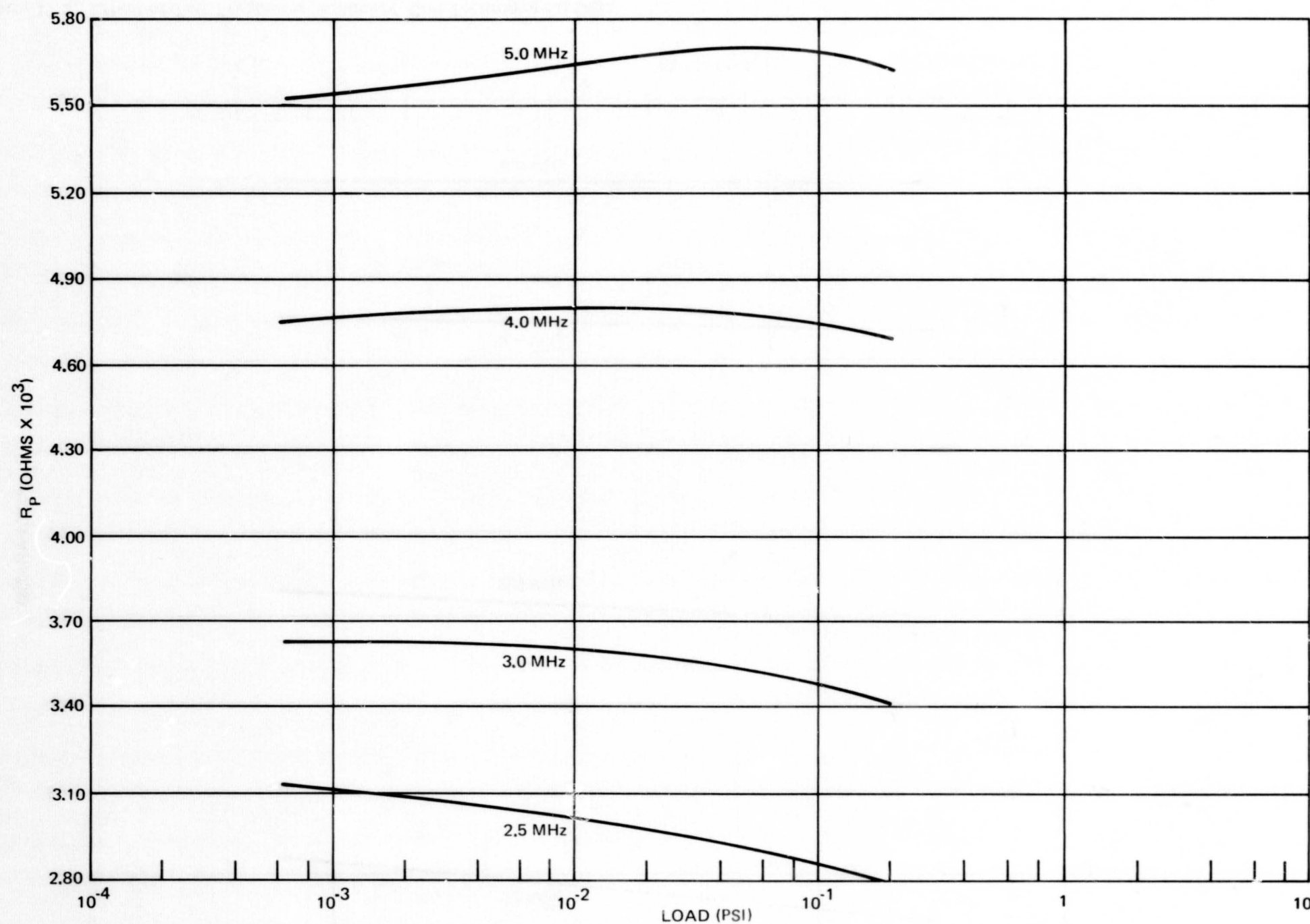


Figure 11-8. Effect of Test Frequency, Induction Coil Technique- C_p Data

Figure 11-9. Effect of Test Frequency, Induction Coil Technique- R_p Data

Induction Coil Tests to Determine Data Repeatability

Two sets of measurements were obtained to assess the repeatability of the compression measurements. Each set of measurements was obtained on a different day and on days different than those on which the previously discussed data was obtained. The first set of measurements was made prior to the tests for determining the effect of changing the frequency. The second set of measurements was made after the effect-of-frequency tests.

The 6-in. square, 24 reflector sheets, specimens of the DAM/NN and DAM/B2A composites were used for the first set of tests. The frequency setting of 2.50 MHz had not been changed since the previous tests. Typical test results are shown in Figure 11-10. Further results are presented in Section 7 of Reference 22. The previously obtained results (Table 11-4) are also shown to allow comparisons. Agreement with the previous results are good.

The 6 in. square, 24 reflector sheets, specimens of the DAM/B2A and DAM/tissuglas composites were used for the second set of tests. Typical test results are shown in Figure 11-11. Further results are presented in Section 7 of Reference 22. As shown, the agreement with the previously obtained data is not as good after a resetting of the frequency. It appears that the discrepancies may have been caused by operating at a slightly different frequency than that used in the original measurements. In future testing or in an actual inspection application, the frequency could be reset more accurately by using auxiliary instrumentation. Another possibility is to pre-align the test apparatus before each series of measurements by using a standard test specimen.

Applicability of Induction Coil Technique to DGK/Dacron B4A Composite

The testing with the induction coil technique reported previously in this section was accomplished prior to the selection of the MLI composite in Task 7. Consequently, after selection of the DGK/Dacron B4A composite in Task 7 (see Section 9), compression detection tests on DGK/Dacron B4A were

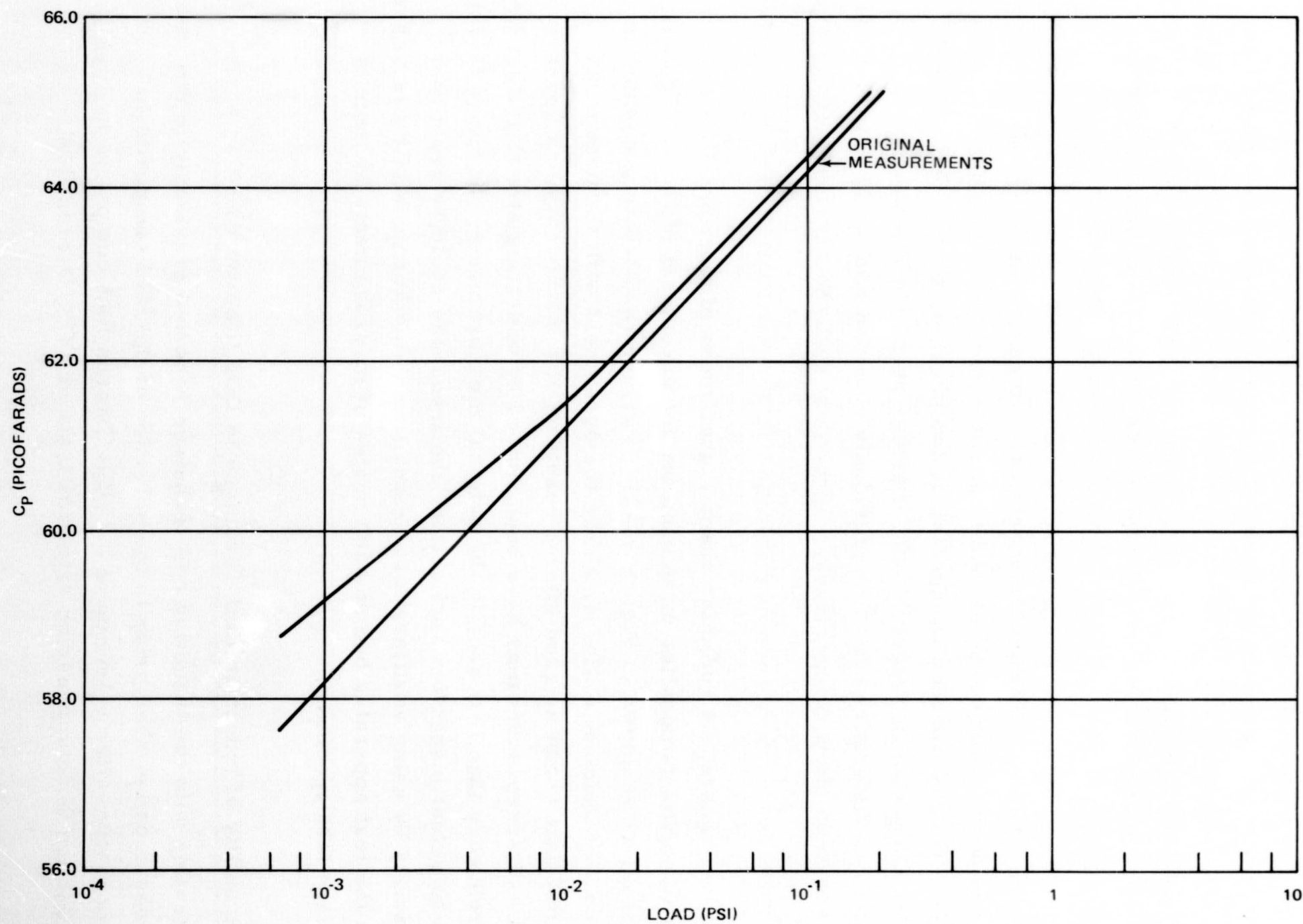


Figure 11-10. Repeatability of C_p versus Load-DAM/B2A Without Frequency Reset

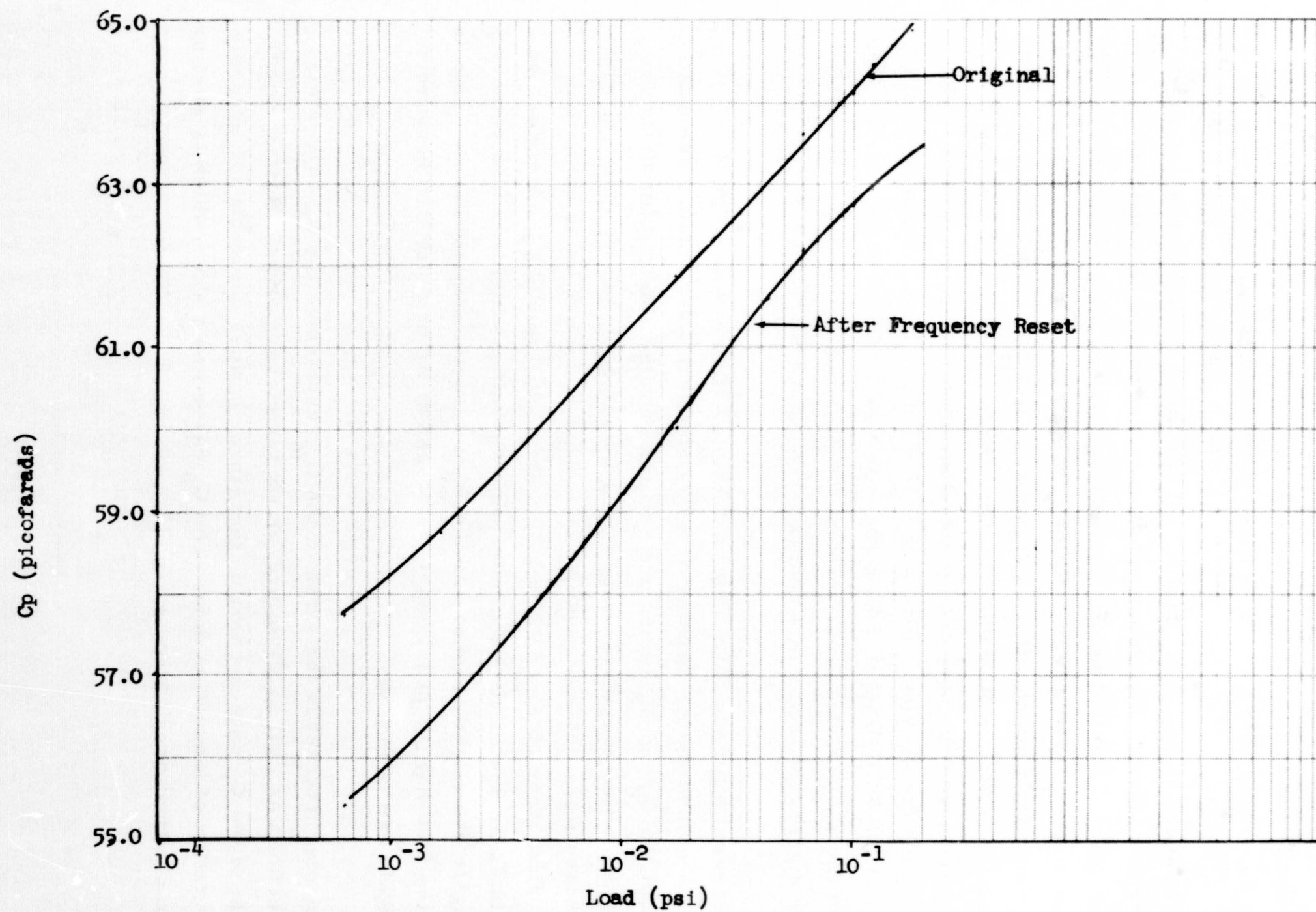


Figure 11-11. Repeatability of C_p vs Load - DAM/B2A With Frequency Reset

conducted using the induction coil technique. The objective of these tests was to verify the applicability of the induction coil technique for the DGK/Dacron B4A composite as well as those previously tested.

The test specimen was 6 in. square and contained 24 reflector sheets and 23 separator layers. This configuration is identical to that used in the previous tests. The test setup, procedure, and apparatus were identical to that used in the previous tests with two exceptions. The RX meter used was not the same instrument. It was, however, the same model (Boonton 250A) as the instrument used previously. The other exception was that the frequency was more precisely set for the DGK/Dacron B4A composite. The frequency for the previous tests was 2.50 ± 0.0125 MHz, whereas the frequency for the DGK/Dacron B4A composite was 2.5000 ± 0.0002 MHz. The effect of these two differences between the previous and recent tests should not be a significant factor in a comparison of the test results.

The test results for the DGK/Dacron B4A specimen are included in Figures 11-5 and 11-6. Tabular data are shown in Table 11-6. The magnitudes of the C_p and R_p values are similar to those obtained for the other composites tested previously with the C_p values being nearly identical with the highest values obtained previously and the R_p values being somewhat lower. Data were obtained while both adding and removing the weights, as shown in Table 11-6. As anticipated, the C_p values obtained while removing the weights are slightly higher and the R_p values are slightly lower. This is due to the fact that the panel has not returned to its original thickness when the weights are removed.

Of particular interest is the slope of the C_p curve since the R_p curves for this specimen as well as those previously tested have slopes which are less than that of the C_p data and would, therefore, be less desirable for accurate interpretation of inspection data. The C_p curve has a slope which is similar to those obtained previously.

Table 11-6

COMPRESSION DETECTION IN DGK/DACRON B4A WITH INDUCTION COIL TECHNIQUE

Incremental Applied Weight (grams)	Applied Pressure (lb/in. ²)	C _p *	R _p #	Incremental Weight Removed (grams)	Applied Pressure (lb/in. ²)	C _p *	R _p #
0	0.0	62.0	2.60	0	1.91×10^{-1}	75.7	2.63
10.6	6.5×10^{-4}	62.8	2.62	-343	1.70×10^{-1}	75.5	2.63
17	1.65×10^{-3}	64.1	2.63	-450	1.43×10^{-1}	75.2	2.63
17	2.73×10^{-3}	65.0	2.64	-450	1.16×10^{-1}	74.9	2.64
45	5.5×10^{-3}	66.6	2.65	-300	9.7×10^{-2}	74.5	2.64
93	1.12×10^{-2}	68.4	2.66	-300	7.86×10^{-2}	74.1	2.65
96	1.71×10^{-2}	69.3	2.67	-300	6.03×10^{-2}	73.6	2.65
99	2.31×10^{-2}	70.0	2.67	-150	5.1×10^{-2}	73.3	2.66
150	3.13×10^{-2}	71.0	2.68	-154	4.16×10^{-2}	72.8	2.66
153	4.16×10^{-2}	71.6	2.69	-153	3.13×10^{-2}	72.2	2.67
154	5.1×10^{-2}	72.2	2.68	-150	2.31×10^{-2}	71.4	2.66
150	6.03×10^{-2}	72.7	2.68	-99	1.71×10^{-2}	70.7	2.66
300	7.86×10^{-2}	73.3	2.67	-96	1.12×10^{-2}	69.7	2.65
300	9.7×10^{-2}	73.9	2.67	-93	5.5×10^{-2}	68.2	2.64
300	1.16×10^{-1}	74.2	2.66	-45	2.73×10^{-2}	66.8	2.63
450	1.43×10^{-1}	74.9	2.65	-17	1.65×10^{-2}	65.9	2.62
450	1.70×10^{-1}	75.3	2.64	-17	6.5×10^{-2}	64.4	2.61
343	1.91×10^{-1}	75.6	2.63	-10.6	0.0	63.1	2.58

*C_p - Capacitance in picofarads#R_p - Resistance in ohms $\times 10^3$

Frequency at start of test = 2.500201 MHz

Frequency at end of test = 2.500159 MHz

11.1.3.3 Eddy Current Technique

Eddy current and induction coil techniques are very similar. However, eddy current testing instrument readout is in terms of units whose significance is determined by comparison with measurements on a material standard specimen. The RX meter induction coil technique was chosen for feasibility studies because the RX meter impedance measurements are more fundamental electrical quantities.

11.1.4 Conclusions and Recommendations—Inspection Technique Evaluation

11.1.4.1 Conclusions

The evaluation of four techniques for nondestructive testing of MLI resulted in the following conclusions:

- A. The infrared and microwave techniques can be eliminated as potential inspection techniques because of the high reflectivity of the MLI reflector sheets to these wavelengths.
- B. The capacitor inspection technique is limited in use to a check on preselected localized areas or as an average indication of the insulation thickness over all of the tank.
- C. The induction coil technique appears feasible for providing a reliable and sufficiently accurate method for nondestructive inspection of MLI. This inspection can be accomplished at randomly selected locations. Corrosion as low as 2 percent, as well as compression of the insulation, can be detected.
- D. An indication of the elasticity properties of an MLI composite can be determined with the induction coil technique.
- E. Repeatability of data can be expected if the working frequency of the RX meter is accurately reset for each series of tests.
- F. The induction coil technique is applicable for use with the DGK/Dacron B4A composite selected in Task 7.

11.1.4.2 Recommendations

The promising results obtained with the induction coil technique show that further evaluation and development, beyond the scope of this study, should be accomplished for this technique. These future evaluation and development studies should include:

- A. Delineation of the interaction of the induction coil response with the insulation condition in order to allow accurate interpretation of inspection data.
- B. Definition of apparatus configuration for full-scale operation.
- C. Definition of techniques for accurate relative positioning of the coil and MLI.
- D. Determination of the optimum frequencies to be used with a given number of layers in the insulation composite.
- E. Proof testing of full-scale apparatus and procedures.

11.2 REPAIR OF DAMAGED AREAS

The design concept for installation of the MLI is based upon the use of pre-fabricated panels which are fastened together at the edges to completely envelop the tank, see Section 10. The panels are fastened together with Velcro and lacing thread. Consequently, replacement of an entire panel can be readily accomplished with this design. Unless the damage is very minor, it is anticipated that damaged insulation would be refurbished by simply replacing the entire panel containing the damaged material. Minor damage such as a tear in an outer reflector sheet can be repaired with tape.

Section 12
SPECIFICATIONS—TASK 10

The objective of Task 10 was to prepare preliminary specifications for the selected MLI composite. The preliminary specifications shown herein include material specifications for the DGK reflectors and Dacron B4A net separators, a fabrication specification for the MLI panels, and an application specification for the panels.

No preliminary specifications were prepared for the purge bag. The purge bag design is shown in Section 10 and has two primary installation constraints:

- A. The MLI shall not be damaged (compressed, ripped, or torn) or contaminated (oil, grease, fingerprints) during bag installation.
- B. The bag shall be installed in a manner which ensures that the maximum leak rate specified on a final design drawing is not exceeded.

The material specification for the DGK reflector material specifies a maximum emittance for the gold surfaces of 0.025. This is consistent with the current specifications from the vendor which indicate that they will certify to a 0.025 maximum emittance. However, it should be noted that the emittance values obtained in this contract for DGK were somewhat higher than 0.025 (see Table 3-16). Further emissivity studies of the latest DGK material will be required before writing a final specification for the DGK material.

PRECEDING PAGE BLANK NOT FILMED

PROCUREMENT REQUIREMENTS
FOR
FILM, POLYIMIDE, GOLD METALIZED

1.0 SCOPE

This document defines the procurement requirements for polyimide film with a vacuum-deposited coating of gold to be used as a multilayer insulation material.

2.0 MATERIAL REQUIREMENTS

2.1 Composition

The material shall consist of polyimide film with a vacuum-deposited gold coating on both surfaces.

2.2 Form

The material shall be supplied as a continuous film wound on hollow fiber-board cores of the dimension specified in the purchase order or contract.

2.3 Dimensions

2.3.1 Thickness—The thickness of the film shall be 0.0003 ± 0.00003 inch.

2.3.2 Width—The width of the material shall be within ± 0.50 inch of the width specified in the purchase order or contract.

2.3.3 Length—Unless otherwise specified in the purchase order, the length of the material supplied shall be within 5 percent of the total specified with each core containing a minimum continuous length of 100 feet and no more than 10 pounds of material.

2.4 Properties

2.4.1 Emittance—Both gold surfaces of the film shall have a maximum emittance at any point of 0.025.

2.4.2 Weight—The weight of the material shall be $0.0022 \pm 0.0002 \text{ lb/ft}^2$.

2.4.3 Coating Adhesion—Transfer of the gold coating from the material shall be confined to scattered spots with a combined area not exceeding 1 percent of the total area tested.

2.5 Product Marking

The inside of the core of each roll shall be legibly and durably identified near the ends with the manufacturer's name and designation, lot number, and total quantity on the roll.

2.6 Workmanship

The material shall be uniform in quality and condition; shall be evenly wound on the cores, shall be free of oil, grease, fingerprints, dirt, wrinkles or other foreign materials; and shall be free of tears, holes, voids in the gold coating, edge distortion, or other defects.

3.0 QUALITY ASSURANCE REQUIREMENTS

3.1 Responsibility

The supplier shall be responsible for the performance of all inspection and testing to demonstrate conformance to the material requirements specified herein. The supplier may utilize his own or any other facilities and services acceptable to the procuring activity. Records of the examination and tests shall be kept complete and available to the procuring activity. The procuring activity reserves the right to perform any inspections deemed necessary to assure that material conforms to the prescribed requirements.

3.2 Lot

For purposes of sampling, inspection and tests, a lot shall consist of material manufactured at one time and offered for acceptance at one time.

3.3 Sampling

3.3.1 Sampling Locations—Samples shall be taken at least 2 feet from the roll end and a minimum of 2 inches in from the sides.

3.3.2 Sampling Frequency—Each roll shall be sampled.

3.4 Quality Assurance Tests

3.4.1 Scope—The tests described below and any additional examinations and tests necessary to demonstrate conformance of the product to the material requirements of Section 2 shall be performed.

3.4.2 Emittance Tests—The emittance of both surfaces of five specimens shall be tested using a Lion Emissometer Model 25B, or equivalent. Tests shall be conducted at 21° to 32°C (70° to 90°F). The low emittance standard shall be 0.025. The instrument shall be calibrated immediately before each test. The calibration standards and the test specimen shall be at the same temperature. The temperatures shall be equalized by placing the specimen and the calibration standards on adjacent areas of the same surface of a block of aluminum or copper of minimum thickness of 0.50 inch and of minimum length and width of 4.00 inches. The specimen and standards shall be in contact with the block for a minimum of 5 minutes prior to calibration and shall remain in contact with the block during calibration and test. The emittance of each specimen shall conform to the requirements of Section 2.

3.4.3 Coating Adhesion Tests—Five specimens shall be tested. The test procedure shall consist of the application and removal of a piece of high-tack, pressure-sensitive tape on each side of each specimen. The tape shall be Scotch No. 250 or equivalent, 0.50 ± 0.12 inch wide, cut into strips 4.00 ± 0.12 inches long. Except for a pull tab, 0.50 ± 0.12 inch long on one end, each tape strip shall be applied with a 0.9 ± 0.1 lb roller. The tape

shall be removed 5 to 10 minutes after application by grasping the pull tab and pulling at a uniform rate. The pull shall be parallel to the surface of the specimen and shall result in a peeling force on the bond between the tape and specimen surface. Tape removal shall require 3 to 5 seconds. The surface of the tape and the area from which it was removed shall be visually examined for evidence of transfer of gold to the tape. For each specimen, the results of this examination shall conform to the requirements of Section 2.

4.0 PACKAGING REQUIREMENTS

4.1 Preservation and Packaging

The material shall be preserved and packaged in a manner that will afford adequate protection against corrosion, deterioration, and physical damage during shipment from supply sources to first receiving activity. Each roll shall be supported within the unit container so that no sections of the material will be flattened or damaged.

4.2 Packing

Material shall be packed to assure acceptance by common carrier at the lowest freight rates and safe delivery from supply source to first receiving activity.

4.3 Marking

All containers shall be marked in accordance with applicable state and federal shipping containers shall be legibly and durably marked with the order number, manufacturer's name and designation, lot number, quantity of material, and special marking, "WARNING—OPTICAL SURFACES—DO NOT CONTAMINATE".

5.0 NOTES

5.1 Intended Use

The material covered by this document is primarily intended for use as a multilayer insulation composite component for space vehicles.

5.2 Lion Emissometer Model 25B

This equipment may be obtained from Lion Research Corporation,
32 Potter Street, Cambridge, Massachusetts 02142.

5.3 Scotch No. 250 Pressure Sensitive Tape

This material may be obtained from Minnesota Mining and Manufacturing Company, 2501 Hudson Road, St. Paul, Minnesota 55119.

PRECEDING PAGE BLANK NOT FILMED

PROCUREMENT REQUIREMENTS
FOR
NET, POLYESTER, RESINLESS FINISH

1.0 SCOPE

This document defines the procurement requirements for a heat-set, polyester net material to be used as a multilayer insulation composite separator.

2.0 MATERIAL REQUIREMENTS

2.1 Composition

The material shall consist of 100 percent polyester (Dacron) net.

2.2 Form

The material shall be supplied as a continuous net fabric wound on hollow fiberboard cores of the dimension specified in the purchase order or contract.

2.3 Dimensions

2.3.1 Width—The width of the material shall be within ± 1.0 inch of the width specified on the purchase order or contract.

2.3.2 Length—Unless otherwise specified in the purchase order, the length of the material supplied shall be within ten percent of the total specified with each core containing a minimum continuous length of at least 130 lineal feet and no more than 10 pounds of material.

2.4 Physical Properties

The net shall meet the following requirements:

Property	Required Value
Weight (oz/yard ²)	0.1622 to 0.2085
Thickness (in.)	0.0058 to 0.0069
Mesh Count	5.2 x 8.2 minimum 6.2 x 9.5 maximum
Meshes/in. ²	43 to 59
Yarn size (denier)	40
Burst strength (lb/in. ²)	10 minimum

2.5 Finish

The material shall be scoured and heat set with a resinless finish to a stiffness of $3\text{-}5/32 \pm 8/32$ inches in the warp direction and $3 \pm 11/32$ inches in the fill direction.

2.6 Outgassing Characteristics

Weight loss by outgassing shall be less than 0.06 percent in 0.5 hour at $25 \pm 4^{\circ}\text{C}$ ($77 \pm 7^{\circ}\text{F}$) and 5×10^{-6} torr.

2.7 Product Marking

The inside of the core of each roll shall be durably identified near one end with the manufacturer's name and designation, lot number, width, and total length of the roll.

2.8 Uniformity

The material shall be uniform in quality and appearance with no creases, folds, tears, apparent foreign matter, or visible edge distortion.

3.0 QUALITY ASSURANCE PROVISIONS

3.1 Responsibility

The supplier shall be responsible for the performance of all inspections and testing to demonstrate conformance to the material requirements specified herein. The supplier may utilize his own or any other facilities and services acceptable to the procuring activity. Records of the examination and tests shall be kept complete and available to the procuring activity. The procuring activity reserves the right to perform any inspection deemed necessary to assure that material conforms to the prescribed requirements.

3.2 Lot

For sampling purposes, lot shall consist of each 4,000 linear yards, or fraction thereof, of net produced at one time and submitted for acceptance at one time.

3.3 Sampling

Each lot of material shall be sampled.

3.4 Quality Assurance Tests

3.4.1 Scope—The tests described below and any additional examinations and tests necessary to demonstrate conformance of the product to the material requirements of Section 2 shall be performed.

3.4.2 Physical Properties—Tests defined below shall be performed to determine conformance to Paragraph 1.3.

Property	Test Method
Weight	ASTM D231
Thickness	ASTM D1777 Using a 1-in. ² presser foot weighted to apply an anvil pressure of 0.5 psi.
Mesh count	ASTM D231
Mesher/in. ²	Paragraph 2.2.2
Yarn size	Paragraph 2.2.3
Burst strength	CCT 191B
Finish	Paragraph 2.2.4

3.4.3 Mesher/In.²—The number of meshes per square inch in both the warp and the fill directions shall be measured per ASTM D231.

3.4.4 Yarn Diameter—The yarn diameter shall be determined by Method 4020 of Federal Test Method Standard 191.

3.4.5 Finish

3.4.5.1 Stiffness—The stiffness shall be determined by Method 5200 of Federal Test Method Standard 191.

3.4.5.2 Outgassing—Outgassing shall be measured in accordance with the standard procedure which shall be furnished to the supplier.

3.4.6 Width—The width of the material shall be measured in accordance with Method 5020 of Federal Test Method Standard 191.

3.4.7 Length—The length of the materials shall be measured in accordance with Method 5010 of Federal Test Method Standard 191. The weight of the roll shall be measured to the nearest 1.0 pound.

3.4.8 Examination—The material shall be examined visually to determine conformance to paragraphs 2.2, 2.7 and 2.8.

4.0 PACKAGING REQUIREMENTS

4.1 Preservation and Packaging

The materials shall be preserved and packaged in a manner that will afford adequate protection against deterioration, contamination, and physical damage during shipment from supply source to the first receiving activity.

4.2 Packing

Packages that require overpacking for acceptance by common carrier shall be packed in uniform quantities in a manner to assure carrier acceptance at the lowest freight rates, and to assure safe delivery from supply source to the first receiving activity.

4.3 Marking

Unit, intermediate, and shipping containers shall be durably and legibly marked with the order number, manufacturer's name and designation, lot number, quantity of material, and special marking, "WARNING-DO NOT CONTAMINATE".

5.0 NOTES

5.1 Intended Use

The material covered by this document is primarily intended for use as a separator in multilayer insulation composites for space vehicles.

PRECEDING PAGE BLANK NOT FILMED

PROCESS REQUIREMENTS
FOR
FABRICATION OF MULTILAYER INSULATION PANELS

1.0 SCOPE

This document defines the process requirements for the fabrication of radiative barrier type, multilayer insulation panels.

2.0 PROCESS REQUIREMENTS

2.1 Environmental Requirements

All operations related to fabrication shall be performed in an enclosed controlled environment area. Incoming air shall be filtered through filters with an 85 percent or greater efficiency (National Bureau of Standards atmospheric dust spot rating). The air system in the enclosed area shall be designed to provide a positive air pressure and to minimize air turbulence at the working level. The temperature and relative humidity in the enclosed area shall be maintained at $21 \pm 3^{\circ}\text{C}$ ($70 \pm 5^{\circ}\text{F}$) and 50 ± 10 percent, respectively. Work surfaces, tools, and clothing shall be maintained free of contact contamination.

2.2 Materials

The materials shall be as specified on the design drawing.

2.3 Thickness Uniformity

The minimum insulation thickness shall be as specified on the design drawing.

2.4 Thickness Control

Fabrication shall be accomplished in a manner which assures that the minimum thickness is as specified on the design drawing.

2.5 Penetrations and Fasteners

Unless otherwise specified on the design drawing, all penetrations and fasteners shall be perpendicular to the composite layers upon installation.

2.6 Tension and Compression Loads

The materials shall not be subjected to tension or compression loads which permanently alter the stacking configuration of the panel.

2.7 Reflectance

The fabrication of the insulation shall be performed in a manner which preserves the reflectance of each film surface within specified tolerance for the films.

2.8 Workmanship

The insulation shall be free of rips, tears, cuts, oil, grease, dirt, fingerprints, or other foreign material which are deleterious to appearance or function. Cut edges shall be free of slivers or chaff. Plies shall be separated at cut edges.

3.0 QUALITY ASSURANCE REQUIREMENTS

3.1 Lot

For purposes of sampling, inspection, test, storage and/or shipment, a lot shall consist of each multilayer insulation assembly offered for acceptance.

3.2 Sampling

Each insulation assembly shall be tested for conformance to the requirements of this inspection.

3.3 Quality Assurance Tests

3.3.1 Thickness Uniformity—Thickness shall be determined by placing the part on a properly contoured surface and measuring the distance to the surface of the part from references suspended at known distances from the contoured surface. Each thickness measurement shall conform to the requirements of Paragraph 2.3.

3.3.2 Examination—The supplier shall make such inspections as are necessary to assure that the requirements of Paragraphs 2.4, 2.5, 2.6, 2.7 and 2.8 are met.

4.0 STORAGE AND PACKAGING REQUIREMENTS

4.1 Preservation and Packaging

The insulation panels shall be preserved and packaged in a manner that will afford adequate protection against deterioration, contamination, and physical damage during storage and/or shipment from supply source to receiving activity.

4.2 Marking

Unit, intermediate and shipping containers shall be durably and legibly marked with manufacturer's name, designation and lot number and special marking, "WARNING—DO NOT CONTAMINATE". Marking shall be accomplished in a manner that will not deteriorate, contaminate, or otherwise damage the insulation panels.

PRECEDING PAGE BLANK NOT FILMED

APPLICATION REQUIREMENTS
FOR
INSTALLATION OF MULTILAYER INSULATION PANELS

1.0 SCOPE

This document defines the minimum application requirements for the installation of prefabricated multilayer insulation panels.

2.0 PROCESS REQUIREMENTS

2.1 Environment

All operations related to installation shall be performed in an area and manner which meets the minimum requirements of the fabrication operation.

2.2 Materials

The materials used for insulation and fastening shall be as specified on the design drawing.

2.3 Surface

The surface to receive insulation shall be maintained free of oils, grease, dirt, fingerprints, or other foreign materials.

2.4 Application of Insulation

2.4.1 Insulation Configuration—The panel configuration shall be as specified on the design drawing.

2.4.2 Panel Positioning—Panels shall be placed on attachment pins in a manner that ensures alignment as specified on the design drawing with no panel buckling or other distortion.

2.4.3 Mechanical Loads—The panels shall not be subjected to mechanical loads which permanently alter the thickness of the fabricated panels.

2.4.4 Blanket Joining—The lacing and Velcro patterns shall be as specified in the design drawing. Lacing and Velcro strips shall be applied in a manner to close adjacent butt joints with maximum contact but no overlap. No materials or procedures other than those specified in the design drawing shall be used to join insulation blankets.

2.4.5 Workmanship—The installed insulation shall be free of rips, cuts, tears, dirt, oil, grease, fingerprints, or other foreign materials or defects detrimental to performance.

2.5 Examination—The supplier shall make such inspections as are necessary to determine conformance to the process requirements.

3.0 STORAGE REQUIREMENTS

3.1 Preservation

The installed insulation panels shall be preserved in a manner that will afford adequate protection against deterioration, contamination and physical damage during storage.

Section 13

REFERENCES

1. McDonnell Douglas Astronautics Company. Investigation of High-Performance Insulation Application Problems. Fourth Quarterly Report. Contract NAS8-21400, MDC G0275, January 1970.
2. McDonnell Douglas Astronautics Company. Investigation of High-Performance Insulation Application Problems. Third Quarterly Report. Contract NAS8-21400, Report MDC-G1238, October 1969.
3. D. R. Krause. Development of Lightweight Material Composites to Insulate Cryogenic Tanks for 30-Day Storage in Outer Space. Second Quarterly Report, Contract NAS8-26006. McDonnell Douglas Astronautics Company Report MDC G0775, December 1970.
4. D. R. Krause. Development of Lightweight Material Composites to Insulate Cryogenic Tanks for 30-Day Storage in Outer Space. Third Quarterly Report, Contract NAS8-26006. McDonnell Douglas Astronautics Company Report MDC G2265, March 1971.
5. D. R. Krause. Development of Lightweight Material Composites to Insulate Cryogenic Tanks for 30-Day Storage in Outer Space. Fourth Quarterly Report, Contract NAS8-26006. McDonnell Douglas Astronautics Report MDC G2348, June 1971.
6. Douglas Missile and Space Systems Division. High-Performance Insulation System Development. Interim Report. Douglas Report DAC-57963, January 1967.
7. McDonnell Douglas Astronautics Company. Investigation of High-Performance Insulation Application Problems. Interim Progress Report. Contract NAS8-21400, Report MDC G2135, February 1971.
8. Lockheed Missiles & Space Company. Handbook of Thermal Design Data for Multilayer Insulation Systems, Design of High-Performance Insulation Systems. Volume VI. Contract NAS8-11347, LMSC Report A742593-VI, August 1965.
9. D. Hender. A Miniature Version of the JA70 Computer Program H800 (MINIVER). MDC Report 60462, June 1970.
10. Marshall Space Flight Center. MSFC Memorandum S&E-ASTN-ADV-70-44. March 9, 1970.

11. McDonnell Douglas Astronautics Company. Saturn S-IVB/Alternate Launch Vehicle Analyses. Interim Final Report. Contract NAS7-101, task authorization No. 5, December 1970.
12. N. R. Folkman and T. G. Lee. Thermodynamic Design Fundamentals of High Performance Insulation. AIAA Paper No. 67-294, April 1967.
13. Frank Kreith. Principles of Heat Transfer. Second Edition. International Textbook Company, 1965, p. 347.
14. McDonnell Douglas Astronautics Company. Thermal Testing of Typical Vehicle Multilayer Insulation Panel Components. IRAD Report MDC G2153, March 1971.
15. Lockheed Missiles & Space Company. Superinsulation Thermal Conductivity Parametric Study. Contract NAS8-20438, LMSC/HREC A784869, October 1967.
16. McDonnell Douglas Astronautics Company. Design of Purge Systems for Multilayer Insulation on Cryogenic Tankage. IRAD Report MDC G2521, September 1971.
17. B. F. Goodrich Company. 2430 Series Pressure Proof Closure. Brochure, Form 1432, October 15, 1961.
18. McDonnell Douglas Astronautics Company. Phase B Final Report, Space Shuttle Program. Report MDC E0377, June 1971.
19. E. I. DuPont de Nemours & Company. Summary of Properties-Kapton Polyimide Film. Technical Information Bulletin F-1A, A-48711.
20. AFMRL Cryogenic Materials Data Handbook. Supplement to ML-TDR-64-280. Air Force Materials Laboratory Research and Technology Division, Wright-Patterson Air Force Base, February 1965.
21. Douglas Missiles and Space System Division. Thermo and Hydrodynamic Experiment Research Module in Orbit, Project Thermo. Final Report. Contract NAS8-18053, Report DAC-60594, March 1967.
22. D. R. Krause. Development of Lightweight Material Composites to Insulate Cryogenic Tanks for 30-Day Storage in Outer Space. First Quarterly Report, Contract NAS8-26006, McDonnell Douglas Astronautics Report MDC G0683, September 1970.